SAND2022-5119R
SAND2020-#####X

Evaluation of Engineered Barrier Systems FY21 Report

Spent Fuel and Waste Disposition

Prepared for US Department of Energy
Spent Fuel and Waste Science and Technology

E.N. Matteo, T. Dewers, T. Hadgu, N. Bell, M. Rodriguez,
P. Kotula, J. N. Kruichak, B.A. Hernande-Sanchez
M.R. Casilas, I. Kolesnichenko
Sandia National Laboratories

F. Caporuscio, K.B. Sauer, and M. Rock
Los Alamos National Laboratories

L. Zheng, S. Borglin, L. Lammers, M. Whittaker, P. Zarzycki
P. Fox, C. Chang, N. Subramanian, P. Nico, C. Tournassat,
C. Chou, H. Xu, and E. Singer
Lawrence Berkeley National Laboratories

November 5, 2021
M2SF-21SN010308053
SAND2020-xxx R

Rev. 11.29.16

Sandia National Laboratories

Sandia National Laboratories is a multi-mission laboratory managed and operated by National Technology & Engineering Solutions of Sandia, LLC., a wholly owned subsidiary of Honeywell International, Inc., for the U.S. Department of Energy's National Nuclear Security Administration under contract DE-NA0003525.

Revision 0
10/7/2019

APPENDIX E
NFCSC DOCUMENT COVER SHEET [1]

Name/Title of Deliverable/Milestone/Revision No.	Evaluation of Engineered Barrier Systems FY21 Report / M2SF-21SN01030805
Work Package Title and Number	Engineered Barrier System R&D – SNL / SF-21SN01030805
Work Package WBS Number	1.08.01.03.08
Responsible Work Package Manager	Edward N. Matteo / (Name/Signature)
Date Submitted	

Quality Rigor Level for Deliverable/Milestone[2]	☐ QRL-1 ☐ Nuclear Data	☐ QRL-2	☒ QRL-3	☐ QRL-4 Lab QA Program[3]

This deliverable was prepared in accordance with Sandia National Laboratories
(Participant/National Laboratory Name)

QA program which meets the requirements of
☒ DOE Order 414.1 ☐ NQA-1 ☐ Other

This Deliverable was subjected to:

☒ Technical Review ☐ Peer Review

Technical Review (TR)
Review Documentation Provided
☐ Signed TR Report or,
☐ Signed TR Concurrence Sheet or,
☒ Signature of TR Reviewer(s) below

Peer Review (PR)
Review Documentation Provided
☐ Signed PR Report or,
☐ Signed PR Concurrence Sheet or,
☐ Signature of PR Reviewer(s) below

Name and Signature of Reviewers
Carlos Jove-Colón

NOTE 1: *Appendix E should be filled out and submitted with the deliverable. Or, if the PICS:NE system permits, completely enter all applicable information in the PICS:NE Deliverable Form. The requirement is to ensure that all applicable information is entered either in the PICS:NE system or by using the NTRD Document Cover Sheet.*

- *In some cases there may be a milestone where an item is being fabricated, maintenance is being performed on a facility, or a document is being issued through a formal document control process where it specifically calls out a formal review of the document. In these cases, documentation (e.g., inspection report, maintenance request, work planning package documentation or the documented review of the issued document through the document control process) of the completion of the activity, along with the Document Cover Sheet, is sufficient to demonstrate achieving the milestone.*

This page is intentionally left blank.

SUMMARY

This report describes research and development (R&D) activities conducted during fiscal year 2021 (FY21) specifically related to the Engineered Barrier System (EBS) R&D Work Package in the Spent Fuel and Waste Science and Technology (SFWST) Campaign supported by the United States (U.S.) Department of Energy (DOE). The R&D activities focus on understanding EBS component evolution and interactions within the EBS, as well as interactions between the host media and the EBS. A primary goal is to advance the development of process models that can be implemented directly within the Generic Disposal System Analysis (GDSA) platform or that can contribute to the safety case in some manner such as building confidence, providing further insight into the processes being modeled, establishing better constraints on barrier performance, etc.

The FY21 EBS activities involved not only modeling and analysis work, but experimental work as well. Progress was made during FY21 in multiple research areas and documented in this report as follows: (1) DECOVALEX2023, Task C Modeling Status: Thermo-Hydrological Modeling of the FE Experiment with PFLOTRAN and COMSOL, (2) Polymer Intercalation Synthesis for Boehmite Nanosheets, (3) Hydrothermal experiments on key EBS materials, (4) Chemical Controls on Montmorillonite Structure and Swelling Pressure, (5) Illitization Mechanisms Revealed by Cryo-Electron Tomography (CRYOET), (6) Molecular Modeling of Radionuclide Retention by Bentonites, (7) sorption and diffusion experiments on bentonite, (8) Coupled Microbial-Abiotic Processes in EBS and Host Rock Materials, (9) Heating and Hydration Column Test on Bentonite, (10) understanding the THMC evolution of bentonite in FEBEX-DP—coupled THMC modeling, and (11) Understanding the THMC Evolution of Bentonite Using Large Scale Field Experiments: FEBEX-DP and HotBENT.

The R&D team represented in this report consists of individuals from Sandia National Laboratories (SNL), Lawrence Berkeley National Laboratory (LBNL), and Los Alamos National Laboratory (LANL). In addition, the EBS R&D work leverages international collaborations to ensure that the DOE program is active and abreast of the latest advances in nuclear waste disposal. For example, the FY21 work on modeling and experiments for coupled THMC processes at high temperatures incorporated bentonite properties from the HotBENT Field Test conducted at the Grimsel Test Site in Switzerland.

Overall, significant progress has been made in FY21 towards developing the modeling tools and experimental capabilities needed to investigate the performance of EBS materials and the associated interactions in the drift and the surrounding near-field environment under a variety of conditions including high temperature regimes.

This page is intentionally left blank.

ACKNOWLEDGEMENTS

This work was supported by the U.S. Department of Energy Office of Nuclear Energy, through the Office of Spent Fuel and Waste Science and Technology (SFWST) Research and Development Campaign (DOE NE-81) within the Office of Spent Fuel and Waste Disposition.

The authors acknowledge contributions in the form of discussions on technical and integration issues from the following people from Sandia National Laboratories: R. Chris Camphouse, Emily Stein, Ernie Hardin(retired), Carlos Jové-Colón, Yifeng Wang, and David Sassani. In addition, the authors thank Jorge Monroe-Rammsy (DOE NE-81), Prasad Nair (DOE NE-81), Tim Gunter (DOE NE-81) and William Boyle (DOE NE-8) for their discussions, oversight, and guidance on topics covered in this report.

The authors thank Deborah Phipps for assistance with formatting and proofing of this document.

Lastly, the authors thank Carlos Jové-Colón (Sandia) for providing a careful and thorough technical review of this document.

This page is intentionally left blank.

TABLE OF CONTENTS

LIST OF FIGURES

LIST OF TABLES

This page is intentionally left blank.

REVISION HISTORY

This page is intentionally left blank.

ACRONYMS

1D	one-dimensional
2D	two-dimensional
3D	three-dimensional
ANL	Argonne National Laboratory
ASTM	American Society for Testing and Materials
BBM	Barcelona Basic Model
BCV	Czech bentonite
BExM	Barcelona Expansive Model
CEC	cation exchange capacity
CSH	calcium silicate hydrate
CT	computed tomography
CURIE	Centralized Used Fuel Resource for Information Exchange
cryoET	Cryo-electron tomography
DFT	density functional theory
DOE	US Department of Energy
DPC	dual-purpose canister
EBS	engineered barrier system
ELSM	Extended Linear Swelling Model
EOS	equation of state
FCRD	Fuel Cycle Research and Development
FE	Wyoming bentonite
FE	full-scale emplacement
FEBEX	Full-scale Engineered Barrier EXperiment
FY	fiscal year
GBM	granulated bentonite material
GCMC	grand canonical Monte Carlo
HLW	high-level radioactive waste
HotBENT	High Temperature Effects on Bentonite)
HPC	hydroxylpropyl cellulose
HRSTEM	High-resolution scanning transmission electron microscopy
IC	Ion Chromatography
ID	inner diameter
INL	Idaho National Laboratory
ISF	interim storage facility
ISFSI	independent spent fuel storage installation
KMMT	Potassium Montmorillonite
LAMMPS	Large-scale Atomic/Molecular Massively Parallel Simulator

LCS	low carbon steel
LLW	low-level radioactive waste
MMT	Montmorillonites
MTU	Metric Tons of Uranium
NAGRA	National Cooperative for the Disposal of Radioactive Waste (Switzerland)
NaMMT	sodium montmorillonite
NFST	Nuclear Fuels Storage and Transportation Planning Project
NPT	National Pipe Thread
NRC	Nuclear Regulatory Commission
OD	outer diameter
OPC	ordinary Portland Cement
ORNL	Oak Ridge National Laboratory
PMF	potential of mean force
PR	Prototype Repository
PT	proton transfer
PVP	polyvinylpyrrolidone (PVP)
PWR	pressurized water reactor
QXRD	Quantitative X-Ray Diffraction
SAD	selected area diffraction
SEM	Scanning electron microscopy
SFWD	spent fuel and waste disposition
SFWST	spent fuel waste science and technology
SMD	steered molecular dynamics
SNF	spent nuclear fuel
SNL	Sandia National Laboratory
SRNL	Savannah River National Laboratory
TI	thermodynamic integration
UNF-ST&DARDS	Used Nuclear Fuel – Storage, Transportation & Disposal Analysis Resource and Data Systems
WHAM	weighted histogram analysis method
XRD	X-ray Diffractometry

SPENT FUEL AND WASTE DISPOSTION EVALUATION OF ENGINEERED BARRIER SYSTEMS FY21 REPORT

1. INTRODUCTION

This report describes research and development (R&D) activities conducted during fiscal year 2021 (FY21) specifically related to the engineered barrier system (EBS) R&D Work Package in the Spent Fuel and Waste Science and Technology (SFWST) Campaign supported by the United States (U.S.) Department of Energy (DOE). It fulfills the SFWST Campaign deliverable M2SF-21SN010308053. The R&D team consists of individuals from Sandia National Laboratories, Lawrence Berkeley National Laboratory (LBNL), and Los Alamos National Laboratory (LANL).

The R&D activities described in this report focus on understanding EBS component evolution and interactions within the EBS, as well as interactions between the host media and the EBS. A primary goal is to advance the development of process models that can be implemented directly within the Generic Disposal System Analysis (GDSA) platform or that can contribute to the safety case in some manner such as building confidence, providing further insight into the processes being modeled, establishing better constraints on barrier performance, etc.

The FY21 EBS activities involved not only modeling and analysis work, but experimental work as well. Progress was still made in a number of different research areas during FY21, as described in this report and summarized below:

- **DECOVLAEX2023 Task C (Section 2)**

  Section 2 presents a status update of participation in DECOVALEX2023, Task C. PFLOTRAN and COMSOL are being used to participate in a multi-institution effort to compare different codes for TH and THM modeling of the Full-scale Emplacement (FE) Heater test at the Mont Terri Underground Rock Laboratory, Switzerland.

- **Polymer Intercalation Synthesis for Boehmite Nanosheets (Section 3)**

  Section 3 presents a study detailing the synthesis of a novel anionic sorbent material, which could have potential application in a repository setting. Novel materials based on the aluminum oxyhydroxide boehmite phase were prepared using a glycothermal reaction in 1,4-butanediol. Under the synthesis conditions, the atomic structure of the boehmite phase is altered by the glycol solvent in place of the interlayer hydroxyl groups, creating glycoboehmite. The structure of glycoboehmite was examined in detail to determine at glycol molecules are intercalated in a bilayer structure, twice the expansion identified previously. This precursor phase enables two new phases that incorporate either polyvinylpyrrolidone or hydroxylpropyl cellulose nonionic polymers. These new materials exhibit changes in morphology, thermal properties, and surface chemistry. All the intercalated phases were investigated using PXRD, HRSTEM, SEM, FT-IR, TGA/DSC, zeta potential titrations, and specific surface area measurement. These intercalation polymers are non-ionic and interact through wetting interactions and hydrogen bonding, rather than by chemisorption or chelation with the aluminum ions in the structure.

- **Hydrothermal Experiments (Section 4)**

  The work presented in Section 4 develops concepts related to mineral and geochemical changes that may occur in the near field of high temperature for a nuclear waste repository hosted in crystalline rock. The core samples used for the experimental program consist of granodiorite from the Grimsel Test Site, a well-characterized lithology, to mimic a generic crystalline rock environment. This section presents the results from FY21 research, which characterized (1) how EBS components (stainless steel/low carbon steel, Wyoming bentonite, Ordinary Portland Cement (OPC)) react and change in the presence of Grimsel granodiorite wall rock and synthetic Grimsel granodiorite groundwater and (2) steel-bentonite interface mineralogy at high temperature and pressure (250°C, 150 bars) in-situ repository conditions.

  The FY 21 experimental work yielded multiple concepts of interest: (1) illitization of montmorillonite in Wyoming bentonite in a Grimsel granodiorite wall rock environment may be restricted due to the bulk chemistry of the overall system (i.e., low potassium) and/or kinetics, (2) montmorillonite structural alterations were not observed in the Wyoming bentonite + Grimsel granodiorite + cured OPC experiment, (3) the inclusion of a cured Portland cement chip did not dramatically increase the solution pH but lead to the formation of diverse secondary mineral formation, (4) analysis of clay mineral structural changes reveals that montmorillonite alteration did not occur, (5) newly crystallized Fe-saponite forms at the steel-bentonite interface and grows perpendicular to the steel surface, (6) Fe enrichment in the bentonite due to interaction with steel corrosion products does not migrate far from steel (<50 μm), (7) calcium aluminum silicate hydrate (C(A)SH) minerals formed within the Wyoming bentonite-Grimsel granodiorite system, (8) zeolite-forming reactions are not favored in the Wyoming bentonite-Grimsel system, and (9) general steel corrosion is observed and thicknesses/rates of Fe-rich clay formation were measured.

- **Chemical Controls on Montmorillonite Structure and Swelling Pressure (Section 5)**

  Section 5 presents the progress of a research activity of combining novel microscopic experimental and simulation studies to address mechanical-chemical coupling for bentonite. While FY20 work focused on measuring the swelling pressure of compacted clay and key aspects of the clay microstructure using synchrotron X-ray methods using specialized oedometer, in FY21 we extended our prior modeling work on clay swelling thermodynamics to higher electrolyte concentrations and specifically investigated the influence of pore fluid on montmorillonite structure and composition at equilibrium.

- **Illitization Mechanisms Revealed by Cryo-Electron Tomography (CRYOET), (Section 6)**

  Section 6 presents the progress of a study on illitization mechanisms using Cryo-electron tomography (CryoET). CryoET data were acquired for samples that were hydrothermally treated at 200ºC for 0, 7, 56 or 112 days by collaborators at Sandia National Laboratory (SNL). Preliminary evidence suggests that illitization of smectite under hydrothermal conditions and low mineral volume fraction proceeds via the simultaneous dissolution of smectite and reprecipitation of illite.

- **Molecular Modeling of Radionuclide Retention by Bentonites (Section 7)**

  Section 7 presents the molecular modeling of radionuclide retention by bentonites, which will be used to parametrize meso- and macroscopic models of radionuclide migration in the bentonite barrier to develop a robust safety assessment model. Although the inclusion of the chemical reactions on the fly in classical molecular dynamics remains a challenge, we showed the progress we made towards reactive molecular simulations by exploring various reduction pathways for uranium ions in the aqueous solutions, the role of the solution composition, and complexation by environmentally most relevant ligands – carbonates.

- **Sorption and diffusion experiments on bentonite (Section 8)**

  Section 8 presents experimental results from ^{3}H and Se(VI) through-diffusion experiments through a well-characterized, purified montmorillonite source clay (SWy-2). Experiments were conducted under a single ionic strength (0.1 M) and three different electrolyte compositions representing pure Na, pure Ca, and a Na-Ca mixture in order to probe the effects of electrolyte composition on clay microstructure, Se(VI) aqueous speciation, and ultimately diffusion. Preliminary modeling results from these experiments are also presented.

- **Coupled Microbial-Abiotic Processes in EBS and Host Rock Materials (Section 9)**

  Section 9 presents the study of microbial-abiotic processes in EBS and host rock materials. Experiments on potential microbial activity present in materials collected from the FEBEX experiment were conducted from materials including high heat, intermediate, and control temperature zones. In FY21 the experiments were continued to completion and broken down for final analysis. The results from these experiments indicate that clay materials maintain microbial communities with potential for microbial growth. However, it is interesting that the material from the hot zone did not show that potential for the time scales in these experiments.

- **Heating and Hydration Column Test on Bentonite (Section 10)**

  Section 10 presents the benchtop-scale high temperature column experiments, HotBENT-Lab, in support of the HotBENT field tests. Since June 2019, a heated column and a non-heated column test have run for over 1.5 years and data were collected via CT scan and ERT. Both columns were dismantled with bentonite samples collected in December 2020. Subsequent analysis of the clay has been completed including hydration, mineralogy, and chemical analysis.

- **Understanding the THMC evolution of bentonite in FEBEX-DP—coupled THMC modeling (Section 11)**

  Section 11 presents coupled THMC modeling of bentonite under high temperature. In FY21, we continued THMC modeling using BExM for MC coupling to examine the mechanical evolution of bentonite under high temperatures, and, at the same time, we attempted to interpret the data collected from the high temperature column tests presented in Section 7 using numerical model. In FY21, we have completed the preliminary THM model for the column test, but further refinement of the model is needed to resolve some discrepancies between model and data.

- **Understanding the THMC Evolution of Bentonite Using Large Scale Field Experiments: FEBEX-DP and HotBENT (Section 12)**

  Section 12 presents an analysis of using large scale field experiments FEBEX-DP and HotBENT to understand the THMC evolution of bentonite. This section contains three parts. In the first part, after the THMC model provided a coherent explanation of THMC data collected at the FEBEX *in situ* test, we used the well-calibrated THMC model to conduct an exploratory simulation to address the question about the long-term alteration of bentonite, up to 10,000. In the second part, we developed a 1D reactive transport model to explain the data collected at the bentonite/concrete interface. The model was able to reproduce some data, but there were also discrepancies between model and data, which warranted further refinement of the model. In the third part, we give an update of the HotBENT project, including the field test, and the modeling platform that is under preparation

This page is intentionally left blank.

2. DECOVALEX 2023, Task C: THM Modeling of the FE Experiment

2.1 Introduction

DECOVALEX 2023, Task C is focused on THM modeling of the FE experiment at the Mont Terri Underground Rock Laboratory, Switzerland. This report summarizes Sandia's progress in the modeling studies of DECOVALEX 2023, Task C.

The FE experiment conducted at Mont Terri involves heating of an in-situ FE tunnel surrounded by Opalinus Clay host rock (NAGRA, 2019). The tunnel contains three heaters placed on pedestals made of bentonite blocks and the rest of the tunnel is filled with a granular bentonite mixture (Figure 2-1).

The focus of this modeling task is to understand pore pressure development in the Opalinus Clay and how this is affected by heating, engineering factors (e.g., shotcrete, tunnel shape) and damage due to tunnel construction and thermal effects (NAGRA, 2019).

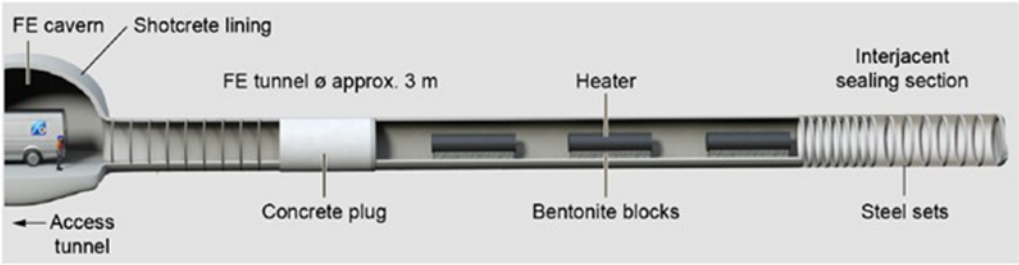

Figure 2-1 Schematic diagram of the FE tunnel (DECOVALEX 2023, Task C).

DECOVALEX 2023, Task C is divided into steps. The first three steps are described below, as defined in the Task C specification. There are also options for additional steps.

- **Step 0 - Preparation phase**: Benchmarking of participating teams computing methods against some simple, tightly defined 2D test cases.

- **Step 1 - FE heating phase**: Modeling the change in pore pressure in the Opalinus Clay because of heating in the FE experiment. This will require 3D THM simulations with representation of partially saturated conditions.

- **Step 2 - FE ventilation phase**: Modeling of absolute pressures in the Opalinus Clay, which will require representation of the ventilation of the FE tunnel prior to heating. Modeling teams can choose the complexity of the representation of excavation and EDZ development.

2.2 Description of Task C, Step 0

Currently the participating modeling teams are in the process of completing Step 0 modeling. Thus, this report focuses on Sandia's Step 0 modeling progress. Step 0 consists of three main modeling cases. These cases were designed to obtain consensus across the modeling teams and to test modeling capabilities. The modeling cases are:

- **Step 0a**: a 2D Thermal-only simulation with saturation dependent thermal properties and saturation held at initial values.

- **Step 0b**: a 2D Thermal-Hydrology with vapor transport simulation. TH model with partial saturation in the bentonite and Opalinus Clay close to the tunnel.

- **Step 0c**: a 2D THM simulation which includes rock mechanics. Linear elastic models for bentonite and Opalinus clay to be used.

2.2.1 Geometry and Measurement Locations

For Step 0 a 2D geometry was chosen to reduce the computing burden. The geometry consists of a cross-section through the center of the middle heater in the FE experiment (Figure 2-2). Note that the Opalinus Clay is bedded and has anisotropic THM properties in directions parallel and perpendicular to bedding. The bedding dips at 34˚ from the horizontal as shown in Figure 2-2. Dimensions of the materials in Figure 2-1 are given in Table 2-1. The heater is centered within the tunnel. The Sandia team selected a 50 m by 50 m domain outer boundary, which generally avoids boundary effects. Measurement locations are given in Table 2-2. Simulation results are to be obtained at these locations.

Table 2-1 Details of the geometry for the 2D model (Task C Specifications).

Description	Value	Reference
Diameter of FE tunnel (Dt)	2.48 m	NAGRA, 2019
Heater diameter (Dh)	1.05 m	NAGRA, 2019
Pedestal width at base (Wp)	0.8 m	NAGRA, 2019
Opalinus Clay domain	50 m x 50 m	Suggestion

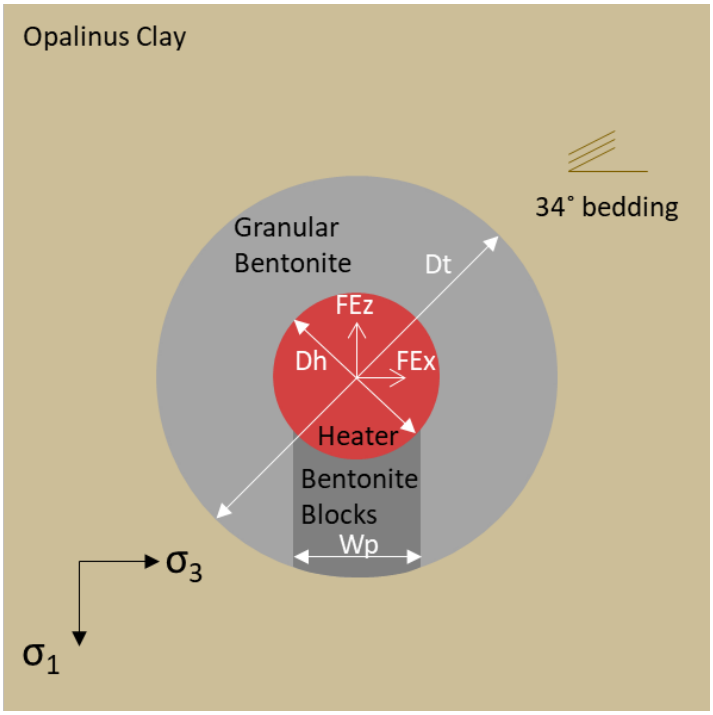

Figure 2-2 Model geometry for Step 0 (Task C Specifications)

Table 2-2 Measurement Locations (Task C Specifications).

Name	Radial distance from heater center (m)	Angle (vertically upwards is zero and measured clockwise)
H_1	0.525	0
H_2	0.525	90
H_3	0.525	180
H_4	0.525	270
H_5	0.525	56
H_6	0.525	326
H_7	0.725	0
H_8	0.725	90
H_9	0.725	180
H_10	0.725	270
H_11	0.725	56
H_12	0.725	326
T_1	1.04	0
T_2	1.04	90
T_3	1.04	180
T_4	1.04	270
T_5	1.04	56
T_6	1.04	326
O_1	5	56
O_2	8	56
O_3	14	56
O_4	5	326
O_5	8	326
O_6	14	326

2.3 Step 0 Modeling

For Step 0 simulations the Sandia team selected the numerical codes PFLOTRAN (Hammond et al., 2014) and COMSOL Multiphysics®. Use of the two codes allowed modeling of the three cases of Step 0, and comparison of results within Sandia. Simulations were run for 5 years from the start of heating.

2.3.1 Material Properties

DECOVALEX, Task C provided material properties to be used for the simulations. Table 2-3 shows parameter values to be used in Step 0 simulations. Several of the specified material property equations are different from what is in PFLOTRAN. Effort was made to add some of the property equations into PFLOTRAN. Some of the differences are shown below:

- The specified thermal conductivity equation as a function of liquid saturation is different from what is in PFLOTRAN. The equation specified in Task C is given as:

$$\boldsymbol{\lambda(\theta) = \lambda_{dry} + (\lambda_{sat} - \lambda_{dry}) \cdot \theta} \quad \textbf{Eq. 2-1}$$

where λ is thermal conductivity in W/m/K
θ is saturation
λ_{sat} is saturated thermal conductivity in W/m/K
λ_{dry} is dry thermal conductivity in W/m/K

- The default thermal conductivity equation in PFLOTRAN is (Somerton et al., 1974):

$$\boldsymbol{k_{th} = k_{dry} + \sqrt{S_l}\left(k_{sat} - k_{dry}\right)} \quad \textbf{Eq. 2-2}$$

where k_{th} = thermal conductivity
k_{dry} = dry thermal conductivity
k_{sat} = fully saturated thermal conductivity

- The specified specific heat equation is a function of various variables, while constant heat capacity is used in PFLOTRAN. The specified Task C equation is:

$$\boldsymbol{C_p = C_p^{solid} \cdot (1 - \phi) \cdot \frac{\rho_g}{\rho_b} + C_p^{water} \cdot \phi \cdot \theta \cdot \frac{\rho_w}{\rho_b}} \quad \textbf{Eq. 2-3}$$

where C_p is specific heat capacity in J/kg/K
C_p^{solid} is specific heat capacity of solid grains in J/kg/K
ϕ is porosity
C_p^{water} is specific heat capacity of water = 4181.3 J/kg/K

- The specified water density equation uses a constant thermal expansion coefficient of water, while PFLOTRAN uses water density (water thermal expansion coefficient) as a function of temperature and pressure. The Task C specified equation for water density is:

$$\boldsymbol{\rho_w = \rho_w^0 \frac{1}{e^{\alpha_w (T - T_0)} e^{c_w (p_0 - p)}}} \quad \textbf{Eq. 2-4}$$

where ρ_w is water density (kg/m^3)
ρ_w^0 is the reference water density (kg/m^3)
α_w is the thermal expansion of water (K^{-1})
T_0 is the reference temperature (273.15 K)
c_w is the compressibility of water
p_0 is the reference pressure (0.1 MPa)
c_w is the compressibility of water
p_0 is the reference pressure (0.1 MPa)

- The specified porosity vs pore compressibility equation is different from that in PFLOTRAN. The specified Task C equation is:

$$\boldsymbol{\varphi = \varphi_0 \left(1 + c_{pore}(p_w - p_{w0})\right)} \quad \textbf{Eq. 2-5}$$

where φ is porosity and φ_0 is initial porosity (-)
c_{pore} is pore compressibility (Pa^{-1})
p_w is water pressure and p_{w0} is initial water pressure (Pa)

The equation in PFLOTRAN is:

$$\boldsymbol{\varphi = \varphi_0 + c_{pore}(p_w - p_{w0})} \quad \textbf{Eq. 2-6}$$

Eq. 2-1 and Eq. 2-4 are now included in PFLOTRAN. In addition, Eq. 2-5 can be utilized using Eq. 2-6. Eq. 2-6 can be manipulated in the PFLOTRAN input deck by using the soil compressibility card and multiplying the value by initial porosity. To get the porosity and pore compressibility of Task C, the following PFLOTRAN cards can be used:

- SOIL_COMPRESSIBILITY_FUNCTION DEFAULT
- SOIL_COMPRESSIBILITY value

where value for the soil compressibility is the pore compressibility defined in Table 2-3multiplied by the initial porosity.

- PFLOTRAN also has anisotropic permeability and thermal conductivity.

Table 2-3 Material parameters for Step 0 (Task C Specifications)

	Input parameters	Symbol	Unit	OPA [1]	GBM [3]	Bentonite blocks [4]	Source
Thermal parameters	Dry thermal conductivity parallel and perpendicular to bedding	$\lambda_{dry,\parallel}$	W/mK	2.4	0.35	0.26	
		$\lambda_{dry,\perp}$	W/mK	1.3			
	Saturated thermal conductivity parallel and perpendicular to bedding	$\lambda_{sat,\parallel}$	W/mK	2.4	1.2	0.96	
		$\lambda_{sat,\perp}$	W/mK	1.3			
	Solid specific heat capacity	c_s	J/kgK	995	800	800	
Hydraulic parameters	Dry Bulk Density	ρ_{bulk}	kg/m^3	2340	1490	1690	NTB 15-02
	Porosity	ϕ	-	0.13	0.331	0.331	
	Intrinsic permeability	$k_{i,\parallel}$	m^2	5.0E-20	3.5E-20	1.0E-22	
		$k_{i,\perp}$		1.0E-20			
	Van Genuchten Entry Pressure	p_e	MPa	20.0	28.6	30	
	van Genuchten n	n	-	2.5	2.0	1.67	
	van Genuchten maximum water saturation	s_{max}	-	1.0	1.0	1.0	
	van Genuchten residual water saturation	s_r	-	0.0	0.0	0.0	
	Pore compressibility	c_{pore}	1/Pa	8.66E-10	1.05E-07	1.13E-07	calculated from E, ν
Mechanical parameters	Young's modulus	$E_\parallel$	MPa	8000	18	24	
		$E_\perp$		4000			
	Shear modulus	$G_\perp$	MPa	3500			
	Poisson ratio	$\nu_\parallel$	-	0.35	0.35	0.2	
		$\nu_\perp$		0.25			
	Linear thermal expansion	α_T	1/K	1.5E-05	3.0E-06	3.0E-06	
	Biot coefficient	α	-	1	1	1	
Fluid parameters	Reference water density	ρ_{fluid_ref}	kg/m^3	1000			
	Fluid compressibility	c_{fluid}	1/Pa	4.65E-10			
	Linear thermal expansion water	α_w	Pa s	4.00E-04			
	Vapour diffusivity (vapour in air)	D_v	m^2/s	2.42E-05			

Note: NTB 15-02 is NAGRA (2019)

2.3.2 Simulation Model Setup

Model geometry and meshing were developed for Step 0 PFLOTRAN and COMSOL® simulations. The geometry and mesh used for PFLOTRAN simulations is shown in Figure 2-3. The domain size is 50 m x 50 m, and the mesh has 138,103 grid blocks. Based on the specified material properties (Table 2-3) and other Task C specifications, the following initial and boundary conditions were used.

- Initial condition:
  - T = 15 °C everywhere
  - Pore water pressure 2 MPa. Hydrostatic pressure assumed at Opalinus Clay.
  - Bentonite blocks initial condition:
    - Initial water content 18 % (NAGRA, 2019). Calculated liquid saturation = 0.919
  - Granular bentonite initial condition:
    - Initial water content 5 % (NAGRA, 2019). Calculated liquid saturation = 0.227

- Initial water saturation at Opalinus Clay = 1
- Initial stress σ1 = 6.5 MPa σ3 = 2.5 MPa (COMSOL® THM)

- Diffusion Coefficient:
  - Liquid phase: 2.0 x 10^{-9} m^2/s
  - Gas phase: 2.0 x 10^{-5} m^2/s
- Boundary Condition:
  - No heat flow, no water flow, no vapour flow, no displacement on outer boundaries.
  - Heater power is 1350 W per heater, and each heater is 4.6 m long.
  - Column outer boundary at 2.0 MPa and 15 °C
  - Heater boundary no water flow, no displacement.
- Opalinus Clay:
  - Anisotropy in permeability and thermal conductivity applied

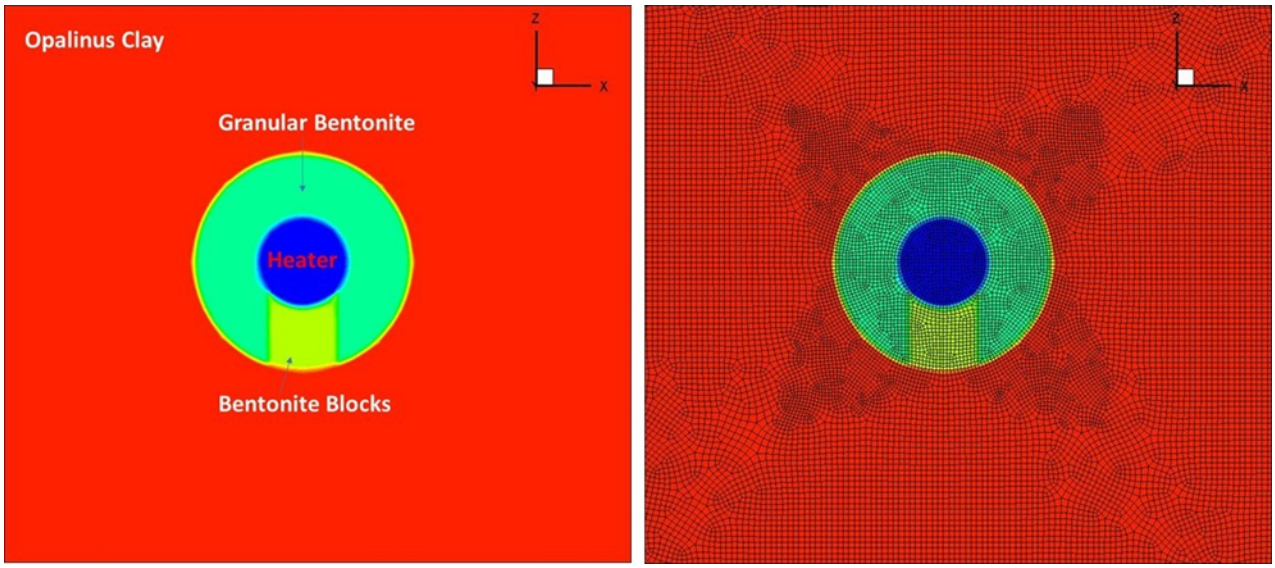

Figure 2-3 Geometry and meshing used for Task C, Step 0 PFLOTRAN simulations.

2.4 Step 0 Simulation Results

Preliminary simulations were made for the Task C, Step 0 cases using the PFLOTRAN and COMSOL® codes. The PFLOTRAN simulations concentrated on Step 0a (thermal-only) and Step 0b (Thermal-hydrology) simulations. The COMSOL® simulations included Step 0c (THM) in addition to Step 0a and Step 0b. Selected preliminary simulations results for each modeling code are shown below. Note that these are interim results and the final results will be reported in the future.

2.4.1 PFLOTRAN Simulation Results

As also specified in Section 2.2, Step 0a is 2D Thermal-only simulation with saturation dependent thermal properties and saturation held at initial values. In PFLOTRAN, Step 0a was modelled by

assigning permeability of 1.0 x 10^{-29} m^2, to represent thermal-only simulation. Figure 2-4 shows predicted evolution of temperature at specified locations at the outside edges of the heater. Locations H1, H2 and H4 are close to the Granular Bentonite, while H3 is close to the Bentonite Blocks. The results at H3 are different because of the different thermal conductivity of the Bentonite Blocks compared to the Granular Bentonite. The small temperature differences between H1, H2 and H4 could be due to their respective locations with respect to the bedded Opalinus Clay.

Figure 2-5 shows distribution of temperature at end of simulation time for PFLOTRAN Step 0b runs. The shape of the distribution reflects anisotropy in permeability and thermal conductivity. Figure 2-6 shows PFLOTRAN predicted evolution of temperature at specified locations for Step 0b. Temperatures decrease at distances away from the heater. Figure 2-7 shows predicted liquid pressure at specified locations in the Opalinus Clay. Predicted results are different for Point O1 are different from the other locations because of its close proximity to the heater and its location parallel to the Opalinus Clay bedding.

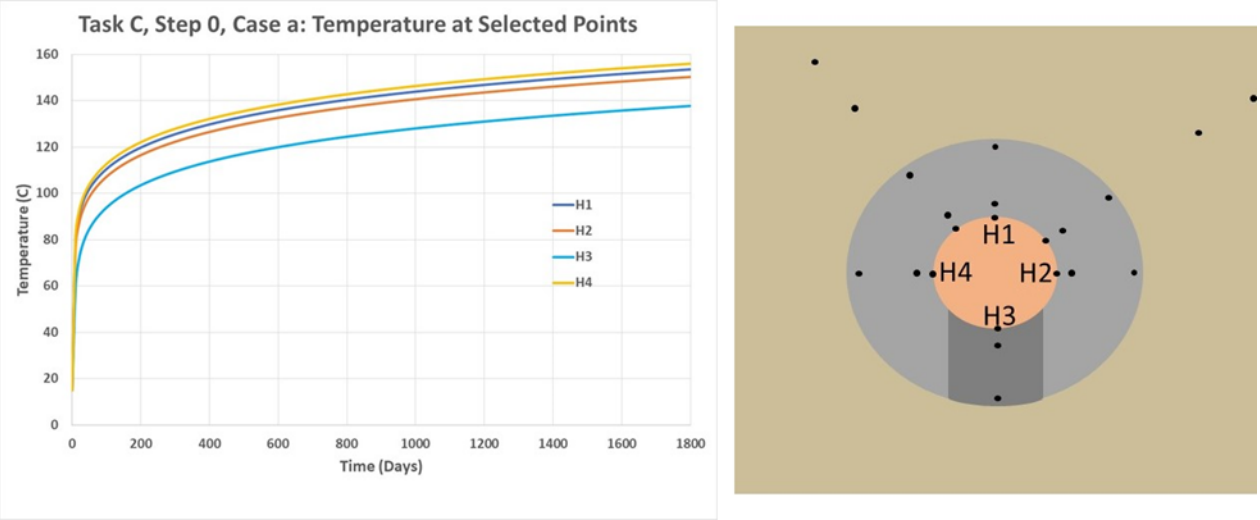

Figure 2-4 Step0a: PFLOTRAN Predicted Evolution of Temperature at Specified Locations.

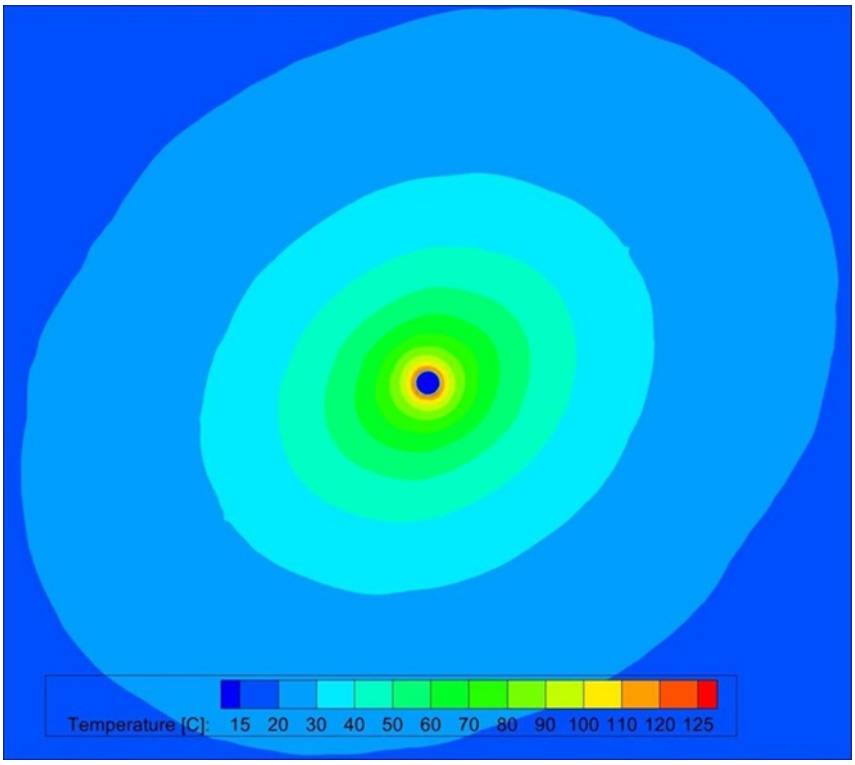

Figure 2-5 Step0b Results: PFLOTRAN Predicted Temperature Distribution at 1800 Days (with anisotropy).

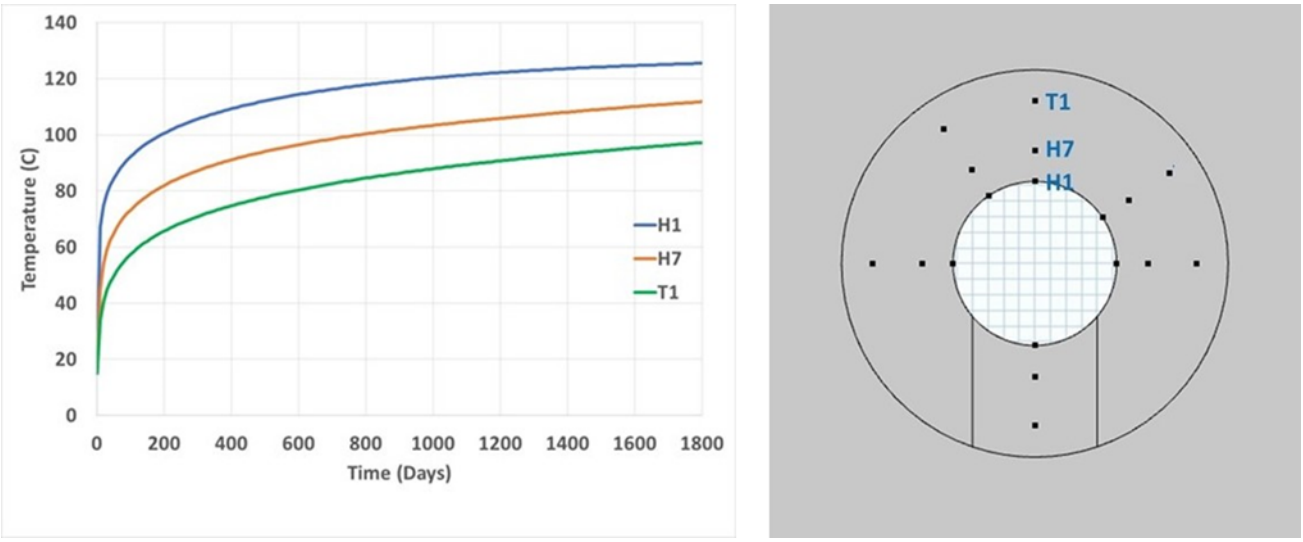

Figure 2-6 Step0b: PFLOTRAN Predicted Evolution of Temperature at Specified Locations.

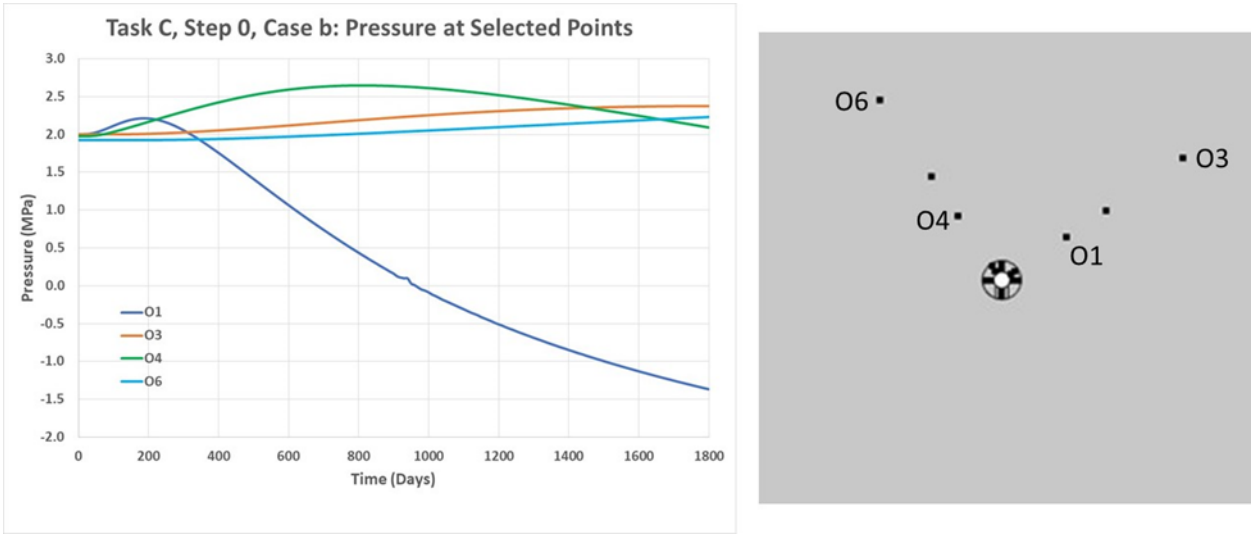

Figure 2-7 Step0b: PFLOTRAN Predicted Evolution of Liquid Pressure at Specified Locations.

Predicted temperature results for the thermal-only case (Step 0a) were about the same for most Task C participating teams. However, there were differences in predictions for the TH (Step 0b) and THM (Step 0c) modeling cases. Simplified extra simulation cases for the TH case (Step 0b) were then added to further identify the causes of differences between teams. The new extra cases were:

- **Case b2**: TH model with all materials assigned Opalinus Clay properties, zero (or very small) permeability in the Opalinus Clay.

- **Case b3**: TH model with all materials assigned Opalinus Clay properties, normal permeability in the Opalinus Clay.

PFLOTRAN simulations were conducted for Step 0, Case b2 and Case 3 specifications. Case b2, with near zero permeability, simulation results are shown in Figure 2-8 and Figure 2-9. Figure 2-8 and Figure 2-9 show predicted evolution of liquid pressure at Points O1 and O4 in the Opalinus Clay. The blue lines in both figures represent results when the default Equation of State (EOS) in PFLOTRAN is used. Comparison of results with other teams that used the Task C specified water density (Eq. 2-4) showed that the PFLOTRAN predicted pressure values were lower. Since then, Eq. 2-4 has been implemented in PFLOTRAN to compare results with other teams. PFLOTRAN has been run with the Task C specified water density and the results are shown in Figure 2-8 and Figure 2-9 (orange lines). The differences between the blue and orange lines are significant, which is the result of using constant thermal expansion coefficient in Eq. 2-4.

Case b3, with Opalinus Clay permeability, simulation results are shown in Figure 2-10 and Figure 2-11. Figure 2-10 and Figure 2-11 show predicted evolution of temperature and liquid pressure at specified locations in the Opalinus Clay. Points O1 and O3 are located parallel to the Opalinus Clay bedding while Points O4 and O6 are located perpendicular to the bedding. The results reflect the anisotropy in permeability and thermal conductivity.

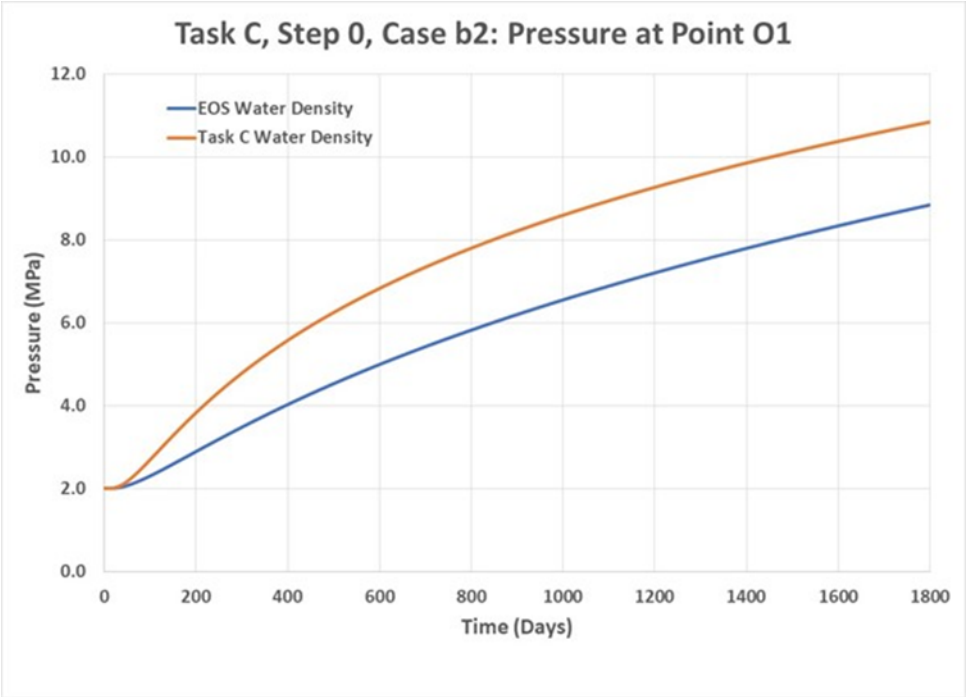

Figure 2-8 **Step 0 Case b2: Predicted Evolution of Pressure at Point O1 with PFLOTRAN Default Equation of State and Task C Specified Density**

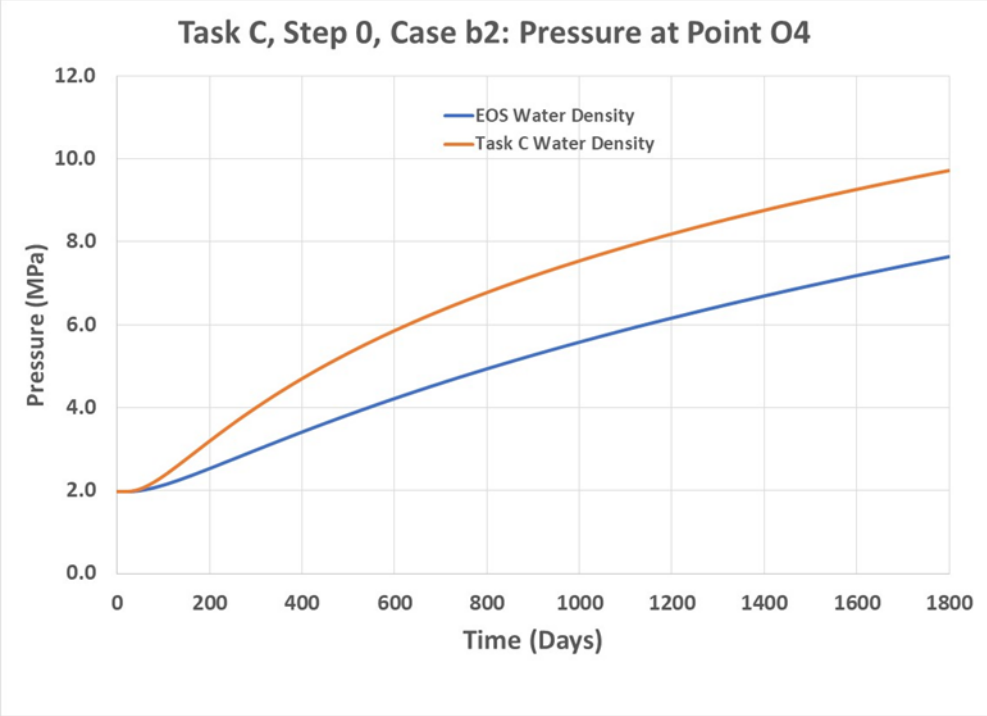

Figure 2-9 **Step 0 Case b2: Predicted Evolution of Pressure at Point O4 with PFLOTRAN Default Equation of State and Task C Specified Density**

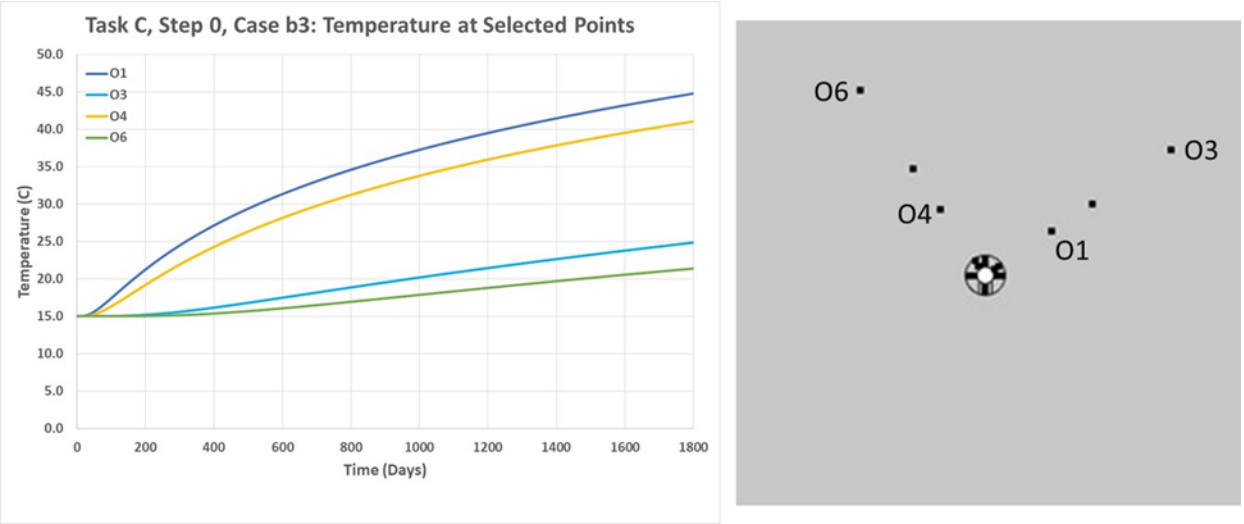

Figure 2-10 Step 0b3: PFLOTRAN Predicted Evolution of Temperature at Specified Locations.

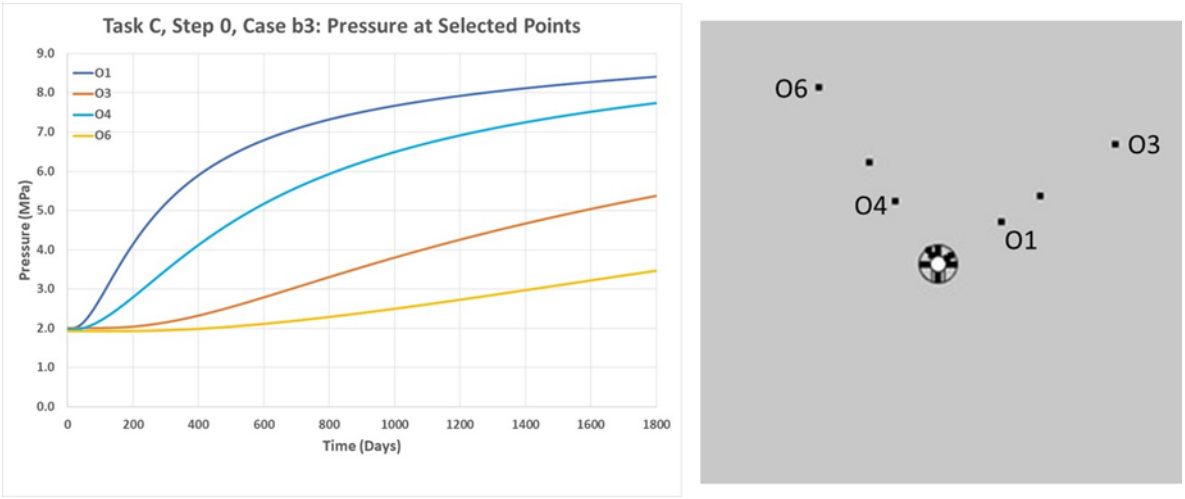

Figure 2-11 Step 0b3: PFLOTRAN Predicted Evolution of Liquid Pressure at Specified Locations.

2.4.2 COMSOL® Simulation Results

COMSOL® simulation results are shown in Figure 2-12 and Figure 2-13. Figure 2-12 shows COMSOL® predicted evolution of temperature at specified locations in the bentonite (Bentonite Blocks and Granular Bentonite) for Step 0b. Figure 2-13 shows COMSOL® predicted evolution of liquid pressure at specified locations in the Opalinus Clay.

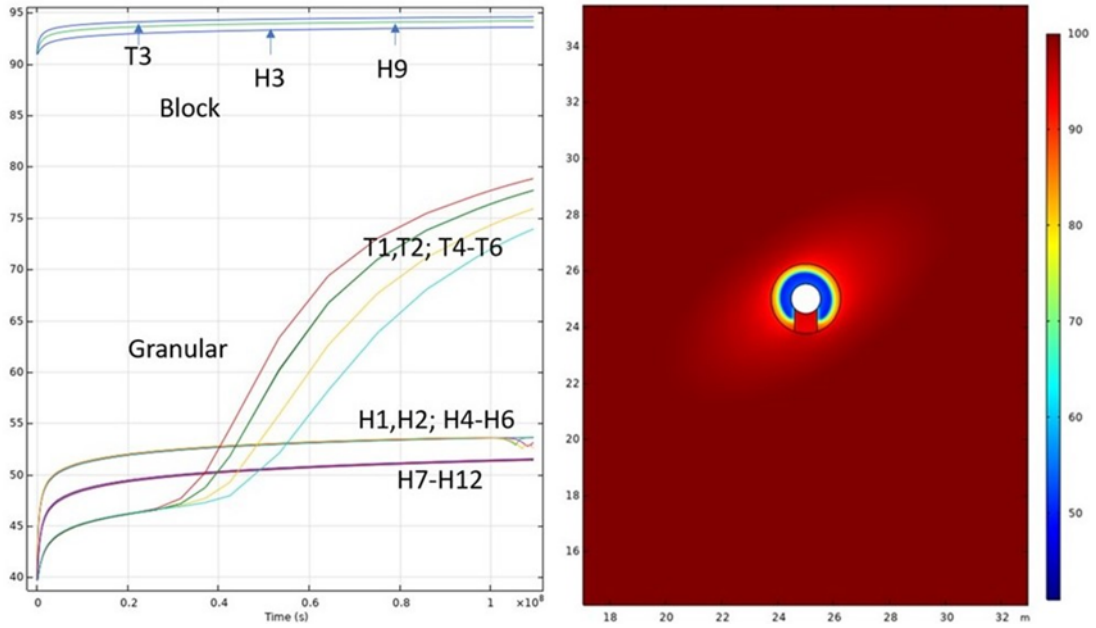

Figure 2-12 Step 0b: COMSOL® Predicted Evolution of Relative Humidity at Specified Locations.

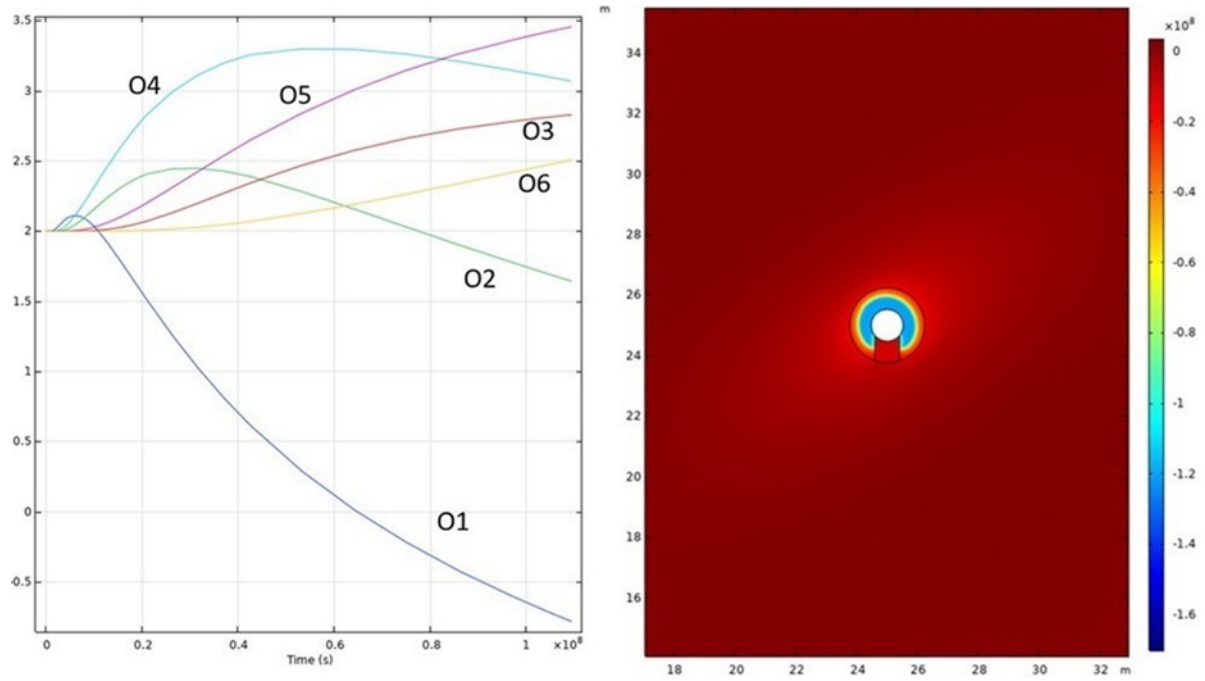

Figure 2-13 Step 0b: COMSOL® Predicted Evolution of Liquid Pressure at Specified Locations.

2.4.3 Preliminary PFLOTRAN and COMSOL® comparison of results

Sandia's COMSOL® simulation results for Step 0 Case b2 compared well with the results of other teams that used constant linear thermal expansion coefficient of water. Sandia's predicted PFLOTRAN liquid pressures were consistently lower because of use of the built-in equation of state that uses temperature varying thermal expansion coefficient (water density). This is discussed in Section 2.4.1. This was also the case with other teams that use EOS for properties of water (example, LBNL team). To explore the

issue of the thermal expansion coefficient of water, intra-Sandia code comparison, PFLOTRAN and COMSOL®, were conducted for Step 0, Case b2. For the simulations the anisotropy in Opalinus Clay was removed for further simplification. In addition, temperature variable thermal expansion coefficient of water was used. Simulation results of temperature and liquid pressure in the Opalinus Clay are shown in Figure 2-14. As shown in the plots the results of the two codes match very well.

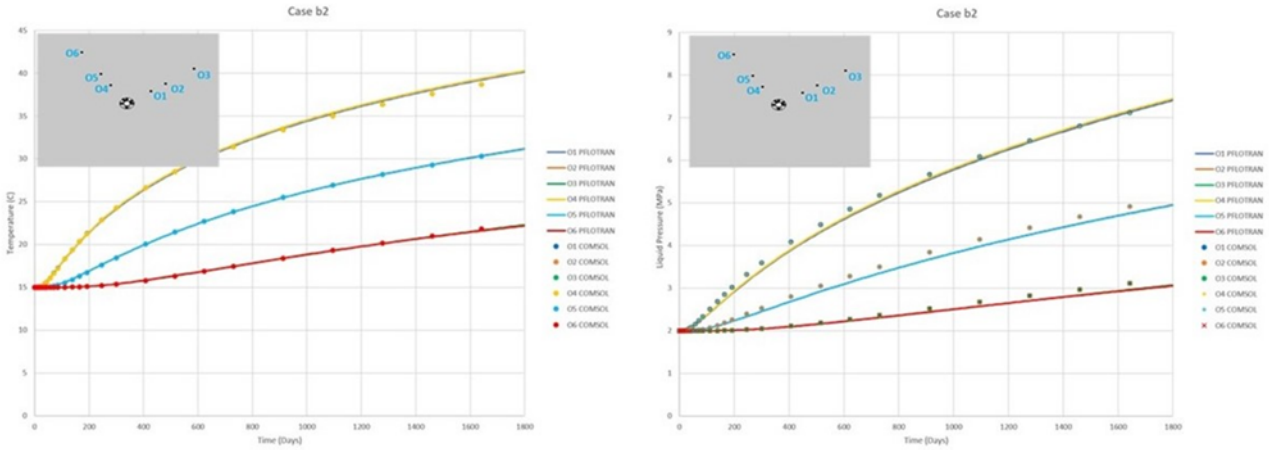

Figure 2-14 Step 0 Case b2: PFLOTRAN and COMSOL® Predicted Evolution of Temperature and Liquid Pressure at Specified Locations.

2.5 Summary and Future Work

Preliminary simulations of Task C, Step 0 were conducted at Sandia National Laboratories using PFLOTRAN and COMSOL® codes. The modeling work allowed building of capabilities at Sandia to model T, TH and THM simulations. Simulations of Step 0 will continue to reduce differences between teams. Sandia's modeling team will also continue to use PFLOTRAN and COMSOL® simulations to identify differences in simulation methods. Modeling will also start on Task C, Step 1. As shown in Figure 2-15, the Step 1 modeling will use full three-dimensional geometry.

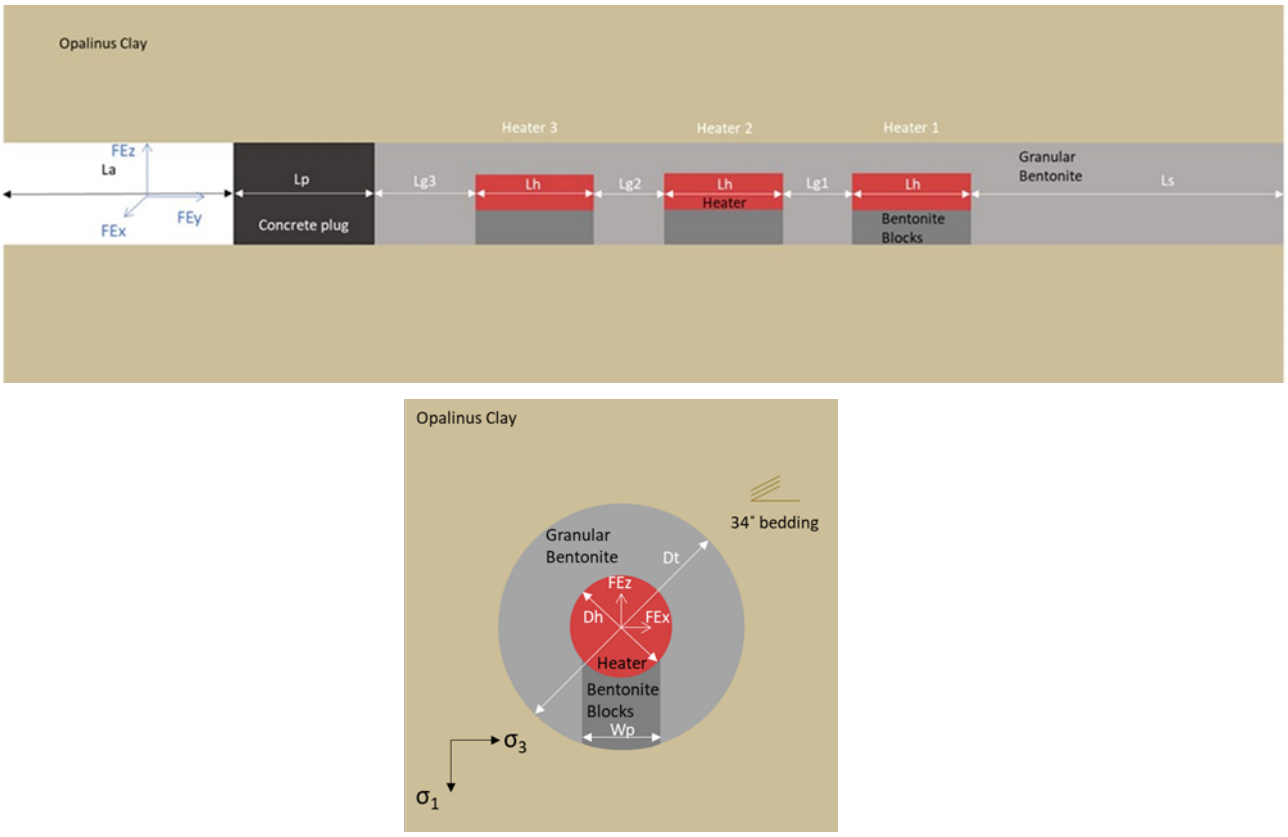

Figure 2-15 **3D model geometry for Step 1 (Task C Specifications).**

This page left intentionally blank.

3. Polymer Intercalation Synthesis of GlycoBoehmite Nanosheets

3.1 Introduction

Interfacial properties are central in nanomaterials development to meet challenges in energy efficiency, energy storage, catalysis, advanced manufacturing, and materials processing. Layered material structures are particularly impacted by interfacial properties since understanding and manipulating their interfacial forces has led to novel exfoliated and delaminated 2D materials such as clays (Letaief and Detellier, 2009; T. Liu et al., 2008), graphene and graphene oxide (Coleman et al., 2011), and several metal oxides (Adachi-Pagano et al., 2000; Ma & Sasaki 2010). These exemplar layered materials have grown in interest for flexible electronics, sensors, gas barriers, and catalytic activity. Many techniques for adjusting interfacial properties require surface chemical modification via oxidation (graphene) or charge substitution as in layered clay materials (Guo et al., 2015; Liu et al., 2006; Matusik et al., 2012; Naguib et al., 2013; Oestreicher et al., 2014). Organic surfactants and polymers have been intercalated into the interlayer region of layered materials for several systems based on ion exchange or transport (Gardolinski & Lagaly, 2005b; Giraudeau et al., 2009; Letaief & Detellier, 2009; Stober & Pollmann, 1999; Tunney & Detellier, 1996a). Although these interactions change electrostatic or wetting interactions between surfaces, layered materials bound by forces like hydrogen bonding via hydroxyl groups in the interlayers have received much less attention. Thus, synthesis approaches that are based on control of hydrogen bonding forces in the layered structure have novel potential for application as hybrid materials.

Boehmite (γ-AlOOH) is a transition alumina with a hydrogen bonded (H-bond) layer structure that can be tailored to control its interfacial behavior. The inorganic AlO_6 octahedra are bonded in a layered structure as sheets in the a-c plane, and the forces between sheets are based on H-bonding by the terminal -OH groups normal to the b-axis. It has long been recognized that the interfacial force bonding the layers together are two strongly bonded H-bond chains (Holm et al., 1958), and DFT-MD simulation of boehmite also demonstrates the strength of H-bonding on surfaces (Motta et al., 2012). Simulation of the structure by DFT shows that water strongly coordinates with the surface hydroxyl groups (Tunega et al, 2011). Modification of the AlOOH surface will require approaches that disrupt the adsorption of water. Chiche et al. utilized the role of H-bonding at boehmite surfaces in studies of the boehmite phase crystal growth (Chiche et al., 2011; Chiche et al., 2009). They showed that polyol materials like xylitol would specifically interact with the surfaces based on molecule topology and configuration, and enabled changes in the growth morphology due to H-bonded surface modification. Boehmite is used for several applications as a catalyst material (Ma et al., 2008b; Suchanek et al., 2010), adsorbent (Yu et al., 2013), membrane additive (Kololuoma et al., 2015; Vatanpour et al., 2012), composite filler (Kololuoma et al., 2015; Malucelli et al., 2013; Tseng et al., 2014), flame retardant (Patra et al., 2014), and precursor to Al_2O_3 ceramics (Iler, 1961). Hybrid materials based on alteration of boehmite material structure could provide unique functionality based on hybrid material properties, where organic moieties could tailor surface chemistry, optical index of refraction, adsorption properties (including capacity and specificity), or porosity from the established aqueous route properties of boehmite. According to Kickelbick (2007), hybrid materials are defined as composites of two moieties at the nanometer or molecular level, often having an organic and inorganic component. Class I hybrid materials utilize weak hydrogen bonding, electrostatics, or van der Waals interactions, whereas Class II have strong chemical interactions between the constituents by covalent or coordinative bonds. Interpenetrating networks of inorganic and polymers fall into the category of Class I hybrid materials, whereas strong bonds due to covalent or coordinating chemistry are categorized as Class II hybrid materials.

In boehmite synthesis, alcohol-water mixtures have been found to have effects upon particle size and morphology (Y. Liu et al., 2008; Ma et al., 2008a). Although alcohols at lower temperatures affect crystal growth through solution complexes and diffusion rates, elevated temperature and pressure induce

chemical bonding via dehydration reactions of surface -OH groups (Tunney & Detellier, 1996b). This elevated temperature chemisorption of alcohols on the surface induces surface growth rate changes via surface chemistry and speciation effects, but alteration of the crystal phase and unit cell is not observed (Li et al., 2010).

Solvothermal synthesis approaches are known to form covalent surface reaction of alcohols with metal oxides under elevated temperature and pressure (Gardolinski & Lagaly, 2005a, b). This has been used to control wetting interactions and dispersion of particle suspensions. Inoue et al. demonstrated that there are hybrid transition aluminas based on boehmite crystal structures formed by gibbsite dehydration synthesis in glycol solvents using autogenous pressure reactors (Inoue et al., 1988). Glycol modified boehmites were reported for solvents varying from ethylene glycol to 1,6-hexandiol (Inoue, 2004; Inoue, 1989; Inoue et al. 1991), showing that glycol solvent molecules are incorporated between boehmite interlayer sheets. This chemisorption process would involve covalent bonding, making these established glycoboehmites a Class II hybrid material. The glycol expands the unit cell along the b-axis to produce a new glycoboehmite phase. The organic material remains terminated with -OH groups and maintains cohesion through H-bonding interactions between inorganic layers. However, the chemisorbed glycol has not been considered for the impact of the H-bonding network in the interlayer. We propose that the strength of the H-bonds between atomic layers is reduced by van der Waals interactions resulting from -CH_2- units of the glycol backbone, and the potential for backbone mobility over the terminal -OH groups between boehmite layers. If this theory is true, it would be possible to insert other molecules or polymers between the atomic layers of glycoboehmite, when the interaction strength of the adsorbate is greater than the interlayer strength or the wetting interaction of the solvent. The inherent surface modification of Class II glycoboehmite hybrid materials would enable a Class I hybrid interphase between atomic layers due to the chemisorbed glycol surfaces.

In this paper we examined the ability of glycol solvents to control the expansion of the boehmite crystal structure through polymer intercalation within the interlayers. This work explores the ability of well-known hydrogen bonding polymers (polyvinylpyrrolidone (PVP) or hydroxylpropyl cellulose (HPC)) to interact during the glycothermal synthesis reaction and form new polymer intercalated phases. Structural and property measurement of the resulting compounds is provided by overall morphology, atomic structure, thermal stability measurements, and zeta potential measurement. Developing new hybrid materials through association or chemisorption via hydroxyl groups is a viable approach for new materials development. As boehmite is the critical precursor to γ -Al_2O_3 used as a catalyst support, the reaction of these materials may create high surface area materials that have not been demonstrated previously.

3.2 Experimental

All reactions described below have been replicated over 10 times to demonstrate reproducibility. All chemicals were used as received without further purification.

3.2.1 Boehmite synthesis

Boehmite was synthesized based on an adaptation of the Yoldas process for the reaction of aluminum isopropoxide $[Al(OPri)_3]_4$ in water at elevated temperature (Buining et al., 1991; Lepot et al., 2008; Yoldas, 1975). The precipitation was performed in purified (Millipore) water using the solution precipitation reaction method by $[Al(OPri)_3]_4$ in a 500 mL round bottom flask equipped with a reflux condenser. The setup was placed in a chemical fume hood and heated to reflux temperature under ambient conditions using a thermal mantle. For the reaction, $[Al(OPri)_3]_4$ (5.00 g, 2.45 mmol, 99% Sigma-Aldrich) was placed into the flask with 375 mL of deionized water. The reactor contents were stirred continuously with a magnetic stir bar for 24 hours. After the reaction cooled, a white precipitate

was collected by centrifugation (3000 rpm for 10 minutes) and the solid was washed by three cycles of centrifugation using methanol (Sigma Aldrich, 99%). The product was then dispersed in methanol for characterization.

3.2.2 Glycoboehmite synthesis

Glycoboehmite (GB) was formed by treating 5.00 g gibbsite $Al(OH)_3$ (64.1 mmol) (1 micron average particle size, Micral 9400, Huber) in 200 mL 1,4-butanediol (Sigma-Aldrich, 99%) at 250 °C for 24 hours under a N_2 atmosphere and autogeneous pressure. This is modified from the procedure of Inoue et al. (Inoue, 1989; Inoue et al., 1988) Potassium hydroxide (KOH, ACS Grade, Sigma-Aldrich) was added as a mineralizer at 0.31 g (5.53 mmol) to the initial dispersion. The materials were added by manual mixing in a mortar and pestle, followed by pouring of the dispersion into the Parr reactor. A Parr Instruments 600 mL stirred reactor was used (Moline, IL). Samples were de-aired under continuous vacuum for 20 minutes to remove trapped or dissolved air, followed by N_2 purge for 20 minutes before sealing, to prevent oxidation of the 1,4-butanediol. The thermal profile was run as described. The autogeneous pressure in the reactor was typical at 20 psi. Cooling of the reactor was set at a 30-minute ramp to 25 °C, but the thermal mass of the heater made this a parabolic decreasing profile. A gel-like solid product was isolated from the synthesis solvent using centrifugation (4000 rpm for 10 minutes) and the solid was washed by four cycles of centrifugation using ethanol (Sigma Aldrich, 99%). Further drying of a sample of the solvent was conducted using a vacuum oven at 70 °C as needed.

3.2.3 Polymer intercalation synthesis

The reactions were conducted using the Parr stirred reactor, with varying conditions based on synthesis of glycoboehmite. Polymer derivatives were tested using 5.00 g of gibbsite, with 1.00 g (0.1 mmol) of polyvinylpyrrolidone (PVP) (10,000 mol. wt., Sigma-Aldrich) or hydroxypropyl cellulose (0.01 mmol) (HPC, Sigma-Aldrich, 100,000 mol wt.), respectively. This ratio was used to provide excess polymer sufficient to fully cover the precursor gibbsite powder and stabilize any nanoparticle product. Each material was added by manual mixing in a mortar and pestle, followed by loading into the Parr reactor. The reactor was purged of air using the same methods as the glycoboehmite synthesis. The thermal schedule was set with a two hour rise time to 220 °C, followed by 24 hours reaction at temperature. The reactor cooled to ambient temperature and was unloaded. Products were collected by centrifugation at 4000 rpm for 10 minutes from the 1,4-butanediol reactor and washed four times using ethanol. Excess unbound polymer is redissolved during these cycles. Glycoboehmite synthesized with PVP is termed GB-PVP, and glycoboehmite synthesized with HPC is termed GB-HPC.

3.2.4 Characterization Techniques

3.2.4.1 XRD

X-ray Diffraction scans were taken of the synthesized glyco-boehmite using a PANalytical instrument, from 2θ angles of 2 to 70 degrees. Phase analysis was determined from patterns collected on a PANalytical powder diffractometer employing a Cu Ka radiation (1.5406 A) and a RTMS X'celerator detector. Jade 9 XRD Pattern Processing software (Materials Data, Inc, Livermore, CA) and powder diffraction file (PDF 00-083-2384) was employed for powder indexing. Samples were prepared by drop casting from ethanol dispersions over a Si wafer with (510) crystallographic orientation to prevent substrate peak interference. An α-Al_2O_3 standard was run in the instrument prior to operation to ensure sample height calibration. Jade software was used to examine data and conduct phase identification.

3.2.4.2 Scanning Electron Microscopy (SEM)

Scanning electron microscopy (SEM) of the glycoboehmite products was performed using a Carl Zeiss Supra™ 55VP SEM (10–20 kV; 8.5 mm working distance). SEM of the initial material shows the morphology for comparison.

3.2.4.3 High-resolution Scanning Transmission Electron Microscopy (HRSTEM)

High-resolution scanning transmission electron microscopy (HRSTEM) was performed with a Thermo Fisher Scientific Titan G2 80-200 STEM operated at 200 kV and equipped with a spherical aberration corrector on the probe-forming optics and four silicon-drift X-ray detectors. Samples were made by dispersing sonicated suspensions of glycoboehmite in ethanol onto carbon coated TEM grids. Platelets were imaged both normal to the platelet face and edge-on or at curled edges to directly measure the b-spacing of the glycoboehmite.

3.2.4.4 FTIR

Spectra were obtained of dried boehmite and glycoboehmite powders using a Nicolet 6700 FT-IR (Thermo Scientific) using a Smart iTR ATR sample accessory. 128 scans of the background and of the sample were taken to obtain the IR spectra of powder materials in air.

3.2.4.5 Thermogravimetric Analysis/Differential Scanning Calorimetry (TGA/DSC)

Thermogravimetric Analysis/Differential Scanning Calorimetry was performed using a TA Instruments Q600 SDT. The method contained an initial 20-minute isothermal hold, followed by a ramp to 800ºC at 10ºC/minute. Each of the samples were weighed (8-17 mg) into a 90 µL alumina cup and run under a 100 mL/min flow rate of argon and separately air.

3.2.4.6 Zeta Potential

A Stabino Particle Charge analyzer with autotitration configuration was used to conduct zeta potential as a function of pH. (Colloid Metrix, Gmbh) For each material, 0.10 g of dried product was dispersed in 10 mL of 10-3 M KNO3 electrolyte solution using an ultrasonic bath. Titrants were freshly prepared as 0.025 M solutions of HNO3 and KOH respectively. Measurements of the zeta potential development as a function of pH were conducted in 10-3 M KNO3 solution at ambient temperature. 20 mL of background electrolyte solution was added to the instrument, with 1 mL of a stock dispersion. The instrument pH meter was freshly calibrated using pH 4, 7 and 10 standard solutions.

3.2.4.7 Surface Area Measurement by BET Method

Glycoboehmite material and polymer intercalated glycoboehmite was first heated for 2 hours in a 100 ºC oven. This ensured the material was dry, to prevent precipitation during degas sample preparation. A portion of each sample was set aside and further calcined at a temperature of 600 ºC for 2 hours. The materials were first purged with nitrogen gas and held at a temperature of 60 ºC for 24 hours using a Micrometerics SmartPrep instrument. Based on nitrogen adsorption the surface area (m^2/g) was measured using a Micrometerics Tristar II instrument.

3.3 Results and Discussion

3.3.1 Structural Characterization

Materials prepared in this study were the aqueous route boehmite (aqB), the glycoboehmite (GB) from literature, as well as the two polymer intercalated materials (GB-PVP, GB-HPC). The aqueous phase synthesized boehmite is a reference for the alteration of the unit cell in the novel glycol-synthesized phases to easily compare structural properties. The crystal structure for each of the synthesized phases is characterized by X-ray diffractometry in Figure 3-1. The boehmite phase has the space group *Cmcm*, and an orthorhombic unit cell, with dimensions as a= 3.07Å. b = 12.53 Å, and c = 3.87 Å. All the boehmite peaks identified from Powder Diffraction File (PDF) 01-088-2111 are present and labeled in Figure 3-1a. The boehmite (aq) in Figure 3-1a matches the unit cell of the prior reports of Christensen (Christensen et al. 1982; Corbató,1985).

The glycothermally synthesized phases all indicate unit cell alterations by the presence and intensity of new peaks (identified with blue text in figures and with a prime as (020)′). Figure 3-1b presents the XRD pattern for the 1,4-butanediol route GB first reported by Inoue et al. (Inoue, 1989; Inoue et al., 1991) The phase formed similarly, and exhibits several peaks in common with aqueous boehmite, identified with the (120), (140), (200), (151), and (231) reflections. These peaks indicated that the atomic arrangements of the (Al-O_6) octahedra in the basal inorganic planes are unaltered from that of the aqB phase. However, there are new peaks clearly evident at 4.8, 9.8, and 24.5 degrees 2θ, which have been tentatively identified with (020)′ (040)’ and (140)′ indices resulting from the intercalated organic glycol. The low angle peak at 4.8 degrees 2θ suggests a much larger expansion of the layers for this compound, and the indexation for the peaks changes due to the larger expansion. In prior work by Inoue (Inoue et al., 1991), XRD data below 5° 2θ was not collected, and it is possible that this enlarged b-axis length was not assessed and that the b-axis was indexed at one half the actual dimension. Both polyvinylpyrrolidone derivative glycoboehmite (GB-PVP) (Figure 3-1c) and hydroxypropyl cellulose derivative glycoboehmite (GB-HPC) (Figure 3-1d) have (020)′ reflections that are expanded relative to the aqB material based on the lower value of the 2θ peak as compared to the Boehmite (020) reflection at 13.9 degrees 2θ. However, these are not as expanded as the GB material. GB-PVP and GB-HPC was also scanned below 5° 2θ and no extra diffraction peaks were observed, ruling out the larger layer expansion. Higher peak intensity is evident for both polymer adducts of GB. The position of the (020)′ plane for the GB-PVP sample is at 7.24° 2θ. There is also a large, broad background peak at ~21.5° 2θ in Figure 3-1c. The GB-HPC material in Figure 3-1d has sharp aqB (020) peak at 14.5 degrees 2θ, but a very strong (020)′ peak at 7.22° 2θ, and the amorphous background is less prominent. This broad background may indicate an amorphous phase related to either the polymer or an alumina based gel.

This structural analysis assumes that the boehmite bonding is not disturbed in the a-c plane between the (Al-O_6) octahedra, but that the interlayer structure is expanded by the glycol substitution for the interlayer hydroxyl groups. This results in the boehmite (020) peak shifting to the lower 2θ values by expansion of the b-axis and retains the 2θ position of reflections exclusive to the a and c plane. Thus, the non-basal reflections are not shifted from the boehmite structure. All peaks that have a b-axis dependence (i.e., k > 0) should shift to lower angle peak positions based on the b-axis expansion. The GB-HPC and GB-PVP samples do not show significant shifts in peaks such as (140), (151), or (231) due to the relatively limited b-axis expansion and rigidity of the a-c plane. This can be understood by a precedent in mixed phase synthesis for the route used here. Inoue et al. described the effect of the precursor Gibbsite particle size, where the dehydration reaction is incomplete in micron-sized particles (Inoue, 2004). GB formation is believed to result from a dissolution-reprecipitation mechanism, with nucleation occurring at the heterogeneous interface. Large particles may undergo direct dehydration to boehmite in the core before surface dissolution reaches the center of the precursor gibbsite phase. As the precursor gibbsite material is

micron sized in this study, it is expected that phase purity is not achieved in this system, and all the GB samples have low aqB phase impurities. This is evidenced in Figure 3-1. Impurity content therefore broadens the shift in high b-axis dependent peaks, which have low overall intensity for the thin samples here (to be discussed further). It is important to point out the inconsistent and remarkable behavior of the GB sample when compared to that of the other samples (aqB, HPG and PVP). In the case of the GB sample is indicating a substantial expansion of the structure as indicated by the low angle peak at 4.8o 2q (~18.4 A). With the assignment of this peak as the (020)' peak, there is a substantial shift in any other (hkl) where k>0. This low angle peak is only observed in the GB sample, and not for the HPG or PVP based materials.

Analysis of the peak shift was conducted to determine the interlayer expansion due to the intercalation of organics into the layered structure. Table 3-1 presents the results assuming that the AlO(OH) layer thickness remains unchanged and noting that there are two layers contained in the unit cell. The layer thickness of the separation in aqB is ~2.0 Å as measured in Mercury software. There is a total change in (020) peak location from an initial (020) = 6.1 Å in aqB to a new (020)′ = 18.4 Å in GB. The interlayer expansion is calculated by subtracting two AlO(OH) layer thicknesses from the (020)' value, e.g. 18.4 Å – 4.0 Å to give 16.4 Å as the total change in the layer thickness for GB as compared to aqB as synthesized. Performing the same calculation for GB-PVP yields a value of ~9.2 Å and GB-HPC a similar value of ~9.2 Å as well. Additional discussion on the interlayer expansion is presented in the next section with HRSTEM analysis.

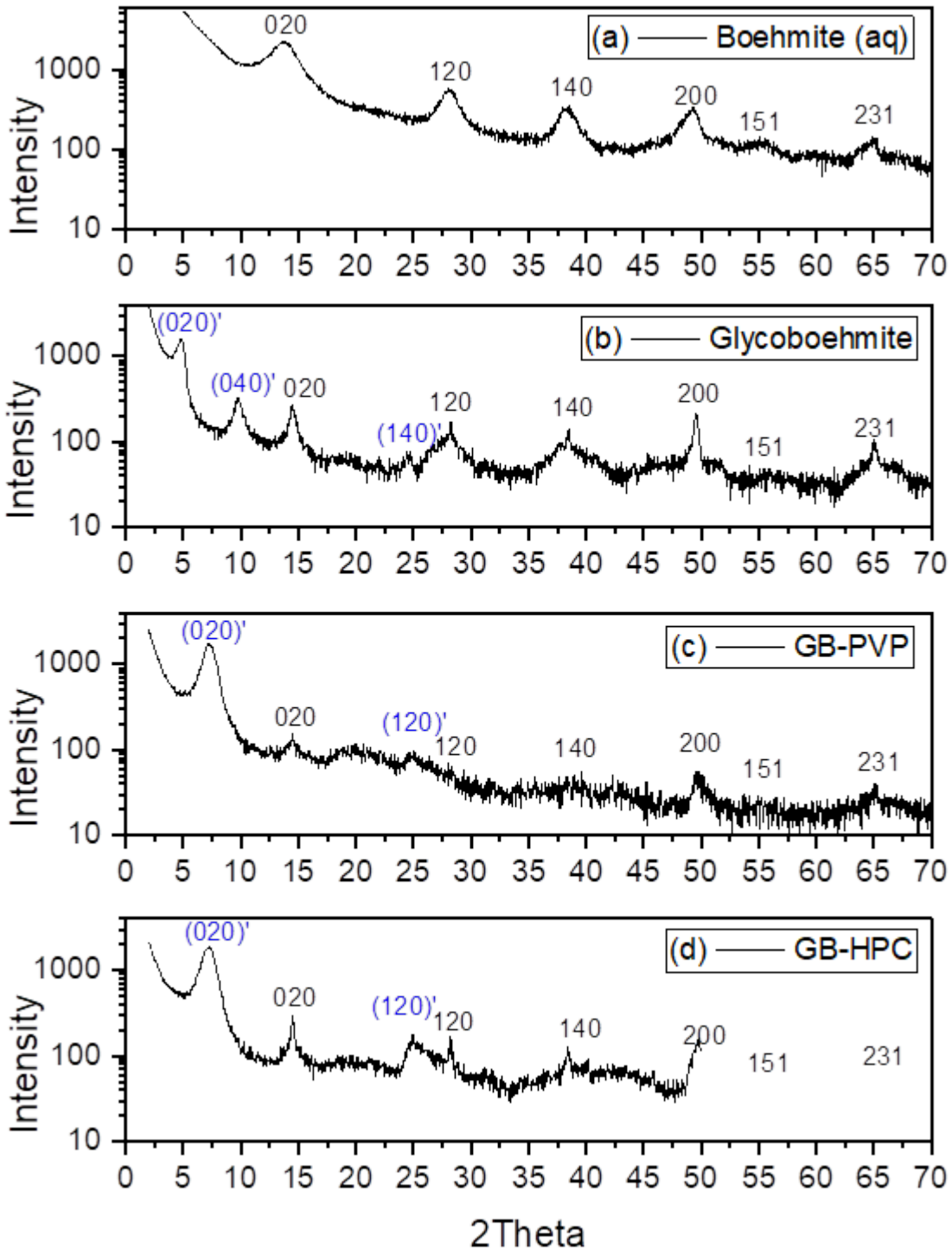

Figure 3-1 **XRD scan of boehmite derivative particles: (a) Aqueous boehmite synthesis, (b) Glycoboehmite, (c) GB-PVP, and (d) GB-HPC.**

Table 3-1 Position of (020)′ values, and estimated interlayer spacing.

Sample	2-Theta Value of (020) or (020)’	Interlayer Spacing d(020)´(Å)	Interlayer Distance (Å)
Boehmite (aqB)	13.9	6.38	4.34
Glycoboehmite (GB)	4.80	18.38	16.4
GB-PVP	7.24	11.2	9.16
GB-HPC	7.22	11.2	9.16

Further structural study was conducted using HRSTEM of the GB samples in Figure 3-2. Figure 3-2a is an atomic resolution image of the platelet face of GB. The regular atomic periodicity of the (Al-O_6) octahedra can be seen with the appearance of a hexagonal-like symmetry of the Al^{3+} ions along the sheet surface, confirming that the sample sheet is being viewed normal to the b-axis (i.e., perpendicular to the a-c plane and denoting the slowest growth direction is perpendicular to the sheet). The inset diagram is the Fourier transform image of the atomic periodicity in the facet, producing a diffraction pattern consistent with the expected symmetry for the a-c directions of the unit cell. Reflections in the structure show a twin boundary in the image, with both unit cell reflections marked for view. This corroborates the assumption that the inorganic sheet structure is unaltered from that of aqB, as used in PXRD analysis. Figure 3-2b shows a selected-area diffraction (SAD) pattern and identification of peak reflections from the nanosheet material. The spots indexed as (02n0) come from a single edge-on sheet and are therefore weak. The faint spots are due to the low number of atomic layers in the platelet but are indicated by arrows to aid in visualization. Figure 3-2c is a HAADF image of some sheets edge-on with integrated intensity profile across the sheet shown in Figure 3-2d. This provides a direct measurement of the interlayer expansion. Diffraction analysis of the (02n0) reflections from six SAD patterns gives d_{020}=17.4 Å ± 0.6 Å which is consistent with the HAADF images of the edge-on sheets and confirm the considerable expansion of the layers for this phase. Figure 3-2e and Figure 3-2f are images of the GB-PVP and GB-HPC products respectively. Direct SAD patterning was attempted for both GB-PVP and GB-HPC, but this analysis failed due to beam damage of the specimen during analysis. However, an estimate of the layer thickness was possible from the image itself. For the case of GB-PVP from Figure 3-2e, a value of 8.8 A interlayer distance was derived, which is consistent with the interlayer value obtained from XRD estimates (i.e. ~9.16 Å).

The layered structure in each sample is clearly visible for both products. Finding a suitable number of edge orientations in the sample was challenging, but an estimated range of 5-10 layers was found during examination of the two polymer versions, namely GB-PVP and GB-HPC. The HRSTEM and SAD analyses are consistent with the structural information from XRD analysis, as the GB material retains the unit cell structure of aqB but exhibits b-axis expansion due to atomic layer modification by the 1,4-butanediol solvent. The b-axis expansion for glycoboehmite compare as $d_{020'}$=17.4 Å ± 0.6 Å from the analysis of six SAD patterns and $d_{020'}$=18.4 Å from XRD. This result is inconsistent with Inoue, et al. (1991) as they documented a smaller lattice expansion. The XRD data in Figure 3-1 as well as Figure 3-2 indicate a much larger opening between the AlO(OH) layers. The presence of the low angle peak (<5° 2θ) dictates a much larger cell expansion for GB compared to the other samples. The very large expansion of the GB interlayer distance (i.e. ~16.4 Å) is slightly larger than twice the end-to-end distance of the 1,4-butanediol molecule alone and suggests a double layer of this molecule between the AlO(OH) sheets of the GB material. GB-PVP or GB-HPC compounds expanded via the polymer intercalation relative to the aqB, but not to the degree of the GB material. These characterizations show that the GB precursor or synthesis environment enables intercalation of the PVP and HPC polymers into the layered structure of boehmite. This is the first example of use of this process for nonionic polymer intercalation into hydrogen bonded interlayers, as will be discussed later in the manuscript. The glycol-based modifications thus make possible new hybrid materials in contrast to the aqB synthesis.

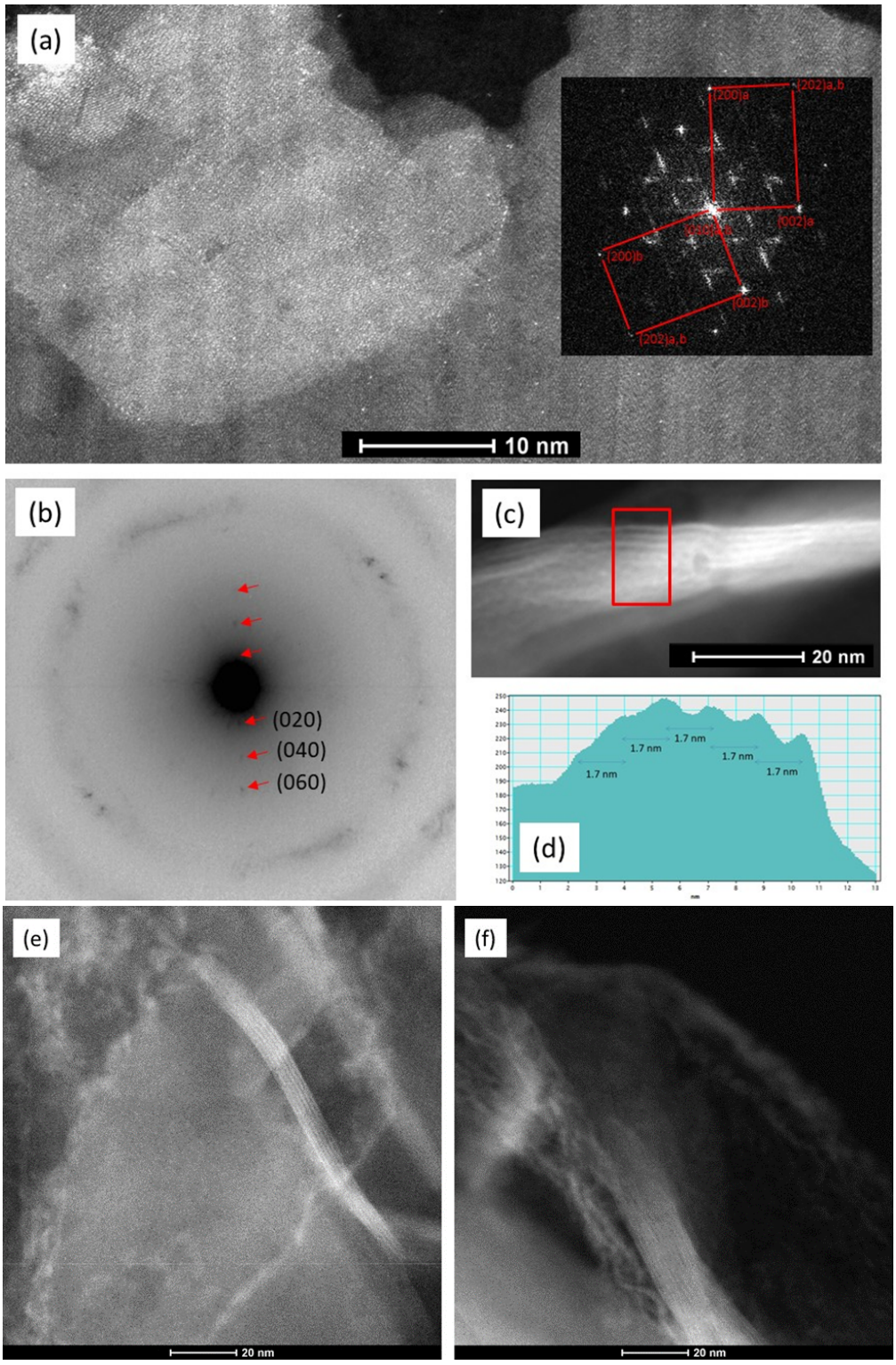

Figure 3-2 Transmission Electron Microscopy images of glycoboehmite materials. (a) HRSTEM image of platelet face with (020) plane normal to the beam direction as shown in the inset Fourier transform (b) Selected-area diffraction pattern (contrast inverted) through glycoboehmite nanosheet (c) HRSTEM image for edge of glycoboehmite nanosheet (d) Integrated intensity profile of glycoboehmite nanosheet edge (e) edge view of PVP-GB nanosheet (f) edge view of HPC-GB nanosheet.

Figure 3-3 shows the SEM images of the products from each synthesis, and significant variation in particle morphology, size, and topology are evident. The magnification in each image is consistent to make the variation in size and structure comparable to visual inspection. The aqB in Figure 3-3a indicates the crystallite size is very small and aggregated in the prepared sample. Edge oriented materials in the image suggest the platelet shape, although the structures may be aggregates of several crystallites. In contrast, the images in Figure 3-3b-d show much larger, flaky particles. Figure 3-3b is the GB material, previously reported to have a "honeycomb" morphology (Inoue, 1989). The samples made here are sheet-like materials, with irregular edges, but a smooth face topology. They are microns in length while being extremely thin. The two samples formed using additional polymers (Figure 3-3c-d) show a nanosheet structure with a greater degree of bifurcation in the sheet, which leads to a more tortuous surface. The density of these bifurcations appears greater for the GB-HPC sample over that of the GB-PVP material.

Peak broadening analysis by the Scherrer equation was used to estimate the effective crystallite size for each phase. The analysis based on the reflections observed in the 6-15° 2θ range so as to achieve relatively consistent comparisons for either the (020) of aqB or the (020)′ peaks from HPG or PVP. For consistency, the GB sample employed the (040)' reflection at 9.76° 2θ. The resulting crystallite size estimates were as follows: aqB (Figure 3-1a) was 3.4 nm, GB (Figure 3-1b) was 9.3 nm, GB-PVP (Figure 3-1c) was 5.5 nm, and GB-HPC (Figure 3-1d) was 5.1 nm. In our evaluation, the GB showed a larger coherence length (~9 nm) along the b-axis direction than the polymer modified phases. This agrees with the larger size and smooth topology of the GB material in Figure 3-3b.

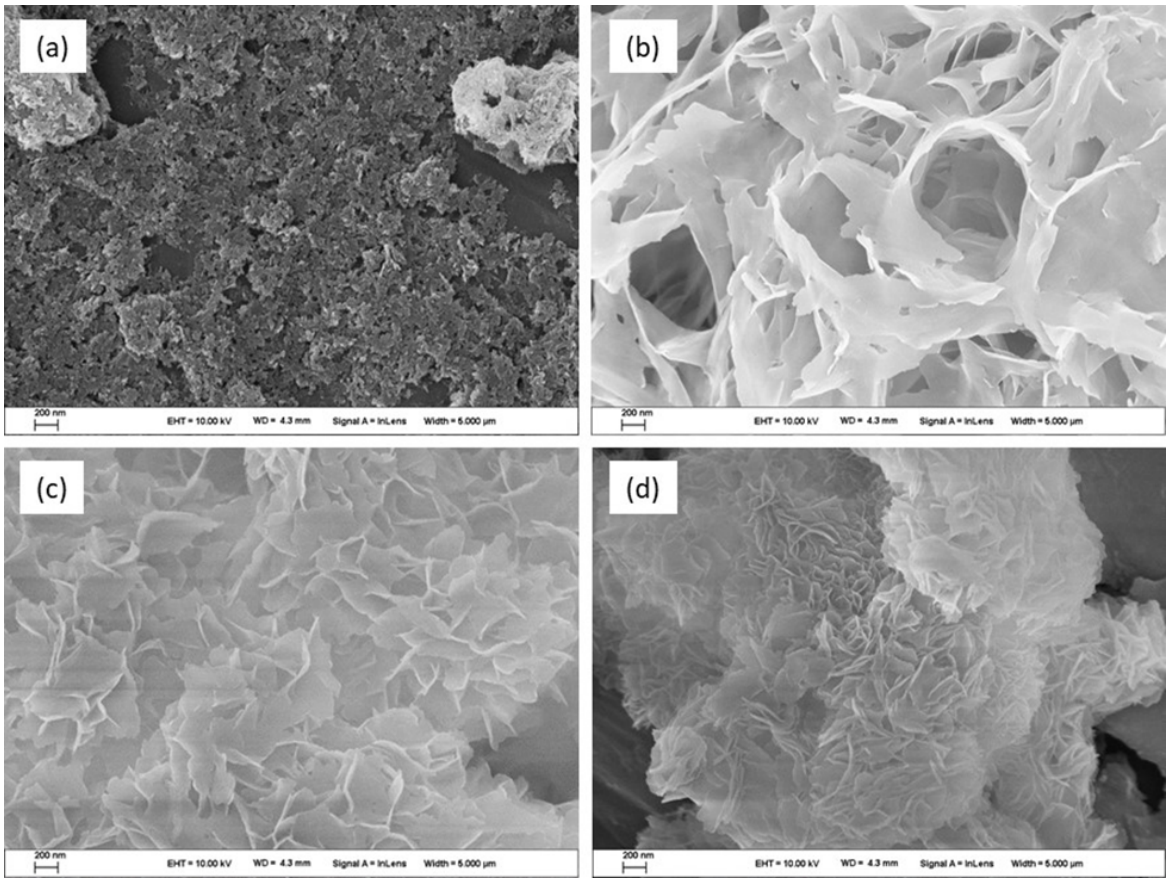

Figure 3-3 SEM images of: (a) aqueous synthesized Boehmite nanopowder (aqB), (b) 1,4-butanediol synthesized Glycoboehmite (GB), (c) Polyvinylpyrrolidone derivative boehmite (PVP-GB), and (d) Hydroxypropyl cellulose derivative boehmite (HPC-GB). Scale bar = 200 nm.

The development of particle morphology during crystal growth is related to nucleation rate, supersaturation, and environmental factors. The growth of aqB vs. GB will be discussed first and extended to the phases containing intercalated polymers. The morphological growth forms of boehmite are sensitive to many factors, including the precursors, temperature, pressure, solution pH, and use of surface growth directing agents. Growth morphologies can vary from nanoparticle platelets (Chiche et al., 2009; Hakuta et al. 1999; Jolivet et al., 2004; Lepot et al., 2008; Mathieu et al., 2007; Yoldas, 1975), nanowires (Buining et al., 1991; Chen et al. 2007; Chen & Lee, 2007; Iler, 1961; Kuang et al., 2003), lamellar (Wu et al. 2013), nanosheets (Chen et al. 2007; Chen & Lee, 2007; Chen et al. 2008; He et al., 2008; Wen et al., 2015), and interpenetrating or intergrown clusters and agglomerates (Cai et al.2009; Hochepied & Nortier, 2002; Li et al., 2010). The proportion of facet dimensions and particle size will also be dependent on nucleation rate and aging, as well as pH (Jolivet et al., 2004).

The synthesis route used in this work is based on alkoxide reaction with water solvent, followed by aging at 95 °C, and prior study of similar systems are found in the works of Yoldas et al. (1975) and Buining et al., (1991). These works treated their alkoxide with acid to form nanowires, having similarity to the aging conditions of Iler et al. (1961). Reaction of an alkoxide precursor with water is rapid and leads to an alkoxide containing amorphous gel (Buining et al., 1991). Boehmite is known to follow *Ostwalds Rule of Stages* in phase transformation through structural rearrangement from an amorphous gel, leading to final formation of boehmite for the Al-H_2O system (Bunker & Casey 2016; Zhang et al. 2018). Temperatures as low as 60 °C have been used to form boehmite in water at pH 9 (Hochepied & Nortier, 2002). Solubility in the Al-H_2O system was measured and modeled for both thermal and salt effects in aqueous conditions from ambient pressure up to hydrothermal conditions of 290 °C (Benezeth et al., 2001; Palmer et al., 2001). In aqueous hydrothermal systems, boehmite shows minimum solubility levels at pH values of 5 -6, and the soluble species in solution is the $Al(OH)_4^-$ anion above pH 6 (Palmer et al., 2001). The solubility rises logarithmically as pH is made more alkaline, and it is clearly the dissolution species. The reaction rate of an amorphous precursor is expected to be more rapid than that of gibbsite $Al(OH)_3$, and will lead to solution species sufficient to precipitate boehmite under elevated temperature annealing in solvent (Bunker & Casey 2016). Development of supersaturation from an amorphous precursor will therefore have a high nucleation rate essential to the formation of nanosized crystallites.

In the approach of this work, no acids, bases, or salts were used, and pH was measured as 5 before thermal treatment. Solubility of Al^{3+} is quite low in neutral conditions without heating (Benezeth et al., 2001). The solubility rises with applied temperature, with a displacement of the solubility minimum to lower pH value and a greater depth. As has been seen in previous literature, boehmite nanoparticles are formed with a platelet morphology in accord with the equilibrium shape and growth rates reported by Jolivet et al. (2004). Literature reports state that water based synthesis at ambient pressure should form as nanosized platelets, with variation from thickness of 5-10 nm and face dimension of 20-35 nm by the method of Yoldas (1975), under acid catalyzed conditions, to the reported values by Chiche et al. (2009), of platelets 6.5 nm thick and 15 nm long. The method used here was similar to that of Lepot et al., using a two stage method (Lepot et al., 2008). Irregular morphology was found at 80 °C, but a second hydrothermal anneal at 200 °C gave very defined rhomobohedral platelets of length 30-80 nm. The morphology of the boehmite nanoparticles by the approach used here is similar to the first stage of the report by Lepot et al., although less regular in topology as a thermal anneal in hydrothermal conditions was not used.

From the SEM images in Figure 3-3, it is clear that the glycothermal route creates much larger nanosheet structures than the aqueous method. Inoue et al. detailed the reaction to form glycoboehmites from gibbsite as a dissolution-recrystallization reaction (Inoue, 1989). The glycothermal synthesis morphologies are described as a “honeycomb” or a curled intergrown cluster. Li et al. reported a similar growth shape for boehmite synthesis reaction in an ethanol-toluene solvent mixture (Li et al., 2010).

Essentially a dehydration reaction, the water reaction product was theorized to dissolve the Al^{3+} ions as $Al(OH)_4^-$ anions similarly to the Al^{3+} speciation in alkaline aqueous condition. The $Al(OH)_4$ species would also be favored by using mineralizers including NaOH or KOH. Inoue et al. used Bayer process Gibbsite with NaOH content as Na_2O ranging from 0.2 to 0.45wt %. (Inoue, 1989).

Growth of the glycoboehmite phase is theorized to nucleate heterogeneously at the surface of the gibbsite precursor where the $Al(OH)_4$ is liberated by the presence of H_2O and/or the KOH used in this work. The morphological expression of the glycoboehmite materials relate to the dissolution rate of the gibbsite and the transport rate to the growing crystal surfaces. Large GB nanosheets as seen here would require that initial surface nucleation is attained, but the rate of the $Al(OH)_4$ generation is low. Slow growth from the initial nuclei by species transport and integration leads to large crystals according to classical treatments of nucleation and growth (Jolivet et al., 2000). The honeycomb morphology would be expressed for systems with high surface area which promote the heterogeneous nucleation rate, and high dissolution of the precursor from small precursor particle size by the Gibbs-Thompson effect. The effect of dissolution and transport was noted by Inoue et al. who showed that ultrafine powders (0.2 micron) generate a phase pure product (Inoue, 1989; Inoue et al., 1988), whereas larger particle size can retain traditional boehmite from a topotactic dehydration and does not experience full dissolution. In later publications, Al isobutoxide was used as precursor (Inoue et al., 1991, 1994). These reports demonstrated more rapid reaction kinetics reaching completion in as fast as 2 hours at 250 °C. Cho et al. also measured reaction rates of gibbsite powders to form glycoboehmite using times of several hours, where pH values must be increased using NaOH, KOH or ammonia base sources (Cho et al., 1996). The work conducted here used KOH as mineralizer with micron size gibbsite particles and required 24 hours to reach completion. The mineralizer content used here is 0.06 wt% to the $Al(OH)_3$ precursor, exceeding the work of Inoue with Na_2O contaminant. Therefore, the lower surface area of the precursor powder and heterogeneous nucleation rate on micron sized Gibbsite used here is key to the formation of the larger sheet-like structures.

The GB-PVP sample in Figure 3-3c has a higher tortuosity and GB-HPC is even higher in crystal interpenetration. The synthesis approach used for the intercalated glycoboehmite phases was a modification of the GB preparation. The polymers were added to the synthesis reaction and the temperature was reduced to 220 °C, on the assumption that lower temperature would have a lower probability of polymer degradation in the glycol solvent. PVP and HPC are both nonionic polymers with good solubility in polar solvents. PVP is commonly used for particle dispersion and has shown surface affinity in aqB synthesis (Farahmandjou & Golabiyan, 2019). HPC has more complex aqueous solution behavior with liquid crystalline properties but is shown to form gel layers at elevated temperature (Makarova et al., 2013). Both systems are expected to impact crystal growth by surface adsorption. Transport species will be mobile through the surface polymer layer and must nucleate within the adsorbed polymer layer.

The morphological expression of the product phases GB-PVP and GB-HPC differ from GB in tortuosity but not in the inorganic layered structure. This indicates that the dissolution-recrystallization chemistry is identical to the GB process and based on an $Al(OH)_4^-$ species. Heteronucleation from the Gibbsite seed is expected but now within an adsorbed polymer layer. Such a surface adsorbed layer will slow the $Al(OH)_4^-$ diffusion rate. This will change in twinning/intergrowth frequency by locally exceeding the supersaturation level at the growing phase. The higher tortuosity in HPC could be an artifact of the local molecular weight. The PVP polymer has a molecular weight of 10,000, whereas HPC is at 100,000 grams/mol. If the HPC inhibits transport more than the PVP, via either thickness or chemical structure, then more nucleation or twinning events would be expected.

The intercalation behavior in the GB variants indicates surface modification of the interlayer structure by the polymer. Alcothermal reactions within layered systems are known to affect properties of interlayer

environments, as seen in kaolinite by Komori et al. (2000), and by Tunney and Detalier (1996b). The surface modification of kaolinite is known to affect surface properties including rheology and delamination properties (Gardolinski & Lagaly, 2005a, b). aqB is known to have attractive forces between the interlayers that form a structured zig-zag series of H-bonds (Holm et al., 1958). In GB, the solvent intercalation should disrupt the regular H-bond network in GB interlayers. In the presence of polymer layers during growth, the polymers may exhibit stronger bonding interaction that that of the glycol solvent, displacing it while capturing the polymer in the interlayer. The incorporation of the nonionic polymers shows that the association of the PVP and HPC are favorable during the inorganic boehmite growth, unlike that of aqB in water. This would require a stronger adsorption energy than that of 1,4-butanediol There is perhaps precedent for then from the comparison between multiple glycols in the GB synthesis. Inoue specifically highlighted the performance of the 1,4-butanediol solvent as superior to other glycols, as the 1,4-butanediol chains are stated to have more conformational flexibility leading to improved phase transformation rates (Inoue, 2004). The two polymers are nearly identical in the expansion of the interlayer distance by PXRD. However, it will be shown these polymers differ in swelling from adsorbed water or glycol solvent in the thermal analysis section. HPC and PVP differ chemically and in molecular weight. Both are hygroscopic, but also can dissolve in glycols. With this number of variables between the examples tested, more definitive exploration must be the subject of a future work.

3.3.2 Zeta Potential

The surface chemistry in water of each material was investigated using zeta potential titrations to compare the surface charging response to pH and the position of the isoelectric point (IEP) of each material. Figure 3-4 presents the titration curve for each material in 10^{-3} M KNO_3 electrolyte solution. In boehmite, Chiche et al. (2011) highlighted the influence of the crystal faces expressed in each nanocrystal, as (010) basal planes are not known to exhibit charging reactions with protons, thus being electrically neutral (Jonsson et al., 2011). Only the edge faces in boehmite are expected to exhibit proton exchange reactions, on the (100), (101), and (001) faces. The position of the IEP is affected by the proportion of those edge planes. Chiche et al. found that IEP could vary from 8.9 to 10.2. The lower value was attributed to (101) terminated nanocrystals, while (001) and (100) facets were responsible for more basic values of IEP. The boehmite sample tested here meets the range of values reported by other studies, with an IEP near 8.6. The magnitude of the developed charge in the plateau regions also is similar to that of Chiche et al., near +35 mV at pH 4 – 6, and -30 mV at pH 10.

The glycothermally produced materials all exhibit zeta potential behavior that differed from standard boehmite, with shifts in IEP to lower pH values, and much stronger electrical potential values under alkaline pH conditions. The glycoboehmite system has the lowest IEP, with the largest variability between the five measurements of 5.2 to 6 for IEP. The GB-PVP system has IEP values ranging from 6.5 to 7, and the GB-HPC has the most consistent IEP at 7.0. These are all significantly lower than boehmite (aq). The nanosheet face surface chemistry is expected to be dominated by the chemisorption of the 1,4-butanediol solvent to the (010) surface, and thereby also creating a neutral charging state for the majority of the particle surface. The edge groups again are expected to be the charge bearing aspects of the materials. The variation in the IEP and development of charge relate to the chemisorption of the 1,4-butanediol molecules in the glycoboehmite structure.

The development of the zeta potential is similar for each material as well, with weaker strength under acid pH values, but much higher values under basic conditions at -70 mV near pH 10. Neither of the polymer intercalated samples exhibit significant IEP shifts from the glycoboehmite material, and as both PVP and HPC polymers are non-ionic, we conclude that the charging groups are non-coordinated by the polymer. Each polymer intercalation material does raise the IEP marginally from the glycoboehmite material itself, which shows that the influence of interlayer spacing for these polymer intercalated compounds is less

critical or dominated by the polarity of the polymer for the charging behavior of edge surface hydroxyl groups.

The development of zeta potential vs. pH is related to the acid-base properties of surface groups, which are primarily modeled as surface -OH species. By summing over the variations of surface groups and their acid dissociation constants (pKa), the surface response can be modeled for a material. Jolivet used the multisite ion complexation approach based on Hiemstra et al. (Hiemstra et al., 1999; Jolivet et al., 2004). In boehmite, the protonation behavior is related to the coordination with Al ions in the crystal lattice, where greater coordination leads to more acidic properties. With this model, they determined that the (010) facets have a weak positive charge but do not have protonation changes over the pH range of 4 to 12, and therefore do not play a strong role in determination of the isoelectric point (IEP). This is evident in the aqB data as the zeta potential approaches a nearly constant value as pH is decreased. Chemical species at the (101), (100) and (001) edge facets all have pKa values of 9.28 or 9.91, which when averaged over the entire particle surface lead to an IEP of ~ 8.5, in agreement with surveys of literature values on boehmite (Kosmulski, 2003). The results in Figure 3-4 for aqB are in agreement with these prior reports. The greater shift in the isoelectric point for the GB based materials indicates a shift in the surface chemistry properties in these materials, which has not been reported before.

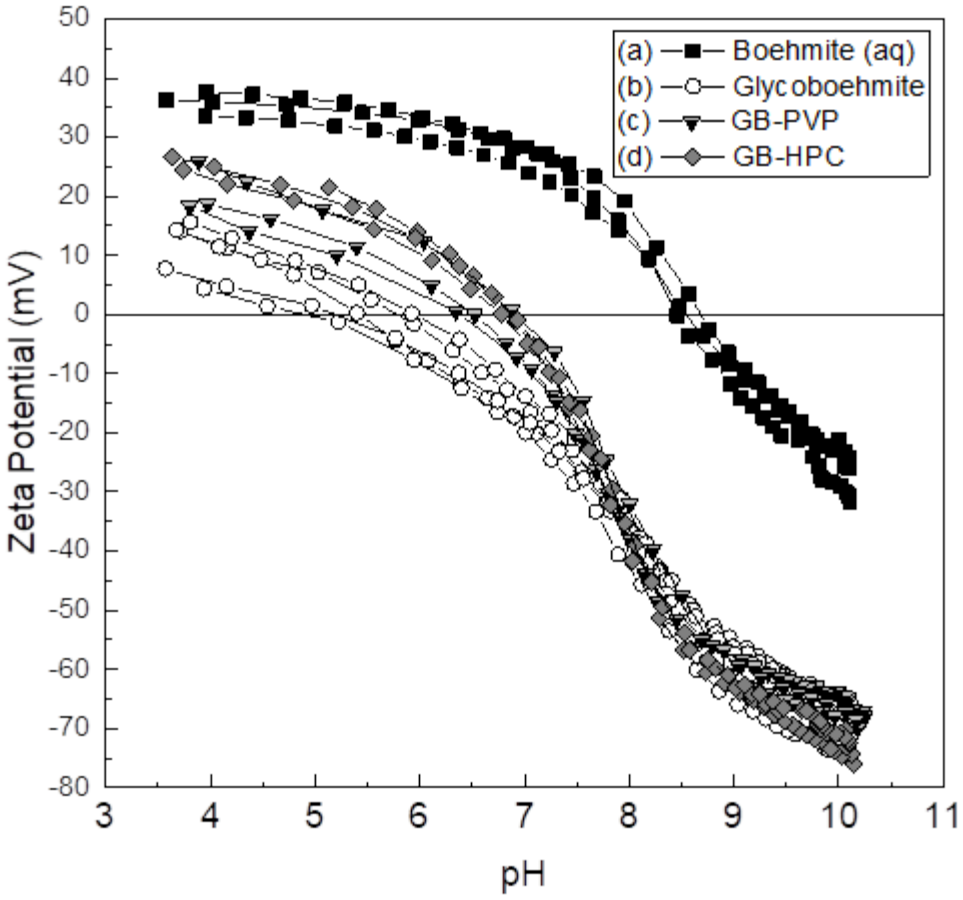

Figure 3-4 **Zeta Potential Measurements for each boehmite material. Three or more measurements are presented for each material with lines to guide the eye.**

In considering the surface groups on GB based materials, we note that strong zeta potentials were found at pH 10, and this requires a significant presence of negatively charged groups. Surface bonded 1,4-butanediol on the (010) surfaces would present a surface like that of n-butanol. The ionization constant of n-butanol is 16.1, and it is therefore unlikely that the (010) surface of the GB compounds has strong charging behavior. The edge groups of the GB compounds therefore would be more likely to have hydrolysis of glycol to create hydroxyl groups at defects and behave more like that of aqB surfaces. Therefore, the acidity of these groups appears stronger than traditional boehmite.

The character of these edge sites is difficult to probe directly at the dimension of the materials produced here. A definitive treatment of the surface charging behavior in GB will require a future study, but potential reasons for the charging behavior can be postulated. First, it is possible that there are greater defects at the surface that increase coordination of surface oxygen or -OH groups. Franks and Gan described that increased coordination of surface oxygen lead to greater acidic properties (Franks & Gan, 2007). Motta et al. used DFT-MD modeling to obtain similar results that Al ion coordination of bridging oxygens led to more acidic behavior (Motta et al., 2012). This would require that there are a higher number of defect groups at these edges. Curvature at these edges may make this hypothesis valid. Alternatively, the edge groups of the glycothermally produced materials are expected to have partial coordinations with glycol rather than the interlayer hydroxyl groups. These would be the interlayer glycols rather than the surface hydroxyl groups. In the MUSIC model, the effect of ion coordination in the Al-O bond is affected by the bond length as well as the cation coordination number. Shorter bond length Al-O would increase the polarity of the bond and affect the acid base character. As a model, this would be similar to the octahedral distortion of an alkoxide precursor. In the GB structure, the interlayer regions contain the intercalated glycol. This region will affect the wetting behavior at the edge surface. Isolation of these effects is beyond the scope of this work and will be investigated in a future publication.

3.3.3 Organic Content Characterization

FT-IR spectroscopy was performed on the boehmite (aq.) and glycoboehmite products after drying under a vacuum (70 °C) for 48 hours. The spectra and resulting peaks are presented in Figure 3-5. Aqueous synthesized boehmite was examined as a reference for the vibrations in boehmite and matches well with the literature values for IR spectral vibrations (Feng et al., 2008). The large peaks at 3290 and 3087 cm^{-1} are typical values of the -OH stretch vibrations, as seen by Ram (2001), and modeled by Tuniga et al. (2011). Adsorbed water is expected to create a band at 1645 cm^{-1}. The aqueous boehmite has the O-H bending vibration at 1155 cm^{-1}, the Al=O stretch at 1068 cm^{-1}, and the torsional mode of the AlO_6 octahedra is assigned at 727 cm^{-1}. There is also a weak peak at 881 cm^{-1} which may be an Al-OH_2 bending mode, identified in some samples by Tettenhorst and Hofmann (1980).

The glycoboehmite sample contains less intense peaks in the -OH stretching region between 3500 and 3000 cm^{-1}, and a more evident trio of -CH_2 peaks at 2938, 2910, and 2861 cm^{-1}, as expected from the intercalation of 1,4-butanediol molecules (Inoue et al., 1991). The -OH bending vibration is altered into two peaks at 1170 and 1118 cm^{-1}, as seen by Inoue et al. (1991). The Al=O stretch matches boehmite at 1066 cm^{-1}, as does the torsional vibration of the AlO_6 octahedra at 727 cm^{-1}. Additional peaks attributed to the intercalated 1,4-butanediol are evident at 947, 877 and a shoulder at 781 cm^{-1}. These are somewhat shifted from that of Inoue, but the reason for the variation is unknown.

Samples GB-PVP and GB-HPC exhibit clear variation from the previously reported materials. In Figure 3-5c, GB-PVP has a single, broad -OH stretch vibration at 3286 cm^{-1}, and a strong set of vibrations at 2937, 2910, and 2867 cm^{-1} which are common in -CH_2 vibrations from the polymer chain and side groups of polyvinylpyrrolidone. The structural vibrations of the Al-O bonds are very similar to boehmite at 1124, 1045, and 866 cm^{-1}, as the O-H bending vibration, Al=O stretch, and an Al-OH_2 bending mode. There is a characteristic peak at 1659 cm^{-1} for the pyrrolidone C=O group, confirming carbonyl moiety from the

PVP. Broadening of the characteristic C-N peak also occurred. There are a series of peaks in the region from 1500 to 1200 cm^{-1} (1473, 1430, 1386, and 1209 cm^{-1}), which are attributed to the vibrations of the -CH_2 groups of PVP. Finally, the peaks at 865, 792, and 765 cm^{-1} are like the glycoboehmite peaks attributed to the intercalated 1,4-butanediol reaction solvent.

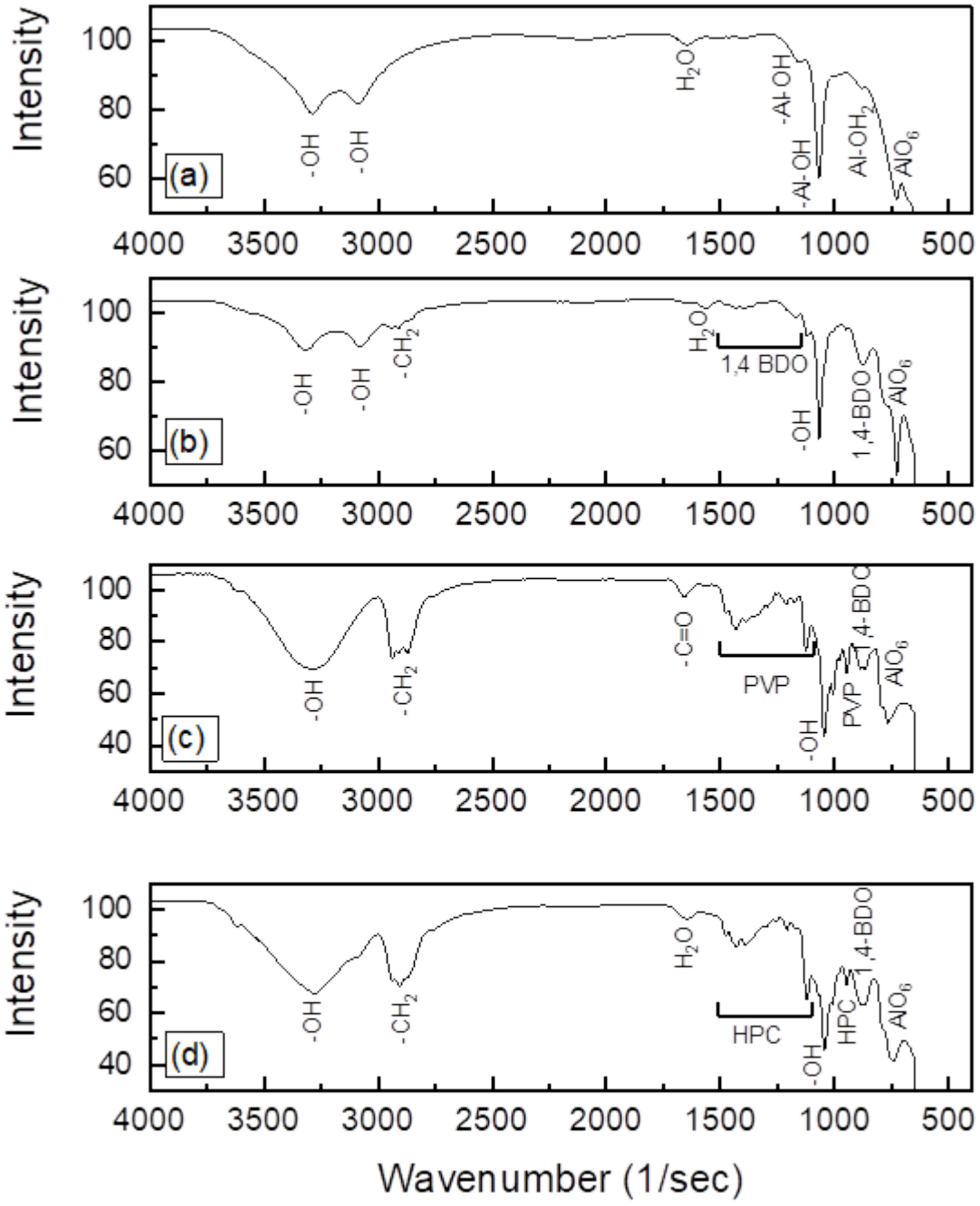

Figure 3-5 **FT-IR data: (a) aqueous synthesized Boehmite nanopowder, (b) 1,4-butanediol synthesized Glycoboehmite, (c) Polyvinylpyrrolidone derivative boehmite (PVP-GB), and (d) Hydroxypropyl cellulose derivative boehmite (HPC-GB).**

The GB-HPC sample likewise shows strong peak additions from the HPC polymer and matches the fingerprint region below 1100 cm^{-1} with the GB-PVP sample. There is a strong set of peaks common to the -CH_2 vibrations at 2931, 2906, 2870, and 2763 cm^{-1}, and the -OH stretch vibrations are centered at 3280 cm^{-1}. The -OH stretch vibration in GB-HPC has a less Gaussian profile than the GB-PVP, but the main character is still present. Again, the Al-O vibrations for the O-H bending vibration at 1120 cm^{-1}, the Al=O stretch at 1043 cm^{-1}, and an Al-OH_2 bending mode at 879 cm^{-1} are all similar to GB-PVP and the glycoboehmite samples. There are other characteristic peaks at 1009 and 946 cm^{-1} that are attributed to the HPC polymer in the sample.

The presence of organic material was further characterized using TGA/DSC analysis. Figure 3-6 provides the results of thermal testing in both air and argon environments. Figure 3-6a and Figure 3-6c contrast the TGA data in air and argon but find broad agreement, while DSC results are in Figure 3-6b and Figure 3-6d. Ultimately, glycoboehmite and boehmite have comparable mass loss by 800 °C, although glycoboehmite is marginally greater. This is expected from the intercalated glycol. Higher temperatures are needed to burn out the intercalated solvent and glycol. The glycoboehmite becomes white after calcination in air, and black in Ar indicating that carbonization is occurring in Ar.

The behavior of boehmite in argon shown in Figure 3-6a matches well with prior examination of Alphonse and Courty (2005), who performed a detailed analysis of the dehydration of boehmite. There are three primary stages; an endothermic mass loss at 200 °C occurs first, followed by a broad endotherm ending before 500 °C. The final stage involves continual mass loss up to 900 °C, to a total loss of ~30% of the initial material mass (i.e. sum of Mass Loss 200 °C and Mass Loss 200-550 °C). These stages are interpreted as relating to the loss of physically adsorbed water, the dehydration conversion into γ-Al_2O_3, and the loss of residual hydroxyl groups. Table 3-2 compares the mass losses in the four samples studied here. This is based on the three stages known in boehmite, (1) where mass lost up to 200 °C is assumed to be physisorbed solvent (water/glycol), (2) the mass lost between 200 and 550 °C as intercalated organics or dehydration of boehmite to γ-Al_2O_3, and (3) the final mass at 800 °C as dry γ -Al_2O_3. The solvent fraction is determined as the mass loss below 200 °C, divided by the mass at 800 °C. The intercalation fraction represents the content of bound glycols and/or intercalated polymer materials. It is calculated as the Mass loss in the thermal range of 200 to 550 °C, with respect to the % Mass at 800 °C. The solvent fraction and intercalation fractions give mass ratios for adsorbed solvent, and intercalated organics in each of the materials.

The boehmite phase behaves similarly to previous results of thermal dehydration data, with a mass loss at 800 °C of 23% composed of 0.076 solvent fraction, and internal water equal to the expected ratio of 20% (Alphonse & Courty, 2005). For the glycoboehmite, mass loss is low at ~ 4% up to 216 °C, which corresponds well with the boiling point of 1,4-butanediol (216 °C) and is interpreted as the retained material that was poorly washed out or intercalated into the interlayer structure. After the initial decrease, a total mass loss of < 25% is noted up to approximately 650 °C, which is qualitatively similar to the behavior of boehmite.

For the polymer intercalated phases, the adsorbed value of water is very high in the GB-PVP sample, at 60% mass loss up to 200 °C. The solvent fraction is well above pure surface adsorption, by a factor of nearly 2.2. This greatly exceeds what is realistic for either a single- or double-layer concentration of the PVP as a surface polymer coverage. As the mass loss is below 200 °C, the excess mass should relate to the presence of residual solvent. In contrast to GB, the endothermic loss for these samples is at 185 °C (1,4-butanediol b.p. 216 °C). Water is a byproduct of the synthesis reaction, and PVP polymers are known to be highly hygroscopic. It is believed that water is present in the swollen PVP interlayers therefore, rather than the glycol alone.

Table 3-2 Mass calculations for physiosorbed solvent and intercalated polymer content in alumina compounds. Values are normalized to a unit mass from the initial mass.

Compound	Mass Loss 200 °C	Mass Loss 200 - 550 °C	% Mass at 800 °C	Solvent Fraction	Intercalation Fraction
Boehmite (aqB)	0.0583	0.1565	0.7698	0.076	0.20
GB	0.0407	0.1862	0.7566	0.054	0.25
GB-PVP	0.6031	0.1100	0.2770	2.177	0.40
GB-HPC	0.2190	0.2403	0.5283	0.414	0.45

GB-HPC also experiences a solvent loss up to 200 °C, but the extent is only 22%. Its solvent fraction is also larger than GB, at 0.414 but is a manageable content for HPC polymer. Above this temperature both polymer adducts show mass loss continuously, until 500 °C in air, or 550 °C in argon. GB-HPC loses about 23% by mass, whereas GB-PVP loses an additional 11%. The presence of water in that interlayer would expand the layer distance therefore, and this helps explain the near equal swelling distance for the two polymer systems. The mass content for each polymer is represented as the intercalation fraction as 0.40 and 0.45 for the PVP and HPC derivatives. These values are quite similar despite the variation in the molecular weight of the polymers used (10,000 for PVP and 25,000 for HPC). The polymers while nonionic, have variable structure and solvation properties for both water and 1,4-butanediol solvents. The chemical structure of PVP and HPC are not identical. PVP can have surface interaction via the pyrrolidone group and a random solvated polymer radius in solution, whereas HPC is known to exhibit solubility with liquid crystal behavior and an upper solution solubility limit. As there are several variations between these samples, it remains a subject to investigate why the swelling and conformation of the polymers between inorganic sheets arrive at a similar value.

Degradation of the organic components provides another verification of the presence of the polymer layers. In the DTA data of Figure 3-6b,d, it is possible to examine the thermal degradation of solvents, hydroxyl groups, or polymer materials for each sample. Endothermic peaks in both GB-PVP and GB-HPC materials are present by 190 °C, proving the mass losses are related to solvent evaporation. In air, the mass loss behavior for all the glycothermal samples between 190 and 500 °C relates to exothermic peaks, as would be explained by the oxidation of organic groups. Under an argon atmosphere, none of the exothermic reactions take place. While in air the PVP sample has two exotherms, which are assigned to the burnout of the PVP sidegroups at 225 °C, and the polymer backbone at 420 °C. The GB-HPC appears to have three exothermic events, at 215, 375, and a weaker event at 410 °C. These are attributed to the progressive loss of sidegroups, glucose ring breakdown, and the combustion of the residual cellulose fragments.

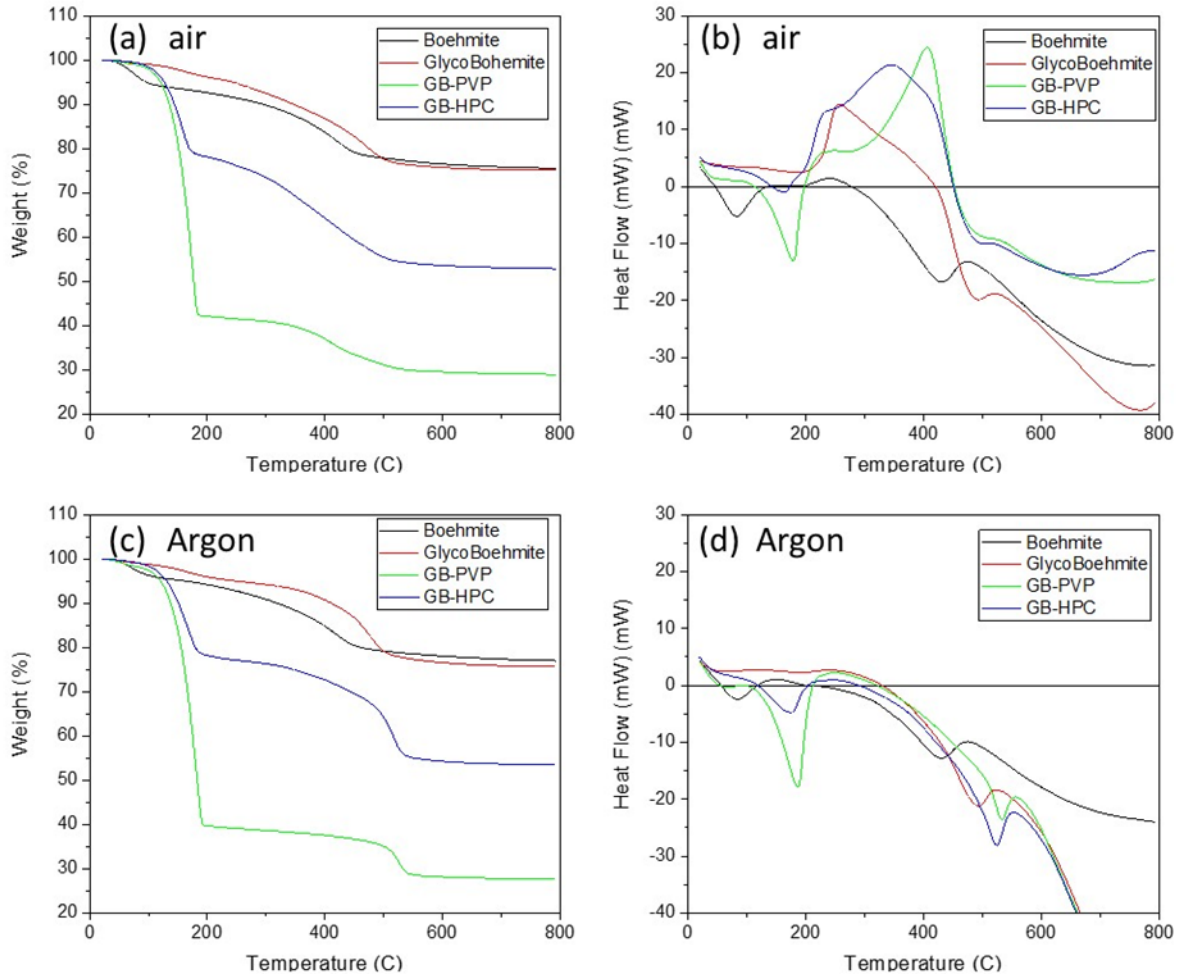

Figure 3-6 TGA/DTA data for each material: (a) TGA in air, (b) DTA in air, (c) TGA in argon, and (d) DTA in argon.

3.3.4 Thermal Phase Conversion

The impact of a calcination treatment of these materials was also studied for the effect on specific surface area, due to the application of boehmite as an absorbent material. The conversion of boehmite to γ-Al_2O_3 is well known to occur from 450 to 550 °C (Iler, 1961). Table 3-3 shows the specific surface area resulting from varying thermal treatments. The BET surface areas in boehmite are initially reflective a very small particles, but conversion to gamma alumina at 600 °C lowers the surface area via aggregation and the formation of new grain boundaries. The glycoboehmite material behaves similarly to aqB, with a reduction in surface area. The removal of the interlayer glycol does not prevent some consolidation. The two polymer intercalation phases have initial surface area results that are lower than the non-polymer compounds. Yet post calcination, both increase in surface area, with the GB-HPC sample having the largest surface area of all the samples. The phase transformation involves the loss of H_2O from the normal crystal structure, but the stages of combustion of the organic polymers in the intercalated compounds may cause further expansion or prevent contact in the GB-PVP and GB-HPC materials. Finally, the HPC adduct has the broadest exothermic set of events from 200 to ~440 °C. This continuous reaction may be the reason for the development of larger surface area compared to the PVP system.

Table 3-3 Surface Area measurements for thermally processed Boehmite materials.

Sample ID	Treatment/Prep. (in air)	BET surface area (m^2/g)	Treatment/Prep. (in air)	BET surface area (m^2/g)
Boehmite (aqB)	heated 100 °C for 2 hours	180.6	heated 100 °C for 2 hours and calcined 600 °C	153.6
GB	heated 100 °C for 2 hours	135.5	heated 100 °C for 2 hours and calcined 600 °C	124.4
GB-PVP	heated 100 °C for 2 hours	133.0	heated 100 °C for 2 hours and calcined 600 °C	166.9
GB-HPC	heated 100 °C for 2 hours	60.3	heated 100 °C for 2 hours and calcined 600 °C	174.4

3.4 Conclusion

New hybrid materials based on the Boehmite phase of oxyhydroxide alumina were successfully synthesized using the glycothermal approach. The use of the glycol solvent system creates an *in situ* surface modification of the boehmite layers by glycol esterification, and thereby changes the bonding forces between the atomic layers. Synthesis using polyvinylpyrrolidone or hydroxypropylcellulose polymers are successfully intercalated into the atomic structure which further expanded the b-axis of the unit cell. The new hybrid phases exhibit increased calcined surface area, stronger surface acidity, and a variation in thermal transformation properties from aqueous synthesized boehmite. This validates the hypothesis that modifying H-bonding from surface –OH groups will enable polymer adsorption to direct crystal growth. This also enabled the formation of a higher surface area adsorbent material post-calcination in comparison to the aqueous phase boehmite.

4. Hydrothermal Experiments for Key Engineered Barrier System Materials

4.1 Background

4.1.1.1 EBS Concepts in Crystalline Rock

The EBS in crystalline rock consists of the waste canister overpack, bentonite buffer, cement liner, and host rock (Figure 4-1), similar to designs for argillite-hosted repositories. Crystalline rock has many favorable characteristics that contribute to waste package longevity, including stability of excavated tunnels, favorable (i.e., reducing) chemical conditions, and low porosity/groundwater fluxes (e.g., Anderson et al., 2013).

Unique concerns for repositories hosted in crystalline rock are related to the physical properties of the host rock, which allow for the sustained presence of natural and manmade fractures. Interconnected networks of fractures can create pathways for radionuclide transport away from the repository near field (e.g., Figueiredo et al., 2016); therefore, the waste canister overpack and bentonite buffer are relied on for radionuclide retention for long term repository function (e.g., Mariner et al., 2011).

Colloid-mediated transport of radionuclides has been identified as a possible concern for crystalline rock hosted repository systems. Colloids, 1 to 1000 nm suspended particles, are present in natural groundwaters and can be formed from bentonite erosion. The hydraulic conductivity of the bentonite buffer when fully saturated is expected to be sufficiently low to prevent transport of radionuclides away from the canister and colloids are expected to be filtered by the low porosity of the bentonite (Missana and Geckis, 2006). However, bentonite colloid formation at the outer edge of the EBS, adjacent to the host rock and in contact with a fracture or flow pathway, may lead to transport of radionuclides away from the repository near field (Missana et al., 2003; Möri et al., 2003; Missana and Geckis, 2006) (Figure 4-1).

Therefore, colloid-facilitated transport must be considered in assessments of crystalline-rock hosted repository systems and has been examined in experiments at URL sites (e.g., Möri et al., 2003; Missana and Geckis, 2006; Kurosawa et al., 2006; Reimus, 2012) and laboratory scale experiments (Missana et al., 2008; Dittrich et al., 2015; Telfeyan et al., 2020).

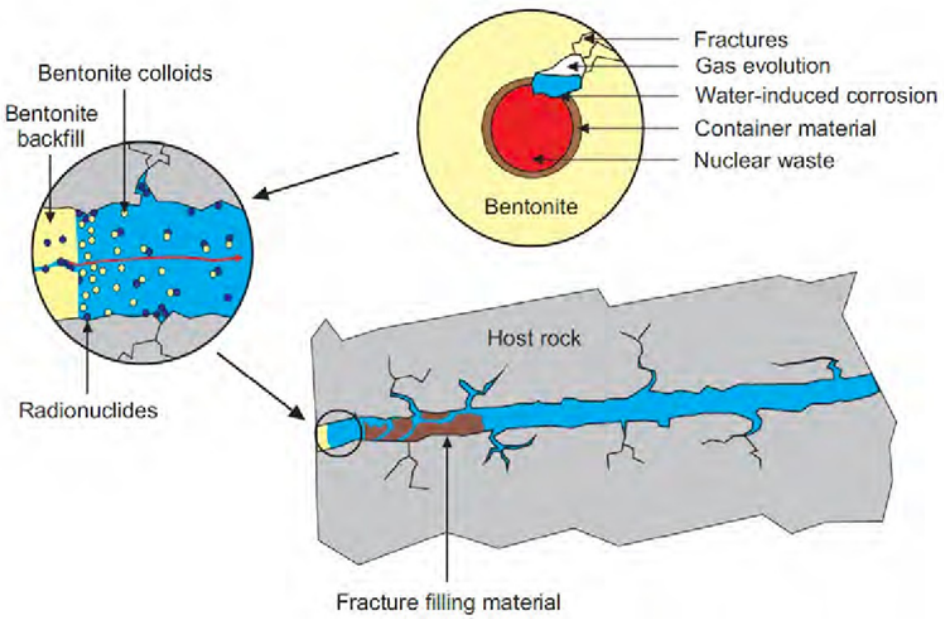

Figure 4-1 Possible scenario for bentonite-colloid facilitated transport of radionuclides away from a corroded waste package. Waste Package breach coincides with fracture formation in the bentonite buffer and the formation of bentonite colloids at the buffer hose rock interface. Radionuclides sorbed to colloids are transported away from the EBS via fractures in the host rock. (Figure from Missana and Geckis, 2006)

Crystalline rock repository concepts have been evaluated in long-term, full-scale, in situ demonstrations at underground research facilities and laboratory experiments, mostly at temperatures <100°C. Foreign repository programs have extensively vetted repository designs, especially Sweden and Finland who have each submitted license applications for repository operations in crystalline rock. Buffer temperature limits in these cases are 100°C. The FEBEX heater test at the Grimsel Test Site was an 18-year long full-scale EBS demonstration in crystalline rock which included a heater that maintained a temperature of 100°C at the dummy canister surface. In the FEBEX experiment, smectite alteration was only observed close to the heater surface (~10 cm) and included recrystallization to saponite and chlorite, accumulation of magnesium near the heater, and decrease in clay mineral cation exchange capacity (CEC) and surface area (Fernandez et al., 2017).

To address the temperatures involved with the disposal of DPCs, there is a need for higher-temperature, full-scale experiments to characterize the changes in bentonite physical and chemical properties. The planned HotBENT (High Temperature Effects on Bentonite) experiment performed by NAGRA at the Grimsel Test Site in the same drift as the FEBEX experiment, is in its initial stages and is ongoing. The experiment will run for 15 to 20 years and will be dismantled over five years (AMBERG, 2019). The peak temperatures will be between 175 to 200ºC. Results will be very useful for evaluating potential alterations to bentonite mineralogy and physical properties in a high temperature crystalline rock repository setting.

4.1.1.2 Previous Research in Bentonite−Portland Cement Interaction

There have been many studies on the interaction of bentonite and cementitious materials in EBS systems as both materials are integral to most repository designs (e.g., Karnland, 1997; Cuevas et al., 2006; Savage et al., 2007; Watson et al., 2009; Fernández et al., 2009; Savage et al., 2010; Watson et al., 2018). Cementitious materials, such as shotcrete, cast-in-place, and/or pre-formed cement blocks, are necessary

elements of repository infrastructure and provide ground support to maintain drift integrity and prevent collapse. However, the reaction of cement with water may have a significant chemical effect on the repository system through the dissolution of portlandite ($Ca(OH)_2$), alkali-rich phases, calcium silicate hydrate (CSH) minerals, and other reactive components of the cement (e.g., sulfates). Thus, cement reactions have the potential to release significant amounts of OH^- and Ca^{2+} into the groundwater migrating into the EBS system, leading to increase in pore water pH in the bentonite buffer, montmorillonite dissolution, and the formation of diverse secondary mineral phases (e.g., Ca-zeolites, CSH phases, feldspars). Cement-bentonite interaction is observed to be a non-linear system that involves multiple coupled processes that occur simultaneously and affect each other (e.g., Savage et al., 2007). These processes include the reaction of concrete to release Ca^{2+} and OH-, transport of hydroxide and cations into bentonite, montmorillonite ion exchange and dissolution, precipitation of secondary phases, dissolution of accessory minerals, and porosity and swelling changes (Savage et al., 2007).

The potential for significant and wide-ranging geochemical and mineralogical effects of bentonite-cement interaction has led repository programs to implement a pH limit for cement porewater (e.g., SKB, pH < 11). The pH limit is achievable using low pH cements that replace traditional cement components (e.g., limestone aggregate) with siliceous materials (e.g., fly ash and silica fume) resulting in the reduced abundance of portlandite in the cured product and a lower Ca/Si ratio in the CSH minerals (Calvo et al., 2010; Lothenbach et al., 2011). Due to the potential for bentonite degradation in alkaline pore waters, low pH cement formulations are becoming increasingly standard for repository concepts. The experimental work presented in this report focuses on the effects of cured Ordinary Portland cement (OPC); next phases will evolve to include low pH formulations.

Observations from long-term, full-scale, in situ demonstrations at underground research facilities provide insight into cement-bentonite interactions in the natural environment, including potential effects on groundwater geochemistry, host-rock properties, and hydrologic processes. Several full-scale experimental studies at underground research laboratories in crystalline rock have been conducted, including the PR (Prototype Repository) at the Äspö Hard Rock Laboratory in Sweden (Johannesson et al., 2007) and FEBEX at the Grimsel Test Site (Martin et al., 2006). Observations of cement-bentonite interaction after 13 years in the FEBEX demonstration are reported in Alonso et al. (2017) and Fernández et al. (2017). The FEBEX experiment consisted of a heater that was held at 100ºC resulting in an observed maximum temperature of 28ºC in the concrete liner (Martinez et al., 2016).

Therefore, the observed alteration was likely due only to water-rock interaction, and not temperature effects. Important observations, reported in Alonso et al. (2017) and Fernandez et al. (2017), include that both the shotcrete plug and bentonite experienced alteration due to groundwater interaction. In the concrete, portlandite dissolution occurred at the host rock- concrete interface and CSH phases in the concrete were altered due to the incorporation of aluminum, sulfur, and magnesium. At the bentonite-concrete interface, the main alteration mineral observed was ettringite ($Ca_6Al_2(SO_4)_3(OH)\cdot 26\ H_2O$), indicating that the breakdown of sulfur-rich phases in the bentonite, concrete, and/or sulfur sourced from the groundwater resulted in mineral precipitation (Alonso et al., 2017). In the bentonite, alteration was mostly limited to the immediate interface zone, mostly in the form of precipitation of Mg-rich phases and the change in exchangeable cations in the bentonite (Fernandez et al., 2017).

These results highlight the potential for alteration at the cement-bentonite interface at ambient temperatures in a realistic crystalline rock repository scenario.

4.1.1.3 Steel Canister—Clay Interface Zone Alteration in Crystalline-Hosted Repository

As discussed above, the U.S. DOE is interested in exploring the disposal of larger waste packages with higher thermal loads. The large amount of SNF in the waste packages, therefore, has the potential to

generate temperatures at the waste package surface in excess of 200°C for long periods of time. The interface between the metal canister and the bentonite barrier in a backfilled repository EBS concept will likely undergo chemical reactions due to the elevated temperatures and infiltration of groundwater. The effect of these high thermal loads and the presence of an aqueous fluid will produce corrosion of the surface of the metal canister, and likely mineral reactions between the steel corrosion products and the bentonite in close proximity to the canister.

This report focuses on the interaction of the EBS and candidate steel overpack materials in a crystalline rock environment. Design concepts for a crystalline rock repository in the United States are still being explored, but the current base case in crystalline rock includes stainless and carbon steel (Matteo et al., 2016). In comparison, all foreign repository designs in crystalline rock include a copper waste package overpack with cast iron inserts to maintain canister structure. Crystalline rock is thought to be a less robust natural barrier in comparison to other host rock lithologies, such as clay and salt. Therefore, in crystalline rock, the waste package is relied on as the primary mechanism to prevent radionuclide release. Copper is selected in repository designs developed by foreign countries due to its corrosion-resistant nature under anoxic conditions and is thought to provide a long-term barrier. Copper, however, will be susceptible to corrosion due to chloride and sulfide, which must be accounted for in the groundwater, EBS, and host rock.

4.1.1.4 Formation of the Fe-Oxide Layer on Steel

The steel will corrode at the bentonite buffer interface in the presence of oxygen according to one of the following reactions (aerobic corrosion) (Kursten at al., 2004):

$$4\ Fe^{o} + 3\ O_2 \rightarrow 2\ Fe_2O_3 \qquad \textbf{Eq. 4-1}$$

$$2\ Fe + 2\ H_2O + O_2 \rightarrow 2\ Fe(OH)_2 \qquad \textbf{Eq. 4-2}$$

The corrosive reaction (Eq. 4-2) can be fairly fast for carbon steel, whereas corrosion can be slowed for stainless steels by an oxide film (i.e., Fe-oxide). The oxide film will act as a protective coating against further corrosion in the effect called passivation. In an alkali solution where a porous $Fe(OH)_2$ develops, a passive layer may not form, but $Fe(OH)_2$ may still decrease the corrosion rate (Kursten et al., 2004). Therefore, stainless steel and carbon steel are protected against corrosion by the presence of a thin "passive" layer in environments with cement that are highly alkaline conditions (Kursten et al., 2004).

Oxide passive films can break down at lower pHs and/or by reactions with aggressive species (e.g., chlorides (Kursten et al., 2004)). The passive film overlaying carbon steel can more easily be broken down by chloride corrosion than on stainless steel. Carbon steel, therefore, tends to suffer for general/uniform corrosion, whereas stainless steel tends to be highly localized (i.e., pitting corrosion, stress corrosion) (Smart et al., 2004).

Previous laboratory studies (25–100ºC) have shown the formations of the Fe-oxide layer at the steel-bentonite interface (i.e., Álvarez, et al., 2008; Bourdelle et al., 2014; Kursten et al., 1996; 1997; Pignatelli et al., 2014; Smailos et al., 1997). A range of different Fe- oxide/hydroxides are observed to precipitate on the steel surface in the laboratory experiments, dependent on experimental conditions. The main corrosion products observed are magnetite (Fe_3O_4) and goethite (FeO(OH)) in experiments below 100ºC, with hematite (Fe_2O_3) occurring in the experiments at 100ºC.

4.1.1.5 Mineral Reactions at the Steel-Bentonite Interface

The interface of the waste canister overpack and the EBS represents a chemical boundary at which material interactions may affect bentonite properties and the canister surface (e.g., Gaudin et al., 2013; Wilson et al., 2006a, b). After initial repository closure and when the boundary is experiencing the thermal peak, this boundary will likely be dry. Under dry conditions, bentonite mineralogy will likely be stable (e.g., Wersin et al., 2007) and corrosion will be minimal. However, the saturation of the bentonite buffer will occur over time due to the infiltration of groundwater, leading to canister corrosion, potential alteration of the bentonite, and reactions between corrosion products and the bentonite.

The assessment of the interactions occurring at the steel-bentonite interface is important to consider in the evaluation of the long-term repository function for waste isolation. For example, iron mobilized by corrosion of the steel canister may affect the properties of the bentonite. In the event of a canister failure, significant changes in the bentonite immediately adjacent to the breached area (i.e., the steel-bentonite interface) will affect the movement of radionuclides and the sealing properties of the bentonite. Higher temperatures at the clay/canister interface may cause a local increase in Fe-activity and dissolved SiO_2. The resulting chemical gradient causes migration of dissolved species radially away from the canister towards the colder rock, potentially leading to the silicification throughout the buffer during the cooling phase (Pusch, 1995; Svemar, 2005).

Interaction of carbon steel and bentonite was examined in the 18-year FEBEX full-scale EBS heater test at the Grimsel Test Site (Martin et al., 2006). Metal corrosion and chemical changes in bentonite chemistry at the buffer-steel interface occurred and is described in Kober et al. (2017) and Hadi et al. (2019). The bentonite in contact with steel examined by Hadi et al. (2019) likely was heated to temperatures of 30 to 60ºC. They observe that corrosion of carbon steel leads to a >140 mm layered zone of iron enrichment extending radially into the bentonite. In the ~30 mm closest to the canister, iron is hosted in newly formed goethite ($Fe^{3+}O(OH)$) within the bentonite. The remainder of the Fe-enriched zone is interpreted to be a result of the diffusion and sorption to the clay mineral edge site of Fe^{2+} (Hadi et al., 2019). This layering is interpreted to be related to the initial diffusion of Fe^{3+} during oxidizing conditions, followed by diffusion of Fe^{2+} when oxygen becomes depleted. Clay mineral alteration was not observed, likely due to the low temperatures achieved.

High-temperature, full-scale experiments are needed to characterize the steel-bentonite interface evolution under conditions relevant to DPC disposal. HotBENT, an experiment conducted by NAGRA in the same drift as the FEBEX experiment, is in its initial stages. The experiment will run for 15 to 20 years and will be dismantled over five years (AMBERG, 2019). The peak temperatures will be between 175 to 200ºC. Results will be very applicable to understanding steel-bentonite interaction in a crystalline rock repository setting.

Lab-scale experiments, in comparison to full-scale demonstrations, lack the long timeframes, realistic scales, and water/rock and clay/steel ratios that are unique to in situ experiments, such as FEBEX (described above), but can provide insight to potential reaction pathways at higher temperatures. To date, many lab-scale experiments have been completed on the interaction of clay minerals/bentonite with steel/Fe-oxide/native iron at temperatures between 25 and 300ºC (e.g., Lantenois, 2003; Perronnet, 2004; Lantenois et al., 2005; Cathelineau et al., 2005; Wersin et al., 2008; Mosser-Ruck et al., 2010; Pignatelli et al., 2013; Bradbury et al., 2014; Kaufhold et al., 2015; Bourdelle et al., 2014; 2017; Cheshire et al., 2018). These studies show that steel corrosion has the potential to have wide ranging effects on the physical and chemical properties of the bentonite buffer, likely dependent on bulk system chemistry.

In low temperature repository settings (<100ºC), iron released through steel corrosion will be likely absorbed by the surrounding clay through cation exchange. This exchange will reduce the self-sealing

ability in the clay (i.e., swelling capacity) and cause the buffer to become stiff (Pusch et al., 2015). Fe^{3+}, generated under initial oxidizing conditions, may replace Al^{3+} in the octahedral sheet of montmorillonite, which can accelerate the alteration to non-swelling phases, due to high crystal stresses and mineral instability due to the large cation size (Nguyen-Thanh et al., 2012). In addition, the combination of heating and the ion exchange between the Na^{2+} in the clay with the Fe^{2+} produced from corrosion under reducing conditions (anoxic) promotes the development of channel-type transport pathways for solutions migrating through the bentonite buffer (Gueven and Huang, 1990; Nguyen-Thanh, et al., 2012; Pusch et al., 2012).

In > 100ºC experimental systems that utilize reaction solutions with circum-neutral pH values (i.e., porewaters buffered by clay and silicate minerals), $Fe^{2+/3+}$ is transferred from either iron shavings or steel coupons to clay minerals in the bentonite to form different Fe-rich phyllosilicate minerals (chlorite, Fe-saponite, berthierine, serpentine phase) (e.g., Guillaume et al., 2004; Mosser-Ruck et al. 2010; Cheshire et al., 2018; Caporuscio et al., 2019; Jove- Colon et al., 2019). For example, in 300ºC hydrothermal experiments that include steel coupons embedded in bentonite, stainless steel corrodes to produce a chromite-like (FeC_r2O_4) passivation layer above unaltered steel, whereas a magnetite-like phase forms on the surface of LCS (Cheshire et al., 2018; Jové Colón et al., 2019). Attached to the corroded surface is a < 100 µm zone of Fe-rich smectite (Fe-saponite) (Cheshire et al., 2018). Results from lab-scale studies indicate that the formation of Fe-rich silicate phases as mantle on the steel surface may provide corrosion protection (e.g, Kaufhold et al., 2015; Cheshire et al., 2018); however, this finding should be confirmed in full-scale/long term experiments.

4.2 Methods: Experimental Design

Hydrothermal experiments were designed to understand geochemical and mineralogical changes that may occur in the EBS of a high-temperature crystalline repository. Different combinations of materials found in the hypothetical repository setting, including wall rock (Grimsel Granodiorite from the Grimsel Test Site), bentonite buffer (unprocessed Wyoming bentonite), waste canister overpack (316SS, 304SS, LCS), cement liner (cured ordinary Portland cement), and groundwater (synthetic Grimsel Granodiorite groundwater) were included in the experiments.

Experiments were conducted under water-saturated conditions. Reactants (Table 4-1) were loaded into a flexible gold reaction cell and fixed into a 500 mL gasket confined closure reactor (Seyfried et al., 1987). The redox conditions for each system were buffered using a 1:1 mixture (by mass) of Fe_3O_4 and Fe° added at 0.07 wt.% of the bentonite mass. Coupons of steel (316SS, 304SS, or LCS), were added to the experiments at approximately 15 to 25 wt.% of the mass of the solid reactants to mimic the presence of a waste canister. Experiments were pressurized to 150 to 160 bar and were heated isothermally to 250°C for 6 to 8 weeks. Reaction liquids were extracted periodically during the experiments and analyzed to investigate the aqueous geochemical evolution in relationship to mineralogical alterations. The sampled reaction liquids were split into three aliquots for unfiltered anion, unfiltered cation, and filtered (0.45 µm syringe filter) cation determination. All aliquots were stored in a refrigerator at 1°C until analysis.

Reaction products and starting materials were characterized using X-ray diffraction, electron microprobe, and SEM. Detailed analytical methods are listed in Caporuscio et al. 2021.

Table 4-1 Initial components and reaction conditions for IEBS experiments in the presence of Grimsel granodiorite.

Exp.	Components	Temp (°C)	Run time	Synthetic GW (g)	Grimsel Granodiorite (g)	WY bentonite (g)	Cured Portland cement (g)	EBS metal (g)	Fe° (g)	Fe_3O_4 (g)	Water: Rock
IEBS-0	WB	250	8 weeks	160	-	16.78	-	-	0.50	0.50	9:1
IEBS-1	GG + WB	250	6 weeks	144	3.47	10.91	-	-	0.49	0.50	10:1
IEBS-2	GG+ WB + 316SS	250	6 weeks	182	3.19	11.02	-	nm	0.49	0.50	13:1
IEBS-3	GG + WB + 304SS	250	6 weeks	110	3.41	11.05	-	2.74	0.50	0.59	8:1
IEBS-4	GG + WB + LCS	250	6 weeks	185	3.28	11.00	-	5.06	0.50	0.51	13:1
IEBS-5	GG + WB + 316SS	250	8 weeks	150	3.29	11.01	-	5.07	0.50	0.50	10:1
IEBS-6	GG + WB + OPC	250	8 weeks	126	2.11	6.60	2.07	-	0.50	0.50	10:1
IEBS-7	GG + WB + 316SS	250	6 months	270	6.51	21.50	-	5.07	0.97	0.97	9:1
IEBS-8	GG + WB + OPC + 316SS	250	8 weeks	171	3.64	10.92	3.62	5.05	0.50	0.50	9:1

Notes: Abbreviations: Low Carbon Steel (LCS), ordinary Portland cement (OPC), Grimsel granodiorite (GG), Stainless steel (SS), Wyoming bentonite (WB), not measured (NM)
Experiments completed in FY21 are highlighted in green.

4.3 Results

4.3.1 Starting Material Characteristics

Synthetic Grimsel Groundwater. A synthetic groundwater was mixed to mimic fluids found at the Grimsel Test Site after the recipe reported in Kersting et al. (2012). Chemistry of the synthetic fluid is presented in Table 4-2. The groundwater at the Grimsel Test Site is a Na-CO_3 type water and has a pH of ~8.6 to 8.8.

Wyoming bentonite. The bentonite used in the present study is unprocessed and was provided by Bentonite Performance Minerals LLC from Colony, Wyoming, U.S.A. It is composed dominantly of Na-montmorillonite (general composition: $Na_{0.33}(Al,Mg)_2(Si_4O_{10})(OH)_2 \cdot nH_2O$), lesser clinoptilolite and feldspar, and minor biotite, pyrite, quartz, opal, and sulfide minerals. The quantitative x-ray diffraction (QXRD) results from unheated bentonite are presented in Appendix C of Caporuscio et al., 2021.

Grimsel Granodiorite. The granodiorite used in the experiments was sourced from a drill core from the Grimsel Test Site. Major mineral phases include K-feldspar, plagioclase, and quartz. Minor phases are muscovite and biotite. Trace phases are allanite, zircon, titanite, and apatite. The QXRD results from unheated granodiorite are presented in Appendix C of Caporuscio et al., 2021.

Cured Portland cement chip. Chips consisting of a mix of 100% ordinary Portland cement and Los Alamos municipal tap water (Table 4-2) were cast in November of 2018. Major mineral phases observed in the XRD pattern the cured cement chip include portlandite ($Ca(OH)_2$), belite (calcio-olivine, Ca_2SiO_4), alite (Ca_3SiO_5), and brownmillerite ($Ca_2(Al,Fe)_2O_5$).

Table 4-2 Initial groundwater chemical composition from Kersting et al. (2012), the synthetic groundwater used in experiments (Missana & Geckeis, 2006), and the Los Alamos municipal tap water.

	Target solution (Kersting et al., 2012)	Synthetic Grimsel GW (this study)	Los Alamos Municipal Tap Water
	(mg/L)	(mg/L)	(mg/L)
Na^+	127	116	2.50
K^+	3	3	12.8
Ca^{2+}	5	7	2.04
Mg^{2+}	13	12	9.62
Cl^-	11	14	3.24
CO_3^{2-}	219	203	24.7
SiO_2	21	34	n.m.
SO_4^{2-}	97	87	75.7
pH	8.6–8.8	8.5	6.93

*n.m. = not measured

316SS. (NIST SRM 160b) is an iron alloy primarily with 18.37 wt.% Cr, 12.35 wt.% Ni, 2.26 wt.% Mo, 1.619 wt.% Mn, 0.5093 wt.% Si, and 0.175 wt.% Cu.

304SS. An ion alloy which differs from 316SS in Cr/Ni ratio. Along with Fe, it contains 18 wt.% Cr, 8 wt.% Ni, < 2 wt.% Mn, < 1 wt.% Si, < 0.045 wt.% P, and < 0.03 wt.% S, and < 0.08 wt.% C.

Low carbon steel (LCS). Composed of Fe along with ~0.2 wt.% C, 0.9 wt.% Mn, < 0.04 wt.% P, and < 0.05 wt.% S.

4.3.2 Aqueous Geochemistry

The pH and concentrations of cations and anions in reaction fluids evolved during the experiment, likely reflecting mineral-brine reactions. The starting solution, synthetic Grimsel Granodiorite groundwater, has a pH of ~8.5. The pH, measured at 25ºC, of the fluids extracted weekly from the reaction vessels dropped over the course of all experiments. In the baseline experiment IEBS-0, pH values were steady between 5.5 and 6 throughout experiment duration. In experiments IEBS-1 through IEBS-5, measured pH values were roughly between 6 and 7. Experiment IEBS-2 had a slightly more acidic solution during the middle of the experiment: the pH dropped to ~5 by week 3 and then increased to ~6.2 by the end of the experiment. The pH values in the 6-month experiment, IEBS-7 remained constant just below 6 for the run duration. The pH values observed in IEBS-6 and IEBS-8, which contained a cured Portland cement chip, evolved to slightly higher pH values (i.e., ~7–7.5) (Figure 4-2).

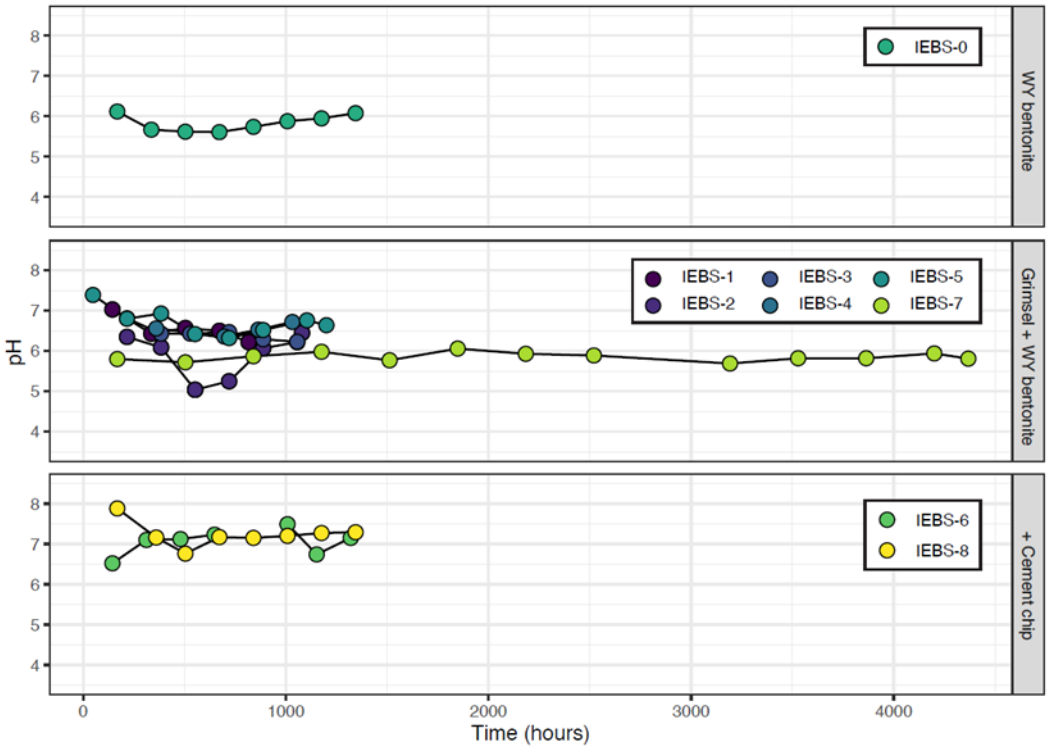

Figure 4-2 Measured pH values (at 25 C) for reaction fluids extracted from experiments IEBS-0 through IEBS-8.

Water:rock. Experiments were performed at a range of water:rock ratios (8:1 to 13:1). As experiments progressed, fluids were gradually extracted from the reaction vessel during sampling, which slightly lowered the water:rock ratio with every fluid extraction.

4.3.2.1 Cations

Alkali/alkaline earth metals. Major alkali and alkaline earth metal cations (K^+, Na^+, Ca^{2+}, Mg^{2+}) follow similar trends in concentrations measured throughout each experiment (Figure 4-3). In the unfiltered and filtered results, concentrations typically decrease slightly from values observed at the first sampling. No significant differences in measured values between the filtered and unfiltered results are observed.

For IEBS-0 through IEBS-5 and IEBS-7, initial Ca^{2+} values are observed to be close to concentrations in the starting Grimsel Granodiorite synthetic groundwater (~7 mg/L). Calcium concentrations in IEBS-5 and IEBS-7, are initially observed to be slightly elevated in comparison to the other experiments. In IEBS-7, [Ca^{2+}] remains around 1.5 to 2.0 mg/L from month two to six of experiment time. In the experiments containing the cured cement chip (IEBS-6 and IEBS-8), [Ca^{2+}] reaches values less than 2 mg/L within a week of the experiment and are roughly similar to values observed in the experiments that do not contain cement.

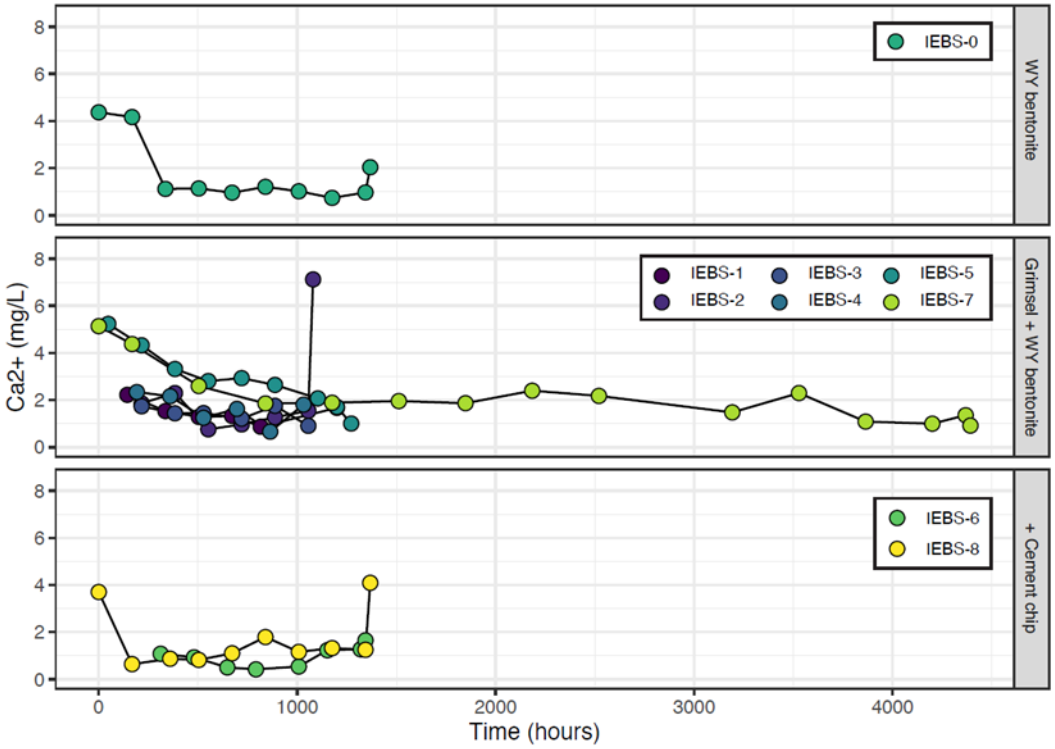

Figure 4-3 Concentration in mg/L of calcium in the unfiltered reaction fluids during each IEBS experiment.

Potassium. Potassium concentrations typically remained constant at values below 5 mg/L for the duration of all experiments (Figure 4-4). Experiments with the cured cement chip had slightly higher and less consistent potassium concentrations.

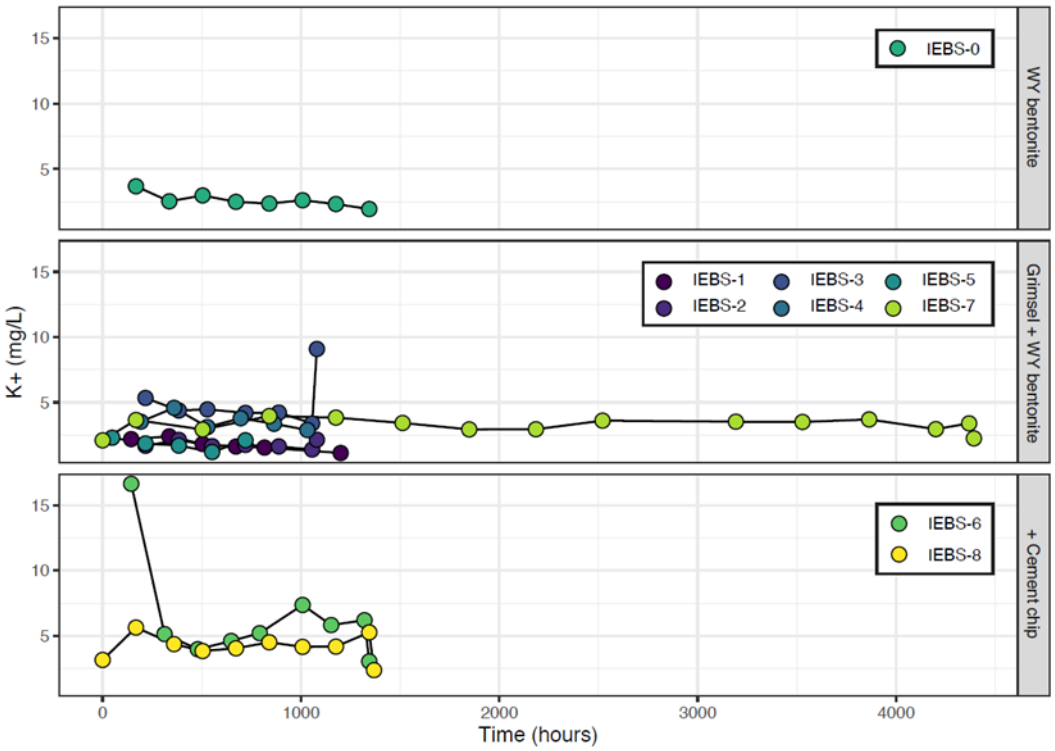

Figure 4-4 Concentration in mg/L of (A) potassium in the unfiltered reaction fluids during each IEBS experiment.

Magnesium. Magnesium concentrations drop from starting solution values (~12 mg/L) to < 0.5 mg/L in the unfiltered aliquot by the first sampling and remain at similar values for the duration of all experiments (Figure 4-5).

Sodium. Observed sodium values in all experiments demonstrate a flat trend (Figure 4-6). Concentrations range from 100 to 200 mg/L but are similar in magnitude to the [Na^+] observed in the starting solution (116 mg/L). There are no differences in the solutions between experiments with bentonite only (IEBS-0), bentonite and Grimsel Granodiorite (IEBS-1 to IEBS-5, IEBS-7), or with the added cement chip (IEBS-6 and IEBS-8).

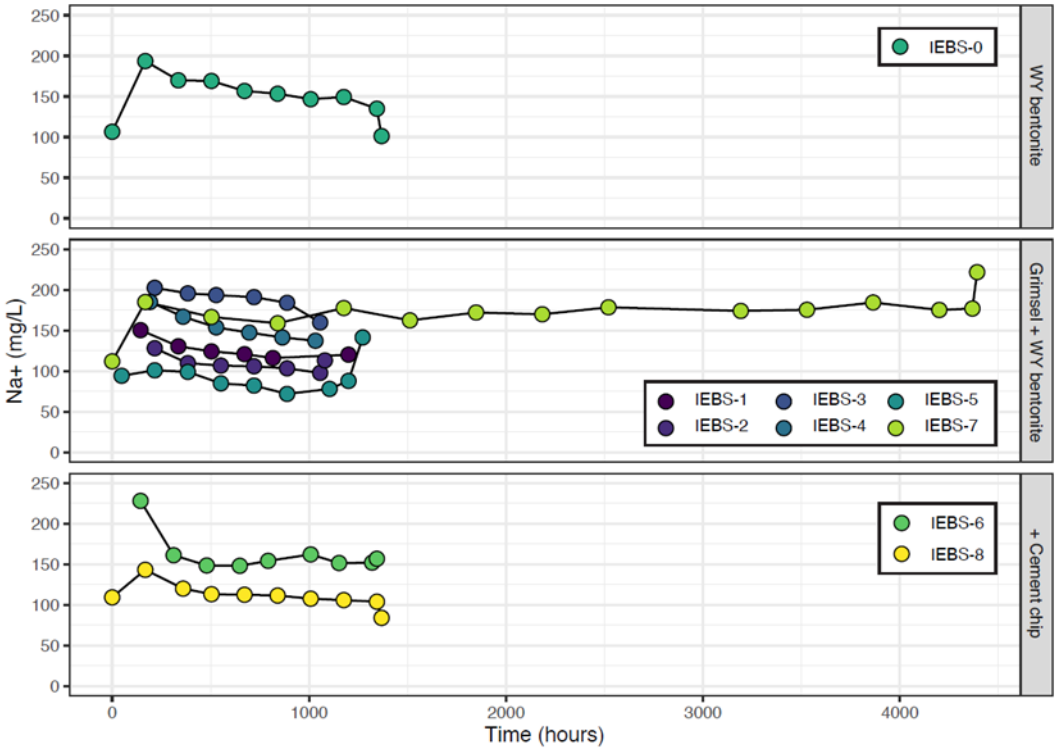

Figure 4-5 **Concentration in mg/L of sodium in the unfiltered reaction fluids during each IEBS experiment**

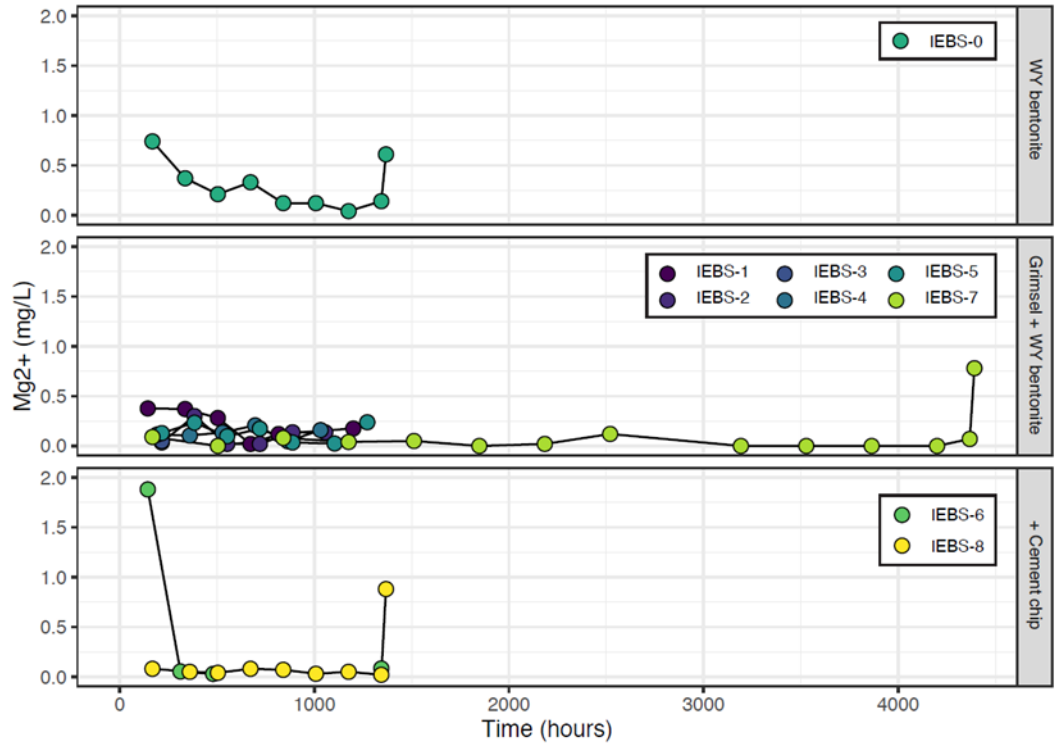

Figure 4-6 **Concentration in mg/L of magnesium in the unfiltered reaction fluids during each IEBS experiment.**

Silica. Measured concentrations in the six completed experiments with Grimsel Granodiorite and Wyoming bentonite (IEBS-1 to IEBS-5, IEBS-7) cover a wide range of values between ~350 and 800 mg/L (Figure 4-7). Starting silica values in the synthetic Grimsel groundwater are ~34 mg/L; values observed in the experiments all increase rapidly during the first week of experiment time. Comparing experiments in this group, the aqueous silica concentrations do not follow consistent trends. For example, values in IEBS-1, IEBS-2, and IEBS-4 decrease after the first sample, before values increase by the third or fourth sample. Concentrations in IEBS-3 initially increased before leveling off around the middle of the experiment, and slightly decreasing over the last two weeks. Concentrations in IEBS-5 remained relatively constant before slightly increasing at the end of the experiment. In the 6-month experiment (IEBS-7), concentrations stabilized by the second month of experiment time to values between 700 and 800 mg/L. Silica concentrations in the Wyoming bentonite only experiments (IEBS-0) remained at between 700 and 800 mg/L as well. In comparison, silica concentrations in the experiments with a cured cement chip (IEBS-6 and IEBS-8) were slightly lower, hovering around 600 mg/L by the end of the experiments.

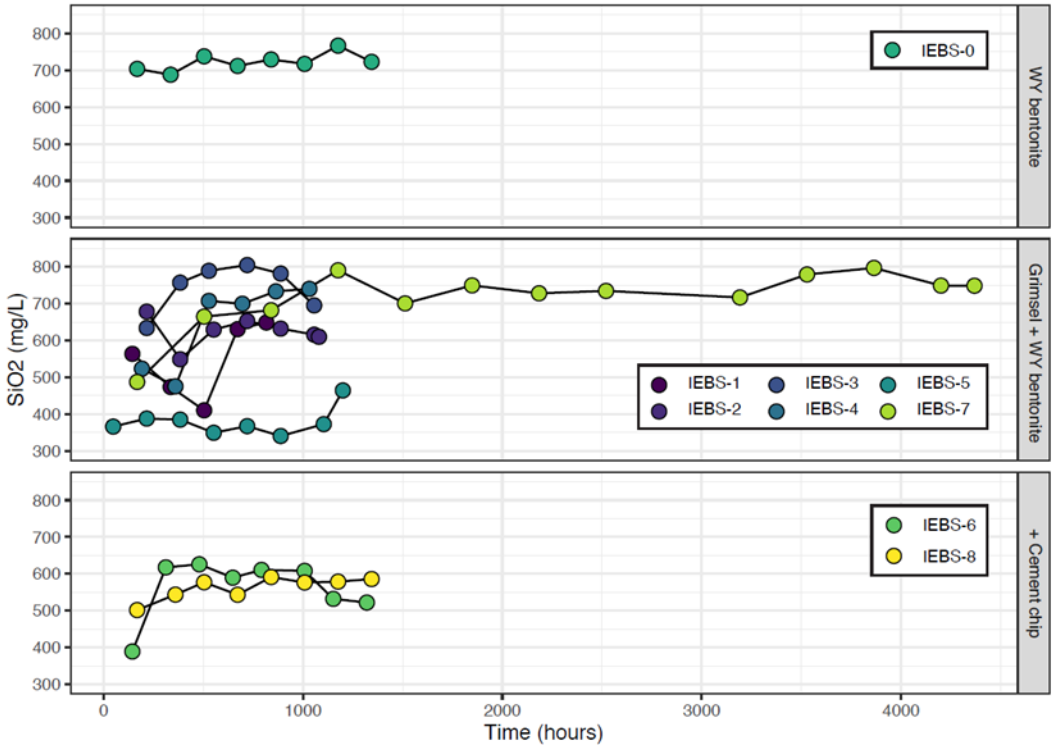

Figure 4-7 Concentration in mg/L of aqueous silica in the unfiltered reaction fluids during each IEBS experiment.

Iron. The [Fe^{2+}] in all IEBS experiments remains below ~1 mg/L in the filtered and unfiltered cation samples for the duration of the experiments (Figure 4-8). A jump to ~10 mg/L is observed around 500 hours experiment time in IEBS-6 in the unfiltered results; this is likely the result of particulate matter present in the sample. The final sample from IEBS-1 that was collected before experiment cooling has Fe concentrations of ~4 mg/L for both filtered and unfiltered samples. Quench samples (collected after experiment cooling) from IEBS-2 and IEBS-3 show sharp increases to >20 mg/L in the unfiltered aliquot (Figure 4-8.

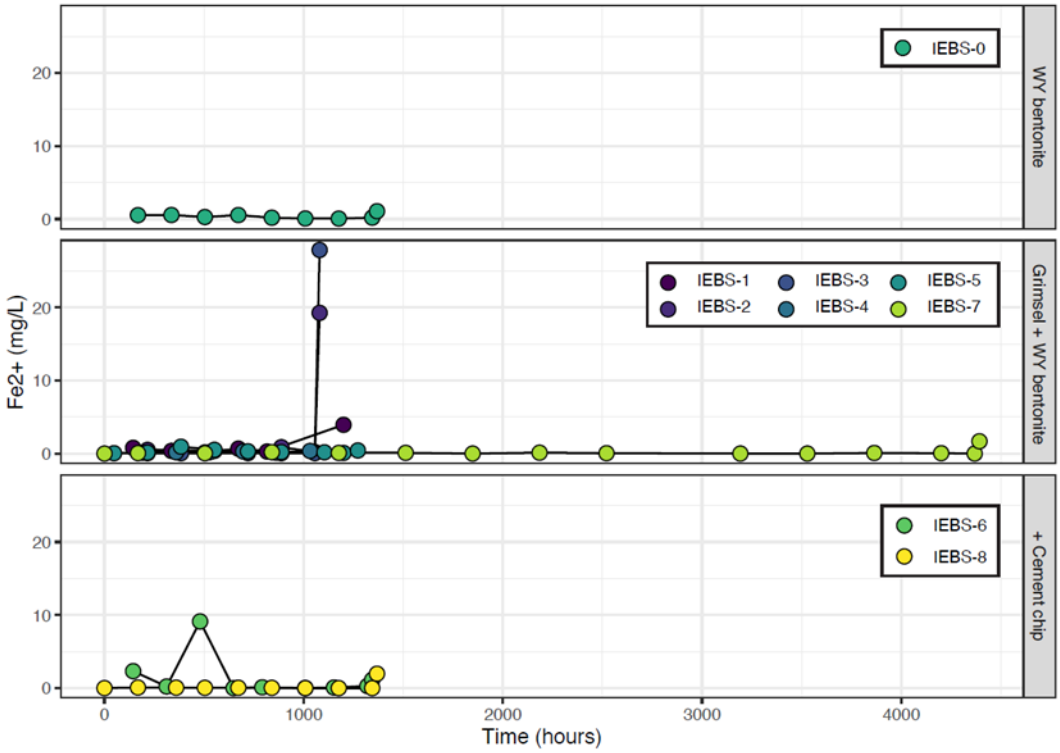

Figure 4-8 Concentration in mg/L of aqueous iron in the unfiltered reaction fluids during each IEBS experiment

Aluminum. Aluminum concentrations in the unfiltered fraction from experiments IEBS-0 through IEBS-5 and IEBS-7 reached concentrations of ~4 to 5 mg/L by the first weeks of experiment time (Figure 4-9). Concentrations slightly decreased or remained near constant for the remainder of the experiment. Quench samples from IEBS-2 and IEBS-3 exhibit a spike in $[Al^{3+}]$ concentrations. In comparison, the $[Al^{3+}]$ concentrations were notably higher in IEBS-6 and IEBS-8, remaining around 5 to 7 mg/L for the duration of each experiment.

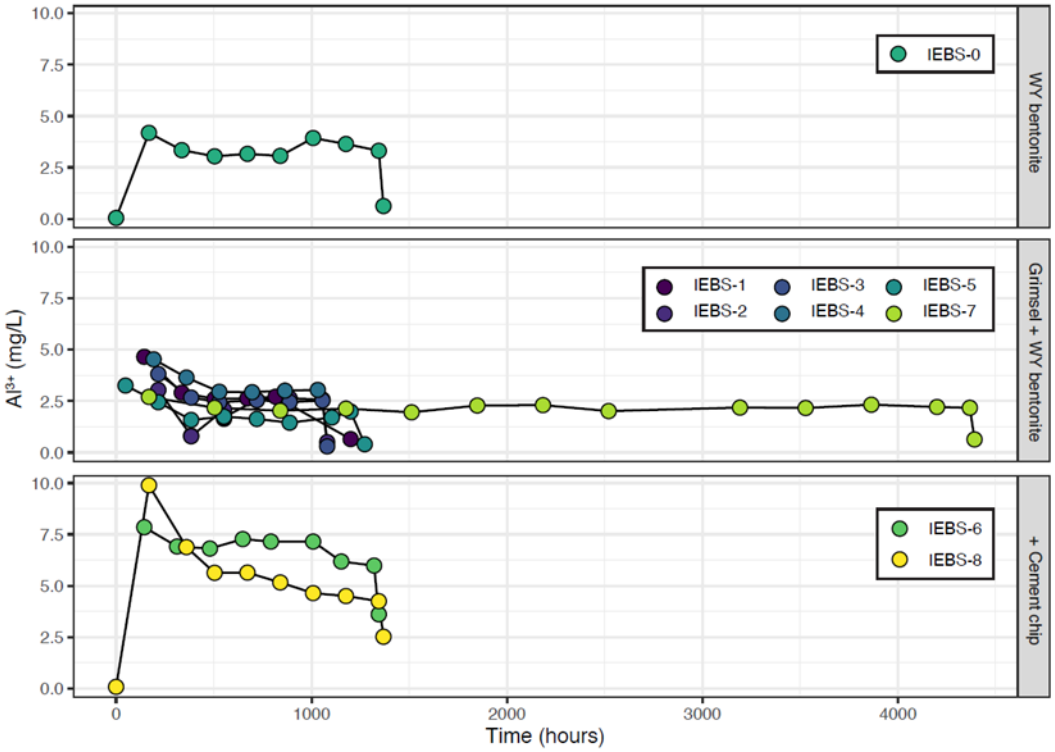

Figure 4-9 **Concentrations in mg/L of aluminum in the unfiltered reaction fluids during each IEBS experiment.**

4.3.2.2 Anions

Chloride. Chloride concentrations in the baseline experiment with Wyoming bentonite and Grimsel synthetic groundwater (IEBS-0) generally remain between 10 and 15 mg/L. Observed concentrations in experiments with Wyoming bentonite and Grimsel Granodiorite generally decrease from the first to second sampling and then remain relatively steady for the rest of the experiment. By the end of each experiment, measured concentrations in IEBS-1 to IEBS-5 and IEBS-7 are between 10 and 25 mg/L (Figure 4-10). In the experiments with the added cement chip, values are initially elevated in IEBS-6 starting around 33 mg/L and lower in IEBS-8 (~13 mg/L). Chloride concentrations in IEBS-6 and IEBS-8 converge by the end of each experiment to values between 10 and 20 mg/L.

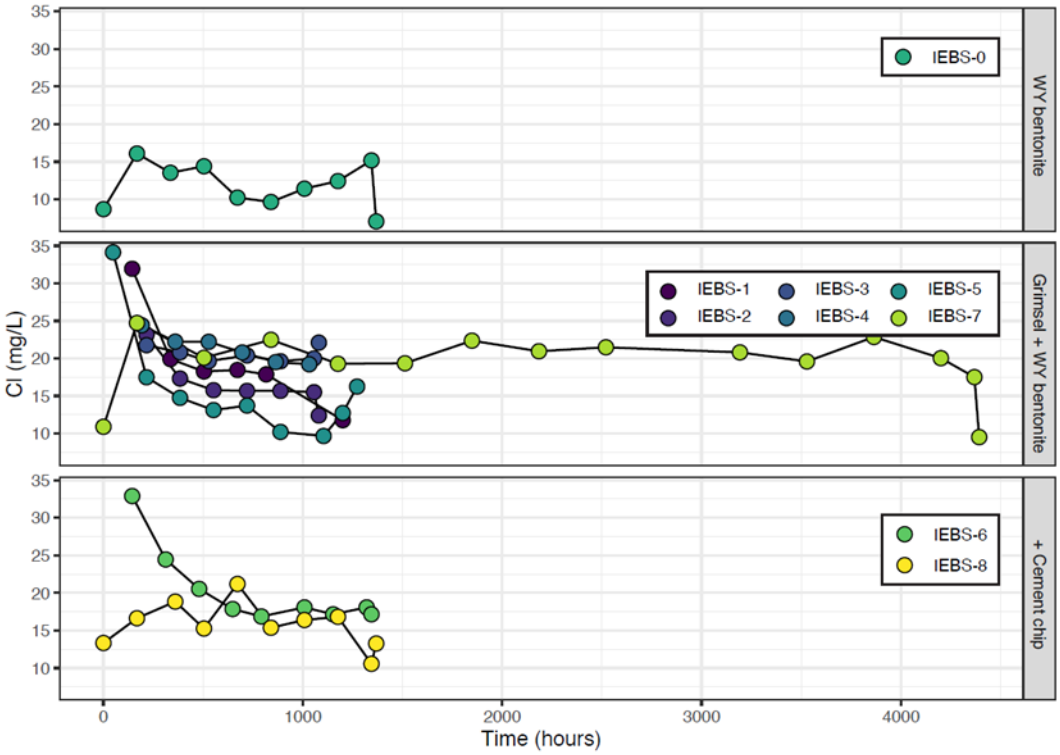

Figure 4-10 Concentration in mg/L of chloride anions in unfiltered reaction fluids during each IEBS experiment

Sulfate. Sulfate concentrations in IEBS-0 initially increase sharply from the first to the second sampling, remain between 200 and 300 mg/L for the remainder of the experiment, and drop to 100 mg/L on experiment quench. In the six experiments with Grimsel and Wyoming bentonite, observed concentrations are between 100 and 300 mg/L and generally stabilize by the fourth sampling (Figure 4-11). Observed initial values are between ~150 and 350 mg/L, which shows an increase from the starting solution values (87 mg/L). The majority of experiments end at concentrations of 100 to 200 mg/L, with the exception of IEBS-3, which ended around 275 mg/L (325 mg/L quench). Sulfate concentrations were less variable in the experiments with the cement chip, which mostly remained between 150 and 250 mg/L.

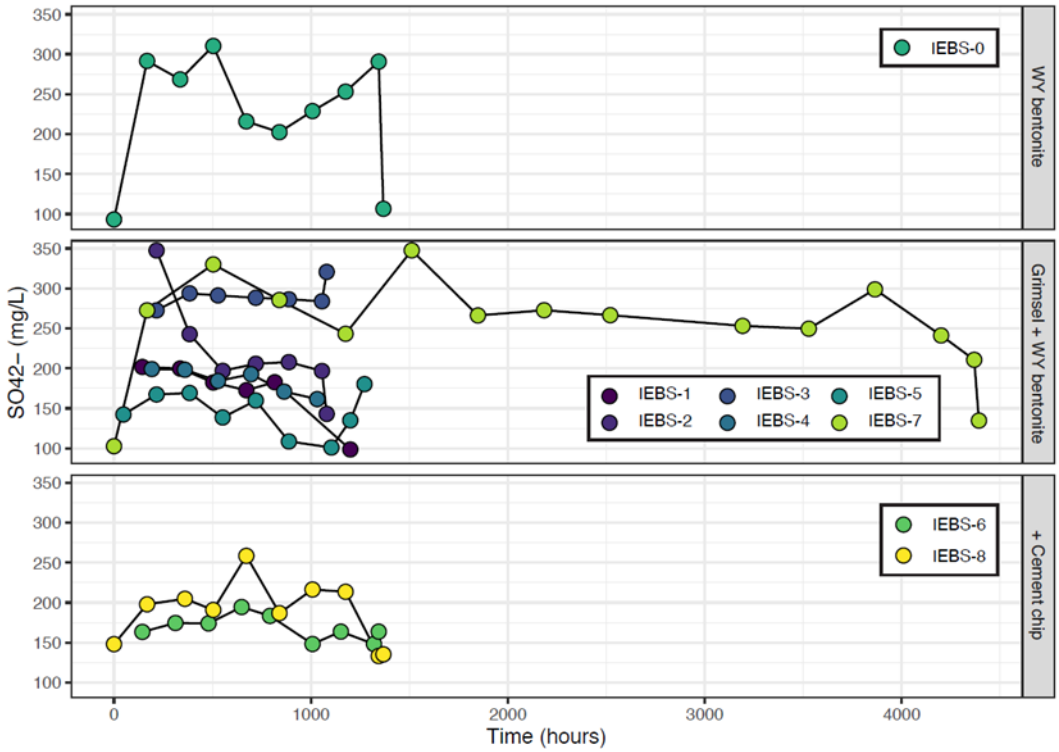

Figure 4-11 Concentration in mg/L of sulfate anions in the unfiltered reaction fluids during each IEBS experiment

4.3.3 Quantitative X-ray diffraction (QXRD)

QXRD analyses of the starting material mixture and the bulk reaction products from IEBS-0 through IEBS-8 cab be found in Caporuscio et al. 2021. The results show changes in bulk mineralogy as the result of the hydrothermal reaction. The approximate starting reaction mixture for each experiment is listed in Table 4-1. The bulk mineralogy of a representative sample of Wyoming bentonite, Grimsel Granodiorite, and the starting mixture is reported in Caporuscio et al. 2021.

IEBS-0. Experiment IEBS-0 was a baseline experiment to explore Wyoming bentonite alteration in the synthetic Grimsel groundwater solution. Observed mineralogy changes include the reduction in feldspar and clinoptilolite and an increase in smectite/illite/illite-smectite.

IEBS-1 to IEBS-5. Results from the experiment products indicate that mineral dissolution, precipitation, and recrystallization reactions likely occurred. For example, in the results from all samples, the abundance of quartz increases by ~1 to 7 wt.%. Clinoptilolite dissolution likely occurred based on the decrease in abundance by 1 to 6 wt.%. Smectite abundance increases by 3 to 11 wt.% and the amount of mica and chlorite decreases by about 5 wt.%. Changes in clay mineralogy were further investigated by detailed clay mineral structural studies, discussed in the next section.

CSH minerals, which were identified in this section and in SEM images, were not identified via XRD, likely due to their low bulk abundance or poorly crystalline nature.

IEBS-7. Mineralogy changes in IEBS-7, which examined long term Grimsel Granodiorite + Wyoming bentonite interaction, shows more pronounced mineralogical changes than the shorter-term experiments

with the same reactants (described above). Feldspar and clinoptilolite were decreased more over the 6-month period and smectite/illite/illite-smectite increased by ~17 wt.%.

IEBS-6 and IEBS-8. The inclusion of a cured cement chip with Wyoming bentonite and Grimsel Granodiorite reactants resulted in different mineralogical changes. The sample analyzed included bentonite and granodiorite components; the cement chip was intact and removed from the mixture for separate post experiment characterization. The main mineralogical changes include reduction in clinoptilolite and the formation of analcime and amorphous material.

4.3.4 Clay XRD

The clay-size fraction (<2 µm) was separated via density separation from a gently crushed portion of the reaction products from each experiment. While crushing, discrete particles of Grimsel Granodiorite were removed. In the case of IEBS-6, the cement chip was separated before the sample was selected. The XRD patterns of the ethylene glycol saturated, oriented clay fractions can be used to determine alterations to the clay mineral structure (i.e., peak position shifts), which can be used to calculate clay mineral expandability. The ethylene glycol saturated peak positions are presented in Table 4-3 and the XRD patterns are plotted in Figure 4-12.

Peak positions from IEBS-1 through IEBS-5 are similar to those of the ethylene glycol saturated smectite peaks of unheated Wyoming bentonite, and calculated expandabilities based on the difference between the d002 and d003 peaks from these samples show an increase in clay expansion. Results from IEBS-0 show less expandability. In comparison, results from IEBS-6 and IEBS-8, which included the cured cement chip, show lower expandabilities than the clay fraction from experiments without cement, but still slightly increased in comparison to unreacted Wyoming bentonite. The six-month experiment, IEBS-7, shows similar expandability estimates and peak positions to IEBS-6 and IEBS-8.

Table 4-3 Glycolated smectite (GS) peak positions for the <2 µm clay fraction separated from the Wyoming bentonite. Expandability was calculated based on the position of the 002 and 003 GS peaks.

Sample	1		2		3		5		002/003	1	2	3
EG-smectite	2θ	d (Å)	2θ	d (Å)	2θ	d (Å)	2θ	d (Å)	Δ 2θ	%Exp	%Exp	%Exp
WY Bentonite	5.2	17.0	10.4	8.5	15.7	5.7	26.3	3.4	5.2	102	105	105
IEBS-1	5.2	16.9	10.4	8.5	15.6	5.7	26.2	3.4	5.2	105	109	109
IEBS-2	5.3	16.6	10.4	8.5	15.7	5.6	26.2	3.4	5.1	108	112	111
IEBS-3	5.2	17.1	10.3	8.6	15.6	5.7	26.2	3.4	5.1	107	111	110
IEBS-4	5.2	17.1	10.3	8.6	15.6	5.7	26.2	3.4	5.1	107	111	110
IEBS-5	5.2	16.9	10.4	8.5	15.6	5.7	26.2	3.4	5.1	107	111	110
IEBS-6	5.2	17.0	10.4	8.5	15.7	5.7	26.3	3.4	5.2	104	107	107
IEBS-7	5.2	17.0	10.4	8.5	15.6	5.7	26.1	3.4	5.2	102	104	105
IEBS-8	5.2	17.0	10.4	8.5	15.6	5.7	26.1	3.4	5.2	100	103	103
IEBS-0	5.2	17.0	10.4	8.5	15.6	5.7	26.2	3.4	5.3	100	102	102

1: %Exp = 973.76 – 323.45Δ + 38.43Δ² – 1.62Δ³ (Eberl et al., 1993)
2: %Exp = 1517.8 – 548.49Δ + 68.35Δ² – 2.90Δ³ (Eberl et al., 1993)
3: %Exp = 766.01 – 194.10Δ + 12.924Δ² (Moore and Reynolds, 1997)

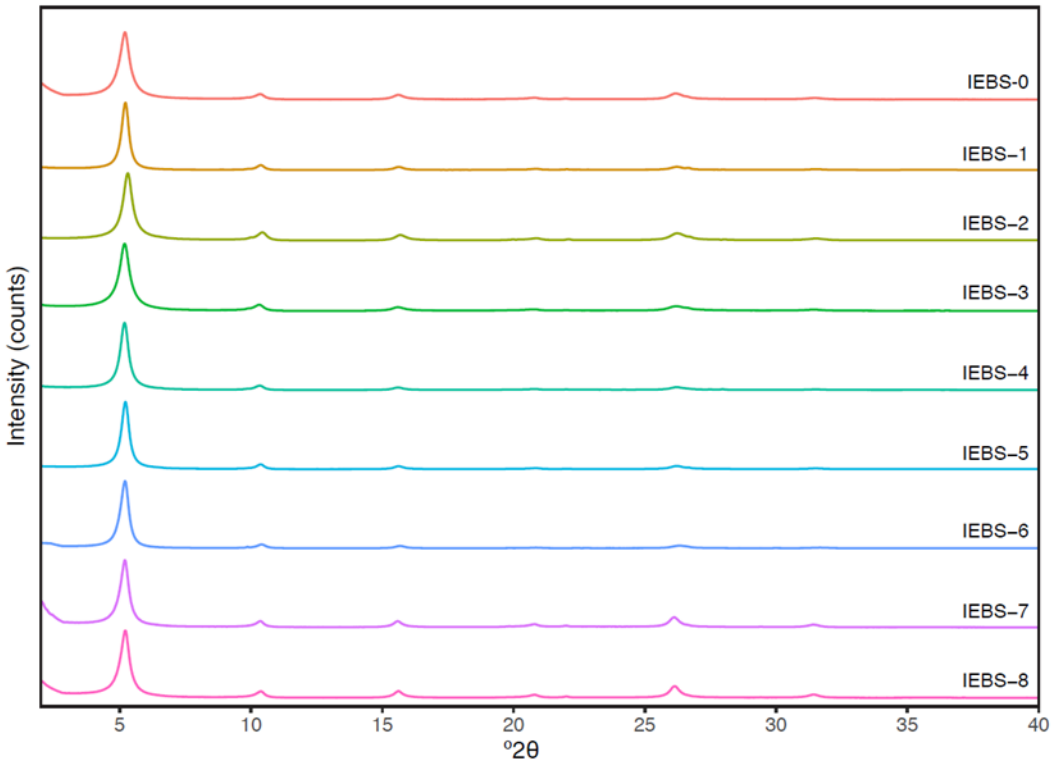

Figure 4-12 XRD patterns the oriented, ethylene glycol saturated <2 µm fraction from IEBS-1 through IEBS-8 showing no significant shifts in smectite peaks.

4.3.5 Electron Microprobe Analyses

Reaction products were analyzed via electron microprobe (EMP) to determine the major element composition of mineral phases. The EMP analyses primarily targeted the clay matrix, steel alteration products, altered glass shards, and other authigenic minerals. Analysis of the reaction products from IEBS-6, IEBS-7, IEBS-8, and IEBS-0 are currently in progress and will be included in the report for FY22. The EMP results of the previous experiments are reported in Caporuscio et al., 2021 and described in Caporuscio et al., 2020.

4.3.6 SEM/EDS

Reaction products, including loose powder, epoxy mounts, and thin sections, from the IEBS experiments were characterized using the SEM and qualitative elemental abundances were evaluated using EDS. The SEM images are presented in Caporuscio et al., 2021 and described below.

4.3.6.1 Clay

IEBS-0. Clay in the reaction products of IEBS-0 has a foily texture (F-25; F-26; F-27 in Caporuscio et al., 2021). Analcime sphere are observed locally. Feldspar with dissolution texture was also observed.

IEBS-1 to IEBS-5. The reaction products show similar features. In all the experiments, montmorillonite clay has a foily texture (i.e., Figure F-1 A, B; F-4 A, B, F-7 A in Caporuscio et al., 2021). Spherical crystals are embedded in the fine-grained clay matrix (i.e., Figure F-1 C, D, E; F-2 C, D; F-3 A, C; F-4 B, C, D, E; F-6 B, C in Caporuscio et al., 2021). The EDS analyses of these crystals reveal large Ca peaks,

with smaller Si, Al, and C peaks, likely corresponding to calcium aluminum silicate hydrate (CASH) minerals.

IEBS-6 and IEBS-8. The clay matrix of IEBS-6 and IEBS-8 is altered throughout to include analcime, garronite, feldspars, and erionite (F-10; F-11; F-18; F-19; F-20 in Caporuscio et al., 2021,).

IEBS-7. In the 6-month experiment, clay is observed to have a foily texture (F-13, F-14 in Caporuscio et al., 2021). Feldspar with dissolution textures is observed.

4.3.6.2 Grimsel Granodiorite

Feldspar surfaces are observed to be variably pitted, indicating dissolution may have occurred at the edge of the grains (Figure 4-13). No significant authigenic mineral precipitation is observed to form rims on the feldspar grains. Further, fragments of Grimsel Granodiorite included in the experiments did not experience any significant mineral reactions. For example, Figure 4-14 shows an intact Grimsel fragment composed of biotite, apatite, and quartz. No alteration textures or new mineral growth is observed within the boundaries of the Grimsel fragment.

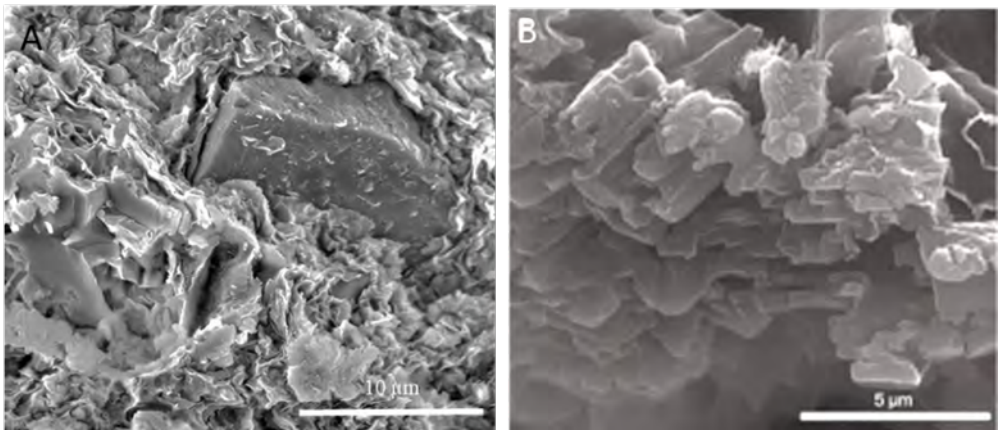

Figure 4-13 Feldspar dissolution textures observed in secondary electron SEM images from (A) IEBS-5 and (B) IEBS-1

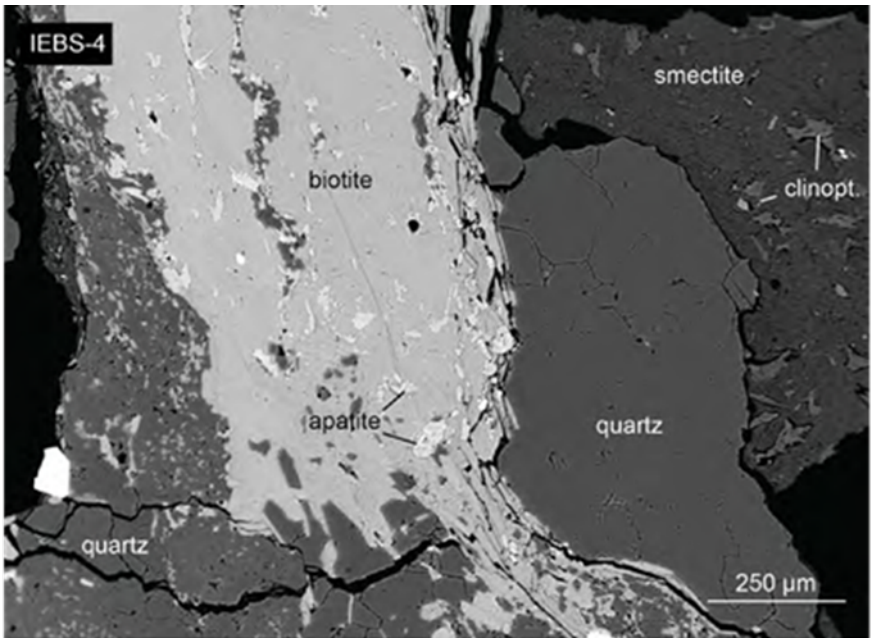

Figure 4-14 Backscattered electron SEM image of a post-reaction fragment of Grimsel Granodiorite from IEBS-4. Authigenic mineral growth/alteration is not apparent within the fragment. Abbreviation: clinopt., clinoptilolite.

4.3.6.3 Post-reaction Gel

At the conclusion of the experiments, a gel-like slurry was present on the top of the reactionproduct for IEBS-3, 4, and 5 (Figure 4-15A). The dried gel was analyzed with EDS and is Si- and Al-rich with minor amounts of Fe (1.4 - 4.3 wt.%) and Na^{2+} (3 - 6 wt.%). The dried gel texture consisted of linear and cross-linked morphology (Figure 4-15B & C).

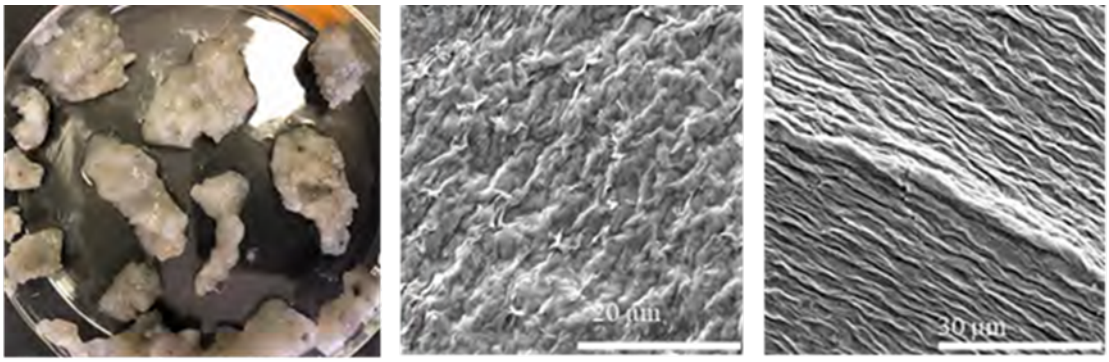

Figure 4-15 [A]. Post-reaction gel mixed with clay from IEBS-4. [B & C]. SEM images of the dried gel. Two different textures were observed: cross-linked and linear

4.3.6.4 Experiments with Cement

SEM images of the surface of the starting cement material show various cement phases (Figures F-28, F-29 from Caporuscio et al., 2021). In IEBS-6 and IEBS-8, which contained cured Portland cement in the starting materials, Na-rich analcime was prevalent throughout the reaction product (Figure 4-16) along with minor erionite-Ca and garronite (Figure F-11 A from Caporuscio et al., 2021). The fragments of the Grimsel Granodiorite did not experience significant alterations and only occasional dissolution texture on

the surface of feldspar grains was observed (Figure F-11 B from Caporuscio et al., 2021). The cured Portland cement chips extracted from IEBS-6 and IEBS-8 both have a layer of clay with zeolite embedded on the surface (Figure 4-16; and F-10 A, B from Caporuscio et al., 2021). A thin section showing a cross section of the cement chip was created and will be characterized in the next FY.

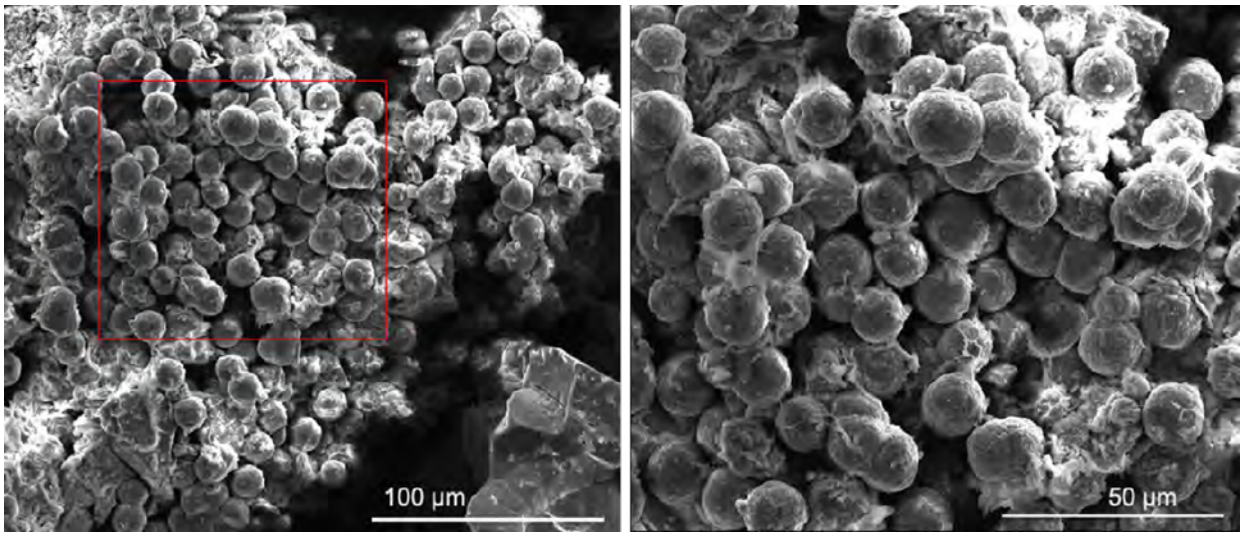

Figure 4-16 Cluster of Na-rich analcime grains from experiment IEBS-6, which included a cured chip of ordinary Portland cement. The image on the right is a magnification of the red box in left image

4.3.7 Colloid Formation

A gel phase was observed on experiment cooling in IEBS-3, IEBS-4, and IEBS-5. When suspended in DI water, particles remained suspended in solution. A dried film of the suspension from IEBS-5 was analyzed via XRD; the colloid phase was identified as montmorillonite. A portion of the suspension fluid from IEBS-5 was also analyzed with a Zetasizer at Los Alamos National Laboratory, in order to assess particle size and colloid stability. The measured zeta potential values centered around -38.9, indicating moderately stable colloids. The average particle size diameter was ~237 nm and the diameters were distributed between ~30 and 1000 nm (Figure 4-17).

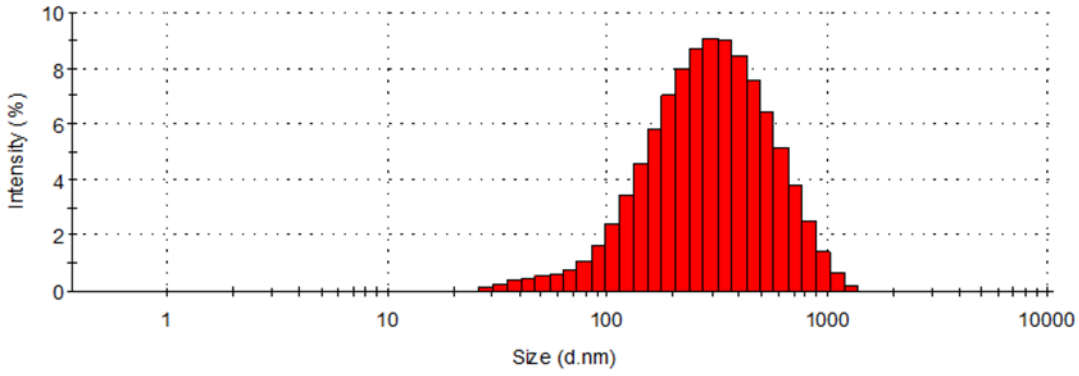

Figure 4-17 Distribution of colloid diameters from sample IEBS-5 measured via Zetasizer

4.3.8 Steel-bentonite Interface Mineralization

Steel coupons (316SS, 304SS, and LCS) were included in IEBS-2 through IEBS-5 (Table 4-4). All of the experiments contained Wyoming bentonite, Grimsel Granodiorite, and synthetic Grimsel Granodiorite groundwater. Experiments were run at 250°C and 150 bar for a period of 6 or 8 weeks. The mineralogy and chemistry of phases that formed on the surface of the steel coupons was characterized and measured via SEM and EMPA.

304SS: IEBS-3. The surface of the 304SS coupon included in IEBS-3 was coated in Fe-saponite with a honeycomb texture. Fe-Ni-Cr sulfides are observed embedded in the Fe-saponite and unaltered smectite is observed attached to the underlying Fe-saponite (Figure 4-11; and F-7 A-F from Caporuscio et al., 2021)

316SS: IEBS-2, -5, -7, and -8. Images of the 316SS coupons from IEBS-2 show two layers of mineral growth that formed perpendicular to the steel surface (Figure 4-11). Fe-saponite forms directly adjacent to the pitted steel surface (Figure 4-11; and F-9 C & D from Caporuscio et al., 2021) and chlorite is observed to form a thin layer locally adjacent to the steel surface, inside of the Fe-saponite. Sulfide minerals, such as pyrrhotite are also observed (Figure 4-11).

The 316SS from IEBS-5 shows two layers of mineral growth similar to IEBS-2. A thin layer of chlorite is observed locally attached to the steel surface and Fe-saponite rosettes form outboard of the chlorite (Figure 4-11; and Figures F-8 C & D from Caporuscio et al., 2021).

Reaction products observed on the surface of the 316SS from IEBS-7 include a mat of Fe-saponite rosettes (Figures F-15, F-16 from Caporuscio et al., 2021). Locally, CSH/smectite is observed to coat the Fe-saponite (Figure F-17 from Caporuscio et al., 2021). Cross section images of the reacted coupon have not yet been collected.

The surface of the 316SS from IEBS-8 is also coated in Fe-saponite (Figures F-23, F-24 from Caporuscio et al., 2021). Clusters of analcime, garronite, and clay are locally attached to the mineralized surface (Figure F-25 from Caporuscio et al., 2021). Cross section images of the reacted coupon have not yet been collected.

LCS: IEBS-4. The post-reaction LCS was coated by a layer of Fe-saponite rosettes. Fe,Ni,Cr-sulfide or other Fe-rich alteration products were not observed

4.3.8.1 Growth Rates of Fe-rick Layer on the Steel Surface

Width measurements of precipitation products perpendicular to the surface of 316SS, 304SS, and LCS coupons were measured for experiments containing stainless-steel coupons.

Precipitation thicknesses (Table 4-4) were measured on backscattered electron images of two coupons per experiment. Fifty measurements were taken at regular intervals from each long side at equal intervals and eight measurements on each short side. Measurements were made in Adobe Photoshop using the measurement tool. Mineral growth rates (Table 4-4) were determined by dividing the average precipitation thickness by the number of experimental run days.

Table 4-4 **Precipitation thickness and rates. Rates are represented in µm per day. Three steel types were examined: 304SS, 316SS and LCS from IEBS-2 through IEBS-5. The water:rock ratios were calculated without the stainless steel. All experiments contained Wyoming bentonite and Grimsel Granodiorite.**

Sample	Steel	Matrix	Temp	Time	Water: Rock	Average Precip. (µm)	Precip./Day (µm/day)
IEBS-3	304	Bent + GG	250°C	6 weeks	7.1	31.60 (±27.01)	0.88
IEBS-2	316	Bent + GG	300°C	6 weeks	11.9	2.27 (±1.40)	0.06
IEBS-5		Bent + GG	300°C	8 weeks	9.4	38.72 (±27.76)	0.69
					AVERAGE:	20.50	0.38
IEBS-4	LCS	Bent + GG	300°C	6 weeks	5.6	40.17 (±30.17)	1.12

* Bent = Wyoming bentonite; GG = Grimsel Granodiorite

The mineral growth rates were the highest in IEBS-4 containing LCS (1.12 µm/day), followed by the 304SS in IEBS-3 (0.88 µm/day). The precipitation rates were the slowest in the experiment containing 316SS. The six-week experiment, IEBS-2, had a lower precipitation rate (0.06 µm/day) versus the 8-week experiment, IEBS-5, at the same conditions (0.69 µm/day). The length of time may have an impact on the thickness of the precipitation, but the difference in the water to rock ratio may be more significant.

4.4 Discussion

4.4.1 Hydrothermal Interaction of Wyoming Bentonite, Grimsel Granodiorite, and Synthetic Groundwater

Synthetic Grimsel Groundwater. A synthetic groundwater was mixed to mimic fluids found at the Grimsel Test Site after the recipe reported in Kersting et al. (2012). Chemistry of the synthetic fluid is presented in Table 4-2. The groundwater at the Grimsel Test Site is a Na-CO_3 type water and has a pH of ~8.6 to 8.8.

Wyoming bentonite. The bentonite used in the present study is unprocessed and was provided by Bentonite Performance Minerals LLC from Colony, Wyoming, U.S.A. It is composed dominantly of Na-montmorillonite (general composition: $Na_{0.33}(Al,Mg)_2(Si_4O_{10})(OH)_2 \cdot nH_2O$), lesser clinoptilolite and feldspar, and minor biotite, pyrite, quartz, opal, and sulfide minerals. The QXRD results from unheated bentonite are presented in Caporuscio et al. 2021.

Grimsel Granodiorite. The granodiorite used in the experiments was sourced from a drill core from the Grimsel Test Site. Major mineral phases include K-feldspar, plagioclase, and quartz. Minor phases are muscovite and biotite. Trace phases are allanite, zircon, titanite, and apatite. The QXRD results from unheated granodiorite are presented in Caporuscio et al. 2021.

Cured Portland cement chip. Chips consisting of a mix of 100% ordinary Portland cement and Los Alamos municipal tap water (Table 4-5) were cast in November of 2018. Major mineral phases observed in the XRD pattern the cured cement chip include portlandite ($Ca(OH)_2$), belite (calcio-olivine, Ca_2SiO_4), alite (Ca_3SiO_5), and brownmillerite ($Ca_2(Al,Fe)_2O_5$).

Table 4-5 Initial groundwater chemical composition from Kersting et al. (2012), the synthetic groundwater used in these experiments (Missana & Geckeis, 2006), and the Los Alamos municipal tap water.

	Target solution (Kersting et al., 2012)	Synthetic Grimsel GW (this study)	Los Alamos Municipal Tap Water
	(mg/L)	(mg/L)	(mg/L)
Na^+	127	116	2.50
K^+	3	3	12.8
Ca^{2+}	5	7	2.04
Mg^{2+}	13	12	9.62
Cl^-	11	14	3.24
CO_3^{2-}	219	203	24.7
SiO_2	21	34	n.m.
SO_4^{2-}	97	87	75.7
pH	8.6–8.8	8.5	6.93

*n.m. = not measured

316SS. (NIST SRM 160b) is an iron alloy primarily with 18.37 wt.% Cr, 12.35 wt.% Ni, 2.26 wt.% Mo, 1.619 wt.% Mn, 0.5093 wt.% Si, and 0.175 wt.% Cu.

304SS. An ion alloy which differs from 316SS in Cr/Ni ratio. Along with Fe, it contains 18 wt.% Cr, 8 wt.% Ni, < 2 wt.% Mn, < 1 wt.% Si, < 0.045 wt.% P, and < 0.03 wt.% S, and < 0.08 wt.% C.

Low carbon steel (LCS). Composed of Fe along with ~0.2 wt.% C, 0.9 wt.% Mn, < 0.04 wt.% P, and < 0.05 wt.% S.

4.4.2 Aqueous Geochemistry

The pH and concentrations of cations and anions in reaction fluids evolved during the experiment, likely reflecting mineral-brine reactions. The starting solution, synthetic Grimsel Granodiorite groundwater, has a pH of ~8.5. The pH, measured at 25ºC, of the fluids extracted weekly from the reaction vessels dropped over the course of all experiments. In the baseline experiment IEBS-0, pH values were steady between 5.5 and 6 throughout experiment duration. In experiments IEBS-1 through IEBS-5, measured pH values were roughly between 6 and 7. Experiment IEBS-2 had a slightly more acidic solution during the middle of the experiment: the pH dropped to ~5 by week 3 and then increased to ~6.2 by the end of the experiment. The pH values in the 6 month experiment, IEBS-7 remained constant just below 6 for the run duration. The pH values observed in IEBS-6 and IEBS-8, which contained a cured Portland cement chip, evolved to slightly higher pH values (i.e., ~7–7.5) (Figure 4-18).

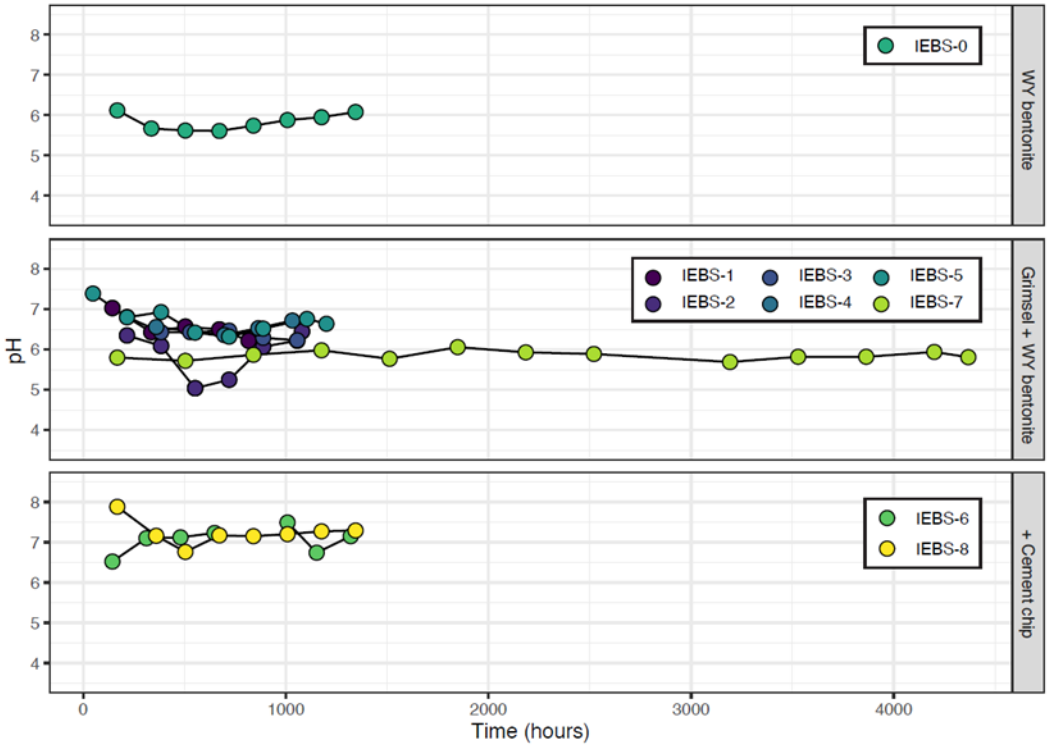

Figure 4-18 Measured pH values (at 25ºC) for reaction fluids extracted from experiments IEBS-0 through IEBS-8.

Water:rock. Experiments were performed at a range of water:rock ratios (8:1 to 13:1). As experiments progressed, fluids were gradually extracted from the reaction vessel during sampling, which slightly lowered the water:rock ratio with every fluid extraction.

4.4.2.1 Cations

Alkali/alkaline earth metals. Major alkali and alkaline earth metal cations (K^+, Na^+, Ca^{2+}, Mg^{2+}) follow similar trends in concentrations measured throughout each experiment (Figure 4-19). In the unfiltered and filtered results, concentrations typically decrease slightly from values observed at the first sampling. No significant differences in measured values between the filtered and unfiltered results are observed.

For IEBS-0 through IEBS-5 and IEBS-7, initial Ca^{2+} values are observed to be close to concentrations in the starting Grimsel Granodiorite synthetic groundwater (~7 mg/L). Calcium concentrations in IEBS-5 and IEBS-7, are initially observed to be slightly elevated in comparison to the other experiments. In IEBS-7, [Ca^{2+}] remains around 1.5 to 2.0 mg/L from month two to six of experiment time. In the experiments containing the cured cement chip (IEBS-6 and IEBS-8), [Ca^{2+}] reaches values less than 2 mg/L within a week of the experiment and are roughly similar to values observed in the experiments that do not contain cement.

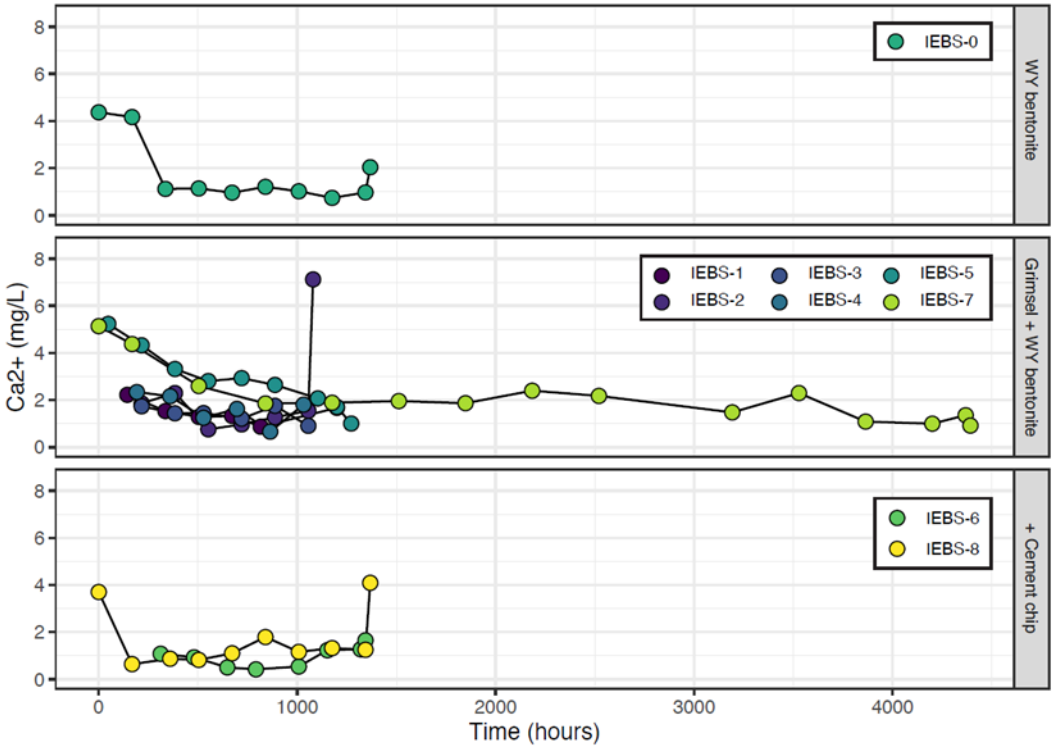

Figure 4-19 Concentration in mg/L of calcium in the unfiltered reaction fluids during each IEBS experiment

Potassium. Potassium concentrations typically remained constant at values below 5 mg/L for the duration of all experiments (Figure 4-20). Experiments with the cured cement chip had slightly higher and less consistent potassium concentrations.

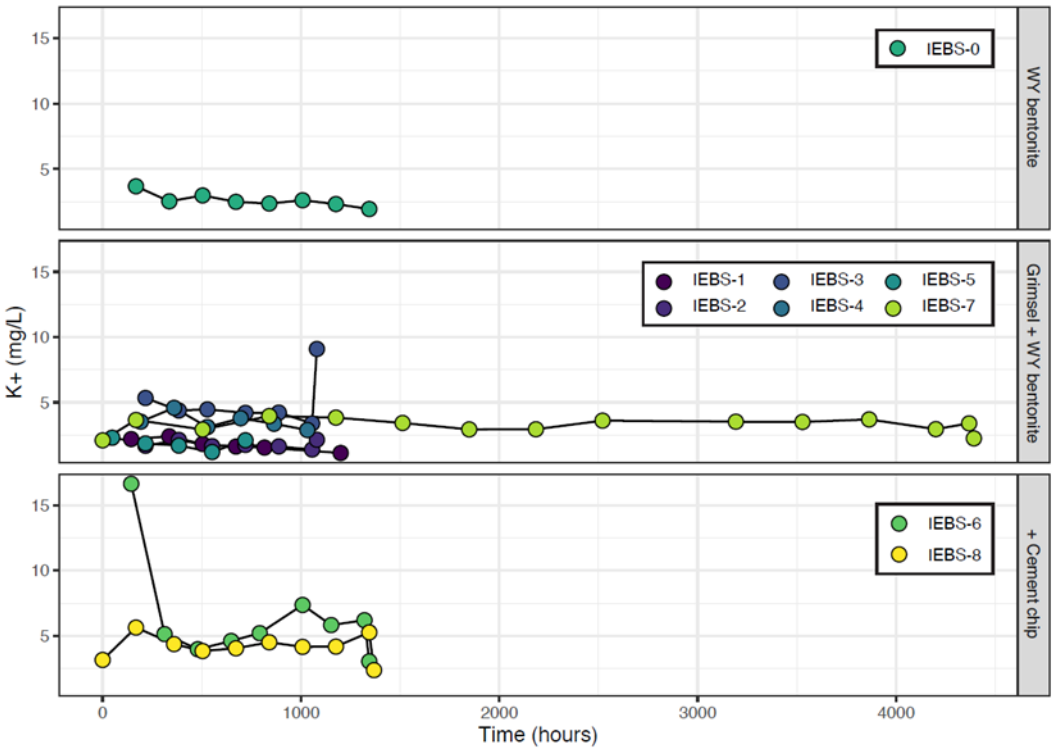

Figure 4-20 Concentration in mg/L of (A) potassium in the unfiltered reaction fluids during each IEBS experiment.

Magnesium. Magnesium concentrations drop from starting solution values (~12 mg/L) to < 0.5 mg/L in the unfiltered aliquot by the first sampling and remain at similar values for the duration of all experiments (Figure 4-21).

Sodium. Observed sodium values in all experiments demonstrate a flat trend (Figure 4-22). Concentrations range from 100 to 200 mg/L but are similar in magnitude to the [Na^+] observed in the starting solution (116 mg/L). There are no differences in the solutions between experiments with bentonite only (IEBS-0), bentonite and Grimsel Granodiorite (IEBS-1 to IEBS-5, IEBS-7), or with the added cement chip (IEBS-6 and IEBS-8).

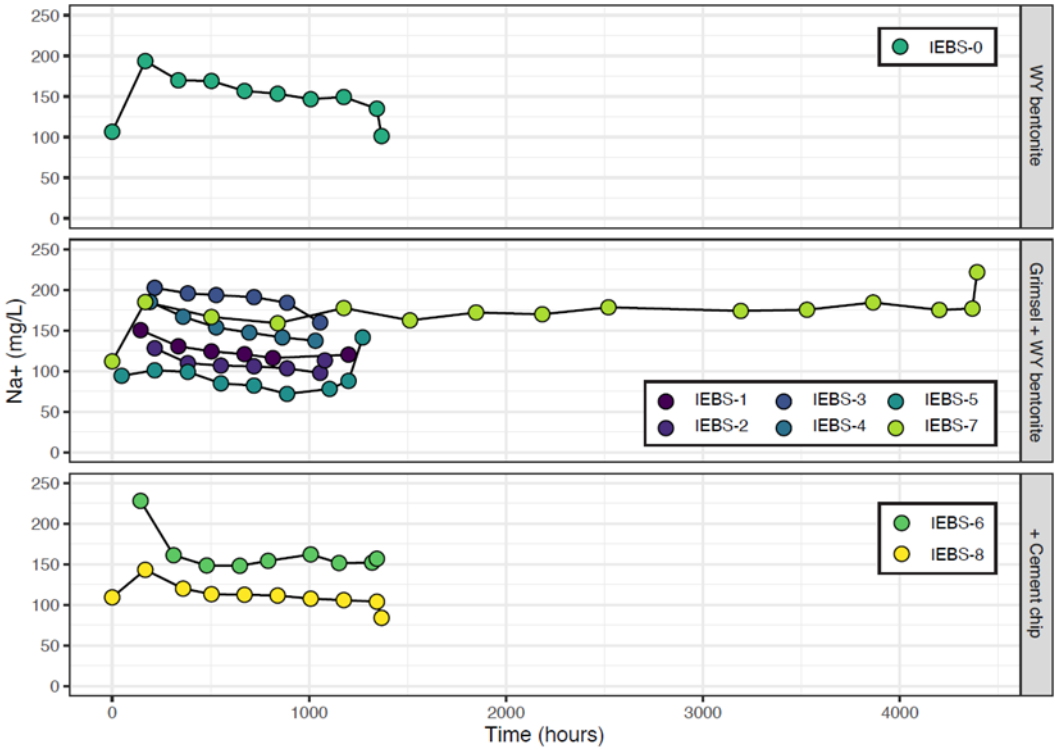

Figure 4-21 **Concentration in mg/L of sodium in the unfiltered reaction fluids during each IEBS experiment.**

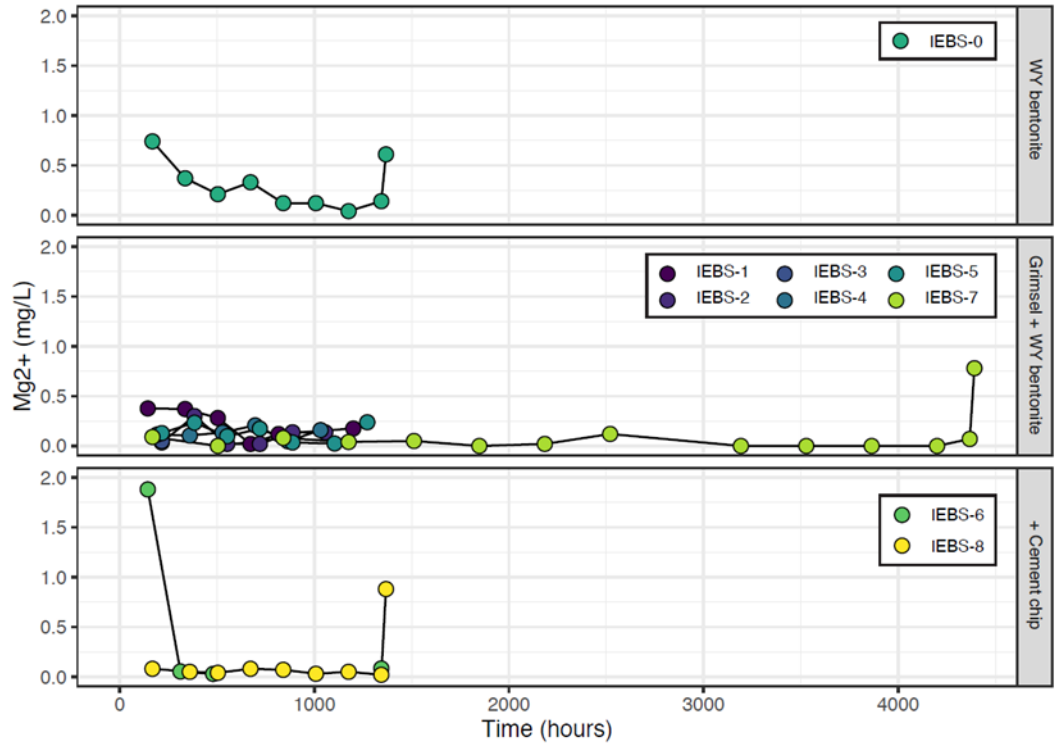

Figure 4-22 **Concentration in mg/L of magnesium in the unfiltered reaction fluids during each IEBS experiment.**

Silica. Measured concentrations in the six completed experiments with Grimsel Granodiorite and Wyoming bentonite (IEBS-1 to IEBS-5, IEBS-7) cover a wide range of values between ~350 and 800 mg/L (Figure 4-23). Starting silica values in the synthetic Grimsel groundwater are ~34 mg/L; values observed in the experiments all increase rapidly during the first week of experiment time. Comparing experiments in this group, the aqueous silica concentrations do not follow consistent trends. For example, values in IEBS-1, IEBS-2, and IEBS-4 decrease after the first sample, before values increase by the third or fourth sample. Concentrations in IEBS-3 initially increased before leveling off around the middle of the experiment, and slightly decreasing over the last two weeks. Concentrations in IEBS-5 remained relatively constant before slightly increasing at the end of the experiment. In the 6-month experiment (IEBS-7), concentrations stabilized by the second month of experiment time to values between 700 and 800 mg/L. Silica concentrations in the Wyoming bentonite only experiments (IEBS-0) remained at between 700 and 800 mg/L as well. In comparison, silica concentrations in the experiments with a cured cement chip (IEBS-6 and IEBS-8) were slightly lower, hovering around 600 mg/L by the end of the experiments.

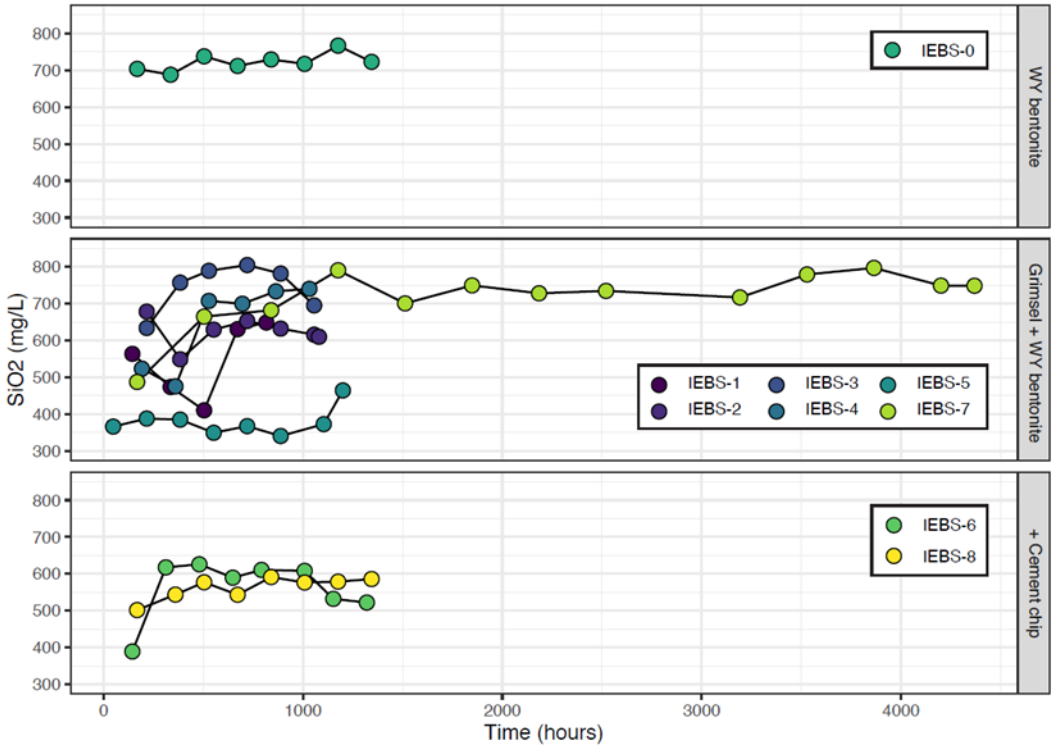

Figure 4-23 Concentration in mg/L of aqueous silica in the unfiltered reaction fluids during each IEBS experiment.

Iron. The [Fe^{2+}] in all IEBS experiments remains below ~1 mg/L in the filtered and unfiltered cation samples for the duration of the experiments (Figure 4-24). A jump to ~10 mg/L is observed around 500 hours experiment time in IEBS-6 in the unfiltered results; this is likely the result of particulate matter present in the sample. The final sample from IEBS-1 that was collected before experiment cooling has Fe concentrations of ~4 mg/L for both filtered and unfiltered samples. Quench samples (collected after experiment cooling) from IEBS-2 and IEBS-3 show sharp increases to >20 mg/L in the unfiltered aliquot (Figure 4-24).

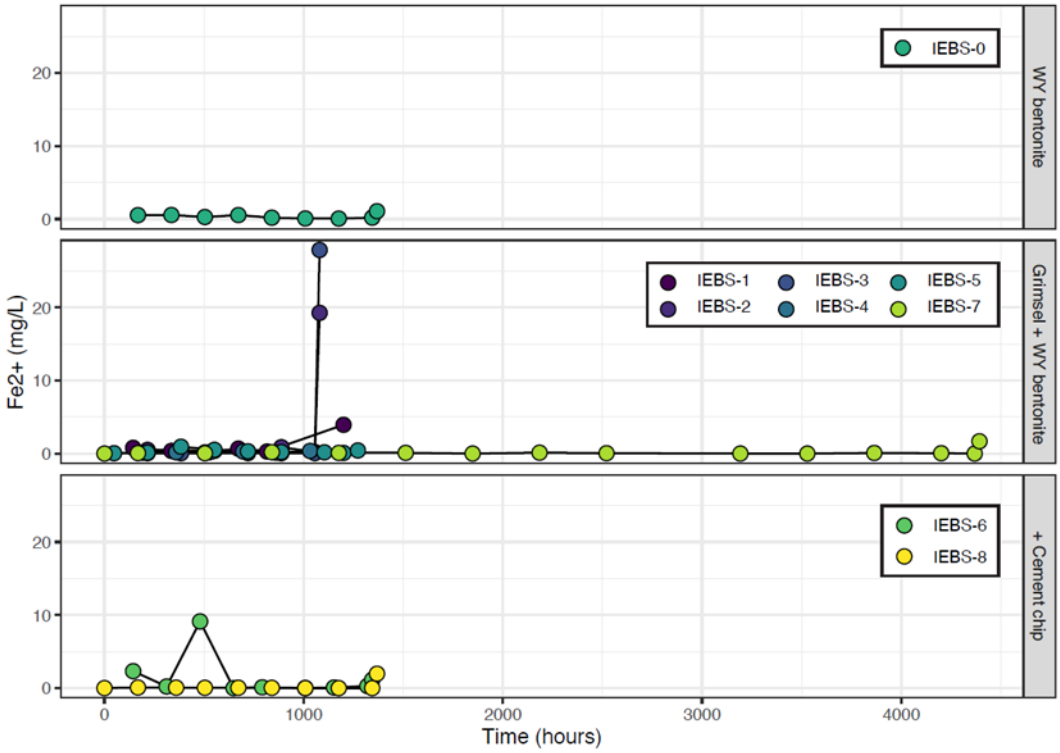

Figure 4-24 Concentration in mg/L of aqueous iron in the unfiltered reaction fluids during each IEBS experiment.

Aluminum. Aluminum concentrations in the unfiltered fraction from experiments IEBS-0 through IEBS-5 and IEBS-7 reached concentrations of ~4 to 5 mg/L by the first weeks of experiment time (Figure 4-25). Concentrations slightly decreased or remained near constant for the remainder of the experiment. Quench samples from IEBS-2 and IEBS-3 exhibit a spike in $[Al^{3+}]$ concentrations. In comparison, the $[Al^{3+}]$ concentrations were notably higher in IEBS-6 and IEBS-8, remaining around 5 to 7 mg/L for the duration of each experiment.

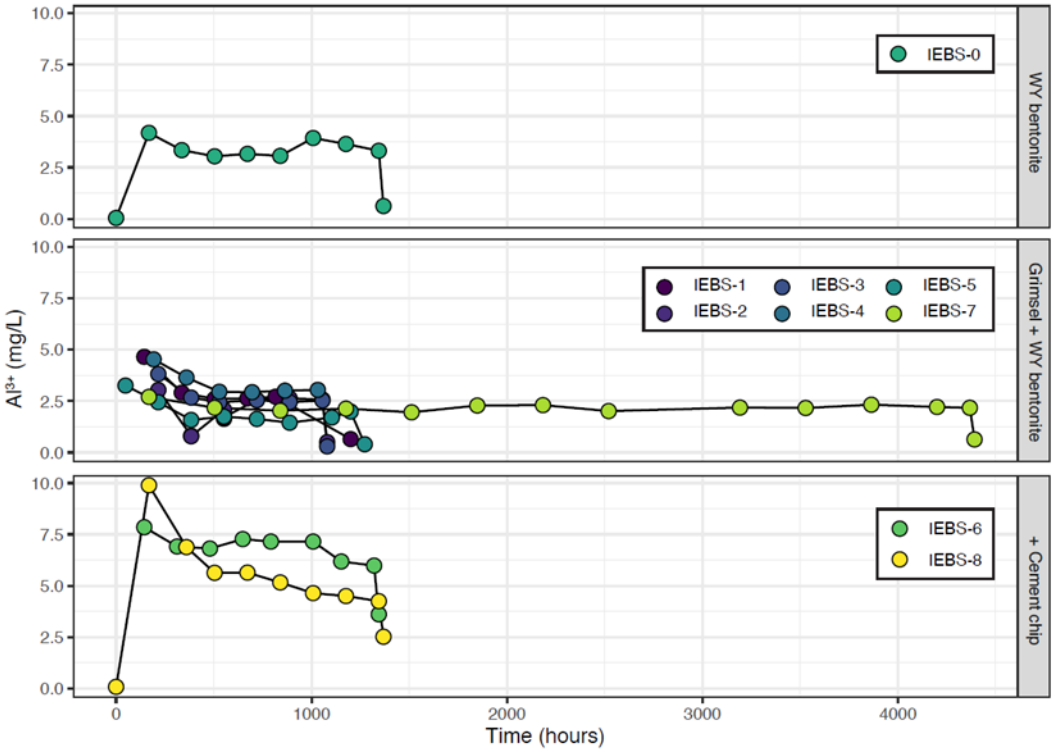

Figure 4-25 Concentrations in mg/L of aluminum in the unfiltered reaction fluids during each IEBS experiment.

4.4.2.2 Anions

Chloride. Chloride concentrations in the baseline experiment with Wyoming bentonite and Grimsel synthetic groundwater (IEBS-0) generally remain between 10 and 15 mg/L. Observed concentrations in experiments with Wyoming bentonite and Grimsel Granodiorite generally decrease from the first to second sampling and then remain relatively steady for the rest of the experiment. By the end of each experiment, measured concentrations in IEBS-1 to IEBS-5 and IEBS-7 are between 10 and 25 mg/L (Figure 4-26). In the experiments with the added cement chip, values are initially elevated in IEBS-6 starting around 33 mg/L and lower in IEBS-8 (~13 mg/L). Chloride concentrations in IEBS-6 and IEBS-8 converge by the end of each experiment to values between 10 and 20 mg/L.

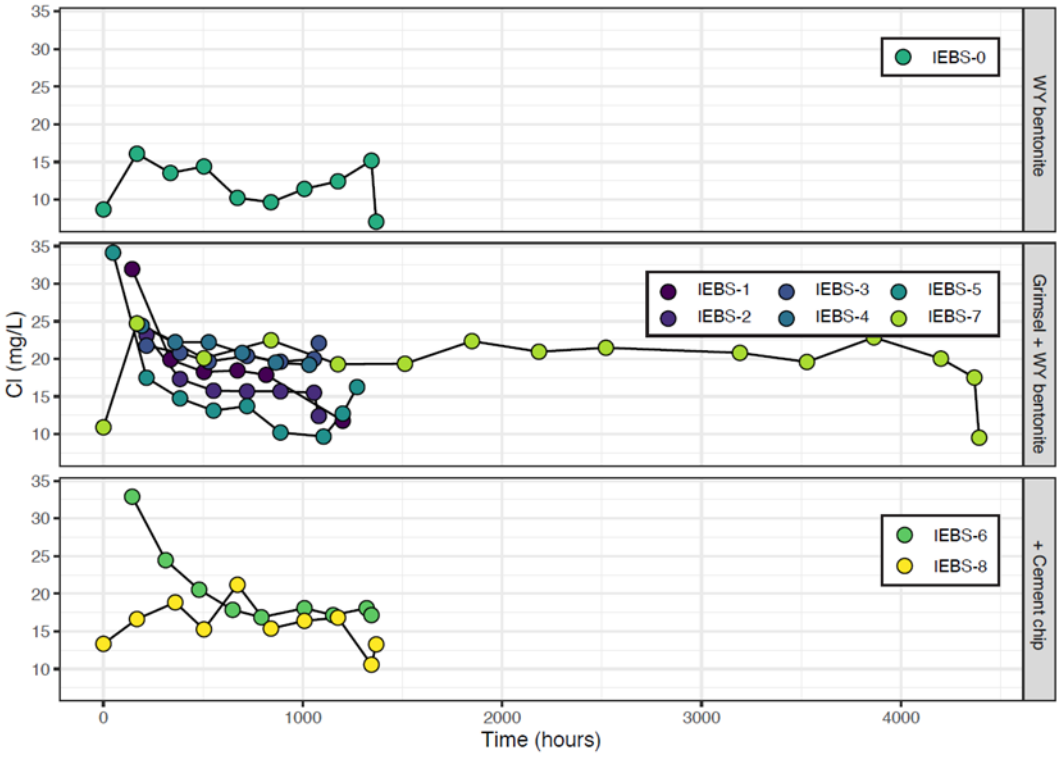

Figure 4-26 Concentration in mg/L of chloride anions in the unfiltered reaction fluids during each IEBS experiment.

Sulfate. Sulfate concentrations in IEBS-0 initially increase sharply from the first to the second sampling, remain between 200 and 300 mg/L for the remainder of the experiment, and drop to 100 mg/L on experiment quench. In the six experiments with Grimsel and Wyoming bentonite, observed concentrations are between 100 and 300 mg/L and generally stabilize by the fourth sampling (Figure 4-27). Observed initial values are between ~150 and 350 mg/L, which shows an increase from the starting solution values (87 mg/L). The majority of experiments end at concentrations of 100 to 200 mg/L, with the exception of IEBS-3, which ended around 275 mg/L (325 mg/L quench). Sulfate concentrations were less variable in the experiments with the cement chip, which mostly remained between 150 and 250 mg/L.

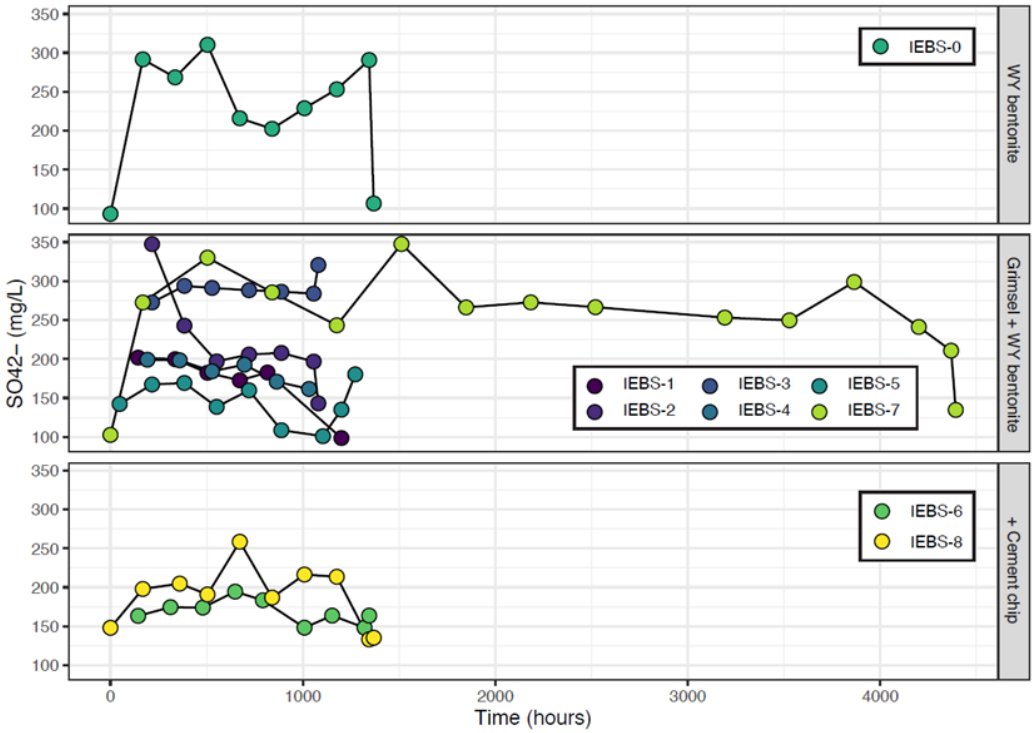

Figure 4-27 Concentration in mg/L of sulfate anions in the unfiltered reaction fluids during each IEBS experiment.

4.4.3 QXRD

QXRD analyses of the starting material mixture and the bulk reaction products from IEBS-0 through IEBS-8 are presented in Table C in Caporuscio et al. 2021. The results show changes in bulk mineralogy as the result of the hydrothermal reaction. The approximate starting reaction mixture for each experiment is listed in Table 4-1. The bulk mineralogy of a representative sample of Wyoming bentonite, Grimsel Granodiorite, and the starting mixture is reported in Caporuscio et al. 2021.

IEBS-0. Experiment IEBS-0 was a baseline experiment to explore Wyoming bentonite alteration in the synthetic Grimsel groundwater solution. Observed mineralogy changes include the reduction in feldspar and clinoptilolite and an increase in smectite/illite/illite-smectite.

IEBS-1 to IEBS-5. Results from the experiment products indicate that mineral dissolution, precipitation, and recrystallization reactions likely occurred. For example, in the results from all samples, the abundance of quartz increases by ~1 to 7 wt.%. Clinoptilolite dissolution likely occurred based on the decrease in abundance by 1 to 6 wt.%. Smectite abundance increases by 3 to 11 wt.% and the amount of mica and chlorite decreases by about 5 wt.%. Changes in clay mineralogy were further investigated by detailed clay mineral structural studies, discussed in the next section.

CSH minerals, which were identified in thin section and in SEM images, were not identified via XRD, likely due to their low bulk abundance or poorly crystalline nature.

IEBS-7. Mineralogy changes in IEBS-7, which examined long term Grimsel Granodiorite + Wyoming bentonite interaction, shows more pronounced mineralogical changes than the shorter term experiments with the same reactants (described above). Feldspar and clinoptilolite were decreased more over the 6-month period and smectite/illite/illite-smectite increased by ~17 wt.%.

IEBS-6 and IEBS-8. The inclusion of a cured cement chip with Wyoming bentonite and Grimsel Granodiorite reactants resulted in different mineralogical changes. The sample analyzed included bentonite and granodiorite components; the cement chip was intact and removed from the mixture for separate post experiment characterization. The main mineralogical changes include reduction in clinoptilolite and the formation of analcime and amorphous material.

4.4.4 Clay XRD

The clay-size fraction (<2 µm) was separated via density separation from a gently crushed portion of the reaction products from each experiment. While crushing, discrete particles of Grimsel Granodiorite were removed. In the case of IEBS-6, the cement chip was separated before the sample was selected. The XRD patterns of the ethylene glycol saturated, oriented clay fractions can be used to determine alterations to the clay mineral structure (i.e., peak position shifts), which can be used to calculate clay mineral expandability. The ethylene glycol saturated peak positions are presented in Table 4-6 and the XRD patterns are plotted in Figure 4-28.

Peak positions from IEBS-1 through IEBS-5 are similar to those of the ethylene glycol saturated smectite peaks of unheated Wyoming bentonite, and calculated expandabilities based on the difference between the d002 and d003 peaks from these samples show an increase in clay expansion. Results from IEBS-0 show less expandability. In comparison, results from IEBS-6 and IEBS-8, which included the cured cement chip, show lower expandabilities than the clay fraction from experiments without cement, but still slightly increased in comparison to unreacted Wyoming bentonite. The six month experiment, IEBS-7, shows similar expandability estimates and peak positions to IEBS-6 and IEBS-8.

Table 4-6 Glycolated smectite (GS) peak positions for the <2 µm clay fraction separated from the Wyoming bentonite. Expandability was calculated based on the position of the 002 and 003 GS peaks.

Sample	1		2		3		5		002/003	1	2	3
EG-smectite	2θ	d (Å)	2θ	d (Å)	2θ	d (Å)	2θ	d (Å)	Δ 2θ	%Exp	%Exp	%Exp
WY Bentonite	5.2	17.0	10.4	8.5	15.7	5.7	26.3	3.4	5.2	102	105	105
IEBS-1	5.2	16.9	10.4	8.5	15.6	5.7	26.2	3.4	5.2	105	109	109
IEBS-2	5.3	16.6	10.4	8.5	15.7	5.6	26.2	3.4	5.1	108	112	111
IEBS-3	5.2	17.1	10.3	8.6	15.6	5.7	26.2	3.4	5.1	107	111	110
IEBS-4	5.2	17.1	10.3	8.6	15.6	5.7	26.2	3.4	5.1	107	111	110
IEBS-5	5.2	16.9	10.4	8.5	15.6	5.7	26.2	3.4	5.1	107	111	110
IEBS-6	5.2	17.0	10.4	8.5	15.7	5.7	26.3	3.4	5.2	104	107	107
IEBS-7	5.2	17.0	10.4	8.5	15.6	5.7	26.1	3.4	5.2	102	104	105
IEBS-8	5.2	17.0	10.4	8.5	15.6	5.7	26.1	3.4	5.2	100	103	103
IEBS-0	5.2	17.0	10.4	8.5	15.6	5.7	26.2	3.4	5.3	100	102	102

1: %Exp = $973.76 – 323.45\Delta + 38.43\Delta^2 – 1.62\Delta^3$ (Eberl et al., 1993)
2: %Exp = $1517.8 – 548.49\Delta + 68.35\Delta^2 – 2.90\Delta^3$ (Eberl et al., 1993)
3: %Exp = $766.01 – 194.10\Delta + 12.924\Delta^2$ (Moore and Reynolds, 1997)

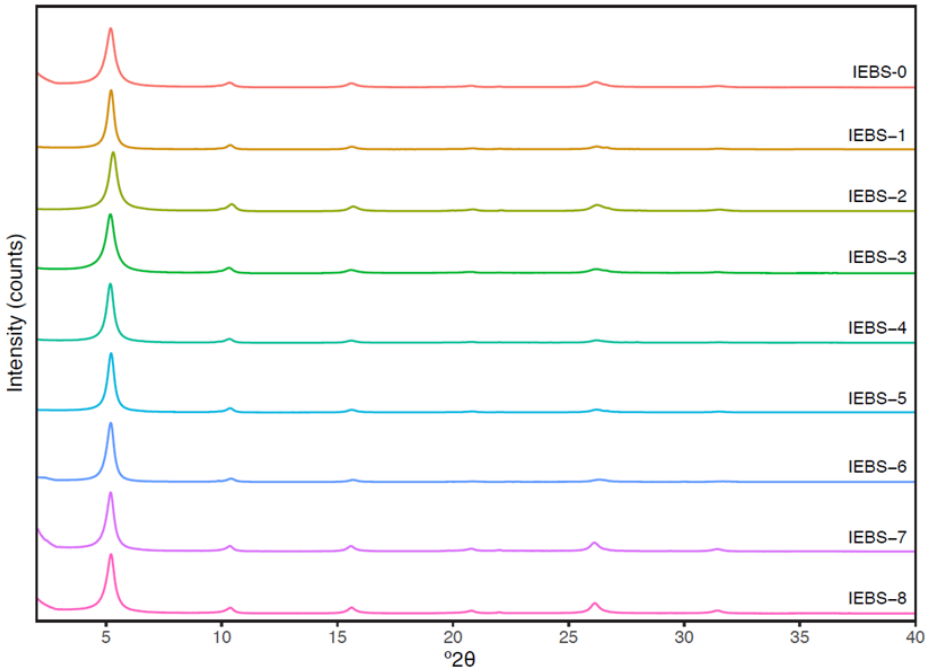

Figure 4-28 XRD patterns the oriented, ethylene glycol saturated <2 µm fraction from IEBS-1 through IEBS-8 showing no significant shifts in smectite peaks.

4.4.5 Electron Microprobe Analyses

Reaction products were analyzed via electron microprobe (EMP) to determine the major element composition of mineral phases. The EMP analyses primarily targeted the clay matrix, steel alteration products, altered glass shards, and other authigenic minerals. Analysis of the reaction products from IEBS-6, IEBS-7, IEBS-8, and IEBS-0 are currently in progress and will be included in the report for FY22. The EMP results of the previous experiments are reported in Appendix D of Caporuscio et al. 2021 and described in Caporuscio et al., 2020.

4.4.6 SEM/EDS

Reaction products, including loose powder, epoxy mounts, and thin sections, from the IEBS experiments were characterized using the SEM and qualitative elemental abundances were evaluated using EDS. The SEM images are presented in Appendix F of Caporuscio et al. 2021 and described below.

4.4.6.1 Clay

IEBS-0. Clay in the reaction products of IEBS-0 has a foily texture (F-25; F-26; F-27 from Caporuscio et al., 2021). Analcime sphere are observed locally. Feldspar with dissolution texture was also observed.

IEBS-1 to IEBS-5. The reaction products show similar features. In all the experiments, montmorillonite clay has a foily texture (i.e., Figure F-1 A, B; F-4 A, B, F-7 A from Caporuscio et al., 2021). Spherical crystals are embedded in the fine-grained clay matrix (i.e., Figure F-1 C, D, E; F-2 C, D; F-3 A, C; F-4 B, C, D, E; F-6 B, C from Caporuscio et al., 2021). The EDS analyses of these crystals reveal large Ca peaks, with smaller Si, Al, and C peaks, likely corresponding to calcium aluminum silicate hydrate (CASH) minerals.

IEBS-6 and IEBS-8. The clay matrix of IEBS-6 and IEBS-8 is altered throughout to include analcime, garronite, feldspars, and erionite (F-10; F-11; F-18; F-19; F-20 from Caporuscio et al., 2021).

IEBS-7. In the 6-month experiment, clay is observed to have a foily texture (F-13, F-14 from Caporuscio et al., 2021). Feldspar with dissolution textures is observed.

4.4.6.2 Grimsel Granodiorite

Feldspar surfaces are observed to be variably pitted, indicating dissolution may have occurred at the edge of the grains (Figure 4-29). No significant authigenic mineral precipitation is observed to form rims on the feldspar grains. Further, fragments of Grimsel Granodiorite included in the experiments did not experience any significant mineral reactions. For example, Figure 4-30 shows an intact Grimsel fragment composed of biotite, apatite, and quartz. No alteration textures or new mineral growth is observed within the boundaries of the Grimsel fragment.

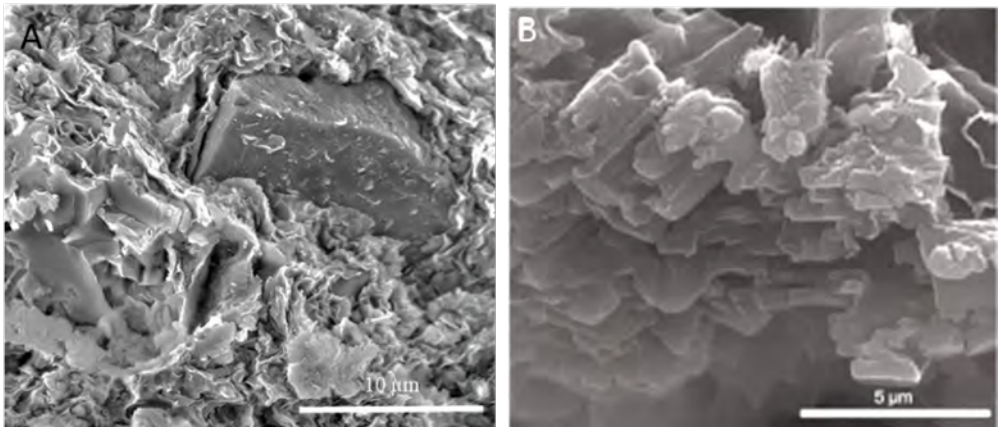

Figure 4-29 Feldspar dissolution textures observed in secondary electron SEM images from (A) IEBS-5 and (B) IEBS-1.

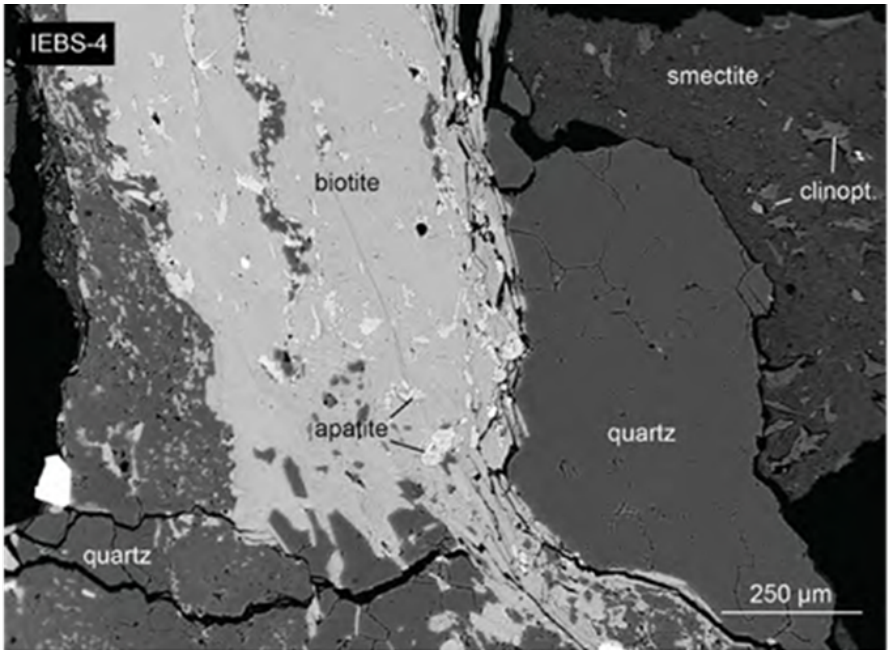

Figure 4-30 Backscattered electron SEM image of a post-reaction fragment of Grimsel Granodiorite from IEBS-4. Authigenic mineral growth/alteration is not apparent within the fragment. Abbreviation: clinopt., clinoptilolite.

4.4.6.3 Post-reaction Gel

At the conclusion of the experiments, a gel-like slurry was present on the top of the reactionproduct for IEBS-3, 4, and 5 (Figure 4-31A). The dried gel was analyzed with EDS and is Si- and Al-rich with minor amounts of Fe (1.4 - 4.3 wt.%) and Na^{2+} (3 - 6 wt.%). The dried gel texture consisted of linear and cross-linked morphology (Figure 4-31B & C).

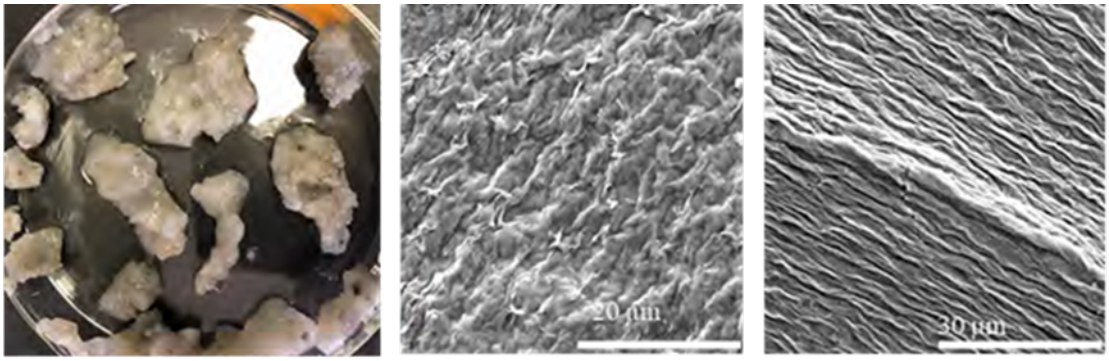

Figure 4-31 [A]. Post-reaction gel mixed with clay from IEBS-4. [B & C]. SEM images of the dried gel. Two different textures were observed: cross-linked and linear.

4.4.6.4 Experiments with Cement

SEM images of the surface of the starting cement material showed various cement phases (see Caporuscio et al., 2021). In IEBS-6 and IEBS-8, which contained cured Portland cement in the starting materials, Na-rich analcime was prevalent throughout the reaction product (Figure 4-32) along with minor erionite-Ca and garronite (not shown here, see Caporuscio et al., 2021). The fragments of the Grimsel Granodiorite did not experience significant alterations and only occasional dissolution texture on the surface of feldspar grains was observed (Figure F-11 B in Caporuscio et al., 2021). The cured Portland cement chips extracted from IEBS-6 and IEBS-8 both have a layer of clay with zeolite embedded on the surface (Figure 4-32). A thin section showing a cross section of the cement chip was created and will be characterized in the next FY.

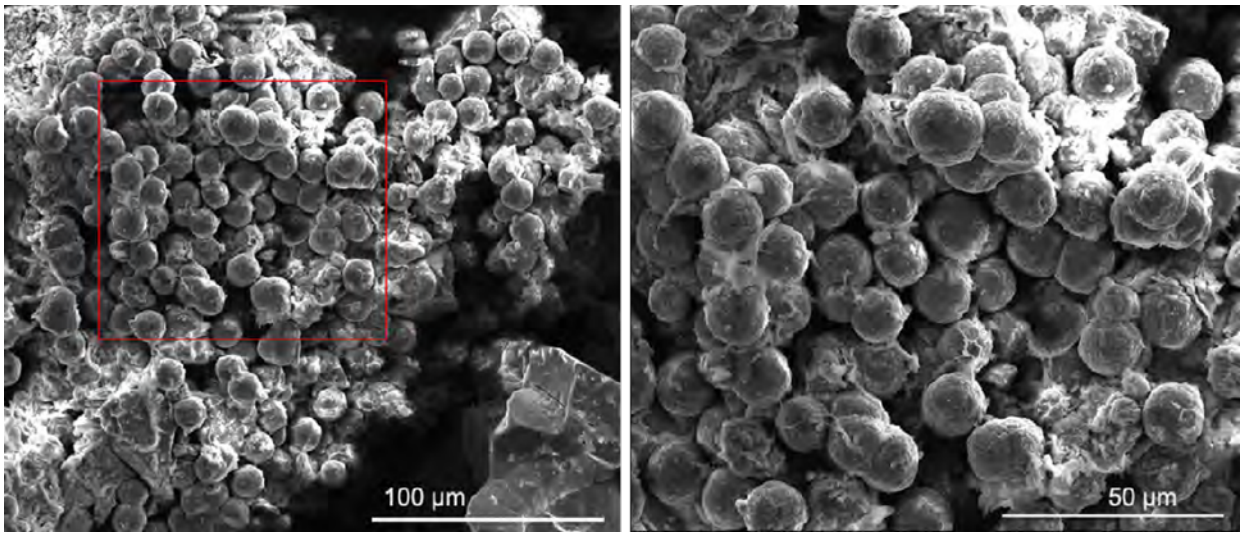

Figure 4-32 Cluster of Na-rich analcime grains from experiment IEBS-6, which included a cured chip of ordinary Portland cement. The image on the right is a magnification of the red box in left image.

4.4.7 Colloid Formation

A gel phase was observed on experiment cooling in IEBS-3, IEBS-4, and IEBS-5. When suspended in DI water, particles remained suspended in solution. A dried film of the suspension from IEBS-5 was analyzed via XRD; the colloid phase was identified as montmorillonite. A portion of the suspension fluid from IEBS-5 was also analyzed with a Zetasizer at Los Alamos National Laboratory, in order to assess particle size and colloid stability. The measured zeta potential values centered around -38.9, indicating moderately stable colloids. The average particle size diameter was ~237 nm and the diameters were distributed between ~30 and 1000 nm (Figure 4-33).

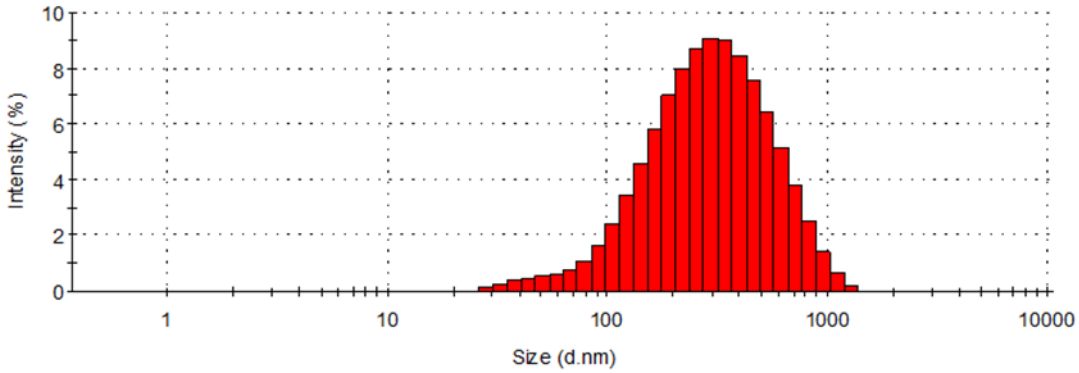

Figure 4-33 Distribution of colloid diameters from sample IEBS-5 measured via Zetasizer.

4.4.8 Steel-bentonite Interface Mineralization

Steel coupons (316SS, 304SS, and LCS) were included in IEBS-2 through IEBS-5 (Table 4-7). All of the experiments contained Wyoming bentonite, Grimsel Granodiorite, and synthetic Grimsel Granodiorite groundwater. Experiments were run at 250°C and 150 bar for a period of 6 or 8 weeks. The mineralogy

and chemistry of phases that formed on the surface of the steel coupons was characterized and measured via SEM and EMPA.

304SS: IEBS-3. The surface of the 304SS coupon included in IEBS-3 was coated in Fe-saponite with a honeycomb texture. Fe-Ni-Cr sulfides are observed embedded in the Fe-saponite and unaltered smectite is observed attached to the underlying Fe-saponite (Figure 4-27; and F-7 A-F from Caporuscio et al., 2021)

316SS: IEBS-2, -5, -7, and -8. Images of the 316SS coupons from IEBS-2 show two layers of mineral growth that formed perpendicular to the steel surface (Figure 4-27). Fe-saponite forms directly adjacent to the pitted steel surface (Figure 4-27; and F-9 C & D from Caporuscio et al., 2021) and chlorite is observed to form a thin layer locally adjacent to the steel surface, inside of the Fe-saponite. Sulfide minerals, such as pyrrhotite are also observed (Figure 4-27).

The 316SS from IEBS-5 shows two layers of mineral growth similar to IEBS-2. A thin layer of chlorite is observed locally attached to the steel surface and Fe-saponite rosettes form outboard of the chlorite (Figure 4-27; and Figures F-8 C & D from Caporuscio et al., 2021).

Reaction products observed on the surface of the 316SS from IEBS-7 include a mat of Fe-saponite rosettes (Figure F-15, F-16 from Caporuscio et al., 2021). Locally, CSH/smectite is observed to coat the Fe-saponite (Figure F-17 from Caporuscio et al., 2021). Cross section images of the reacted coupon have not yet been collected.

The surface of the 316SS from IEBS-8 is also coated in Fe-saponite (Figure F-23, F-24 from Caporuscio et al., 2021). Clusters of analcime, garronite, and clay are locally attached to the mineralized surface (Figure F-25 from Caporuscio et al., 2021). Cross section images of the reacted coupon have not yet been collected.

LCS: IEBS-4. The post-reaction LCS was coated by a layer of Fe-saponite rosettes. Fe,Ni,Cr-sulfide or other Fe-rich alteration products were not observed

4.4.8.1 Growth Rates of Fe-rich Layer on the Steel Surface

Width measurements of precipitation products perpendicular to the surface of 316SS, 304SS, and LCS coupons were measured for experiments containing stainless-steel coupons.

Precipitation thicknesses (Table 4-7) were measured on backscattered electron images of two coupons per experiment. Fifty measurements were taken at regular intervals from each long side at equal intervals and eight measurements on each short side. Measurements were made in Adobe Photoshop using the measurement tool. Mineral growth rates (Table 4-7) were determined by dividing the average precipitation thickness by the number of experimental run days.

Table 4-7 Precipitation thickness and rates. Rates are represented in µm per day. Three steel types were examined: 304SS, 316SS and LCS from IEBS-2 through IEBS-5. The water:rock ratios were calculated without the stainless steel. All experiments contained Wyoming bentonite and Grimsel Granodiorite.

Sample	Steel	Matrix	Temp	Time	Water:Rock	Avg. Precipitation (µm)	Precipitation/day (µm/day)
IEBS-3	304	Bent + GG	250°C	6 weeks	7.1	31.60 (±27.01)	0.88

IEBS-2		Bent + GG	300°C	6 weeks	11.9	2.27 (±1.40)	0.06
IEBS-5		Bent + GG	300°C	8 weeks	9.4	38.72 (±27.76)	0.69
		Average:				**20.50**	**0.38**
IEBS-4	LCS	Bent + GG	300°C	6 weeks	5.6	40.17 (±30.17)	1.12

* Bent = Wyoming bentonite; GG = Grimsel Granodiorite

The mineral growth rates were the highest in IEBS-4 containing LCS (1.12 µm/day), followed by the 304SS in IEBS-3 (0.88 µm/day). The precipitation rates were the slowest in the experiment containing 316SS. The six-week experiment, IEBS-2, had a lower precipitation rate (0.06 µm/day) versus the 8-week experiment, IEBS-5, at the same conditions (0.69 µm/day). The length of time may have an impact on the thickness of the precipitation, but the difference in the water to rock ratio may be more significant.

4.5 Discussion

4.5.1 Hydrothermal Interaction of Wyoming Bentonite, Grimsel Granodiorite, and Synthetic Groundwater

Interaction of Wyoming bentonite and synthetic Grimsel groundwater was documented in IEBS-0. QXRD results show a decrease in clinoptilolite and plagioclase and increase in smectite. XRD results show that smectite structure is not altered during the 8-week experiment. Locally, analcime crystals are observed. Observed pH values are around 6. Overall, at 250ºC smectite appears to remain stable, and form from the alteration of minerals such as plagioclase feldspar during the experiment.

In experiments that included Wyoming bentonite, Grimsel Granodiorite, and the synthetic brine (IEBS-1 through IEBS-5), reaction products include a fine-grained, recrystallized clay matrix with phenocrysts derived from the starting Grimsel Granodiorite and accessory minerals in Wyoming Bentonite, such as feldspars, micas, and quartz. Newly formed mineral phases include calcite, quartz, gypsum, and a C(A)SH phase. The following describes our preliminary observations on hydrothermal mineralization and alteration in the 6–8 week Wyoming bentonite + Grimsel Granodiorite experiments.

4.5.1.1 Montmorillonite

Secondary electron SEM imaging of loose powder mounts of the reaction products show the development of a foily texture in the fine-grained clay matrix.

Recrystallization of montmorillonite to non-swelling phases, such as illite or muscovite, is not observed. The XRD patterns from the oriented clay fraction show no alteration to the montmorillonite structure or expansion capacity (Figure 4-7, Table 4-7). In addition, the QXRD analyses of the reaction products from IEBS-1 through IEBS-5 show increased abundance of montmorillonite.

The EMP analyses from the clay matrix of all the IEBS experiments have very similar compositions (Appendix E, Caporuscio et al., 2021). In terms of alkali elements, the matrix is most enriched in Na (0.15–0.17 atoms per formula unit) in comparison to K (0.02–0.03 apfu) and Ca (0.02–0.03 apfu). The bulk chemistry of the starting materials (i.e., Na-rich montmorillonite in the unheated Wyoming bentonite) may prevent illitization due to low K^+ content in the system. Stability of Na-montmorillonite in hydrothermal experiments with low bulk system potassium has also been observed in our experimental work with Wyoming bentonite ± Opalinus Clay, in which illitization was prohibited by the bulk chemistry of the system (Cheshire et al., 2014; Sauer et al., 2020)

4.5.1.2 Feldspars

Low temperature feldspars have been identified in all the experimental runs; however, further characterization is needed in future experiments to understand their significance.

4.5.1.3 Calcium (aluminum) Silicate Hydrates

In all the experiments with Grimsel Granodiorite and Wyoming bentonite, spherical, C(A)SH phases formed within the fine-grained clay matrix. Small amounts of this mineral are observed in IEBS-1, and it is abundant in IEBS-2 through 5 (Figure 4-6). Based on the composition of this mineral (Appendix E, Caporuscio et al., 2021), it is likely a hydrated calcium silicate, such as tobermorite ($Ca_5Si_6O_{16}(OH)_2$•$4(H_2O)$).

The formation of C(A)SH minerals contrasts with the products of previous experiments with Wyoming bentonite ± Opalinus Clay host rock in which zeolite phases (analcime–wairakite solid solution) formed. The EMP analyses of the spherical minerals formed in the IEBS experiments had significantly lower SiO_2 and Al_2O_3 content and very high CaO in comparison to the analcime–wairakite. Further, analcime–wairakite is interpreted to crystallize from dissolution/precipitation of clinoptilolite and/or clay minerals in Opalinus Clay (Cheshire et al., 2014; Sauer et al., 2020). In the Grimsel system, clinoptilolite is observed to survive the hydrothermal experiment (e.g., Figure 4-29F). Tobermorite crystals are embedded in the clay matrix of the IEBS reaction products and may form from the dissolution/precipitation of smectite. Other studies have identified the formation of tobermorite from montmorillonite during lower temperature (<120°C) hydrothermal reactions (e.g., Fernandez et al., 2017). Tobermorite has also been observed in experiments involving bentonite and cement with highly alkaline bulk chemistries and pH > ~10 (Savage et al., 2007). In comparison, the solution pH over the course of the IEBS experiments did not exceed ~7 (Figure 4-18) and the experiments did not involve cement. Future investigations will focus on CSH mineral reactions in the IEBS experiments with Grimsel Granodiorite and Wyoming bentonite.

4.5.1.4 H_2S Generation

Fluid extraction from the IEBS experiments was accompanied by strong $H_2S_{(aq,g)}$ smells during the course of the 250°C experiments. The $H_2S_{(aq,g)}$ is most likely related to pyrite solubility from the starting Wyoming Bentonite in a chloride-bearing solution (Crerar et al. 1978; Ohmoto et al. 1994) and the sulfate concentration in the synthetic Grimsel groundwater solution. The reducing nature of the experimental system likely preserved the $H_2S_{(aq,g)}$ species. Pyrite contents obtained by QXRD analyses for the Colony Wyoming bentonite (0.4 wt.%) are listed in Table 4-3. Grimsel Granodiorite lacks pyrite, but the synthetic Grimsel groundwater contains appreciable SO_4^{2-} (Table 4-2). The QXRD results show a slight decrease in the abundance of pyrite in the reaction products; however, the low bulk abundance likely resulted in some uncertainty in the result.

Sulfide-induced corrosion of the waste canisters is the primary concern for the Swedish repository systems (Börjesson et al., 2010), therefore the Swedish Nuclear Fuel and Waste Management Company (SKB) have emplaced fairly strict sulfur specifications (sulfide content <0.5 wt.%; total sulfur <1 wt.%) for the bentonite buffer used in their repositories (Börjesson et al., 2010).

4.5.1.5 pH Effects

In IEBS-1 through IEBS-5, the solution starts with a pH of 8.5 and ends between 6 and 7.5. All the experiments drop in pH in the middle of the experiment to less than 6.7 before slightly rebounding (Figure 4-18). Many of the mineral-forming reactions described above are strongly influenced by the pH of the system. Most mineral reaction rates that are of concern to a repository are increased under high pH

systems. Chermak (1992) showed that under pH conditions of 11 to 13, Na-rectorite was formed at 150 to 200°C within 17 days. Fully formed Na-mica (paragonite) developed after 32 days. Work from Eberl and Hower (1977) and Eberl (1978) do not show illitization until 260 to 400 °C at quenched pH's ranging from 4 to 5. These observations are consistent with the current IEBS research; illitization was not observed and Na-rich phyllosilicates formed.

The formation of C(A)SH minerals may also affect the pH of the system. Savage et al. (2002) describe the formation of tobermorite with the generalized reaction:

$$Ca^{2+} + SiO_{2\,(aq)} + H_2O \rightarrow \text{tobermorite} + H^+ \qquad \textbf{Eq. 4-3}$$

in which H^+ is produced. Thus, the formation of C(A)SH minerals, such as tobermorite, may buffer the solution to lower pH values. Savage (1997) reported that zeolite formation within bentonite in contact with cement occurs at lower pH values and C(A)SH mineral formation is favored at high pH (> 11.5). In the IEBS experiments, C(A)SH minerals formed, but solution pH values remained below ~7 for the duration of the run. The formation of C(A)SH minerals at low pH (<7) in the IEBS experiments is at odds with previous experiments and will be the subject of our future investigations.

4.5.1.6 Six Month Experiment

The six-month experiment (IEBS-7) was conducted to observe kinetic effects of a longer heating time. The aqueous geochemical and mineralogical changes in changes observed were similar to the observations from the shorter experiments described above. The solution chemistry stabilized by 6 to 8 weeks of experiment time (Figure 4-18 through Figure 4-27). The pH and concentrations of cations and anions were similar to those observed in the 6 to 8-week experiments.

The mineralogical changes in the 6-month experiment were more pronounced than in the shorter experiments. Similarly, no zeolites have been observed in the reaction products so far. Electron microprobe analyses are in the process of being collected. The QXRD results show that more silicate mineral transformations occurred. More plagioclase feldspar and clinoptilolite dissolution occurred. An increase in the weight percent of smectite was observed, likely from the alteration of minerals like plagioclase feldspar. Significant formation of non-swelling clays was not observed, indicating that montmorillonite remained stable at the experimental conditions.

4.5.1.7 Summary

The mineralogical and geochemical changes observed in the Wyoming bentonite- Grimsel Granodiorite experiments can be applied to understanding potential material interactions in a high-temperature, crystalline repository. Montmorillonite remained stable in the 250ºC hydrothermal experiments, indicating the bulk composition of the system likely prevented smectite illitization. Quartz precipitation occurred, likely related to breakdown of precursor zeolite (clinoptilolite) in the Wyoming bentonite. Minor CSH phases were observed and may be precursor phases to zeolites. Preliminary findings suggest that the clay barrier may only experience slight alteration in the initial thermal pulse in a repository setting, but this finding should be supported by longer term experiments and full-scale demonstrations (e.g., HotBENT).

4.5.2 Colloid Generation

The formation of bentonite colloids is likely significant for process models of repository function, as colloid-facilitated transport of radionuclides may occur in a crystalline system (e.g., Missana and Geckeis, 2006). Moderately stable colloids were observed in re-suspensions of gel formed in IEBS-5, and likely

are present in the other experiments that are yet to be characterized. Colloid stability at the high temperatures utilized in this experimental study is not well known. According to the DLVO theory, colloids are likely not stable in solution at the temperature of the experiment (250ºC) due to reduction in surface charge density and electric double layer thickness of the colloid particles (e.g., Garcia-Garcia et al., 2009). Therefore, in our reaction products, colloids were likely stabilized in solution to form a gel phase upon experiment cooling. Future work will investigate if colloids are present in aqueous samples extracted while the experiment is at temperature and the effects of hydrothermal treatment on the physical properties of bentonite colloids.

4.5.3 Effects of Ordinary Portland Cement

Two experiments containing a cured chip of ordinary Portland cement have been completed. The inclusion of the cured cement chip introduced multiple mineral phases and chemical species that were reactive at the temperature and pressure conditions of the experiment. The cement chip represented ~18 wt.% of the total solid reactants and resulted in slightly increased solution pH values and diverse mineral reaction products in comparison to the results from IEBS-1 through IEBS-5 and IEBS-7 described above.

The effect on the system pH was not dramatically different from the experiments without cement (e.g., pH = ~7.5 versus pH = 6 – 7, respectively). It appears that OH^- derived from the cement chip was either quickly consumed by mineral-forming reactions and/or the system was buffered by zeolite/clay mineral forming reactions. Concentrations of anions and cations in solution were a similar magnitude to those observed in the experiments without cement.

SEM characterization of the reaction products from IEBS-6 and IEBS-8 show that zeolite formation occurred throughout the experiment groundmass, on the cement chip surface, and on the surface of the steel coupon included in IEBS-8 (Figure F-12 A & B, F-18, -19, -20 from Caporuscio et al., 2021). Zeolite phases identified by SEM-EDS include garronite and analcime.

Quantitative XRD results from the clay groundmass show the proportion of clay and other precursor mineral phases that were consumed in zeolite and CSH mineral forming reactions. These analyses provide insight to potential volume decreases/porosity development at the cement-bentonite interface. The formation of 3 to 6 wt.% analcime in the clay groundmass of experiments IEBS-6 and IEBS-8 was observed, coupled with a decrease of similar magnitude in wt.% of smectite. Changes in the abundance of other mineral phases was similar to as observed in the experiments without cement. Thus, the formation of zeolite reaction products likely occurred from the interaction of experimental fluids with a slightly higher pH, cement components, and clay.

In full-scale EBS demonstrations, such as FEBEX, the alteration zone in the bentonite at the cement-bentonite interface (at ambient temperatures) only extends several cm into the buffer (Fernández et al., 2017). The experimental results described here provide insight into changes that may be expected at higher temperatures (i.e., the formation of zeolite minerals, pH effects). Characterization that is still in progress includes the observation of local changes in mineralogy of the cement piece included in the experiment and chemistry from the edge to the interior of the cement chip of a thin section of a cross section of the cement chip. These analyses will reveal important information on the stability of cement phases such as portlandite on the exterior and interior of the cement chip.

4.5.4 Steel-bentonite Interface: Mineral Precipitation and Steel Corrosion

The results from these experiments show a dynamic environment in the experimental systems at the bentonite-metal interface. The bulk chemistry likely controls the alteration mineralogy, as demonstrated by the similarities in mineral precipitation in the experiments. The new growth of surface-bound minerals

is likely due to direct crystallization in the localized environments surrounding the metal with the steel material acting as a substrate for mineral growth in response to corrosion.

The findings of our previous investigations on mineral precipitation at the steel-bentonite interface in hydrothermal experiments mimicking a crystalline rock environment have been described in Caporuscio et al. (2018; 2019). These previous reports describe the layered alteration sequence observed on the surface of steel coupons included in experiments with Wyoming bentonite, Grimsel Granodiorite, and synthetic Grimsel groundwater. In general, an Fe-oxide layer is observed to form an alteration layer on the surface of the steel coupons after six to eight weeks of hydrothermal treatment. The Fe-oxide layer is followed by a thin layer of chlorite and sulfides precipitated from sulfide-bearing fluids, likely from pyrite dissolution in the bentonite/host rock. This thin layer is followed by a ~0.30 to 150 µm thick layer of newly crystallized Fe-saponite. The Fe-enriched phyllosilicate minerals observed are interpreted to be the results of the interaction of Fe supplied by steel corrosion and clay minerals in the bentonite (i.e., montmorillonite). Locally, chlorite and CSH minerals are also observed attached to the steel surface. A six-month experiment was completed in FY21 and measurements of corrosion rates for the steel included in that experiment are in progress. The following describes our findings from a general crystalline rock environment.

4.5.4.1 Steel-bentonite Interface Reactions

The steel corrosion products from the interaction with bentonite produced four layers onto the steel substrate: (1) general corrosion, (2) Fe-oxide, (3) CSH and/or chlorite (if present), and (4) Fe-saponite outer layer with occasional minor sulfides. The post- experiment steel shows uniform corrosion at the conditions of these experiments. The occurrence of the Fe-saponite is associated with the corrosion of the steel, but there is no significant alteration of the bentonite away from the steel surface (>100 µm) (Figure 4-33). The precipitation of sulfides, such as pentlandite, formed at early stages of corrosion and is likely due to pyrite decomposition in the bentonite. The occurrence of the sulfides is closely associated with the Fe-saponite at the steel interface. Fe-saponite formation is related to the interaction of the Fe-bearing/Si-rich fluids from the leaching of the steel and bentonite dissolution (Cheshire et al., 2018; Jove-Colon et al., 2019). The surface-bound Fe-rich minerals likely directly crystallized from solution in the local environments surrounding the metal plates as these phases are not observed elsewhere in the clay reaction products. The localized presence of the newly formed Fe-rich phases together with the lack of significant increase in aqueous Fe in the reaction fluids indicate that steel coupon reactions did not influence solution chemistry of the bulk system. Further testing needs to be performed (i.e. Raman spectroscopy or XRD) to identify the Fe-oxide phase of the steel surface.

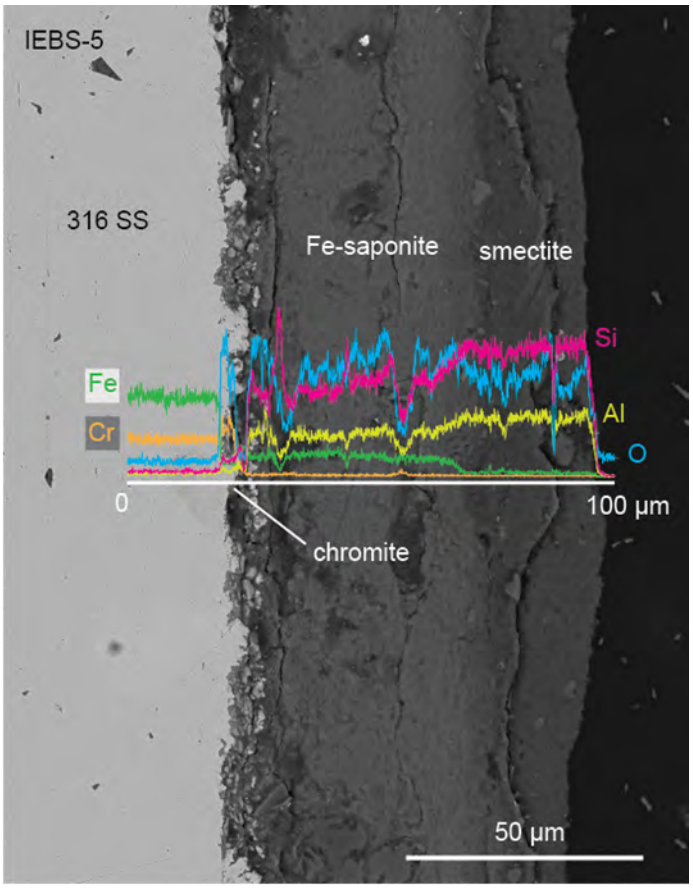

Figure 4-34 Energy dispersive X-ray spectroscopy (EDS) chemical results from a line scan (white line) across the steel-clay boundary. A layer of chromite followed by Fe-saponite is observed attached to the steel surface. A layer of unaltered smectite is observed outboard of the Fe-saponite layer.

The rate of alteration of the bentonite in proximity to the steel corrosion is dependent on the ability of the iron to migrate through the clay as Fe^{2+}. This is regulated by the rate of corrosion, the rate of formation of the Fe-oxide, which may reduce the Fe^{2+} released, and the system dynamics (Mosser-Ruck et al., 2010). The general reaction between the steel and bentonite is depicted in Figure 4-34. The stainless-steel interaction with bentonite via congruent dissolution/oxidation can be detailed by the following reactions:

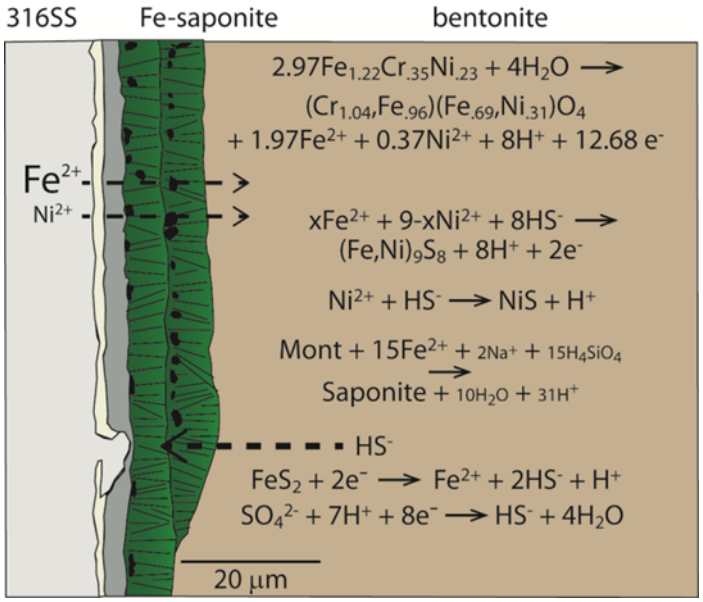

Figure 4-35 A stylized representation of phyllosilicate mineral growth at the steel interface. Of particular interest is the reaction: montmorillonite → Fe-saponite.

Synthetic Fe-saponites have been crystallized in dilute solutions and gels of silica, Fe-, Al- chlorides at temperatures up to 850°C and pH of 8.5 to 9.5 (Kloprogge et al., 1999). This is consistent with a partial dissolution of the steel plates contributing ferrous iron into a fluid phase with silica and aluminum, thereby facilitating Fe-saponite (smectite) crystallization with the steel surfaces acting as a growth substrate. Further, Fe-saponite alteration into chlorite has been suggested (Mosser-Ruck et al., 2010) in the presence of ferrous iron at temperatures approaching 300°C and near-neutral pH. This was confirmed by Mosser-Ruck et al (2016) through long duration experiments (up to 9 years). The authors were able to demonstrate that smectite is consumed by dissolution to produce chlorite (chamosite) by precipitation. Mosser-Ruck et al. (2016) depicts this reaction by:

$$3\ \text{smectite} + 3\ \text{Fe} + 4\ H_2O \rightarrow 1\ \text{chlorite} + 3\ \text{quartz} + 2\ \text{albite} + 3\ H_2 + \text{zeolite} \qquad \textbf{Eq. 4-4}$$

The stainless-steel interaction with bentonite via congruent dissolution/oxidation can be detailed by the following reactions (Cheshire et al., 2018).

Stainless steel dissolution

$$Fe_{1.22}Cr_{0.37}Ni_{0.22} \rightarrow 1.22\ Fe^{2+} + 0.37\ Cr^{3+} + 0.22\ Ni^{2+} + 3.99\ e^- \qquad \textbf{Eq. 4-5}$$

Formation of Fe-saponite and sulfides

$$Fe^{2+} + Ni^{2+} + Cr^{3+} + H_2S_{(aq)} + (Na,K,Ca)_{0.33}(Al_{1.67},Fe_{0.20}^{3+},Mg_{0.13})Si_4O_{10}(OH)_2 \rightarrow \text{smectite} \qquad \textbf{Eq. 4-6}$$

$$(Fe,Ni,Cr)_9S_8 + (Na, K, Ca)_{0.33}Fe_3(Si_{3.67},Al_{0.33})O_{10}(OH)_2 \qquad \textbf{Eq. 4-7}$$

Pentlandite Fe-saponite

4.5.4.2 Effects of Portland Cement on Steel Corrosion

Experiment IEBS-8 included both a cured cement chip and a coupon of 316SS. SEM images of the reacted coupon show that a layer of Fe-saponite formed on the steel surface (see Figure F-23 & -24, in Caporuscio et al., 2021). Future analyses of the cross section view of the coupon will document the alteration products. Measurement of mineral precipitation thickness/growth rate will be compared to results obtained from experiments without cement (described above). In general, it is expected that the higher pH environments associated with cement will inhibit steel corrosion (Kursten et al., 2004). Ongoing characterization of the steel from IEBS-8 and future experiments will quantify the effect of the cement on steel corrosion in the EBS environment.

4.5.4.3 Steel Corrosion Summary

The results from the experiments discussed here indicate that the waste container will act as a substrate for mineral growth in response to steel corrosion. These surface-bound minerals likely formed via direct crystallization from the solution in their specific localized environment surrounding the metal plates. The iron in the newly precipitated mineral layers at the steel interface is sourced as the steel corrodes; however, the steel coupons from this study have yet to be evaluated for general versus localized (e.g., pitting) corrosion. Future work is needed to address the extent these mineral precipitants influence the engineered barrier performance or the repository system as a whole, and to whether these minerals (e.g., Fe- saponite) will act as a passive protecting layer against further corrosion of the waste containers.

4.6 Conclusions

This document summarizes the EBS Grimsel Granodiorite wall rock hydrothermal experiments IEBS-1 through IEBS-8 that include combinations of Wyoming bentonite + Grimsel granodiorite + Grimsel Granodiorite synthetic groundwater ± stainless/LCS ± cured ordinary Portland cement. Results from experiments IEBS-1 through IEBS-8 are presented and include: (1) SEM images and EDS data, (2) QXRD data, (3) clay mineral XRD data, (4) electron microprobe data for major mineral phases, and (5) aqueous geochemistry data.

Concepts developed so far include:

- Illitization of montmorillonite in Wyoming bentonite in a Grimsel granodiorite wall rock environment may be restricted due to the bulk chemistry of the overall system (i.e., low potassium) and/or kinetics
- Montmorillonite structural alterations were not observed in the Wyoming bentonite + Grimsel granodiorite or the Wyoming bentonite + Grimsel granodiorite + cured ordinary Portland cement experiments
- The inclusion of a cured Portland cement chip did not dramatically increase the solution pH but lead to the formation of diverse secondary mineral formation
- Newly crystallized Fe-saponite forms at the steel-bentonite interface and grows perpendicular to the steel surface in both experiments with and without cement.
- C(A)SH minerals formed within the Wyoming bentonite-Grimsel granodiorite system
- Zeolite-forming reactions are not favored in the Wyoming bentonite-Grimsel system

- Abundant zeolite formation is observed in experiments containing OPC, clay is likely consumed in zeolite-forming reactions
- Fe enrichment in the bentonite due to interaction with steel corrosion products does not migrate far from steel (<50 μm)
- General steel corrosion is observed and thicknesses/rates of Fe-rich clay formation were measured for IEBS-2 through IEBS-5.

Research needs to be emphasized in the following areas for FY21:

- Continue to build a database of Grimsel granodiorite and EBS experiments
- Further work to understand formation of C(A)SH minerals at relatively low pH (<8.0)
- Complete characterization of the reaction products from the experiments with cement, including mineral reactions in the bentonite and within the cement chip
- Develop understanding of the role of secondary mineral formation in systems that include ordinary Portland cement
- Include low-pH cement formulations in EBS experiments
- Corrosion of steels/interface silicate mantling effects
- Detailed geochemical modelling of geochemical changes observed in the bentonite-granodiorite system
- Incorporate results into generic modeling codes

The database, along with summary conclusions, will be of use to other experimental teams in the DOE complex, system modeler, and the international repository science community in the development of concepts related to high-temperature crystalline repository environments.

4.7 EBS International Collaborations Background

Personnel at NAGRA began construction of the long-term, full-scale HotBENT experiment at the beginning of 2020 at the Grimsel Test Site underground research laboratory (URL). The ongoing experiments will be heated and dismantled in stages that have durations from five years to 15 to 20 years. The draft experiment plan (AMBERG, 2019) describes all aspects of the experiments (materials, dimensions, etc.) A summary is presented below.

The HotBENT experiment aims to investigate higher temperature repository concepts. Specific objectives of the experiment include: (1) study the effects of high temperatures (i.e., high thermal loading) (>150°C) at and in the vicinity of the heater surface on the performance of bentonite and/or bentonite-mixtures as buffer materials at realistic scales and in-situ conditions, (2) enhance the existing geochemical databases and the understanding of buffer performance, in particular in terms of robustness, (3) assess the effect on the generally agreed safety functions at high temperatures, (4) evaluate corrosion of potential canister materials and potential microbial activities, and (5) consider interaction of bentonite buffer with cement-based liners and/or plugs.

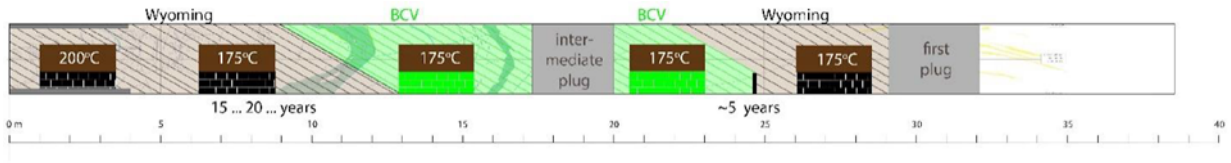

Figure 4-36 Schematic of the HotBENT heater test. Heaters are depicted in brown with the temperature indicated. BCV, Czech bentonite

Construction for the HotBENT experiment began in November 2019, with construction operations anticipated to end in August 2021. The first phase, located between the first and intermediate plugs, will be dismantled after five years (Figure 4-36). The second phase, located behind the intermediate plug, will be dismantled after 15 to 20 years. These long-term experiments are constructed with two types of bentonite, Wyoming bentonite and Czech bentonite (BCV), and will be emplaced in the former FEBEX heater test tunnel, which is excavated from Grimsel Granodiorite. The maximum temperatures at the heater surface will be 200°C (one heater, Wyoming bentonite) and 175°C (four heaters, Wyoming bentonite and BCV). Table 4-1 lists the expected temperature gradient for the 200ºC heater scenario. The support pedestals will be composed of compacted bentonite blocks (either Wyoming bentonite or BCV) whereas the rest of the tunnel will be backfilled with granulated bentonite material. Plugs will be constructed with low pH shotcrete (Table 4-8).

Table 4-8 Summary of expected temperatures from Heater surface (AMBERG, 2019)

Radial Distance from Heater Surface (cm)	Expected Max. Temperature Values (ºC)
10	178
20	147
30	128
40	114
50	103
60*	93
70	83

*Interface between the buffer and rock. With a heater of 1.05 m in diameter, the buffer has a thickness of 61.5 cm.

The proposed parameter measurements that will be measured by implemented instrumentation in the HotBENT setup (identified high priority parameters are pressure, temperature, and humidity) are listed below:

- Temperature at the heater surface
- Total pressure and temperature at the heater surface, plugs, and tunnel walls
- Porewater pressure (hydraulic pressure) in the rock
- Porewater pressure, water content, and temperature in the buffer
- Movements of the heaters and potentially plugs
- Power applied to the heaters
- Gas concentration in the buffer (O_2 and H_2)
- Gas pressure in the buffer
- Thermal conductivity in the buffer

4.8 LANL Hydrothermal Experiments

Bentonite was received from Florian Kober (NAGRA) which included Czech bentonite (BCV) and leftover Wyoming bentonite material from the FE experiment at the Mont Terri URL. The "FE" and BCV bentonites both arrived as either granulated bentonite material (GBM) or compressed block material. At the time of sample shipment, NAGRA had not yet received the Wyoming bentonite to be used in the HotBENT test. The leftover (unheated) material from the FE test, however, closely replicates the Wyoming-type bentonite that will be used in HotBENT and will be utilized in our experimental program.

4.8.1 Methods

Hydrothermal experiments were designed to understand geochemical and mineralogical changes that may occur in the EBS at the HotBENT conditions. These preliminary experiments include a different combination of the two bentonites with groundwater (synthetic Grimsel Granodiorite groundwater).

The experiments were conducted under water-saturated conditions. Reactants (listed in Table 4-9) were loaded into a flexible gold reaction cell and fixed into a 500 mL gasket confined closure reactor (Seyfried et al., 1987). The redox conditions for each system were buffered using a 1:1 mixture (by mass) of Fe_3O_4 and Fe° added at 0.07 wt.% of the bentonite mass. Experiments were pressurized to 150 to 160 bar and were heated isothermally to 200°C for eight weeks. Reaction liquids were only extracted periodically during HBT-3 experiments and analyzed to investigate the aqueous geochemical evolution in relationship to mineralogical alterations. The sampled reaction liquids were split into three aliquots for unfiltered anion, unfiltered cation, and filtered (0.45 µm syringe filter) cation determination. All aliquots were stored in a refrigerator at 1°C until analysis. We could not sample HBT-1 and -2 due to COVID-19 restrictions in the lab. Detailed analytical methods are listed in Appendix A, Caporuscio et al. 2021.

Characterization of the solid reaction products include X-ray diffraction, SEM, and electron microprobe analyses. Concentrations of major anions and cations in the sampled aqueous fluids were collected and are reported in Appendix B, Caporuscio et al. 2021.

Table 4-9 Initial components and reaction conditions for HBT experiments. Abbreviations: LCS, low carbon steel; FE, Wyoming bentonite; BCV, Czech bentonite

Exp.	Components	Temp (°C)	Synthetic GW (g)	FE Bentonite (g)	BCV Bentonite (g)	LCS	Fe° (g)	Fe_3O_4 (g)	Water:Rock
HBT-1	FE + LCS	200	133	21.0	-	5.05	0.55	0.55	6:1
HBT-2	BCV + LCS	200	127	-	21.0	5.03	0.55	0.55	5:1
HBT-3	FE + BCV + LCS	200	105	8.6	8.6	5.04	0.50	0.50	6:1

4.8.2 Results

4.8.2.1 Starting Material Characteristics

Wyoming bentonite from the FE test. The bentonite used in the present study is an unprocessed, Na-rich Wyoming bentonite that was leftover material from the FE experiment at the Mont Terri URL, which closely replicates the Wyoming-type bentonite that will be used in HotBENT. The bentonite is required to contain: >75% smectite (Na- montmorillonite), <1% pyrite, <0.5% sulfur, and <1% organic carbon as

specified in Karnland (2010) and Leupin et al. (2013). No additives to the bentonite are allowed. Granulated bentonite material and compressed block material are both used in the experiments.

Czech (BVC) Bentonite. BCV bentonite is enriched in iron and is an unprocessed Czech bentonite. This bentonite formed from the in-situ alteration of Fe-rich tuffs and augite-biotite-type tuffites (Villar et al., 2020a).

The smectite content in the BCV is 88.6 wt.%. In addition to smectite, the BVC contains quartz (2.1 wt.%), calcite/dolomite (1.5 wt.%), apatite (1.3 wt.%), goethite (1.1 wt.%), anatase (1.2 wt.%), chlorite/kaolinite (1.5 wt.%), and mica (0.7 wt.%).

Synthetic Grimsel Groundwater. A synthetic groundwater was mixed to mimic fluids found at the Grimsel Test Site after the recipe reported in Kersting et al. (2012). Chemistry of the synthetic fluid is presented in Table 4-3 in Section 4.3.4. The groundwater at the Grimsel Test Site is a Na-CO_3 type water and has a pH of ~8.6 to 8.8.

Low carbon steel (LCS). Composed of Fe along with ~0.2 wt.% C, 0.9 wt.% Mn, < 0.04 wt.% P, and < 0.05 wt.% S.

4.8.2.2 Aqueous Geochemistry

Reaction fluids were sampled twice during the HBT-1 experiment: first, after one week of heating, and second, when the experiment was dismantled, due to unusual circumstances surrounding COVID-19. HBT-2 was only sampled pre- and post-experiment. HBT-3 was sampled every week of the experiment duration. The aqueous geochemistry is described below and reported in Appendix B, Caporuscio et al., 2021.

pH. HBT-1 began with a pH of 7.9 at 25ºC. The pH of reaction fluids initially dropped to 6.5 after the first sampling and concluded at 6.4 after experiment quench. The starting pH of HBT-2 was 8.5 before reducing to 5.4 after quenching. HBT-3 started at a pH of 8.3 and gradually decreased to a pH of ~6 at the end of the eight weeks. (Figure 4-37).

Silica. An increase in aqueous silica concentration was observed in the unfiltered samples (403 to 513 mg/L) but decreased in the unfiltered samples (390 to 174 mg/L), from the initial sampling to the end of the experiment in HBT-1. The silica concentration in HBT-2 saw an increase of both the filtered and unfiltered samples. HBT-3 had a sharp increase of aqueous silica between the pre-experiment and the first experimental sample (18 to 185 mg/L filtered and 22 to 218 mg/L unfiltered). Both filtered and unfiltered silica samples increased to ~300 mg/L through the 8 weeks before decreasing to ~250 mg/L after quenching. (Figure 4-37).

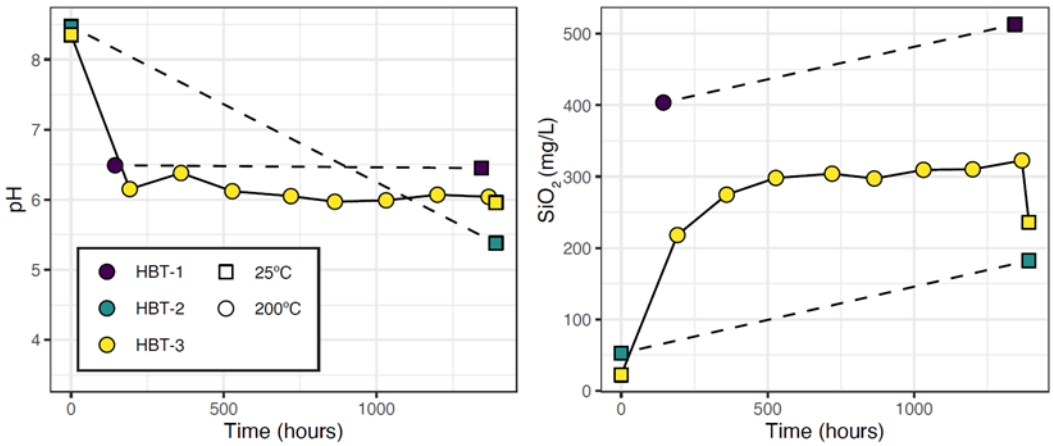

Figure 4-37 Measured pH values (at 25ºC) and silica concentrations in mg/L for reaction fluids extracted from experiments HBT-1 through -3.

Iron. The iron concentration from the initial to post-experiment increased across the experiments (Figure 4-38). HBT-3 saw a fluctuation of iron in solution between 0.5 to 0.1 mg/L but has a general downtrend.

Aluminum. Aqueous aluminum concentrations were similar in the initial sample collected in the filtered and unfiltered aliquots for HBT-1 and -2 (~0.6 mg/L and ~0.07 mg/L, respectively). Concentrations in the filtered aliquot decreased for each experiment at quench (Figure 4-38). In comparison, the unfiltered quench sample showed an increase in [Al^{3+}], indicating suspended particulates were likely present in the sample. HBT-3 had an initial increase in Al^{3+}, but after the first sampling, the aluminum decreased to ~0.04 mg/L and remained at similar concentrations for the rest of the experiment (Figure 4-38).

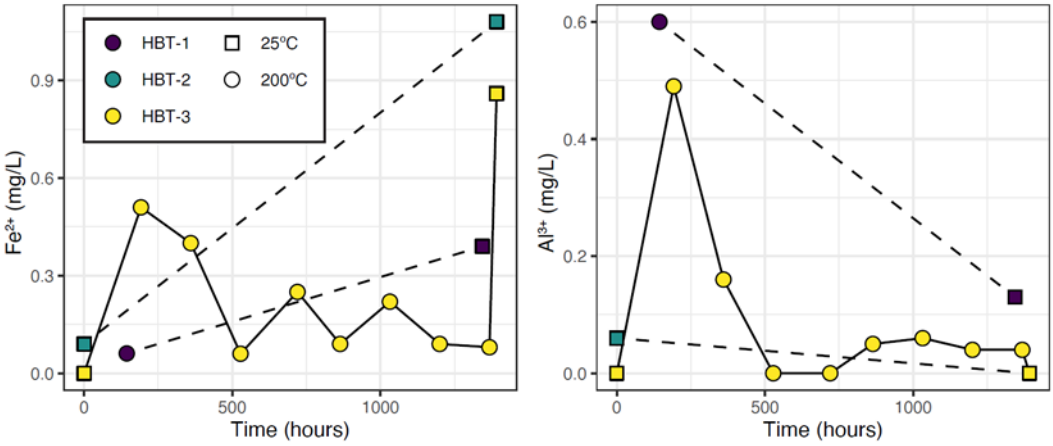

Figure 4-38 Concentration in mg/L of iron and aluminum cations in the unfiltered reaction fluids during each HBT experiment.

Magnesium. In HBT-1, the magnesium concentrations increased in the filtered samples (0.3 - 0.6 mg/L) from the initial to post-experiment sampling. In the unfiltered samples, a sharp increase (0.2 - 26 mg/L) from the first sample to quench indicates fine particulates in solution. HBT-2 had a decrease in both the unfiltered and filtered Mg^{2+} (8 - 5 mg/L and 11 - 8 mg/L, respectively). The magnesium concentrations in HBT-3 had a drastic decrease in both the unfiltered and filtered samples. Both Mg^{2+} samples began at ~11 mg/L and decreased to ~0.4 mg/L, where it stayed less than ~1 mg/L for the duration of the experiment. (Figure 4-39).

Alkali/alkaline earth metals. Potassium, sodium and calcium concentrations in solution generally increase between the collected HBT samples (Figure 4-39). In HBT-1, K^+ and Na^+ concentrations increased in the unfiltered aliquots, whereas Ca^{2+} concentrations stayed relatively constant in the filtered aliquot (~10 mg/L), and only increased in the filtered samples (9 - 74 mg/L). HBT-2 had relatively consistent concentrations from pre- and post-experimental filtered and unfiltered samples for each cation. The cations all increased over the duration of the experiment. HBT-3 also saw increases with all three cations. The Ca^{2+} concentration began at ~3 mg/L and after an initial uptick in the first week, stayed between ~10.5 to 12 mg/L for both the filtered and unfiltered aliquots. Potassium and sodium show the same trend of an initial jump in concentration in the first week before leveling out for the remainder of the experiment.

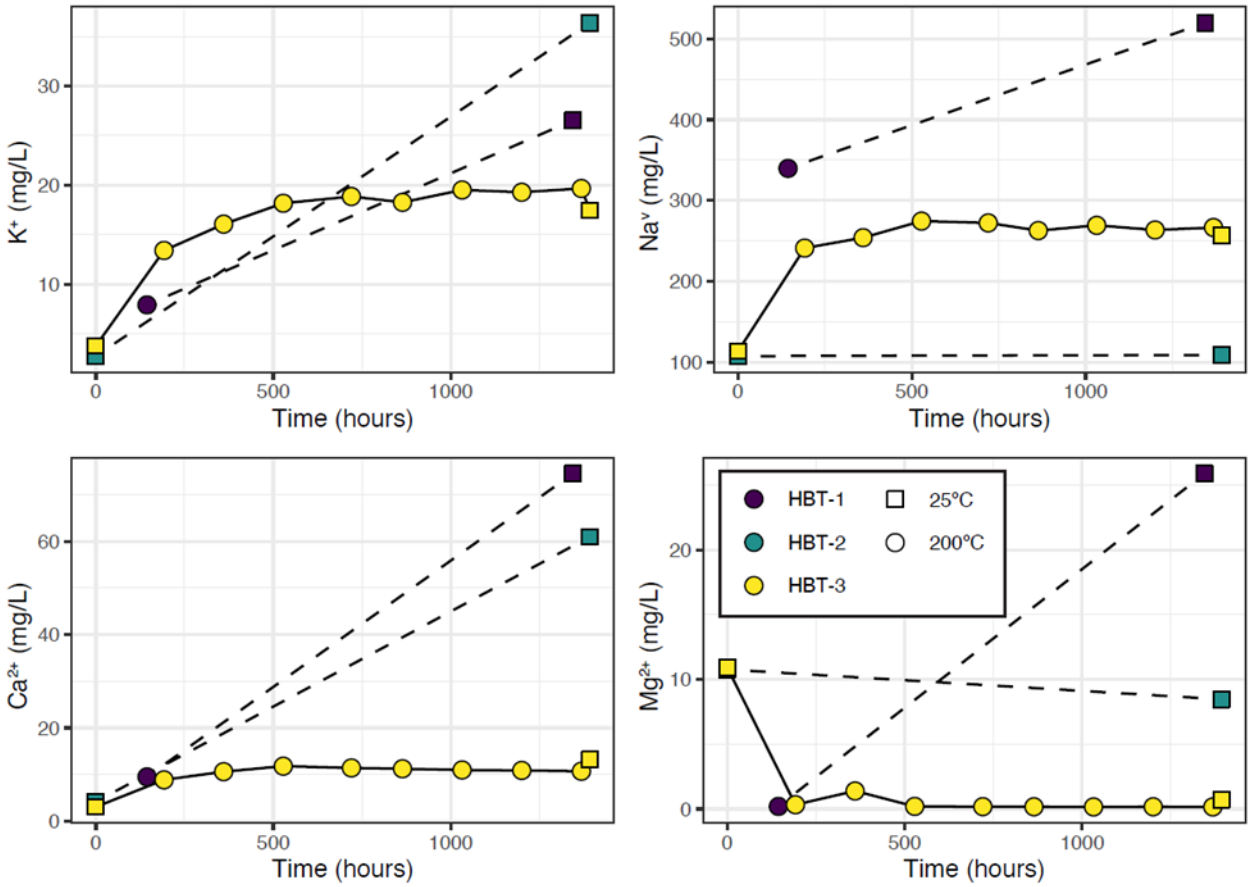

Figure 4-39 Concentration in mg/L of potassium, sodium, calcium, and magnesium cations in the unfiltered reaction fluids during each HBT experiment.

Sulfate. Sulfate concentrations in HBT-1 generally increased over the experiment duration from ~245 mg/L to ~300 mg/L. HBT-2 had a decrease in sulfate from pre- to post-experiment (102 - 82 mg/L). The sulfate concentrations increased initially in HBT-3 from 117 mg/L to 295 mg/L and varied over the 8 weeks between ~210 mg/L and ~450 mg/L before decreasing to 138 mg/L at the end of the experiment (Figure 4-40).

Chloride. The Cl- concentration in HBT-1 and -2 shows a decrease from beginning to the end of the experiments (20.3 - 19.3 mg/L and 8.5 - 9.0 mg/L, respectively). Although HBT-3 shows the same trend from the initial and final chloride concentrations (10.9 - 6.4 mg/L), there was a gradual increase of the concentration to 27.3 mg/L in week three before beginning to decrease (Figure 4-40).

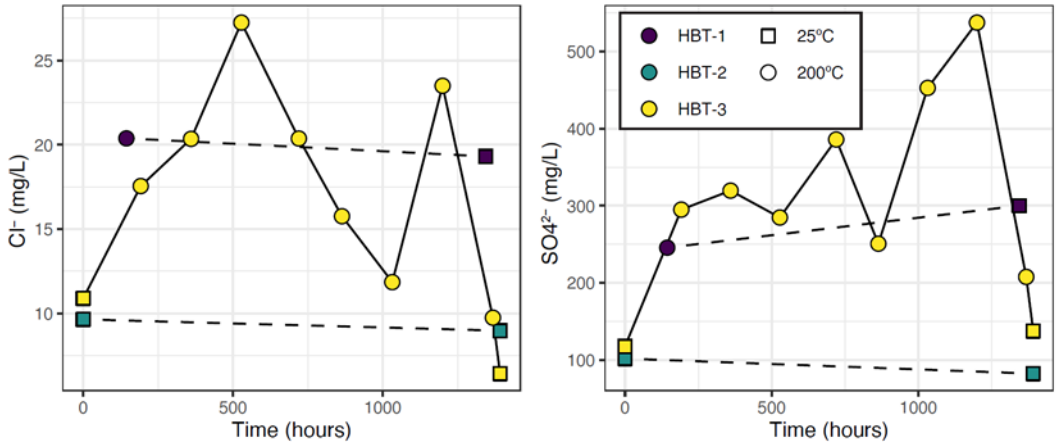

Figure 4-40 Concentration in mg/L of chloride and sulfate anions in the unfiltered reaction fluids during each HBT experiment

4.8.2.3 SEM

HBT-1. The matrix of primarily smectite (cornflake texture) with minor quartz and plagioclase observed (Figure F-30 & -31 in Caporuscio et al., 2021). The LCS included in the experiment was coated in a layer of Fe-saponite (Figure F-32 & -33 in Caporuscio et al., 2021).

HBT-2. The clay matrix consisted mainly of smectite and was locally more Fe-rich than HBT-1. Minor siderite and quartz were also observed in the matrix (Figure F-34 & -35 in Caporuscio et al., 2021). There were honeycombed Fe-saponite on the LCS along with lesser amount of siderite (Figure F-36 through F-38 in Caporuscio et al., 2021).

HBT-3. Smectite dominated the clay matrix with minor apatite and plagioclase. The steel was almost entirely coated with a siderite precipitate (Figure F-39 & F-40 in Caporuscio et al., 2021). Fe-saponite was present in between siderite crystals or atop of the siderite layer (Figure F-41 through F-43 in Caporuscio et al., 2021).

4.8.2.4 QXRD

QXRD analyses of the starting materials and the bulk reaction products from HBT-1 through -3 are presented in Table 4-10. The results show changes in the bulk mineralogy as a result of hydrothermal reactions.

Table 4-10 Quantitative X-Ray Diffraction (QXRD) analyses of the unreacted starting material and experiments run products

Mineral-Fraction	HBT-1	HBT-2	HBT-3	FE Block	BVC Block	50: 50 FE:BVC
Non-Clay						
Quartz	1.6	2.6	2.2	2.1	2.1	3.4
Feldspar	0.5	-	0.2	1.5	-	2.4
Apatite	-	1.0	-	-	1.3	-
Dolomite	-	0.7	-	-	0.7	-
Calcite	-	0.3	1.9	-	0.8	0.9

Magnetite	-	2.4	0.4	-	-	-
Anatase	-	0.8	0.4	-	1.3	1.2
Cristobalite	3.4	-	3.8	1.2	-	1.7
Goethite	-	-	-	-	1.1	0.8
Amorphous	2.0	0.5	3.7	1.0	1.9	5.9
Total	**7.6**	**8.3**	**12.7**	**5.8**	**9.3**	**16.4**
Clay						
Smectite	92.4	88.5	82.0	94.2	88.6	81.2
Mica	-	1.5	1.3	-	0.7	1.6
Chlorite / Kaolinite	-	0.6	1.8	-	1.5	0.8
Illite	-	1.2	-	-	-	-
Saponite	-	-	2.1	-	-	-
Total	**92.4**	**91.7**	**87.3**	**94.2**	**90.7**	**83.6**
SUM	**100.0**	**100.0**	**100.0**	**100.0**	**100.0**	**100.0**

FE bentonite. The unreacted FE bentonite contained 94.2 wt.% smectite with minor amounts of quartz (2.1 wt.%), feldspars (1.5 wt.%), cristobalite (1.2 wt.%), and an amorphous phase (1.0 wt.%). The bentonite is slightly different from the Wyoming bentonite used in the IEBS experiment because the FE test used pure Wyoming sodium bentonite (DOPAS, 2016).

BCV bentonite. The Czech bentonite had less montmorillonite (88.6 wt.%) than the FE bentonite but contained mica (0.7 wt.%) and chlorite/kaolinite (1.5 wt.%). This bentonite also contained quartz, cristobalite, and amorphous phase, along with apatite, anatase, carbonates, and goethite.

FE:BCV. A 50:50 mixture of FE and BCV bentonite were also analyzed. The clay fraction accounted for 83.9 wt.% of the sample and was composed of smectite (81.2 wt.%), mica (1.6 wt.%), and chlorite/kaolinite (1.5 wt.%). The non-clay portion contained quartz, feldspars, calcite, anatase, cristobalite, and goethite. An amorphous phase accounted for ~6 wt.% of the sample. The observed totals that are different from a calculated 50:50 mix of FE and BCV likely reflect natural variation in the bentonite mineralogy.

HBT-1. The FE bentonite included in this experiment only had a slight decrease in the smectite fraction (94.2 - 92.4 wt.%). The amorphous phase increased 1 wt.% to 2.0 wt.%.

HBT-2. The smectite content remained unchanged after the experiment, but the clay fraction gained the addition of illite (1.2 wt.%). Goethite was expended and magnetite is present from the buffer added. The amorphous phase decreased from 1.9 wt.% to 0.5 wt.%.

HBT-3. From the starting material to post-experiment, the smectite content remained unchanged. There was an increase of chlorite/kaolinite and newly formed saponite. There was a decrease in the amorphous phase (5.9 - 3.7 wt.%) and again goethite is no longer present.

4.8.2.5 Clay XRD

The clay-size fraction (<2 μm) was separated via density separation from a gently crushed portion of the reaction products from each experiment. The XRD patterns of the ethylene glycol saturated, oriented clay

fractions can be used to determine alterations to the clay mineral structure (i.e., peak position shifts), which can be used to calculate clay mineral expandability. The ethylene glycol saturated peak positions are presented in Table 4-11 and the XRD patterns are plotted in Figure 4-41. Results from the clay mineral fraction do not indicate significant formation of interlayered illite or of other phyllosilicate phases.

Table 4-11 Ethylene glycol saturated smectite peaks from the <2 µm fraction from unheated starting material and the clay groundmass of the HBT experiments. Expandability (%Exp) is calculated based on the difference between the d002 and d003 peaks using the Scherer Equation.

Sample	1		2		3		5		002/003	1	2	3
EG- Smectite	2Θ	d (Å)	2Θ	d (Å)	2Θ	d (Å)	2Θ	d (Å)	Δ 2θ	%Exp	%Exp	%Exp
FE bentonite	5.2	17.0	10.4	8.5	15.6	5.7	26.2	3.4	5.2	102	104	105
BCV bentonite	5.2	16.9	10.5	8.5	15.8	5.6	26.5	3.4	5.3	97	98	99
HBT-1	5.2	17.0	10.4	8.5	15.7	5.7	26.2	3.4	5.3	99	101	102
HBT-2	5.3	16.8	10.5	8.4	15.8	5.6	26.5	3.4	5.3	96	98	99
HBT-3	5.3	16.7	10.5	8.4	15.8	5.6	26.4	3.4	5.3	97	98	99

1: %Exp = 973.76 – 323.45Δ + 38.43Δ² – 1.62Δ³ (Eberl et al., 1993)
2: %Exp = 1517.8 – 548.49Δ + 68.35Δ² – 2.90Δ³ (Eberl et al., 1993)
3: %Exp = 766.01 – 194.10Δ + 12.924Δ² (Moore and Reynolds, 1997)

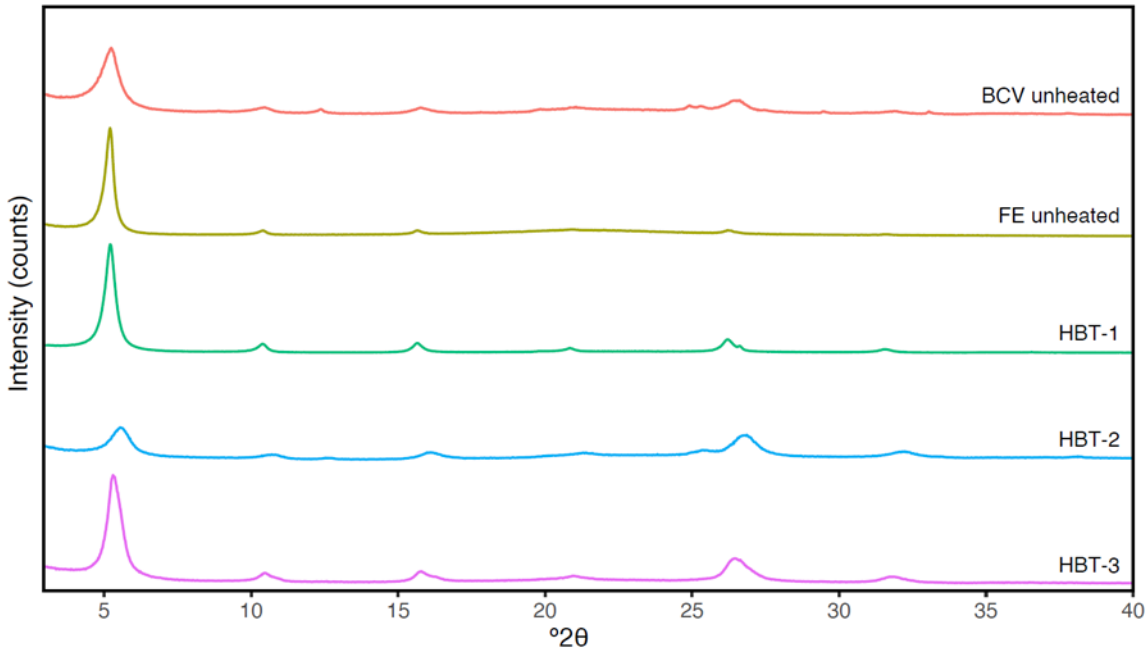

Figure 4-41 XRD patterns the oriented, ethylene glycol saturated <2 µm fraction from HBT-1 through HBT-8 showing no significant shifts in smectite peaks.

4.8.2.6 XRF

XRF analyses for bulk rock oxide chemistry were performed on the unreacted starting material and the bulk reaction products (Table 4-12).

Table 4-12 X-Ray Fluorescence (XRF) analyses of the unreacted starting material and experiments run products. Abbreviation: LOI= loss on ignition.

XRF (wt.%)	HBT-1	HBT-2	HBT-3	FE Block	BCV Block	FE:BCV
CaO	1.34	3.89	2.54	1.39	4.17	2.86
K_2O	0.59	0.80	0.70	0.57	0.85	0.77
SiO_2	59.05	44.90	51.74	63.37	48.82	55.73
Al_2O_3	18.76	14.75	16.87	19.69	14.48	17.87
Na_2O	2.04	0.24	1.00	2.12	0.45	1.21
MgO	2.31	3.34	2.85	2.41	3.23	3.07
P_2O_5	0.06	0.56	0.28	0.05	0.58	0.33
Fe_2O_3	9.28	19.11	15.99	4.13	11.43	7.92
TiO_2	0.26	3.50	1.84	0.16	3.37	1.92
MnO	0.06	0.20	0.14	0.03	0.19	0.10
LOI	6.11	8.43	5.81	5.99	12.21	8.06
TOTAL	99.8	99.7	99.8	99.9	99.8	99.8

Across all the experiments, the weight percent oxides values only showed slight variations between the unreacted and reacted bentonite. All the experiments experienced a decrease in SiO_2 weight percent compared to their unreacted counterparts. HBT-2 and -3 also decreased in the LOI (loss on ignition) compared to the unreacted bentonite. The weight percent of Fe_2O_3 increased for all the experiments, possibly as a result of the addition of the buffers to the experiments or transfer of Fe from the LCS coupons added to the experiment.

4.8.2.7 Electron Microprobe Analyses

Analyses for HBT-1 through -3 are due to be completed in September 2021.

4.9 Discussion

4.9.1 Hydrothermal Interaction of FE and BCV Bentonite

Secondary electron SEM imaging of loose powder mounts of the reaction products shows the development of a foily texture in the fine-grained clay matrix. Minor recrystallization of montmorillonite to non-swelling phases, such as illite or muscovite, was observed in experiments that included BCV bentonite in the QXRD results. Characterization of the smectite structure using XRD analyses of ethylene glycol saturated mounts shows a more detailed look at the alteration of the smectite during the hydrothermal experiments. The experiment with FE bentonite only (HBT-1) saw a reduction in expandability of ~4% versus ~1% in the BCV bentonite only (HBT-2) experiment. The experiment,

HBT-3, which has equal portions of FE:BCV had a reduction in expandability similar to HBT-1 (FE only). The formation of illite-smectite mixed layers was not detected in the XRD patterns of the clay separations (Figure 4-41).

4.9.2 Steel Interface Mineral Precipitation

Steel coupons extracted from the three experiments were characterized by SEM of the mineralized surface. Cross sections images and electron microprobe analyses will be made in the upcoming FY. The SEM images from these experiments demonstrate the active environment at the bentonite-metal interface in experimental systems. The alteration mineralogy is likely controlled by the bulk chemistry as demonstrated by the differences in mineral precipitation in the three different experiments with different combinations of FE and BCV bentonite (Figure 4-42). The steel material acts as a substrate for mineral growth in response to corrosion and allows for the direct mineralization for new growth of surface-bound minerals in the localized environment surrounding the metal.

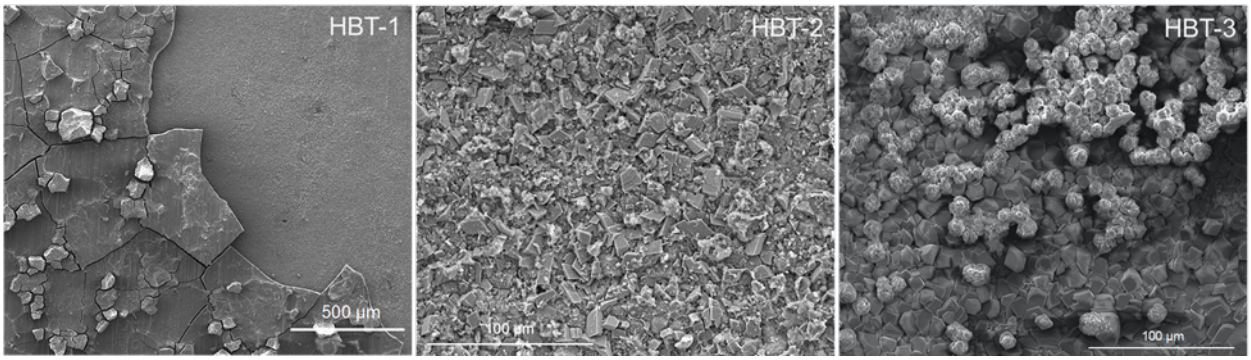

Figure 4-42 Overview of the steel coupons included in each experiment. HBT-1 is overlain with smectite, whereas HBT-2 and -3 was overlain with siderite + smectite

4.9.2.1 FE Bentonite

HBT-1, containing FE only, the LCS was covered with black, orange, red, and white precipitants. The formation of a phyllosilicate iron corrosion product, Fe-saponite, was observed on the steel coupon surface during SEM analyses. These reaction products are only observed in a thin (< ~50 µm) rind on the reacted coupons. Unaltered montmorillonite was observed along with the Fe-saponite. Other observed Fe-rich corrosion products include Fe-oxides.

In the Wyoming bentonite-only experiment series described in Cheshire et al. (2018), a magnetite-like oxide layer developed at the outermost surface of the steel coupon. In addition to the crystallization of this oxide product, precipitation of Fe-rich phyllosilicates (Fe-saponite) was observed. The Fe-saponite forms a more reactive zone with a higher surface area than the original steel surface. The Fe-saponite likely precipitated directly on the steel from the solution interacting with smectite in the local environment surrounding the steel coupons. The clay matrix is not enriched in Fe like the clay observed at the steel interface. The low concentration of Fe ions in the bulk system solution (>0.50 mg/L) and the presence of a new Fe-rich phase indicates that the reaction at the interface does not affect the chemistry of the bulk experimental system.

The stainless-steel interaction with bentonite via congruent dissolution/oxidation can be detailed by the following reactions (Cheshire et al., 2018):

Stainless steel dissolution

$$Fe_{1.22}Cr_{0.37}Ni_{0.22} = 1.22Fe^{2+} + 0.37Cr^{+} + 0.22Ni^{2+} + 3.99e^{-} \quad \textbf{Eq. 4-8}$$

Smectite evolution

$$Fe^{2+} + Ni^{2+} + Cr^{3+} + H_2S_{(aq)} + (Na,K,Ca)_{0.33}(Al_{1.67},Fe^{3+}_{0.20},Mg_{0.13})Si_4O_{10}(OH)_2 = \underset{\text{smectite}}{}$$
$$(Fe,Ni,Cr)_9S_8 + (Na, K, Ca)_{0.33}Fe_3(Si_{3.67},Al_{0.33})O_{10}(OH)_2 \quad \textbf{Eq. 4-9}$$
$$\text{pentlandite} \qquad \text{Fe-saponite}$$

4.9.2.2 Presence of BCV Bentonite

In the BCV-containing experiments, HBT-2 and -3, SEM images showed the LCS surface completely covered in a layer of rhombohedral siderite ($Fe_xCa_yCO_3$) with smectite in between (Figure 4-43). In other experiments with LCS, the formation of a magnetite inner layer under the siderite is observed in the presence of bentonite/clay-rich environments (Mendili et al., 2014; Necib et al., 2016; Romaine et al., 2013). Magnetite may have formed in our experiments, and future characterization of a cross section of the steel coupons will make that determination.

The transportation of the dissolved Fe species produced by the corrosion of the steel is limited to the clay-steel interface. This corrosion product forms a siderite-smectite layer, creating a transitional layer between the LCS and the bentonite. One of the suggested precipitation mechanisms to describe the corrosion of LCS to the precipitation of siderite is (Mendili et al., 2014):

$$CO_{2\,(aq)} + H_2O = 2H_2CO_{3\,(aq)} \quad \textbf{Eq. 4-10}$$

$$H_2CO_{3\,(aq)} = HCO_3^{-}{}_{(aq)} + H^{+}{}_{(aq)}$$
$$\text{or} \quad \textbf{Eq. 4-11}$$
$$HCO_3^{-}{}_{(aq)} = CO_3^{2-}{}_{(aq)} + H^{+}{}_{(aq)}$$

$$Fe_{(s)} \rightarrow Fe^{2+} + 2e^{-} \quad \textbf{Eq. 4-12}$$

$$Fe^{2+}{}_{(aq)} + CO_3^{2-}{}_{(aq)} = FeCO_{3\,(s)}$$
$$\text{or} \quad \textbf{Eq. 4-13}$$
$$Fe^{2+} + HCO_3^{-} = FeCO_3 + H^{+}$$

The carbon species (CO_2, HCO_3^-, CO_3^{2-}) in aqueous solution is determined primarily by pH. Carbon dioxide is prevalent at low pH, bicarbonate at near neutral ($6.4 < pH < 10.3$), and carbonate at high pH (Mendili et al., 2014). Based on the experimental pHs, the reaction most likely followed the bicarbonate pathway, leading to the precipitation of siderite.

The siderite that forms at the LCS interface has additional Ca^{2+} incorporated into its structure. The incorporation of Ca^{2+} into the siderite structure for an iron calcium carbonate product causes an in-step or spiral dislocation, similar to the manner of growth seen for calcite (Figure 4-43). The inclusion of Ca^{2+} inhibits the normal growth process of siderite and may lead to a rounded type of the siderite crystal morphology (Matomoros-Veloza et al., 2020).

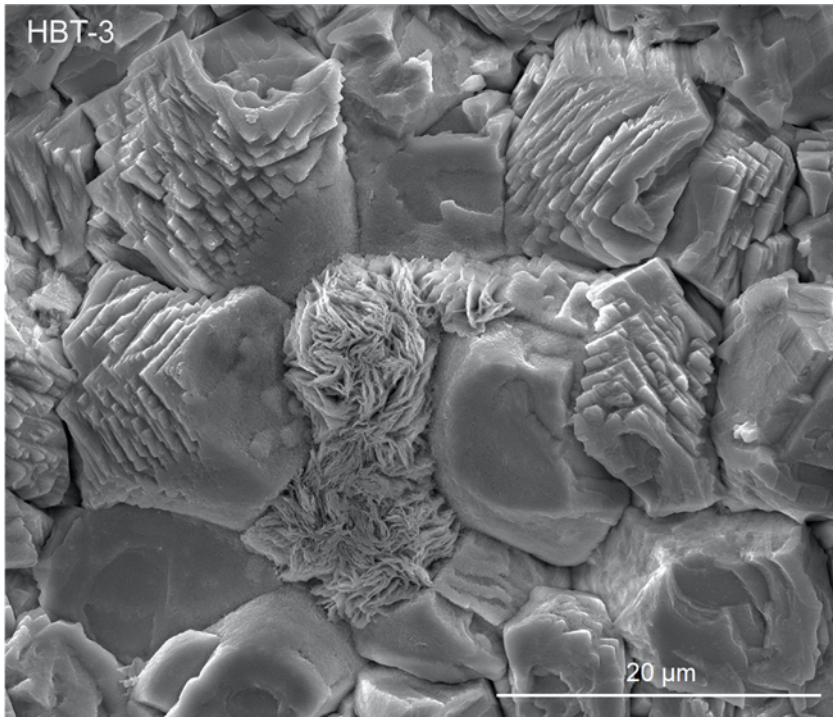

Figure 4-43 Example of in-step dislocation of siderite crystal structure from HBT-3

The siderite layer may provide protection to the LCS and may protect against corrosion to an extent. The dense Fe-mineral layer on the steel surface forms a protective corrosion product film, limiting the amount of dissolved Fe from the LCS and maintaining a low Fe concentration in solution (<0.51 mg/L during the experiment).

4.10 Conclusions and Future Work

The three completed experiments document the potential mineralogical and geochemical changes in the FE and BCV bentonite at 200ºC and water saturated conditions. The main observed effects of heating for the eight-week period is the slight reduction in montmorillonite swelling, formation of carbonate phases in experiments that contained BCV, and the lack of formation of silicate minerals such as zeolites. Reaction fluids in the mixed BCV-FE system remained around a pH of 6. LCS coupons included in the experiments were variably corroded and provided a substrate for Fe-rich mineral precipitation. Fe-oxides and phyllosilicates were observed in the experiment with FE only. In experiments with BCV, Fe-rich carbonates (siderite) were observed on the reacted steel surface in addition to oxides and Fe-saponite.

For future experiments we will need to consider the low-pH shotcrete mixture, which has a complicated formula, and potentially lower temperatures (90°C, the predicted temperature at the buffer/rock interface). We would also want to consider:

- Length of experiments
- Water:rock ratio
- Differences in results related to granulated bentonite material vs. compacted vs. powdered
- Relative humidity X-ray diffraction experiments to determine changes in clay swelling behavior

5. Chemical Controls on Montmorillonite Structure and Swelling Pressure

5.1 Introduction

The swelling properties of smectite clays (the main component of bentonite) one of the main factors affecting water and mass transport in EBSs. The development of effective transport models requires a realistic model of clay microstructure as a function of stress state and solution chemistry, which depends on the physiochemistry of clay-water-ion interactions. Smectite ion exchange reactions are coupled to water uptake and swelling pressure generation in a chemo-mechanical process. Ion exchange reactions are also extensively used for the selective removal of heavy metals from wastewater, water softening, and the recovery of critical elements from geologic resources and from spent metal ion batteries. Due to its wide-ranging applications, ion exchange is considered the second most important reaction on earth following photosynthesis (Meetei et al., 2020) Exchangers that enable the transfer of ions could be engineered membranes (with targeted selectivities; Hassanvand et al., 2017), polymeric resins (Christensen, 2005), or natural materials such as zeolites (Wang and Sun, 2013) and smectites.

Smectites (swelling clays) exhibit high CEC. Montmorillonites (MMT – a common type of smectite clay mineral) are effective barriers because their expansive behavior, upon contact with water, fill the voids between the container and the wall rock sealing the nuclear waste repository, thus mitigating liquid advective transport. Furthermore, the intrinsic negative charge on the MMT layers mitigates the diffusion and transport of radionuclides that tend to form oxyanions (Sellin and Leupin, 2013). It is well established that montmorillonite clays adopt crystalline hydration states, with fixed water contents (Norrish, 1954; Bourg and Sposito, 2011; Teich-McGoldrick et al., 2015; Ho et al., 2019; 1-, 2- and 3- water layer states). The dominant hydration content in the clay-rich barrier corresponds to stable swelling states with 2- and 3-layers of water (2W & 3W). Numerous physical and chemical variables have a major influence on swelling behavior, such as water activity (Whitley and Smith, 2004), cation composition (Teich-McGoldrick et al., 2015; Salles et al., 2013; Laird, 1997), and confining pressure (Massat et al., 2016; Hsiao and Hedstrom, 2017)). Additionally, the type and composition of cations in the interlayer determine the equilibrium water content and basal spacing for a specific hydration state (Teich-McGoldrick et al., 2015; Honorio et al., 2017).

Due to their high CEC, swell/shrink reactions and ion exchange processes in smectites are tightly coupled. Interlayers of different hydration states are distinct phases that exhibit unique selectivities of adsorption for alkali metal cations. Li & Schultess (2020) modeled competitive ion exchange among isovalent cations by curve-fitting X-ray diffraction data using model parameters from first-principles density functional theory (DFT) and a priori knowledge of the clay composition. They confirmed that the exchange of Cs+ with NaMMT was accompanied by a collapse of the interlayer region and observed the broadening and presence of multiple basal spacing peaks suggesting that in the case of incomplete ion exchange, the interlayers are segregated with unique cations. Recently, a comprehensive study (Zhou et al., 2020) addressed critical questions pertaining to the coupling between swelling states and ion exchange in montmorillonite. The authors predicted stable equilibrium hydration states as a function of water and ion activities in solution and the cationic partition in clay when aqueous activity conditions are changed in a dynamic environment. Furthermore, Whittaker et al. (2019) showed that an ion exchange driven change in water content (swelling state) is often associated with a restructuring of the interlayer depending on the cation that is exchanged into the clay phase. Evidence, thus, suggests that the ion exchange can drive the swelling or collapse of interlayers in smectites, and that the hydration and ion exchange reaction energetics are tied to each other. Understanding this coupling is critical to model the feedbacks arising

from changes to microstructure and chemical composition that eventually control diffusion and transport in nuclear waste barriers.

Studies spanning several decades have established that the selectivity of swelling clays for alkali metal ions follows the lyotropic series (Jenny, 1936; Bolt, 1955; Shainberg 1987; Whittaker et al., 2019). The interaction between the cation and the mineral basal surface/edges (depending on the pH) as well as the relative tendencies of the cations to be hydrated in the mineral interlayers were considered to be factors determining the order of selectivity. A paradigm shifting study on the ion exchange selectivity of clay minerals argued that exchange among isovalent cations is controlled by the selectivity of the solution phase for the strongly hydrated cation (the one with lower hydration enthalpy) rather than by clay particle surface selectivity (Teppen and Miller, 2006). The weakly hydrated cation, thus, tends to partition into the solid phase, while the other cation remains in the aqueous phase. Rotenberg et al. (2009) supported this conclusion with microcalorimetry measurements and molecular dynamics simulations to explain that the preferential adsorption of Cs+ over Na+ in montmorillonite is driven by the relative 'hydrophobicity' of Cs compared to Na in solution, and not its affinity for clay mineral surfaces. While this shift in understanding explains the progressive clay selectivity for alkaline ions according to the lyotropic series, the influence of the aqueous phase composition (and concentration) on the selectivities has not been explored sufficiently. The two studies referenced above consider saturated clay minerals in dilute suspension (water activity, $\boldsymbol{a_w \sim 1}$) and computations of the free energy of exchange in the aqueous phase are performed based on a trace exchange of the cation without the presence of the anion. Therefore, the effect of aqueous ion pairing interactions (Tournassat et al., 2009) on the exchange free energy is neglected.

Cs^+ sorption on smectite, investigated in the presence of competing cations (Na^+, K^+, Ca^{2+}), highlighted a strong dependence of adsorption selectivity on ionic strength. This study emphasized the importance of accounting for competition from even trace ions in solution (Missana et al., 2014). When multiple types of adsorption sites exist in the clay mineral (surface and edge sites, for example), the selectivity of a particular adsorption site can be enhanced or diminished as a function of electrolyte concentration (Baeyens and Bradbury, 2004). Additionally, a study that computed the free energy of exchange between Na^+ and NH_4^+ in solution as a function of the mole fraction of NH_4^+ in the mixed electrolyte revealed a significant dependence of the exchange free energy on the solution composition (Wang and Sun, 2013). Since it is established now that the state of hydration of cations in solution drives the favorability of exchange, there is a need to investigate how the energetics of ion exchange are altered in the presence of concentrated and mixed electrolytes in which the hydration shells of the cations may not be fully occupied (Afanasiev et al., 2009; Marcus, 2014; Teychené et al., 2019).

Here, we address two key questions that persist from our work reported in FY20 and limit our ability to predict equilibrium pore structures in compacted bentonite barriers: (i) what effect does electrolyte composition (relative ion activities) exert on spontaneity of smectite ion exchange? (ii) how can we account for as well as isolate contributions from transition between swelling states and the deviations from equilibrium water content within the same swelling state in montmorillonite during ion exchange at a given water activity?

5.2 Methodology

5.2.1 Theory

In FY20, we reported a series of simulations on smectite swelling free energy in dilute aqueous solution and on layer-state mixing energetics. Our work in FY21 expanded these simulations to include swelling free energy calculations in different compositions, high ionic strength electrolytes, as well as a thermodynamic study of coupled ion exchange and water uptake for a fixed swelling state. In this context,

the term 'swelling state' corresponds to an equilibrium 2W or 3W hydration state and a change to the swelling state corresponds to the transition between them. The overall swelling reaction, resulting in a change to the swelling state, for a pure end-member MMT can be written as follows, with equilibrium water content per layer of water per unit cell of clay for NaMMT and KMMT represented by $\boldsymbol{n}$ and $\boldsymbol{m}$, respectively.

$$NaMMT_{2W} + n\,H_2O \leftrightarrow NaMMT_{3W} \quad \textbf{Eq. 5-1}$$

$$KMMT_{2W} + m\,H_2O \leftrightarrow KMMT_{3W} \quad \textbf{Eq. 5-2}$$

The overall ion exchange reaction for a fixed swelling state (2W represented by double overbar, for instance) can be written as shown in Reaction (3). Note that the change in water content (*m-n)* from the exchange reaction contains a factor of *2* owing to the ion exchange taking place at a fixed 2W swelling state. Equilibrium is achieved when the chemical potentials in MMT and the solution are equal at a given composition.

$$\overline{\overline{NaMMT}}_q^{nH_2O} + qK_{aq}^{+} + 2(m-n)H_2O \rightarrow \overline{\overline{KMMT}}_q^{mH_2O} + qNa_{aq}^{+} \quad \textbf{Eq. 5-3}$$

As the reaction proceeds, the degree of exchange varies from 0 (exchange of traces of K+ in a $\overline{\overline{NaMMT}}$) to 1 (complete exchange from homoionic $\overline{\overline{NaMMT}}$ to homoionic $\overline{\overline{KMMT}}$). In order to define reaction quantities, it is necessary to carefully set up the initial and final reference states and ensure that mass (including water) is conserved during the exchange reaction. In our definition of states, the number of water molecules in the ion exchange end-members is not equal. Therefore, for the solid phase ion exchange, we consider two sets of initial and final reference states with *n* and *m* water molecules per layer of water per clay unit cell, respectively. The overall exchange free energies are expressed as a function of the water activity in solution, and the water content in the clay interlayers (*m, n*). The reference state of the solution follows the conventional definition of the chemical potential of pure, non-interacting ions at 1M concentration, and the activity coefficients for isovalent dissimilar ions are not assumed equal.

This overall reaction for ion exchange in a fixed swelling state (Eq. 5-3 for 2W) can be broken up into three parts: the exchange in the aqueous phase, another exchange in the solid/clay phase, and the hydration/dehydration reaction resulting in a change in the equilibrium water content.

$$K_{aq}^{+} \rightarrow Na_{aq}^{+} \text{ (aqueous phase)} \quad \textbf{Eq. 5-4}$$

$$\overline{\overline{NaMMT}}_q^{nH_2O} \rightarrow \overline{\overline{KMMT}}_q^{nH_2O} \text{ (solid phase)} \quad \textbf{Eq. 5-5}$$

$$\overline{\overline{KMMT}}_q^{nH_2O} + 2(m-n)H_2O \rightarrow \overline{\overline{KMMT}}_q^{mH_2O} \quad \textbf{Eq. 5-6}$$
(deviation from equilibrium water content)

The Gibbs free energy for the overall reaction can be decomposed into its three contributions with $\Delta G_{ex,aq}$ and $\Delta G_{ex,\overline{\overline{MMT}}}$ representing the exchange free energies in the aqueous and solid phases, respectively. $\Delta G_{hyd,\overline{\overline{MMT}}}$ corresponds to the free energy change from the change in equilibrium water content between stable end-members of the exchange reaction (Eq. 5-6). We assume here that the free energy change pertaining to the deviation in water content at a fixed swelling state is equal for the K- and Na- end-members (i.e., the free energy change for reaction 6 is assumed equal for $\overline{\overline{KMMT}}$ and $\overline{\overline{NaMMT}}$).

$$\Delta G_{ex,rxn} = \Delta G_{ex,aq} + \Delta G_{hyd,\overline{\overline{MMT}}} + \Delta G_{ex,\overline{\overline{MMT}}} \quad \textbf{Eq. 5-7}$$

The Gibbs free energy of exchange in the aqueous phase is computed as a function of the ratio of ion activity coefficients in a mixed electrolyte.

$$\mu_{Na^+} = \mu^0_{Na^+} + RT\ ln\ (\gamma_{Na^+}(1 - x_{K^+}));\ \mu_{K^+} = \mu^0_{K^+} + RT\ ln\ (\gamma_{K^+}x_{K^+});$$
$$\Delta G_{ex,aq} = \Delta G_{K\rightarrow Na,aq} = \left[(\mu^0_{Na^+} - \mu^0_{K^+}) + RTln\frac{\gamma_{Na^+}}{\gamma_{K^+}} + RTln\frac{1 - x_{K^+}}{x_{K^+}}\right] \quad \textbf{Eq. 5-8}$$

where $\boldsymbol{\mu_i}$, $\boldsymbol{\gamma_i}$, and $\boldsymbol{x_i}$ are the chemical potential, aqueous activity coefficient, and mole fraction of *i.* Ion exchange calculations in the solid phase are realized through two ion exchange reactions at fixed water contents (Eq. 5-9 and Eq. 5-10). The corresponding free energies of the two reactions are written in terms of their free energies of formation in a dilute suspension ($G^f_{\infty H_2O}$) and the immersion free energy of clay in aqueous solution (G^i_{aq}). Note that in Reaction 2.11b, there is an extra component ($G^{\Delta hyd}_{aq}$) to the free energy of formation of an ion exchange end-member whose water content deviates from its equilibrium value (as described in Eq. 5-6).

$$IE1: \overline{\overline{NaMMT}}^{nH_2O}_q + qK^+_{aq} \rightarrow \overline{\overline{KMMT}}^{nH_2O}_q + qNa^+_{aq} \quad \textbf{Eq. 5-9}$$

$$IE2: \overline{\overline{NaMMT}}^{mH_2O}_q + qK^+_{aq} \rightarrow \overline{\overline{KMMT}}^{mH_2O}_q + qNa^+_{aq} \quad \textbf{Eq. 5-10}$$

$$\Delta G_{IE1} = \left(G^f_{\overline{\overline{KMMT}},nH_2O} - G^f_{\overline{\overline{NaMMT}},nH_2O}\right) + q\Delta G_{ex,aq} \quad \textbf{Eq. 5-11}$$

$$\Delta G_{IE2} = \left(G^f_{\overline{\overline{KMMT}},mH_2O} - G^f_{\overline{\overline{NaMMT}},mH_2O}\right) + q\Delta G_{ex,aq} \quad \textbf{Eq. 5-12}$$

Where $\left(G^f_{\overline{\overline{KMMT}},nH_2O} - G^f_{\overline{\overline{NaMMT}},nH_2O}\right)$ is the free energy of exchange in the solid phase ($\Delta G_{ex,\overline{\overline{MMT}}}$) in Eq. 5-7. For the $\overline{\overline{NaMMT}}$ endmember, free energies of formation for the n and m hydration states,

$$G^f_{\overline{\overline{NaMMT}},nH_2O} = G^f_{NaMMT,\infty H_2O} - G^i_{NaMMT,\ aq} \quad \textbf{Eq. 5-13}$$

$$G^f_{\overline{\overline{NaMMT}},mH_2O} = G^f_{NaMMT,\infty H_2O} - \left(G^i_{NaMMT,\ aq} + G^{\Delta hyd}_{NaMMT,\ aq}\right) \quad \textbf{Eq. 5-14}$$

Similar expressions can be written for $\overline{\overline{KMMT}}$. Substituting these equations and Eq. 5-13 and Eq. 5-14 in Eq. 5-11and Eq. 5-12 we get:

$$\Delta G_{IE2} - \Delta G_{IE1} = \left(G^{\Delta hyd}_{NaMMT,\ aq} + G^{\Delta hyd}_{KMMT,\ aq}\right) = 2\Delta G_{hyd,\overline{\overline{MMT}}} \quad \textbf{Eq. 5-15}$$

As mentioned before, the influence of hydration/dehydration at a fixed swelling state is assumed equal for the $\overline{\overline{NaMMT}}$ and $\overline{\overline{KMMT}}$ end-members. Therefore, the contribution of the hydration/dehydration reaction that occurs during ion exchange can be isolated.

5.2.2 Simulations

We recently developed a new cis-vacant molecular model for Wyoming-MMT, consistent with atomic-scale high-resolution transmission electron microscope imaging (Subramanian et al., 2020). We showed that the interlayer water is more structurally ordered with stronger hydrogen bonding in cis-vacant MMT than its commonly-used trans-vacant equivalent and the structure of the interlayer varies depending on the cations occupying it. Through grand canonical Monte Carlo (GCMC) simulations (Bennet, 1976), we obtained the equilibrium basal spacing and water contents for stable hydration states of cis-vacant NaMMT and KMMT in a dilute suspension. We performed all our simulations on the cis-vacant molecular structure for MMT in this study. The clay unit cell parameters were a = 5.20 Å, b = 9.00 Å, c = 10.07 Å, $\alpha = \gamma = 90°$, and $\beta = 99.5°$. This unit cell was repeated in the a-b plane followed by isomorphic substitution of Mg++ for Al+++ in the octahedral sheet resulting in a structural charge of -0.57e per unit cell (O20(OH)4). It must be noted that the constraint of preventing two adjacent Mg++ substitutions is not applicable to cis-vacant MMT. The simulations carried out in LAMMPS (Plimpton et al., 2020), use ClayFF (Cygan et al., 2004) to describe the van der Waals and electrostatic forces in the mineral and cations, and SPC/E for water (Pullman, 2010). Lennard-Jones interaction terms between dissimilar atom types were calculated via Lorentz-Berthelot mixing rules. We employed a cutoff distance of 15 Å for short-range interactions, and Ewald's summation method with an accuracy of 99.99% for long range electrostatics.

5.2.2.1 Swelling Simulations

Evaluation of the energetics associated with the transition between hydration states requires the calculation of free energy changes through perturbation (Landau et al., 1980; Bennett, 1976), alchemical transformations with thermodynamic integration (TI) (Zacharias et al., 1994)), or reaction coordinate based simulations (Jarzynski, 1997). The calculation of the free energy difference between stable hydrates yields the swelling free energy at a given solution composition. Significant focus has been dedicated to the estimation of swelling free energies using molecular modeling (Whitley and Smith, 2004; Honorio et al., 2017; Smith et al., 2006; Svoboda et al., 2018; Underwood & Bourg, 2020) of trans-vacant MMT in dilute suspension. We employed the potential of mean force (PMF) approach in combination with umbrella sampling (along a pre-defined reaction co-ordinate), in a related study, to compute the swelling free energy of NaMMT as a function of ionic strength in homoionic solutions. As a result, the minima from the PMF profile yielded the equilibrium basal spacings and the relative probability for each hydration state as a function of bulk solution concentration. We also explored the likelihood of mixed hydration states existing in an interstratified microstructure within MMT tactoids (Lammers et al., *in prep*).

Here, we focus on a bulk solution with a total ionic concentration of 1M or 1.9M. Our molecular system consists of two parallel clay layers, made up of 175-unit cells each (9.35 nm × 9.05 nm), suspended in solution (see Figure 5-1). The edges of clay layers perpendicular to the *x*-*z* plane were made unreactive with OH, OH_2 terminations that result in neutral edge charge. The system was equilibrated in the NPT (T = 298 K, P = 1 atm) ensemble for 1 ns, following which, a steered molecular dynamics (SMD) simulation was performed over 3 ns in the NP_zT ensemble. In the SMD run, the bottom MMT layer was tethered while the top MMT layer was translated along the *z*-direction with a constant velocity of 2 Å /ns by a harmonic stiff spring (Park & Schulten, 2004). Subsequently, we segmented the entire SMD run into trajectory windows of 1 Å change in basal spacing and used the initial step of each window as input to perform umbrella sampling. The umbrella sampling, which was implemented using the Collective Variables (COLVARS) library in LAMMPS (Fiorin et al., 2013), spanned 40 stages per window, and each stage sampled the distance between the layers and the harmonic potential of the spring for a translation of 0.025 Å. The small size of umbrella windows ensured that there was sufficient sampling of the entire reaction coordinate (here, the reaction coordinate is the basal spacing) and overlap among the

umbrella windows. Since the umbrella sampling approach imposes a biasing potential (here, the biasing potential is the harmonic potential of the stiff spring), we need an unbiasing algorithm to compute the PMF. We used the Weighted Histogram Analysis Method (WHAM) code (Grossfield et al., 2019) to extract the PMF profile from the umbrella sampling results. Ho et al. (2019) showed that the ClayFF parameter set does not predict the dry to one-water layer (0W – 1W) hydration process well. The authors of the study modified ClayFF to capture the dry to hydrated state transition. Since we used the traditional ClayFF parameters, and because we are interested in the swelling states applicable to engineered barriers, our focus is restricted to the 2W to 3W transition.

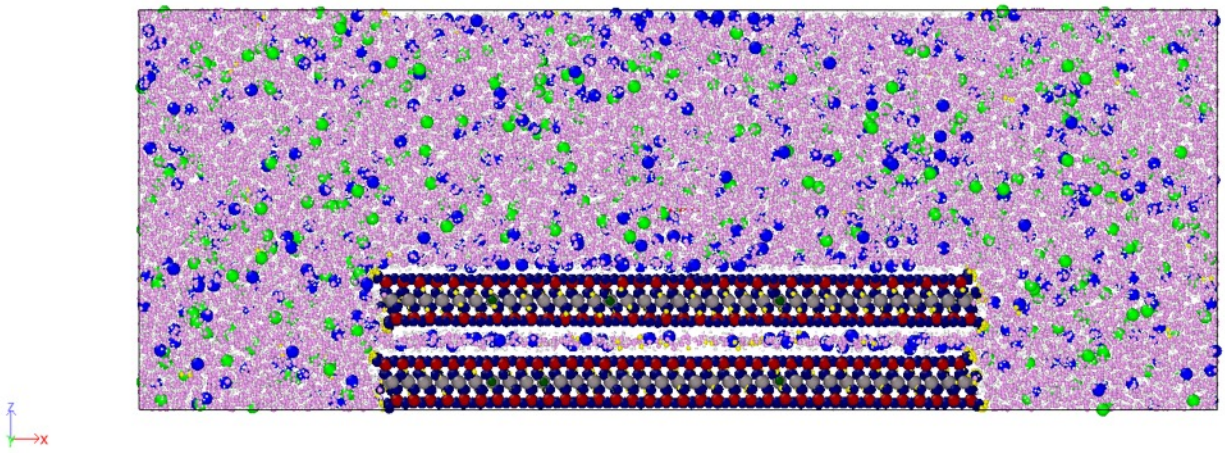

Figure 5-1 **System set-up for PMF simulations with umbrella sampling. The top mineral layer is translated away parallel to the bottom layer, which is fixed along *x* and *z*. The atoms along the *x-z* edges of the clay layers are terminated for neutral edge charge; the clay layer is infinitely large along the *y* direction. The atom color scheme is as follows: Al – grey, Mg – dark green, Si – dark red, O – navy blue, H atoms in clay layer – yellow, Na – blue, Cl – green, water O – pink, water H – white.**

5.2.2.2 Ion Exchange Simulations

The energetics associated with the replacement of ions in clay minerals have been studied over the last two decades using TI employed via molecular simulations (Rotenberg et al., 2009; Lammers et al., 2017; Zhou et al., 2020). However, as explained earlier, these studies assume a dilute aqueous phase, whereas we consider homoionic as well as mixed electrolyte solutions at higher ionic strength. The TI calculations are performed separately in the solution phase and the solid phase. In the solution phase, we start with homoionic 1M NaCl and progressively transform 25% of Na^+ ions transformed into K^+ ions by changing their pairwise Lennard-Jones interaction potentials (i.e., $\boldsymbol{\sigma}$ for the distance of zero intermolecular potential and $\boldsymbol{\varepsilon}$ for the potential well depth) in a series of 11 steps, using a coupling parameter $\lambda \in [0,1]$, with 0 representing Na^+, and 1 representing K^+, using equations given by:

$$\sigma(\lambda) = \sigma_{Na} + \lambda(\sigma_{Na} - \sigma_K) \qquad \textbf{Eq. 5-16}$$

$$\varepsilon(\lambda) = \varepsilon_{Na} + \lambda(\varepsilon_{Na} - \varepsilon_K) \qquad \textbf{Eq. 5-17}$$

At each step, an NPT equilibration for 3 ns followed the change in the Lennard-Jones interaction parameters. The result at the end of the transformation yields a mixed electrolyte solution containing 0.75M NaCl and 0.25M KCl. This series of progressive transformation steps were carried out until we arrived at solutions of 0.5M, 0.75M, and 1M KCl (with progressively decreasing NaCl concentration). The variation in the Hamiltonian of the system (H) during the transformation as a function of the coupling

parameter λ allows the free energy calculation for the exchange reaction. The outcome of each series of TI simulations in the solution phase is the corresponding $\Delta G_{ex,aq}$ term in Eq. 5-7.

$$\Delta G_{ex} = \int_{\lambda=0}^{\lambda=1} \langle \frac{\partial H}{\partial \lambda} \rangle \, d\lambda \qquad \textbf{Eq. 5-18}$$

We performed a similar series of TI simulations in the 2W clay phase, starting with a volume containing four mineral layers (see Figure 5-2) containing 24-unit cells of MMT each, with equilibrium basal spacings and water contents determined from the swelling simulations in the previous section. The MMT layers in this simulation are periodically replicated in *x* and *y* directions and are therefore, infinitely large without terminated edges. The system is equilibrated (NPT) initially, followed by 3 ns of NP_zT equilibration with the modified force field potentials. The clay layers are rigid during the TI transformation, keeping the basal spacings fixed.

We simulated partial ion exchange in the clay tactoid. However, a 25% partial ion exchange corresponds to one out of the four interlayers being exchanged for K^+. The individual interlayers consist of homogeneous cations and the choice of this methodology is supported by experimental data suggesting that interlayers contain unique cations during partial ion exchange (Whittaker et al., 2019; Li and Schulthess, 2020).

Ion exchange simulations in the clay phase were performed at 3 different equilibrium water contents for 2W state: 9.6 H_2O/uc, 10.2 H_2O/uc, and 11H_2O/uc, which correspond to the equilibrium water contents for 2W KMMT, 2W NaMMT, fully saturated 2W MMT, respectively.

From these TI simulations, we calculated the term $\Delta G_{ex,\overline{\overline{MMT}}}$ in Eq. 5-7 for both partial and complete ion exchange. Furthermore, we also compute the term $\Delta G_{hyd,\overline{\overline{MMT}}}$ as a function of the deviation in water content based on Eq. 5-15.

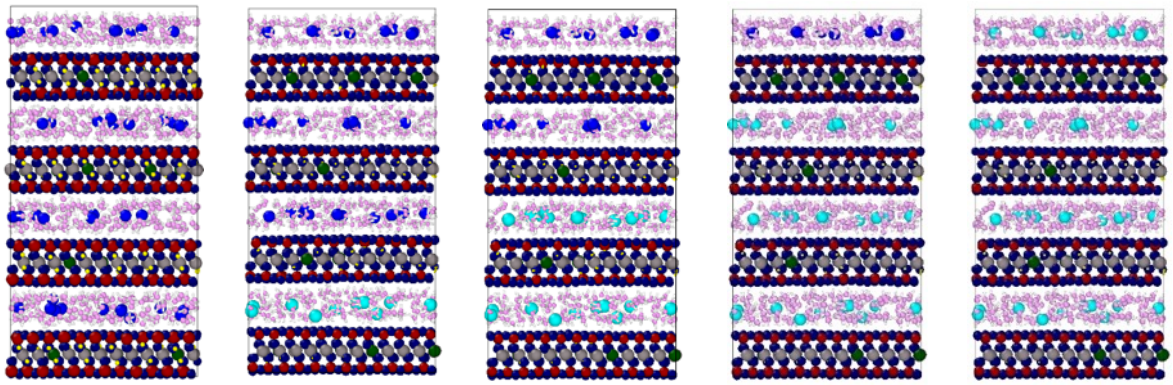

(a) (b) (c) (d) (e)

Figure 5-2 (a) System set up for clay-phase TI simulations. The clay layers are infinitely large in x and y directions. The initial basal spacings are determined based on the 2W minima from the swelling simulations. Na ions are alchemically transformed to K ions in a series of 11 steps. (b) 25% exchange of Na ions to K ions; (c) 50% exchange; (d) 75% exchange; (e) 100% exchange. The atom color scheme is as follows: Al – grey, Mg – dark green, Si – dark red, O – navy blue, H atoms in clay layer – yellow, Na – blue, K – cyan, water O – pink, water H – white.

5.3 Results

The PMF profiles from the swelling simulations of two parallel clay mineral layers suspended in aqueous solutions are presented in Figure 5-3. The profiles yield the minima, equilibrium basal spacings, equilibrium water contents for each stable hydrate/layer state and the energy to transition between them at a constant water and ion activity. The suspension of the clay particle in bulk water yields equilibrium 2W (d_{001} = 15.8 Å), 3W (d_{001} = 18.7 Å), and 4W (d_{001} = 21 Å) crystalline swelling states with accessible free energy minima before the osmotic swelling regime begins. The 3W hydration state is, however, the most favored swelling state with the lowest free energy containing 15 H_2O/uc. As the solution concentration in which the clay particle is saturated increases, the preference shifts towards lower swelling states (2W) and the free energy difference to access the higher swelling state increases, i.e., $\Delta G_{3W-2W,1.9M\ NaCl} > \Delta G_{3W-2W,1M\ NaCl}$. We do not observe a crystalline 4W hydration state for the clay particle in 1M and 1.9M NaCl solutions from the PMF profiles. This indicates the occurrence of clay compaction in the presence of concentrated solutions, which has been supported by recent experimental and computational studies (Shen and Bourg, 2021; Zhou et al., 2020; Ferrage, 2005). Furthermore, it is evident that solution concentration exerts a significant influence on the equilibrium basal spacing (and therefore, the equilibrium water content since the interlayer cation does not vary) of stable hydrates.

The equilibrium basal spacings for the 2W and 3W KMMT layers are 15.9 Å and 18.9 Å, respectively, whereas the 2W and 3W basal spacings for the NaMMT layers are 16.05 Å and 18.8 Å, respectively. The equilibrium water contents for the 2W state are 9.6 H_2O/uc and 10.2 H_2O/uc for KMMT and NaMMT, respectively. A 2W hydrate seems favorable in both cases when suspended in 1M solution and the swelling free energy difference between the 2W and 3W states appear to be ~ 5.5 kJ/mol of clay. However, the slopes leading up to the 2W minima are opposite in magnitude for the two systems, indicating that there may be a more favorable minimum corresponding to a 1W state for KMMT at this water/ion activity. In the case of the NaMMT system, the 2W state appears to be the global minimum and the higher crystalline and osmotic states are accessible within 12 kJ/mol.

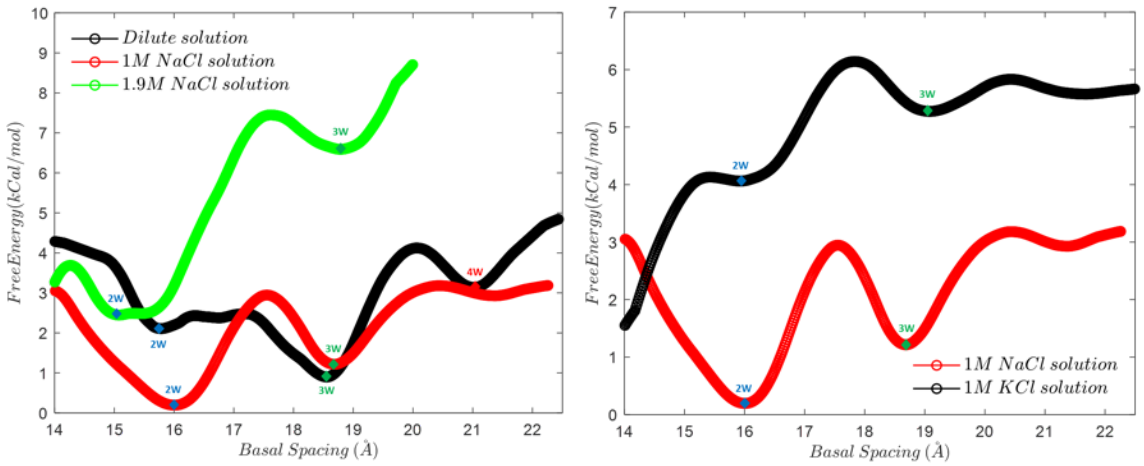

Figure 5-3 Potential of mean force (PMF) profile as a function basal spacing (d001 which was defined as the reaction coordinate) between MMT layers (a-left) suspended in bulk water and NaCl solutions of different concentrations; (b-right) suspended in 1M aqueous solutions with different cations. Results indicate the equilibrium basal spacings for the 2W and 3W state in the respective solution conditions and the difference in their free energies.

The free energies of isovalent ion exchange in aqueous solution as a function of solution composition (at fixed concentration) are presented in Figure 5-4. In the past, the free energy of ion exchange in aqueous solution has been computed as the difference in the ion hydration energies assuming a dilute solution. Based on this computation, the exchange free energy of $Na^+ \rightarrow K^+$ in solution is found to be 72 – 84 kJ/mol (Marcus, 2014; Pettit, 1979). However, we observe a strong concentration dependence on this value implying that the exchange of K^+ for Na^+ is more favorable in concentrated solutions. This could be because the hydration shells of ion in 1M solution are partially complete and contain fewer water molecules per ion to shed as they undergo exchange. We also observe a small composition dependence from the data in Figure 5-4. The aqueous exchange of $K^+ \rightarrow Na^+$ in solution (which in turn, drives the formation of KMMT) is more favorable in a mixed electrolyte with a higher mole fraction of K^+ to begin with. Therefore, potassium-rich mixed electrolytes exhibit a stronger drive for exchange reactions in MMT because the solution has a higher tendency to accept Na^+ ions. Data from our TI simulations in the solid and aqueous phases are combined to obtain the overall free energy of the exchange reaction. Figure 5-5 illustrates this information as a function of solution composition for different equilibrium water contents.

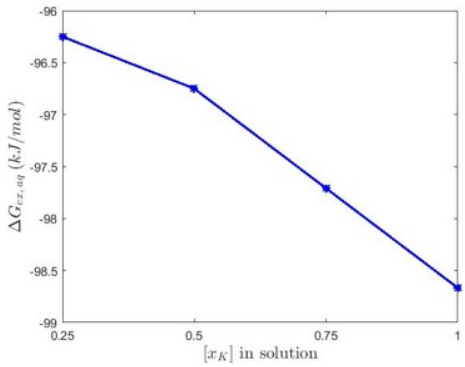

Figure 5-4 Free energy of ion exchange ($K^+ \rightarrow Na^+$) in aqueous solution of total ionic strength of 1M. The plot shows a dependence of the free energy of ion exchange on the equilibrium composition of the mixed electrolyte solution at a fixed concentration.

The reaction constants for the overall exchange reaction are plotted against the mole fraction of K^+ in solution (composition of mixed electrolyte) for each degree of ion exchange (ranging from partial to complete ion exchange) in the clay phase (Figure 5-6). Results demonstrate that the reaction constant (K_c) increases exponentially with increasing KCl fraction in solution. This implies that the solution phase, initially consisting of a high fraction of K^+ ions, is more readily accepting of Na^+ ions from the solid phase, consistent with our findings in Figure 5-4. The exchange of K for Na (both partial and complete) favors the interlayer with a lower water content, explaining the higher selectivity of interlayers with a lower water content (at a fixed hydration state) for potassium over sodium ions. To elaborate this further, we illustrate the equilibrium constants for the overall exchange reaction in different mixed electrolytes in Figure 5-7. When $\overline{\overline{NaMMT}}$ is suspended in 1M KCl solution, the exchange reaction – both partial and complete – is favorable across all three equilibrium water contents. However, as we consider mixed electrolyte solutions that are rich in sodium, the exchange reaction of $\overline{\overline{NaMMT}}$ to $\overline{\overline{KMMT}}$ is feasible only for $m = 4.8$ and a complete exchange is barely favorable. Interlayers with a higher water content do not undergo exchange spontaneously. The data exhibits a strong sensitivity to the composition of the solution and the equilibrium interlayer water content, but not to the degree of exchange in neighboring layers (i.e., the exchange selectivity is almost unaffected by the solid phase composition in our simulations).

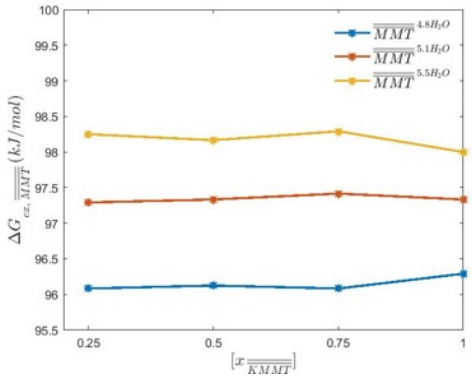

Figure 5-5 Free energy of ion exchange ($Na^+ \rightarrow K^+$) as a function of the extent of the exchange reaction (partial to complete exchange) in a clay platelet containing different equilibrium water contents. The data shows that the equilibrium water content in the clay interlayer exerts a larger influence on the exchange free energy than the composition of the clay phase ($x_{\overline{KMMT}}/x_{\overline{NaMMT}}$).

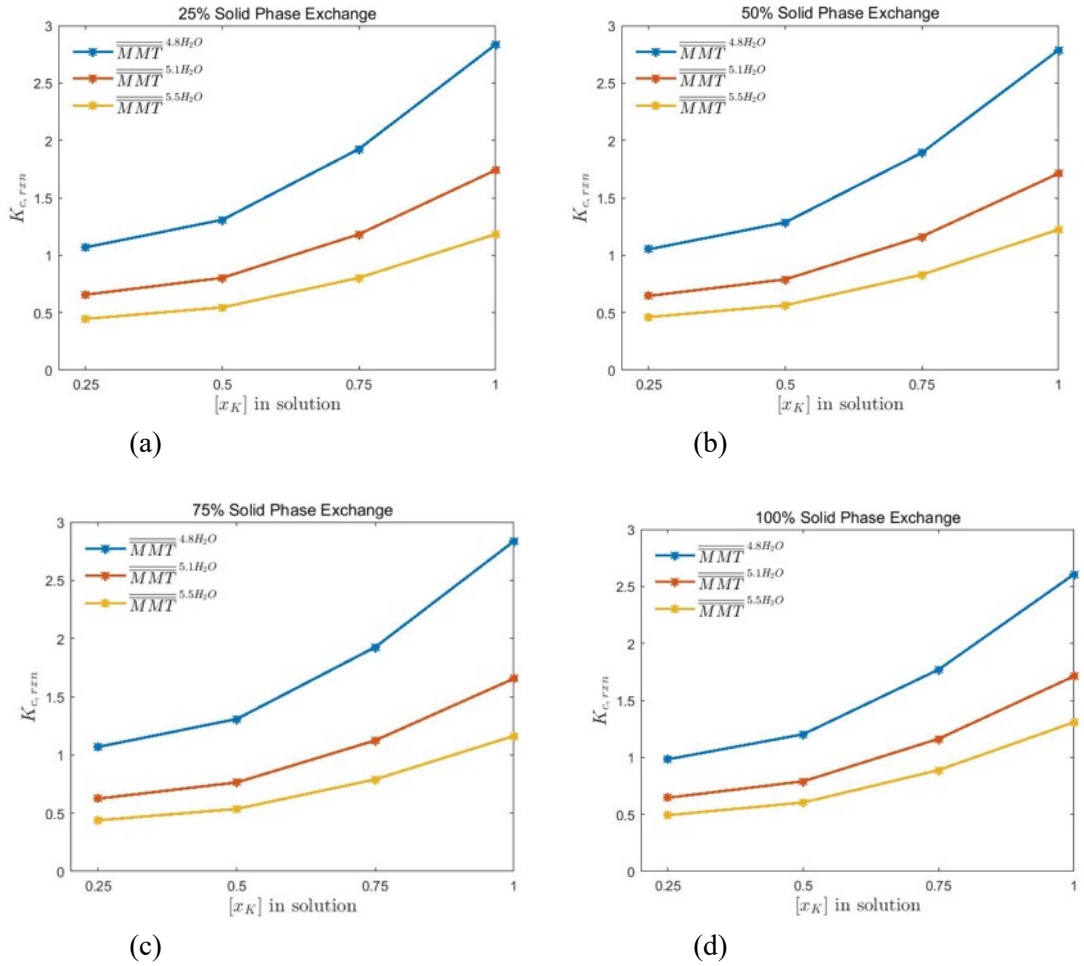

Figure 5-6 Equilibrium constants for the overall ion exchange reaction as a function of solution composition and different degrees of exchange. (a) 25% ion exchange in clay platelet with interlayers consisting of unique cations; (b) 50% ion exchange; (c) 75% ion exchange; (d) complete ion exchange in clay platelet.

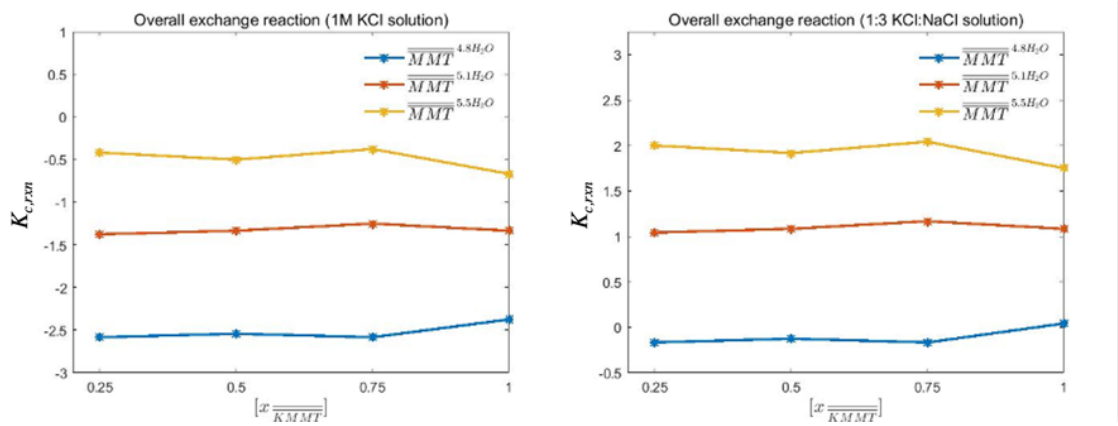

Figure 5-7 Equilibrium constants for the ion exchange reaction as a function of degree/extent of exchange at various mixed electrolyte compositions. (a-left) 1M KCl aqueous solution; (b-right) mixed electrolyte with 0.25KCl + 0.75M NaCl

5.4 Discussion

The exchange of isovalent ions in clay minerals is tightly coupled with a change in water content in the interlayers, which occurs from an overall change in the swelling state or a change in the hydration structure at a constant swelling state. The swelling and ion exchange reactions simulated in this study enable us to understand the influence of solution chemistry (concentration and composition) on the coupled processes. The TI simulations in the aqueous phase yield the free energy of cation exchange in a solution of given composition. Using these free energy values ($\Delta G_{ex,aq}$) in the aqueous phase to compute the chemical potentials/activity coefficients of the ions in solution using Eq. 5-8 allows us to relax the assumption of equal activity coefficients for isovalent ions. Furthermore, we find that the $\Delta G_{ex,aq}$ is not equal to the difference in hydration energies of Na^+ and K^+ ions in dilute solution. There is a significant concentration dependence ($\Delta G_{ex,\infty} \sim 80\ kJmol^{-1}, \Delta G_{ex,1M\ aq} \sim 105\ kJmol^{-1}$) and a small composition dependence ($\pm 2\ kJmol^{-1}$) for the aqueous exchange free energy.

The equilibrium constants of the overall ion exchange reactions expressed as a function of ion activities (a_{Na}/a_K) and the interlayer water content indicate that the equilibrium composition ($x_{\overline{KMMT}}, x_{\overline{NaMMT}}$) of the solid clay phase plays an insignificant role in our simulations. The equilibrium water content, however, is an important factor for the spontaneity of ion exchange ($Na \rightarrow K$) in the solid phase. At clay interlayers with a high equilibrium water content *m= 5.1 or 5.5,* for example, exchange favorability in the solid phase significantly reduces in the presence of mixed electrolytes. Furthermore, the mineral does not exhibit any selectivity to the exchange when a_{Na}/a_K is high. This supports why poorly hydrated clay is more selective to K+ whereas saturated clay is more selective to Na+ even while not being accompanied with a change in the swelling state. Thus, the results in Figure 5-5 and Figure 5-6 strongly highlight the influence of interlayer solvation structure on driving exchange favorability for a given water and aqueous ion activity.

We also observed a strong dependence on the solution composition for the ion exchange reaction. At a given concentration, the ratio of ion activities (composition of the mixed electrolyte) appears to drive the exchange selectivity particularly for equilibrium water contents. In the case of $\overline{MMT}^{5.1H_2O}$, the overall exchange reaction is favorable only when the aqueous solution is rich in K+ whereas for $\overline{MMT}^{5.5H_2O}$, spontaneous ion exchange occurs only in the case of pure KCl solution.

The lack of influence of the solid phase composition on the ion exchange reaction could be an artefact of the clay particle simulations involving rigid clay layers and fixed water contents (NVT ensemble). Evidence in literature points to the favorable occurrence of partial exchange (homostructured interlayers populated with unique cations). Whittaker et al. (2019) showed this to be the case at low- to mid-range a_{Na}/a_K. The study also confirmed the presence of coexisting phase-separated clay particles based on their hydration state although no conclusion could be drawn on phase separation based on cation type. Our simulations model partial ion exchange resulting in "interstratified" interlayers with unique cations in an interlayer. Relaxation and equilibration of the structure allowing for changes to the basal spacing and changes to the water content, perhaps with concurrent GCMC simulations could help quantify the influence of solid phase composition on the ion exchange reaction. However, designing a closed thermodynamic cycle to perform TI simulations can be challenging with this added degree of freedom. The extracted stress data from the interlayers in our NPT simulations confirms the tendency of the interlayers to relax their basal spacings as the degree of exchange progresses (as the solid phase has a greater $x_{\overline{KMMT}}$ composition). For example, we observe greater compressive stresses in the clay particle when the solid phase is $\overline{KMMT}$-rich ($x_{\overline{KMMT}} > 0.5$). The magnitudes of compressive stresses also increase with an increase in the equilibrium water content, i.e., $\overline{KMMT}^{5.5\ H_2O}$ interlayers exhibit a stronger tendency to collapse subsequent to partial and/or ion exchange than $\overline{KMMT}^{4.8\ H_2O}$.

5.5 Summary and Future Work

In FY21 we extended our prior results on clay swelling thermodynamics to higher electrolyte concentrations and specifically investigated the influence of pore fluid on montmorillonite structure and composition at equilibrium. We modeled the swelling and ion exchange reactions in a swelling clay mineral (MMT) and computed the free energies of the reactions using PMF and TI based molecular simulations, respectively. The free energies of phase transformation and ion exchange were used to compute the selectivities of hydration states for cations. Furthermore, we tested a straightforward relationship between the equilibrium constants for the hydration reaction and the selectivities for the ion exchange reaction. Studies that usually model ion exchange do not account generally for varying water contents (from changes to the equilibrium swelling state and the equilibrium water content for the same swelling state), whereas our ion exchange simulations yielded the ratio of activity coefficients of the ion exchange end-members as a function of ion activities and the change in interlayer water content. We also considered the effect of aqueous electrolyte composition on the ion exchange energies. Instead of performing trace exchange via TI simulations, we allowed for ion-ion interactions in the aqueous phase. The free energy of ion exchange in aqueous solution, therefore, is not just the difference of the hydration enthalpies (in dilute suspension) of the exchanged ions in this case but varies based on the initial composition of the aqueous solution. Thus, we are able to explicitly model activities of the ions in aqueous solution as well as make a connection between the ratio of activity coefficients of the ion exchange end members ($\overline{NaMMT}$ and $\overline{KMMT}$) as a function of the water content change between them during the ion exchange process. Our future efforts will involve updating the microstructural thermodynamic model reported in FY 2020 to include a layer state water content dependence. Theoretical results will be compared with the results of ongoing swelling pressure and microstructural measurements.

6. Illitization Mechanisms Revealed by Cryo-Electron Tomography (CRYOET)

6.1 Introduction

Illitization is a chemical transformation that reduces the swelling capacity of bentonite. The effects of illitization include a reduction in nanoporosity that inhibits swelling, an increase in hydraulic permeability due to the formation of micropores, and variability in the ionic conductivity due to the changing ratios and connectivity of these two pore types. While temperature is a strong driver of illitization, the underlying mechanisms by which illitization proceeds are not well understood. Inhibiting illitization at the temperatures found at the surface of nuclear waste storage cannisters would prolong the absorptive and healing capacity of bentonite barriers that make them attractive storage media. Therefore, elucidating the mechanism(s) by which illitization is activated will inform strategies for improving the performance of bentonite storage technologies.

Chemical changes in clay minerals, including smectites that comprise bentonites and the illite transformation products that form from them, are difficult to visualize directly because clay structures are highly heterogeneous at atomic- and molecular scales. Furthermore, the hydrated interfaces that pervade clay mineral fabrics are sensitized to damage from electromagnetic probes typically used for imaging, such as X-rays and electrons. Cryo-electron tomography (cryoET) allows for the direct visualization of hydrated clay minerals by plunge-freezing a thin film of sample to quench molecular motion and reduce the rate of beam-induced damage while enabling a thin film to be imaged under cryogenic conditions. Images are acquired over a range of angles as the sample is tilted, and these images are algorithmically reconstructed into a three-dimensional representation of the fully hydrated structure.

Section 6.2 below outlines the process for data processing and reconstruction, the Section 6.3 discusses preliminary results obtained by this method, and Section 6.4 concludes with work that will be performed in subsequent performance periods.

6.2 cryoET Data Acquisition and Processing Pipeline

Mechanisms of illitization were investigated by imaging a model smectite (SWy-2) that was exchanged with KCl to homogenize the interlayer cation binding sites with K^+. Samples with liquid/solid mass ratios of 1000 were hydrothermally treated at 200°C for 0, 7, 56 and 112 days by collaborators at Sandia National Laboratory. Aliquots of these suspensions were deposited onto TEM grids and plunge frozen in a Vitrobot Mark IV cryo-robot.

Image collection was performed with a Thermo-Fischer Titan Krios electron microscope equipped with a Gatan K3 direct electron detector and a BioQuantum energy filter. Automated acquisition was enabled by SerialEM 3.8 software and a custom script for dose-symmetric tilt/defocus series data acquisition. Dose-fractionated movies consisting of between 2-20 frames were acquired at each tilt and defocus setting. Frames were aligned and summed with MotionCor2 version 1.4.2 to produce an aligned image (Figure 6-2). Images with defocus values, Δf, set to 0nm, 250 nm, and 1000nm were acquired at each tilt angle, which sampled reciprocal space at many frequencies (Figure 6-2). Tilt images were acquired at sample tilt angles between ±64° in 1° increments starting at 0°, alternating between positive and negative tilts every two images producing a maximum of 64x3 = 192 images. A reconstruction algorithm that accounts for multiple electron scattering was used to capture the electron-sample interactions that produce strong contrast in mineral samples, which fundamentally differ from conventional cryoET approaches for biomolecules.

Reconstruction was performed with IMOD version 4.11 and with a custom script written in Python. Reconstructions were segmented with the Weka 3D segmentation package for ImageJ and visualized with Tomviz. Custom analysis was performed in Python.

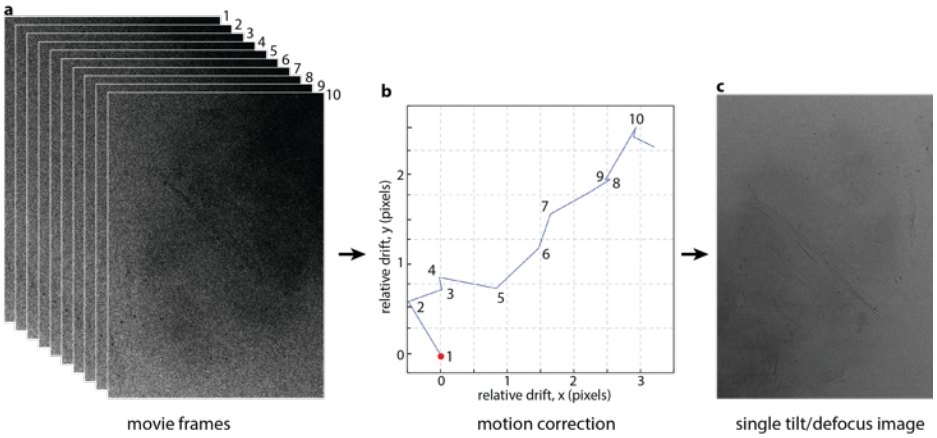

Figure 6-1 **cryoET image generation at a single tilt and defocus value from dose-fractionated movie.**

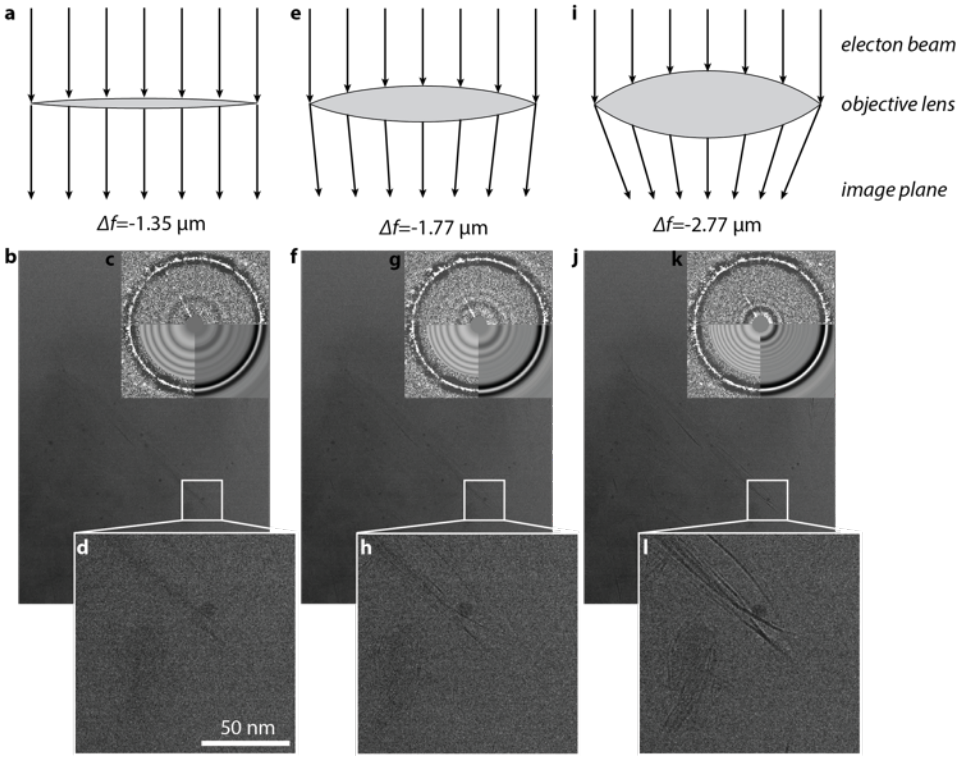

Figure 6-2 **Defocus image acquisition: (a) Defocus image acquired with low objective lens excitation, resulting in little image contrast (b) and only a few zero-crossings in the Fourier Transform, making even high-contrast objects difficult to resolve (d). (e-l) Higher defocus produces more zero-crossings in reciprocal space and higher contrast, but lower resolution.**

6.3 Illitization is a 2D/3D Coarsening Process

Hydrothermally treated smectite undergoes at least four important morphological changes after 112 days.

(1). The average lateral diameter, $\langle L \rangle$, in the electron-transparent region of aggregates viewed at high magnification (Figure 6-3a and Figure 6-3d) decreases, while much larger layers are also resolved when imaged at lower magnification (Figure 6-3b and Figure 6-3e), indicating a shift in the L distribution.

(2). Layers stack into particles with no (hydrated) interlayer gap (Figure 6-3c and Figure 6-3f)

(3). Illitized particles exhibit increased faceting

SWy-2 layers have an average lateral diameter, $\langle L \rangle$, of approximately 250 nm(1), which is consistent with cryoET images (Figure 6-3a). After 112 days of hydrothermal treatment $\langle L \rangle$ decreases considerably in the portion of the images that are electron transparent (Figure 6-3d). However, large layers exceeding 1 μm appear in lower-magnification images (Figure 6-3e) suggesting that some layers grow while others shrink.

Formation of compact particles with no interlayer water (Figure 6-3f) from particles that were originally delaminated (Figure 6-3c) suggests that the evolving particle size distribution redistributes chemical species that contribute to structural charge among the layers. Higher structural charge is associated with stronger interlayer interactions and reduced swelling that is the hallmark of illitization. This is strong evidence that that the illitization process proceeds via the dissolution of smectite and reprecipitation as illite.

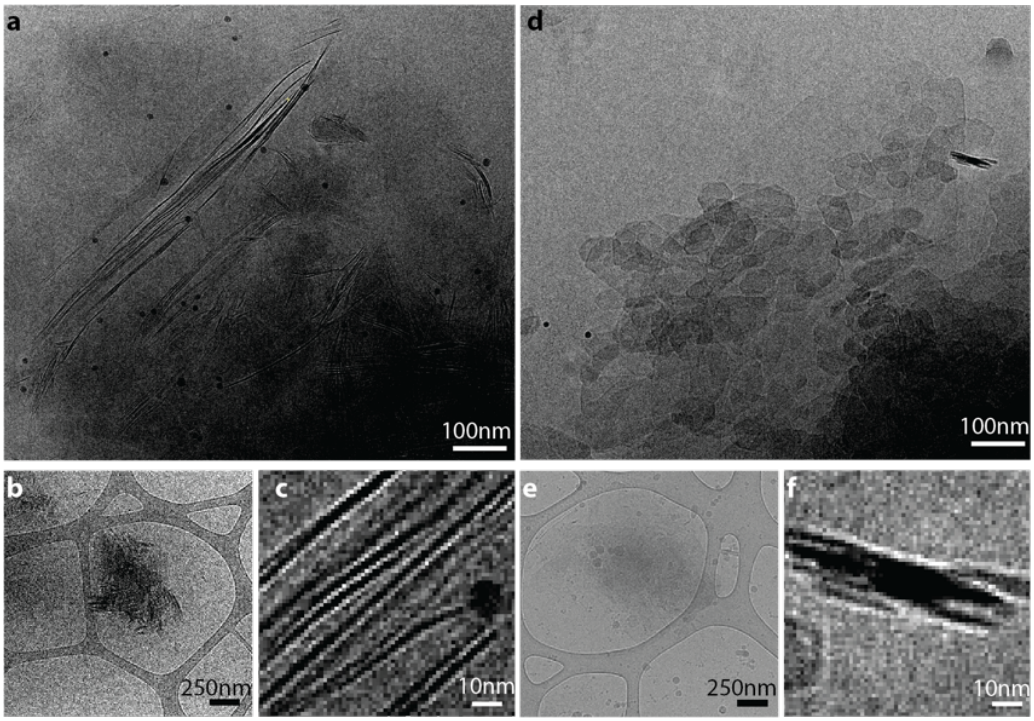

Figure 6-3 Comparison of (a-c) K-exchanged SWy-2 with no hydrothermal treatment and (d-f) after 112 days at 200°C. (a) Electron transparent portion of aggregate. (b) Representative opaque SWy-2 aggregate. (c) Layers are mostly delaminated, with clear separation between them. (d) Electron transparent portion of aggregate. (e) Partially-transparent aggregate of hydrothermally treated SWy-2

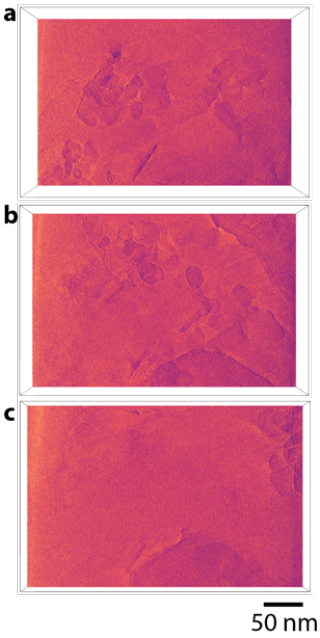

Figure 6-4 Slices through tomogram of 112 day sample. Layers are clearly stacked into thick, planar tactoids and facted at approximately 60° angles, consistent with the underlying crystallographic symmetry.

Faceted, compacted illite particles are also evidence that the illitization process is driven by differences in both the edge and basal interfacial energy between smectite and illite. Rough, unaligned smectite edges are likely to have a much higher energy than faceted edges in compacted particles. Faceting in layers that shrink relative to their original dimensions requires that the layers partially dissolve and reprecipitate at their edges. However, layer stacking also alters the average interfacial energy, as the energy associated with the basal surface does not contribute significantly to the overall interface in a compacted particle, while the edges remain exposed.

6.4 Conclusions and Future Work

Preliminary evidence suggests that illitization of smectite under hydrothermal conditions and low mineral volume fraction proceeds via the simultaneous dissolution of smectite and reprecipitation of illite. The distinction between the two phases is primarily in the higher structural charge of illite, which favors compacted particles with no hydrated gap separating the layers. Therefore, it is hypothesized that the unfavourability of smectite interfaces, and particularly edges, drives the coarsening of smectite particles into illite. More datasets at intermediate timepoints have been collected to better understand the progression of this reaction over time. Further analysis can be applied to quantify changes in the morphological characteristics, such as $\langle L \rangle$, that would help confirm the hypotheses generated by the data presented here.

Important questions for future work include how the chemical composition changes with the layer size. Disproportionation of elements that are expected to contribute to structural charge in SWy-2 smectite (primarily Mg^{2+}) is thought to drive the illite/smectite coarsening process, which suggests that there should also be compositional differences between the two end-members. This also suggests that smectite would not fully convert to illite and would instead increasingly resemble pyrophyllite as Mg^{2+} becomes concentrated in illite. These questions will be answered in the remainder of FY21 and FY22.

7. Molecular Modeling of Radionuclide Retention by Bentonites

7.1 Introduction

The capability of a bentonite barrier to impede the transport of long-lived radionuclides is an essential aspect of the performance evaluation of any storage strategy. A scenario for radionuclide release involves groundwater reaching a corroded canister and mobilizing radionuclides, such as ^{233}U and ^{239}Pu. Thus, knowledge of these radionuclides' aqueous speciation and chemistry under relevant conditions, their interactions with clay minerals, and their mobility within the bentonite matrix is critically vital for evaluating repository performance. The ultimate goal of this work is to develop the predictive computational model of radionuclide retention in bentonites – relevant for nuclear waste disposal technologies. In particular, we propose using molecular modeling to parametrize meso- and macroscopic models of radionuclide migration in the clay barriers and clay-rich rocks and soils to develop a robust safety assessment model.

It is often difficult to experimentally determine the radionuclide migration in clay-rich soil or engineered clay barrier. The radionuclide toxicity requires strict safety protocols, which limits the number of laboratories in which measurements can be carried out and the analytical chemistry techniques that can be safely applied. Molecular modeling offers an attractive alternative to the experimental approach. Using molecular modeling one can estimate transport, speciation, and fluid properties required by the larger scale, continuum radionuclide transport models, and macroscopic/field-scale safety assessment models. For example, molecular dynamics simulations allow one to estimate the radionuclide diffusion coefficient in complex solutions. Molecular modeling gives insight into the transport properties dependence on the system composition, or porosity, and connectivity in the clay matrix. In Figure 7-1, we show the snapshots of the molecular modeling systems we explore in our simulation study to understand the role of clay surface charge, clay hydration state, and solution composition on the mobility of U^{4+}, Pu^{4+}, UO_2^{2+} ions in the bentonites.

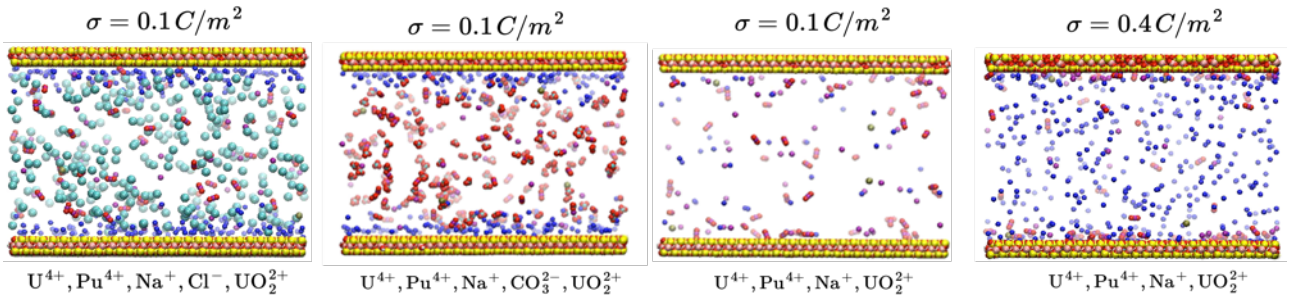

Figure 7-1 Examples of the molecular systems used to model the radionuclides retention by bentonites using molecular dynamics simulations.

In general, the overall trends in the speciation of radionuclides in aqueous solution and how their affinity to clay minerals changes with oxidation state and solution pH are relatively well understood (Bradbury & Baeyens, 2006; Bradbury & Baeyens, 2009). The preference of actinide ions to accumulate in compacted bentonites follows their effective charge of their aqueous species. However, complexation and ion-pairing in the solution phase can effectively alter the affinity of radionuclides to the clay surface.

In the natural environment, hydroxides and carbonate/bicarbonate ions are the most common complexing ligands. Similar to solubility and sorption discussed above, the complexation and complex solubility depend primarily on the actinide oxidation state. For instance, U(IV) hydroxy and carbonate complexes are an order of magnitude less soluble than analogous U(VI) complexes (Ewing, Runde et al., 2010). In principle, complexation by carbonate prevents radionuclides from being retained by bentonites as surface

complexes are typically weaker than those formed in bulk. These complexes prefer to remain in the solution, even though they are effectively less mobile than U(VI) ions (Tachi, Nakazawa et al., 2010). To predict radionuclides mobility in the environment, we need to understand the complexation and speciation in the aqueous solution and near the mineral surface. Knowing energetics and dynamics of sorption and complexation we will be able to rigorously predict radionuclide mobility in the environment and assess the safety of the geological disposal of radioactive waste.

However, the inclusion of the chemical reactions on the fly in classical molecular dynamics remains a challenge. Here, we show the progress we made towards reactive molecular simulations by exploring various reduction pathways for uranium ions in the aqueous solutions, the role of the solution composition, and complexation by environmentally most relevant ligands – carbonates.

7.2 Reduction and Oxidation Pathways of Uranium

The radionuclide mobility in nature is primarily determined by oxidation state, complexation, and sorption to the surfaces of naturally occurring minerals/soils or engineered barriers. The radionuclides in the reduced form are highly immobile (e.g., $X^{3+/4+}$, where X=U, Np, Pu), whereas in the oxidized state ($XO_2^{+/2+}$) they are more soluble and highly mobile. Here, we developed a computational framework to study the reduction and oxidation of radionuclides in complex systems and incorporate such reactions into the reactive molecular dynamics.

The oxidation state of uranium ions spans a wide range from III to VI. The transition from U(III) to U(VI) or from U(V) to U(VI) is one-electron transfer process, and it can be theoretically studied in terms of Marcus' electron transfer (ET) theory (Marcus 1956; Marcus 1957a; Marcus 1957b)

$$U^{3+} - e^- \rightarrow U^{4+} \qquad \textbf{Eq. 7-1}$$

$$UO_2^+ - e^- \rightarrow UO_2^{2+} \qquad \textbf{Eq. 7-2}$$

The U(III) and U(VI) ions are mononuclear species coordinated by 8 and 9 water molecules. However, hexavalent and pentavalent uranyl cations are linear molecules with two axial oxygen atoms coordinated by 5 to 6 water molecules in the equatorial plane around the uranium ion and four water molecules coordinating the axial oxygen atoms in the uranyl molecule. The reduction from U(V) to U(IV) involves protonation of axial oxygen atoms and breaking of covalent bonds between oxygen and uranium:

$$U^{4+} + 2H_2O - e^- \rightarrow UO_2^+ + 4H^+ \qquad \textbf{Eq. 7-3}$$

Similarly, the formation of oxyanion requires that two water molecules in axial position deprotonate completely. The reaction requires four proton transfers and one electron transfer, and from the theoretical point of view, it is considered the proton-coupled electron transfer process, PCET (Cukier & Nocera, 1998; Mayer, 2004; Weinberg et al., 2012) . The elementary reaction in which only proton is transferred is referred to as proton transfer (PT).

In practice, this PCET-type process may follow various pathways, with the mechanism changing according to the reaction conditions and environment. For example, one or two water ligands coordinating U(VI) can deprotonate partially prior to charge transfer and form metastable intermediate $U^{4+}(OH^-)$, $U^{4+}(OH^-)_2$, which upon electron extraction oxide to other intermediate uranium (V) ions, $U^{5+}(OH^-)$, $U^{5+}(OH^-)_2$. The water ligands deprotonation and formation of covalent bonds (oxyion) can also happen after the electron transfer, in a sequential or concerted fashion. Finally, the electron and proton transfers can all occur at the same time.

The first task in our project is to identify energetics of various plausible PCET/PT/ET pathways using DFT calculations and then determine the rate of oxidation/reduction using a combination of molecular dynamics and the first-principle calculations. In Figure 7-2 we show the DFT calculations of relative energetics of stable reduction state and intermediates. The concerted PCETs (Figure 7-2 a,b,d) represent the most energetically favorable redox transformations, whereas sequential ET followed by PTs are associated with the high energy barrier. Our analysis shows that U(V) ion cannot be formed spontaneously in the solution without water hydrolyzing and forming covalent bonds (Figure 7-2), that is, the ion $U^{5+}(H_2O)_n$ is energetically unstable. Surprisingly, the pathways with only one axial oxygen covalently bounded and another being either H_2O or OH^- are energetically possible (Figure 7-2d).

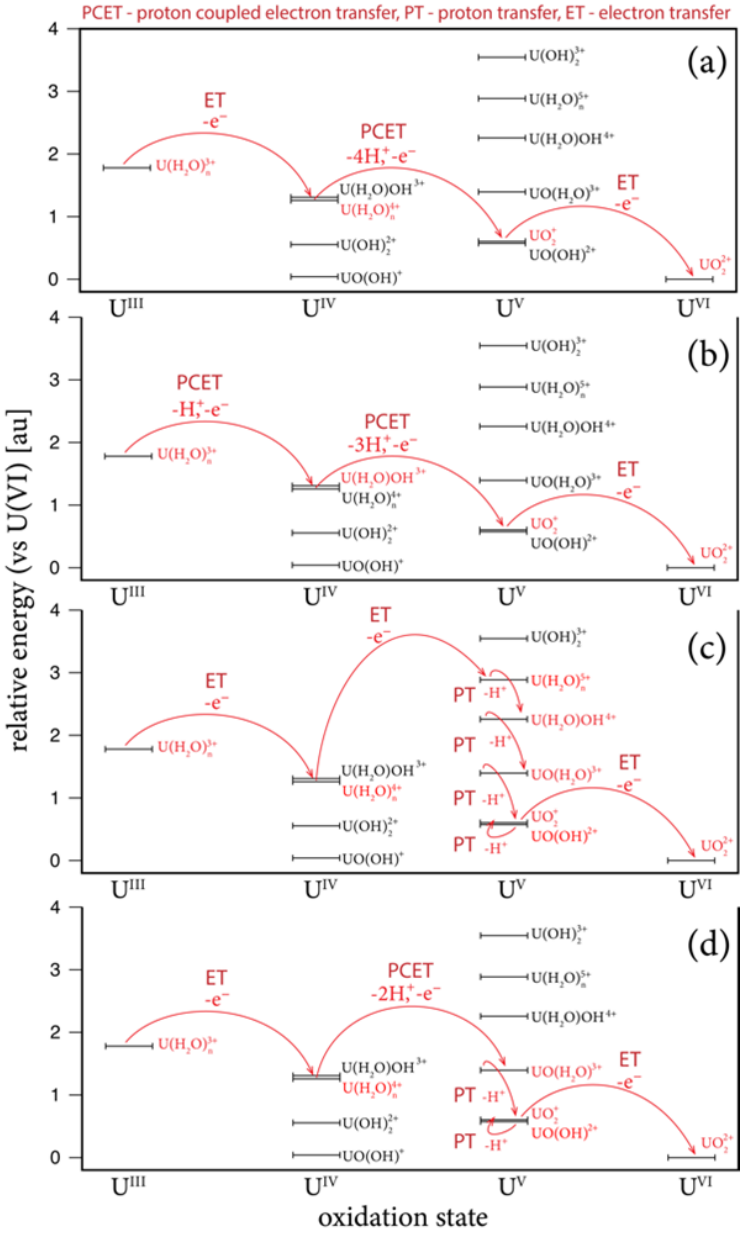

Figure 7-2 Relative energetics of uranium ions with varying oxidation state and coordination environment, and a few possible redox transformation pathways from U(III) to U(VI). Results are obtained using relativistic DFT calculations carried out using an open-source NWChem computational package.

Figure 7-2 plays the role of the energetics guideline for possible redox pathways, but the DFT calculations were carried out for the isolated ion with its first water coordination shell. In order to account for the effect of other ions and solution environment and energetic factors governing the charge transfer rate, we carried out combined molecular dynamics simulations with first-principle methods.

7.3 U(VI) Reduction Rate in the Presence of Carbonate

The association of dissolved uranium, plutonium, and neptunium with organic and inorganic ligands in solution has a significant impact on its environmental mobility – as it affects their solubility, sorption capacity, and redox equilibrium. We extended our previous molecular modeling efforts to better understand the role of complexation by carbonate in uranium oxidation state transformations.

The theoretical framework we used to understand charge transfer is based on Marcus' electron transfer theory (Marcus, 1956; Marcus, 1957a; Marcus, 1957b). In order to estimate the ET rate, one needs to determine the number of microscopic parameters that enter into ET equations in Marcus' theory. The ET is a Franck-Condon process, which means that the electron is transferred instantaneously between fixed nuclei positions. For charge transfer to occur, the electron donor, acceptor, and solvent environment need to reorganize to the transition state geometry/configuration that allows the Franck-Condon process. The energetic cost of this molecular reorganization prior to charge transfer is known as the reorganization energy (λ). Another important microscopic parameter governing ET rate is the electronic coupling between electron donor and acceptor wavefunctions (V_{AB}), which lowers the energy barrier for the ET. In practice, depending on the strength of electronic coupling, we have two regimes with slightly different expressions for the rate constant: adiabatic (strong electronic coupling) and nonadiabatic (weak electronic coupling):

$$k_{nonadiabatic} = \frac{2\pi V_{AB}^2}{\hbar^2\sqrt{4\pi k_B T}} e^{-\frac{\left(\Delta G^0+\lambda\right)^2}{4\lambda k_B T}} \quad \textbf{Eq. 7-4}$$

$$k_{adiabatic} = \nu_n e^{-\frac{1}{k_B T}\left[\frac{\left(\Delta G^0+\lambda\right)^2}{4\lambda} - V_{AB}\right]} \quad \textbf{Eq. 7-5}$$

where ΔG^0 is the electron transfer free energy, k_B is the Boltzmann constant, T is the temperature, and ν_n is the vibration frequency projected on the collective motion vector from the reagents to the transition state.

In this part of the project, our aim is to determine the charge transfer rate and mechanisms for uranium reduction and oxidation pathways in natural environments. The first step is to determine how complexation affects ET/PCET mechanisms and quantify the effective redox rates; the latter can be used in the lower resolution reactive transport and speciation models. One of the key processes is the reduction of U(VI) reduction to U(V) in the presence of coordinating carbonates and Fe(II)/Fe(III) ions. We used several computational methods (Zarzycki et al., 2011; Kerisit et al., 2015; Zarzycki, Kerisit, et al., 2015, Zarzycki, Smith et al., 2015, Zarzycki & Rosso 2017, Zarzycki & Rosso 2018) to determine all microscopic parameters entering charge transfer rate equations defined above.

In Figure 7-3 we show the molecular representations of the U(VI) carbonate complex (oxidized state) and U(V) carbonate complex (reduced state) in contact with iron ion. The presence of carbonate ions in all reactive complexes is key to preserve close proximity between electron donor and acceptor by pairing two positively charged ions (U, Fe) into a reactive complex. The distance between uranium and iron is within 0.34-0.4 nm in all cases, and there are no intervening water molecules or carbonate ligands shielding electron donor and acceptor. This is clear evidence that ET is not ligand-mediated but rather a direct

charge transfer process. What is more, the close proximity of Fe and U results in relatively large electronic coupling between their wavefunctions, suggesting that reduction occurs in the adiabatic ET regime.

In the case of the U(VI) carbonate with Fe(II), two carbonate ligands participate in the mutual coordination of iron and uranyl, and one carbonate ion coordinate only uranyl. This coordination is to a large extent preserved in the transition state geometry, but it changes drastically in the U(V) carbonate complexes with Fe(III). The presence of Fe(III) disrupts the carbonate coordination around U(V), because the negatively charged carbonate ions prefer to coordinate highly positively charged Fe^{3+} rather than UO_2^+. Because the TS geometry is similar to the U(VI), the relaxation from the TS to U(V) needs to involve reconfiguration of carbonate ligands. This substantial change in the complex geometry is associated with considerable reorganization energy (~5.4 eV). Still, despite that energetic cost, the uranium (VI) reduction is a fast process due to strong electronic coupling between acceptor and donor wavefunctions and favorable free energy difference.

The estimated rate of the uranium (VI) carbonate complexes reduction by Fe(II) in aqueous solution is about 0.125 s^{-1}, and it is relatively close to experimentally determined (Ilton et al., 2007) or estimated from the DFT calculations (Wander et al., 2006). Our results agree with the notion that U(V) is the most stable oxidation state in the carbonate-rich environment (Wester & Sullivan, 1980; Mizuguchi et al., 1993; Docrat, Mosselmans et al. 1999). The reduction of U(V) to U(IV) is energetically not favorable in the carbonate environment, and therefore reduction of U(VI) to U(IV) is effectively inhibited by the trapping uranium as U(V) (Wester & Sullivan, 1980; Mizuguchi et al., 1993; Docrat, Mosselmans et al. 1999).

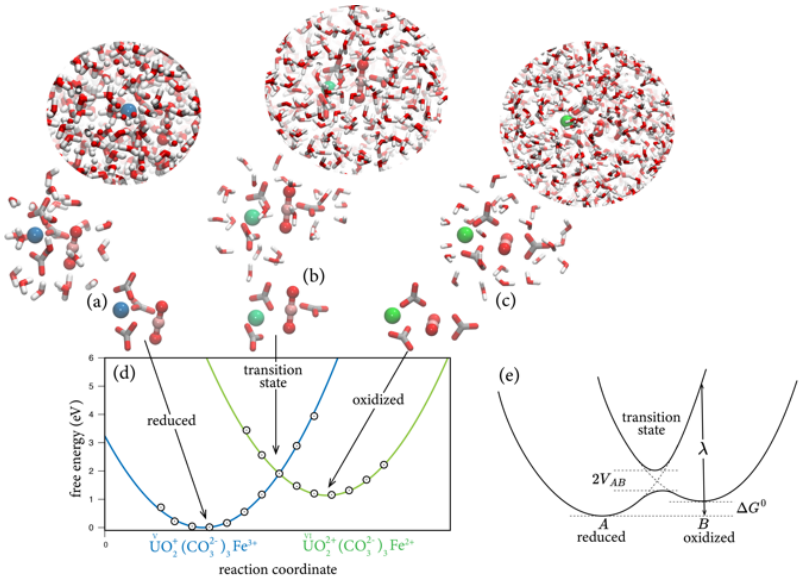

Figure 7-3 **Snapshots of the molecular systems used to model electron transfer from iron to uranium in the presence of carbonate ligands (a-c). In panel (d) we show the electron transfer free energy as calculated using umbrella sampling free energy scheme similar to our previous studies of charge transfer at the iron oxide interfaces and solvated iron ions (Zarzycki et al., 2011, Zarzycki, Kerisit et al., 2015). Points on curves stand for the center of the umbrella sampling window; see (Zarzycki et al., 2011) for details. In panel (e) we show the scheme of the Marcus' electron transfer model (adiabatic ET); λ stands for the reorganization energy, V_{AB} for the electronic coupling between donor and acceptor wavefunctions at the transition state geometry, and ΔG^0 is the electron transfer free energy – a driving force for charge transfer.**

7.4 Radionuclides Chemistry Under the Influence of Radiation

All the actinides are radioactive, and it is expected that their chemistry, speciation, and remediation are affected by their radioactivity. In order to accurately predict the radionuclide mobility in the repository, one needs to account not only for the heat generation associated with radiation, but also for the radiation damage in solution, or radiation-induced dislocation of atoms/ions in the bentonites and associated minerals.

The effect of ionizing radiation is typically divided into the physical, physicochemical, and chemical stages. The physical stage consists of the ionization and excitation of molecules (10^{-15} to 10^{-12} s), in the case of water solution the excited (*) and super-excited (**) water species are formed (H2O*, H2O**) as the products of water radiolysis. In the next physicochemical stage (~ 10^{-12} s) step, they dissociate to form radicals ($H^{\bullet}$, $OH^{\bullet}$, $O^{\bullet}$), hydroxonium ion (H_3O^+) and molecular hydrogen (Obodovskiy, 2019):

$$H_2O^* \rightarrow H^{\bullet} + OH^{\bullet} \quad \textbf{Eq. 7-6}$$

$$H_2O^* \rightarrow H_2 + O^{\bullet} \quad \textbf{Eq. 7-7}$$

$$H_2O^{**} \rightarrow H_2O^+ + e^- \quad \textbf{Eq. 7-8}$$

$$H_2O^+ + e^- \rightarrow H_2O^* \rightarrow H + OH^{\bullet} \quad \textbf{Eq. 7-9}$$

$$H_2O^+ + H_2O \rightarrow H_3O^+ + OH^{\bullet} \quad \textbf{Eq. 7-10}$$

In the last chemical stage of water radiolysis (~ 10^{-7} s), the chemical reactions between the radiolysis products formed in the reactions above led to formation of hydrogen peroxide and hydroxyl ions, for example (Obodovskiy, 2019):

$$H_2O + H^{\bullet} + e^- \rightarrow H_2 + OH^- \quad \textbf{Eq. 7-11}$$

$$OH^{\bullet} + e^- \rightarrow OH^- \quad \textbf{Eq. 7-12}$$

$$H_3O^+ + e^- \rightarrow H^{\bullet} + H_2O \quad \textbf{Eq. 7-13}$$

$$H^{\bullet} + H^{\bullet} \rightarrow H_2 \quad \textbf{Eq. 7-14}$$

$$OH^{\bullet} + OH^{\bullet} \rightarrow H_2O_2 \quad \textbf{Eq. 7-15}$$

All radiolysis products can interact with each other and all ions and molecules in the system, affecting their protonation and oxidation state. In particular, the radical and peroxide species are relevant as they can lead to the oxidation of uranium, ferrous iron present in the bentonite clays or generated other oxidative and corrosive species.

However, our understanding of the radical and redox chemistry of radionuclides and products of the water radiolysis is limited. First, these are typically fast nonequilibrium processes that cannot be easily accounted for in the speciation analysis of the solution or followed experimentally. Second, they are also challenging to model, because there is a lack of interaction models describing excited and radical species. Note that typical molecular mechanics interaction models and ab-initio molecular dynamics schemes are developed to either reproduce the ground state potential energy surface or follow atoms movement on that surface, and therefore not applicable to the radicals and excited molecules. Finally, the chemical reactions occur on the timescale comparable to the time increment in the integrator used to evaluate Newton equations of motions of particles in the system.

Here, we propose to expand our simulation approach described above and in the previous report to account for the chemical reactions between species formed in the solution due to exposure to ionizing radiation. In the first stage, we will develop the interaction models for the radical and excited ions and molecules similar to our previous molecular modeling of the photoexcitation of the iron oxalate complexes (Mangiante et al., 2017). In the next step, we will add the ultrafast radical chemistry events to the molecular dynamics scheme similar to our previous studies of the proton and electron transfer at the iron oxide/electrolyte interfaces (Zarzycki, Smith et al., 2015; Zarzycki & Rosso, 2018) and polaron transfer inside iron oxide particles (Katz et al., 2012; Soltis et al., 2017).

7.5 Future Work

We plan to continue molecular modeling of the uranium oxidation and reduction processes by exploring the various possible proton-electron transfer pathways and the role of the solution composition or presence of the charged clay surface in the uranium and other actinides redox dynamics.

In addition, we are planning to extend our molecular modeling efforts to include the effect of the radioactivity and products of the radiation damage in the solution. This aspect of radionuclide chemistry, although critically important, is often neglected in safety assessments and larger scale modeling efforts. We believe what the molecular-level insight gained by our modeling efforts will allow others to incorporate the radical and excited radionuclides chemistry into speciation and reactive transport models.

This page left blank

8. Sorption and Diffusion Experiments on Bentonite

8.1 Introduction

Most nuclear waste disposal options currently under investigation use clay media (i.e., bentonite or shale) as engineered barriers or as the host rock for geologic storage (Altmann, 2008; Altmann et al., 2012; Delay et al., 2007; Guyonnet et al., 2009; SKB, 2011; Tournassat et al., 2015). Clays are good barriers for HLW due to their low hydraulic conductivity, which restricts contaminant mobility to slow diffusion-based transport, and their high adsorption capacity for radionuclides, which slows transport even further. Montmorillonite ($M^{+}_{0.33}(Al_{1.67}Mg_{0.33})Si_4O_{10}(OH)_2$) is the dominant clay mineral found in bentonite. It has a 2:1 layer-type phyllosilicate structure, with a large specific surface area (~750 m^2/g) and CEC (~1 mol_c/kg), and strongly-sorbing surface complexation sites on clay edge surfaces.

In compacted clay, solute transport is controlled by diffusion, and adsorption of solutes to the clay can significantly retard transport. Uranium is the primary constituent of SNF, and the long half-lives of ^{238}U and ^{235}U (4.5×10^9 and 7.0×10^8 years, respectively) and high toxicity of U underscore the importance of understanding the transport of U through engineered barriers. While present at lower total amounts than U, ^{79}Se is a major driver of the safety case for nuclear waste disposal due to its long half-life (3.3×10^5 yr) and presence as relatively mobile anionic species under a range of chemical conditions (*e.g.*, HSe^-, SeO_3^{2-}, SeO_4^{2-}). Se redox chemistry is complex, with oxidation states ranging from -II to +VI over environmentally relevant conditions. While Se(-II) and Se(0) are relatively immobile due to the formation of low solubility precipitates, Se(IV) and Se(VI) exist as the oxyanions selenite (SeO_3^{2-}) and selenate (SeO_4^{2-}) and are highly mobile in water due to their high solubility. Se adsorption to clay minerals is quite low compared to other important radionuclides such as U. K_d values for selenite adsorption to smectite are in the range of 1-10 L/kg (Missana et al., 2009; Montavon et al., 2009) compared to values up to 10^4 for U(VI) (Tournassat et al., 2018). Selenite and selenate adsorption to the clay minerals kaolinite and Ca-montmorillonite were studied by Bar-Yosef & Meek (1987) over the pH range 4-8. Both selenite and selenate adsorption decreased with increasing pH, with very low or negligible adsorption above pH 8 and selenate adsorption to kaolinite was lower than selenite adsorption (Bar-Yosef & Meek, 1987). Similar trends of lower selenate vs selenite adsorption and decreasing adsorption with increasing pH are observed on iron oxides and oxyhydroxides (Balistrieri and Chao, 1987, 1990).

Selenite diffusion through bentonite has been investigated in several studies (García-Gutiérrez et al., 2001; Idemitsu et al., 2016; Wang et al., 2016; Wu et al., 2017). Idemitsu et al. (2016) measured apparent diffusion coefficient (Da) values of 2.5 x 10-11 to 1.9 x 10-13 m2/s over a range of dry bulk densities (0.8-1.6 kg/L), ionic strengths (0.01-1.0 M NaCl), and temperatures (10-55°C) for purified bentonite consisting of 99% montmorillonite. Measured Da values for bulk bentonite (i.e., with lower smectite content) under similar conditions are 1-2 orders of magnitude higher (Sato et al., 1994; Wu et al., 2014). Under anaerobic conditions, it is possible for Se(IV) to become reduced to Se(0) or Se(-II) (Charlet et al., 2012; Charlet et al., 2007; Ma et al., 2019). Due to the lower adsorption of selenate compared to selenite, selenate diffusion may be even higher than observed for selenite, although we could find no studies on selenate diffusion through bentonite in the literature.

In this report, we present experimental results from ^3H and Se(VI) through-diffusion experiments through a well-characterized, purified montmorillonite source clay (SWy-2). Experiments were conducted under a single ionic strength (0.1 M) and three different electrolyte compositions representing pure Na, pure Ca, and a Na-Ca mixture in order to probe the effects of electrolyte composition on clay microstructure, Se(VI) aqueous speciation, and ultimately diffusion. Preliminary modeling results from these experiments are also presented.

8.2 Materials and Methods

8.2.1 Clay Samples

Selenium diffusion experiments were conducted using a well-characterized montmorillonite source clay (SWy-2) obtained from the Clay Minerals Society. The montmorillonite was purified in order to remove minor impurities (quartz, feldspars, and calcite). The purification procedure was adapted from (Tinnacher et al., 2016). The procedure included the following major steps: (1) dialysis against sodium acetate at pH 5 for carbonate mineral removal, (2) dialysis against NaCl to remove acetate and complete Na-saturation, (3) dialysis against water to remove excess salts, and (4) centrifugation to remove particles greater than 2 m. Montmorillonite (50 g) was suspended in 1 L of 1 M sodium acetate solution buffered at pH 5 with acetic acid, placed into pre-rinsed dialysis tubing (SpectraPor7, 8 kDa), and dialyzed against acetate buffer for 1 week, changing dialysis solution daily. The acetate buffer dialysis solution was then replaced with 1 M NaCl (dialyzed for 3 days), then with MilliQ water (dialyzed for two weeks), again changing dialysis solution daily. The clay suspensions were then transferred into plastic bottles and diluted and dispersed in MilliQ water to reach a clay concentration of approximately 15 g/L, and centrifuged at 1000 x g for 7 minutes. This centrifugation speed and time was deemed sufficient to remove all particles > 2 μm as calculated from Stoke's Law. The replicate < 2 μm clay fractions were then combined into a glass beaker, dried at 60°C and ground in ball mill with tungsten carbide balls.

In order to ensure that aqueous porewater chemical concentrations were constant during the diffusion experiments, purified montmorillonite was pre-equilibrated with the appropriate background electrolyte prior to packing in diffusion cells. 2 g of purified clay was suspended in 100 mL of electrolyte solution and the clay suspension was transferred to pre-rinsed dialysis tubing (SpectrPor7, 8 kDa). Clay samples were dialyzed against 1 L of background electrolyte for 1.5 weeks, changing dialysis solution at least 3 times and manually adjusting pH daily. Once the pH was stable, the background electrolyte solution was replaced with MilliQ water, and dialysis was continued for 5 days, changing the MilliQ water daily. After dialysis was complete, the clay suspension was transferred to 40 mL polycarbonate centrifuge tubes and centrifuged at 39,000 x g for 20 minutes. The supernatant was removed and the clay was dried at 60°C and ground in ball mill with tungsten carbide balls and stored at room temperature prior to packing the cells. At the time of packing, a subsample of each clay was dried at 150°C to determine the moisture content.

8.2.2 Diffusion Experiments

Diffusion experiments were conducted with purified, pre-equilibrated montmorillonite at a dry bulk density (ρ_d) of approximately 1.3 kg/L using the diffusion cell design shown in Figure 8-1. The diffusion cells used for experiments were machined in-house at LBNL, which are based on the design of (Van Loon et al., 2003), with dimensions adjusted to accommodate smaller samples. Because preliminary experiments with stainless steel filters showed evidence of corrosion, PEEK filters with a PCTFE ring were used instead (IDEX # OC-815, overall D=0.95 cm, filter D=0.74 cm, thickness=0.16 cm, pore size=5 μm).

Experiments were conducted under a single ionic strength (0.1 M) and three different electrolyte compositions: 0.1 M NaCl, 0.033 M $CaCl_2$, and 0.085 M NaCl + 0.005 M $CaCl_2$, representing pure Na, pure Ca, and a Na-Ca mixture, respectively. All experiments were performed at room temperature at pH 6.5 in equilibrium with atmospheric conditions (~20% O_2 and 400 ppm CO_2). The pre-equilibrated dry clay samples were carefully weighed into PEEK diffusion cells and compacted using a custom PEEK packing rod. Three phases of the diffusion experiment were conducted: (1) saturation, (2) tritiated water (^3H) diffusion, and (3) Se(VI) diffusion. The clay was saturated by circulating 200 mL of background

electrolyte at both ends of the cell at approximately 1 mL/min using a peristaltic pump for 40-42 days. After the saturation period, the ^{3}H through-diffusion phase was started by replacing the background electrolyte solutions with a high ^{3}H reservoir containing background electrolyte spiked with 30 nCi/mL ^{3}H (200 mL) at one end and a low ^{3}H reservoir containing only background electrolyte (20 mL) at the other end. The high concentration reservoir was sampled at the beginning and the end of the ^{3}H diffusion experiment and did not change significantly over that time period. The low ^{3}H reservoir was changed at time intervals of 3-36 hr, and the ^{3}H concentration was measured in the low reservoir samples by liquid scintillation counting. An in-house built autosampler using a 3D printer (Creality Ender 3Pro) as the base was used to change the low reservoir samples at regular time intervals. The ^{3}H concentration in the low reservoir never exceeded 0.5% of the concentration in the high reservoir. The ^{3}H diffusion was continued for 16 days. After this period, the high concentration reservoir was replaced with a Se(VI)-spiked solution containing 1.0 mM sodium selenate in background electrolyte with a total volume of 190 mL, marking the start of the Se(VI) diffusion experiment. The low concentration reservoirs containing only background electrolyte (5-10 mL) were changed at time intervals of 12-48 hours for the first 44 days, then 48-170 hours for the remaining 33 days and Se concentrations were measured by ICPMS. Se concentrations in the low reservoir never exceeded 1% of the concentration in the high reservoir. Subsamples of the high concentration Se(VI) reservoir were collected at the beginning and end of the experiment and did not change significantly over the experiment.

At the end of the Se(VI) diffusion period, the diffusion cells were disassembled, and the clay plug was extruded using the PEEK packing rod and sliced into thin slices. The thickness of the clay slices was measured using a digital caliper with a precision of 0.1 mm. The clay slices were placed into 20 mL glass scintillation vials and dried at 150°C for 24 hours. The PEEK filters were removed from each end of the clay plug, suspended in 10 mL of MilliQ water in a glass scintillation vial and shaken vigorously to dislodge any clay that was stuck to the filter. The filter was then transferred to a new vial and 5 mL of 0.5 M hydrochloric acid was added to the filter to dissolve Se(VI). The clay slices were extracted with 5 mL of 0.5 M trace metal grade hydrochloric acid for 3-days, then centrifuged at 39,000 x *g* for 20 min and filtered through a 0.45 μm PVDF syringe filter. Selenium concentrations were measured in the acid extracts by ICPMS. The small amount of clay which was removed from the filters with MilliQ water was dried at 150°C, weighed, and extracted in the same manner as the clay slices. Both the dry bulk density (ρ_d) and Se concentrations in the clay plug are expressed in terms of the 150°C oven dry weight of clay.

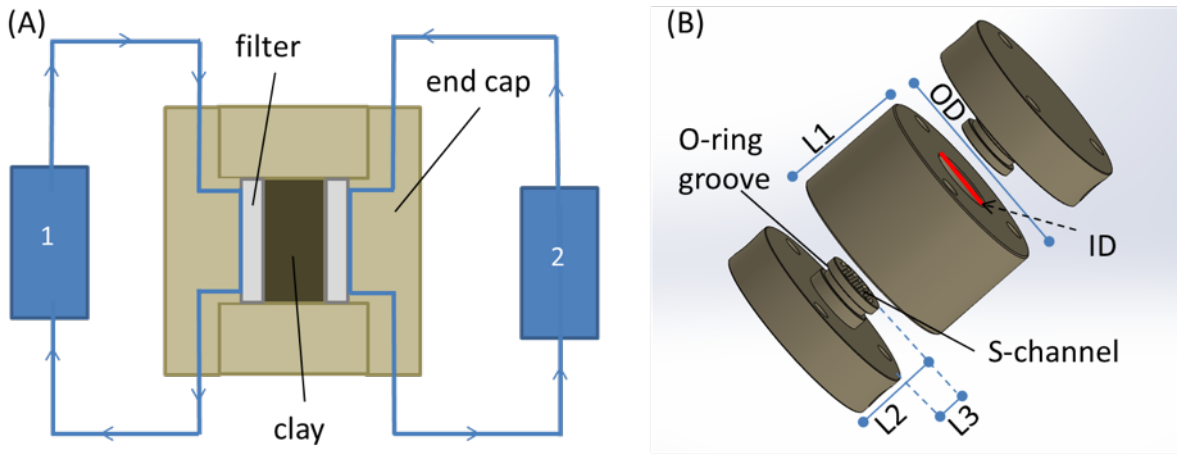

Figure 8-1 **Schematic of diffusion cells machined in house. (A) Cross-sectional view of the diffusion cell showing the clay plug, filters and two solution reservoirs. During saturation and ^{3}H diffusion, both reservoirs are used, and during U(VI) in-diffusion, reservoir 2 is removed and the cell is plugged at that end. (B) Detailed schematic of the cell design, with groves for the o-rings and an S-shaped channel which allows the solution to distribute evenly over the entire filter of the diffusion cell. The dimensions for the cell are as follows: OD = 30 mm, ID = 9.5 mm, L1 = 17.8 mm, L2 = 12.2 mm, L3 = 4.9 mm. O-rings measure 7.5 mm ID and 9.5 mm OD.**

8.2.3 Analytical Techniques

Samples were analyzed for Se by ICP-MS (Perkin-Elmer Elan DRC II) after acidification and dilution with ultrapure (ultrex grade) 0.15 M nitric acid and internal standard addition. Selenium was measured using oxygen as the cell gas in DRC mode and using Rh as an internal standard. Spike recoveries with known concentrations of Se were run every 5 samples, and recoveries ranged from 0.80-1.25. Independent QC samples were run every 10 samples, with recoveries ranging from 0.9-1.1. Samples were analyzed for ^{3}H using liquid scintillation counting (Perkin-Elmer Liquid Scintillation Analyzer Tri-Carb 2900TR) by mixing 4 mL of sample with 18 mL of Ultima Gold XR liquid scintillation cocktail.

8.2.4 Modeling Approach

Modeling of diffusion experiments was carried out using CrunchClay (Steefel et al., 2015; Tournassat & Steefel, 2019a) taking full advantage of the capabilities of this reactive transport code developed at LBNL. CrunchClay is currently one of only two codes that can handle diffusion processes in the diffuse layer, in which the solution is not electroneutral, and for which coupled interdiffusion processes must be taken into account to model diffusion properties with a mechanistic approach (Tournassat & Steefel, 2019b). CrunchClay has the ability to treat both electrical double layer and bulk porosity with differing anion and cation diffusivities, which makes it possible to simulate the diffusion of a range of tracers with different charges in a single run, and with the same input parameters. CrunchClay also has surface complexation and cation exchange modeling capabilities, thus making it possible to couple mechanistic adsorption models with diffusion models in clay media. Our goal is to derive consistent diffusion and adsorption parameters for Se, ^{3}H and other trace elements as a function of ionic strength and electrolyte composition, which will be probed experimentally in this project.

8.3 Results and Discussion

8.3.1 Tritium and Selenium Diffusion

Normalized mass flux (J_N, in m/day) reaching the low concentration reservoir was calculated using Eq. 8-1:

$$J_N = \frac{C_{low} V_{low}}{C_{high} A \cdot \Delta t} \quad \textbf{Eq. 8-1}$$

Where C_{low} is the concentration in the low concentration reservoir, C_{high} is the concentration in the high concentration reservoir, V_{low} is the volume of the low concentration reservoir (approximately 20 mL), A is the cross-sectional area of the diffusion cell (0.709 cm^2), and Δt is the time interval since the previous sampling event. The normalized mass flux for tritium diffusion in the three cells is shown in Figure 8-2. Note that the autosampler missed the vial for the Na-Ca cell at 23 hours. Tritium diffusion reached steady-state after approximately 100 hours, with slightly higher flux in the Ca cell compared to the Na and Na-Ca cells. Small differences in the measured ^3H normalized flux may result from small differences in cell packing, which can in turn affect porosity or pore structure (*i.e.*, pore constrictivity or tortuosity). Total porosity (ε) depends on bulk density and can be calculated using Eq. 8-2:

$$\varepsilon = 1 - \frac{\rho_d}{\rho_g} \quad \textbf{Eq. 8-2}$$

where ρ_g is the crystal density of clay mineral layers (*i.e.*, grain density). For montmorillonite, ρ_g is approximately 2.84 kg/L (Bourg et al., 2006; Tournassat and Appelo, 2011). There were some small differences in the calculated bulk density and porosity for the three cells due to differences in the moisture content of the clays at the time of packing. A summary of the diffusion cell parameters, including an average normalized flux at steady state (>100 hr) is shown in Table 8-1.

Normalized flux for Se(VI) (Figure 8-3) reached steady state after approximately 300 hours, with the Ca cell showing the greatest normalized flux. Notably, the differences in the normalized flux between the cells for Se are much greater than was observed for tritium and therefore are not due to differences in total porosity alone. Rather, differences in aqueous Se speciation, clay swelling, and effective porosity in the presence of Na and Ca are expected to play a large role in the diffusive flux of Se(VI). Se(VI) aqueous speciation over the pH range of 5-8 is shown in Figure 8-4, where three major Se(VI) species with different charge dominate: SeO_4^{2-}, $HSeO_4^-$, and $CaSeO_4^0{}_{(aq)}$. While the SeO_4^{2-} species with a charge of -2 is the most abundant species under all conditions in the pure Na electrolyte, the neutral $CaSeO_4^0{}_{(aq)}$ species accounts for 30% of the total Se at pH 6.5 in the pure Ca electrolyte, and 6% of the total Se in the Na-Ca mixture. The diffusive fluxes of anionic species are typically lower than those of neutral or cationic species due to anion exclusion from the electrical double layer, and our results are consistent with this. Furthermore, porewater composition also affects the solute accessible (or effective) porosity due to effects on clay layer stacking, with higher Ca concentrations resulting in larger effective porosities (Tournassat and Appelo, 2011).

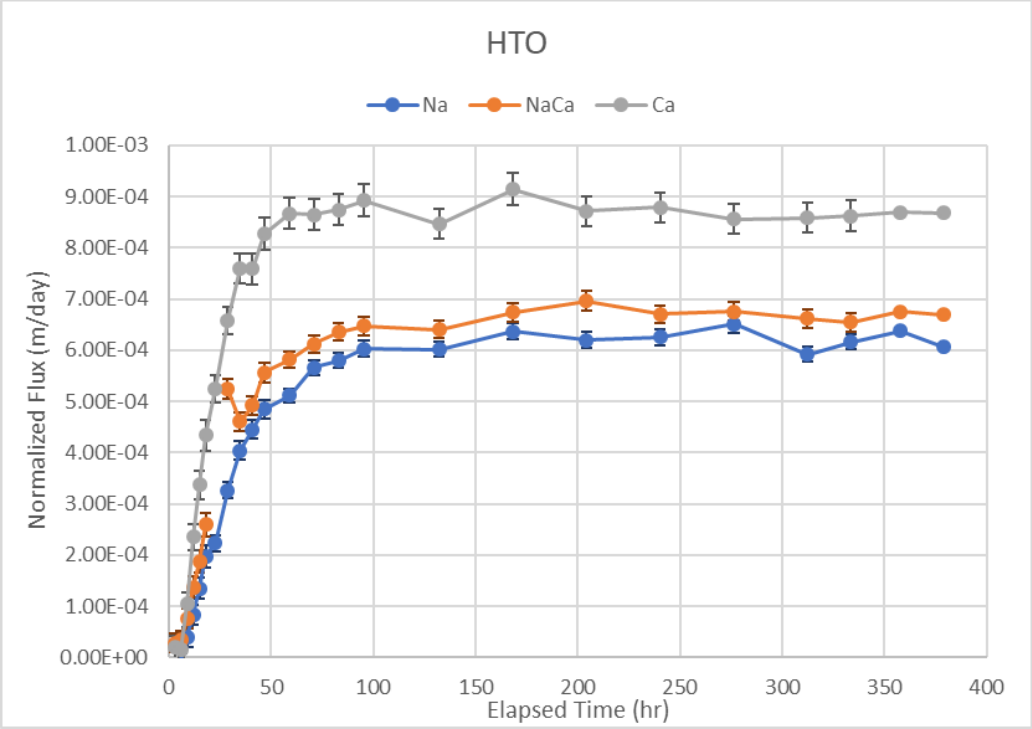

Figure 8-2 Normalized tritium flux in the three diffusion cells. Error bars represent analytical error.

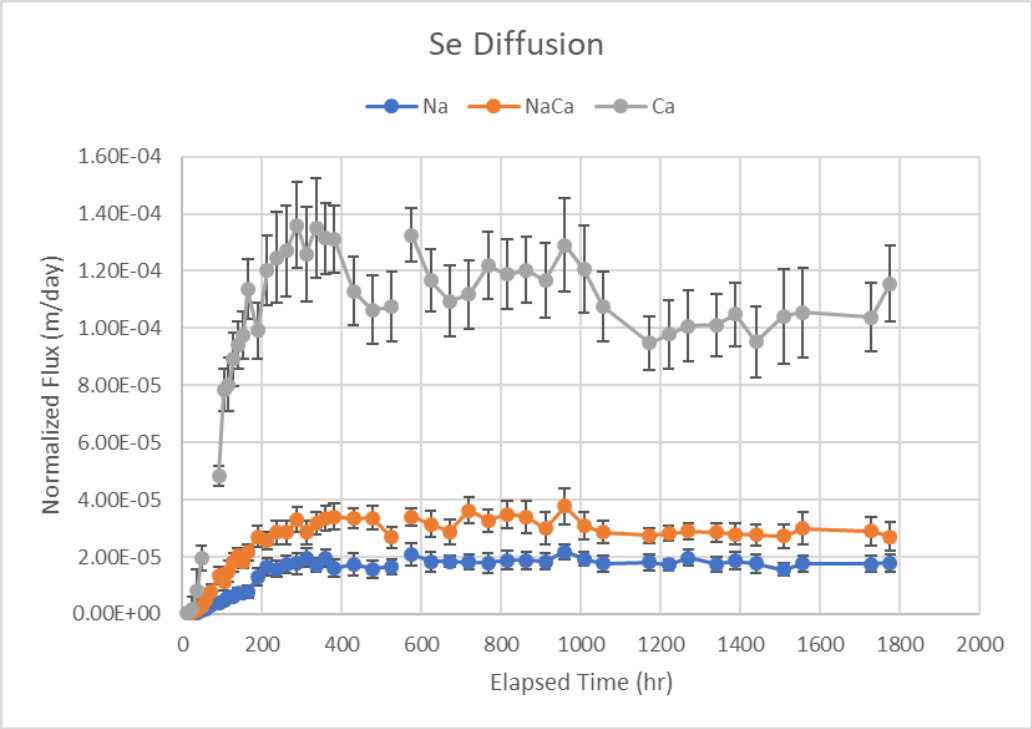

Figure 8-3 Normalized Se flux in the three diffusion cells. Error bars represent analytical error

Table 8-1 Summary of diffusion cell parameters.

Cell	ρ_d, kg/L	ε	Tortuosity[(a)]	^{3}H Avg J_N, m/day[(b)]	Se Avg J_N, m/day[(c)]
Na	1.35	0.52	0.037	$6.19 \pm 0.19 \times 10^{-4}$	$1.82 \pm 0.14 \times 10^{-5}$
Na-Ca	1.28	0.55	0.040	$6.66 \pm 0.16 \times 10^{-4}$	$3.08 \pm 0.31 \times 10^{-5}$
Ca	1.24	0.56	0.058	$8.72 \pm 0.22 \times 10^{-4}$	$1.14 \pm 0.12 \times 10^{-4}$

(a) Preliminary modeled value from ^{3}H diffusion.

(b) Average steady state for ^{3}H for 95-379 hours.

(c) Average steady state for Se for 310-1775 hours.

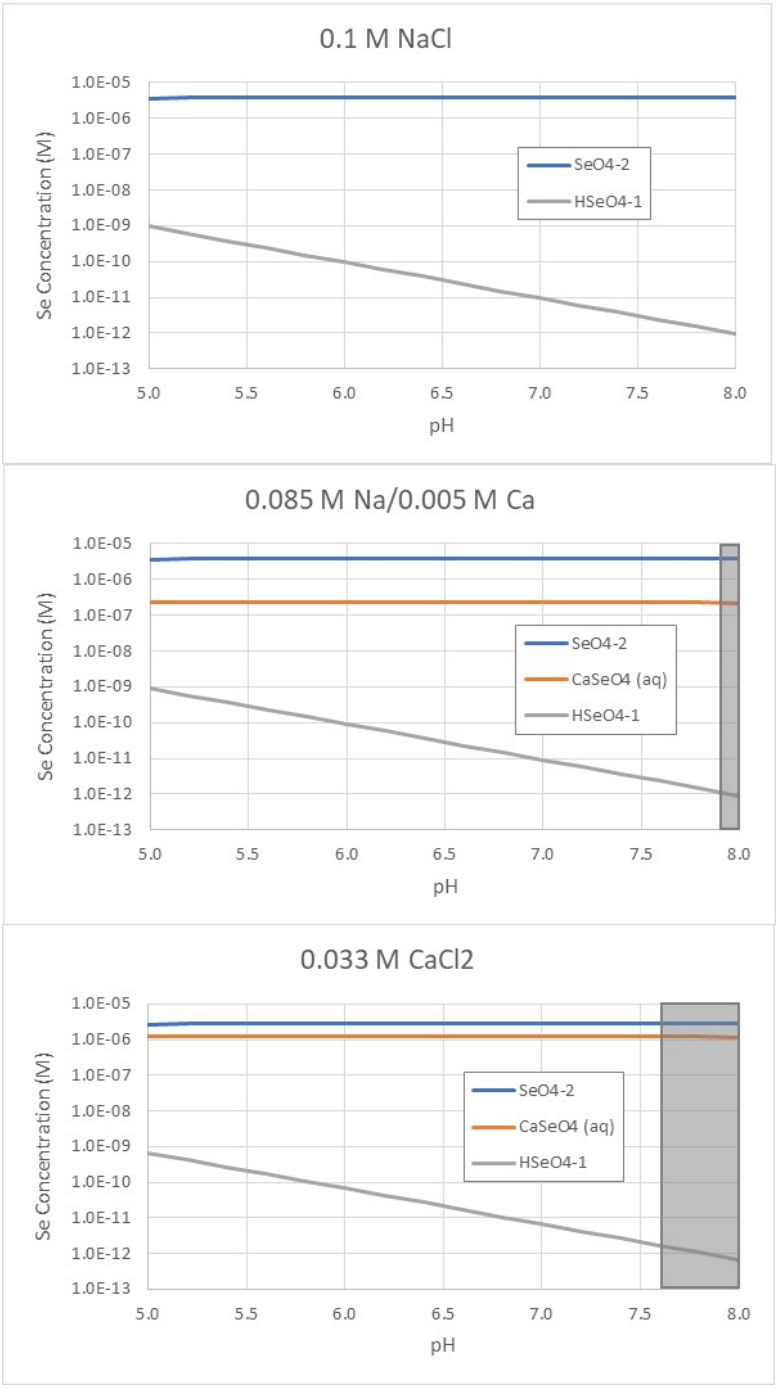

Figure 8-4 **Aqueous speciation of Se(VI) as a function of pH in equilibrium with atmospheric CO_2 (380 ppm) for three different electrolyte compositions. Total Se(VI) concentration is 4 μM. The area shaded in grey represents conditions which are oversaturated with respect to calcite.**

8.3.2 Clay Slicing

Selenium clay profile concentrations from HCl extractions at the end of the diffusion experiments are shown in Figure 8-5. Clay slices ranged in thickness from 0.3 to 0.9 mm. The Se concentrations are expressed in terms of the total porewater volume, and follow the trend Na<Na-Ca<Ca. This trend is

consistent with the Se diffusion data which suggest that the Ca-saturated clay has the highest effective porosity for Se(VI). Se concentrations in the clay slice closest to the high concentration reservoir (at ~4.5-5.0 mm) are 0.18, 0.25, and 0.77 mM for the Na, Na-Ca, and Ca cells, respectively. The profiles in all three cells are linear with depth as expected for steady-state conditions. These data will be used in conjunction with diffusion data to model adsorption and effective porosity under the different electrolyte conditions.

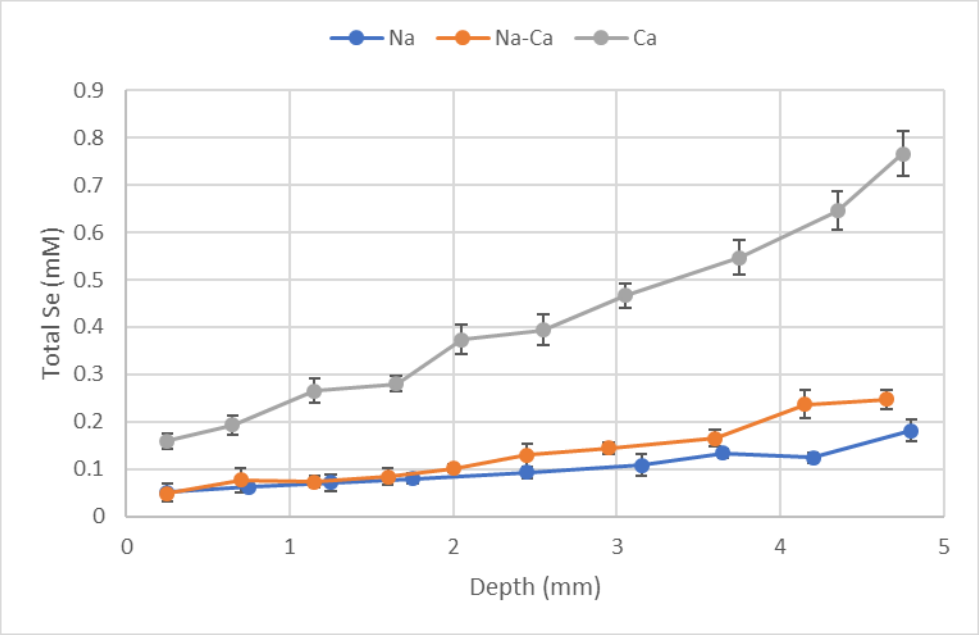

Figure 8-5 Se profiles extracted from clay using 0.5 M HCl at the end of diffusion experiments. Se concentrations are expressed as a concentration in the total porewater volume.

8.3.3 Modeling Results

In a first step HTO diffusion data were modeled considering that the whole porosity was accessible to HTO (Figure 8-6 to Figure 8-8). These calculations evinced differences of connectivity in the diffusion pathways (tortuosity parameter) as a function of pore water composition (Table 8-1). In order to model diffusion through the clay, the diffusion through the filters at either end of the cell must also be considered. Filter diffusion values were adapted from Aldaba et al. (2014), however, the modeled tortuosity given in Table 8-1 must be considered as preliminary because the effect of the filter properties must be further investigated. Notwithstanding the error in the parameters estimation because of the filter effects, diffusion experiments and simulation results showed a clear increase of the connectivity with a change of electrolyte from Na dominated to Ca dominated pore water composition. This change is interpreted as a consequence of differences in microstructure driven by pore water composition differences, and hence surface composition differences: Ca dominated surfaces have the tendency to stack clay layers, and so to open larger inter particles pores compared to Na dominated surfaces.

This finding is consistent with SeO_4^{2-} diffusion results, showing a large increase of SeO_4^{2-} steady state flux value with increasing Ca concentration in the system. As Ca concentration increases, the volumetric proportion of porosity water influenced by the vicinity of charged clay surfaces decreased because of clay layer stacking (Tournassat and Appelo, 2011). Consequently, the proportion of porosity accessible to SeO_4^{2-} increased, leading to larger steady state fluxes. Reactive transport simulations with CrunchClay are on-going to quantify this phenomenon.

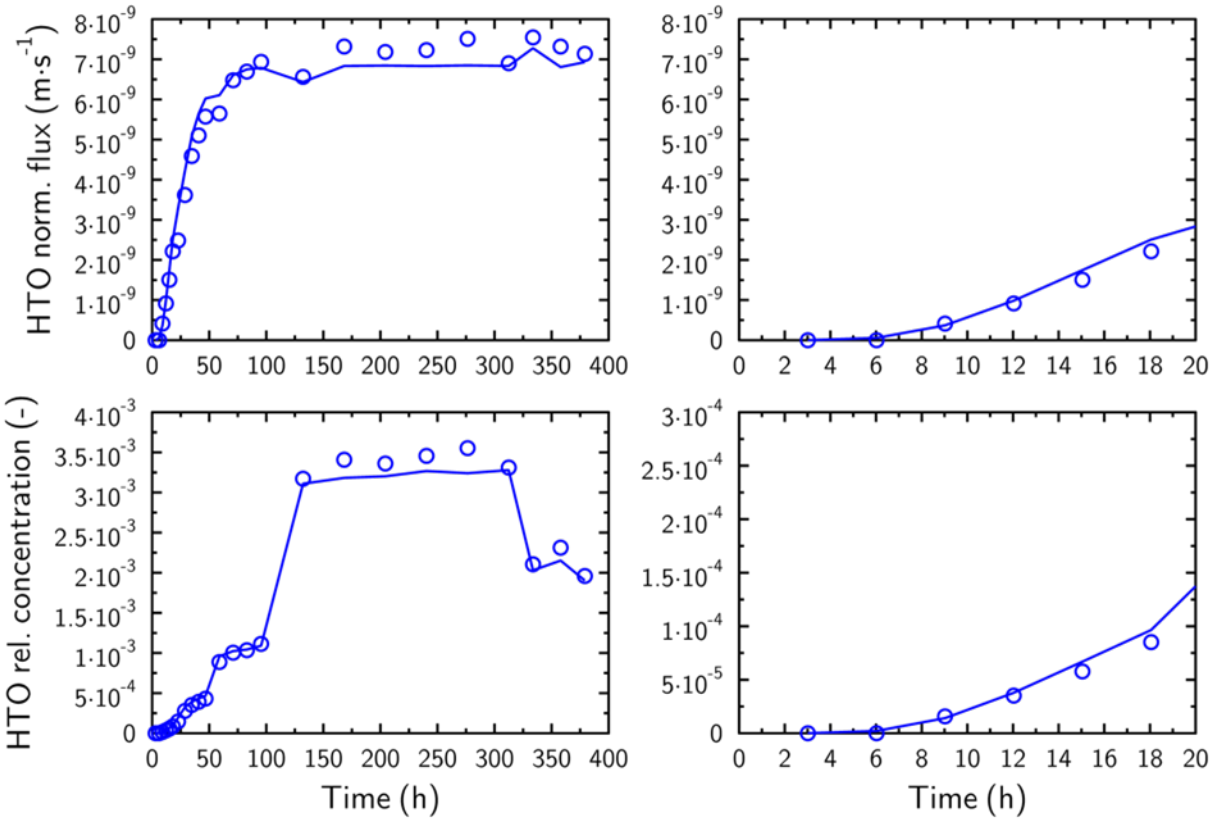

Figure 8-6 **Modeling (lines) of ^{3}H (HTO) diffusion in experiment (circles) with 0.1 M NaCl background electrolyte composition. Top: HTO normalized flux. Bottom: HTO relative concentration (C_{low}/C_{high}).**

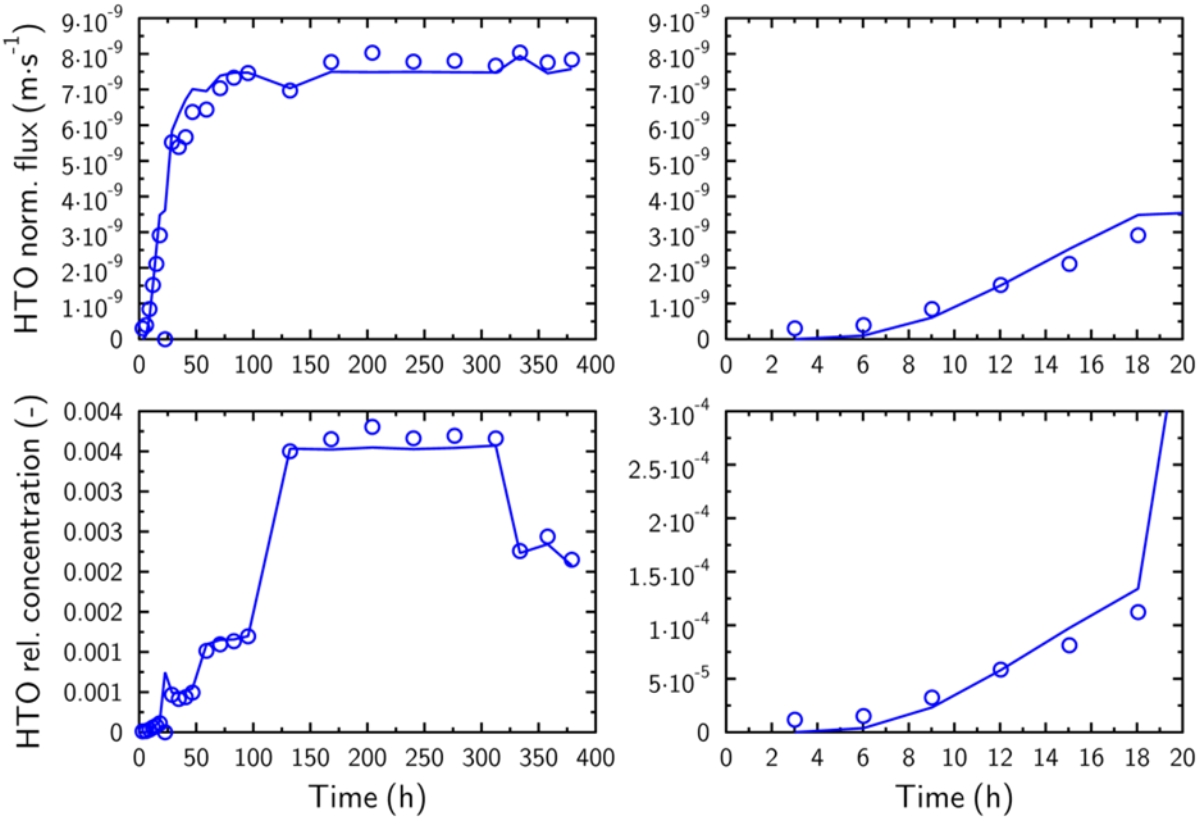

Figure 8-7 **Modeling (lines) of ^{3}H (HTO) diffusion in experiment (circles) with 0.085 M NaCl + 0.005 M M $CaCl_2$ background electrolyte composition. Top: HTO normalized flux. Bottom: HTO relative concentration (C_{low}/C_{high}).**

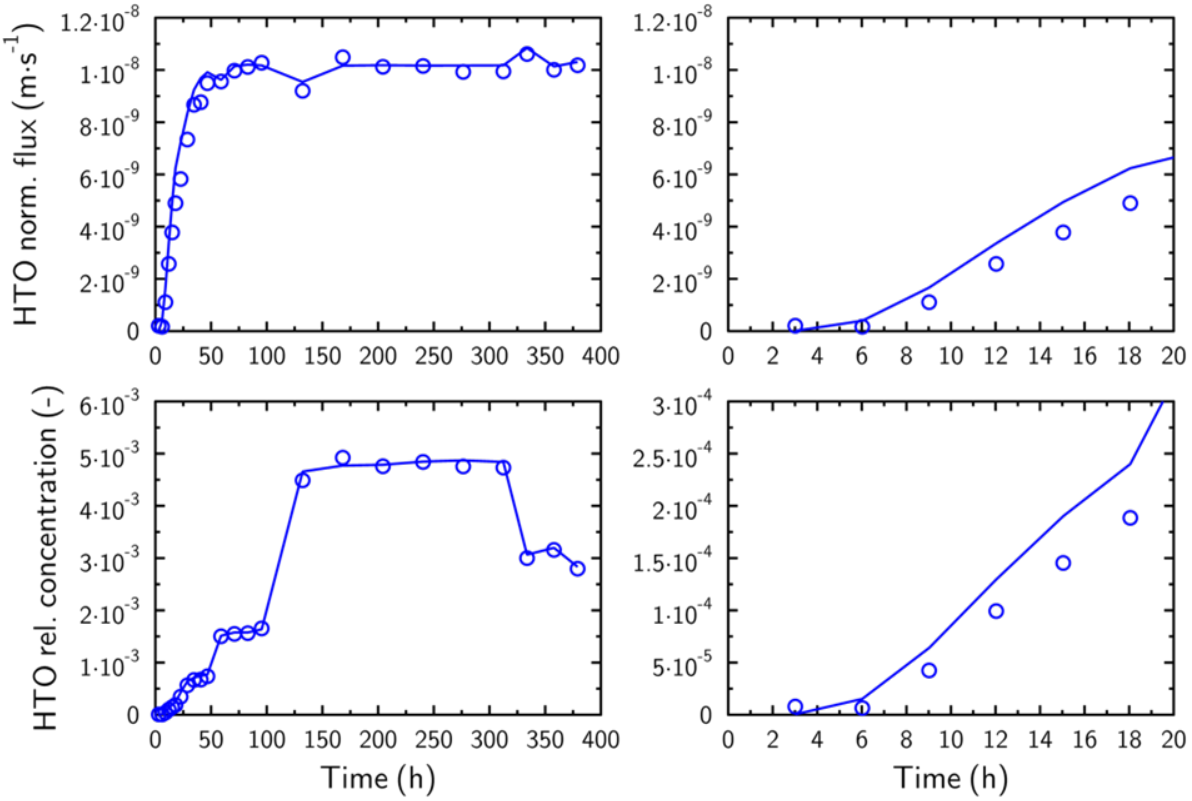

Figure 8-8 **Modeling (lines) of ^{3}H (HTO) diffusion in experiment (circles) with 0.033 M $CaCl_2$ background electrolyte composition. Top: HTO normalized flux. Bottom: HTO relative concentration (C_{low}/C_{high}).**

8.4 Summary and Future Work

In FY21, ^{3}H and Se(VI) through-diffusion experiments were conducted with compacted montmorillonite at a bulk density of approximately 1.3 kg/L. The experiments were conducted under a single ionic strength (0.1 M) and three different electrolyte compositions: 0.1 M NaCl, 0.033 M $CaCl_2$, and 0.085 M NaCl + 0.005 M $CaCl_2$, representing pure Na, pure Ca, and a Na-Ca mixture, respectively. Results showed that both ^{3}H and Se diffusion was greatest in the pure Ca system and lowest in the pure Na system. These results are consistent with an increase in pore connectivity from Na dominated to Ca dominated pore water composition. This change is interpreted as a consequence of differences in microstructure driven by pore water composition differences: Ca dominated surfaces have the tendency to stack clay layers, and so to open larger inter particles pores compared to Na dominated surfaces. Differences in Se diffusion as a function of electrolyte composition are even greater, with Se normalized fluxes approximately 6 times higher in the pure Ca system compared to the pure Na system. This suggests that the accessible (or effective) porosity for Se in the Ca system is higher than for the Na system, likely due to differences in clay stacking, electrical double layer, and Se(VI) aqueous speciation.

Future work will focus on refining the ^{3}H diffusion model, including the filter diffusion model, and modeling the Se(VI) diffusion through montmorillonite in the three different electrolyte compositions. We will then begin to investigate redox transformations of Se in clay systems and the effect on Se transport.

9. Coupled Microbial-Abiotic Processes in EBS and Host Rock Materials

Experiments on potential microbial activity present in materials collected from the FEBEX experiment were conducted from materials including high heat, intermediate, and control temperature zones. Details of the samples can be found in previously published reports (Villar et al., 2020b; Bárcena, 2015). The tested samples were recovered from the FEBEX site in 2015. Before sampling, clays were cooled in the formation. After removal they were subsampled, removing external surfaces that had been in contact with extraction equipment. The final samples had an average volume of 18 cm^3 and were wrapped in plastic, vacuum sealed in aluminized Mylar bags, and stored at room temperature.

Current experiments are designed to determine if these materials possess microbial communities capable of metabolizing H_2 or other substrates, and how the FEBEX treatment impacted those capabilities. In FY19, two sets of materials were tested from a 'heater zone' (BD-48-6, high temperature) and from a 'cold zone' (BD-59-10) (Figure 9-1). In FY20, two sample locations were added, one at BD-48-5 (mid high temperature) and the other at BD-48-4 (mid low temperature). In FY21 the experiments were continued to completion and broken down for final analysis.

9.1 Methods

9.1.1 Sample Incubation

To prepare the sample of each clay type, the Mylar bags containing the subsamples were opened and a piece was broken away from the large block. This subsample was placed on an autoclaved piece of Al foil in the biosafety cabinet and 0.5 cm was scraped with a sterilized razor blade to remove the outer surfaces. Scrapings and foil were removed, and the sample was placed on a new autoclaved piece of foil. A fresh sterile razor blade was then used to remove about 5 g of clay. This 'fresh' (newly exposed) layer of clay was mixed and distributed amongst 60 mL serum vials (6 for each clay type) containing 10 mL of sterile minimal salts media (Sigma M9 minimal salts, MSM), which contains 15 g/L KH_2PO_4, 64 g/L $Na_2HPO4 \cdot 7H_2O$, 2.5 g/L NaCl, 5.0 g/L NH_4Cl. MSM was purchased 5x concentrated (Sigma), so actual addition was 2 mL of medium and 8 mL of DI water (milliQ). The medium and water were added to 60 mL serum bottles through a 0.2 µm filter. 15 psi of gas mix was added to each serum bottle. This was done by starting with a full serum bottle of air, adding 7 mL of CO_2, and pressuring to 15 psi with a N_2/5% H_2 mix. All gas was filtered through a 0.2 µm filter. This method provided a consistent gas mix for all bottles, with an average final composition of 5% CO_2, 2.8% H_2, 9% O_2, with a balance of N_2.

Sample designations were 59-10 (control, non-heated); 48-4 (35°C); 48-5 (50°C); 48-6 (95°C) (Villar et al., 2018). For Experiments 1 and 2, only 59-10 and 48-6 were tested. In Experiments 3 and 4, all four samples were included (Table 9-1, Figure 9-1). Sterile control samples (autoclaved clay) and blanks (no clay, only media) were run for comparison purposes. Although the number of replicates varied slightly for each experiment, 4-6 samples were prepared of each clay type, and additional 2-3 samples of autoclaved controls for each clay, and 3 blank controls for the experiment.

Samples were placed horizontally on a rocking table and incubated at 35°C. To monitor activity, gas composition of the serum bottle headspace was analyzed periodically. Gas analysis was performed on a Shimadzu GC-8AIT with Ar carrier gas, which allowed for simultaneous quantitative determination of H_2, O_2, N_2, and CO_2. GC conditions were as follows: Ar flow 0.4 kg/cm^2, detector and injection temperature 150°C, column temperature 35°C, 80 mA current, CTRI packed column. Calibrations of H_2, O_2, N_2, and CO_2 were completed prior to sampling bottles with known concentrations of gases. Samples were analyzed immediately after removing from the incubator and replaced in the incubator after

sampling. To sample, an alcohol saturated wipe was put on the serum stopper for 5 min to sterilize the surface of the stopper. A sterile 22-gauge needle connected to a gas tight syringe was then inserted into the stopper and 100 µL of headspace was removed and injected into the GC. A new needle was used for each bottle when sampled. With a headspace volume of 50 mL, and with each bottle sampled approximately 18 times over the incubation, this resulted in a 3.6 % loss of gas pressure over the entire incubation period.

At the conclusion of the experiment, bottles were either maintained at 35°C without shaking or destructively sampled to analyze pH, solids content, chemical analysis and microbial community.

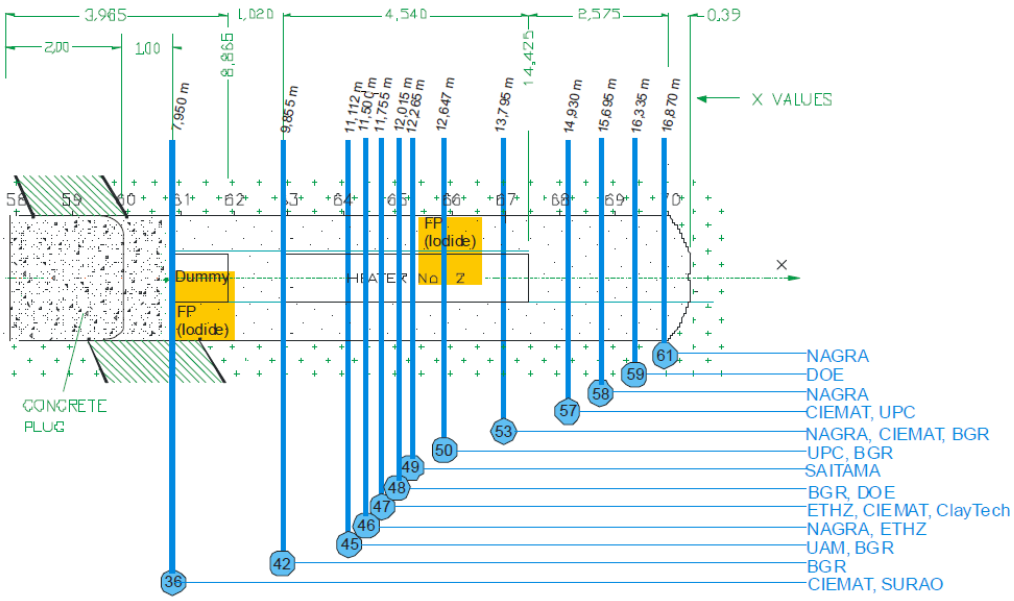

(a)

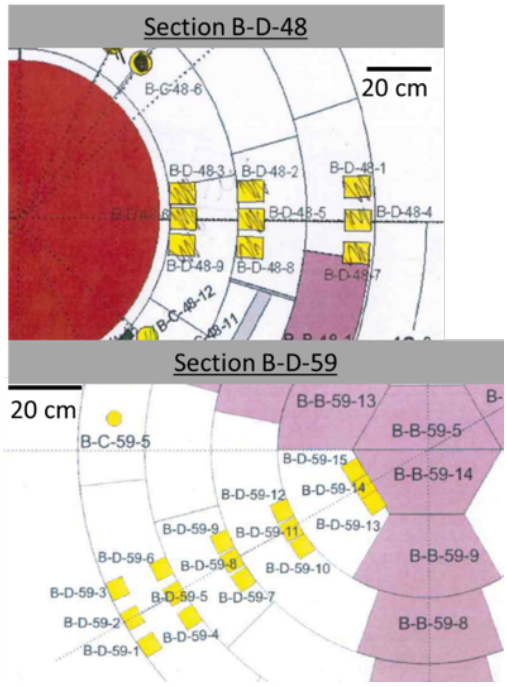

(b)

Figure 9-1 **Locations of bentonite samples in original FEBEX experiment: (a) Longitudinal cross-section along FEBEX tunnel, and (b) cross-sections B-D-48 and B-D-69 (modified from Villar et al., (2017))**

Table 9-1 Experimental descriptions

Experiment	FEBEX samples	Outcome	Average initial O_2	Average initial CO_2	Average initial H_2	Solid/liquid ratio (mg/mL)	Test duration (days)
1	48-6; 59-10	Stopped due to experimental difficulties	3-5.5%	1-3%	3-5%	na	60
2	48-6; 59-10	H_2 consumption in 59-10 samples, controls and 48-6 showed no activity	9.2%	5.9%	2.9%	TBD	379
3	48-6, 48-5, 48-4, 59-10	Low Activity observed, possibility to high solids content	10.6%	4.8%	2.2%	TBD	296
4a	48-6, 48-5, 48-4, 59-10	Low Activity observed	12.4%	5.4%	2.0%	46	120
4b	48-6, 48-5, 48-4, 59-10	O_2 consumption and CO_2 production in 59-10 and to a lesser extent 48-4 samples. No activity in controls or 48-5 and 48-6 samples.	8.6%	6.5%	2.7%	46	287

9.1.2 DNA extraction

Incubated samples were depressurized and de-crimped and the total sample (clay and media) were transferred to a sterile 15 mL tube and stored at -80°C until extraction. Total genomic DNA was collected in duplicates from each sample using the DNeasy PowerSoil kit (QIAGEN) following the manufacturer's instructions. The duplicate DNA extractions were combined prior to PCR amplification. The 16S rRNA gene was amplified for the identification of bacteria and archaea using 515F and 806R primers. The reverse PCR primer was modified to include Illumina Nextera adapters and 12-bp Golay barcodes. The PCR reactions were performed in triplicates in 25 µL reactions with the following reagents: Takara Ex Taq (0.025 units μL^{-1}), 1X Takara Ex Taq PCR buffer, Takara dNTPs mix (200 µM), Roche bovine serum albumin (0.56 mg mL^{-1}), PCR primer (200 nM) and approximately 10 ng uL^{-1} DNA template. 16S gene amplification was performed with the following thermocycler settings, 95 °C for 3 min, 25 cycles of 95 °C for 45 s, 50 °C for 60 s, and 72 °C for 90 s with a final extension of 10 min at 72 °C. The PCR product triplicates were composited and purified using Sera-Mag (Thermo Scientific) Solid-Phase Reversible Immobilization (SPRI) paramagnetic beads. Quantification of the purified PCR products was done using the Qubit hs-DS-DNA kit (Invitrogen) and pooled in equimolar concentrations (10ng/µL for 16S) and sequenced on a single lane for 300 bp (basepair) paired-end Illumina v3 MiSeq sequencing completed at the Vincent J. Coates Genomics Sequencing Laboratory at UC Berkeley.

9.1.3 Experiment 4 Porewater analysis

For Experiment 4 only, at the end of the incubation, the serum bottles were depressurized and opened, and the pH was measured immediately. The bottles were then mixed to suspend the solids and 0.5 mL of suspension was removed to quantify solid/liquid ratio. Porewater was then separated for geochemical analysis by centrifugation (at 8000x g for 15min) and porewater was filtered through a 0.45 µm PVDF

syringe filter. Porewater samples were analyzed for anions by ion chromatography (Thermo Scientific Dionex ICS-2100) and metals by ICP-MS (Perkin-Elmer Elan DRC II).

9.2 Results

Four experiments have been completed, as described in Table 9-1. Experiment 1 focused on working out experimental protocols. Experiment 2 consisted of the high heat samples (48-6) and the control, non-heated sample (59-10). Gas composition data for H_2, CO_2 and O_2 from Experiment 2 is shown in Figure 9-2 and Figure 9-3. These plots show the average of all replicates for each condition. On Day 150, the samples were re-gassed to the original gas composition due to low H_2 in the 59-10 samples, and again with the H_2 mix only for the 59-10 samples only on day 350, which lowered percent CO_2 content from 8% to 4%. Gas consumption was only observed in the 59-10 samples, and was not evident until Day 50, when loss of H_2 and O_2 was observed. Note that the rate of H_2 consumption in the replicates was not consistent, with a range of consumption rates observed (Figure 9-3). No significant loss of gas was seen in the controls and 48-6 sample. At the conclusion of the experiment, three samples from the 59-10 incubation bottles, two with high, and one with low H_2 consumption rates, and one sample from the 48-6 bottles (with no H_2 consumption) were sent for DNA microbial analysis. The results are shown in Figure 9-4 and Figure 9-5. The 48-6 sample had very low DNA extraction amounts, but results show a variety of species present. In contrast, the 59-10 samples show enrichment of a specific organisms which have the potential for hydrogen metabolism, including Actionbacerium, firmucutes, and Acidobaceria (Giguere, 2020; Greening, 2014; Piche-Choquette, 2019; Kalam, 2020). Because DNA extraction efficiencies are related to several factors, including the difficulty in extracting from clay, we cannot infer absolute bacterial abundance or determine if there was selective harm to a specific group of microorganisms during heating. However, it does appear that certain organisms existing on the clay can become active in the non-heated clay.

Based on these results, Experiment 3 was initiated, this time adding two intermediate heated samples, 48-5 and 48-4. After 157 days, little or no change in the gas composition was observed, whereas in the previous experiment consumption of H_2 was observed in the 59-10 sample after 50 days. These experiments contained a higher solid to liquid ratio than the previous experiment, which caused an increase in viscosity that limited the ability of the shaking tables to mix the slurry. It is suspected this was limiting activity, perhaps because of reduction in gas dissolution in the media due to poor mixing during incubation. An additional 5 mL of media was added at 157 days. This experiment ran for 296 days, and although some activity in the 59-10 and 48-4 samples was observed, there was also some changes in the sterile controls (Figure 9-6). Some contamination from the media addition was suspected so the experiment was restarted. Overall, the results of Experiment 3 were to emphasize the potential important role of solid to solution ratio in the rate of community development.

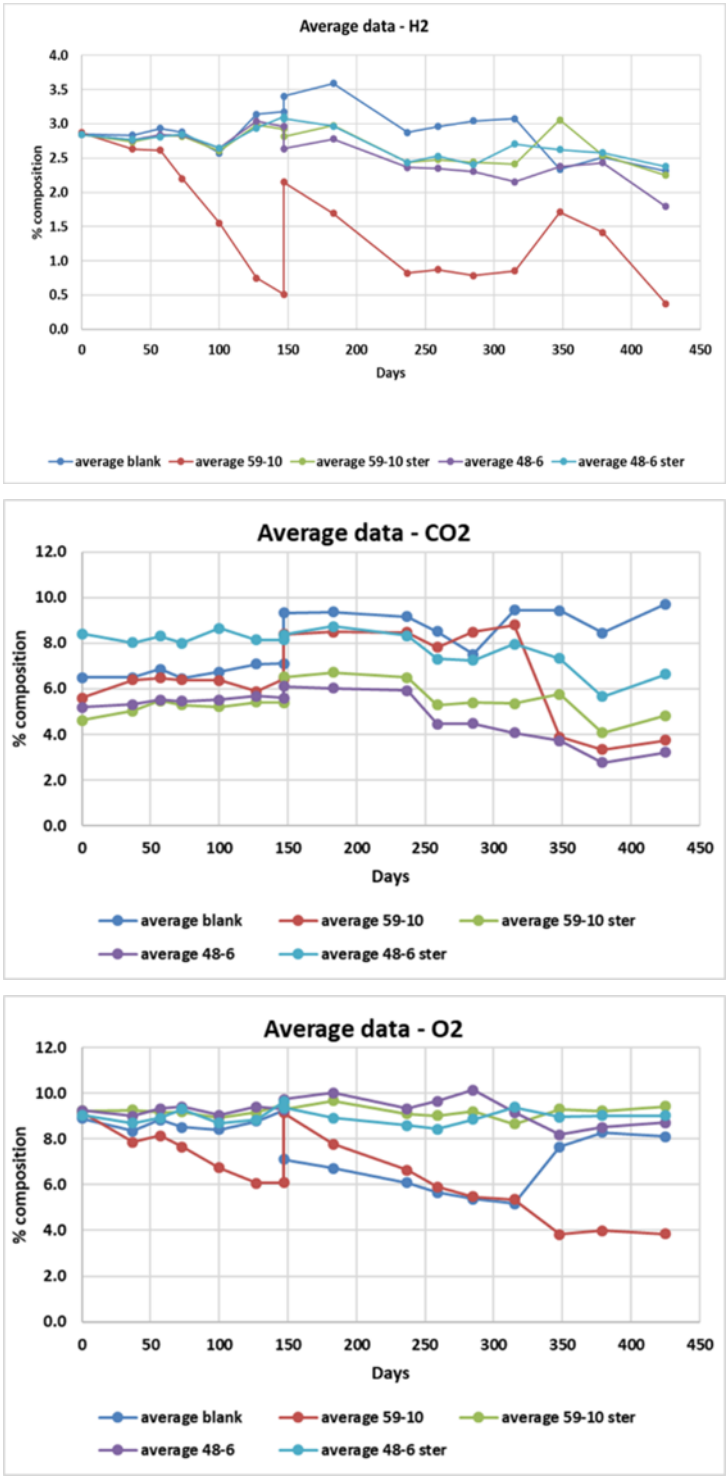

Figure 9-2 **Averages of H_2 CO_2, and O_2 concentrations in each condition for Experiment 2. For the 59-10 and 48-6 samples there are 6 replicates, for the sterile control there are 3 replicates, and there are 2 blanks. Spikes of H_2 concentration at day 150 and 350 are due to regassing of the headspace to replace depleted H_2.**

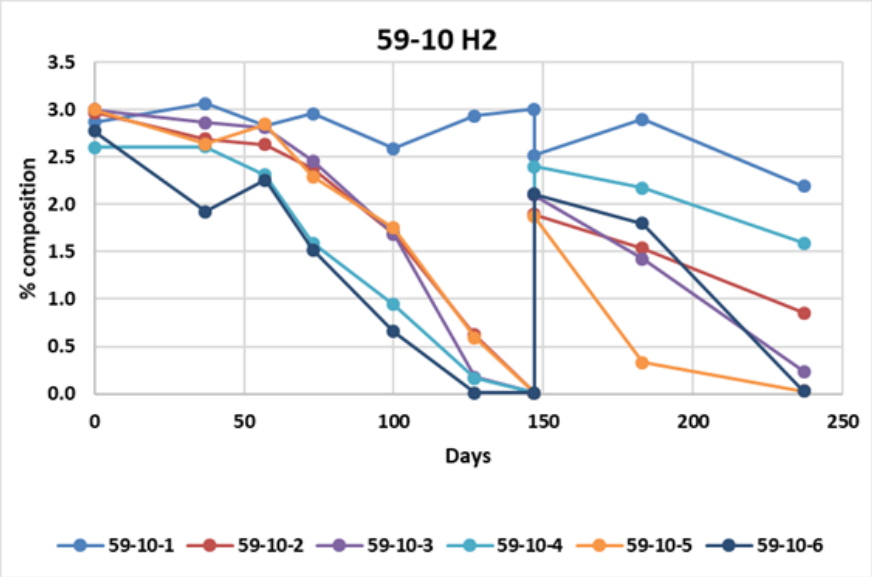

Figure 9-3 **Above are individual plots of the six 59-10 bottles for the first 237 days from Experiment 2. 59-10-1 is showing very little consumption of H_2, 59-10-2 and 59-10-4 are showing moderate activity and 59-10-3,5, and 6 are showing higher activity. Bottles 59-3, 4, and 5 were sacrificed for DNA sequencing**

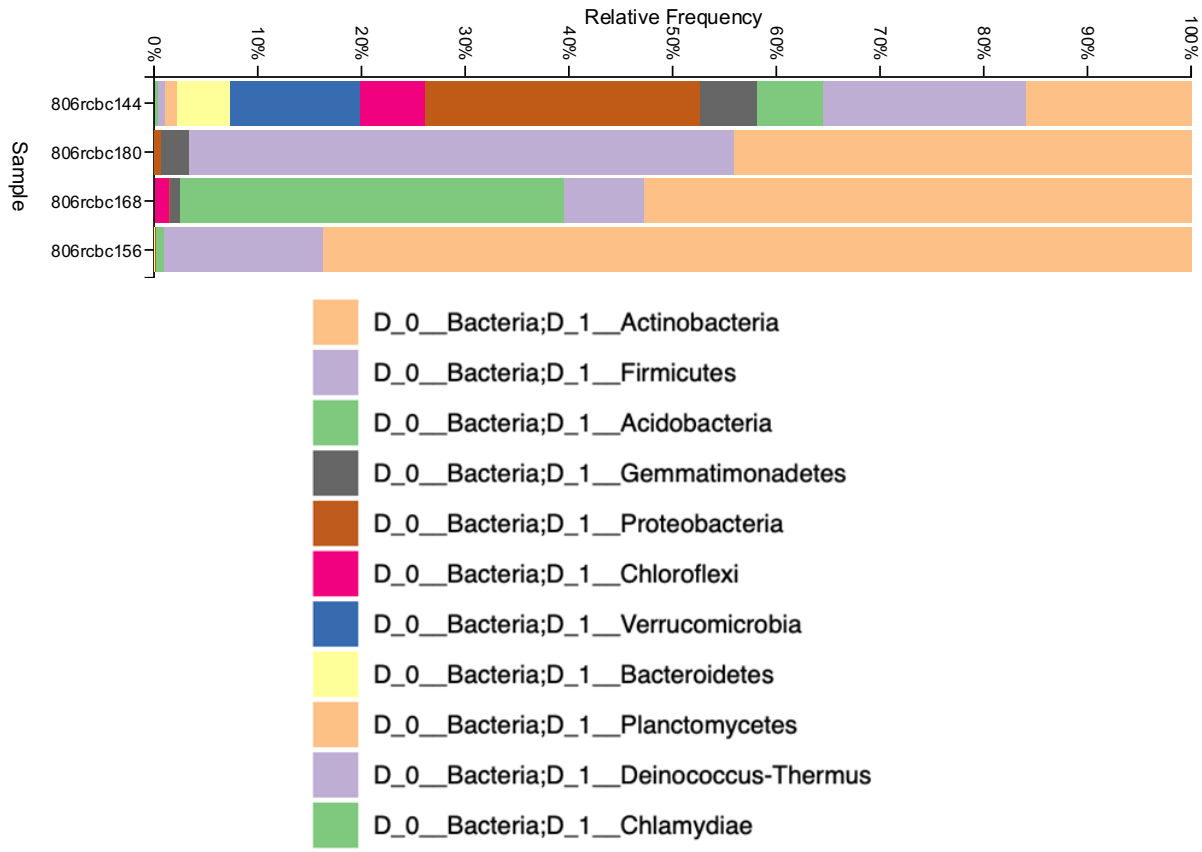

Figure 9-4 DNA sequencing results showing Taxonomy by Phylum. ID -144 is 48-6; IDs 180, 168,156 are 59-10 samples.

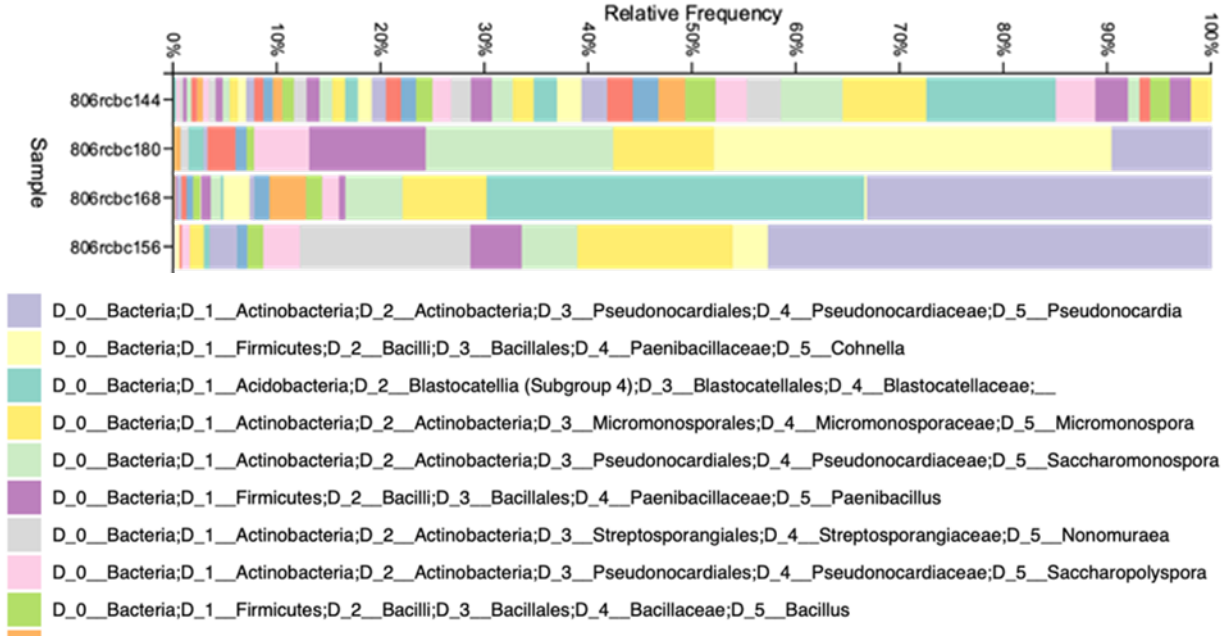

Figure 9-5 DNA sequencing results showing Taxonomy by species.

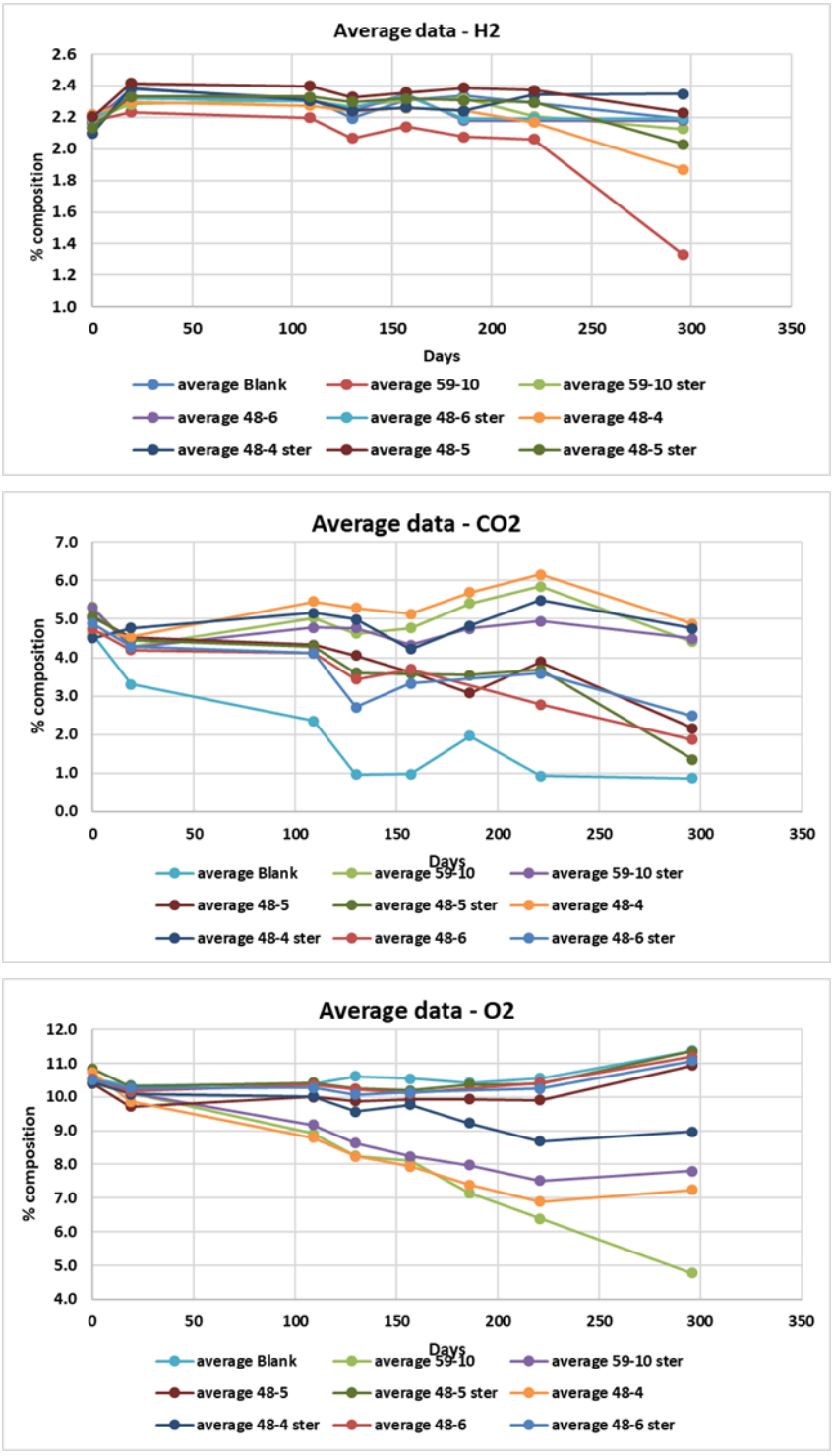

Figure 9-6 **Averages of H_2, O_2, and CO_2 concentrations in Experiment 3. H_2 is showing some depletion at the 300 day sampling, but activity was much slower to start in this experiment, possibly due to the high solids content in the bottles.**

Experiment 4 had the same sample set as Experiment 3, with the addition of ground water (GW) media (Table 9-2) in place of the Sigma MSM media to a set of 59-10 samples and to lower the solid to solution ratio. The GW media was based on pore water composition from compacted MX-80 clay (Bradbury and

Baeyens, 2003). For the first few sampling points, no activity was noted. It was noted that the oxygen levels were higher than in previous tests, so at 120 days the gas composition in the bottles were adjusted to lower the oxygen content. To accomplish this the bottles were completely depressurized and evacuated by pulling a vacuum on the system. The bottles were allowed then to equilibrate with air, follow by the addition of 7 mL of CO_2, and then pressurized to 15 psi with 5% H_2 in N_2. Shortly after this adjustment, an increase in consumption of oxygen in the 59-10 replicates and production of CO_2 were measured (Figure 9-7). Overall, activity was seen in all the 59-10 replicates, and moderate activity in the 48-4 and 59-10 GW replicates. The other samples, 48-5, 48-6, and the controls did not show changes in gas composition. Contrary to the 2nd experiment incubations, the gas consumption showed more consumption of oxygen and production of CO_2, and only two of the four 59-10 replicates demonstrated H_2 consumption, one much more than the other (Figure 9-7). This clearly indicates that the capacity for H_2 oxidation is retained in many of the FEBEX samples, with the possible exception of the hottest and direst samples. It also indicates that other metabolisms are also possible. The consumption of O_2 and increase in CO_2 are clear evidence for an active microbial community. At this point it is unclear what other metabolisms are, but it further supports the importance of considering the metabolic potential of barrier materials. One of the reasons that H_2 metabolism was less frequent within the individual samples as that the oxygen levels at setup may have played a role selecting for particular organisms, or simply that a different community developed in these sets of samples. Subsamples of some of the replicates have been sent for community analysis, but challenges due to low biomass have delayed the results.

Table 9-2 Groundwater media used for Experiment 4.

Compound	Molarity (mM)	Ion	Molarity (mM)
$NaHCO_3$	0.798	Na	243
Na_2SO_4	104	C	0.881
NaCl	34.2	SO_4	104
KCl	1.23	Cl	68.3
$CaCl_2*2H_2O$	9.35	K	1.23
$MgCl_2*6H_2O$	7.06	Ca	9.46
CaF_2	0.109	Mg	7.06
$SrCl_2$	0.0831	F	0.218
Si	0.183	Si	0.183
		Sr	0.0831

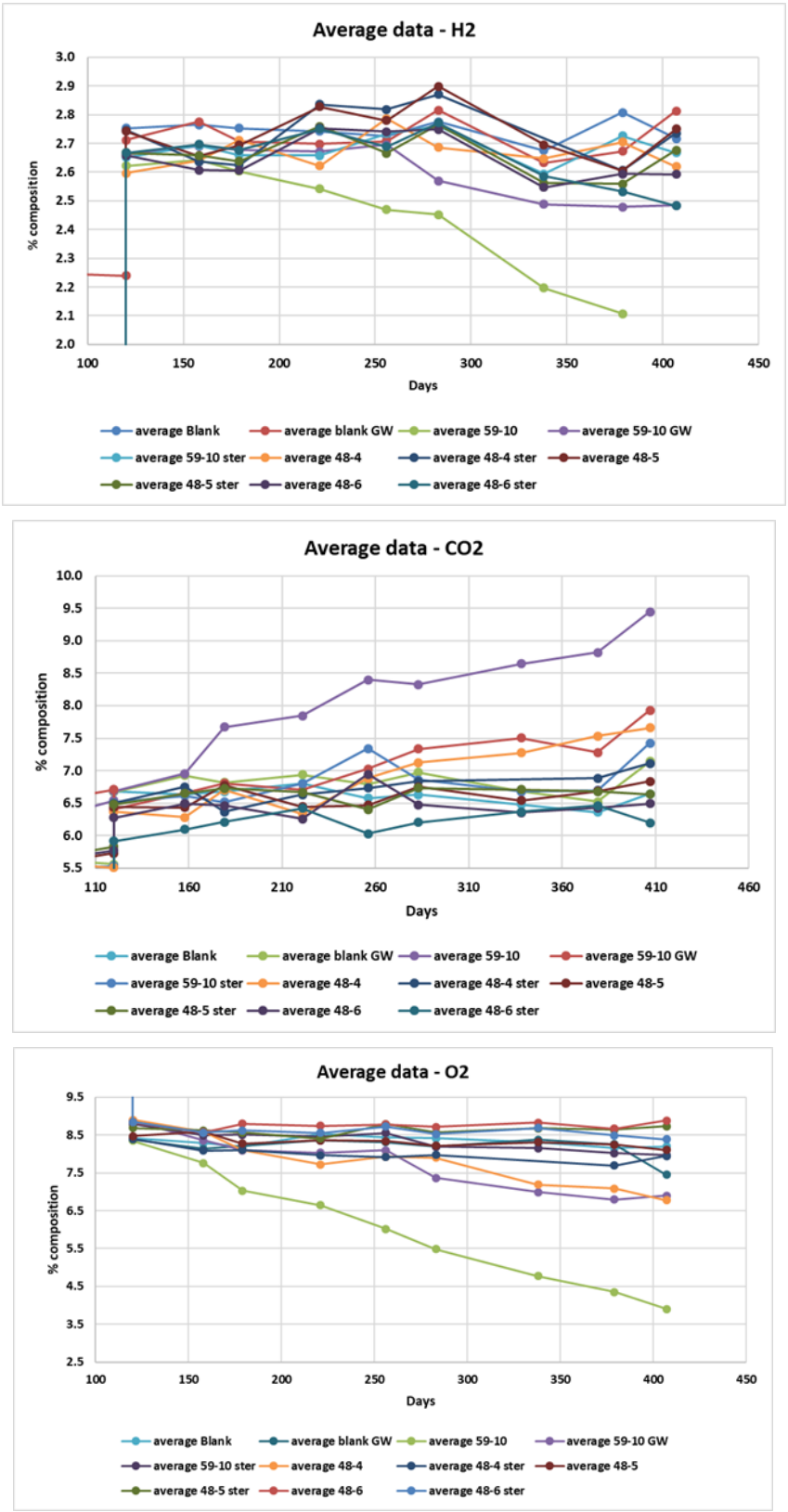

Figure 9-7 Averages of H_2, O_2, and CO_2 concentrations in Experiment 4.

The results of initial geochemical measurements of Experiment 4 samples are shown in Table 9-3 to Table 9-5. The variation in pH between the samples was small (Table 9-3), the only notable difference was between the media (average pH 6.62) and the GW sample (average pH 6.45). There was no significant difference between the samples (pH 6.60) and sterile controls (pH 6.63). There was some variability in the solids (Table 9-3) content, but no correlation of solids content was seen with CO_2, O_2, or H_2 composition (R^2 = 0.062, 0.072, 0.024, respectively).

Table 9-3 pH and solids content for Experiment 4. (GW = artificial groundwater, ster = sterilized sample).

	pH	dry sample (g/mL)
B1	6.75	0.004
B2	6.73	0.004
B3	6.76	0.004
B1GW	6.45	0.009
B2 GW	6.45	0.010
59-10-1	6.64	0.056
59-10-2	6.61	0.039
59-10-3	6.45	--
59-10-4	6.56	0.037
59-10-1 gw	6.37	0.050
59-10-2 gw	6.35	0.077
59-10-3 gw	6.75	0.053
59-10-4 gw	6.35	0.068
59-10-1 ster	6.70	0.030
59-10-2 ster	6.56	0.043
48-4-1	6.71	0.057
48-4-2	6.57	0.050
48-4-3	6.52	0.090
48-4-4	6.62	0.048
48-4-1 ster	6.62	0.032
48-4-2 ster	6.63	0.034
48-5-1	6.69	0.042
48-5-2	6.62	0.027
48-5-3	6.58	0.051
48-5-4	6.61	0.042
48-5-1 ster	6.65	0.038
48-5-2 ster	6.56	0.037
48-6-1	6.64	0.054
48-6-2	6.56	0.053
48-6-3	6.58	0.033
48-6-4	6.52	0.055
48-6-1 ster	6.65	0.020
48-6-2 ster	6.68	0.021

Cation analyses for Li, Be, Al, Fe, Se (as SeO), Co, Mo, Ag, Cd, Sn, Sb, Ca, Eu, Pb, Th, and U were below detection limits. Cations that were detected in the porewater are shown in Table 9-4, and the major anions in Table 9-5. There are differences in the cation and anion content in the GW samples, notably higher sulfate, Na, and Cl. Some of the cations were affected by the solids content, as can be seen in the differences between the blanks and the samples due to the influence of the clay. The blank samples have higher Na, P, K, B and the clay samples have higher Ca. No nitrate was added with the media or groundwater and no significant amounts are seen in the porewater.

Table 9-4 Cation data for Experiment 4. BDL = below detection limit. GW = artificial groundwater, ster = sterilized sample.

	Na	P	K	Si	Ca	B	Ti	Mg	V	Cr	Mn	Ni	Cu	Zn	Rb	Sr	Ba	AsO
B1	109.26	53.82	21.95	0.97	0.02	0.25	0.11	0.02	BDL	BDL	BDL	BDL	1.23E-03	BDL	1.16E-04	9.64E-05	7.55E-04	BDL
B2	110.38	57.23	22.22	0.97	0.05	0.29	0.11	0.02	BDL	BDL	6.94E-04	BDL	6.67E-04	BDL	1.14E-04	2.82E-04	9.53E-04	BDL
B3	153.76	77.68	30.97	1.00	0.02	0.29	0.15	0.02	BDL	1.89E-04	7.21E-05	BDL	9.65E-04	BDL	1.43E-04	1.25E-04	8.79E-04	BDL
B1GW	273.53	34.47	15.36	1.12	0.83	0.29	0.06	5.44	BDL	BDL	2.29E-04	BDL	1.83E-03	1.15E-03	9.86E-05	3.64E-02	1.11E-03	BDL
B2 GW	288.53	52.73	22.31	1.30	0.13	0.38	0.10	3.70	BDL	BDL	BDL	BDL	2.55E-03	1.04E-03	1.18E-04	1.06E-03	4.56E-04	BDL
59-10-1	82.84	30.27	4.54	0.56	0.30	0.13	0.07	2.55	2.73E-04	BDL	4.14E-03	BDL	7.16E-04	BDL	2.89E-04	9.01E-03	BDL	2.78E-03
59-10-2	78.86	27.87	4.79	0.57	0.29	0.12	0.06	2.55	2.77E-04	1.80E-04	4.01E-03	BDL	7.32E-04	BDL	2.82E-04	8.55E-03	BDL	2.99E-03
59-10-3	82.13	28.98	4.62	1.06	0.22	0.14	0.06	2.63	4.67E-04	3.53E-04	4.27E-03	BDL	7.26E-04	BDL	3.33E-04	1.12E-02	2.56E-04	3.83E-03
59-10-4	123.35	49.95	11.26	1.17	0.28	0.12	0.11	2.32	6.68E-04	BDL	4.59E-03	BDL	1.02E-03	BDL	5.57E-04	1.32E-02	BDL	2.40E-03
59-10-1 gw	220.03	16.98	6.05	0.92	1.42	0.14	0.03	11.80	2.54E-04	1.05E-04	2.01E-02	BDL	1.76E-03	1.54E-03	7.29E-04	6.72E-02	4.70E-04	2.32E-03
59-10-2 gw	237.13	24.17	8.18	1.15	0.99	0.13	0.04	8.59	3.00E-04	BDL	9.00E-03	BDL	1.80E-03	3.30E-03	7.20E-04	5.59E-02	7.23E-04	3.50E-03
59-10-3 gw	243.45	27.89	9.61	0.74	0.94	0.09	0.05	6.37	1.78E-04	BDL	9.27E-03	3.05E-04	1.97E-03	1.15E-03	6.55E-04	4.40E-02	1.66E-04	2.80E-03
59-10-4 gw	238.61	24.10	8.51	1.14	0.96	0.11	0.04	8.07	3.19E-04	BDL	9.35E-03	BDL	1.80E-03	1.90E-03	7.61E-04	5.46E-02	5.12E-04	3.77E-03
59-10-1 ster	98.04	41.64	11.40	1.16	0.24	0.15	0.10	2.10	5.30E-04	1.47E-03	3.27E-03	BDL	9.96E-04	1.38E-03	4.51E-04	1.04E-02	2.67E-04	1.18E-03
59-10-2 ster	82.75	30.32	5.38	1.21	0.24	0.12	0.07	2.41	5.75E-04	BDL	2.87E-03	BDL	7.10E-04	BDL	3.39E-04	1.07E-02	1.86E-04	2.73E-03
48-4-1	85.94	32.96	5.02	0.72	0.30	0.11	0.07	2.96	3.65E-04	2.19E-04	7.88E-03	BDL	7.16E-04	1.62E-03	4.07E-04	9.11E-03	1.59E-04	2.93E-03
48-4-2	90.33	36.16	5.73	1.33	0.23	0.12	0.08	3.05	6.14E-04	2.01E-04	9.94E-03	BDL	7.32E-04	BDL	6.30E-04	1.17E-02	3.60E-04	3.44E-03
48-4-3	83.34	31.46	4.63	1.24	0.23	0.10	0.07	2.66	4.78E-04	BDL	9.50E-03	BDL	5.75E-03	2.63E-03	4.98E-04	1.12E-02	3.07E-04	5.01E-03
48-4-4	97.23	40.41	7.06	1.33	0.26	0.11	0.09	3.14	5.65E-04	BDL	7.83E-03	5.67E-04	7.98E-04	BDL	6.01E-04	1.21E-02	3.12E-04	2.59E-03
48-4-1 ster	93.13	37.70	7.14	1.35	0.25	0.10	0.09	3.25	6.97E-04	2.38E-04	8.60E-03	BDL	7.29E-04	BDL	4.08E-04	1.04E-02	2.15E-04	2.09E-03
48-4-2 ster	98.17	42.07	8.06	1.38	0.21	0.11	0.09	3.33	6.27E-04	BDL	8.69E-03	BDL	7.99E-04	BDL	4.33E-04	1.10E-02	1.83E-04	2.13E-03
48-5-1	85.22	34.11	4.74	0.58	0.26	0.11	0.07	2.55	3.27E-04	1.06E-04	3.76E-03	BDL	6.69E-04	BDL	2.96E-04	8.11E-03	BDL	2.47E-03
48-5-2	93.39	39.42	6.52	1.23	0.23	0.10	0.08	2.39	6.38E-04	1.48E-03	3.14E-03	BDL	7.24E-04	BDL	4.08E-04	1.05E-02	1.77E-04	2.50E-03
48-5-3	89.95	36.30	5.99	1.28	0.25	0.12	0.08	2.50	5.57E-04	BDL	3.32E-03	BDL	7.05E-04	BDL	3.87E-04	1.05E-02	2.34E-04	2.60E-03
48-5-4	91.30	36.37	5.71	1.29	0.24	0.12	0.08	3.42	6.00E-04	BDL	8.47E-03	BDL	1.43E-03	2.83E-03	4.05E-04	1.15E-02	3.19E-04	2.68E-03
48-5-1 ster	87.31	34.33	6.46	1.22	0.26	0.13	0.07	2.36	6.09E-04	BDL	2.47E-03	BDL	7.09E-04	BDL	3.75E-04	9.08E-03	2.58E-04	2.04E-03
48-5-2 ster	84.94	32.86	4.91	1.27	0.26	0.12	0.07	2.85	6.20E-04	3.02E-04	5.52E-03	BDL	7.40E-04	BDL	3.45E-04	1.13E-02	1.86E-04	3.59E-03
48-6-1	89.36	32.28	4.60	0.87	0.29	0.10	0.07	2.67	3.16E-04	1.15E-04	3.52E-03	BDL	6.26E-04	BDL	3.04E-04	7.98E-03	BDL	2.39E-03
48-6-2	90.90	33.87	5.36	1.41	0.28	0.12	0.07	2.57	4.82E-04	BDL	3.52E-03	BDL	6.26E-04	1.75E-03	3.83E-04	9.50E-03	1.26E-04	2.25E-03
48-6-3	102.02	41.94	7.92	1.37	0.25	0.09	0.08	2.22	5.49E-04	BDL	2.79E-03	BDL	6.97E-04	BDL	4.47E-04	9.63E-03	BDL	1.64E-03
48-6-4	90.24	31.41	4.95	1.33	0.29	0.12	0.07	2.54	5.03E-04	BDL	3.79E-03	BDL	7.19E-04	BDL	4.00E-04	9.46E-03	2.27E-04	3.35E-03
48-6-1 ster	103.35	44.66	11.03	1.33	0.26	0.12	0.09	2.39	6.67E-04	1.29E-04	3.24E-03	BDL	7.00E-04	BDL	4.75E-04	1.07E-02	1.53E-04	1.29E-03
48-6-2 ster	104.06	45.94	12.11	1.32	0.27	0.09	0.10	2.09	5.72E-04	2.49E-04	2.53E-03	BDL	8.22E-04	BDL	5.01E-04	8.31E-03	1.46E-04	1.08E-03

Table 9-5 Anion data for Experiment 4. BDL = below detection limit

	Cl (mM)	SO4 (mM)	NO3 (mM)	PO4 (mM)
B1	35.01	BDL	BDL	230.11
B2	35.91	BDL	BDL	235.83
B3	49.80	BDL	BDL	327.82
B1GW	84.63	87.13	BDL	112.71
B2 GW	91.54	81.75	BDL	185.09
59-10-1	40.69	0.83	BDL	125.26
59-10-2	39.17	0.83	BDL	116.81
59-10-3	42.32	1.09	BDL	123.25
59-10-4	58.53	0.61	BDL	227.99
59-10-1 gw	#N/A	#N/A	#N/A	#N/A
59-10-2 gw	97.56	85.29	BDL	64.48
59-10-3 gw	98.98	84.35	BDL	79.82
59-10-4 gw	98.74	84.77	BDL	63.69
59-10-1 ster	38.69	0.55	BDL	186.89
59-10-2 ster	38.31	0.81	BDL	129.78
48-4-1	37.87	0.12	BDL	138.94
48-4-2	35.57	0.12	BDL	154.47
48-4-3	37.51	0.16	0.15	132.01
48-4-4	37.87	0.10	BDL	174.41
48-4-1 ster	36.14	0.08	BDL	169.60
48-4-2 ster	37.07	0.07	BDL	111.30
48-5-1	36.35	0.51	BDL	139.50
48-5-2	37.61	0.47	BDL	159.98
48-5-3	36.13	0.46	BDL	103.24
48-5-4	40.43	0.56	BDL	153.63
48-5-1 ster	34.36	0.61	BDL	142.27
48-5-2 ster	35.87	0.96	BDL	137.19
48-6-1	42.66	0.77	BDL	127.21
48-6-2	43.51	0.72	0.12	134.26
48-6-3	42.46	0.40	BDL	171.74
48-6-4	44.86	0.76	BDL	127.38
48-6-1 ster	37.49	0.47	BDL	187.02
48-6-2 ster	37.23	0.37	BDL	193.58

Table 9-6 ID and sample names for DNA sequencing

ID	Clay	H2 cons. level	Growth	Sample name
806rcbc144	48	low	No	48-6-1
806rcbc180	59	high	Yes	59-10-5
806rcbc168	59	medium	Yes	59-10-4
806rcbc156	59	high	Yes	59-10-3

9.3 Conclusions

The results from these experiments indicate that clay materials maintain microbial communities with potential for microbial growth. However, it is interesting that the material from the hot zone did not show that potential for the time scales in these experiments. Whether this is due to the heating or the drying or both is unknown at this point. Furthermore, the specific communities that develop appear sensitive to the gas composition and solids content. Because no growth was observed in the control sample this observed enrichment of communities is derived from bacteria existing in the clay prior to the start of incubation. While long by laboratory standards, these experiments are clearly extremely short by the time scales of repository dynamics. At that time scale it is clear that microbial activity within the barrier material is likely to be significant. Given the limitations in moisture and other chemical species, it is reasonable to assume that this microbial activity is most likely to be concentrated along fractures and at the formation boundaries. This tendency is emphasized by the impact that high solid to solution ratio appear to have on microbial activity in our Experiment 2. It is also emphasized by the fact that the only samples to not show some significant microbial activity in our experiments were those closest to the heaters. Lastly, the impact on the groundwater media samples as compared to the minimal salt media and the non-H_2 metabolisms observed in many of the samples indicate that a clear understanding of the composition of the fluids within the formation will be important in predicting what metabolic processes are likely to dominate. To our knowledge this is the only experimental work to demonstrate the activity of the microbial communities from FEBEX materials under minimal media conditions, as opposed to growth media and also to show the presence of H_2 metabolism. Further work should focus on the variety of metabolisms possible from the inoculate community present within the barrier material and how specific chemical and physical conditions control its rate of growth.

10. Heating and Hydration Column Test on Bentonite

10.1 Introduction

This Chapter of the report details of laboratory-scale experimental results in support of the HotBENT field-scale experiment, which is designed to study THMC behavior during long-term heating of clay to 200°C. This effort is built upon previous efforts of long-term laboratory-scale clay heating experiments conducted at lower temperatures (Fernandez & Villar, 2010; Gomez-Espina, 2010; Villar et al., 2008). This benchtop-scale laboratory experiment, HotBENT-Lab, provides a laboratory analog of the HotBENT field experiment to obtain a comprehensive set of characterization data and monitoring measurements, which are difficult to conduct at the field scale. The primary goal of this laboratory experiment is to obtain well-characterized datasets to (1) improve understanding of bentonite THMC processes under heating and hydration for model parameterization and benchmarking, (2) compare the HotBENT-Lab data with HotBENT field-scale test results, and (3) develop a prototype of an experimentation platform for future studies of bentonite under conditions of high temperature.

In support of this effort, and as described in the FY18-20 reports, the HotBENT-Lab experiment a cylindrical pressure column was constructed to reproduce realistic heating and hydration conditions of the field-scale experiment. The design of the experimental apparatus and monitoring tools are based on estimated ranges of temperature and pressure, ability to accommodate characterization methods (i.e., X-ray computed tomography (CT) and ERT) and safety. In order to better separate the effects of heating and hydration, two identical test columns are used, with the control column undergoing only hydration, and the experiment column experiencing both heating and hydration. Since June 2019, the column tests have run for over 1.5 years and both columns were dismantled with bentonite samples collected in December 2020.

10.2 HotBENT-Lab Design

10.2.1 Column Design

A schematic diagram of the column design is shown in Figure 10-1and was described in detail in the FY18-20 progress reports. To review, clay was packed in an Aluminum 7071 pressure column designed to withstand a maximum working pressure of 1000 psi (~6.9 MPa) at 200 °C. The inner diameter (ID) of the column is 6.5 inches, an outer diameter (OD) is 7.5 inches, and a height is 18 inches. A cartridge heater of 12-inch-long and 0.25-inch OD is housed in a titanium shaft of 3/8 inch OD penetrating through the center of the column. Using MX-80 bentonite (Cetco), we packed two columns at an initial gravimetric water content of 15%, and a bulk dry and wet density of ~1.2 and 1.5 g/cm3. A 0.25-inch thick layer of sand pack (12/20 mesh grain size) was installed between the clay column and the column wall as a high-permeability boundary. Hydration was achieved by flowing a synthetic brine (Table 10-1) continuously through the sand layer via a flow port at each of the end caps (Figure 10-2) via a syringe pump (ISCO pumps, 500 ml capacity).

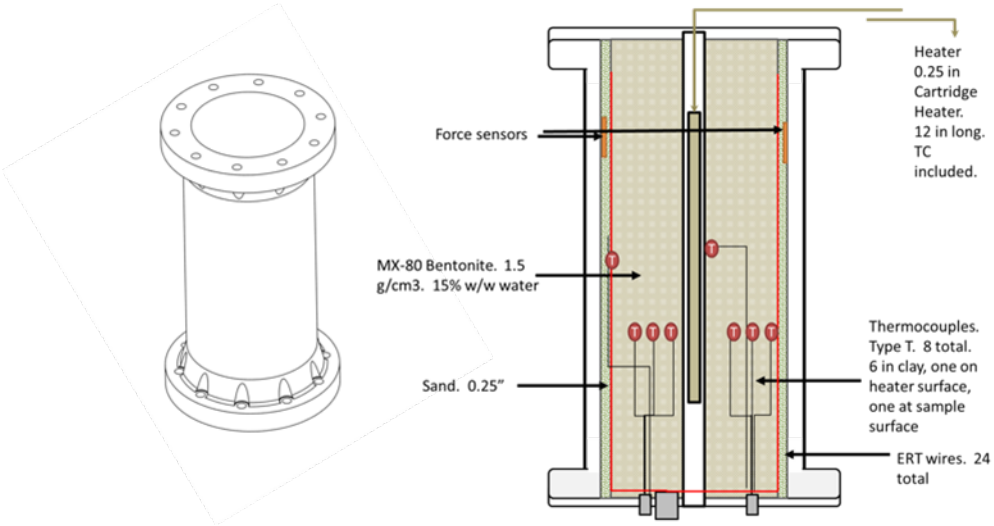

Figure 10-1 **Schematic diagram of the column design for HotBENT-Lab experiment. Left: 3D rendering of the column exterior; right: interior design of the bentonite column, showing locations of sensors and the heater. The 1.5 g/cm^3 in the figure represents the bulk wet density of packed clay.**

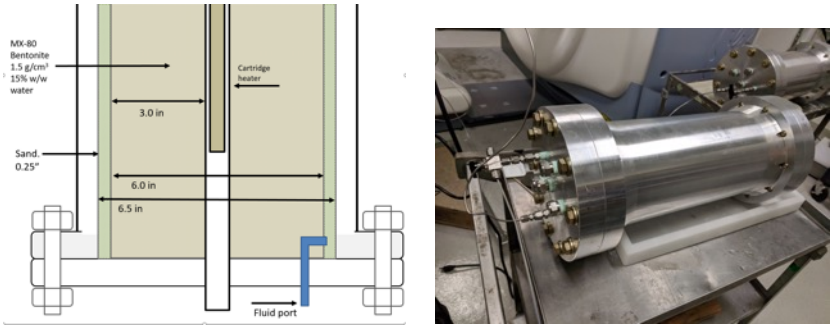

Figure 10-2 **Schematic diagram showing the geometry of the different components of the test column (left) and an image of the completed column (right)**

Table 10-1 Chemical composition of the artificial groundwater used to saturate the column (from Bradbury and Baeyens, 2003)

Compound	Molarity (mM)	Ion	Molarity (mM)
$NaHCO_3$	0.798	Na	243
Na_2SO_4	104	C	0.881
NaCl	34.2	SO_4	104
KCl	1.23	Cl	68.3
$CaCl_2*2H_2O$	9.35	K	1.23
$MgCl_2*6H_2O$	7.06	Ca	9.46
CaF_2	0.109	Mg	7.06
$SrCl_2$	0.0831	F	0.218
Si	0.183	Si	0.183
		Sr	0.0831

10.2.2 Characterization and Monitoring

To characterize the sample during the heating process, the following techniques were employed:

10.2.2.1 X-Ray CT-imaging

X-ray CT images were collected to provide a 3D visualization of the density distribution in the column, which can be used to visualize density changes due to water saturation, clay swelling or structural deformation during the experiments. A GE Lightspeed 16 medical CT scanner was used to scan the experimental columns periodically throughout the experiment. Based on the column dimensions, the spatial resolution of the CT images is 400 × 400 × 625 μm. Because of the large weight of the experimental columns (~55 lbs), a cart/lift is used to move the columns onto and off the CT scanner table. Alignment of the scans is achieved via markings on the CT table and on the outside of the column, as well as key features in the CT images (high and low-density anomalies) inside the column during post processing. The post processing and analysis of the obtained CT scan images are conducted using self-developed codes in ImageJ software (Schneider et al., 2012).

10.2.2.2 Continuous temperature monitoring

Temperature monitoring was conducted using thermocouples (type T) installed in the column. A total of 8 thermocouples were installed in each column between the heater shaft and the column wall. The distances of other thermocouples from the heater shaft were 0 (on the heater), 0.5, 1, 1.5 2, 2.5, 3, and 3.5 inches (the latter was on inside of the column wall). These feedthrough-coupled thermocouples, with an accuracy of 0.1°C, were acquired from Conax Technologies. The temperature readings from the thermocouples were recorded at 30s intervals with a data logger (Keithley 2701) throughout the experiment. In addition to the thermocouples inside the columns, additional temperature measurements were taken on the outside wall of the column.

10.2.2.3 Time lapse electrical resistivity tomography (ERT) monitoring

The ERT data acquisition is conducted using a DAS-1 ERT system (Multi-phase Technologies), combining electrodes used to send electrical current or measure electrical potential. Measurements were conducted using a pre-defined monitoring schedule (Figure 10-3). A total of ~2600 data points were collected for a single resistivity survey in each column, which takes ~ 40 minutes. The voltage used for ERT data acquisition was targeted at < 50 V, but it varied depending on the resistivity of the tested clay

and its hydration status during the experiment. Both the heated and unheated columns were configured to allow for sequential data collection during the same data acquisition event. Tri-hourly data collection is designed for the initial stage of the experiment, and this frequency was adjusted based on the observed rate of changes during the experiment and was reduced for the long-term experiment. Data collection was autonomously carried out via a control software. Analysis of the post-experiment collected datasets included data quality assessment, inversion and visualization. The open software BERT (boundless ERT, Günther & Rücker, 2012) and Paraview (Kitware, NY) were used for data inversion and visualization.

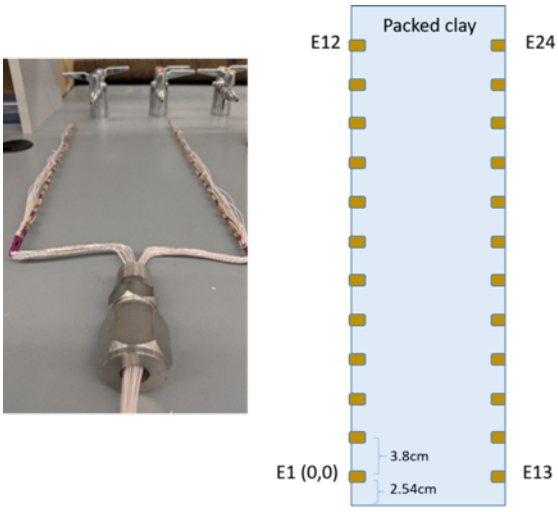

Figure 10-3 ERT monitoring design and a geometric layout of the column

10.2.2.4 Influent and effluent fluid geochemical analysis

The fluid (Table 10-1) used to hydrate the bentonite was sampled and analyzed to monitor geochemical changes in the bentonite system. Changes in water chemistry are being used to understand the geochemical processes in the column due to evaporation, dilution, diffusion and other transformations. Samples collected from the experiments were filtered, acidified, when necessary, prepared and analyzed using the standard Ion Chromatography (IC) and Inductively Coupled Plasmas – Mass Spectrometry (ICP-MS) protocols.

10.2.2.5 Pre- and post- experiment clay analysis following a gradient from the heater

Preliminary measurements have been made on the pre-experiment clay and more extensive tests are planned when the experiment is dismantled. The post-experiment clay analysis data will be compared with those from the pre-experiment clay samples to understand changes in physical, chemical and hydrological characteristics of bentonite due to hydration and heating, including gravimetric water content analysis and mineralogical analysis with X-ray Diffractometry (XRD).

10.2.2.6 Lab petrophysical studies

In addition to the heating and hydration experiments conducted in the pressure column, parallel experiments with non-pressurized and smaller columns were set up for petrophysical model studies. The main goal of such studies is to determine petrophysical correlations that can be used to link indirect geophysical measurements to parameters of interests. For instance, resistivity-moisture content correlations can be determined from the results of such studies, so the electrical resistivity map acquired from the pressure columns can be translated into a moisture distribution map. Such studies can also be

used to acquire water content-density calibration datasets for CT images as well as for porosity-permeability correlation studies.

10.3 Experimental Operation

Packing and startup of the system occurred in June 2019, and hydration and heating have been continuous since inception. Two columns have been continuously operated, a heated and unheated column. After the baseline scan and testing other components, hydration and heating were started. A schematic diagram of the experimental setup with the column and supporting components is shown in Figure 10-4.

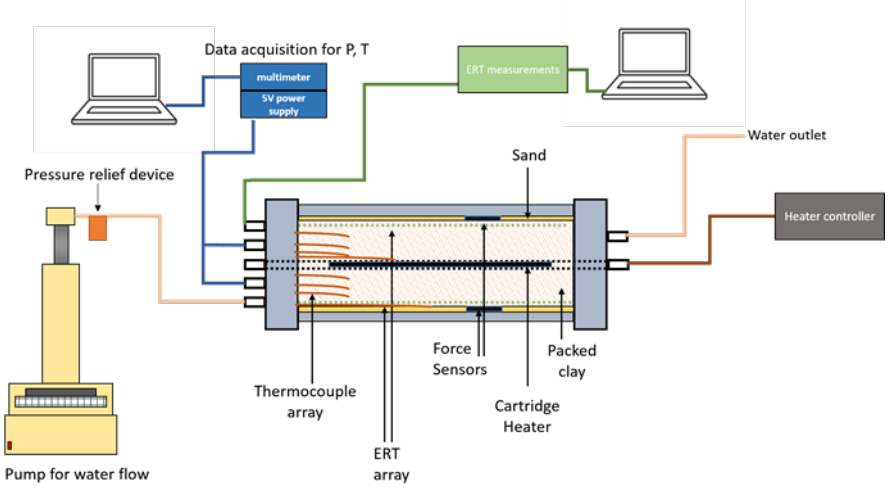

Figure 10-4 Schematic diagram of the entire experimental setup including the column, flow control, and sensors. The inner diameter (ID) of the column is 6.5 inches, an outer diameter (OD) is 7.5 inches, and a height is 18 inches.

10.4 Monitoring Results

10.4.1 X-ray CT

10.4.1.1 Baseline CT

The baseline CT image provides information on the clay and sand packing, and the layout the column sensors. The cross-sectional CT images of the Column 1 (C1), which was used for the heating and a hydration experiment, is shown in Figure 10-5. The color scale in the images is CT numbers that are proportional to the bulk density. In general, the higher numbers (i.e., brighter color) represent higher density. As shown on the image, the bright yellow color on the column perimeter represents the Al pressure column. The white shining spots are either the copper electrodes, the copper wires connecting the electrodes, or the metal in the pressure sensors. Blue color represents low-density features, which include the interior open space of the heater shaft, penetrating through the middle of the bentonite column, and some lower density features created during packing. The brownish color between the column and the clay pack represents the sand layer packed into the column with the purpose to evenly saturate the bentonite. Visible strikes running horizontally across the column are resulting from the dry packing process. Overall, the density variability as the artifact of packing is generally very small. We selected a representative 2D image (marked by the yellow dotted line in Figure 10-5) to discuss the clay hydration subject to heating in Section 10.4.2c.

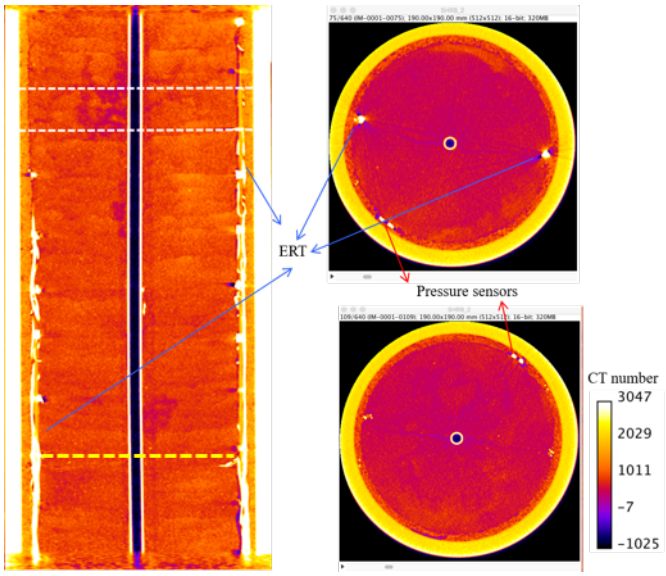

Figure 10-5 Cross sectional CT images of Column 1 that is used for a heating and hydration experiment. The two circular cross sections are from locations marked with the dashed lines on the vertical cross section image on the left. The yellow dashed line indicates locations of the 2-D image selected in Figure 10-6.

The cross-sectional CT images of Column 2 (C2), which was subject to hydration only, are shown in Figure 10-6, which show similar density features in this column, but some visible variances can be observed as well. Noticeably, some local low-density features on the top of the column are visible resulting from uneven packing. In addition, a seemingly slightly larger lateral heterogeneity exists, which is also related to packing. In Section 10.4.2b, we will discuss two representative 2D images (marked by the yellow dotted line in Figure 10-6) of the clay that was subject to hydration only.

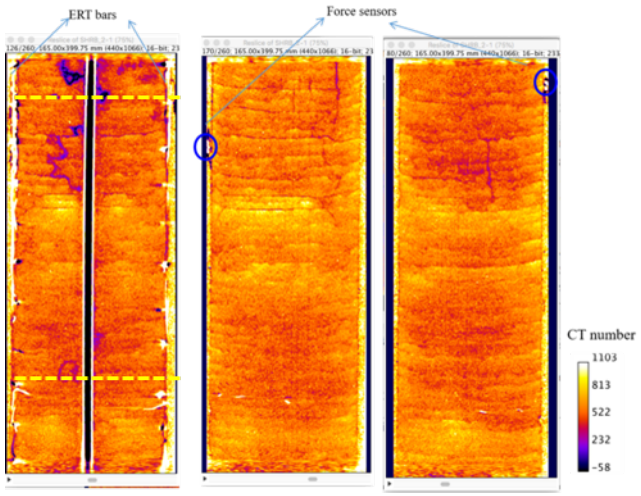

Figure 10-6 Cross sectional CT images of Column 2 that are used for hydration only experiment as the control. The three different cross sections represent different slices at different depths in the axis-normal direction. The two yellow dotted lines indicate locations of the two 2D image selected for the time series presentation in Figure 10-5.

A 3D rendering of C1 is shown in Figure 10-7, and a similar image for C2 is shown in Figure 10-8, with marked key features.

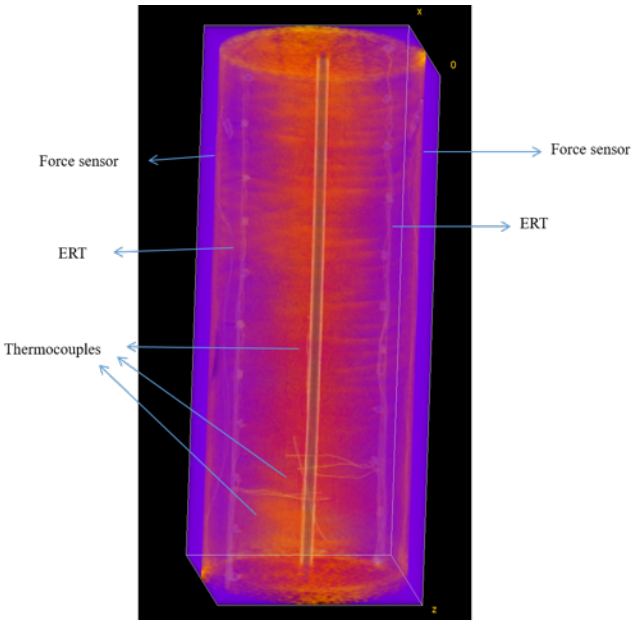

Figure 10-7 3D CT image of C1 with key instrumentation—thermocouples, ERT and force sensors, and sensor wires.

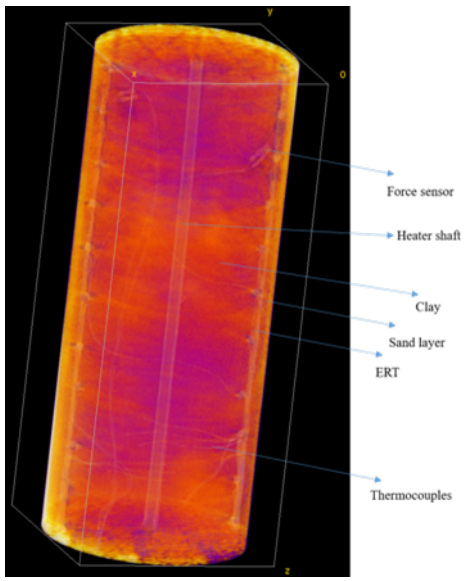

Figure 10-8 3D CT image of C2 with key features indicated.

Overall, the CT images provide well-defined visualization of the column density structure. This can be used to determine precise locations of the sensors and boundaries in the sample column, which are needed for interpreting and modeling the behavior of the system as experimental data are being collected. Additionally, the images can be used to understand changes in density and structure during clay hydration and heating. We built the relationship between CT number vs. density by scanning columns compacted with bentonite clay of different bulk wet density. Columns were packed with the same bentonite clay but different water contents and compaction (thus dry densities), resulting in variable bulk wet densities.

Figure 10-9 represents calibration curve, which was used to interpret the correlation between the CT number and the clay density for both heated and non-heated columns. It should be also noted that the clay density is dependent on the bulk dry density and water content, i.e., the value increases with increasing water content and clay dry density. Also noted that no hysteretic or dynamic wetting-drying processes were considered in Figure 10-9 as it was built on static conditions with pre-packed columns.

After the heating and hydration tests, we dismantled both columns and collected bentonite samples at different locations (see more details in Section 10.5). These samples were used to further verify the calibration curve by directly comparing the measured gravitational density vs. interpreted CT density.

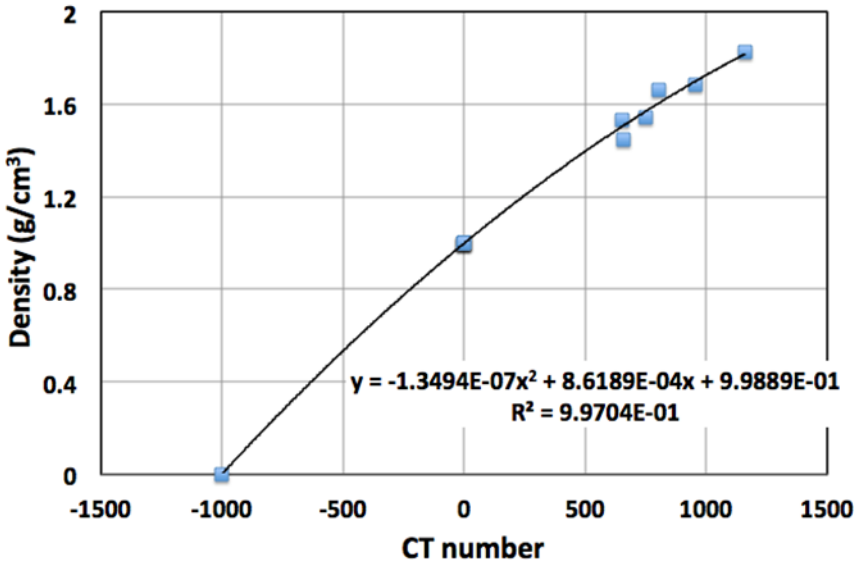

Figure 10-9 The calibration curve used to interpret the correlation between the CT value and bulk wet density.

Since June 2019, we have run the experiments and monitored the density distributions and temporal changes in both columns through frequent CT scans for over 1.5 years. In the following sections, we will update the 3D density map of the heated column subject to hydration, and the non-heated column to both hydration and heating. Comparisons will focus on (1) the temporal changes of 3D clay density distributions due to water intrusion, swelling and structural deformation subject to hydration in the non-heated column, and hydration and heating in the heated column, (2) the swelling and deformation of clay subject to hydration and heating by image-tracking the transit movement of the thermocouple sensors, and (3) the density averaged over the entire clay column and its changes as a function of time.

10.4.1.2 3-D hydration

Figure 10-10 depicts the 3D orthogonal view of CT density distribution and temporal changes in the non-heated column. The color bar bounds density changes from 1.2 to 2.4 g/cm3, and a brighter color indicates a higher density. The image at T=0 day shows the initial conditions and density distribution after packing, including the heater and heater shaft in the center (white color), the sand layer surrounding the clay (orange color), the ERT bars emplaced at the sand-clay boundary (white line in the top slice, the other ERT bar was emplaced in the opposite position that cannot be directly seen in the figure), and clay packed between the sand layer and the central shaft (blue to orange color). The density variations, bedding layers and the dark fracture patches (bounded by the white dotted lines) close to one end of the column are attributed to uneven packing. The uneven packing, especially the fracture patches, affect the hydration process and induce preferential brine flow pathway. The CT density of clay averaged over the

entire column is 1.46 g/cm3, similar to the measured value of 1.44 g/cm3 by weighing the clay mass used for packing and the column volume. The measured water content was 0.17, the dry density and porosity were then calculated as1.23g/cm3 and 0.53, respectively.

At T=1 day, we saturated the sand layer with brine and kept flowing at 0.11 mL/min under 120 psi. Hydration was then initiated and indicated by the changes of clay density. At T=8 days in Figure 10-12, the increase of CT density in the column indicates the considerable hydration. The density distribution, however, is not uniform. As shown in the figure, the high-density front represents the hydration front, which has advanced halfway towards the center shaft. We also observe great density reduction at the sand-clay boundary relative to the hydration front. This can be attributed to the more considerable reduction in clay dry density by swelling after hydration. The clay swelling initiated at the sand-clay boundary may push and compact the interior clay and contribute to the high-density hydration front. We also show at T=8 days the seal of the fracture patches by swelling, which hinders the propagation of hydration along the center shaft (see the magnified image, Figure 10-10). The clay swelling meanwhile smoothens the density variations and impedes preferential flow of brine from the surround sand layer. All these are in favor of retardation of radionuclide and securing the SNF and waste disposal. At T= 255 days, the density distribution become more uniform. From T=255 to 561 days, the overall CT density and distributions maintain constant. We then depressurized and dismantled the column, collected bentonite samples at different locations (see more details in Section 10.5).

The 3D images indicate radial symmetry of hydration distribution from the sand layer to the center shaft. We thus applied the radially averaged images to show the 3D hydration process. For each CT scan, the obtained CT image stack was first orthogonally reconstructed by rotating a line at 360° around the center shaft. Then, an image was obtained by averaging over the 360° radially reconstructed images, and the CT number was converted into the density using the calibration curve shown by Figure 10-9.

Figure 10-11(A) presents the radially averaged images of the non-heated column, which show the CT density distribution and temporal changes subject to hydration from the sand layer up to 561 days. Note that each sub-image was radially averaged, thus the density profile along a single line (e.g., the white dotted line at T=561 days) represents the average density vs. radial distance from the heater shaft, as shown in Figure 10-11(B). Figure 10-11(A) clearly shows that the hydration was initiated from the peripheral sand layer and the top and bottom boundaries, where brine invaded the clay column from gaps between the column end caps. The hydration along the center shaft, however, stopped at T=7 days, because of clay swelling and sealing of the gaps after hydration (also see the magnified images in Figure 10-10). The continuous propagation of hydration occurred from the peripheral sand layer, as indicated by the temporal changes of the peak density in Figure 10-11(B). At T=33 days, the hydration front approached the center shaft. After that, the clay density increased at a location close to the shaft, along with the density reduction in the middle part (~40 mm from the shaft), resulting in a more uniform density distribution in the entire column.

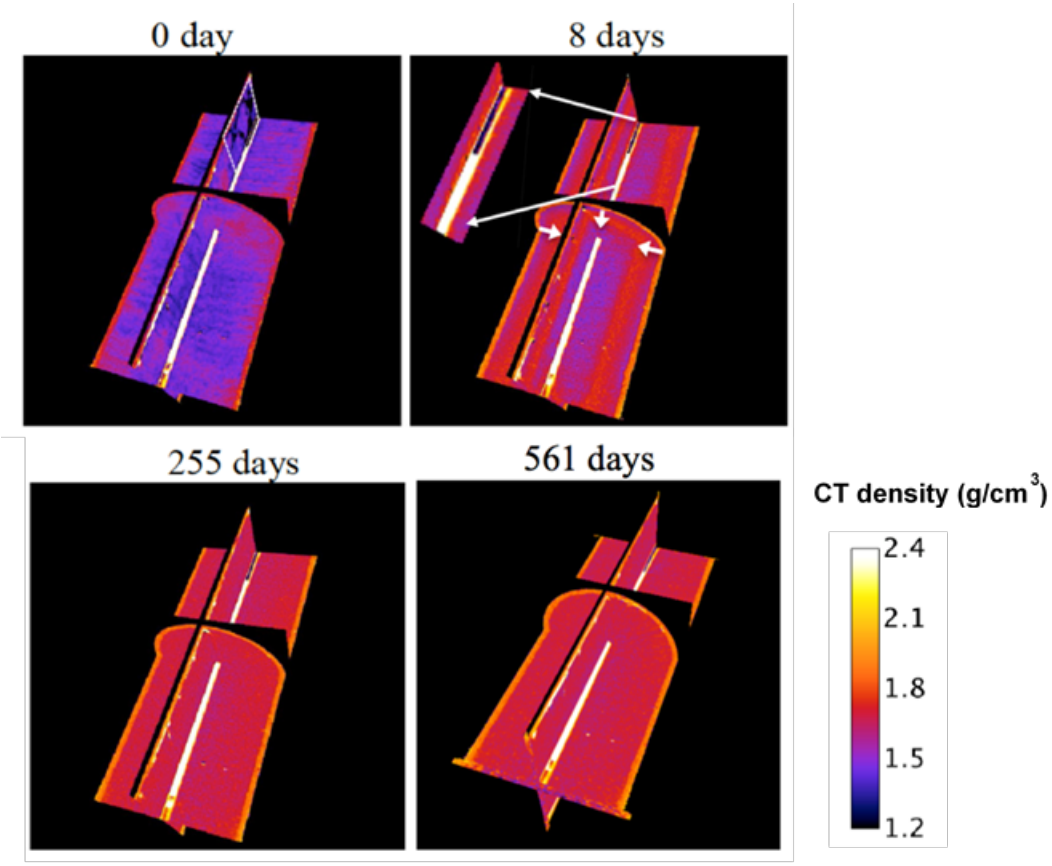

Figure 10-10 The 3D clay density maps showing the spatial and temporal variations of clay density in the non-heated column. The sub-image at T=0 day shows the initial condition after packing, with the uneven-packing induced fracture marked by the white dotted box. The white arrows at T=8 days depict the continuous hydration from the surrounding sand layer, while the magnified image at T=8 days presents the preferential water intrusion along the center shaft at early time. At T=561 days, the column was dismantled with bentonite sample collected at different locations.

The clay swelling and density reduction along the sand-clay boundary can also be observed at early times (T=4 and 8 days) in Figure 10-11(A) and (B). The swelling of clay at the boundary may compact the interior clay, resulting in the sharp density increase ahead of the hydration front. For example, in Figure 10-11(B) and at T=4 days, at the distance of <40 mm from the center shaft, the density of clay increased by ~0.05 g/cm3, when compared to the density at T=2 days. At T=8 days, the density increased another 0.03 g/cm3 ahead of the hydration front (<20 mm from the center shaft). As hydration continued and propagated to the center, the compaction weakened, the density at the sand-clay boundary gradually rebounded, along with the density reduction in the middle part (20-50 mm away from the center shaft). These induced flattening of the density profile along the white dotted line perpendicular to the center shaft, and the uniform density distribution in the entire column. The frequent X-ray CT images and changes in clay density represent the spatial and temporal dependent processes of increasing saturation and clay swelling due to hydration. At T=255 days, the column averaged clay density was stable at 1.68 g/cm3, 0.21g/cm3 higher than the initial value before hydration. At T=561 days, the average clay density was measured at 1.68 g/cm3, without considerable changes since T=255 days.

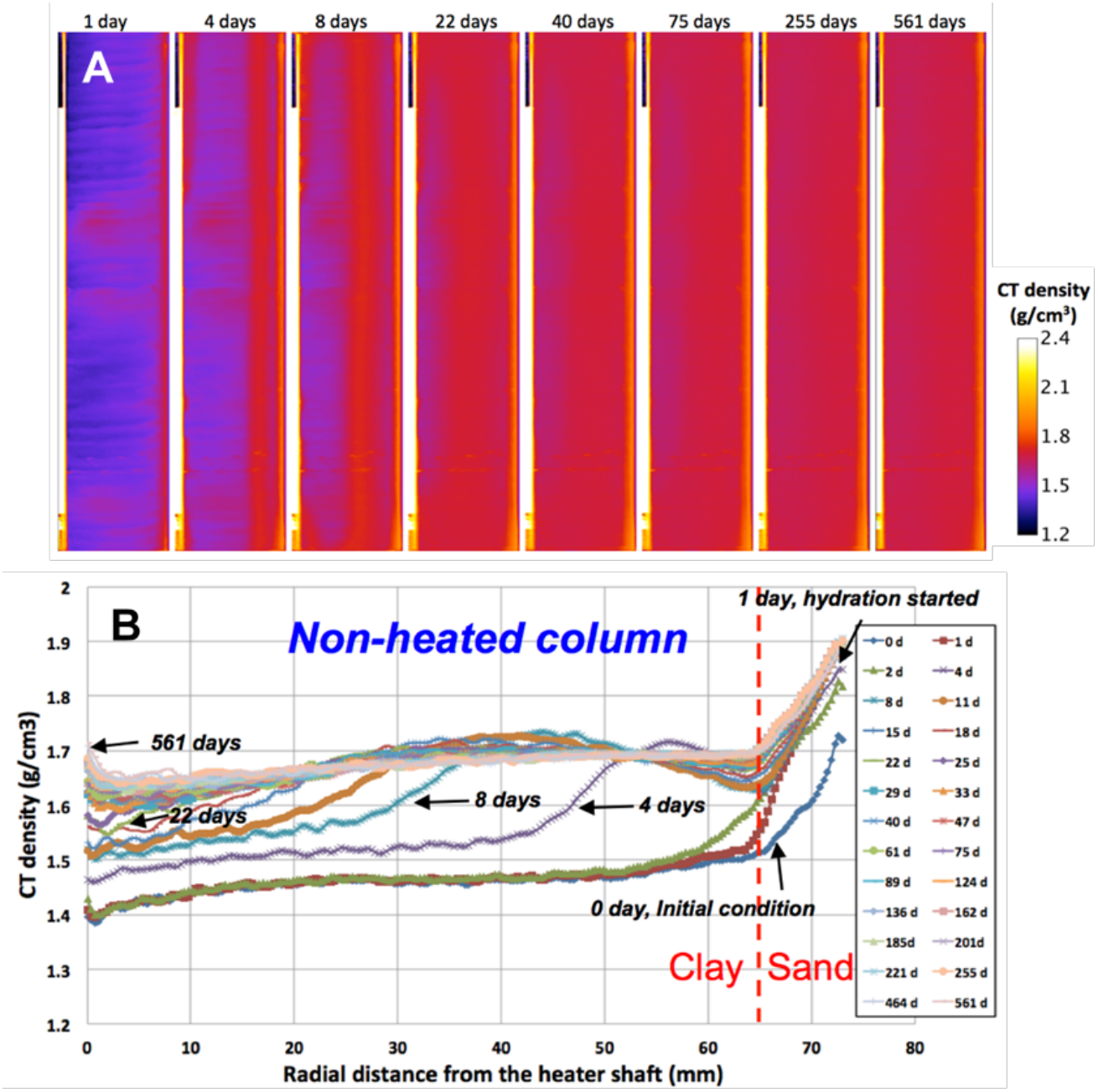

Figure 10-11 (A) The radially averaged density map and changes with time for the non-heated column subject to hydration for 561 days. (B) The average density vs. radial distance from the center shaft along the white dotted line in (A).

10.4.1.3 3-D heating hydration

In the heated column at T=1 day, we also saturated the surrounding sand layer with brine and kept it flowing at 0.11 mL/min under 120 psi. At T=2 days, we turned on the heater and kept the temperature of clay on the heater shaft constant at 200 °C since T=8 days. Figure 10-14 depicts the selected 3-D density distribution and changes with time in the heated column for 564 days, while Figure 10-15 shows the radially averaged density map (A) and the average density profile vs. radial distance from the heater shaft (B). Image at T=0 day presents an initial condition similar to that in the non-heated column. The column

averaged CT density was 1.44 g/cm3, close to the measured value of 1.41 g/cm3 by weighting the packed clay mass and vessel volume. The measured water content for the heated column was 0.18, the dry density and porosity were then calculated as1.20 g/cm3 and 0.54, respectively. The image also presents the patterned layers and density variations, as well as the fracture close to one end of the column. At T=8 days, we observe similar (1) swelling of clay and sealing of the fracture after hydration, (2) density reduction at the sand-clay boundary due to clay swelling, and (3) clay density increases ahead of the hydration due to compaction.

Differing from the non-heated column, however, Figure 10-14and Figure 10-15(A) at T=8 days present a dry-out zone of a lower density close to the heater shaft. Because of heating, the average density within this dry-out zone was 1.32, 1.38, and 1.40 g/cm3 at T=2, 4, and 8 days, respectively, lower than the values of 1.43, 1.52 and 1.56 g/cm3 within the same region of the non-heated column. The heating, thus, induced a larger density gradient (thus, larger gradient of water content) and vapor outward transport (from the innermost heating zone) and condensation in the middle part as temperature decreased (also see Figure 10-15(B)). The hydration front approached to the location 5 mm away from the middle shaft at T=25 days, after that a dry-out zone sustained. At T=564 days, the dry-out zone was confined in location <5mm away from the heater shaft, while the overall density distribution in the column became more uniform.

Within the dry-out zone, we observe bright, high-density deposition on the heater shaft, as shown by the magnified image in Figure 10-14 at T=255 and 564 days. More frequent CT images (Figure 10-15(A) and (B)) indicate the deposition initiated at T=75 days (the sharp increase in the CT density in the dry-out zone in Figure 10-15(B)), followed by the quick increase to 1.83 g/cm3 until T=124 days. After that, the density increased slowly and stabilized at 1.90 g/cm3 at T=564 days. The deposition also occurred along the heater shaft, as shown in Figure 10-15(A). After T=255 days, the deposition continues to grow on the shaft up to ~4 mm thick by the end of the experiment at T=564 days. We dismantled the column and collected the deposited samples for XRD analysis (see Section 10.5 for more details).

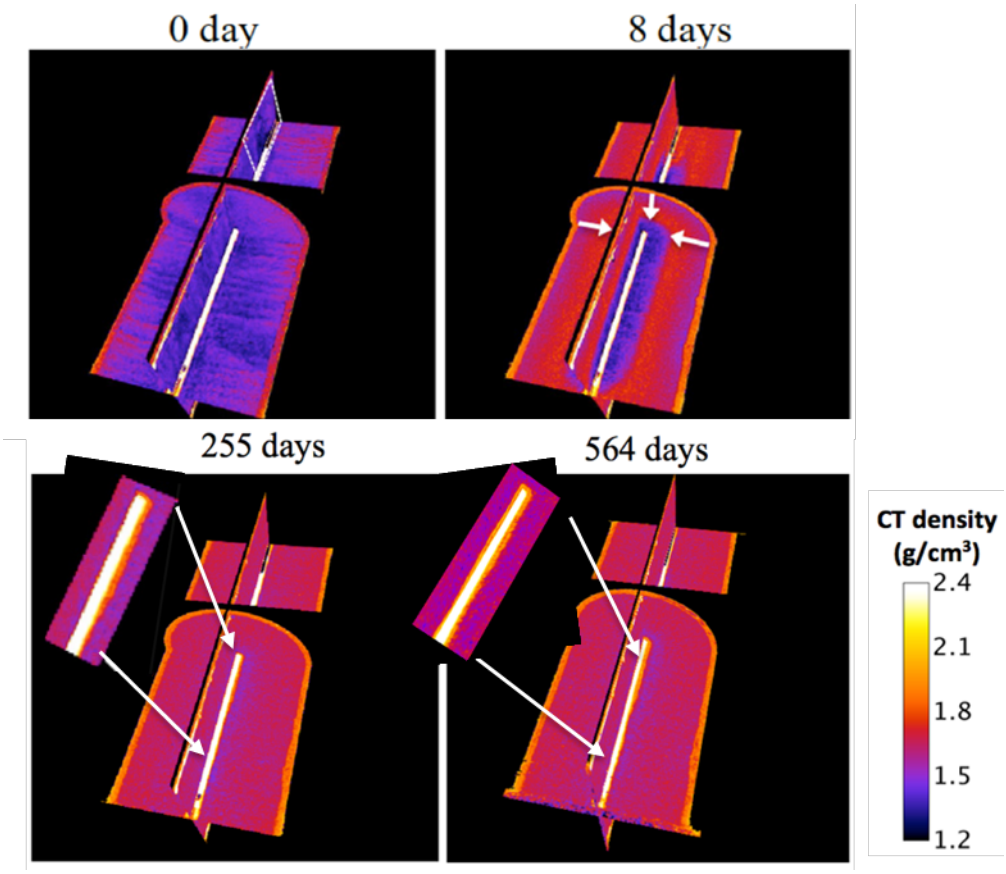

Figure 10-12 **The 3-D clay density map and temporal variations in the heated column. The sub-image at T=0 day shows the initial condition after packing, with the uneven-packing induced fracture marked by the white dotted box. The white arrows at T=8 days depict the continuous hydration from the surrounding sand layer. The magnified image at T=255 and 564 days presents the bright high-density deposition on the heater shaft subject to heating and water vaporization. At T=564 days, the column was dismantled with bentonite sample collected at different locations.**

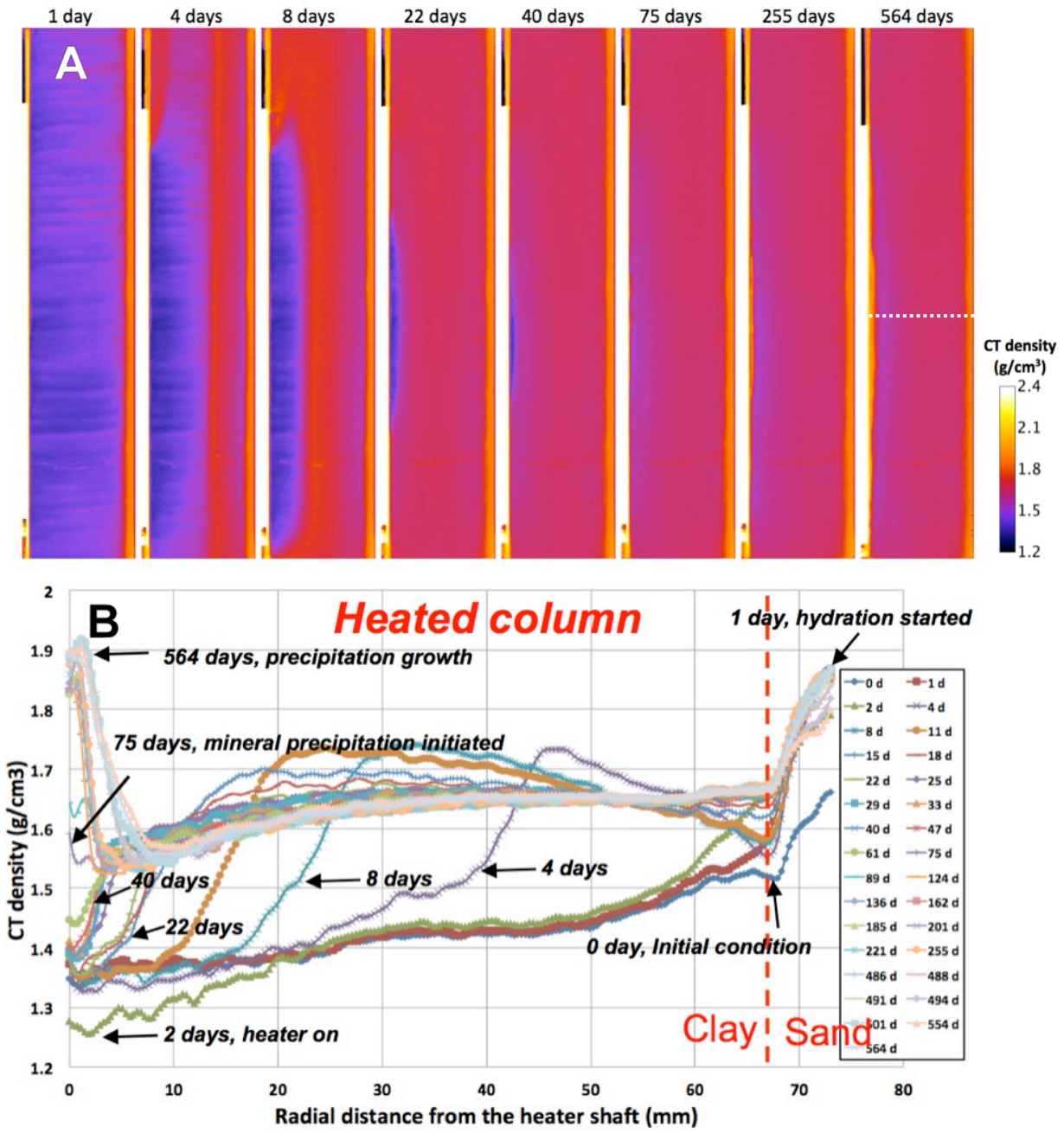

Figure 10-13 (A) The radially averaged density map and changes with time for the heated column subject to heating and hydration. (B) is the average density profile vs. radial distance from the heater shaft along the white dotted line in (A).

10.4.1.4 Displacements at different locations

We have shown in our FY20 milestone report the spatio-temporal displacement of bentonite induced by hydration and heating. We continued to investigate the spatially variable deformations of clay by tracking all six thermocouple sensors emplaced in both of the non-heated and heated columns. Figure 10-14(A) and (B) present the locations of each thermocouple sensor in the non-heated (A) and heated (B) columns during the experiments. Figure 10-14(C) and (D) depict their displacements and variations as a function

of time up to 1.5 years. We define a negative displacement value when displacements towards to the center shaft occurred, while a positive value represents displacements away from the center shaft. In both columns, thermocouple *a* was closest to the center shaft, while thermocouple *f* was closest to the sand-clay boundary. Thermocouples *b, c, d, e* located 20 to 60 mm away from the center shaft. In the non-heated column, as shown in Figure 10-14(A) and (C), all six thermocouples showed similar trending of displacement variations vs. time. For instance, at early time (1-8 days), all thermocouples along with their surrounding clay were compacted toward the center shaft with continuous decrease in displacement. Spatially, the displacement decreased from exterior to interior clay, where displacements were confined by the rigid boundary at the center. After that, as hydration propagates to the center, all the thermocouples were pushed backward to their initial positions. By the end of the experiment at T=561 days, the displacements for all the thermocouples thus gradually rebounded and kept constant at -0.4 to -0.9 mm relative to their initial positions.

Figure 10-14(B) and (D) show the initial locations of the six thermocouple sensors in the heated column, and their displacement changes as a function of time. Comparing to the non-heated column in Figure 10-14(C), the clay presents more considerable displacements subject to heating and hydration. The displacements could be both inward (negative displacement values) and outward (positive displacement values), depending on the location and time. At early times (1-8 days), all thermocouples along with their surrounding clay were similarly compacted toward the heater shaft by swelling at the sand-clay boundary. The displacement values, however, ranged from -1.0 to -3.8 mm, showing larger compaction than that in the non-heated column at -0.2 to -2.4 mm. This indicates larger compaction induced by hydration and clay swelling at the sand-clay boundary when heating at the center. Note the clay CT density (1.58 g/cm^3) at the clay-sand boundary (marked by the black dotted line) at T=8 days in the heated column is lower than that in the non-heated column (1.63 g/cm^3). While more water was sucked into the column by larger water saturation gradient, the reduced clay CT density indicates larger reduction in clay dry density after more considerable swelling. It should be also noted that for thermocouple *f*, the compaction and displacement were limited by the clay available for swelling as its location was too close to the clay-sand boundary.

While the other thermocouples more or less recovered to their initial positions, the displacements of thermocouple *a* were affected by larger heating-induced swelling, as it was closest to the clay dry-out zone. It can be inferred that more interior clay would be drier as more pronounced water vaporization. The more considerable clay swelling after hydration and heating at some locations (e.g., locations around the thermocouple *a* and closer to the heater) may hinder fracture development near the shaft-clay interface by heating, which is in favor of securing the SNF and waste disposal. By the end of the experiment at T=564 days, the displacements of the six thermocouples vary from -0.82 (towards to the heater shaft) to 1.25 mm (away from the heater shaft) relative to their original locations.

The mm-scale displacement subject to heating and hydration will inevitably induce changes in clay dry density and porosity. While these changes in bentonite cannot be determined directly from CT images since CT density represents the bulk bentonite density affected by both water content and solid dry density, we collected bentonite samples after the experiments, conducted physical and chemical analysis to have a better understanding on the impacts of heating and hydration. More details can be found in Section 10.5.

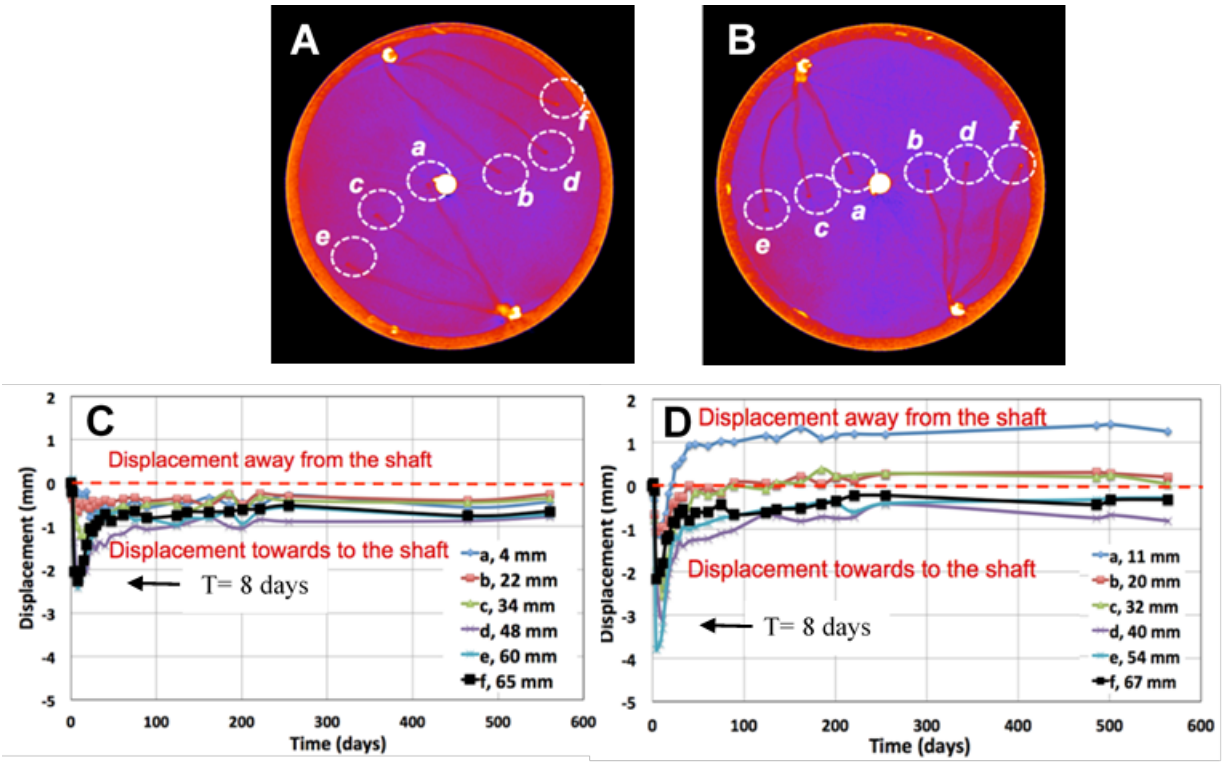

Figure 10-14 The six thermocouple sensors that are used for tracking clay displacement at different locations in the non-heated (A) and heated (B). (C) and (D) present the displacement changes relative to their original positions vs. time for the six thermocouple sensors. A negative displacement value represents displacement towards to the center shaft, while a positive value represents displacement away from the center shaft.

10.4.1.5 Average density change of the clay columns

Through the frequent X-ray CT imaging, we are able to calculate the average CT clay density over the entire clay column and show in Figure 10-15 the density increase after hydration in the non-heated column and heated column subject to heating and hydration. In the non-heated column, the clay density increased quickly once hydration started and at T= 22 days, the average density was 1.68 g/cm3, increased by 0.21 g/cm3, when compared to the initial condition. After that, the value kept relatively constant by the end of the experiment at T=561 days. By comparison and in the heated column, the density increased faster and at T= 15 days, the density increase reached the peak value of 0.21 g/cm3. After that, clay density decreased slowly, but was 0.18 g/cm3 higher than the initial one, and finally stabilized at 1.64 g/cm3 at T= 564 days. Overall, Figure 10-15 presents a faster hydration of clay and density increase subject to heating and hydration, followed by a slow density reduction and finally stabilized. The observed bright deposition on the heater shaft after 75 days in the heated column indicates potential mineral precipitations and chemical interactions (e.g., indicated by 10.4.2), and coupled THMC processes of bentonite clay subject to heating and hydrations. As we discussed earlier, these processes are spatial and temporal dependent. We have dismantled both columns and collected clay samples for detailed structural properties, mineralogical and chemical analysis. These will help in understanding the complex processes and provide a complete dataset for modeling the behavior of bentonite based EBS system, which is key to the evaluation and prediction of its performance in the long term.

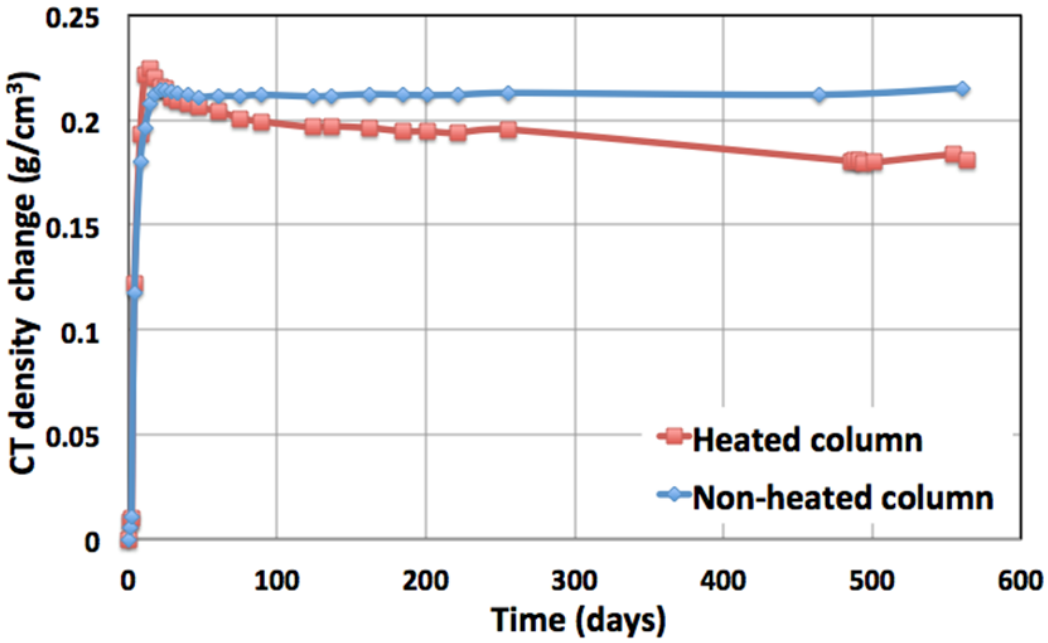

Figure 10-15 The CT density changes in the heated Column 1 and non-heated Column 2.

10.4.2 Geochemistry

Effluent water was collected, weighed and sampled from the influent mixture (see Table 10-1) and from the effluent of both columns (Figure 10-16 to Figure 10-19). Within the influent mixture, the effluent of the heated column showed sulfur reduction (also identified observed through the smell of sulfide), excess of silicon and retention of calcium and magnesium.

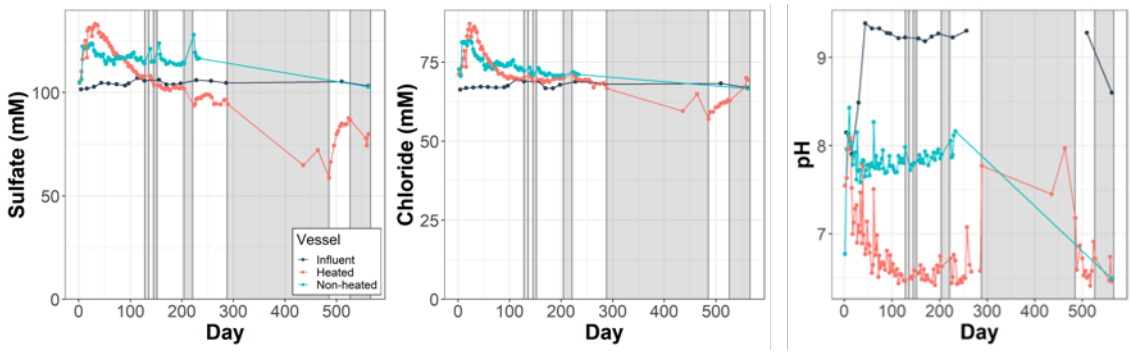

Figure 10-16 Influent and effluent anion concentration and pH. The grey out periods were where constant pressure was maintained without flow through.

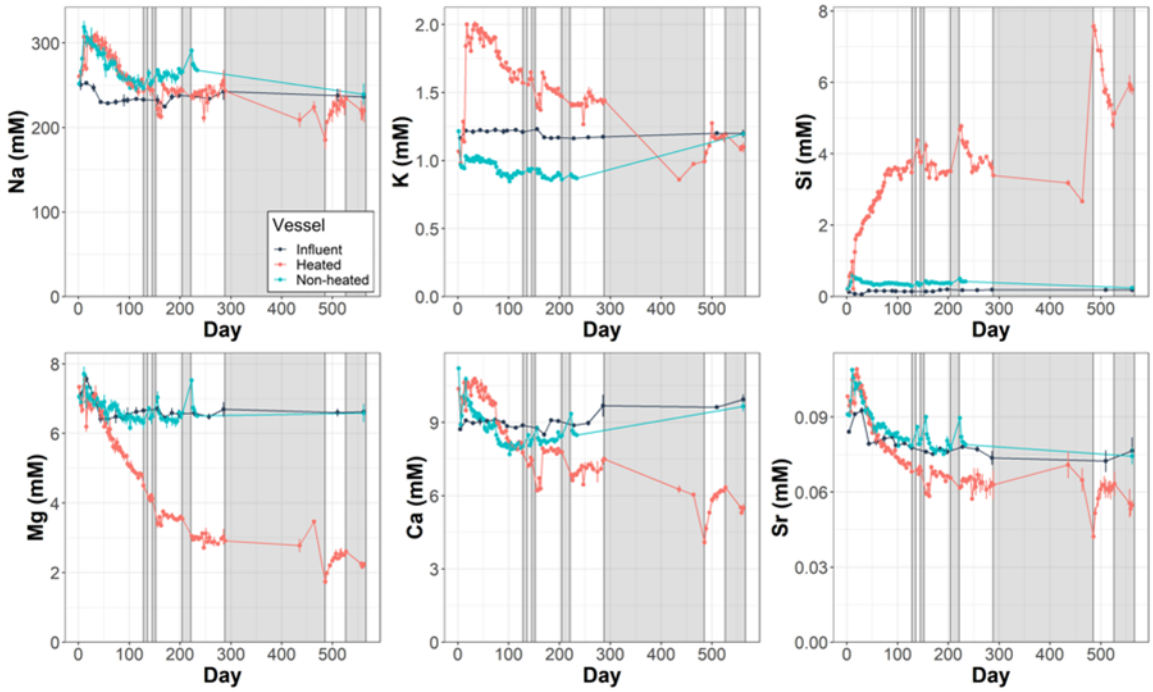

Figure 10-17 Influent and effluent concentration of cations present in the influent water.

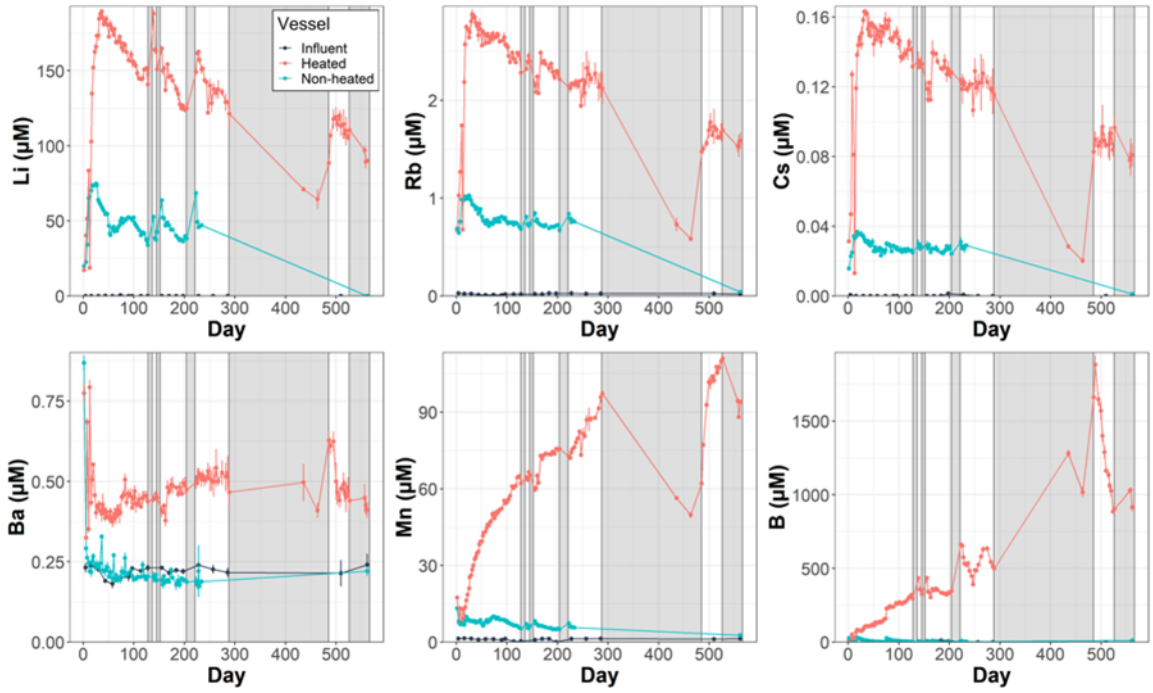

Figure 10-18 Influent and effluent concentration of cations that are not in the influent mixture and showed overall flushing in the heated column.

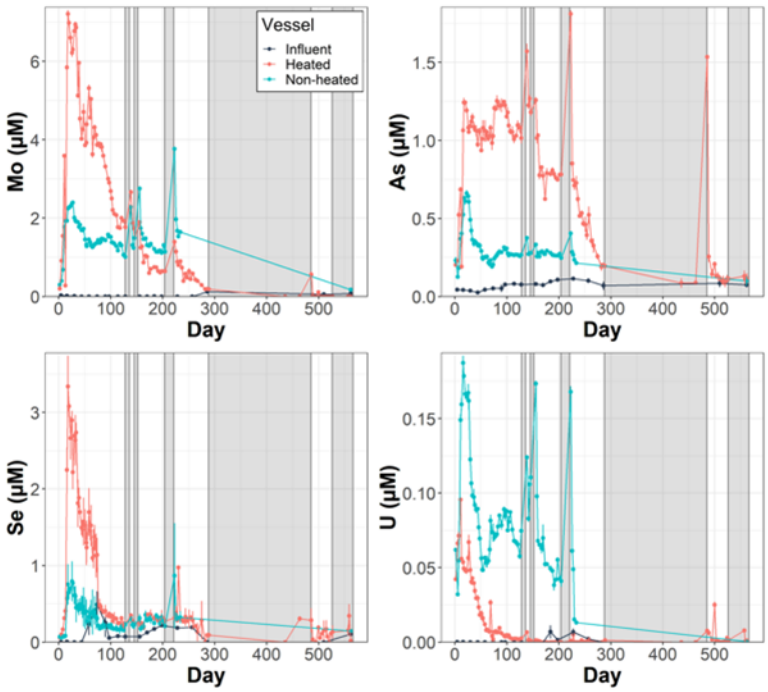

Figure 10-19 Influent and effluent concentration of cations that are not in the influent mixture and showed initial flushing in either column.

10.4.3 Electrical Resistivity Tomography

We continued to monitor the hydrological dynamics of the bentonite clay pack using electrical resistivity tomography (ERT) in the HotBent-Lab experiment. Some crucial aspects of the long-term field test are to understand the THMC processes and maintain the integrity of the barrier system subject to radial thermal gradient and naturally occurring water infiltration from the peripheral bedrocks. Therefore, temporal and spatial water saturation datasets remain desirable, while measuring water content at the field scale is challenging due to the operational thermal and geochemical conditions and the low accessibility of the barrier system. With ERT, the electrodes and cables could be embedded into the clay prior to the backfilling process, and time lapse ERT allows continuous characterization of the electrical resistivity in the clay volume, which could be further correlated to water content. In this section, we would continue the discussion of (a) ERT data acquisition and processing, (b) the calibration between resistivity and water content using laboratory datasets (including CT and temperature), and (c) the visualization of the water content distribution from ERT time lapse. The limitations of the current analyses and the improvements that would be made for the next experiments would also be addressed.

(a) ERT data acquisition and processing

Our ERT setup included (1) an electrical impedance tomography system (MPT DAS-1) and (2) 24 square copper electrodes (0.5 by 0.5 cm) evenly spaced on a pair of fiberglass rods (12 electrodes on each rod, with a 3.8 cm inter-electrode distance) (Figure 10-3 and Figure 10-4). We placed the two rods in a cross-well manner at the sand-clay boundary and embedded the electrodes inside the clay to ensure adequate physical contact between clay and electrodes. Since the columns were laid horizontally, the rods were positioned in the top and bottom halves of the columns to allow inspection of gravitational effects on infiltration. To minimize disturbances to the clay structure, the wires were soldered onto the copper electrodes, traveled along the rods, exited through a feed-through port at the end-cap and connected to the system for electrical measurements. We selected the materials of the rods and wires that could tolerate the

thermal and saline conditions, and we coated the aluminum columns, end caps and the titanium heater shafts with electrically-insulated silicone gel to minimize current conduction from the metal components of the vessels.

During an electrical resistivity measurement, an electrical field was actively created in the clay volume by applying an electrical potential across a pair of selected electrodes, and meanwhile the potential difference between multiple combinations of the other electrodes in pair was measured. The electrical potential was applied in the frequency domain at 1 Hz with a target voltage at 10 V, and the measurement sequence followed a dipole-dipole electrode configuration (combining skip-0, 1, 2, 4, 6, 11 arrays) which summed up to 1326 lines of data in one acquisition session. Our setup allowed automatic measurements of both columns with a specifiable time interval, and the data could be retrieved remotely, producing spatially and temporally dense datasets. A python-based algorithm BERT (Günther & Rücker, 2012) was used for simulating ERT data and generating a 3D electrical resistivity distribution in the clay volume. Figure 10-20 shows the numerical mesh used to perform forward and inverse simulations.

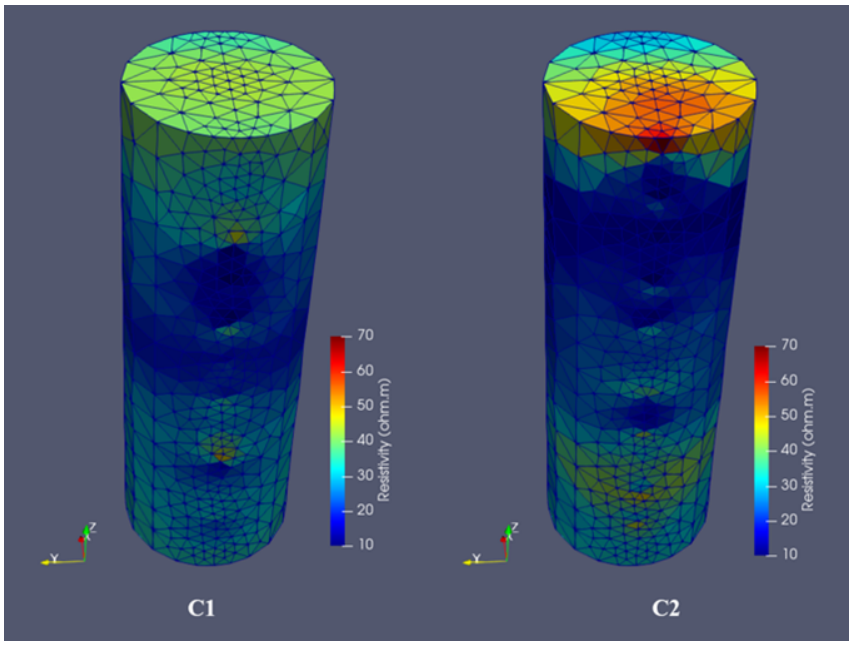

Figure 10-20 Numerical mesh used for ERT inversion and 3D visualization of the electrical resistivity structure of the columns after packing (T=0 day). C1 is the heated column, and C2 is the non-heated. Both columns are packed at ~21% (v/v) volumetric water content and ~1.2 g/cm^3 dry bulk density.

In alignment with CT analysis, we averaged the ERT resistivity radially to investigate the radial heating and infiltration processes. Figure 10-20 shows the data coverage of ERT measurements. The electrode rods were located at (-7.6, 0) and (+7.6, 0) in Figure 10-21(A) and at r = ±7.6 in Figure 10-21(B). Due to the cross-well positioning of the rods, current flow paths concentrated in the plane defined by the two rods, yielding higher ERT coverage near the x-axis. Therefore, when calculating the radial resistivity, we only included the data inside the cuboid bounded by the red lines, systematically filtering out the data from the sand layer and near the electrodes where the data quality was highly subject to the accurate positions of the electrodes (Figure 10-21(A)). We used a 1 cm (radius, chosen as the interspace of the thermocouples) by 1.9 cm (depth, chosen as the electrode half space) mesh grid and acquired the average resistivity in each cell using an inverse distance weighing function with a 1.9 cm moving window (Figure 10-21(B)). Figure 10-21(B) also shows two column depths which would be used to compare with CT results: (1) thermocouple depth z = 11cm, and (2) mid-heater depth z = 21cm.

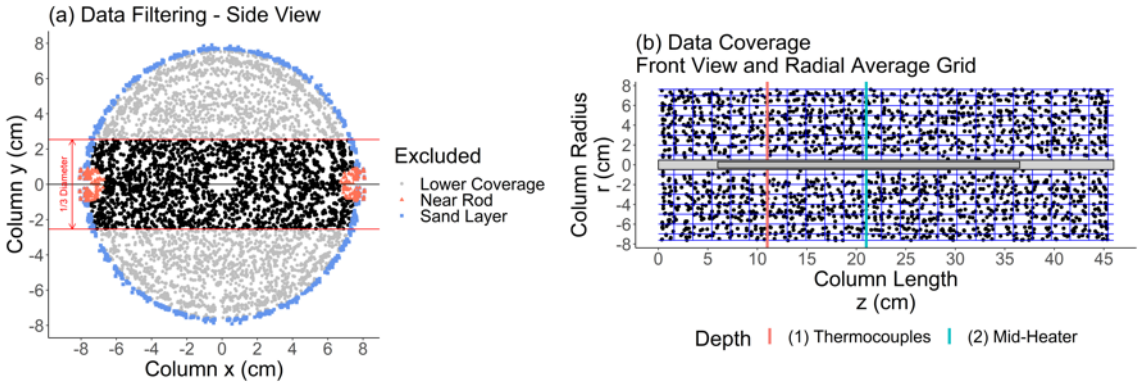

Figure 10-21 (A) Radial data coverage from the ERT inversion model in the cross-sectional view. Each point is the center of a cell from the numerical mesh (Figure 7-21) and carries a resistivity value. (B) Mesh grid for radial-averaged resistivity and selected depths for joint analysis with CT.

In this report, we updated the ERT results beyond day 255. Both the non-heated (Figure 10-22) and heated (Figure 10-23) columns did not show substantial changes in resistivity after day 75, which was also suggested by the CT imaging. In the non-heated column (Figure 10-22), the major change was still the early sprawl of the low resistivity zone that spatially and temporally matched with the CT. CT images showed that (1) water infiltration created a high-density front moving inward, and that (2) clay swell induced a low-density zone near the sand-clay boundary, which gradually equilibrated as clay volume redistributed (Figure 10-13). Figure 10-22 shows a similar progression in the resistivity term, with (1) a low-resistivity zone migrating inward and (2) a high conductive region developing and fading near the sand-clay boundary. As the water content increased, CT density first increased then decreased when clay swell significantly displaced higher density clay minerals with water, while ERT resistivity continued to decrease as clay saturated. In the heated column (Figure 10-23), the relationship between water content and resistivity was masked by the thermal gradient. When the temperature increased (below the boiling point, 175 oC at the applied pressure of 120 psi), the resistivity of the clay also decreased due to vigorous movements of ions in the pore fluid and on the clay surfaces. Comparing the two methods, CT is less sensitive to temperature, and ERT has a more straight-forward relationship with water content. To decouple the effect of temperature on resistivity from that of the water content, our lab experiment allowed joint ERT-CT analysis to correlate time lapse ERT and moisture dynamics.

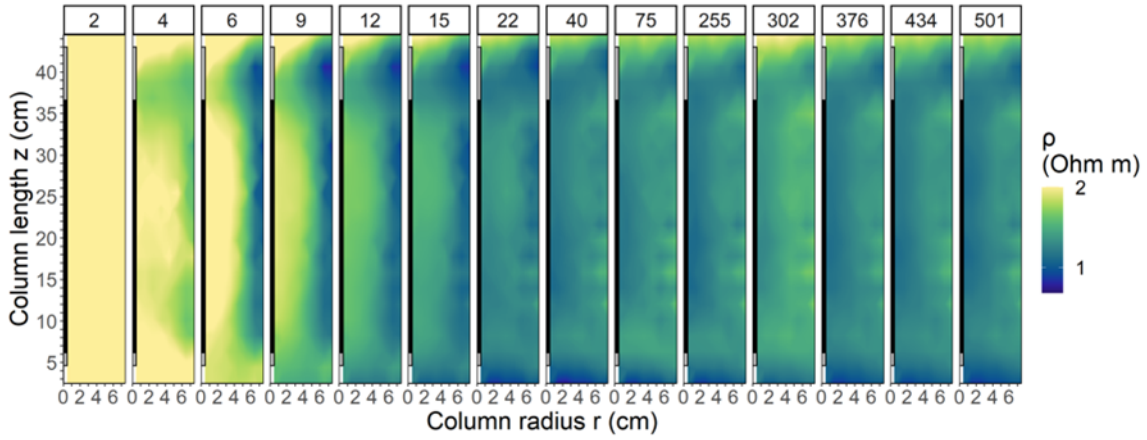

Figure 10-22 Radial resistivity map of the non-heated column (C2) after flow started (day 2 to 501). Flow is along the positive *z* direction. Color bar is log-scaled from 0.8 to 2.0 Ωm.

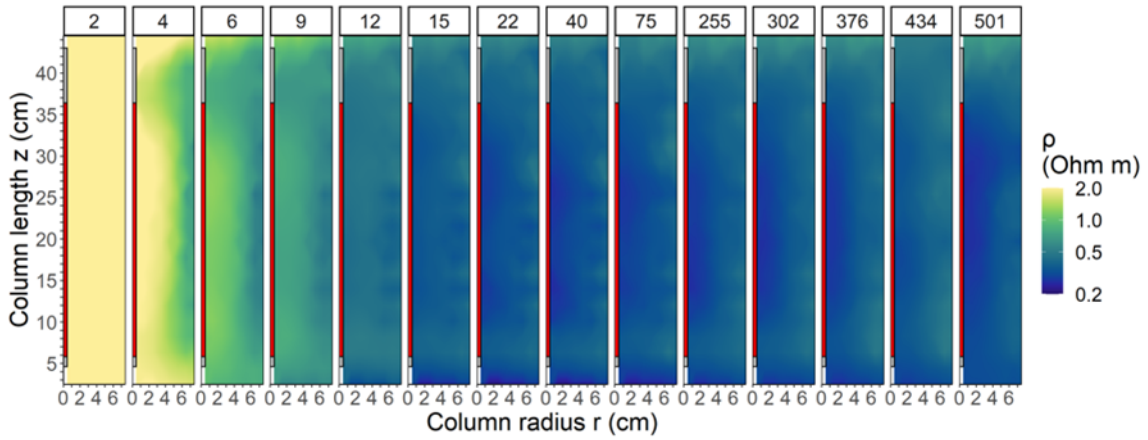

Figure 10-23 Radial resistivity map of the heated column (C1) after flow started (day 2 to 501). The red rectangle at the center is the location of the heater. Color bar is log-scaled from 0.2 to 2.0 Ωm.

10.4.3.1 Joint ERT-CT calibration

We established material-specific relationship between resistivity and water content. As discussed, (1) water content determines pore fluid connectivity, and (2) temperature affects the movement of electrolytes in pore fluid and cations on clay surfaces. In addition, (3) chemical diffusion alters pore fluid conductivity, and (4) mechanical compaction and swell changes the pore structure. Since montmorillonite, the main mineral of the MX-80 bentonite, has high surface conductance, (5) resistivity also decreases with increasing surface area of the clay. A typical petrophysical relationship between resistivity and the factors mentioned above for porous media can be described by Waxman-Smits Model (Eq. 10-1 to Eq. 10-3), which includes an additional surface conductance term, bQv, suitable for the clay application:

$$\rho_S = \Phi^{-m} S^{-n} \left(\sigma_f + \frac{bQ_v}{S}\right)^{-1} \quad \textbf{Eq. 10-1}$$

$$b = \left(1 - 0.83e^{-e^{\sigma f\left(-2.38+\frac{42.17}{T}\right)}}\right) * (-3.16 + 1.59\ln(T))^2 \quad \textbf{Eq. 10-2}$$

$$Q_v = CEC * D_{grain} * \frac{1-\Phi}{\Phi} \quad \textbf{Eq. 10-3}$$

where ρ is the resistivity of the clay (Ω_m), Φ porosity (m^3/m^3), m (-) cementation exponent (typically 1.5 ~ 4.0 and increases with cementation), S degree of saturation (m^3/m^3), n (-) saturation exponent (typically ~ 2), σ_f conductivity of pore fluid (S/m), b equivalent ionic conductance of clay exchange cations (S/m cm^3/meq), T temperature (C), and Q_v is the CEC per unit pore volume (meq/cm^3) as a function of porosity, CEC (meq/g), and Dgrain grain density (g/cm^3). Based on the SKB TR-10-60 technical report for MX-80 bentonite (Karland, 2010), we set CEC = 0.75 meq/g and D_{grain} = 2.75 g/cm3.

Figure 10-24(A) lays out the joint ERT-CT calibration. From the in-situ datasets, we selected ERT and CT at two vertical depths (thermocouples at z = 11 cm and mid-heater at z = 21 cm) and co-registered them at 6 radial distances (Figure 10-24), and the temperature (T) was interpolated at the matching radii (Figure 10-25). Firstly, we used CT data to estimate porosity (Φ) and saturation (S), assuming that the three phases (air, fluid, solid) contributed to the CT values based on their volumetric fraction (θ_a, θ_v, θ_s) and CT intensity (CT_{air}, CT_{water}, CT_{solid}). The dependency of CT_{water} on temperature and density was

considered, and the CT intensity of the MX-80 bentonite was fitted ex-situ with separately packed clay columns with known water content and dry bulk density (CT_{solid} = 2187). Since three variables (θ_a, θ_v, θ_s) were required to determine Φ and S, to reduce one variable, we only included (1) initial data when CT has not showed significant clay swell (therefore assuming initial dry bulk density θ_s) and (2) saturated data (θ_a = 0) based on CT temporal trends in the training dataset, and the rest was set as testing dataset. Secondly, we used ERT data to estimate pore fluid conductivity (σ_f), based on the volumetric fraction of the three phases determined by CT and their permittivity contribution (ε_{air}, ε_{water}, ε_{solid}), where the effect of temperature on ε_{water} was also considered. Finally, the cementation exponent (m) and saturation exponent (n) were fitted separately for the two columns: m = 2.10 and n = 1.74 for the heated column and m = 1.90 and n = 1.97 for the non-heated column.

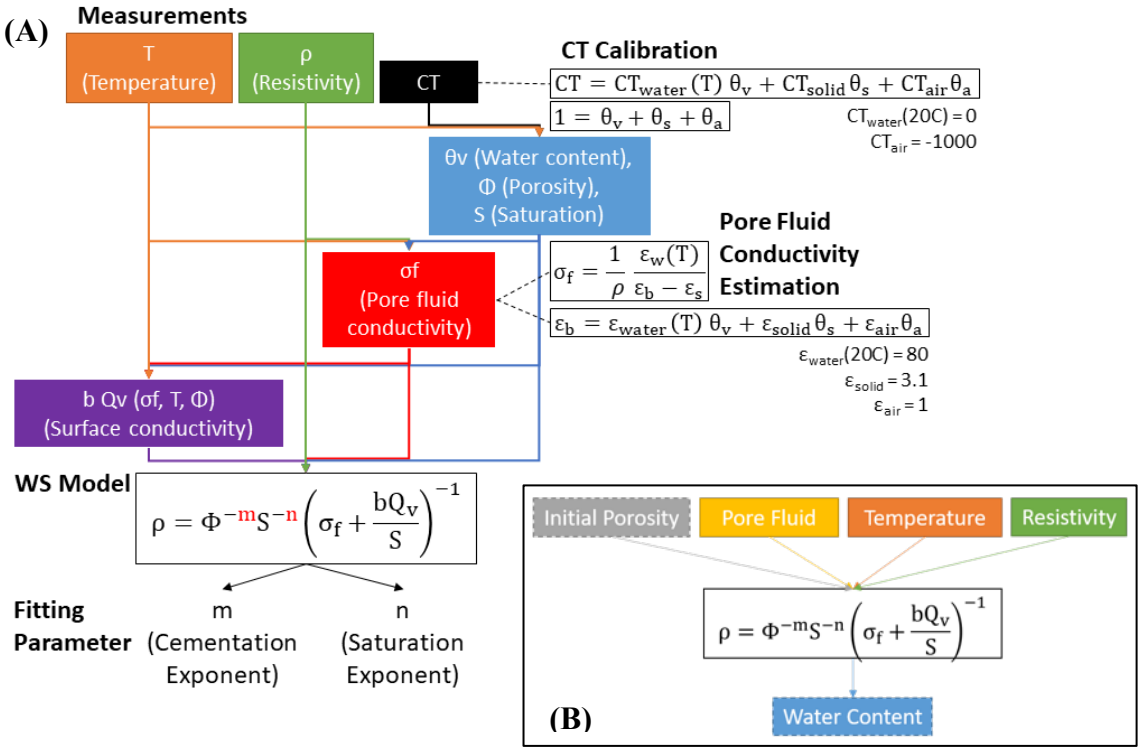

Figure 10-24 (A) Schematic flowchart of the *in-situ* joint ERT-CT calibration. (B) Model application during ERT-moisutre calibration.

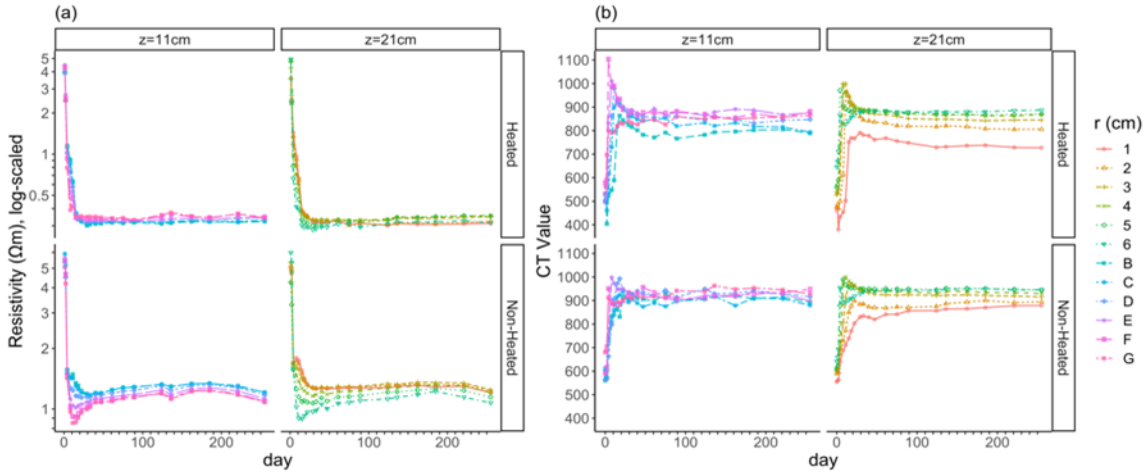

Figure 10-25 Temporal (A) resistivity (after day 1) and (B) CT values of heated (top) and non-heated (bottom) columns at two selected depths. Data in the left panel are sampled near the thermocouples (z = 11 cm) labeled as B-G, where B is closer to the heater and G to the sand-clay boundary. Data in the right panel are sampled at 6 radial distances (1 to 6 cm) from the heater shaft at the mid-heater depth (*z* = 21 cm).

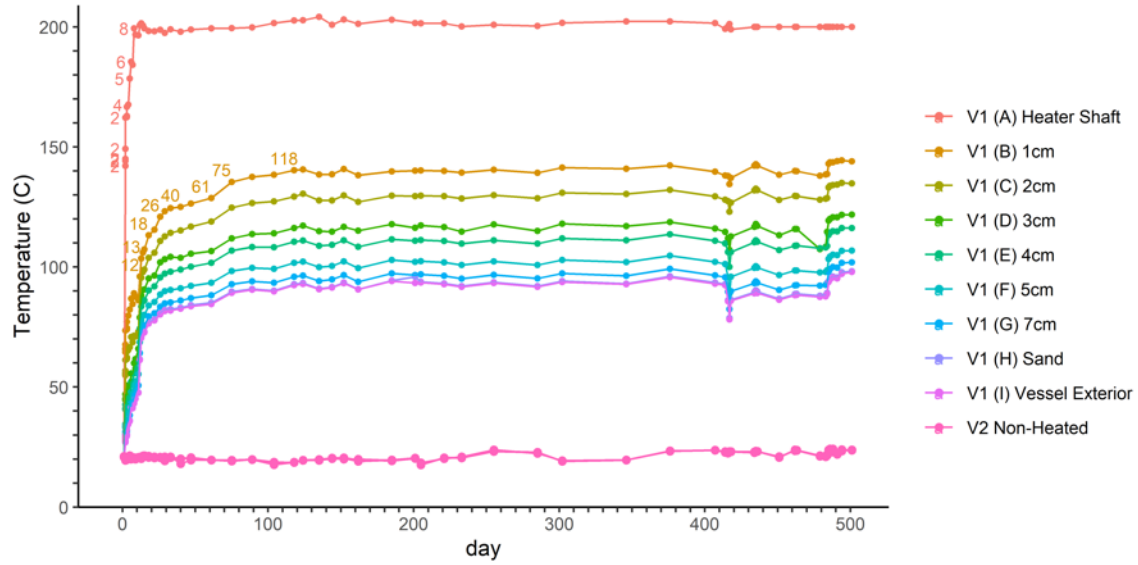

Figure 10-26 Clay temperature measured by the thermocouples in the heated (A through I) and non-heated columns.

10.4.3.2 Time-lapse clay water dynamics

We evaluated if ERT alone would be sufficient to characterize water content distribution. Using the calibrated Waxman-Smits model, we input resistivity, temperature and pore fluid conductivity (estimated during the calibration and temporally/spatially interpolated) without direct constraints from CT (Figure 10-26(B)). The model searched for the combinations of degree of saturation (S) and porosity (Φ) that would yield the observed resistivity value, and it minimized the difference between the estimated and initial porosity (0.56 based on 1.2 g/cm^3 dry density) for the output, which is generally acceptable with high dry bulk density and in a confined volume.

Figure 10-27shows the calibrated water content distribution. Note that in the heated column (left), the cold zones beyond the heater coverage were excluded due to the lack of temperature data. Calibration is not applicable around a small region (few millimeters) around the heater where water was mostly in the vapor form. We also calculated the depth averaged (mid-column depths, z = 11 to 31 cm) water content along the column radii (Figure 10-28). In general, the dynamics of ERT-derived water content agreed with the changes in CT density. THM processes such as (1) initial drying and slower saturation near the heat source, (2) water infiltration from the sand boundary, and (3) clay swell followed by clay volume redistribution were captured in both columns.

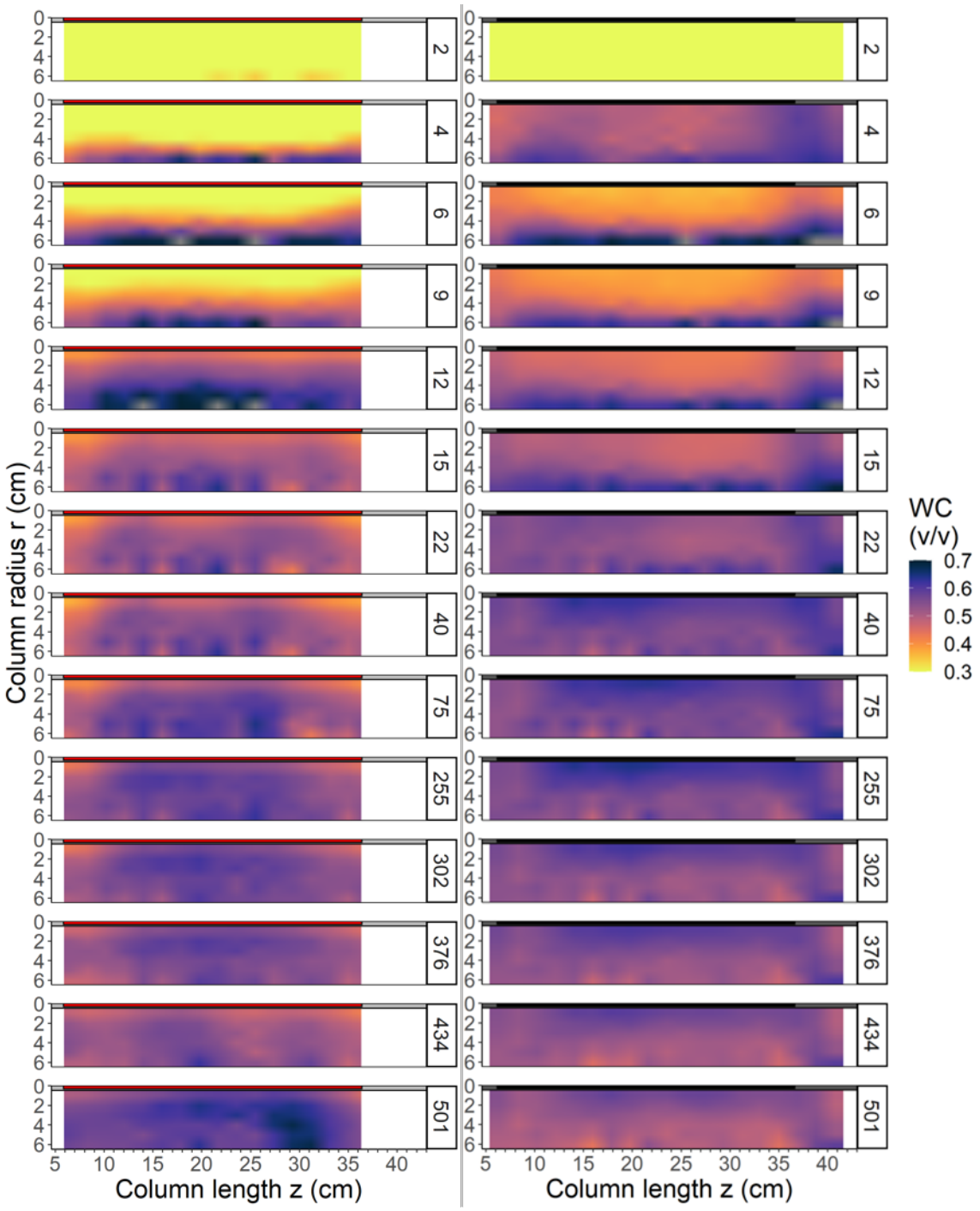

Figure 10-27 Radial water content distribution of the heated (C1, left) and non-heated column (right, C2) on selected days (day 2-501). Color bar is volumetric water content (cm^3/cm^3) scaled from 0.3 to 0.7.

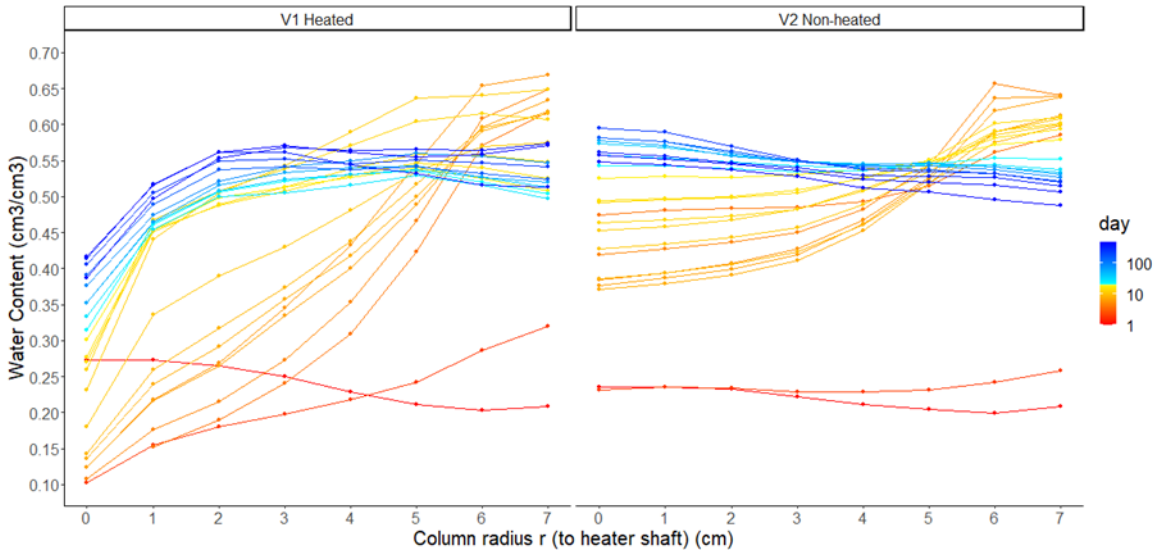

Figure 10-28 Radial averaged water content from the mid-column depths (z = 11 cm to 31 cm). The days are log-scaled for visualization.

At the column level, the water content derived from ERT was compared against the water content estimated from mass balance (Figure 10-29). The ERT water content was averaged in the mid-column depths (z = 11 to 31 cm, weighted by the volume of each cell), and the mass balance was calculated from the mass difference between influx and efflux, or how much of the injected fluid was retained inside the column. The influx was continuously recorded by the inlet pumps, and the efflux was routinely collected and measured gravimetrically. For the non-heated column, the two analyses generated overall similar water content estimates, while ERT overestimated the initial water content because of the lack of unsaturated training dataset. The final water content was also lower than the initial porosity (0.56), which could be due to clay swell and porosity drop. For the heated column, the water content during the unsaturated period was also overestimated. During the period (between day 288 and 485) when the column was held at constant pressure mode, structural changes (fractures) were observed in CT scans. After the flow was re-established, these fractures were sealed promptly, while the dynamic changes in local porosity could have affected the model that tried to converge to initial porosity. Moreover, the mass balance water content of the heated column was also subject to pump leakage due to high salinity after day ~200.

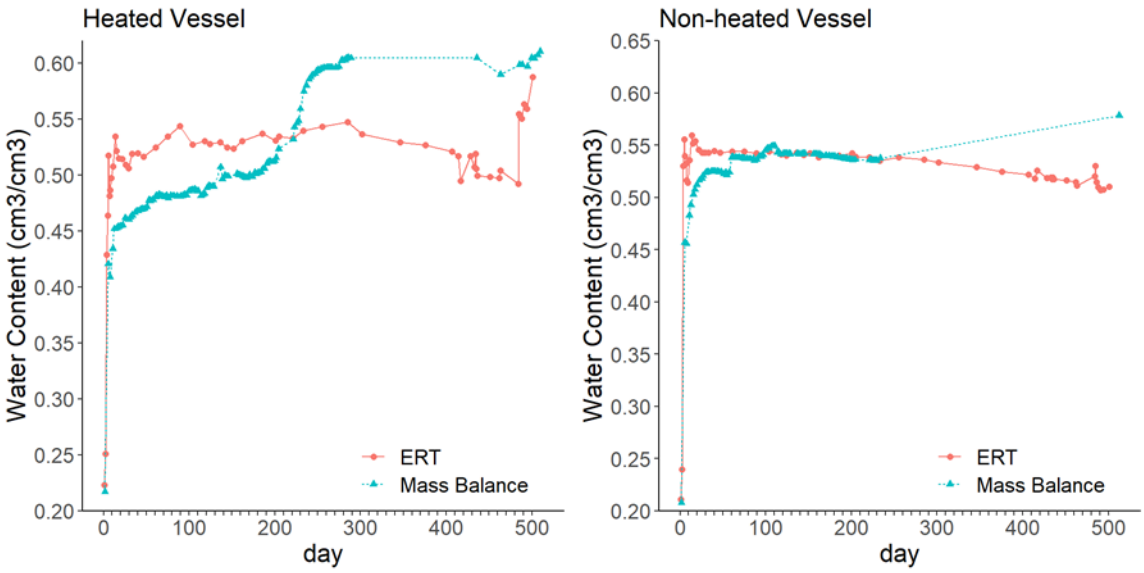

Figure 10-29 Mass balance water content versus ERT-derived water content from the mid-column depths.

The calibration results show that ERT can be used to capture local and temporal moisture variation given temperature, chemistry and porosity estimation inputs. In the next experiment, we would improve our ERT set-ups with (1) increased electrodes (60) and rods (6) for a full 3D resistivity tomography, and (2) an improved design of the electrodes for good contacts with the clay. These efforts could increase both data quality and coverage and reduce the needs for smoothing during the inversion simulation, resolving radial differences especially at the start of the infiltration. For the resistivity - water content calibration, we would also increase the number of thermocouples (12) for a more detailed temperature distribution. Also, the increased 3D coverage of ERT would allow a more spatially distributed calibration with CT.

10.5 Post-experimental Sampling

In this section, we present detailed sampling plans and characterizations after the heating and hydration tests. The objectives are to (1) verify the CT calibration curve by comparing CT density vs. gravitational bulk density, and help in improving the CT image interpretations; (2) obtain a detailed sample characterization dataset on the structural and chemical properties of bentonite after heating and hydration.

Sampling procedures

The sampling plan was developed according to the CT image observations for both heated and non-heated columns. Figure 10-30 presents examples to show the two tube samplers used and their locations in a sampling layer. For the non-heated column, each sampling layer was segmented into 3 sampling zones (R1, R2 and R3) by inserting 0.75'' thick rings at 6'', 4'' and 2'' diameters. The 6'' ring was inserted at the sand-clay boundary to help separating bentonite from sand. In R1 and R2, four 0.25-inch diameter samples were collected from each zone by the 1-inch long tubes, meanwhile eight and four 0625-inch diameter samples were collected separately from R1 and R2. In R3, five 0.25-in diameter samples were collected. For all the three sampling zones, the remaining bulk clay were collected and sealed in whirlpak bags. In the heated column, four 0.25-in diameter samples were collected in R3. Bulk bentonite samples in an additional zone (R4) at 1-inch diameter closest to the heater shaft (marked by the white circle in Figure 10-30) was also collected to investigate the bentonite behavior in the dry out zone.

When dismantling both columns, water flow was first stopped. For the non-heated column, pressure was step-wise reduced to atmospheric. For the heated column, heater was turned off after water flow was stopped, along with step-wise depressurization to eliminate any water evaporation. When cooled down, the two end caps were removed from the vessels. Both columns were CT scanned during the process to monitor if any structural changes in bentonite.

Samples were collected from the two ends of each column at the same time to minimize exposure of sample to air and any potential changes. Each sampling layer was labeled by its depth relative to the vessel ends, the size and location of each tube samplers (Figure 10-30(C)). After inserting the tubes, a CT scan was conducted so that the location of each sample and corresponding CT density distribution (Figure 10-30(D)) can be determined and correlated with the labels (Figure 10-30(C)). Figure 10-30(D) presents an example of the CT image showing the big and small tubes inserted to collect bentonite sample. Figure 10-30(E) is photograph of the 0.625-inch tube sample collected and frozen. In total over 800 bentonite samples were collected from the two columns at different locations and depths.

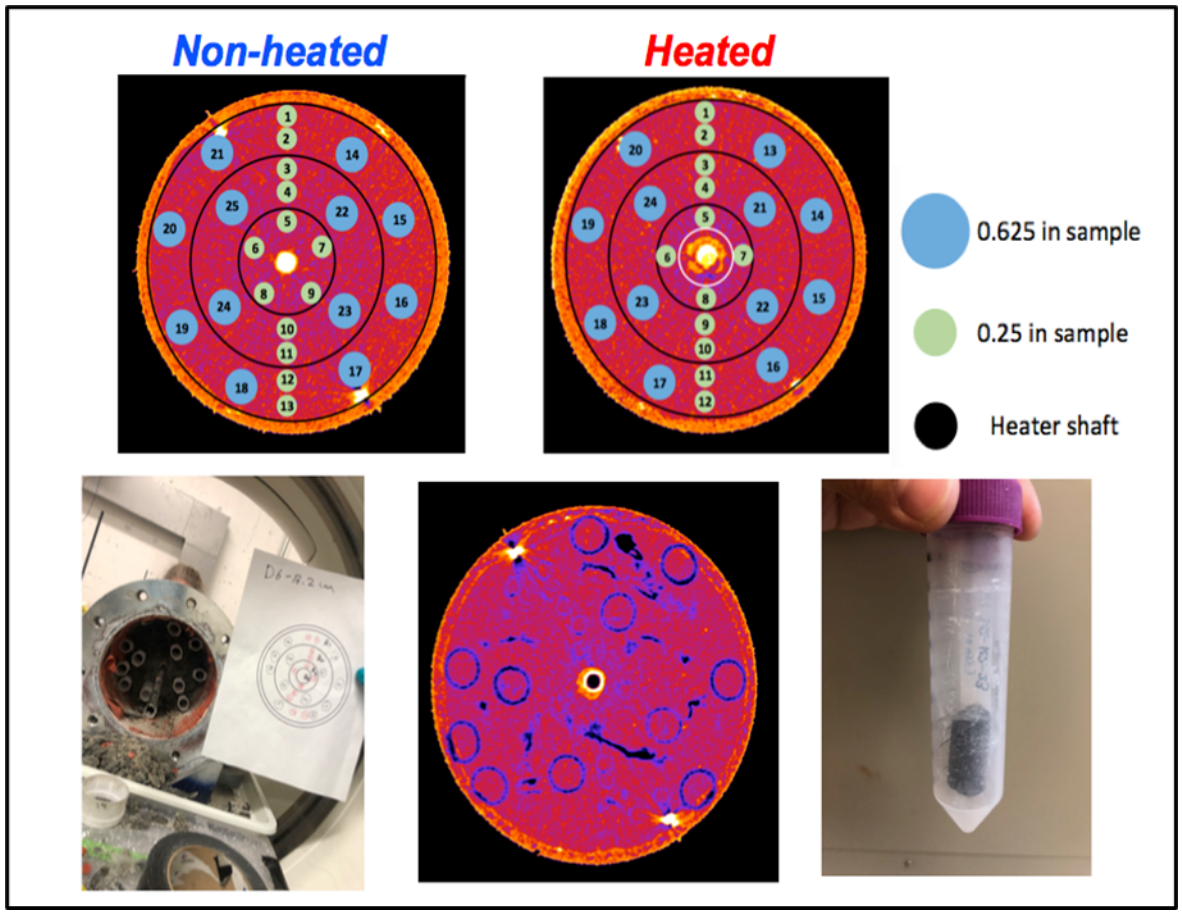

Figure 10-30 Procedures for the post-experimental samplings in the non-heated and heated columns. (A) and (B) are designed locations of two size tube samplers in each sampling layer, which were segmented to 3 and 4 sub-sampling zones in the non-heated and heated column, respectively. (C) is a photograph taken during the sampling with a copy drawing of the location of each sampler. (D) presents a CT image showing the corresponding sample layers and inserted samplers. (E) is a photograph of the 0.625-inch diameter, 1-inch-long sample in a tube sampler.

Sample characterizations: physical parameters

The relationship between CT number vs. density, i.e., the calibration curve, was obtained by scanning columns independently compacted with bentonite clay of different bulk wet density (see Figure 10-9). To further verify the calibration curve, seven samples collected into 0.625-inch tubes were CT scanned for precise volume measurements, along with their wet mass weighed. Figure 10-31compares the gravitational bulk wet density vs. interpreted CT density for the seven samples, with errors within 5%, indicating the effectiveness and precision of CT images in predicating bentonite bulk wet density. Assuming $\rho_{CT=}\rho_{wet}$, the clay dry density, porosity and water saturation can then be calculated as follows:

$$\rho_{dry} = \frac{m_{dry}}{m_{wet}/\rho_{CT}} \quad \textbf{Eq. 10-4}$$

$$\phi = 1 - \frac{\rho_{dry}}{\rho_{mineral}} \quad \textbf{Eq. 10-5}$$

$$s_w = \frac{m_{wet} - m_{dry}}{\phi\, m_{wet}/\rho_{CT}} \quad \textbf{Eq. 10-6}$$

where m_{dry} refers to the sample mass after oven dried, $\rho_{mineral}$ is the mineral density (=2.623g/cm^3). Figure 10-32 presents the bulk wet density (ρ_{CT}), water content (water mass/clay mass) and water saturation of samples obtained at different radial distance from the heater shaft and their variations at different depth for both columns.

In the non-heated column, the bulk wet density varies from 1.72 to 1.63 g/cm^3, showing a decrease trending towards to the heater shaft, similar to the CT density changes vs. radial distance to the heater shaft shown in Figure 10-13. The water contents, however, decrease in values from the boundary to 40 mm away from the center shaft, then keep constant at locations <40 mm away from the shaft. Figure 10-32 indicates high water saturations of samples at 1.0 (fully saturated by water) at 60-70 mm away from the center shaft, while the values gradually deceased to 0.9 at 40 mm and remained constant at locations closer to the shaft. It is also noted that the there were no considerable variations between sample layers for bulk wet density, water content and water saturations, indicating a radial symmetry of hydration was dominant from the sand layer to the center shaft, while water intrusion along the long-axis of the column was not considerable.

Figure 10-32 depicts that in the heated column bentonite was fully water saturated at 40-70 mm away from the heater shaft. The values gradually decreased to 0.90 at 40 mm and were constant at 7-40 mm away from the heater shaft. Similar to the non-heated column shown by Figure 10-31, no variations occurred along the depth. The bulk wet densities, however, showed a large decrease in values from 1.65 to 1.57 g/cm^3, at sampling depths of 21 and 23 cm and at 10-20 mm away from the heater shaft. On the contrary, water content increased from 0.45 to 0.55 at the same sampling locations. Note that at the depths of 21 and 23 cm, the two sampling layers are normal to the middle heater shaft, where the most pronounced heating effect is expected. These differences imply the impacts of heating and hydration on bentonite structure that were not observed in the non-heated column.

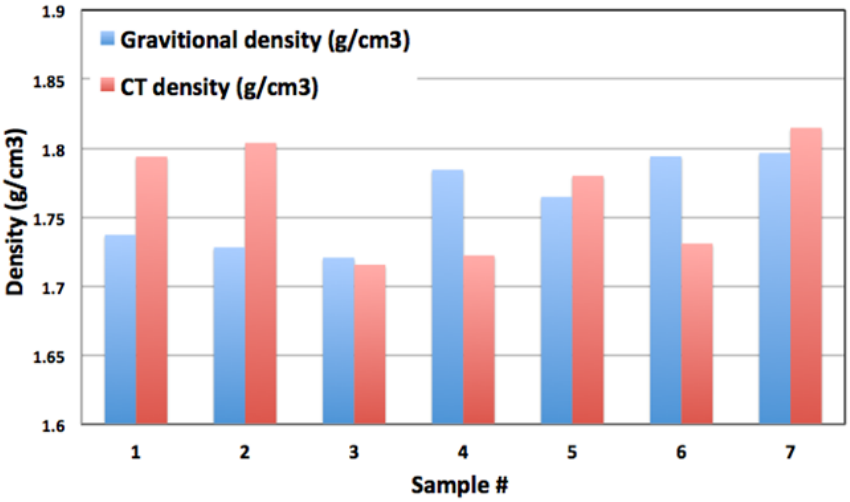

Figure 10-31 Comparisons of the bulk gravitational density vs. CT density for 7 collected bentonite samples

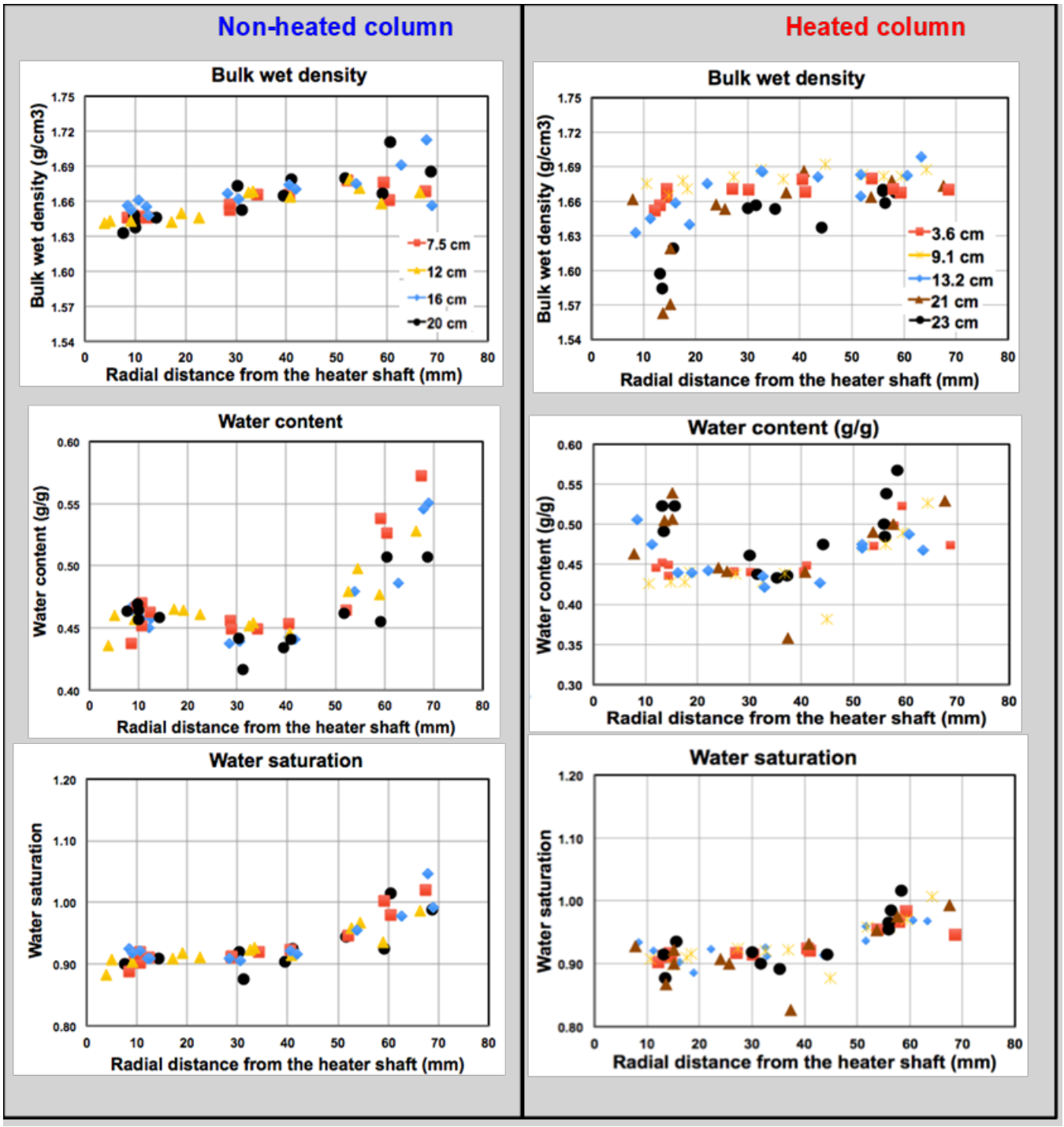

Figure 10-32 The bulk wet densities, water contents and water saturations of the post-experimental bentonite samples, and their variations as a function of the radial distance from the heater shaft. Samples were collected at different depths from the non-heated and heated columns.

To compare bentonite behavior in the non-heated and heated columns, and to better understand the heating impacts, we show in Figure 10-33 the bentonite porosity and dry density, and their variations at different sampling depths and radial distances from the heater shaft. In the non-heated column, the over

higher porosity and lower dry density of bentonite at 50-70 mm away from the center shaft indicate swelling of clay subject to water intrusion from the surrounding sand layer, which induced inward displacement in neighboring clay toward to the shaft, and thus decreased the porosity and increased dry density at 30-50 mm. At locations ~10 mm away from the shaft, the slight increase of porosity from 0.56 to 0.57 and a decrease of dry density from 1.16 to 1.12 g/cm^3 represent swelling of clay, resulting from hydration and water intrusion occurred in the inner bentonite. This swelling of clay, however, is much less significant compared to that occurred close to the clay and the boundary. The overall displacement is thus inward (marked by the blue arrows in Figure 10-33), which is consistent with the CT image observations discussed in Section 10.4.1.

Differing from the non-heated column, the porosity in the heated column was 0.60 at 10-20 mm away from the heater shaft, higher than that of the neighboring clay (0.56) and bentonite at the same location in the non-heated column (0.57). Correspondingly, the dry density at 10-20 mm away from the heater shaft is smaller. This increased clay porosity and decreased dry density indicate more pronounced swelling of clay at 10-20 mm away from the heater shaft than that in the non-heated column. Note that thermocouple *a* located at 11 mm away from the heater shaft (Figure 10-14) indicated larger swelling of clay close to the clay dry-out zone, which is consistent with changes in the porosity and dry clay density measured from *in-situ* bentonite samples.

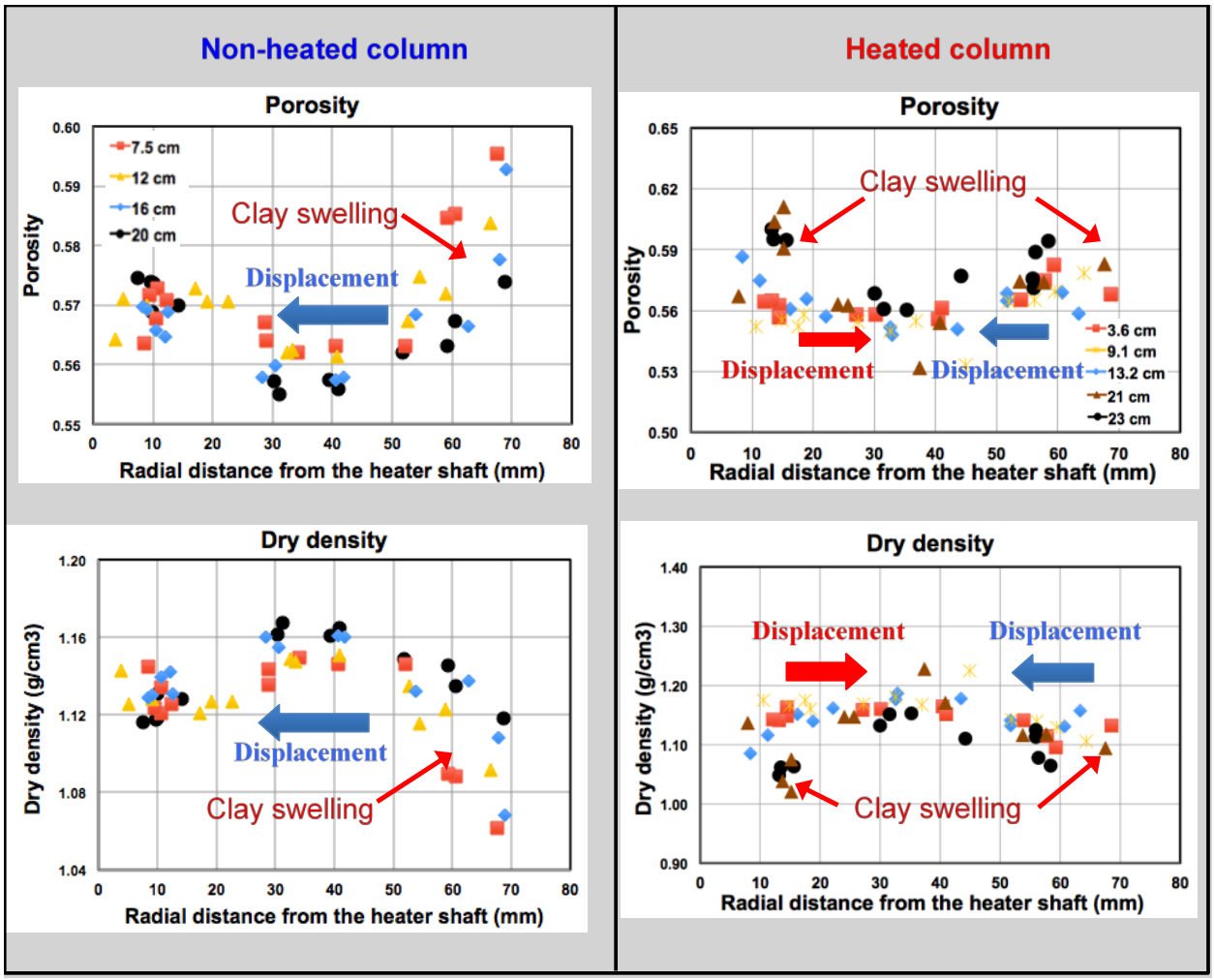

Figure 10-33 The porosity and dry density of the post-experimental bentonite samples, and their variations as a function of the radial distance from the heater shaft. Samples were collected at different depths from the non-heated and heated columns.

XRD analysis of the "HotBent" bentonite material

To characterize the crystalline phases in the "HotBent" samples, X-ray powder diffraction was used. The instrument employed was a Rigaku SmartLab working in a theta-theta Bragg-Brentano configuration, equipped with a spinning sample holder (to improve data collection statistics), and a D/teX Si strip linear detector. Filtered Cu Kα radiation was used, and an interval between 3° and 68° of 2θ was measured. Scanning time depended on the nature of the sample (e.g.,"wet" samples were measured at a faster pace than dry samples, to avoid dehydration issues).

The data were analyzed via the Rietveld method using the MAUD software, which is equipped with advanced tools for modeling both lattice preferred orientation and turbostratic disorder, two very important factors when working with materials containing smectites (see Lutterotti et al., 2009).

A series of different samples were chosen to monitor differences in mineralogical characteristics in function of the processes. The following samples were analyzed from the in-situ experiment: 1) One sample of material collected form the surface of the heating tube ("precipitate"). 2) Four samples from a section of the system with the heater, in the section by the inlet ("V1darN", where N is the distance from

the outer surface, with N=1 being the outside sample, and N=4 being the sample in the center of the section). 3) Four samples again from the heated vessel, but in a section at the middle ("V1dfrN"). 4) Four samples from an unheated vessel, center section ("V2dfrN"). 5) A sample of raw bentonite ("MX-80_raw").

All the samples from the vessels were collected and immediately sealed to prevent moisture loss. The samples from the vessels were opened immediately before each XRPD profile scan to be able to use the signal from the smectite basal peal to measure the hydration state of the smectite in the samples. Being sensitive to moisture changes, the sample preparation was done very quickly by filling a recess in the sample holders with the sample (usually with a consistency of a very thick paste) and flatten with a glass slide. The sample was then immediately scanned, with the time required to measure the whole main basal peak of smectite being around two minutes. This process minimizes the loss of moisture to the air for the time needed for the measurement.

The Rieveld analysis of the samples was rather challenging for several reasons: (1) Characteristics of the smectite phase(s). Montmorillonite typically displays low crystallinity, causing a (anisotropic) peak broadening. The sample preparation method causes preferred orientation of the clay particles at the surface, and a correction for this is needed. Montmorillonite typically displays a stacking disorder, and this characteristic needs to be modeled as well. The presence of more than one montmorillonite phase (e.g., a montmorillonite with two different hydration states needs to be modeled using two montmorillonite phases) makes the analysis more challenging (and slow). (2) Number and the amount of accessory phases. In addition to the montmorillonite issue, a sample with several phases (especially with low symmetry and/or low crystallinity) makes the analysis more challenging. The amount itself of accessory phases is another source of potential errors. In Rietveld analysis in multi-phase samples, it is commonly thought that a <1% by volume amount being non quantifiable, or non-detectable. But this number is strictly dependent on the nature of the sample: e.g., in sample with highly crystalline, high symmetry, phases this number can become much smaller. In the samples we analyzed numbers below 1% should not be trusted. But for some phases the main diffraction peak is present in parts of the profile with no overlapping, therefore the presence of a very small amount of phases is still clearly detectable (e.g., phlogopite, gypsum, pyrite), while other phases, such as feldspars, are more problematic. (3) Sample statistics. In the "wet" samples, given the amount of material available, the nature of the grains in the sample (and not being able to grind a powder from the samples) the sample statistics is sub-optimal, especially for minor phases, generating oscillations in the accessory phase amounts, for example, due to the presence of a few specific grains enriched in those accessory phases. (4) Lack of reliable measured structural models.

The results of all the analyses have been summarized in Table 10-2 and Figure 10-34. There are three montmorillonites, representing the three different hydration states found in the samples. The results have also been color-coded to represent three different segments of minerals: phyllosilicates (orange), other silicates (blue), and non-silicate phases (green). The results of the three groups of minerals are also shown in Figure 10-35 in a graph form, based on the quantitative phase analysis.

Table 10-2 XRD results from clay and precipitate

Phases	Precipitate	v1dar1	v1dar2	vidar3	v1dar4	v1dfr1	v1dfr2	v1dfr3	v1dfr4	v2dfr1	v2dfr2	v2dfr3	MX-80_raw
Montmorillonite 19Å (trihydrated)	0	57.9	73.4	69.8	65.4	63.3	62	63.7	36.4	7.8	12.6	49.6	0
Montmorillonite 16Å (dihydrated)	0	0	0	0	0	0	0	0	29.2	42.5	37.3	1.9	0
Montmorillonite 12.5Å (monohydrated)	0	0	0	0	0	0	0	0	0	0	0	0	78.5
Phlogopite	0	3.3	2	2.7	1.6	1.4	2.1	2.1	1.8	0.9	2.3	2.6	0.1
K-feldspar	0	0.8	1	1.8	1.3	0.5	1.1	1.5	0.9	2.4	3.1	3	1.2
Quartz	0	28.7	11	10.5	10.8	17	12.5	10.7	15.2	15.1	14.4	16.4	9.2
Cristobalite	0	3.6	3.9	3.6	4.5	3.9	4.2	2.4	0.1	5.6	6	8.3	3.5
Plagioclase	0	2.2	0.5	5.7	9.8	2.7	8.7	6.6	6.6	14.9	17.2	7.1	6.2
Calcite	0	0.2	0	0.1	0	0	0.4	0	0.1	3	2.9	0	0.9
Halite	0	0.1	0.1	0	0	0.1	0	0.1	0	0	0	0.3	0
Pyrite	0	0.5	0.6	0.5	0.4	0.3	0.6	0.5	0.9	0.7	0.3	0.9	0.4
Anhydrite	100	0	0.5	0.1	0	0	0	0	0	0	0	0	0
Gypsum	0	2.7	7	5.2	6.2	10.8	8.4	12.4	8.8	7.1	3.9	9.9	0

Phases	Precipitate	v1dar1	v1dar2	vidar3	v1dar4	v1dfr1	v1dfr2	v1dfr3	v1dfr4	v2dfr1	v2dfr2	v2dfr3	MX-80_raw
Clays	0	61.2	75.4	72.5	67	64.7	64.1	65.8	67.4	51.2	52.2	54.1	78.6
Lithics (silicates)	0	35.3	16.4	21.6	26.4	24.1	26.5	21.2	22.8	38	40.7	34.8	20.1
Other (sulfates, halides,...)	100	3.5	8.2	5.9	6.6	11.2	9.4	13	9.8	10.8	7.1	11.1	1.3

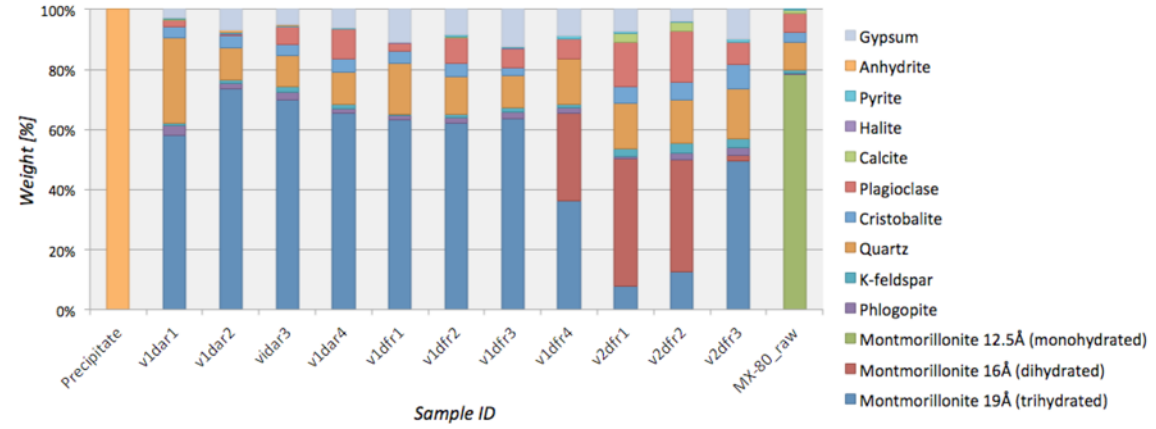

Figure 10-34 XRD results from clay and precipitate

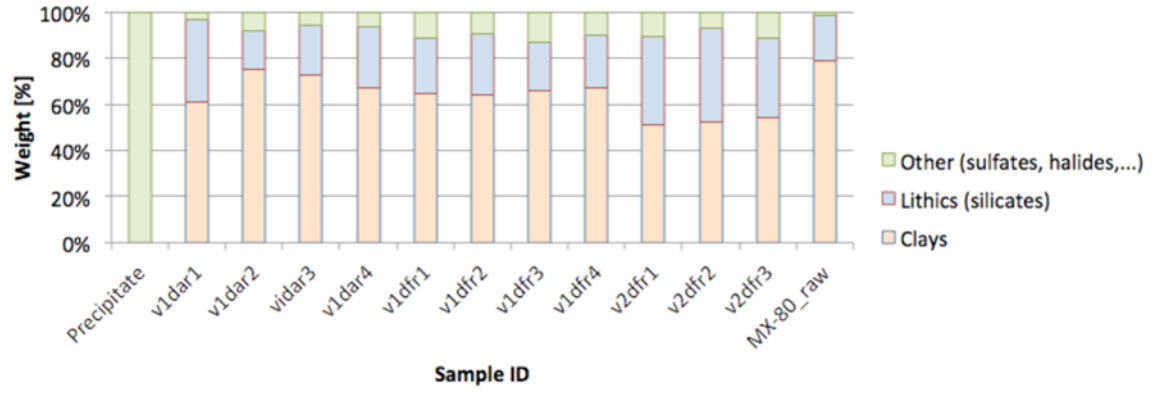

Figure 10-35 Clays, Lithics, and other mineral phases as determined by XRD analysis.

The results show several interesting features. The most evident one is that the precipitated material is pure anhydrite. The presence of anhydrite is not surprising by itself, since the presence of gypsum (highly soluble in water) in the bulk material is expected to provide the sulfate and Ca able to precipitate it, given favorable conditions. The most interesting feature is the absence of any other phase: if the bentonite would have been in direct contact with the heating element, then the only chance for anhydrite to precipitate would have likely been as a cementing phase, as some carbonates do in shales. These results suggest that a gap between the heating element and the bentonite was present, providing the space for anhydrite to crystallize. It cannot be excluded that a mechanism similar in concept to the sulfate attack described in concrete weathering was present, where the crystallization of anhydrite also pushed the

bentonite increasing the gap filled with anhydrite. No anhydrite was found anywhere in any sample, even in the sample taken in the heated sample closer to the heater, strengthening the hypothesis above of a very local phenomenon occurring just in contact with the heating element.

The second most interesting result is related to the behavior of the smectite. In the "raw" bentonite material we found that the hydration state compatible with the basal d-spacing is with a single water molecule per reduced unit cell. In the samples collected from the heated vessel all the samples contain montmorillonite with three water molecules per reduced unit cell, except for the sample closer to the heating element ("V1dfr4") where about 45% of the total montmorillonite amount is dihydrated (montmorillonite 16A), showing a loss in moisture as compared to the montmorillonite 19A (Figure 10-34). The sample without the heater (V2) is dryer (this was also directly observable during the sample preparation, being more brittle in nature), with the hydration level in the montmorillonite increasing towards the center of the vessel, but never reaching a 100% amount of tri-hydrated montmorillonite. No amounts of the mono-hydrated structure, as the starting dry material, have been found anywhere.

The amount of quartz displays some large variability, but this is mostly due to the presence of sand grains in the sample, left from the outer buffer sand layer of the vessels (samples of the vessels where N=1 tend to have larger amounts of quartz because of the contamination with sand).

Relatively large amount of gypsum is present throughout the samples in the vessels, highlighting a substantial source for the precipitation of anhydrite. The oscillations in gypsum amounts seems to suggest its presence in specific grains, rather than being finely distributed in the bentonite. Interestingly, in the "raw" bentonite sample no gypsum is found (different batch of the material?). The similar (low) amount of pyrite excludes that an oxidation of the sulfur in pyrite provided the sulfate needed to crystallize such a large amount of gypsum due to weathering.

The Rietveld fit of the precipitate collected from the crust surrounding the heater is shown in Figure 10-36. The Rietveld fit of the V1dfr4 (sample from the heated vessel close to the heater) in shown in Figure 10-37. Note the shoulder on the main montmorillonite peak that required the use of both tri- and di- hydrated montmorillonite structures to achieve an acceptable fit.

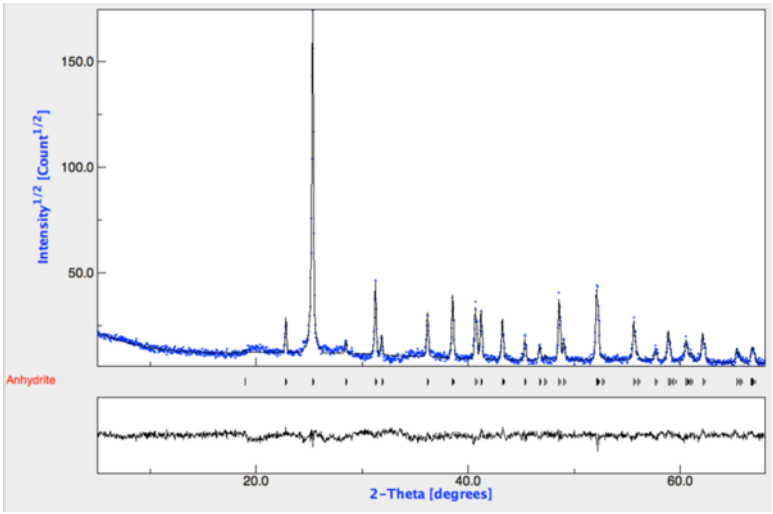

Figure 10-36 Rietveld fit of precipitate sample.

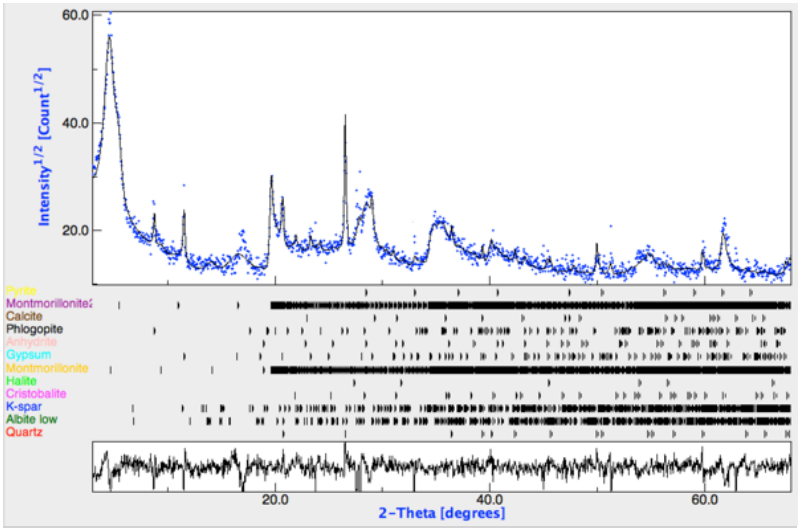

Figure 10-37 Rietveld fit of V1dfr4 sample.

The analysis revealed the probable mechanisms involved it the precipitation of the anhydrite layer around the heather, and the measurements of the samples preserving their hydration state, albeit being more difficult and time-consuming, shed some light about the hydration state of the montmorillonite in the samples. This information coupled with other measurement sensitive to water migration can provide a comprehensive story of the behavior of water in these simulated engineered barriers.

Total digestion of removed clay material

Material from the 0.25 inch samples, the general position of which are shown in Figure 10-30 were used for determination of the cation content in the removed clay. Before digestion, the samples were dried and ground into a fine powder. The digestion was conducted using EPA method 3051A, digested with concentrated HNO_3 and HCl at 175°C in the microwave. The result shows only 11- 20% solids are digestible. As explained during the sampling plan description, V1 is the heated vessel and V2 is the non-heated vessel. Samples were extracted by ring, with R1 being closest to the sand layer, and R4 adjacent to the heater. Figure 10-38 shows the results of selected metals from the overall results, and Table 10-3 compiles results from major cations. In the figure, the red color designates V1, blue V2, and green the original MX-80 clay used for packing. The two grouping for V1 are samples taken near the inlet (da) and samples taken near the sample center (df). For V2 these two groups are plotted together. In Figure 10-35, metals were selected that aligned with the effluent data, including those cations which were both flushed and retained from the clay. The specific samples selected were from V1 (heated) were layer da (depth 0 cm) samples R1- R4 and layer df (depth 15 cm) R1-R4. From V2 (non-heated) Layers da R1 and R3, and layer df R1 1R3. The original MX-80 clay was also included.

In Figure 10-38 (a) and (c), silicon and boron show clear differences in amount recovered from the digested samples. In Figure 10-38(b), manganese appears to be depleted at the center of the sample near the heater. For the other metals no clear trend can be seen from this data, and more replicates will have to be completed to understand the results. In addition, pore water extraction will be completed and analyzed for both cations and anions to understand which chemicals are more active in the clay pores. It should be noted also that the vessel was constructed of Al, and substantial corrosion was observed in the heated vessel. However, these results no significant difference in the Al content in the clay between the heated and non-heated vessel. Calcium showed retention in the column and we know from the XRD results that anhydrite, $CaSO_4$, precipitated on the heater shaft, which like accounts for the Ca retention observed.

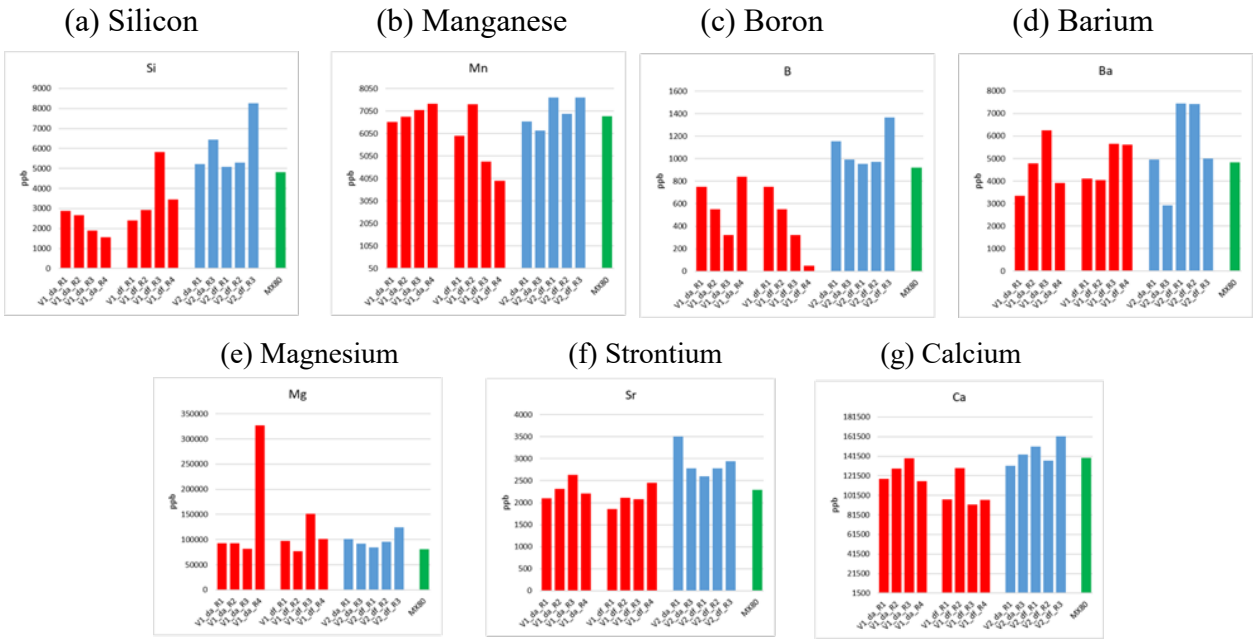

Figure 10-38 Selected cations (in ppb) from total digestion of extracted clay samples. Si, Mn, B, Ba showed flushing from the effluent. Mg, Sr, Ca showed retention in the column

Table 10-3 Major cations found in the digested sample, in ppm

Sample ID	Al ppm	Fe ppm	Na ppm	Ca ppm	Mg ppm	K ppm	Mn ppm	P ppm	Ba ppm	Si ppm	Sr ppm	Ti ppm	B ppm	Pb ppm	Th ppm	U ppm
V1_da_R1	633.1	284.4	229.5	118.2	92.6	30.0	6.56	5.78	3.35	2.87	2.10	1.25	0.92	0.68	0.56	0.16
V1_da_R2	639.5	311.1	228.1	128.9	92.5	30.0	6.79	5.52	4.78	2.67	2.32	1.13	0.93	0.62	0.58	0.16
V1_da_R3	500.7	297.9	236.3	139.6	81.3	29.6	7.10	6.01	6.25	1.89	2.64	0.87	0.82	0.69	0.60	0.16
V1_da_R4	583.9	277.0	199.3	115.9	327.1	20.8	7.38	5.41	3.91	1.57	2.20	0.70	0.75	0.58	0.55	0.17
V1_df_R1	655.2	310.8	244.1	97.5	97.2	29.5	5.95	5.47	4.11	2.41	1.86	1.25	0.55	4.38	0.58	0.16
V1_df_R2	438.8	191.2	239.3	129.6	77.0	28.1	7.34	5.70	4.05	2.92	2.11	0.92	0.32	0.68	0.58	0.16
V1_df_R3	744.2	300.7	229.4	92.1	151.0	26.1	4.80	5.55	5.67	5.82	2.08	1.41	0.05	0.62	0.59	0.17
V1_df_R4	713.8	287.4	222.5	96.8	101.6	29.8	3.95	5.44	5.62	3.45	2.45	2.17	0.84	0.67	0.58	0.16
V2_da_R1	670.2	215.1	229.3	131.9	101.4	30.0	6.58	5.30	4.95	5.23	3.50	1.35	1.15	0.68	0.58	0.15
V2_da_R3	593.6	227.6	222.3	143.4	91.6	27.8	6.18	5.27	2.92	6.45	2.78	1.17	0.99	0.64	0.57	0.15
V2_df_R1	451.9	259.6	246.1	151.3	84.4	30.7	7.65	6.07	7.44	5.09	2.60	0.90	0.95	0.70	0.67	0.18
V2_df_R2	583.7	209.1	235.1	137.2	95.4	31.1	6.92	5.86	7.42	5.30	2.78	1.05	0.97	0.71	0.62	0.16
V2_df_R3	825.0	251.5	247.3	161.6	124.2	33.2	7.65	6.08	5.00	8.26	2.94	2.63	1.37	0.70	0.63	0.18
MX80	485.9	182.9	235.6	139.9	80.7	27.6	6.81	5.16	4.82	4.81	2.29	0.90	0.92	0.87	0.57	0.16

10.6 Summary and Future Work

During FY18-19, pressure columns were designed, built, and instrumented for the HotBENT-lab experiment. In June 2019, hydration was started in both columns, and heating was applied to one column. In FY19-21, columns were monitored continuously for hydration, temperature distribution, effluent chemistry, and density changes. Detailed in this report are results that show steady state hydration for both columns, with some density, hydration and chemistry differences between the heated and non-heated condition. In December 2020, both columns were dismantled, and subsequent analysis of the clay has been completed including hydration, mineralogy, and chemical analysis.

Major results of observations in the column test are:

- CT imaging clearly showed the hydration front moving radially inward. Density measurements from CT images were also indicated that clay swelled upon hydration, which caused clay swelling at the clay/sand interface, localized compaction, and closed fast flow paths created from column packing heterogeneities.

- In the center of the heated column, the bentonite showed lower water saturation, but higher CT density due to mineral precipitation. XRD analysis demonstrated that this precipitation was 100% anhydrite.

- Bentonite was compacted before the arrival of hydration front (e.g., at the early time) due to swelling at area where is hydrated, and then swelled after the arrival of hydration front. Spatially it exhibits a displacement first moving inwards towards the heater and then moved back to its initial location as hydration propagated to the center.

- The hydration of bentonite was delayed in the heated-column in comparison with the non-heated column, whereas the former presented larger compaction of inner bentonite under heating, followed by larger and sustained swelling near the heater shaft.

- Heated and non-heated columns differed in the chemical composition of effluent water with the heated column showing lower sulfate, calcium, and magnesium concentration, but higher silicon, potassium and manganese concentration.

- XRD results shows differences in the hydration of the clays and accumulation of soluble mineral phases from the influent water.

- The Al vessels, made of alloy 7071, were coated with RTV silicone to both prevent corrosion and provide insulation for the ERT probes. However, substantial corrosion was observed in the heated vessel. For the next experiment, the RTV was removed, the vessels were anodized, and coated with a viton sealant to make them more resistant to corrosion.

10.6.1 External collaborations on sample characterization

Subsequent to sampling we have had the opportunity to share some samples with external researchers to extend the analysis beyond the capabilities at LBNL. In particular:

(1). Samples were sent to Dr. Carlos Jove-Colon of SNL to test an application of a specialized XRD technique to evaluate hydration and mineralization changes in the clay.

(2). Samples were sent to Dr. Xiao-Ying Yu of PNNL to examine samples using TOF-SIMS.

(3). Long cores were removed from both vessels and prepared for micro-CT analysis at the Advanced Light Source (ALS) to closer investigate the clay structures in the heated and non-heated vessels.

10.6.2 Future plans for repacking new column

For the remainder of FY21, we will complete post-experimental characterization on bentonite samples. We will also start packing two new columns, with bentonite clay collected from the HotBent field site with an increased dry density to 1.5 g/cm^3. More ERT arrays and thermocouple sensors will be emplaced

to improve the ERT monitoring and temperature profile. New strain gauges will be implemented on the vessel shell for clay swelling pressure measurements. More markers will be emplaced in the column for more detailed characterizations on the spatio-temporal deformation. We will also change water recipe to simulate the Grimsel groundwater, which is significantly lower in salt content.

11. Investigation of the Impact of High Temperature on EBS Bentonite with THMC Modeling

11.1 Introduction

Radioactive waste from spent fuel emanates a significant amount of thermal energy due to decay processes, which causes temperature increases in the surrounding environment particularly in the early stages of waste emplacement. The temperature to which the EBS and natural rock can be exposed is one of the most important design variables for a geological repository because it determines waste package spacing, the distance between disposal galleries, and therefore the overall size (and cost) of repository for a given amount of heat-emanating waste (Horseman & McEwen, 1996). This is especially important for a clay repository because argillaceous rocks have relatively small heat conductivity. Temperature governs chemical alteration and the subsequent changes in mechanical properties of the EBS. A high temperature could result in chemical alteration of buffer and backfill materials (bentonite) within the EBS through illitization and cementation, which compromise the function of these EBS components by reducing their plasticity and capability to swell when wetting (Pusch and Karnland, 1996; Pusch et al., 2010; Wersin et al., 2007). The swelling capability of clay minerals within the bentonite is important for sealing gaps between bentonite blocks, between bentonite and other EBS components, and between the EBS and the surrounding host rock. The chemical alteration may also occur in the near-field host rock, which could reduce the clay capability for self-sealing within the excavation damaged zone (EDZ). Because the permeability of clay rock is low, a high temperature may induce significant pore pressure build-up (through pore water expansion and vaporization) in the near field, which could generate adverse mechanical deformation (such as fracturing), damaging the integrity of the host rock (Horseman & McEwen, 1996).

Evaluation of the long-term geochemical alteration of bentonite buffer and its effect on the mechanical process of bentonite requires coupled THMC models. In this multiple years' effort, we have developed simulators that are capable of simulating THMC simultaneously, TOUGHREACT-FLAC3D, implemented several schemes for MC coupling, and conducted coupled THMC simulations for a generic argillite repository, focusing on illitization and the resulting change in swelling stress in bentonite and argillite host rock (Zheng et. al, 2015, Zheng et al., 2017, Xu et al., 2021). The coupling between chemical and mechanical processes was implemented via an Extended Linear Swelling Model (ELSM), the double structure Barcelona Expansive Model (BExM) (Sánchez et al., 2005; Gens, 2010; Guimarães et al., 2013). In FY21, we continued using MC couping via BExM to examine the mechanical evolution of bentonite under high temperatures.

While THMC simulations of generic case shed light on the anticipated alteration of bentonite and its impact on the swelling stress of bentonite, the underline assumptions in the model, the conceptualization of the THMC processes, the parameterizations of the key constitutive relationships need to be tested against experimental data. Although FEBEX in situ test (Chapter 9 in this report) provided a unique chance to test the THMC model with a heating temperature of 100 oC, the THMC model under high temperature, namely 200 oC, has not been tested yet. Data collected in the high-temperature heating and hydration column experiments for MX-80 bentonite (Chapter 7) can be used to test the THMC model at column scale and will prepare us for testing THMC model with data collected at HotBENT field test. Thus, the modeling effort was dedicated to interpreting the high temperature column tests, starting with a simple TH model, and gradually increasing the level of complexity to THM, eventually THMC model. In FY21, we have completed the preliminary THM model, which will be reported in the second half of this chapter.

11.2 Generic THMC Model for an Argillite Repository Using BExM

One of the key constitutive relationships in the THMC model is MC coupling. The earlier model effort (Zheng et al., 2015b; Zheng et al., 2017) employed an Extended Linear Swelling Model (ELSM), which is simple, and numerically stable, but does not describe the transient state of swelling. Therefore, in the later modeling effort (Zheng et al., 2019; Zheng et al., 2020b), MC coupling via BExM was implemented in TOUGHREACT-FLAC3D. THMC model for the generic case using BExM allows not only quantify the impact of chemical changes on the swelling stress, but also analysis of the stress path. Because the model used in this report has been reported in previous milestone reports (e.g. Zheng et al., 2019), we briefly describe MC coupling via BExM and modeling scenario first and then focus on the discussion of the stress path.

11.2.1 Barcelona Expansive Model (BExM) for MC Coupling

The numerical simulations in this study are conducted with TOUGHREACT-FLAC3D, which sequentially couples the multiphase fluid flow and reactive transport simulator, TOUGHREACT (Xu et al., 2011), with the finite-difference geomechanical code FLAC3D (Itasca, 2009). The coupling of TOUGHREACT and FLAC3D was initially developed in the work by Zheng et al. (2012) to provide the necessary numerical framework for modeling fully coupled THMC processes. Recently, the model was equipped with multiple constitutive models, such as the dual structural BExM and ELSM.

For unsaturated soils, usually, only the macrostructure is considered in a constitutive model, such as the Barcelona Basic Model (BBM). The microstructure is incorporated to extend BBM to a dual structure model such as BExM, which enables simulating the behavior of expansive soils, such as the dependency of swelling strains and swelling pressures on the initial stress state and the stress path, strain accumulation upon suction cycles and secondary swelling. Thus, in the dual structure model, the total volume (V), the total void ratio (e), and porosity (ϕ), of the material are divided into a micro-structural part and a macro-structural part. The microstructure can swell to invade the macro-porosity, depending on the mechanical confinement and load level. This is relevant when considering permeability changes during the soil swelling because fluid flow takes place mostly through the macro-porosity, which is not proportional to the total strain and deformation of the expansive soil. Equations to describe the mechanical behavior of micro-structural and macro-structural levels and the interaction between structural levels are not expressed here for the sake of simplicity.

A one-way coupling approach, in which chemical changes affect mechanical behaviors of bentonite through the evolution of volume fraction of smectite, exchangeable cation concentration, and ionic strength (via osmotic suction), is utilized in this section. These effects are taken into account through BExM. The mathematical formulations for C-M coupling are summarized below.

The original BExM predicts the micro-strains induced by the effective stress for the whole microstructure, ignoring the effects of the evolution of volume fraction of smectite. When the material is hydrated, only the smectite in the micro-structures interacts with the water invasion and swells. Here, we introduce the volume fraction of smectite, f_s, into the micro-structure in BExM for C-M coupling. The swelling capacity of the material should be proportional to the volume fraction of smectite. Thus, the micro-structural volumetric strains are assumed to depend on the change in the microstructural effective stress as follows:

$$\mathrm{d}\varepsilon_{vm}^{e} = \frac{f_s}{K_m}\mathrm{d}\hat{p} \qquad \textbf{Eq. 11-1}$$

where $\hat{p} = p + s_m$, $\hat{p}$ is the effective mean stress, p is the net mean stress, which is the total mean stress $\bar{\sigma}$ minus gas pressure p_g, and s_m is the microstructural suction. The total suction, s_m, contains two components, matric suction, s, and osmotic suction, s_o, i.e. $s_m = s + s_o$. Apparently, liquid saturation affects the suction through the matric suction term, s. The effect of ionic strength of the pore water on microstructural strain is carried out via the osmotic suction, which is computed as:

$$s_o = -10^{-6}\frac{RT}{V_w}\ln a_w \qquad \textbf{Eq. 11-2}$$

where V_w is the molar volume of water (in m^3/mol), R is the ideal gas constant, T is the temperature (in K), and a_w is the activity of water. a_w is calculated in TOUGHREACT (Xu *et al.*, 2011) as follows:

$$\ln a_w = -\Phi m^* \frac{1}{55.51} \qquad \textbf{Eq. 11-3}$$

where Φ is the osmotic coefficient of the solution and m^* is the sum of the molarities of all species in the solution.

In Eq. 11-1, K_m is calculated as

$$K_m = \frac{e^{\alpha_m \hat{p}}}{\beta_m} \qquad \textbf{Eq. 11-4}$$

where α_m is the material parameter. The effect of exchangeable cations is linked to mechanics through the dependence of β_m (Eq. 11-5) on exchangeable cation concentration as shown in the following equation (Gens, 2010):

$$\beta_m = \sum_i \beta_m^i x_i \qquad \textbf{Eq. 11-5}$$

Gens (2010) and Guimaraes *et al.* (2013) proposed that β_m^i is proportional to the ionic hydrated radius and inversely, proportional to its valence. β_m is the sum over ionic species. Based on this hypothesis, we will calibrate the values of β_m^i for different cations against laboratory experiments.

11.2.2 Modeling Scenarios

The model is applied to a hypothetical bentonite-backfilled nuclear waste repository, which involves a horizontal nuclear waste emplacement tunnel at 500 m depth in Opalinus clay (Figure 11-1, from Rutqvist et al., 2013). The case is a pseudo-2D model with Y-axis aligned parallel to the tunnel, with 1 m thickness in y. The Z-axis is vertical, while the horizontal X-axis is perpendicular to the tunnel.

An initial stress field is imposed by the self-weight of the rock mass. Zero normal displacements are prescribed on the lateral boundaries of the model. Zero stress is applied to the top and vertical displacements are prevented at the bottom. Liquid pressure is constantly constrained at the top and bottom, and the model domain is in a hydrostatic state. The initial temperature at the top is 11 ºC, while it is 38 ºC at the bottom, with a thermal gradient of 27 ºC /km along with the depth. The model simulation was conducted in a non-isothermal mode with a time-dependent heat power input. The power curve in Figure 11-1 was scaled from representative heating data from the U.S. DOE's Used Fuel Disposition campaign for Pressurized Water Reactor (PWR) used fuel for the current "high T" case. This heat load is

then scaled in the 2D model to represent an equivalent line load, which depends on the assumed spacing between individual waste packages along an emplacement tunnel. The heat load corresponds to an initial thermal power of 520 W/m along the length of the heater. The EBS bentonite has an initial water saturation of 65% and the argillite is fully saturated. From time zero, the EBS bentonite undergoes simultaneously re-saturation, heating, chemical alteration, and stress changes.

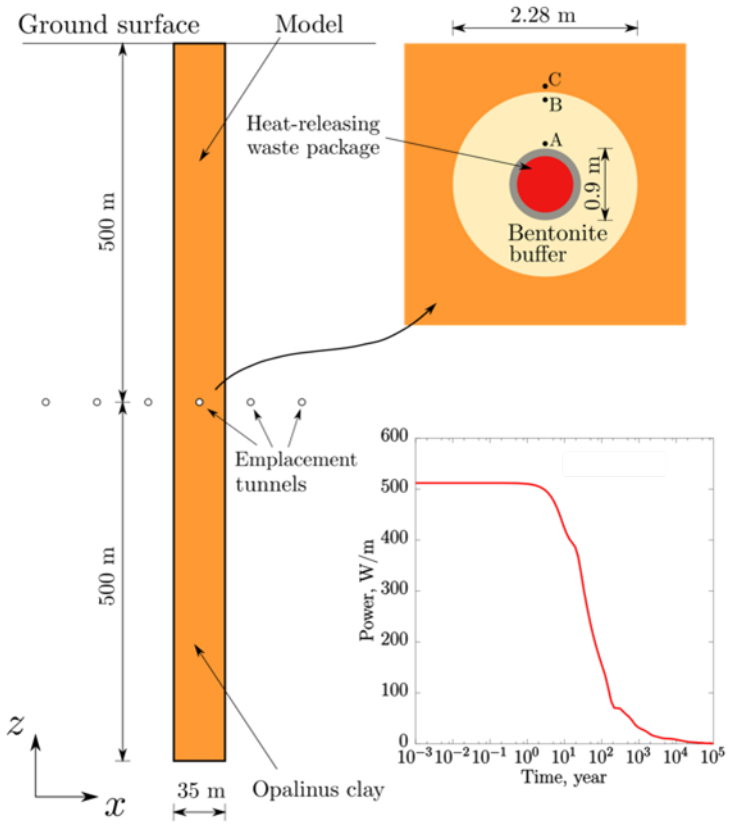

Figure 11-1 Domain for the test example of a bentonite back-filled horizontal emplacement drift at 500 m (Rutqvist et al., 2013). Modeling monitoring points: A: inside the bentonite near the canister, B: inside the bentonite and near the EBS-NS interface, C: inside the clay rock formation and near the EBS-NS interface. Power curves in simulations: 200 ºC peak temperature in the buffer.

11.2.3 Model Results

As aforementioned, C-M coupling is achieved through the dual-structure BExM model, allowing us to evaluate how the chemical changes may affect the mechanical behavior of the EBS bentonite in terms of effective/net and total stress. The chemical effects considered in the model come from three components, mass fraction of smectite, exchangeable cation concentration, and osmotic suction, and they occur in addition to strongly coupled THMC processes induced in this early repository phase due to (1) waste canister emplacement and waste heat decay, (2) backfilling with bentonite which is heated near the waste canisters and hydrates from the host rock side, (3) pore water and gas pressure changes from thermal expansion, hydration, and swelling, (4) stress redistribution due to swelling pressure, and thermal expansion, and (5) chemical reactions triggered by flow and transport and temperature changes. These processes are coupled in many ways and are often associated with strong changes in material properties, such as the permeability of the bentonite being a function of hydration. To set the stage for discussing the stress path, we recap some THC results first.

11.2.3.1 THC Results

We analyze the evolution of THC behavior by looking at two selected locations in the bentonite, one being Point A adjacent to the waste canister and the second being Point B near the host rock wall (see locations depicted in Figure 11-1). Figure 11-2 (a), (b), and (c) show the temperature changes, the evolution of the pore pressure, and the liquid saturation at Points A and B, respectively. At Point A, near the heat source, the temperature reaches up to 200 °C at around 20 years and then slowly decreases to the ambient temperature, 25 °C, after 100,000 years. Point B has a lower maximum temperature, about 170 °C, and a slightly slower initial temperature increase, because of the longer distance to the heater. The liquid saturation at Point A decreases firstly due to evaporation in the vicinity of the waste package and reaches its minimum in about 1 year (Figure 11-2 (c)). Then, the saturation starts to increase due to water inflow from the surrounding Opalinus Clay; Point A reaches full saturation in about 20 years. Point B is close to the host rock, so it does not go through any dehydration and becomes fully saturated in around 8 years. There is only a slight difference in the pore pressure between Points A and B (Figure 11-2 (b)). Both start out at the atmospheric pressure (the bentonite is initially at partial saturation). Since Point B is closer to the host rock than Point A, the pore pressure at Point B increases earlier than point A. Pore pressures peak at 10.5 MPa at around 100 years, then decrease to 2 MPa at around 30,000 years (when the temperature has decreased to almost ambient), and then they increase again to reach the hydrostatic equilibrium.

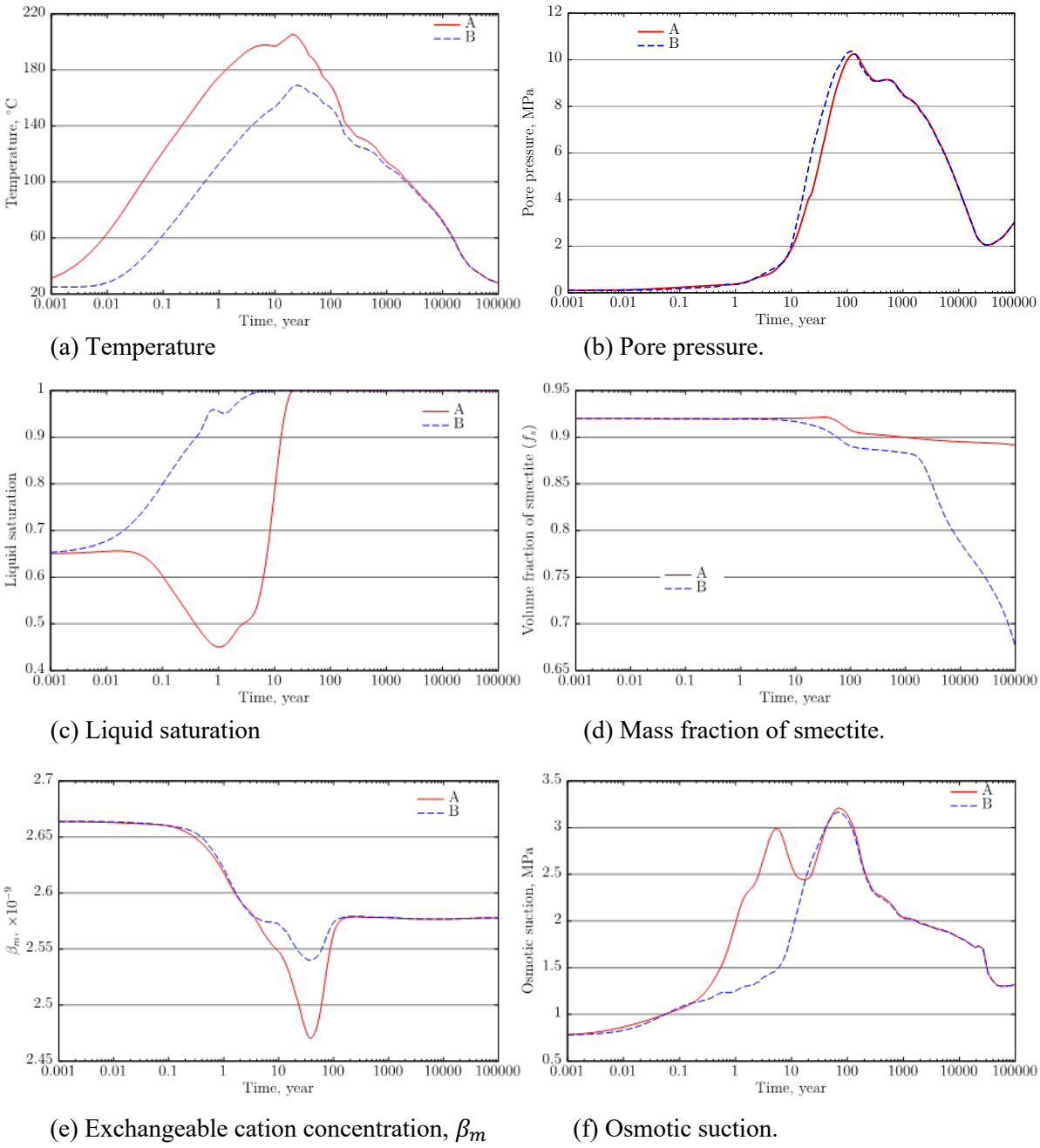

Figure 11-2 Simulation results of THMC evolution at Points A and B within FEBEX bentonite.

The chemical behavior of bentonite under high temperature has been studied extensively and the amount of smectite varied greatly depending on the thermal and chemical conditions. Our model shows the dissolution of smectite, in particular in the bentonite region close to the host rock (Figure 11-2(d)). The mass fraction of smectite, f_s, decreases from 92% to 89.1% at Point A, and to 67.6% at Point B. Figure 11-2(e) shows the evolution of β_m at Points A and B. In the current model, β_m depends on the concentration of the exchangeable cations, Na^+, K^+, Ca^{2+}, and Mg^{2+}. The model predicts a reduction of β_m from 2.66×10^{-9} to 2.48×10^{-9} at Point A and from 2.66×10^{-9} to 2.54×10^{-9} at Point B in the first 40 years (Figure 11-2(e)), which is due to exchangeable K^+ being replaced by exchangeable Na^+. After that, both β_m values recover back to 2.58×10^{-9}. The increases of β_m indicates the accumulation of the

exchangeable cations in the interlayer space of bentonite, resulting in that the adsorption of water is reduced, and, in turn, the swelling of bentonite decreases. The impact will be that the degree of swelling stress increment due to resaturation could be suppressed during the first 40 years due to the initial drop of β_m, but should then rise since β_m bounces back. Figure 11-2(f) shows the evolution of osmotic suction at Points A and B. An increase of osmotic suction indicates the water movement in the porous medium is suppressed, as a result of that, it tends to reduce the swelling of bentonite, whereas a decrease of osmotic suction enhances swelling. For Point A, the osmotic suction shows a two-peak behavior, with one peak of about 3 MPa after 3 years and the second at 3.25 MPa after 80 years, then starts to decrease until the end of the simulation. At Point B, the peak magnitude of 3.25 MPa is reached at around 80 years. The osmotic suction reduces to 1.3 MPa at both points by the end of the simulation.

11.2.3.2 Mechanical Results

To better understand the transient mechanical behavior of the swelling clay and how the BExM represents this behavior, we discuss here the evolution of both macro- and micro-structures. We start by analyzing the stress path at Points A and B as predicted with the BExM. Figure 11-3 presents the stress path in the 3D q-p-s_m space and shows the corresponding projection onto the p-s_m plane. Figure 11-4 (a) and (b) display the 2D stress path again together with the evolution of p_0 in terms of suction. Figure 11-4(c) and (d) present the changes of void ratio (macro, micro and total) in terms of suction. Figure 11-4(e) and (f) depict the evolution of the values of the interaction functions during the various stages of the analysis.

Very early on after waste and bentonite emplacement, since thermal effects are not strong yet and the temperature is still relatively low, the bentonite at Point A starts to swell, and the interaction function f_{is} is triggered, as Figure 11-4(e) shows. Later when the temperature rises beyond 100°C, the bentonite at Point A is subjected to drying—the liquid saturation decreases, and the suction increases, activating a MC mechanism at the micro-scale. The interaction function f_{ic} is positive in Figure 11-4(e) and induces small compressive plastic macro-structural deformation. Moreover, confinement accumulation from the external zones of the buffer and the host rock leads to contraction of the macro-structure due to the increase of the mean net stress. As a result, the macro-structure is compacted, as shown by the growth of p_0 in Figure 11-4(a), and the reduction of total void ratio in Figure 11-4(c). After about one year, the bentonite at Point A returns to hydration, as fluids from the host rock migrate towards this location: the liquid saturation increases again, as shown in Figure 11-4(c), and suction subsequently decreases, resulting in swelling of bentonite and activation of the interaction function f_{is}. As Figure 11-4F(e) displays, f_{is} is positive and induces tensile plastic macro-structural strain, but then it changes to negative and, consequently, induces compressive plastic strain. The mean net stress still increases during this stage, which results in macro-structural contraction. However, at this stage, the temperature increases above 180 °C (Figure 11-2(a)), inducing significant thermal expansion at the macro-scale and causing a macro-void ratio increase. The total void ratio increases during this phase (Figure 11-4(c)), while p_0 follows a complicated increase/decrease path until it becomes steady when the bentonite is fully saturated (Figure 11-4(a)). At full saturation, the state variables at Point A do not change much, except the interaction function continues to switch between f_{ic} and f_{is} paths due to numerical fluctuations of calculated state variables. In Figure 11-2(a), the final LC curve is to the right of the initial one, indicating the increment of the elastic domain, and the hardening of the material.

Point B is close to the host rock and here the bentonite undergoes hydration from the very beginning, so a different behavior is observed in Figure 11-4(b), (d), and (f). The initial state at Point B is under compression due to confinement from the host rock. Thus, in the beginning, the simulated results in Figure 11-4(d) show a slight contraction at the macro-scale while the total and the macro-void ratios decrease. The micro-structure is also under compression, which is implied by the interaction function following a f_{ic} path with MC mechanism in Figure 11-4(f). As Figure 11-4(c) displays, early hydration at Point B leads to increased liquid saturation and reduced suction. In turn, the bentonite starts swelling and

a MS mechanism is activated. The evolution of f_{is} at Point B is similar to that at Point A during the wetting phase as the system evolves to full saturation. Firstly, f_{is} is positive in Figure 11-4(f) and induces tensile plastic macro-structural strain, then it changes to negative and induces compressive plastic strain. Later, thermal expansion at the macro-scale also happens when this position reaches full saturation condition, causing a slight increase of the macro-void ratio (Figure 11-4(d)). The total void ratio increases during this phase mainly due to contributions from micro-structural swelling. During this phase, some suction increases occur as well, so the interaction function changes to a MC mechanism with $f_{ic} > 0$ for a short period, then it goes back to a MS path (Figure 11-4(f)). This implies strong micro-structural swelling due to the strong reduction of micro-structural effective stresses. After 100 years, the macro-structure contracts again mainly due to the accumulation of effective stresses at the macro scale when liquid pressure dissipates. This fact causes a reduction of the macro and total void ratio. In Figure 11-4(b), the final LC curve moves to the right, which indicates the growth of the elastic domain, and hardening of the material.

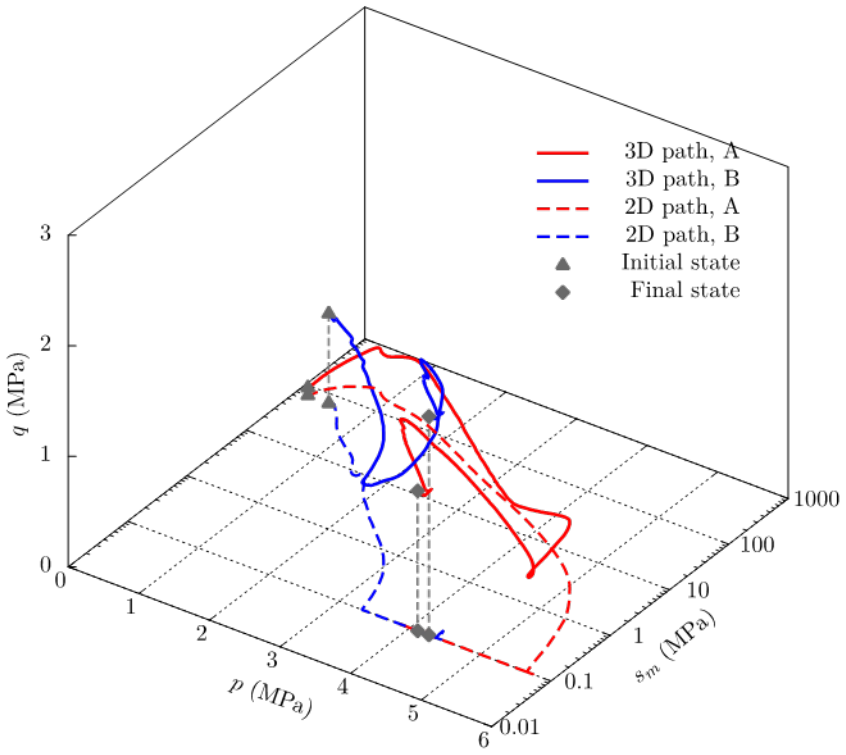

Figure 11-3 Stress path at points A and B in 3D q-p-s_m space.

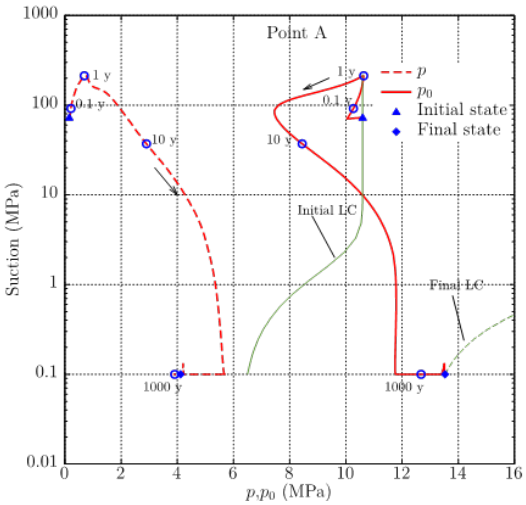

(a) Stress path of Point A on p-s_m plane.

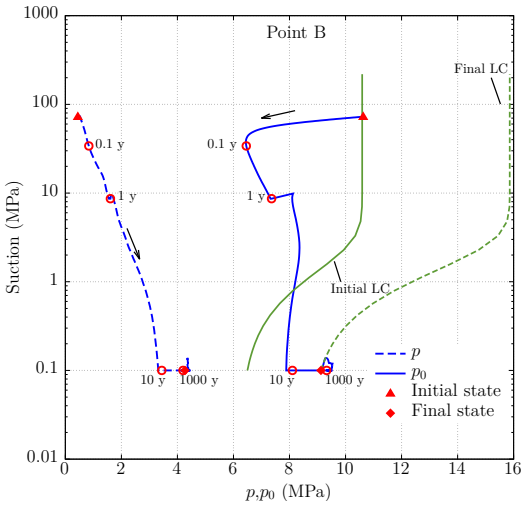

(b) Stress path of Point B on p-s_m plane.

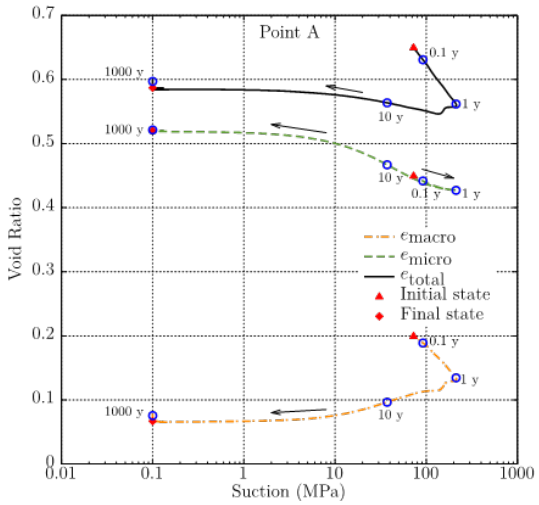

(c) Void ratio evolution at Point A.

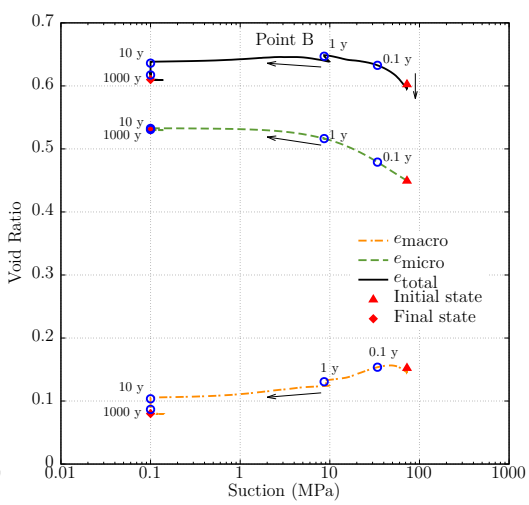

(d) Void ratio evolution at Point B.

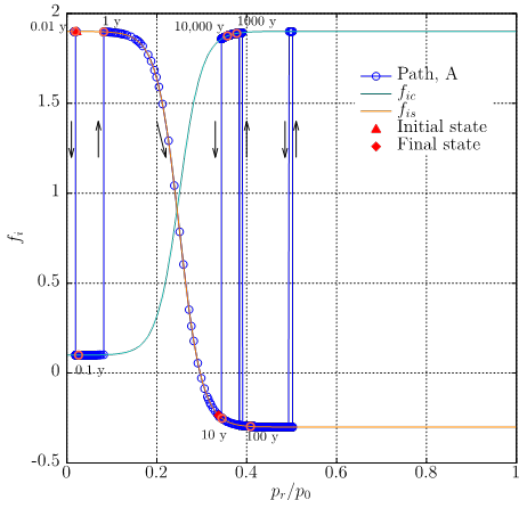

(e) Interaction function at Point A.

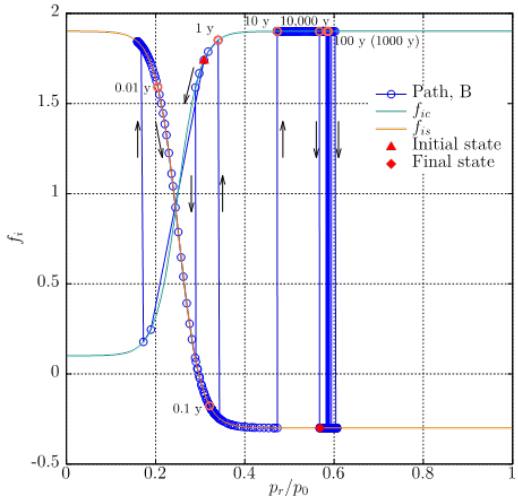

(f) Interaction function at Point B.

Figure 11-4 Simulation results of bentonite behavior at Points A and B within FEBEX bentonite. LC is the Loading-Collapse curve or the yield locus for the macro-structure.

Usually, swelling stress is associated with effective stress when a soil sample is subjected to hydration. In Figure 11-5, we present the mean effective/net stress, i.e., the mean net stress for unsaturated bentonite and the mean effective stress for fully saturated bentonite during the simulation (marked as "W C-M")) to illustrate the accumulation of swelling stress in the solid skeleton of the bentonite. At Point A, the mean effective/net stress is about 5.7 MPa at peak, around 20 years after emplacement. The reason for the increase of peak swelling stress is that an initial drying of the bentonite enhances the peak swelling pressure at full saturation. Additionally, thermal expansion due to heating also contributes to stress accumulation. As the status of bentonite changes from unsaturated condition to fully saturated, effective stresses are plotted instead of net stresses. The effective stress decreases after the full saturation because pore pressure increases (Figure 11-2(b)) and stress redistribution occur. After 100 years, the effective stress starts to increase again, which is due to the decline of osmotic suction and a strong pore pressure reduction. It should be noticed that no volumetric collapse happens at Point A since the material does not reach the LC curve, as indicated in Figure 11-4(a). The key variables affecting the LC curve are the net mean yield stress at full saturation, p_0^*, and macro-structural stiffness parameters, $\lambda(s_m)$ and κ, which are obtained from laboratory experiments but depend on the compaction status of the samples. At Point B, the peak stress at full saturation is 1.2 MPa lower than the stress at Point A due to the fast saturation process and strong confinement induced by strong thermal stresses. However, later, the stress recovers to about 4.2 MPa around 40,000 years. Figure 11-5 also presents another case that was simulated without C-M coupling (marked as "W/o C-M"), meaning the mass fraction of smectite, exchangeable cation concentration, and osmotic suction were all kept constant using the initial input values. By accounting for C-M coupling, the peak stress at Point A is 0.6 MPa lower than the case without C-M coupling, while the peak stress at Point B is only 0.2 MPa lower, which is caused by the different cation exchange at the time that stress peaks, as manifested by the β_m in Figure 11-2(e). For the final recovered stress, both Points A and B exhibit lower stress values if C-M coupling is considered, indicating that chemical effects reduce the effective/net stress in the bentonite buffer. However, the reduction in stress magnitude is generally less than 1 MPa.

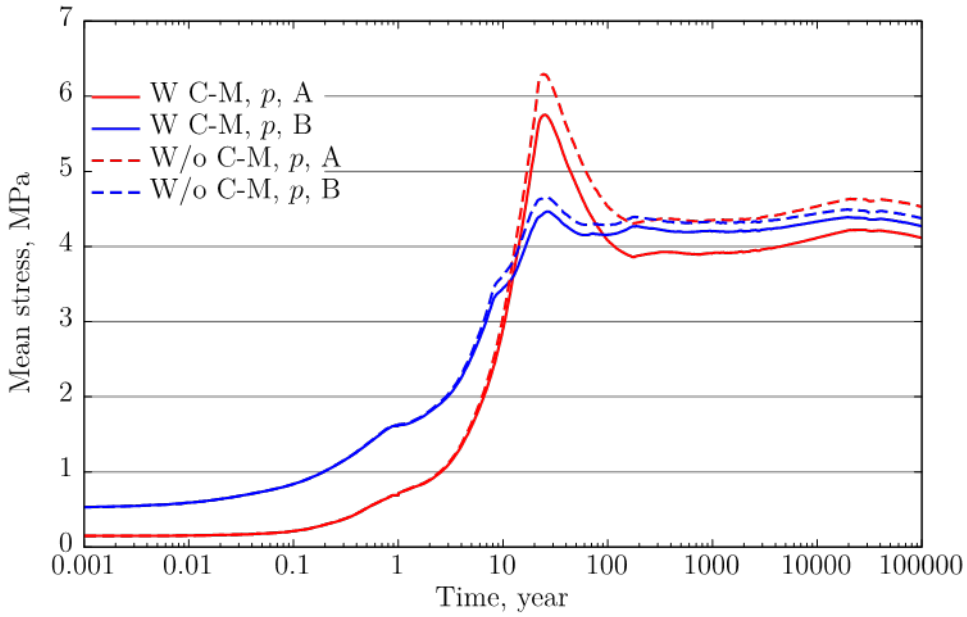

Figure 11-5 Simulation results of stress at points A and B within FEBEX bentonite.

11.3 Modeling the High Temperature Column Tests

Section 11 presents the details of the high temperature column test and the latest result collected by CT-scan when the columns were under heating and hydration and by sample characterization after the column was dismantled. The objective of this modeling effort is to interpret the data collected at high temperature column tests to better understand the coupled THMC processes in bentonite under simultaneously heating and hydration, test the THMC modeling capability, improve the parameterization for the THMC model in preparation for the coupled THMC model for HotBENT field test. In FY21, we started with a simple TH model to calibrate the temperature boundary conditions because of some "irregularity" in the experimental procedures, then expand the model to THM models.

11.3.1 Model Setup

In the preliminary THM model, the model considered the heat conduction and convection, Darcy-type multiphase phase flow, and elastic model for bentonite swelling in which swelling stress is a linear function of water saturation.

Figure 11-6 shows the configuration of the test and the geometry used for modeling. To save computation time, the model was a 2-D cross-section that cut through the middle of the column. The simulation domain contains 3 materials: heater, bentonite, and sand. Although the heater was emplaced in a shaft in the test, to simplify the model, the heater/shaft was described by one layer of grid blocks with high thermal conductivity, very small permeability. The properties of the bentonite and sand layer are listed in Table 11-1. The effective vapor diffusion and parameters of Van Genuchten are taken from the THMC model for a generic repository (Zheng et al., 2015b). The porosity for bentonite was calculated based on the initial water content and bulk density of bentonite. The permeability was calibrated based on the matching between calculated and measured CT density.

Initially, the bentonite has a water saturation of 33%, corresponding to a measured initial water content of about 18%. The sand layer is fully saturated. Water is injected through the sand layer at a constant pressure of 0.8 bars, just like what was running at the test. No displacement boundary condition is applied to the heater and sand layer for mechanical processes.

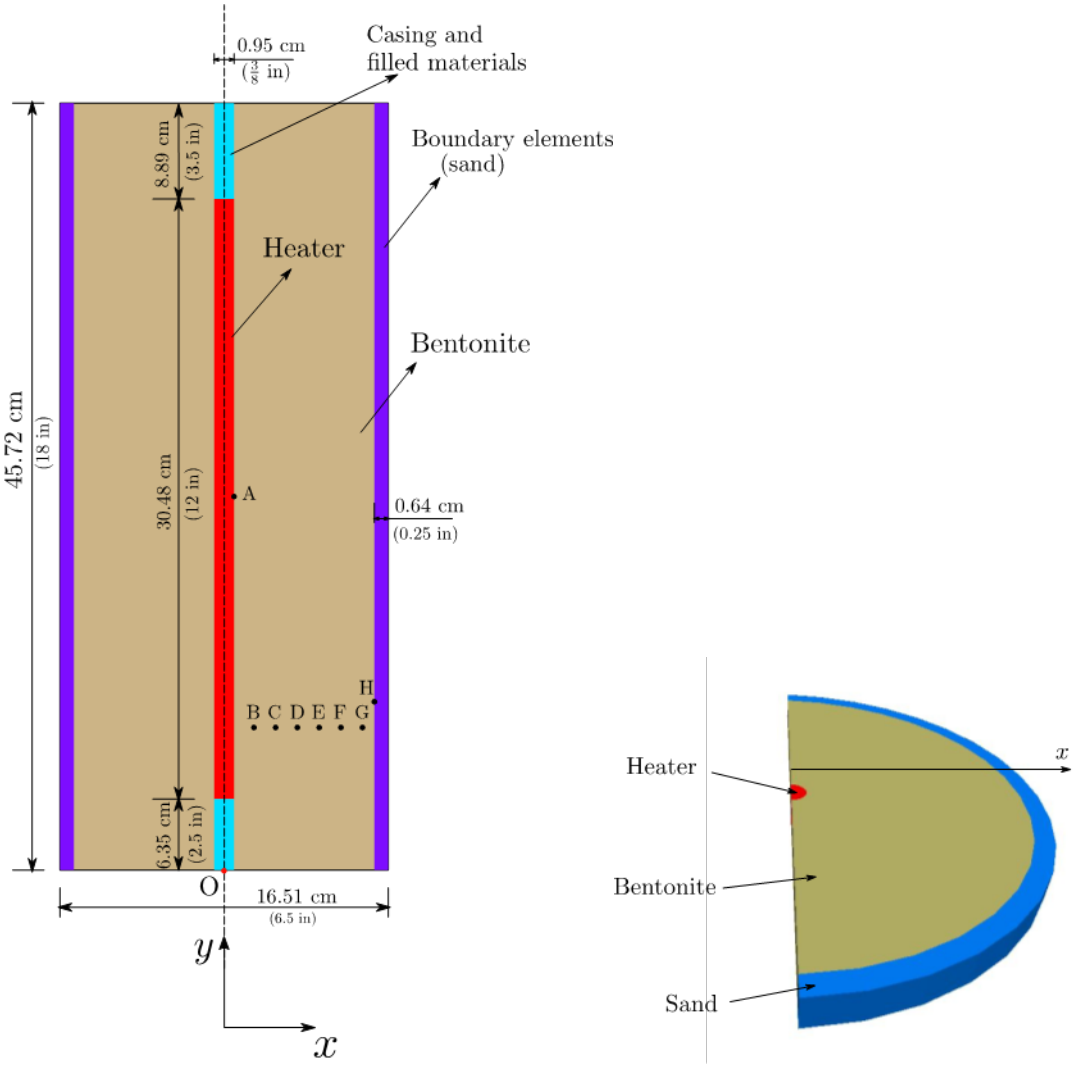

Figure 11-6 **(a) The configuration of the high temperature column test (see chapter 10 for details) and (b) geometry of the model.**

Table 11-1 THM parameters for bentonite and sand layer in the model

Parameter	Sand	Bentonite
Grain density [kg/m^3]	2700	2623
Porosity	0.6	0.54
Saturated permeability [m^2]	2.0×10^{-13}	2×10^{-20}
Relative permeability, k_{rl}	-	$k_{rl} = S^3$
Van Genuchten [1/Pa]	-	1.1×10^{-8}
Van Genuchten m	-	0.32
Compressibility, [1/Pa]	3.2×10^{-9}	3.3×10^{-8}
Thermal expansion coeff. [1/^{o}C]	1.0×10^{-5}	1.0×10^{-5}
Dry specific heat [J/kg- ^{o}C]	1000	800
Thermal conductivity [W/m-^{o}C]	2.0	0.5, 1.1
Effective vapor diffusion coefficient (m^2/s)	5×10^{-5}	5×10^{-5}
Young's modulus (GPa)	24.9	0.2
Poisson's ratio	0.3	0.3

The heater's output power was measured. However, there is a heat loss through the shaft, which means the heat was not totally applied to the bentonite. We, therefore, calculated the heat output (Table 11-2) based on the match between the calculated and measured temperature at point A (Figure 11-7). Another uncertainty related to the thermal boundary conditions is the insulation added about a week after the hearing started. A slight amount of power was added to the sand layer to mimic the heat conservation due to insulation.

Table 11-2 Calibrated heat output based on the temperature near the heater

Time	Heat (W or J/s)
0 – 5.5 hours	0
5.5 hours – 7 days	11
7 days – 13 days	12
13 – 365 days	10

11.3.2 Results of the Base Model

With the calibration of that output at the heater, the model matches temperature at monitoring points (whose radial distances are listed in Table 11-3) reasonably for the monitoring points within the bentonite (Figure 11-7). Temperature profile from point B to G can be explained well with thermal conductivity of

1.1 W/m-°C. However, there is a sharp drop of temperature from point A to point B, which was matched by the model using a low thermal conductivity of 0.5 for a layer about 1 cm thick next to the heater. Note that in this preliminary modeling effort. The change of thermal conductivity as a function of water saturation was not considered but will be added to the model in the refined model soon.

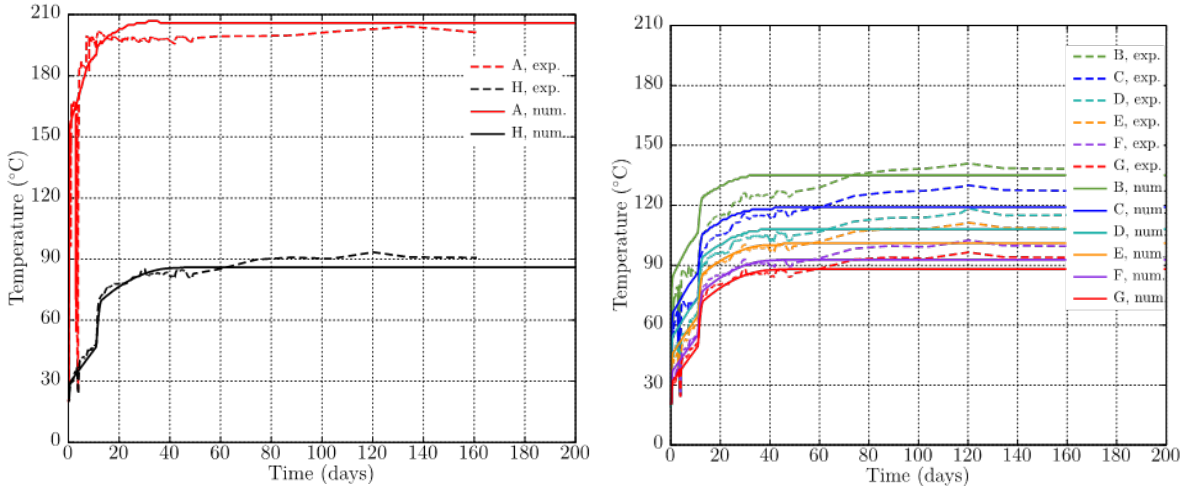

Figure 11-7 (a) Computed and measured temperature at monitoring points.

Table 11-3 Monitoring points in the model

Points	Radial (cm)
A	0.47625
B	1.47625
C	2.36625
D	3.61625
E	4.47625
F	5.87625
G	7.12625
H	7.67625

The evaporation caused by heating drives the pore pressure up within the bentonite, especially the area close to the heater (Figure 11-8, left). When the bentonite becomes fully saturated (Figure 11-8, right), pore pressure is equal to the hydration pressure at the sand layer.

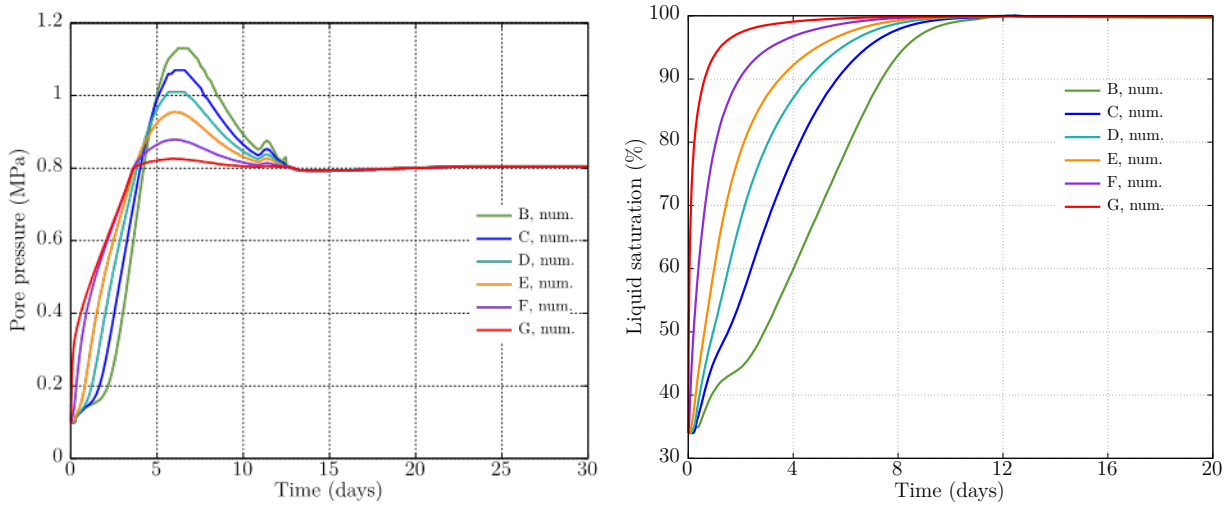

Figure 11-8 Computed pore pressure and liquid saturation at monitoring points.

The swelling of bentonite was computed with a linear elastic swelling model as follows:

$$\Delta\sigma' = K\Delta S_l \beta_{sw} \qquad \textbf{Eq. 11-6}$$

where $\sigma'$is swelling stress (MPa), K is Young's modulus (200 MPa in the model), S_l is the liquid water saturation and β_{sw} is the linear swelling coefficient. A β_{sw} of 0.0238 is used in the model,

Frequent CT scans were conducted to track the progression of hydration. The density calculated from the CT scan is the mass of soil and water per unit volume of the medium. The density change obtained by CT scan is the result of an increase in water content and swelling/compression. Figure 11-9 shows the comparison of measured and computed density and there is remarkable discrepancies between model and data. In the model the behavior of density reflects mostly water content change; swelling/compression seems have little effect, suggesting current mechanical model needs revision.

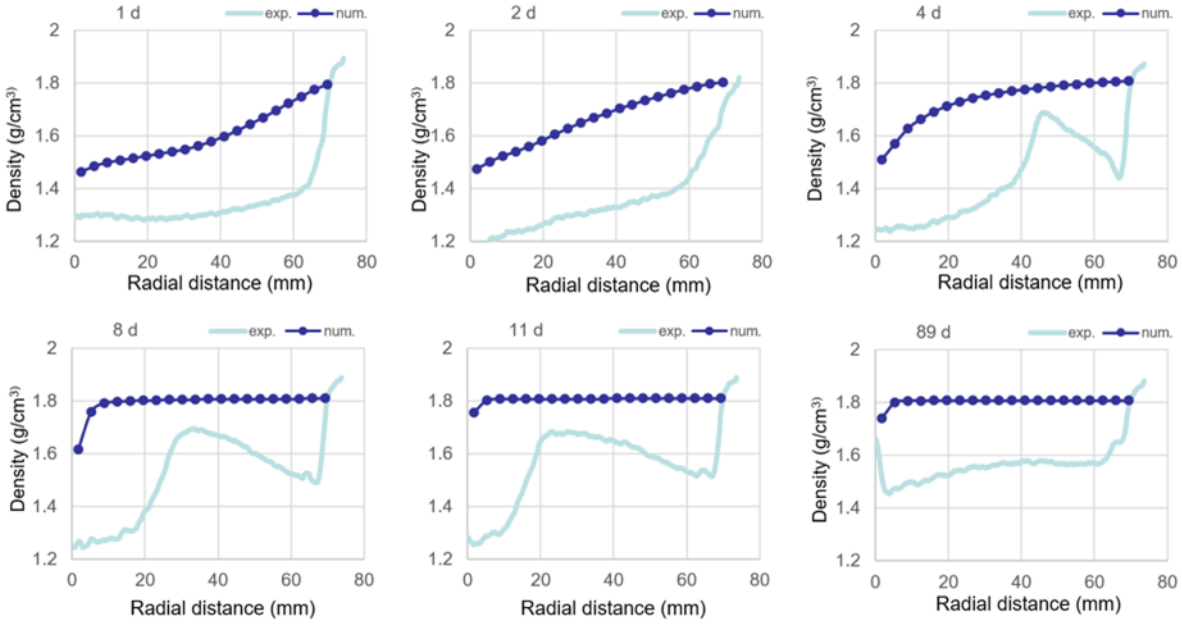

Figure 11-9 Computed density in the base model and measured density from CT scan.

The thermal couples appeared as a bright spot in the CT scan, comparing the CT scan at different times can track the movement of those thermal couples and provide data of displacement (Figure 11-10). Data show that bentonite was first pushed towards the heater because of the swelling at areas near the sand layer, and then moves back to roughly its original place (displacement is equal to zero) when the inner part of bentonite becomes saturated and swells. The largest displacement towards the heater is around 3-4 mm. Although the model (Figure 11-11) matches the movement trend, but the magnitude is only about 0.2 mm.

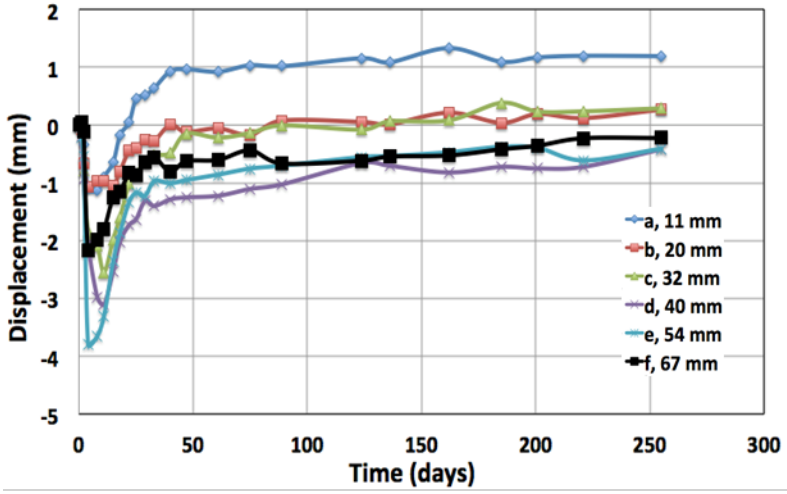

Figure 11-10 Measured displacement based on CT scan. The negative value means displacement towards the heater and a positive value means towards the sand layer.

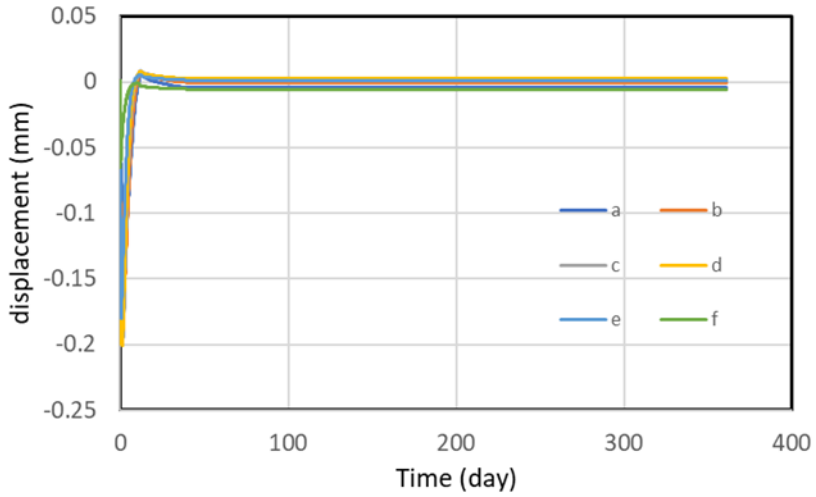

Figure 11-11 Computed displacement in the base model, negative volume means displacement towards the heater, and a positive value means towards the sand layer.

11.3.3 Results of the Revised Model

The base model did not provide a satisfactory match of data collected from the test. The model was therefore revised to improve the match between model and data. One simulation, named "run R1" is to use BExM for the mechanical processes. The parameters for the BExM are the same as FEBEX bentonite (Xu et al., 2020). However, the discrepancies between measured density and model results remain (Figure 11-12) and the computed displacement is still much lower than the data (Figure 11-13).

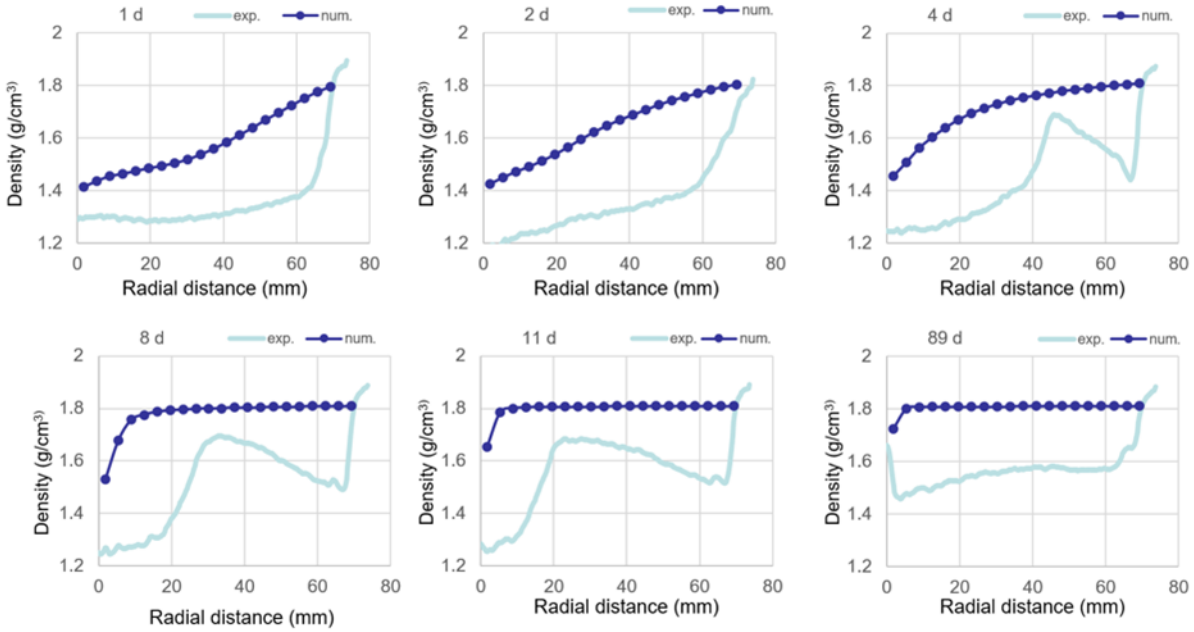

Figure 11-12 Computed density in the revised model "run R1" with BExM and measured density from CT scan.

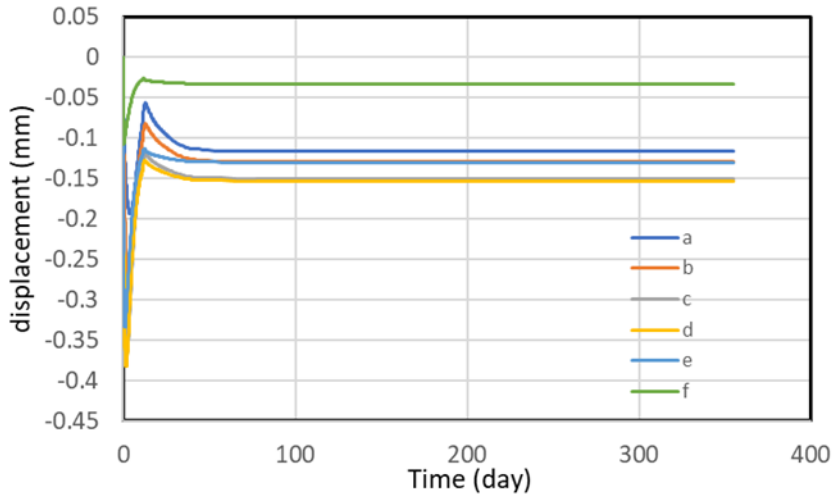

Figure 11-13 Computed displacement in the revised model "run R1" using BExM, a negative value means displacement towards the heater and a positive value means towards the sand layer.

Another run, "run R2", was conducted with two changes comparing with the base model: the linear swelling coefficient β_{sw} is 0.238, one order of magnitude higher than that in the base model; the zero displacement boundary for the sand layer is removed. The model match well with the density data (Figure 11-14). However, because of the removal of the zero displacement boundary at the sand layer, the direction of initial displacement is opposite to what is shown by data.

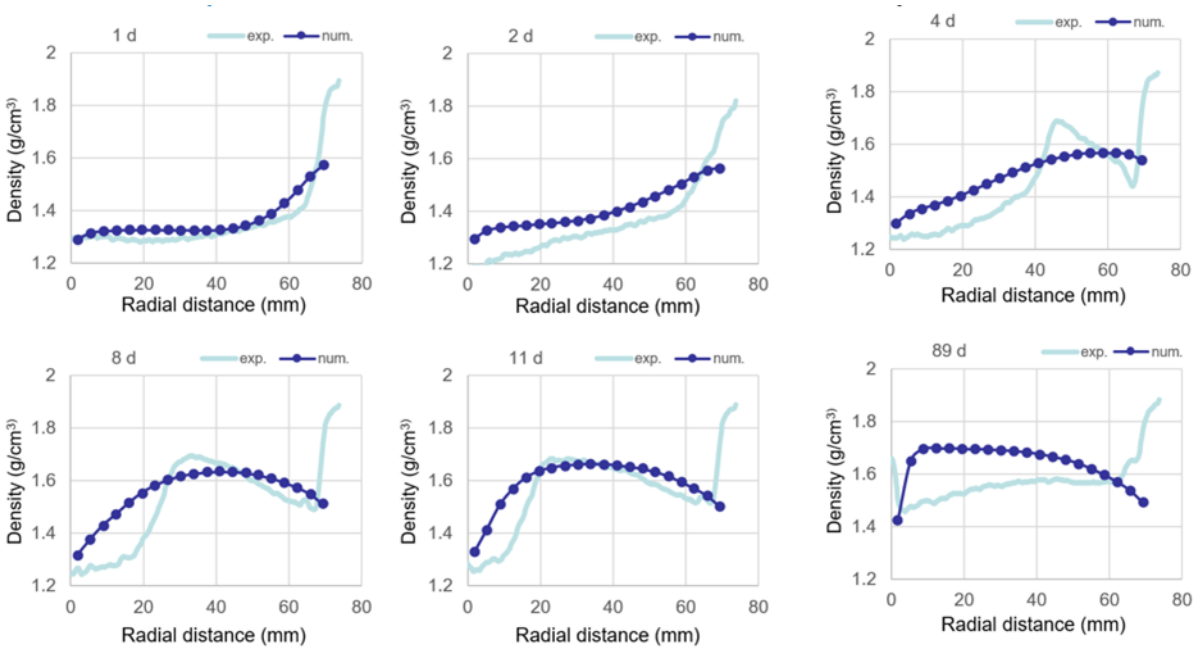

Figure 11-14 Computed density in the revised model 'run R2" and measured density from CT scan.

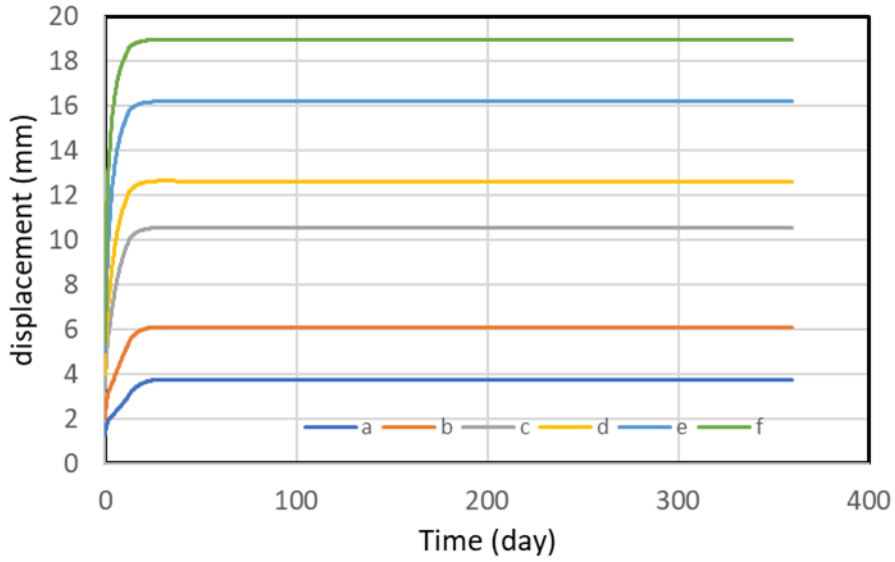

Figure 11-15 Computed displacement in the revised model "run R2", a negative value means displacement towards the heater and positive value means towards the sand layer.

11.4 Summary and Future Work

11.4.1 Summary of Current Modeling Work

In the past few years, we have dedicated our effort to developing coupled THMC models to evaluate the chemical alteration and associated mechanical changes in a generic repository and to consider the interaction between EBS bentonite and the NS clay formation. In FY21, on the one hand, we continued using MC couping via BExM to examine the mechanical evolution of bentonite under high temperature and reported the stress path results; on the other hand, the modeling effort was dedicated to interpreting the high temperature column tests, starting with simple TH model, and gradually increasing the level of complexity to THM, eventually THMC model. We have completed the preliminary THM model up to now. Some observations from the preliminary modeling are as follows:

- Model match well the temperature data, but thermal boundary conditions have to be calibrated because of the heat loss at the heater and the insulation added in the test.

- There are discrepancies between density data and computed results from both the base model that used the linear swelling model and the revised model using BExM.

- Displacement was measured at a couple of monitoring points, which shows initial inwards movement to the heater and later outwards movement to the sand layer. The base model using the linear swelling model and the revised model using BExM reproduce the general trend, but the computed displacement is much lower than measured data

- A revised model using the linear swelling model with a large swelling coefficient and removal of the displacement constrain at the sand layer provides a nice fit of density data but failed to match the displacement data.

11.4.2 Future Work

The current coupled THMC model on the Windows platform greatly improves our understanding of the coupled processes. However, for solving large in-field problems and better modeling efficiency, the simulator for conducting coupled THMC modeling needs to be improved. In the future, we will continue improving the simulator.

Regarding the modeling of the high temperature column tests, we will continue refining the model in the following aspects:

- Extend the simulations to 1.5 years so that the model can be compared with data collected after the columns were dismantled,
- Improve the conceptualization and parameterization of the model to achieve a better fit between density and displacement data and model results
- Conduct simulations for the non-heated column,
- Once the THM model can match data, the model will be expanded to THMC so that we can understand the chemical changes measured in the test.

12. Understanding the THMC Evolution of Bentonite Using Large Scale Field Experiments: FEBEX-DP and HotBENT

12.1 Introduction

The most common buffer material for EBS is compacted bentonite, which features low permeability and high retardation of radionuclide transport. The safety functions of EBS bentonite include limiting transport in the near field; damping the shear movement of the host rock; preventing the sinking of canisters (if emplaced in the center of the tunnel), limiting pressure on the canister and rock, and reducing microbial activity. To assess whether EBS bentonite can maintain these features when undergoing heating from the waste package and hydration from the host rock, we need a thorough understanding of the thermal, hydrological, mechanical, and chemical evolution of bentonite under disposal conditions. While numerous laboratory experiments, field tests, and numerical models have been conducted to improve the understanding of each individual process or coupled THC/THM processes, there is a lack of studies on coupled THMC processes due to the challenges of conducting experiments and developing models that can cover all the THMC processes. Recently in the Spend Fuel and Waste Science and Technology (SFWST) program, coupled THMC models have been developed for a generic disposal system in clayey host rock with EBS bentonite (Liu et al., 2013; Zheng et al., 2014; Zheng et al., 2015b; 2016; 2017;2018; 2019a). However, model validation was difficult due to the lack of THMC data from long-term, large-scale experiments. The FEBEX (Full-scale Engineered Barrier EXperiment) *in situ* test (ENRESA, 2000), which has been operated for 18 years, provides a unique opportunity for validating coupled THMC models, and HotBENT, a large-scale field experiment, which is under construction, will significantly improve the understanding of coupled THMC processes in bentonite under high temperature.

The first part of the chapter documents the progress of modeling the FEBEX *in situ* test. In the FEBEX *in situ* test, two heaters surrounded by bentonite blocks about 0.7 m thick were emplaced in a tunnel excavated in granite. The heaters were switched on in 1997. In 2002, Heater #1 was dismantled; in 2015, Heater #2 was dismantled. LBNL/DOE joined the FEBEX-DP project in FY15. The ultimate goal is to use THMC data from FEBEX-DP to validate THMC models and therefore enhance our understanding of coupled THMC process. From 2015 to 2019, extensive THMC characterization of bentonite samples collected during the dismantling of Heater #2 were carried by partners of FEBEX-DP. Ion concentrations in the pore-water of bentonite were obtained via an indirect method of aqueous extraction: these concentrations were used to initially constrain the chemical model. After the THMC model provided a coherent explanation of THMC data collected at the FEBEX *in situ* test, we used the well-calibrated THMC model to conduct more exploratory simulations. The simulations conducted in FY21 addressed the question about the long-term alteration of bentonite, for a period of up to 10,000 years under conditions similar to the FEBEX *in situ* test, which is discussed in the first part of this chapter.

Because the THMC model is 1D axisymmetric and covers only the bentonite and granite, the bentonite/concrete interfacial area has not been modeled. Because the concrete liner is part of the EBS in some design concepts, understanding the evolution of bentonite/concrete interface is critical for the long-term performance of EBS. In FY21, we developed a 1D reactive transport model to explain the data collected at the bentonite/concrete interface. The model was able to reproduce some data, but there were also discrepancies between model and data, which warranted further refinement of the model. This work is documented in the second part of the chapter.

The third part of the chapter gives an update on the HotBENT project, including the field test, and the modeling work is under preparation.

12.2 Geochemical Interpretation of the FEBEX in situ test Using THMC Model and Prediction of the Long-term Alteration of Bentonite

Because the THMC model had been reported in previous reports (e.g., Zheng et al., 2019, 2020b), in this section we just briefly describe the test, the basic elements of the THMC model, then focus on the model results of the long term simulations.

12.2.1 Brief Description of FEBEX Experiments

FEBEX *in situ* test was conducted at the Grimsel underground laboratory from 1997 to 2015, Switzerland (ENRESA, 2000). It consisted of five basic components: the drift, the heating system, the bentonite barrier, the instrumentation, and the monitoring and control system. The main elements of the heating system are two heaters (#1 and #2), 1 m apart. Heaters were placed inside a cylindrical steel liner. Heaters were at constant-temperature control mode to maintain a maximum temperature of 100 ºC at the steel liner/bentonite interface 20 days after the heating started. The bentonite barrier is made of blocks of highly compacted bentonite. The average values of the initial dry density and the gravimetric water content of compacted bentonite blocks are 1.7 g/cm^3 and 14.4%, respectively.

The *in situ* test began on February 27, 1997 and went through two dismantling events (see Table 12-1 for the operation timeline). A comprehensive post-mortem bentonite sampling and analysis program were performed during both dismantling events (Bárcena et al., 2003; Garcia-Sineriz et al., 2016), especially after the dismantling of heater #2 in 2015. After Heater #2 was switched off and a short cool-off time period, dismantling was carried out from the shotcrete towards the bentonite section by section (Figure 12-1) and samples were taken for THMC and microbiological characterization. (Garcia-Sineriz et al., 2016).

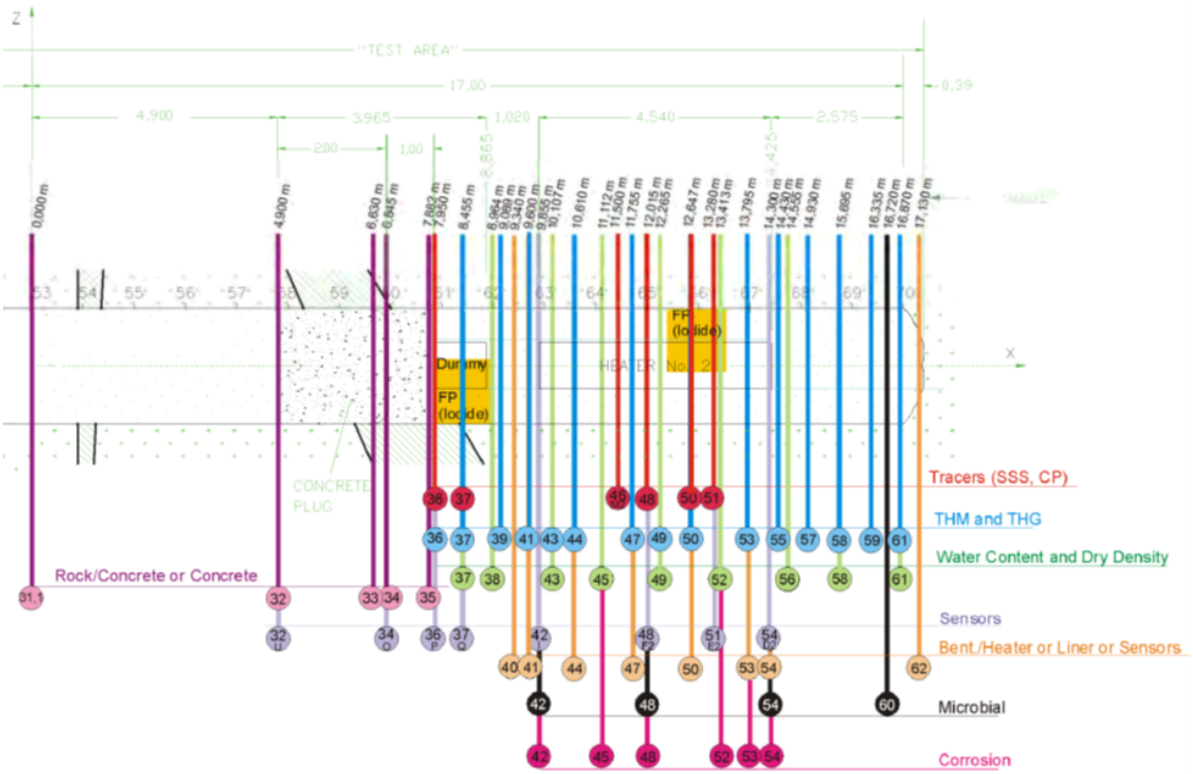

Figure 12-1 Section layout during the dismantling operation of heater #2 (Detzner & Kober, 2015)

In the FEBEX *in situ* test, some data were collected by the sensors installed in the bentonite blocks such as temperature, relative humidity and stress; and some of them were measured in the laboratory using the bentonite samples that were taken after dismantling of test sections, including water content and dry density. The dismantling of Heater #1 in 2002 and Heater #2 in 2015 (Table 12-1) provides two snapshots of measured water content and dry density, and ion concentrations in pore water of bentonite, which are very valuable for understanding the temporal evolution of these key data. A more detailed description of the FEBEX *in situ* test and available THM data were given in Zheng et al. (2018).

Table 12-1 Timeline of FEBEX *in situ* test.

Event	Date	Time (day)	Time (year)
Commencement of heating	2/27/1997	0	0.0
Shutdown of Heater #1	2/2/2002	1827	5.0
Sampling after heat #1 was dismantled	5/2/2002	1930	5.3
Shutdown of Heater #2	4/24/2015	6630	18.2
Sampling after Heater #2 was dismantled	7/3/2015	6700	18.3

Zheng et al. (2018) described the details of chemical data available in the FEBEX *in situ* test and the chemical data have the following features:

- ✓ Data for solid-phase are too scattered to show a clear spatial trend.
- ✓ Data for exchangeable cations are problematic but could be used with caution.

- ✓ The concentration data were not directly measured and geochemical modeling was involved to infer the ion concentration in pore water from data obtained by the aqueous extract test.
- ✓ Ion concentrations in pore water of bentonite are still the primary data to validate the model.
- ✓ Ion concentrations in the pore-water of granite were collected and measured in the two boreholes parallel to the *in situ* test tunnel, which can be used to evaluate the diffusion of bentonite water into granite.

12.2.2 Model Development

After an extensive calibration, the THMC model was able to provide a reasonable interpretation of all THMC data (Zheng et al., 2018; Zheng et al., 2019). The long-term simulations have almost the same setup as the THMC model for the *in-situ* test, except for the thermal boundary condition at the heater. We briefly describe the model below and details of the model were documented in Zheng et al. (2017; 2018).

The numerical simulations were conducted with TOUGHREACT-FLAC3D, which sequentially couples the multiphase fluid flow and reactive transport simulator, TOUGHREACT V3.0-OMP (Xu et al., 2014), with the finite-difference geomechanical code FLAC3D (Itasca, 2009).

12.2.2.1 Modeling Setup

Because the hydration of bentonite is fairly symmetrical, we use an axisymmetric mesh (Figure 12-2) to save computation time so that we can focus on the key coupling processes. However, such a model can only be used to interpret and predict the THMC behavior in the "hot sections", i.e., sections of bentonite block surrounding the heater including sections 41-54 (or more typically section 49) in Figure 12-1.

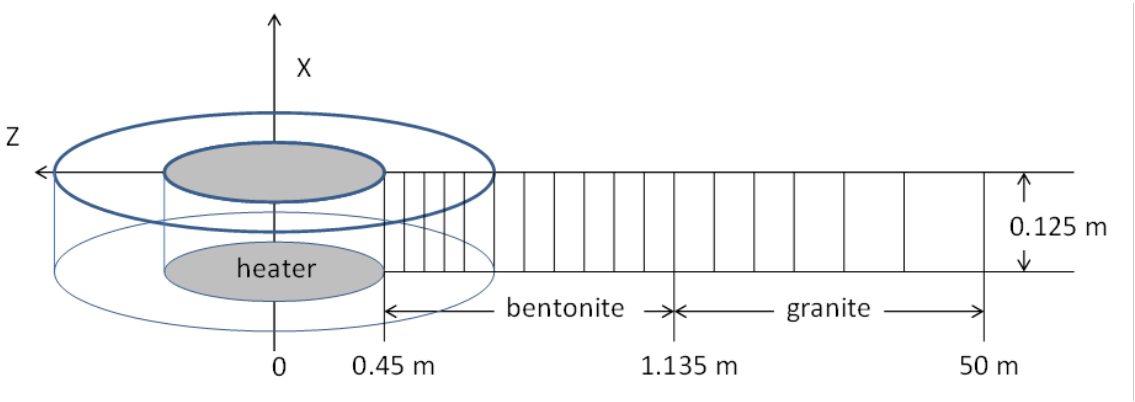

Figure 12-2 Mesh used for the model, not to the scale.

The model considers two material zones: one for the bentonite and the other for the granite. The first two nodes (1 and 2) are located on the external wall of the heater (r = 0.45-0.46 m). Bentonite is located within 0.45 m < r < 1.135 m. The remaining domain up to 50 m is used to simulate the granite. The simulation time starts on February 27, 1997, and ends on July 1, 2015, a total of 6,698 days (18.3 years).

The initial temperature is uniform and equal to 12 ºC. A constant temperature of 100 ºC is prescribed at the heater/bentonite interface (r = 0.45 m) while the temperature is assumed to remain constant at its initial value of 12 ºC at the external boundary (r = 50 m) because the thermal perturbation induced by the heaters over the time frame of the experiment does not extend to this boundary. The bentonite has initially a gravimetric water content of 14%, which corresponds to a saturation degree of 55% and a suction of

1.11×10^5 kPa. The boundary conditions for flow included: 1) no flow at r = 0.45 m and 2) a prescribed liquid pressure of 7 bars at r = 50 m.

The model considers non-isothermal two-phase (air and water) flow, with each individual phase fluxes given by a multiphase version of Darcy's Law. For the vapor flow in the air phase, in addition to Darcy flow, mass transport can also occur by diffusion and dispersion according to Fick's law. In the current model, both conductive (Fourier's law) and convective heat flux are considered in the model and thermal conductivity is the key parameter. Details of the THM model were given in Zheng et al. (2018). In Zheng et al. (2016), we tested two mechanical models for bentonite: a linear swelling model and dual structure BExM and found out that both models led to similar fits to measured THM data. Both methods have pros and cons: BExM provide a mechanistic description of the swelling of bentonite, but it is more computationally expensive and parameters are difficult to calibrate, whereas linear swelling models have simple parameterization and parameters can be easily calibrated, but it does not describe correctly the transient state of swelling. Eventually, for the THMC model for the FEBEX in situ test, we use a method that is somewhat in between — the state surface approach.

12.2.2.2 Chemical Model

Although the chemical model was described in Zheng et al. (2018), we present it here to facilitate the discussion in the next section. The establishment of the chemical model requires first the knowledge of initial chemical conditions in bentonite and granite, i.e., the initial mineralogical and pore water compositions. In this report, the mineral phases and their volume fraction (Table 12-2) were applied with reference to ENRESA (2000), Fernández et al. (2004), Ramírez et al. (2002) and Villar et al. (2018). Note that all these publications used a mass fraction which is transformed to the volume fraction (ratio of the mineral volume to the total volume of medium) using a porosity of 0.41. Note that the minerals that have zero initial volume fractions are the secondary minerals that could be formed. In the current model, we consider quartz, K-feldspar, plagioclase in granite with their volume fractions listed in Table 12-2.

Table 12-2 Mineral volume fraction (dimensionless, ratio of the volume for a mineral to the total volume of medium) FEBEX bentonite (ENRESA, 2000; Fernández et al., 2004; Ramírez et al., 2002) and granite (Zheng et al., 2011).

Mineral	FEBEX Bentonite	Granite
Calcite	0.00472	0
Smectite	0.546	0
Gypsum	0.00059	0
Quartz	0.018	0.37
Cristobalite	0.0059	0.00
K-Feldspar	0.0059	0.35
Plagioclase	0.0059	0.27
Dolomite	0.0	0
Illite	0.0	0
Kaolinite	0.0	0
Siderite	0.0	0
Ankerite	0.0	0
Anhydrite	0.0	0
Chlorite	0.0	0

FEBEX bentonite blocks have an initial gravimetric water content of 13.5–14% (ENRESA 2000). The model presented in this report uses the pore water composition (Table 12-3) inferred by Fernández et al. (2000) from aqueous extract data. The pore water composition for granite (Table 12-3) is taken from Zheng et al. (2011).

Table 12-3 Pore-water composition (mol/kg water except for pH) of FEBEX bentonite (Fernández et al., 2000) and granite (Zheng et al., 2011).

	EBS Bentonite: FEBEX	Granite
pH	7.72	8.35
Cl	1.60E-01	1.31E-05
SO_4^{-2}	3.20E-02	7.86E-05
HCO_3^-	4.1E-04	3.97E-04
Ca^{+2}	2.2E-02	1.81E-04
Mg^{+2}	2.3E-02	1.32E-06
Na^+	1.3E-01	3.76E-04
K^+	1.7E-03	7.80E-06
Fe^{+2}	2.06E-08	2.06E-08
$SiO_2(aq)$	1.1E-04	6.07E-04
AlO_2^-	1.91E-09	3.89E-08

In the chemical model, we consider aqueous complexation, cation exchange, surface complexation and mineral dissolution/precipitation. Details of aqueous complexes and their disassociation constants for reactions, solubility and reaction rate for minerals are given in Zheng et al. (2018).

12.2.3 Coupled THMC Model

The ultimate goal of using coupled THMC model to interpret the data collected in the FEBEX *in situ* test is to understand the THMC evolution of bentonite under simulated repository conditions so that we can use the most plausible processes and parameters to describe the behavior of bentonite. Once the coupled THMC model can simultaneously match the measured temperature, relative humidity, water content, stress, aqueous concentrations, and mineral phase changes, we can further use it to predict the long-term alteration of bentonite buffer under different conditions, such as under higher temperature as was done by Zheng et al. (2015a). In this section, we first recap the chemical results for the base THMC model developed in the last couple of years. Then model simulations with longer running time are presented to show the evolution of the bentonite barrier in the long run.

12.2.3.1 Base THMC Model

From FY16 to FY19, the model for FEBEX *in situ* tested evolved from TH model (Zheng et al., 2016) to THMC model that can reasonably interpret THMC data collected at the test site (Zheng et al., 2018, Zheng et al., 2019, Zheng et al., 2020a). Here we briefly recap the chemical results with some examples to facilitate the discussion in the following sections.

Geochemical evolution is the consequence of coupled THMC processes. THM processes strongly affect the geochemical evolution but usually not vice versa, which is why a great deal of effort was dedicated to having a sound THM model that can match the THM data. Once the THM processes are relatively well

established, before we study the possible chemical reactions, we need to constrain the transport process. While the advection of chemical species is fixed in the THM model, diffusion has to be calibrated in the chemical model.

Because chloride is only controlled by transport processes, its temporal and spatial evolution is a good indicator of the transport processes. The THMC model nicely fit the data near the heater (Figure 12-3), indicating that the chloride concentration could be fairly high at the canister-bentonite interface. If such a trend persists for an extended time period until the canister is fully corroded, the high chloride concentration might significantly affect the degradation of waste. As granite pore water (which has a much lower chloride concentration than bentonite pore water) infiltrates into the bentonite, it dilutes the bentonite pore water significantly as shown by the very low chloride concentration near the granite (radial distance between 0.8 and 1.1 m). Meanwhile, bentonite pore water was pushed further near the heater and evaporation causes an increase in chloride concentration, as manifested by the high chloride concentration near the heater.

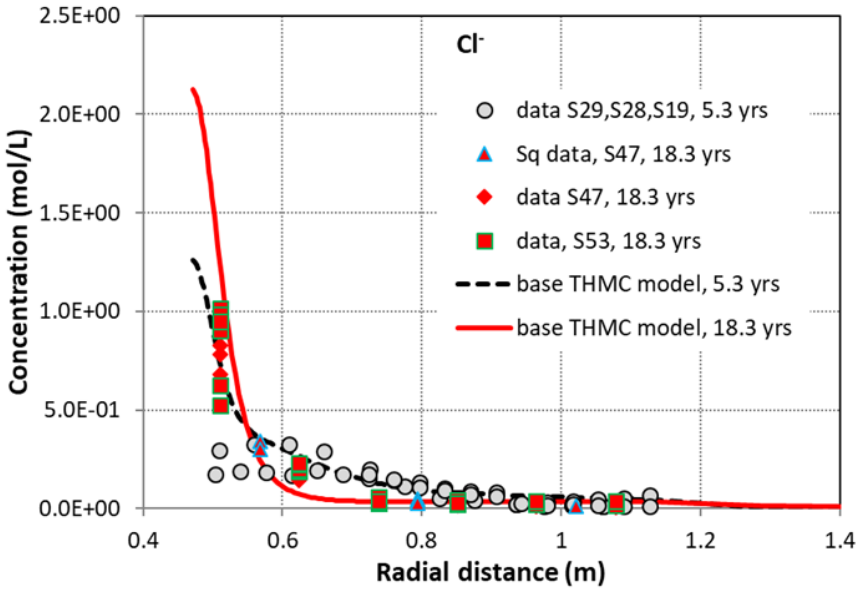

Figure 12-3 Calibrated chloride concentration data at 5.3 years from aqueous extract test for sections 29, 28, and 19 (Zheng et al., 2011), calibrated chloride concentration data at 18.3 years from aqueous extract test for section 47 ("data S47, 18.3 yrs") and section 53 ("data S53, 18.3 yrs"), chloride concentration data from squeezing test for section 47 ("Sq data, S47, 18.3 yrs") and model results from the base THMC model.

The base THMC model (Zheng et al., 2018; 2019) also showed that the key coupling processes that were required to match THM data and concentration of conservative species (e.g., chloride) include vapor diffusion, porosity change due to swelling, permeability change as a function of dry density (or porosity), and thermal osmosis.

Concentration profiles of cations were largely shaped by transport processes while their concentrations are also affected by mineral dissolution/precipitation and cation exchange; the spatial profiles of pH, bicarbonate and sulfate were largely determined by chemical reactions. Potassium (Figure 12-4) is an example of chemical species for which the concentration profiles are largely shaped by transport processes, although potassium is also affected by cation exchange and precipitation of illite. The pH profile is shaped by chemical reactions. Because of the buffer by surface protonation, the spatial profile of pH is also fairly flat, except in the areas near the granite and the heater (Figure 12-5). The increase in pH

in bentonite pore water at the vicinity of the heater is related to the dissolution of montmorillonite (Figure 12-6).

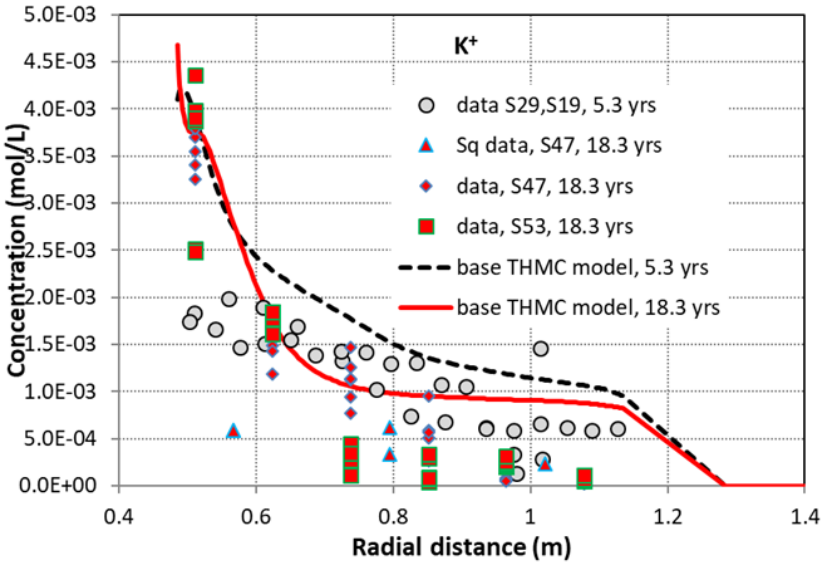

Figure 12-4 **Calibrated potassium concentration data at 5.3 years from aqueous extract test for sections 29, 28, and 19 (Zheng et al., 2011), calibrated chloride concentration data at 18.3 years from aqueous extract test for section 47 ("data S47, 18.3 yrs") and section 53 ("data S53, 18.3 yrs"), chloride concentration data from squeezing test for section 47 ("Sq data, S47, 18.3 yrs") and model results from the base THMC model.**

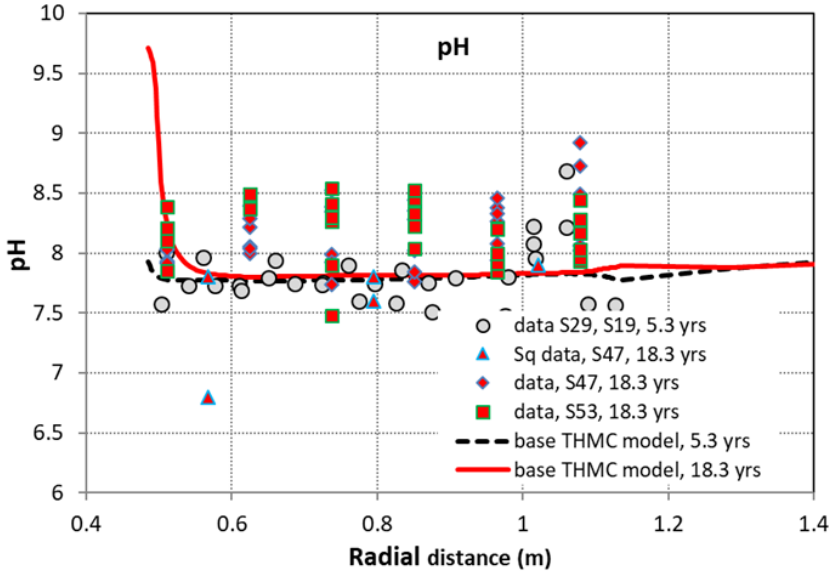

Figure 12-5 **Calibrated pH data at 5.3 years from aqueous extract test for sections 29, 28, and 19 (Zheng et al., 2011), calibrated chloride concentration data at 18.3 years from aqueous extract test for section 47 ("data S47, 18.3 yrs") and section 53 ("data S53, 18.3 yrs"), chloride concentration data from squeezing test for section 47 ("Sq data, S47, 18.3 yrs") and model results from the base THMC model.**

The evolution of clay minerals, namely smectite and illite, has implications for the long-term stability of the bentonite barrier. While many laboratory heating tests are often too short to show a significant change

in clay minerals or conditions in the laboratory tests are very different from the *in situ* condition and the implications of these test results require interpretation. The mineral characterization of the sample collected after the final dismantling provides insight into the possible change of clay minerals after long-term heating and hydration. Unfortunately, given the large variation of the illite fraction in the illite/smectite mixed layer between samples, it is impossible to delineate if there is any increase or decrease of the illite mass fraction by comparison with the reference bentonite. Models show illitization near the heater, as manifested by illite precipitation and montmorillonite dissolution, but on the order of less than 1%, which cannot be proved or disapproved by the data.

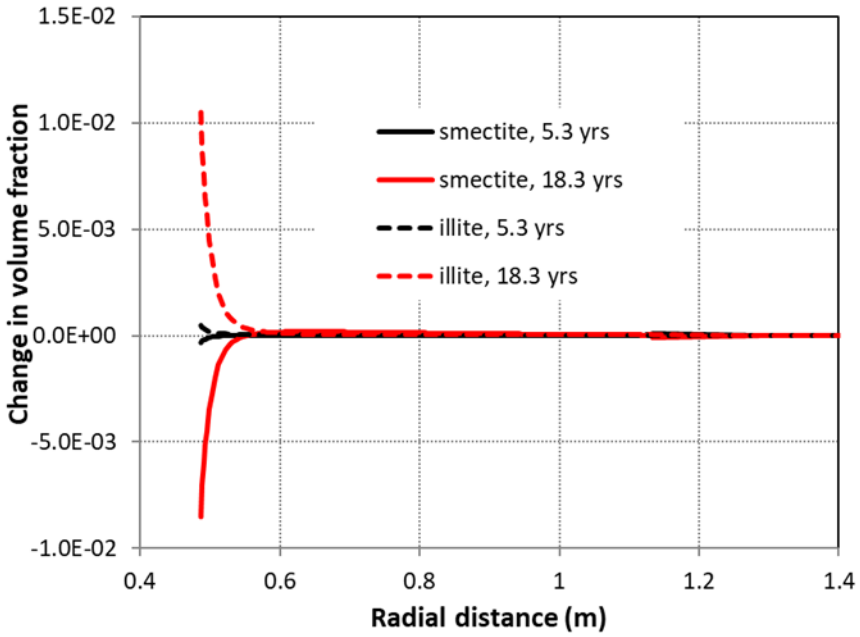

Figure 12-6 Model results of smectite and illite volume fraction change at 5.3 and 18.3 years. The negative value means dissolution and the positive value means precipitation.

12.2.3.2 The Long-term Evolution

One of the most challenging issues for the performance assessment of geological disposal of high-level radioactive waste is the prediction of the long-term evolution of the repository. Typically, the safety performance assessment requires an evaluation of up to 100,000 years. But this is way beyond the time any experiment can run. So far, the longest experiment is the FEBEX *in situ* test that had been running for 18 years, which is incomparable to the required safety evaluation time. What researchers in the community of radioactive waste disposal can best do is to build a validated model and rely on the numerical model for long-term prediction. After the THMC models were well tested to make long-term predictions of the evolution of the bentonite barrier, we extended the base THMC model to a longer time. High ion concentrations near the heater shown by the base THMC model are of particular interest because such high concentrations could significantly affect the spent fuel degradation. The question, however, is whether high ion concentration in pore water is expected in bentonite in the vicinity of a canister in the long run. Although high Cl concentration was observed in the area near the heater, after bentonite becomes fully saturated, do concentrations remain at a high level? And another question is the long-term evolution of smectite. The THMC model for the FEBEX *in situ* test showed a relatively small amount of illitization (dissolution of smectite and precipitation of illite) at an area near the heater after 18 years of heating and hydration. 18 years is very long as a test, but still very short compared with the life span of a repository. Then, the question is whether there will be a significant amount of illitization in such

conditions if we run the model much longer? To answer these questions, the THMC model was run for 20,000 years. The model kept all other conditions the same except that a heat decay curve was applied to the heater, and it is named the "L-THMC model" when discussing results. The shape of the function is similar to that used in Rutqvist et al. (2011) for a 2-D model, but the magnitude is scaled down so that the temperature in the EBS close to the heat source is around 100 ºC, as shown in Figure 12-7. After 10,000 years, the temperature returns to the ambient condition.

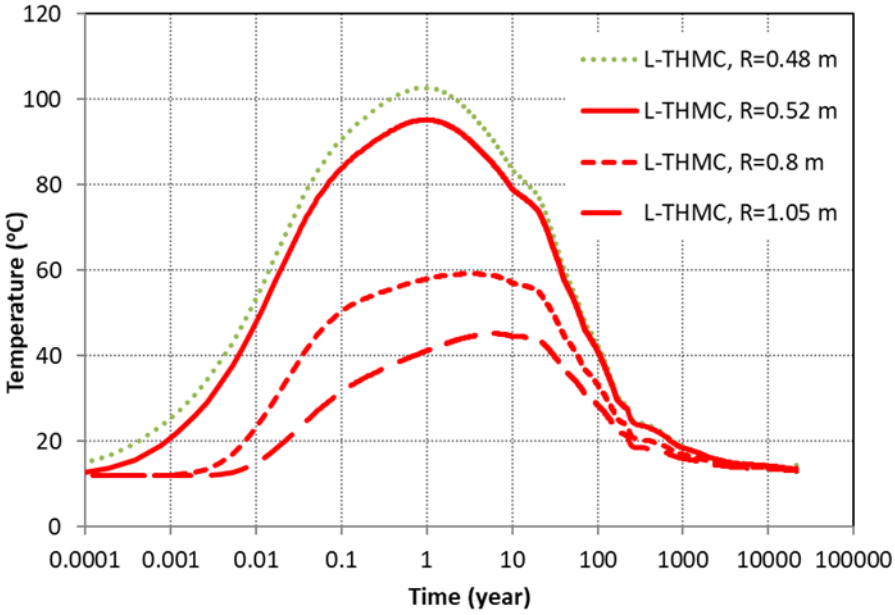

Figure 12-7 Temporal evolution of temperature at several radial distances in the 'L-THMC model".

Models show that inside the bentonite barrier at the very vicinity of the heater/canister, the evolution of relative humidity goes through 3 phases. An early desaturation phase lasts about 1 year and is featured with a sharp decrease of relative humidity; A rapid re-saturation phase that ends around 35-40 years in the current model. Then bentonite barrier enters into a low re-saturation phase: relative humidity at R = 0.48 m increases from 92% at 35 years to 97 % at 200 years and 99 % at 10,000 years in the "L-THMC" model (Figure 12-8). However, the water saturation is 100% after about 50 years (Figure 12-9).

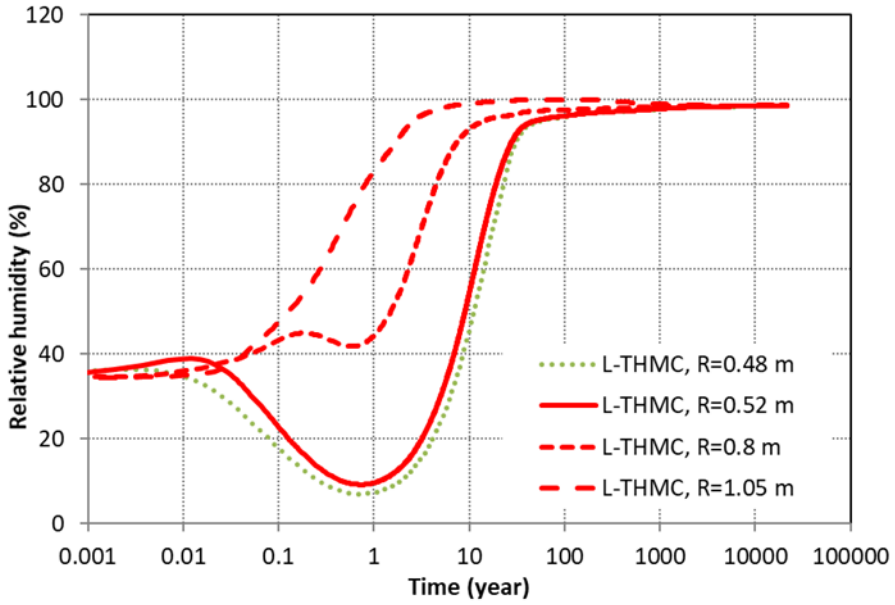

Figure 12-8 Temporal evolution of relative humidity at several radial distances in the 'THMC model".

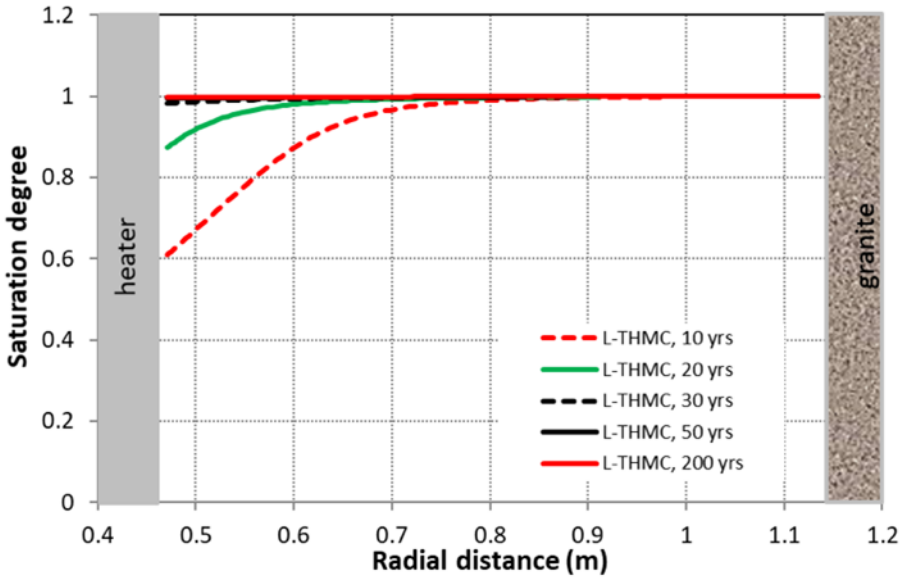

Figure 12-9 Spatial distribution of water saturation at different times in the "L-THMC model".

In the FEBEX *in situ* test, high ion concentration in the pore water of bentonite was observed. For example, as shown by chloride concentration profiles in Figure 12-3, the chloride concentration reached about 2 mol/L near the heater. Such high concentrations are largely the result of evaporation. Then the question is whether the concentration will decrease when the bentonite barrier becomes fully saturated. Figure 12-10 shows that chloride concentration is almost evenly distributed in the bentonite barrier with a concentration of about 0.1 mol/L, slightly lower than the initial chloride concentration in the pore water of bentonite (0.16 mol/L).

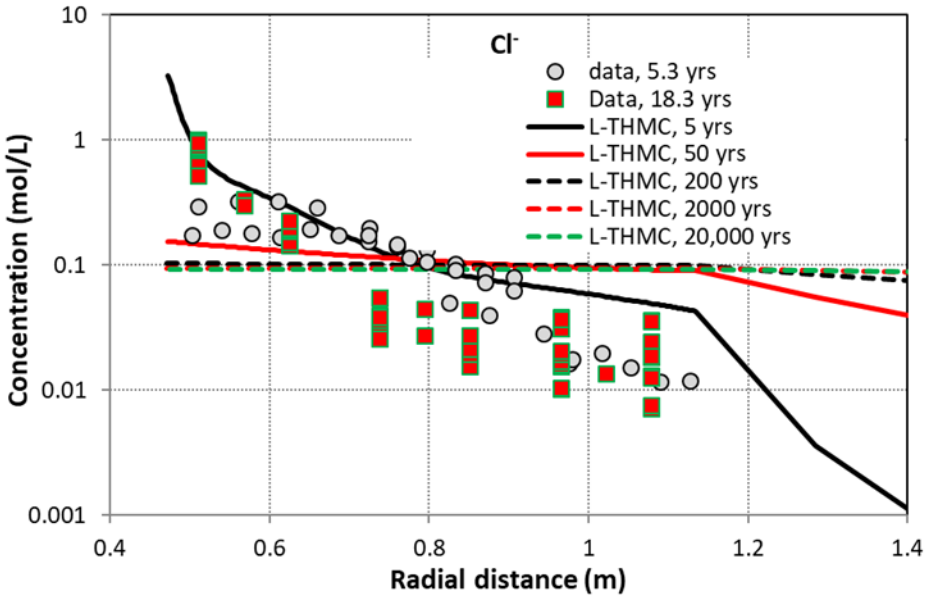

Figure 12-10 Spatial profiles of chloride concentration at several time points in the "L-THMC model".

As it was shown in previous modeling work (e.g., Zheng et al., 2016; 2017), the concentration profiles of cations (calcium, potassium, magnesium, and sodium) were largely shaped by transport processes despite their concentration levels being affected by mineral dissolution/precipitation and cation exchange. In terms of spatial trend, just like chloride, the spatial profile of potassium flattens out in the bentonite barrier: the concentration near the heater was just slightly higher than that near the granite.

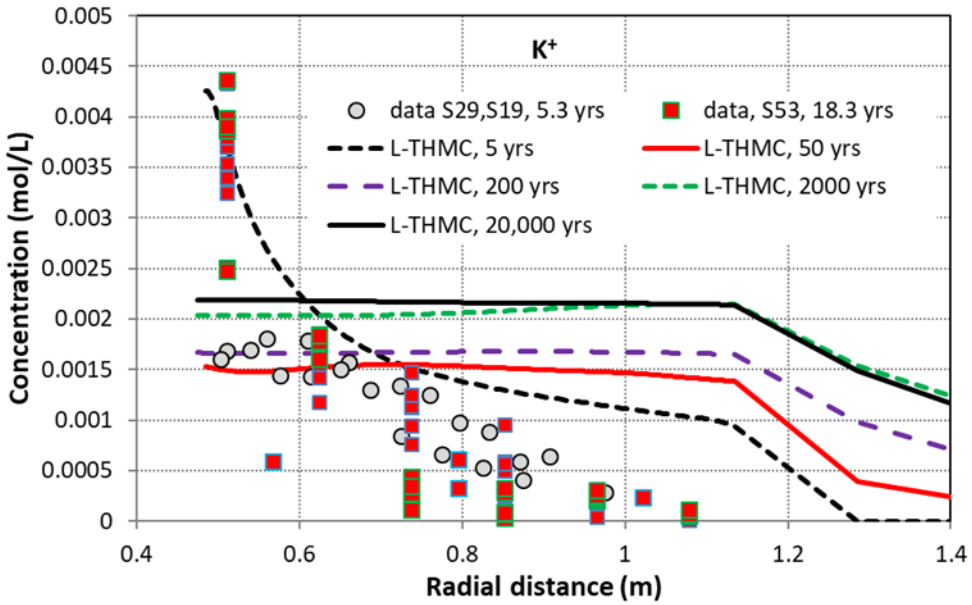

Figure 12-11 Spatial profiles of potassium concentration at several time points in the "THC model" and "THMC model".

Illitization (transformation of montmorillonite to illite) was one of the major concerns throughout the world that lead to the establishment of a thermal limit of 100 ºC for argillite and crystalline repository

with bentonite barrier (Zheng et al., 2015b). The base THMC model shows that montmorillonite dissolves and illite precipitates (illitization is usually expressed as the dissolution of montmorillonite and precipitation of illite, but here we only show the dissolution of montmorillonite) in bentonite near the heater with an amount less than 1% after 18 years, which was neither disapproved nor approved by the data because the data for mineral phase was too scattered (Zheng et al., 2018). It is known that illitization is a very slow process (Zheng et al., 2015a). The question raised here is, if the model runs longer, will there be a significant amount of illitization? The long-term THMC simulation "L-THMC" (Figure 12-12) shows that dissolution of montmorillonite does not progress further, instead, at 20,000 years, only 0.5% mass fraction of montmorillonite dissolves. However, the model shows that there is about 2% dissolution of montmorillonite at the granite/bentonite interface. It is also noteworthy that there is precipitation of montmorillonite across the bentonite barrier at 20,000 years.

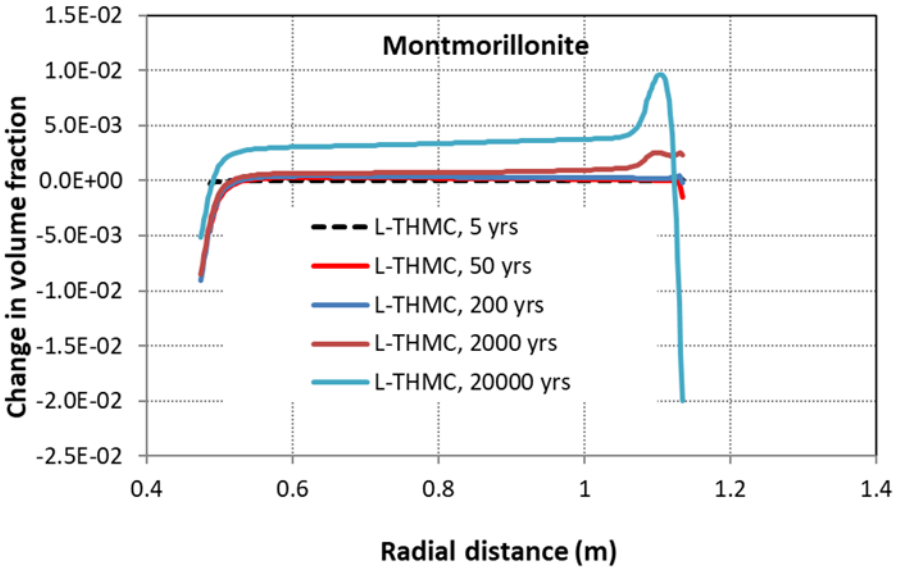

Figure 12-12 Model results for montmorillonite volume fraction change at several times in the "L-THMC model".

In the long run, when bentonite passes the initial high temperature and unsaturation-to-saturation transition time, the chemical change at the granite/bentonite interface becomes pronounced. For example, there is a remarkable dissolution of calcite at the bentonite side and precipitation at the granite side around the granite/bentonite interface. The long-term results indicate the importance of understanding the geochemical changes at the interfacial area, which will be discussed in the next section.

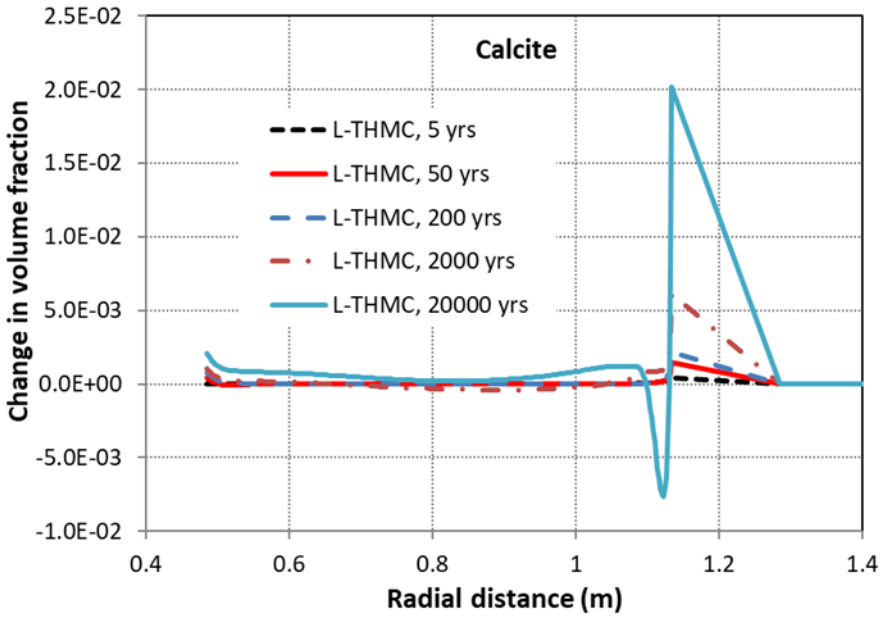

Figure 12-13 Model results for calcite volume fraction change at several time points in the "L-THMC model".

12.3 Modeling the Concrete/Bentonite Interface in the FEBEX *in situ* Test

12.3.1 Characterization of Bentonite/Concrete Interface at FEBEX *in situ* Test

After Heater #1 was dismantled in 2002, a concrete plug was constructed (see Figure 12-1). During the final dismantling in 2015, a series of cores were taken at the interfacial area (see Figure 12-14) and geochemical properties of concrete and bentonite were measured (Turrero & Cloet, 2017), which provide an opportunity to understand the long term (13 years) interaction of concrete and bentonite under *in situ* conditions.

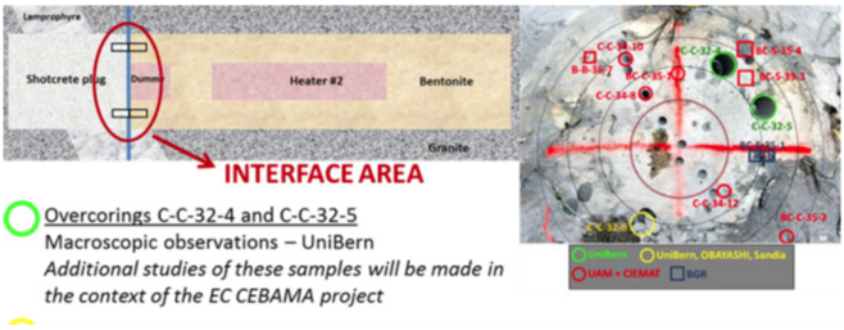

Figure 12-14 Overcoring at the concrete/bentonite interface during the final dismantling of the FEBEX in situ test (Turrero and Cloet, 2017).

Turrero and Cloet (2017) documented comprehensive measurements of the physical and geochemical properties of bentonite and concrete by various institutions around the concrete/bentonite interface. Some general observations are as follows:

After 13 years of interaction, the area with noticeable alterations extended up to 12 mm on both sides based on physical examination of the samples (see Figure 54 in Turrero and Cloet, 2017).

The impact of granite water on concrete was examined by comparing cores in the middle of the tunnel with cores in the vicinity of granite. These results suggest that the interaction with the granite rock is limited to the formation of calcite and the leaching of potassium towards the granite.

Within concrete, for sulfate, sodium, and potassium, a strong decrease at the bentonite interface was observed, while the calcium concentration was much higher at the interface based on the measured soluble ion in core C-C-32-2 (Figure 43 and Table 5-2 in Turrero and Cloet, 2017). However, there are only three data points: one close to the bentonite, two are 85 cm and 190 cm away from the interface. There is only one data point within 30 cm of the interface. Such observation does not reflect the sharp change around the interface.

Within concrete, precipitation of ettringite was observed both far and near the interface, and dissolution of portlandite at the interface was observed by XRD, which was depleted within 2 mm from the interface.

There is an increase in specific surface area on both side of the interface, indicating there might be pore size/structure change that is caused by mineral dissolution and precipitation in both concrete and bentonite.

Chloride content is an order of magnitude lower in the first 5 cm of bentonite analyzed close to the concrete than that in the reference (samples far away from the interface). Chloride diffuses into the concrete plug and Friedel's salt precipitates on the concrete side of the interface.

Na^+ concentration measured in aqueous extracts either on bentonite or concrete samples is lower than the value measured for the reference FEBEX bentonite or the reference concrete. K^+ concentration increased significantly in the first 2 mm of the bentonite. Thus, Ca^{2+} from portlandite diffuses towards the bentonite, where an increase in concentration is observed in the first centimeters compared to the FEBEX original. Soluble Mg^{2+} gets accumulated in the first 2 cm from the interface in concrete. In bentonite, however, Mg^{2+} measured in aqueous extracts is negligible, as precipitation of Mg silicates occurs.

12.3.2 Model Development

We designed a 1-D reactive transport model to simulate the interaction between bentonite and concrete: the model extends 30 cm on each side and no-flux boundary conditions are imposed such that there is only diffusive flux across the interface. The model runs for 13 years, simulating the time from 2002 to 2015 (the period from the construction of the concrete plug in 2002, when Heater #1 was dismantled to the dismantling Heater #2 in 2015). The porosity is 0.125 for concrete and 0.41 for bentonite. Up to now, we were able to finish a set of preliminary simulations which focused on the chemical reactions and have the following key simplifications or assumptions: porosity remains constant and the change of porosity due to mineral precipitation/dissolution is neglected; effective diffusion coefficient is 2×10^{-10} m^2/s; and the effects of porosity change and tortuosity are disabled. In the near future, these simplifications will be removed and their effect on the bentonite/concrete interaction will be tested.

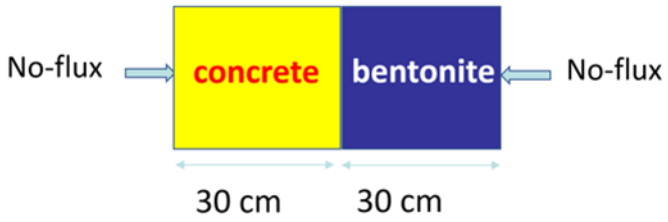

Figure 12-15 Setup of the 1-D reactive transport model

The model considered aqueous complexation, mineral dissolution/precipitation, cation exchange, surface complexation. Table 12-4 lists the initial pore water composition of bentonite and concrete. Because when concrete was constructed and concrete/bentonite interaction started, bentonite has been reacting with granite for 5.3 years (from 1997 to 2002), we took the model results of pore water composition from the coupled THMC model (see Section 12.2.2) for a location at a radial distance of 0.9 m at 5.3 years. The mineral composition of FEBEX bentonite is listed in Table 12-5, which is also the calculated results from the coupled THMC model.

Table 12-4 Pore-water composition (mol/kg water except for pH) of FEBEX bentonite and concrete.

Concentration (molal)	Concrete	Bentonite
pH	7.872	1.30E+01
Cl^-	7.0239E-02	2.30E-02
SO_4^{-2}	4.8882E-02	3.44E-03
HCO_3^-	1.0316E-03	6.75E-06
Ca^{+2}	8.2668E-03	3.20E-03
Mg^{+2}	1.1951E-02	7.76E-05
Na^+	1.3571E-01	6.29E-02
K^+	1.2963E-03	1.98E-02
$SiO_2(aq)$	3.3423E-04	5.21E-03
AlO_2^-	2.4820E-10	3.53E-05

Table 12-5 Mineral composition and their saturation index of FEBEX bentonite.

	Saturation index	Mass fraction
calcite	0	2.00E-02
illite-kk	-2.130684	1.05E-04
kaolinite	-1.822063	2.97E-04
smectite-ca-	0.000372	9.20E-01
quartz	0.318345	3.00E-02
k-feldspar	-0.001467	9.90E-03
cristobalite	0.057903	1.00E-02
ab80an20-lo	-7.928693	1.00E-02
gypsum	-0.269308	0.00E+00
dolomite-2	-2.055845	0.00E+00
albite	-0.722134	0.00E+00
anorthite	-9.856761	0.00E+00
anhydrite	-0.49045	0.00E+00
portlandite	-10.208138	0.00E+00
sepiolite	0.497437	0.00E+00
brucite	-4.382247	0.00E+00
ettringite	-23.001554	0.00E+00
csh(1.6)	-11.103212	0.00E+00
csh(0.8)	-4.28886	0.00E+00

The determination of initial conditions for pore water, and minerals, for concrete requires static long-term equilibrium simulations. To establish these equilibrium simulations, we first took the minerals composition measured in two cores C-C-34-10 and C-C-32, with reference to other publications (Mon et al., 2017 and Marty et al., 2015) and decide the initial estimates of minerals composition. Then, we used the measured water composition in C-C-32-2 at locations far away (190 cm) from the interface as an initial estimates of pore water composition. With the initial estimates of mineral and pore water composition, we ran the model for 1000 years for the water-minerals system to reach a quasi-equilibrium condition. The final results of this equilibrium simulation are used as the initial conditions for concrete in the reactive transport model: Table 12-4 lists the pore water composition for concrete and Table 12-6 lists the minerals and their saturation index. Note that in Table 12-5 and Table 12-6, the minerals with zero mass fraction are secondary minerals—they can be formed during the simulation but not initially present in the model.

Table 12-6 Mineral composition and their saturation index of concrete.

Minerals	SI	Mass fraction
calcite	0	2.80E-01
quartz	-1.83607	3.30E-01
k-feldspar	0.000386	6.00E-02
albite	-2.27878	8.00E-02
portlandite	-0.03279	4.99E-02
muscovite	-2.43862	6.00E-02
ettringite	4.416736	5.04E-02
brucite	4.078015	0.00E+00
csh(1.6)	3.022906	0.00E+00
csh(0.8)	1.696726	0.00E+00
gypsum	-1.34945	0.00E+00
illite-kk	-3.58415	0.00E+00
kaolinite	-6.02046	0.00E+00
smectite-ca-	-4.78108	0.00E+00
dolomite-2	-3.77093	0.00E+00
anorthite	-3.88299	0.00E+00
anhydrite	-1.57271	0.00E+00
cristobalite	-2.09651	0.00E+00
ab80an20-lo	-7.97926	0.00E+00
sepiolite	21.41516	0.00E+00

12.3.3 Model Results

Diffusion and reactions shape the concentration profiles at the end of the simulation (i.e., 13 years). Conservative species, such as chloride (Figure 12-16) are controlled by the diffusion following the concentration gradient whereas highly reactive species are largely controlled by reactions (e.g., carbonate and pH in Figure 12-16). The concentration profile of species like sulfate (Figure 12-16) and major cations (Figure 12-17) are largely shaped by the diffusion, but the irregularity at the vicinity of the interface illustrates the effect of chemical reactions. So far, we only have pH data in pore water of concrete, which are in general matched by the model. Data for the concentration of other species in concrete and bentonite were reported in Turrero and Cloet (2017), but were not used here for comparison because (1) information is incomplete (e.g., for concentration in concrete, sample locations were given as "section 1 close to the dummy" without specific distance), and (2) the graph resolutions are not enough to extract data. We are in the process of contacting the editors of the report to obtain a data table.

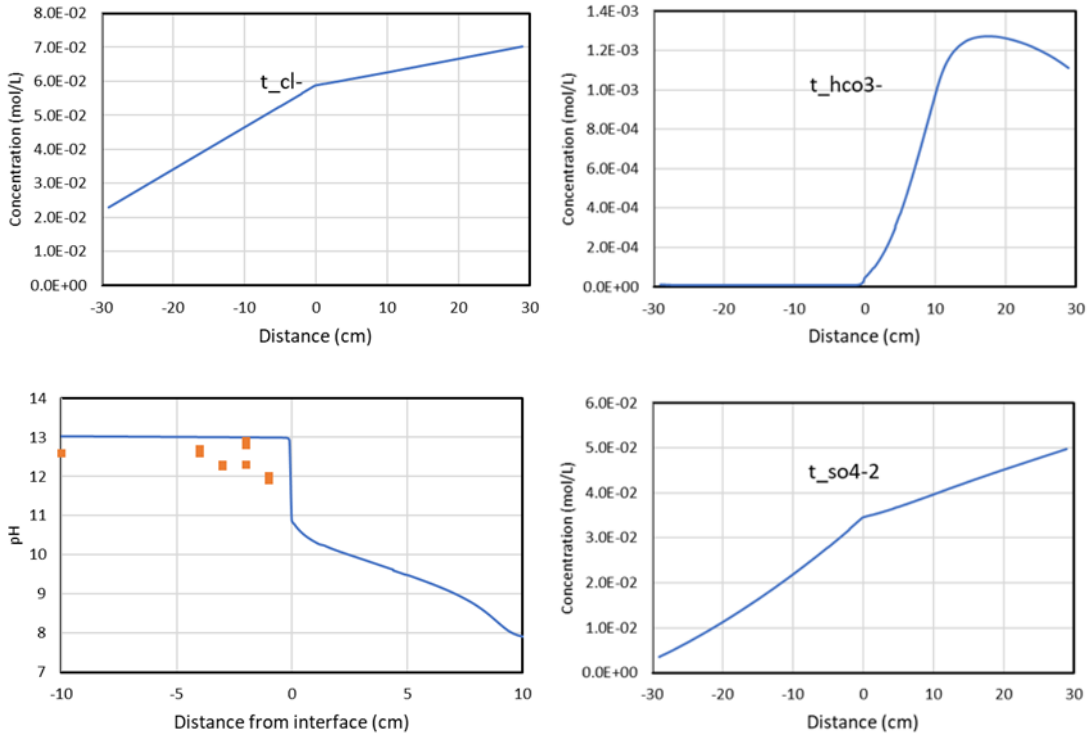

Figure 12-16 Computed total concentrations of chloride, carbonate, sulfate, and pH at the end of the simulation. Also shown are measured pH in concrete. The interface locates at X=0, negative values are on the concrete side and positive values are on the bentonite side.

Data show that chloride content is an order of magnitude lower in the first 5 cm of bentonite than that in the reference (samples far away from the interface). But the model shows a less degree of decreasing trend towards the interface within bentonite. One possible reason is that the model does not consider Friedel's salt whose precipitation may significantly decrease the concentration of chloride around the interfacial area.

Data show that within the concrete, sulfate has a strong decrease at the bentonite interface based on the measured soluble ion in core C-C-32-2 (Figure 43 and Table 5-2 in Turrero and Cloet, 2017). However, the model shows the opposite trend, which suggests that the calculation of initial sulfate concentration in concrete was not correct. ***

Na concentration measured in aqueous extracts either on bentonite or concrete samples is lower than the value measured for the reference FEBEX bentonite or the reference concrete, which are not reproduced by the model, suggesting that there might be significant precipitation of Na-bearing minerals that have been missed in the current model. Data also show that potassium within concrete has a strong decrease at the bentonite interface, and potassium within bentonite increases significantly in the first 2 mm of the bentonite, which is qualitatively matched by the model.

Data show that an increase in calcium concentration is observed in the first centimeters compared to the FEBEX original, however, the model does not exhibit such behavior, which may be attributed to precipitation of calcite in bentonite although calcium from portlandite diffuses towards the bentonite.

Measured data show soluble magnesium within concrete gets accumulated in the first 2 cm from the interface in concrete, which is generally matched by the data. In bentonite measured magnesium in aqueous extracts is negligible, but the model shows different behavior. Turrero and Cloet (2017) mentioned that this is caused by the precipitation of Mg silicates occurs. But it is unclear what the exact mineral phases are.

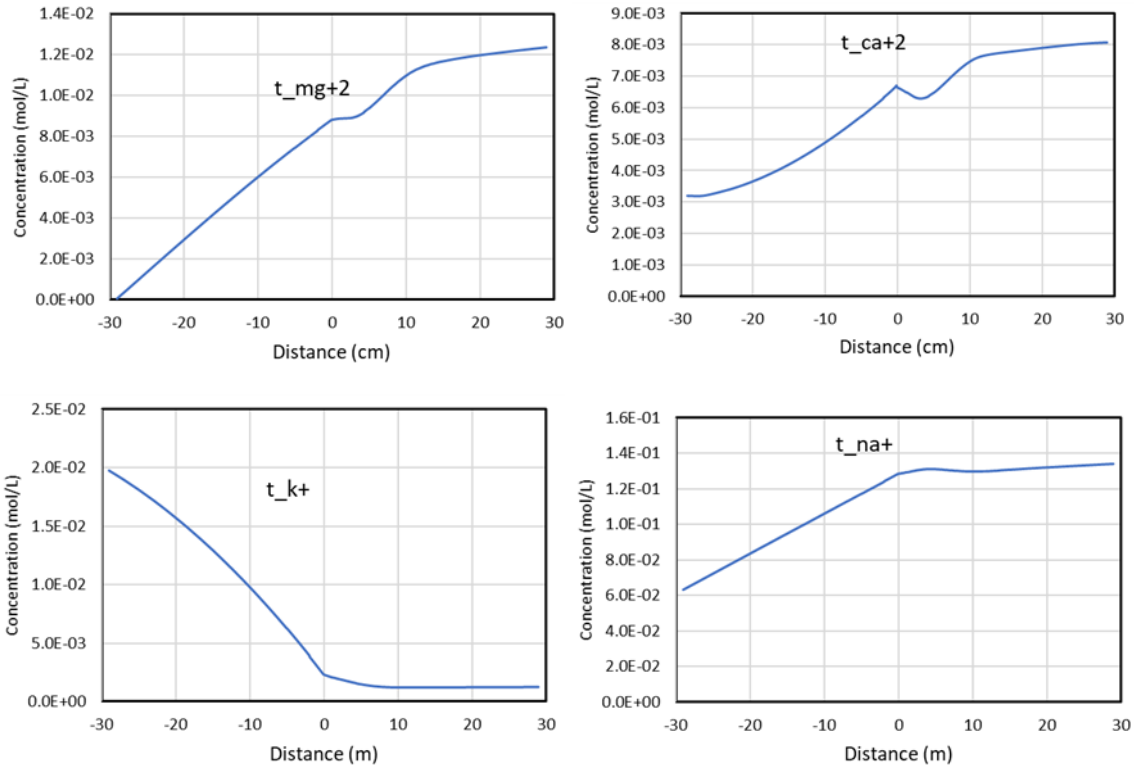

Figure 12-17 Computed total concentrations of major cations at the end of the simulation. Also shown are measured pH in concrete. The interface locates at X=0, negative values are on the concrete side and positive values are on the bentonite side.

Regarding mineralogical changes, pH and calcium changes involve changes in minerals like portlandite, ettringite, calcite, and C-(A)-S-H. Turrero and Cloet (2017) reported that on the concrete side, portlandite dissolves, and losing Ca destabilizes ettringite, and there is decalcification in about 15 mm and formation of C-(A)-S-H. The model confirms the dissolution of portlandite (Figure 12-18) and ettringite (Figure 12-19). However, the model shows precipitation of calcite (Figure 12-20) instead of decalcification as data suggest, which is probably why the model does not show noticeable precipitation of CSH (Figure 12-21)

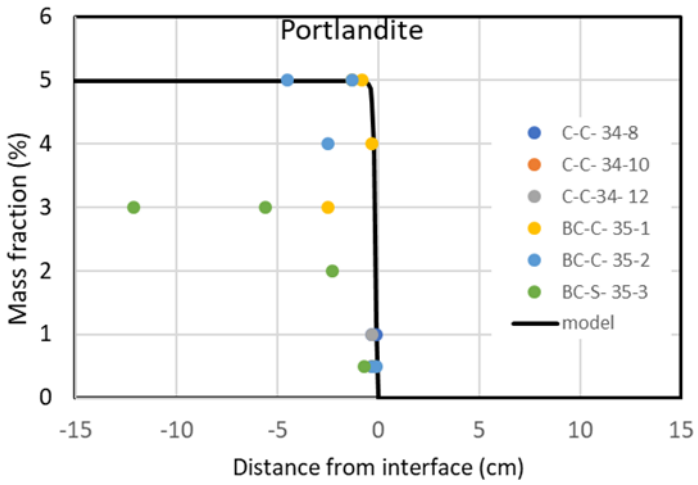

Figure 12-18 Computed mass fraction of portlandite at the end of the simulation.

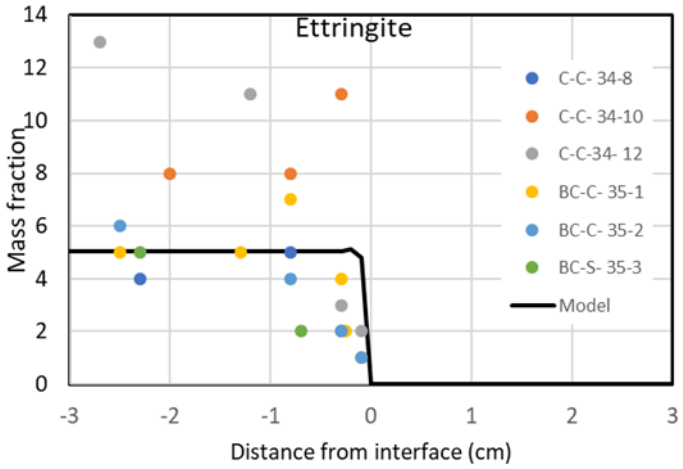

Figure 12-19 Computed mass fraction of ettringite at the end of the simulation.

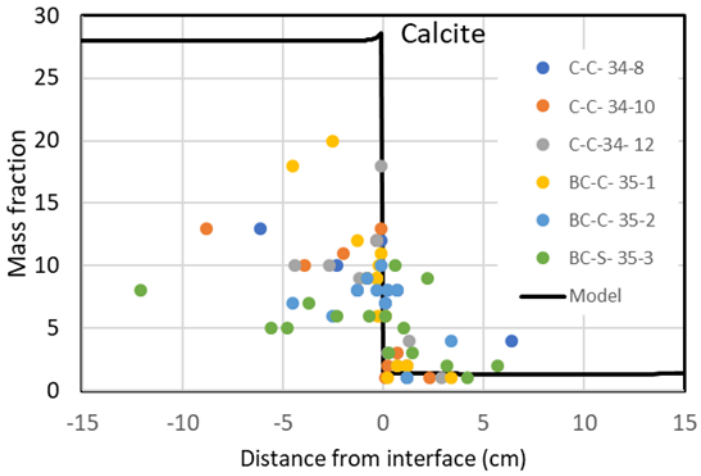

Figure 12-20 Computed mass fraction of calcite at the end of the simulation.

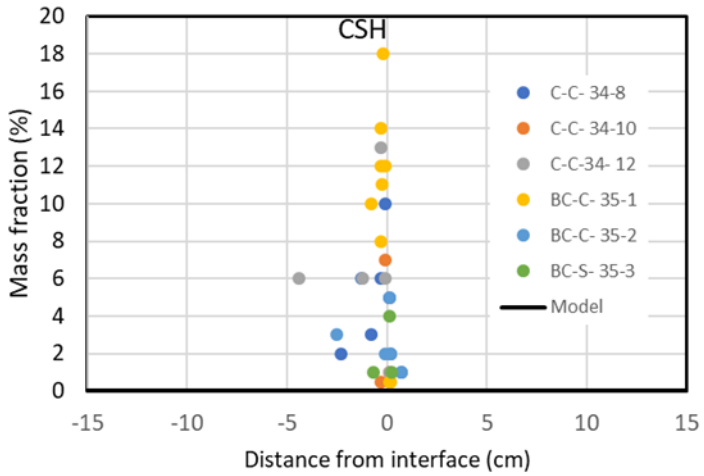

Figure 12-21 Computed mass fraction of CSH at the end of the simulation.

On the bentonite side, the model and data are consistent in terms of precipitation of calcite which is caused by the diffusion of calcium from concrete to bentonite because of the dissolution of portlandite in concrete. The model also confers the observation of the dissolution of montmorillonite (Figure 12-22) due to silicate depletion. The preliminary model explains the behavior of some species and mineral, but some discrepancies need to be resolved by revising the model.

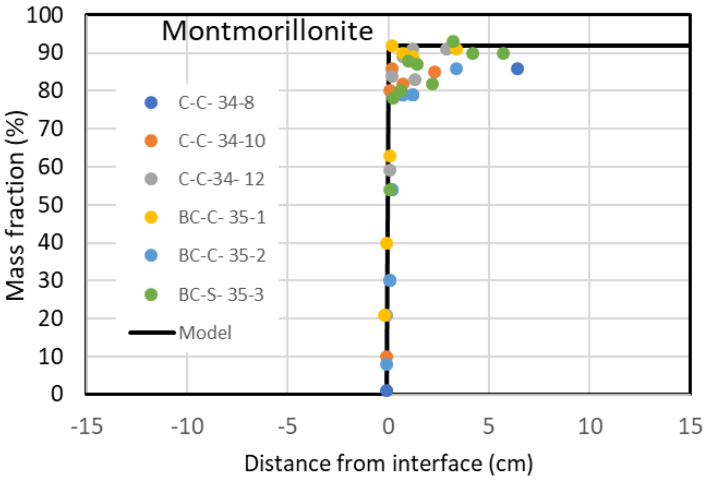

Figure 12-22 Computed mass fraction of montmorillonite at the end of the simulation.

12.4 HotBENT Updates

HotBENT project that is composed of a large-scale test, accompanied by a laboratory program and modeling platform has made milestone progress in FY21. The construction of the field test is close to being finished and a model platform is launched. In this section, we give an update of the lasted development of the HotBENT project, list the opportunities that SFWST can participate in. DOE's participation in this new collaborative effort could be extremely beneficial; substantial cost savings would be achieved in the design of a repository if HotBENT demonstrates that the maximum temperature of bentonite backfill can be raised without drastic performance implications.

The field test is currently under construction in the FEBEX gallery (drift) that starts at the northern entrance of the Grimsel Test Site (Figure 12-23). The experiment is constructed in a modular fashion, whereby a module represents a heater rested on a bentonite block pedestal and encapsulated by a granular bentonite backfill (Figure 12-24). Modules differ in their design temperature, bentonite type, experimental duration, and whether a liner is used or now. The two modules deepest in the drift are separated from the others by an insulation plug to enable excavation of part of the experiment with minimal perturbations to the remaining modules. The THM evolution of the HotBENT experiment will be monitored with ~1200 instruments, including parameters such as temperature, mechanical pressure, hydraulic pressure, water content, saturation, and humidity, displacements, gas concentration, and gas pressure.

From FY16 to the present, NAGRA and partners of the HotBENT project held partners meetings roughly twice a year to develop a plan/design for the HotBENT project and discuss the progress of the project. The latest meeting was held in May 2021 (Kober & Vomvoris, 2021). The overall timeline of the project is listed in Figure 12-25. LBNL actively participated in the project from the very beginning, including conducting scoping calculations to support the design (Zheng et al. 2017; 2018). The official HotBENT Project start was in 2018 once all agreements with the partner institutions had been in place. In addition to DOE and NAGRA, the joint project has three full partner institutions (SURAO from the Czech Republic, RWM from the United Kingdom, and NUMO from Japan) and four associated institutions (NWMO from Canada, BGR from Germany, ENRESA from Spain, and Obayashi from Japan).

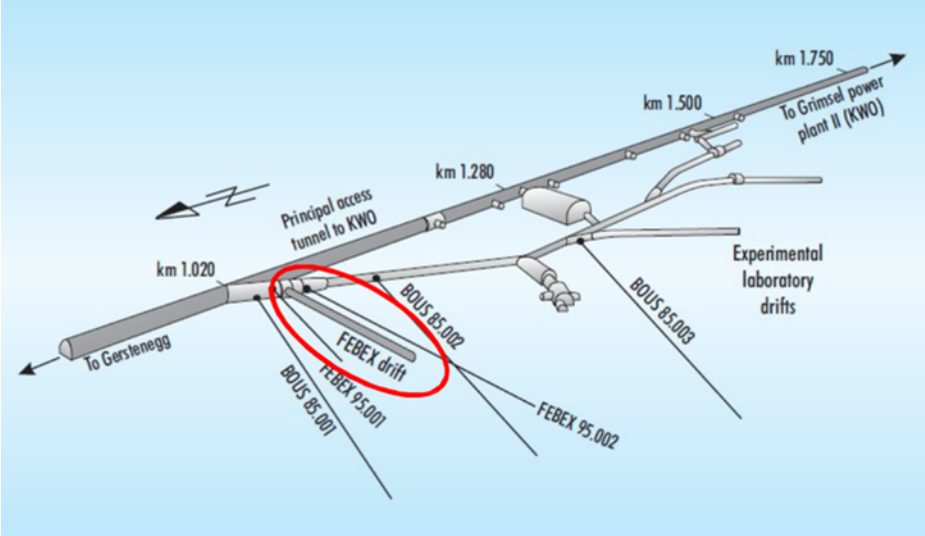

Figure 12-23 Location of the FEBEX Drift at the Grimsel Test Site (NAGRA, 2019)

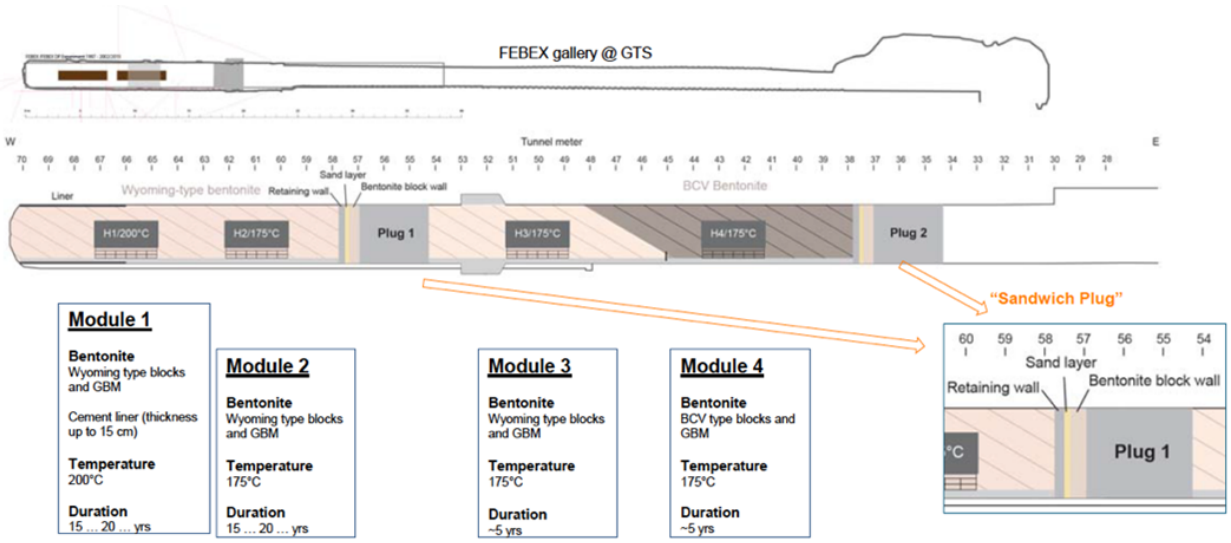

Figure 12-24 Final HotBENT design with individual modules (Kober, 2020)

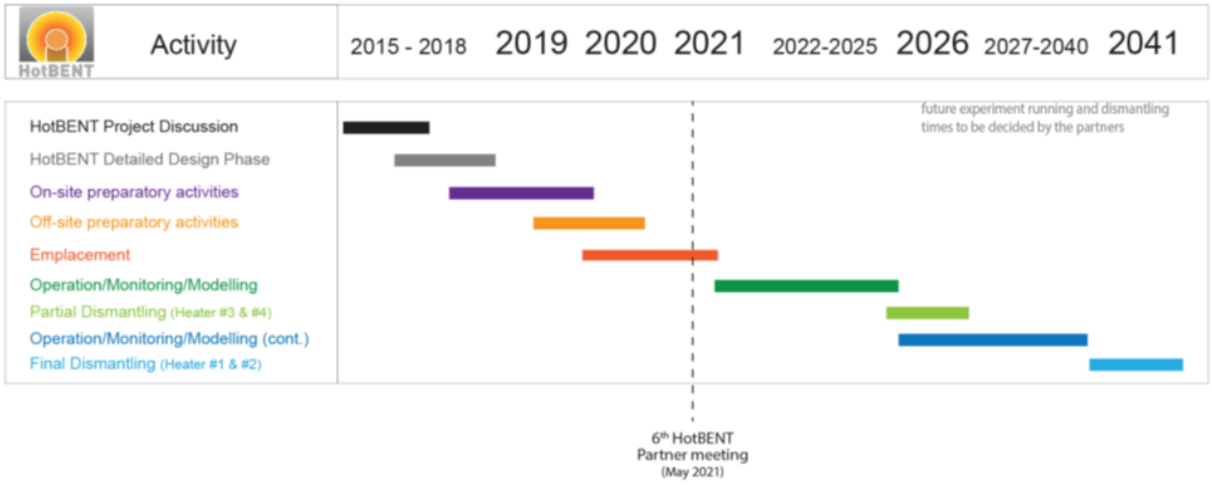

Figure 12-25 Planned timeline for HotBENT experiment (Kober & Vomvoris, 2021).

As to the time of the partner meeting in May 2021, all the area that use Wyoming bentonite was constructed (Figure 12-26). The construction of the entire test is scheduled to be finished in July 2021. Different heating schemes were discussed in the partner meeting (Kober & Vomvoris, 2021), and heating of Sector 1 could start at the end of May.

Meanwhile, NAGRA and partners have discussed the initiation of a HotBENT Modeling Platform and the first kickoff meeting was held in 2020. In this modeling platform, modeling groups associated with the individual partner organizations are working on predictive and interpretative modeling of the test data. The preliminary tasks are listed in Table 12-7. The multi-institutional group will be structured so as to (a) increase the support provided to the HotBENT experiment and its interpretative evaluation, (b) broaden questions being addressed to advance fundamental understanding, and (c) address modeling issues, specifically the quantification of conceptual uncertainties. All partners encourage the Modeling Platform to pursue a broad spectrum of alternative conceptual models that address a common question or support a decision to be made jointly by the HotBENT participants. In addition, specific expertise and skills of the modeling groups can be used to examine particular aspects raised by the data collected as part

of the HotBENT experiment or to make specific predictions. SFWD scientists from LBNL and SNL plan to participate in the Modeling Platform. LBNL's modeling plan is to start with a 3-D TH model and gradually increase the level of complexity until 3-D coupled THMC model is developed and tested with data.

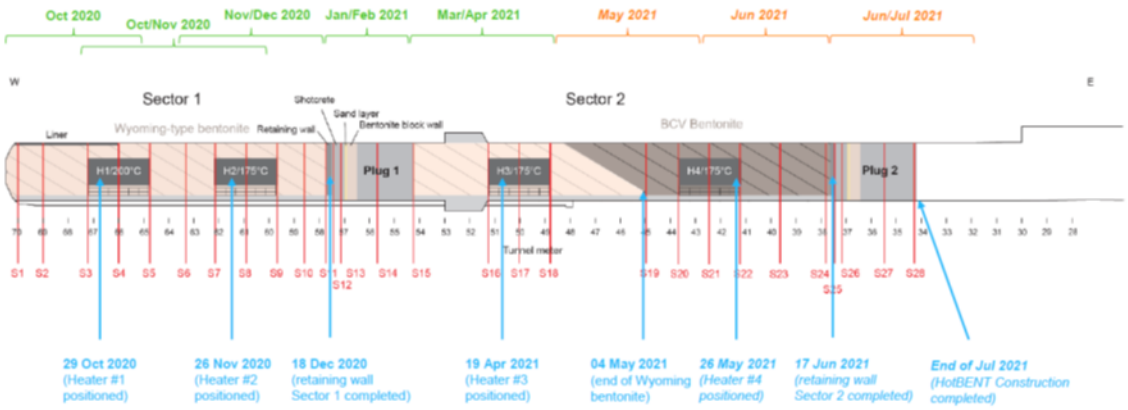

Figure 12-26 HotBENT emplacement milestones (Kober & Vomvoris, 2021).

Table 12-7 Task description of the model platform in the HotBENT project.

Tasks	Task Description (*proposal, to be discussed in first Modelling Meeting*)
1	Perform coupled TH (reference), TM/THM, THC, and THMC simulations of HotBENT
2	Repeated blind predictions of observable variables using models of different complexity
3	Model calibration or data assimilation using different conceptual models
4	Prediction of critical performance measures that affect decision points
5	Direct comparison of simulated output variables
6	Data-worth analysis
7	Conceptual models/uncertainty (summary task)

In addition to the field test and modeling platform, laboratory programs that mainly target the measurement of bentonite properties are also established. One such effort is the high-temperature column tests, but certainly, other laboratory tests are encouraged.

12.5 Summary and Future Work

The FEBEX *in situ* test, which lasted more than 18 years, is extremely valuable for validating the coupled THMC model and deepening our understanding of the evolution of the bentonite barrier throughout heating and hydration. The ultimate goal is to use THMC data from FEBEX-DP to validate THMC models and therefore enhance our understanding of coupled THMC processes in bentonite. After the THMC model provided a coherent explanation of THMC data collected at the FEBEX *in situ* test, we were using well-calibrated THMC to conduct more exploratory simulations. The simulations conducted in FY21 addressed the question about the long-term alteration of bentonite, up to 10,000 years under conditions similar to the FEBEX *in situ* test.

In FY21, we also developed a 1D reactive transport model to explain the data collected at the bentonite/concrete interface. The model was able to reproduce some data, but there were also discrepancies between model and data, which warranted further refinement of the model. In the remaining time of FY21 and FY22, we will expand the model by firstly adding new secondary minerals and refining the thermodynamic and kinetic database to resolve the discrepancies between measured aqueous concentration and model results, and secondly introducing the effect of changing porosity on tortuosity and diffusion coefficient to understand the effect of mineral dissolution/precipitation on the transport process at the interface.

As the HotBENT field test is scheduled to start heating in July 2021, in the remaining part of FY21, our effort will focus on developing a 3D TH model for the field test as part of the modeling platform launched by the HotBENT project.

REFERENCES

Adachi-Pagano, M., Forano, C., & Besse, J. P. (2000). Delamination of layered double hydroxides by use of surfactants. *Chemical Communications*, *1*, 91–92. https://doi.org/10.1039/a908251d

Afanasiev, V. N., Ustinov, A. N., & Vashurina, I. Y. (2009). State of Hydration Shells of Sodium Chloride in Aqueous Solutions in a Wide Concentration Range at 273.15−373.15 K. *The Journal of Physical Chemistry B*, *113*(1), 212–223. https://doi.org/10.1021/jp711542j

Aldaba, D., Glaus, M., Leupin, O., van Loon, L., Vidal, M., & Rigol, A. (2014). Suitability of various materials for porous filters in diffusion experiments. *Radiochimica Acta*, *102*(8), 723–730. https://doi.org/10.1515/ract-2013-2176

Alonso, M. C., García Calvo, J. L., Cuevas, J., Turrero, M. J., Fernández, R., Torres, E., & Ruiz, A. I. (2017). Interaction processes at the concrete-bentonite interface after 13 years of FEBEX-Plug operation. Part I: Concrete alteration. *Physics and Chemistry of the Earth, Parts A/B/C*, *99*, 38–48. https://doi.org/10.1016/j.pce.2017.03.008

Alphonse, P., & Courty, M. (2005). Structure and thermal behavior of nanocrystalline boehmite. *Thermochimica Acta*, *425*(1–2), 75–89. https://doi.org/10.1016/j.tca.2004.06.009

Altmann, S. (2008). 'Geochemical research: A key building block for nuclear waste disposal safety cases. *Journal of Contaminant Hydrology*, *102*(3–4), 174–179. https://doi.org/10.1016/j.jconhyd.2008.09.012

Altmann, S., Tournassat, C., Goutelard, F., Parneix, J. C., Gimmi, T., & Maes, N. (2012). Diffusion-driven transport in clayrock formations. *Applied Geochemistry*, *27*(2), 463–478. https://doi.org/10.1016/j.apgeochem.2011.09.015

Alvarez, M., Lapitz, P., & Ruzzante, J. (2008). AE response of type 304 stainless steel during stress corrosion crack propagation. *Corrosion Science*, *50*(12), 3382–3388. https://doi.org/10.1016/j.corsci.2008.08.028

AMBERG. (2019). HotBENT: Experiment Plan (Draft 20190927 v2.docx). Distributors: Florian Kober (NAGRA) & Stratis Vomvoris (NAGRA).

Andersson, J., Skagius, K., Winberg, A., Lindborg, T., & Ström, A. (2013). Site-descriptive modelling for a final repository for spent nuclear fuel in Sweden. *Environmental Earth Sciences*, *69*(3), 1045–1060. https://doi.org/10.1007/s12665-013-2226-1

Baeyens, B., & Bradbury, M. H. (2004). Cation exchange capacity measurements on illite using the sodium and cesium isotope dilution technique: effects of the index cation, electrolyte concentration and competition: modeling. *Clays and Clay Minerals*, *52*(4), 421–431. https://doi.org/10.1346/ccmn.2004.0520403

Balistrieri, L. S., & Chao, T. (1990). Adsorption of selenium by amorphous iron oxyhydroxide and manganese dioxide. *Geochimica et Cosmochimica Acta*, *54*(3), 739–751. https://doi.org/10.1016/0016-7037(90)90369-v

Balistrieri, L. S., & Chao, T. T. (1987). Selenium Adsorption by Goethite. *Soil Science Society of America Journal*, *51*(5), 1145–1151. https://doi.org/10.2136/sssaj1987.03615995005100050009x

Bárcena, I., Fuentes-Cantillana, J.L. & García-Siñeriz, J.L. (2003). Dismantling of the Heater 1 at the FEBEX "“in situ”" test. Description of operations. Enresa Technical Report 9/2003.

Bárcena, I., García-Siñeriz, J.L. . (2015). FEBEX-DP (GTS) Full Dismantling Sampling Plan (in 492 situ Experiment). Nagra Arbeitsbericht NAB 15-14. 103 pp.

Bar-Yosef, B., and Meek, D. (1987) Selenium Sorption by Kaolinite and Montmorillonite. *Soil Science*, *144*(1), 11–19. https://doi.org/10.1097/00010694-198707000-00003

Bénézeth, P., Palmer, D. A., & Wesolowski, D. J. (2001). Aqueous high-temperature solubility studies. II. The solubility of boehmite at 0.03 m ionic strength as a function of temperature and pH as determined by in situ measurements. *Geochimica et Cosmochimica Acta*, *65*(13), 2097–2111. https://doi.org/10.1016/s0016-7037(01)00585-3

Bennett, C. H. (1976). Efficient estimation of free energy differences from Monte Carlo data. *Journal of Computational Physics*, *22*(2), 245–268. https://doi.org/10.1016/0021-9991(76)90078-4

BOLT, G. H. (1955). Ion Adsorption by Clays. *Soil Science*, *79*(4), 267–276. https://doi.org/10.1097/00010694-195504000-00004

Börjesson, L., Gunnarsson, D., Johannesson, L-E., and Jonsson, E. (2010). Design, production and initial state of the buffer. Svensk Kärnbränslehantering Technical Report, TR-10-15, 89.

Bourdelle, F., Mosser-Ruck, R., Truche, L., Lorgeoux, C., Pignatelli, I., & Michau, N. (2017). A new view on iron-claystone interactions under hydrothermal conditions (90 °C) by monitoring in situ pH evolution and H2 generation. *Chemical Geology*, *466*, 600–607. https://doi.org/10.1016/j.chemgeo.2017.07.009

Bourdelle, F., Truche, L., Pignatelli, I., Mosser-Ruck, R., Lorgeoux, C., Roszypal, C., & Michau, N. (2014). Iron–clay interactions under hydrothermal conditions: Impact of specific surface area of metallic iron on reaction pathway. *Chemical Geology*, *381*, 194–205. https://doi.org/10.1016/j.chemgeo.2014.05.013

Bourg, I. C., & Sposito, G. (2011). Molecular dynamics simulations of the electrical double layer on smectite surfaces contacting concentrated mixed electrolyte (NaCl–CaCl2) solutions. *Journal of Colloid and Interface Science*, *360*(2), 701–715. https://doi.org/10.1016/j.jcis.2011.04.063

Bourg, I. C., Sposito, G., & Bourg, A. C. M. (2006). Tracer diffusion in compacted, water-saturated bentonite. *Clays and Clay Minerals*, *54*(3), 363–374. https://doi.org/10.1346/ccmn.2006.0540307

Bradbury, M., & Baeyens, B. (2009). Sorption modelling on illite. Part II: Actinide sorption and linear free energy relationships. *Geochimica et Cosmochimica Acta*, *73*(4), 1004–1013. https://doi.org/10.1016/j.gca.2008.11.016

Bradbury, M. H., & Baeyens, B. (2003). Porewater chemistry in compacted re-saturated MX-80 bentonite. *Journal of Contaminant Hydrology*, *61*(1–4), 329–338. https://doi.org/10.1016/s0169-7722(02)00125-0

Bradbury, M. H., & Baeyens, B. (2006). Modelling sorption data for the actinides Am(III), Np(V) and Pa(V) on montmorillonite. *Radiochimica Acta*, *94*(9–11), 619–625. https://doi.org/10.1524/ract.2006.94.9-11.619

Bradbury, M. H., Berner, U., Curti, E., Hummel, W., Kosakowski, G., and Thoenen, T. (2014). The long term geochemical evolution of the nearfield of the HLW repository (No. NTB-- 12-01). Paul Scherrer Institute (PSI).

Buining, P. A., Pathmamanoharan, C., Jansen, J. B. H., & Lekkerkerker, H. N. W. (1991). Preparation of Colloidal Boehmite Needles by Hydrothermal Treatment of Aluminum Alkoxide Precursors. *Journal of the American Ceramic Society*, *74*(6), 1303–1307. https://doi.org/10.1111/j.1151-2916.1991.tb04102.x

Bunker, B. C., & Casey, W. H. (2016). *The Aqueous Chemistry of Oxides* (Illustrated ed.). Oxford University Press.

Cai, W., Yu, J., & Mann, S. (2009). Template-free hydrothermal fabrication of hierarchically organized γ-AlOOH hollow microspheres. *Microporous and Mesoporous Materials*, *122*(1–3), 42–47. https://doi.org/10.1016/j.micromeso.2009.02.003

Calvo, J. G., Hidalgo, A., Alonso, C. and Luco, L. F. (2010). Development of low-pH cementitious materials for HLRW repositories: Resistance against ground waters aggression. *Cement and Concrete Research*, 40(8), 1290-1297.

Caporuscio, F. A., Migdissov, A., Rock, M. J., Sauer, K. B., and van Hartesveldt, N. F. (2019). Engineered Barrier System R&D and International Collaborations–LANL (FY19) (No. LA-UR-19-24222). Los Alamos National Lab. (LANL), Los Alamos, NM (United States).

Caporuscio, F.A., Sauer, K.B., Rock, M.J., and Houser, L.M., (2018), Engineered System R&D and International Collaborations – Los Alamos National Laboratory (FY18). Deliverable. SF&WD R&D Work package # SF18LA01030801/SF-18LA01030805, LA-UR-18- 27601.

Caporuscio, F.A., Sauer, K.B., and Rock, M.J. (2020), Engineered System R&D and International Collaborations – Los Alamos National Laboratory (FY18). Deliverable. SF&WD R&D Work package # SF-02LA01030801 Rev2/SF-20LA01030805, LA-UR-20-25330.

Caporuscio, F.A., Sauer, K.B., and Rock, M.J. (2021), Engineered System R&D and International Collaborations – Los Alamos National Laboratory (FY21). Deliverable. SF&WD R&D Work package # SF-02LA01030801 Rev2/SF-20LA01030805, LA-UR-21-28735.

Cathelineau, M., Guillaume, D., Mosser-Ruck, R., Dubessy, J., Charpentier, D., Villiéras, F., Michau, N., (2005). Dissolution–crystallization processes affecting di-octahedral smectite in presence of iron metal: implication on mineral distribution in clay barriers. *Clays in Natural and Engineered Barriers for Radioactive Waste Confinement*. ANDRA, France, p. 35.

Charlet, L., Kang, M., Bardelli, F., Kirsch, R., Géhin, A., Grenèche, J. M., & Chen, F. (2012). Nanocomposite Pyrite–Greigite Reactivity toward Se(IV)/Se(VI). *Environmental Science & Technology*, *46*(9), 4869–4876. https://doi.org/10.1021/es204181q

Charlet, L., Scheinost, A., Tournassat, C., Greneche, J., Géhin, A., Fernández-Martı´nez, A., Coudert, S., Tisserand, D., & Brendle, J. (2007). Electron transfer at the mineral/water interface: Selenium reduction by ferrous iron sorbed on clay. *Geochimica et Cosmochimica Acta*, *71*(23), 5731–5749. https://doi.org/10.1016/j.gca.2007.08.024

Chen, X. Y., Huh, H. S., & Lee, S. W. (2007). Hydrothermal synthesis of boehmite (γ-AlOOH) nanoplatelets and nanowires: pH-controlled morphologies. *Nanotechnology*, *18*(28), 285608. https://doi.org/10.1088/0957-4484/18/28/285608

Chen, X. Y., & Lee, S. W. (2007). pH-Dependent formation of boehmite (γ-AlOOH) nanorods and nanoflakes. *Chemical Physics Letters*, *438*(4–6), 279–284. https://doi.org/10.1016/j.cplett.2007.03.020

Chen, X. Y., Zhang, Z. J., Li, X. L., & Lee, S. W. (2008). Controlled hydrothermal synthesis of colloidal boehmite (-AlOOH) nanorods and nanoflakes and their conversion into - Al2O3 nanocrystals. *Solid State Communications*, *145*(7–8), 368–373. https://doi.org/10.1016/j.ssc.2007.11.033

Chermak, J. A. (1992). Low Temperature Experimental Investigation of the Effect of High pH NaOH Solutions on the Opalinus Shale, Switzerland. *Clays and Clay Minerals*, *40*(6), 650–658. https://doi.org/10.1346/ccmn.1992.0400604

Cheshire, M. C., Caporuscio, F. A., Rearick, M. S., Jove-Colon, C., & McCarney, M. K. (2014). Bentonite evolution at elevated pressures and temperatures: An experimental study for generic

nuclear repository designs. *American Mineralogist*, *99*(8–9), 1662–1675. https://doi.org/10.2138/am.2014.4673

Cheshire, M. C., Caporuscio, F. A., Jove Colón, C. F., Norskog, K. E. (2018). Fe-saponite growth on low-carbon and stainless steel in hydrothermal-bentonite experiments. *Journal of Nuclear Materials*, 511, 353-366.

Chiche, D., Chanéac, C., Revel, R., & Jolivet, J. P. (2011). Use of polyols as particle size and shape controllers: application to boehmite synthesis from sol–gel routes. *Physical Chemistry Chemical Physics*, *13*(13), 6241. https://doi.org/10.1039/c0cp02075c

Chiche, D., Chizallet, C., Durupthy, O., Chanéac, C., Revel, R., Raybaud, P., & Jolivet, J. P. (2009). Growth of boehmite particles in the presence of xylitol: morphology oriented by the nest effect of hydrogen bonding. *Physical Chemistry Chemical Physics*, *11*(47), 11310. https://doi.org/10.1039/b914062j

Cho, S. B., Venigalla, S., & Adair, J. H. (1996). Morphological Forms of alpha-Alumina Particles Synthesized in 1,4-Butanediol Solution. *Journal of the American Ceramic Society*, *79*(1), 88–96. https://doi.org/10.1111/j.1151-2916.1996.tb07884.x

Christensen, S.G. (2005). Thermodynamics of Aqueous Electrolyte Solutions - Application to Ion Exchange Systems, Department of Chemical Engineering, Technical University of Denmark: København.

Christensen, A. N., Lehmann, M. S., Convert, P., Beyer, L., Bastiansen, O., Braathen, G., Fernholt, L., Gundersen, G., Nielsen, C. J., Cyvin, B. N., & Cyvin, S. J. (1982). Deuteration of Crystalline Hydroxides. Hydrogen Bonds of gamma-AlOO(H,D) and gamma-FeOO(H,D). *Acta Chemica Scandinavica*, *36a*, 303–308. https://doi.org/10.3891/acta.chem.scand.36a-0303

Coleman, J. N., & Et Al., E. A. (2011). ChemInform Abstract: Two-Dimensional Nanosheets Produced by Liquid Exfoliation of Layered Materials. *ChemInform*, *42*(18), no. https://doi.org/10.1002/chin.201118179

COMSOL Multiphysics® v. 5.6. www.comsol.com. COMSOL AB, Stockholm, Sweden.

Corbató, C. E. (1985). Structure Refinement of Deuterated Boehmite. *Clays and Clay Minerals*, *33*(1), 71–75. https://doi.org/10.1346/ccmn.1985.0330108

Crerar, D. A., Susak, N., Borcsik, M., & Schwartz, S. (1978). Solubility of the buffer assemblage pyrite + pyrrhotite + magnetite in NaCl solutions from 200 to 350°C. *Geochimica et Cosmochimica Acta*, *42*(9), 1427–1437. https://doi.org/10.1016/0016-7037(78)90048-0

Cuevas, J., De La Villa, R. V., Ramírez, S., Sánchez, L., Fernández, R. and Leguey, S. (2006). The alkaline reaction of FEBEX bentonite: a contribution to the study of the performance of bentonite/concrete engineered barrier systems. *Journal of Iberian Geology*, 32(2), 151- 174

Cukier, R. I., & Nocera, D. G. (1998). PROTON-COUPLED ELECTRON TRANSFER. *Annual Review of Physical Chemistry*, *49*(1), 337–369. https://doi.org/10.1146/annurev.physchem.49.1.337

Cygan, R. T., Liang, J. J., & Kalinichev, A. G. (2004). Molecular Models of Hydroxide, Oxyhydroxide, and Clay Phases and the Development of a General Force Field. *The Journal of Physical Chemistry B*, *108*(4), 1255–1266. https://doi.org/10.1021/jp0363287

Delay, J., Vinsot, A., Krieguer, J.-M., Rebours, H., and Armand, G. (2007) Making of the underground scientific experimental programme at the Meuse/Haute-Marne underground research laboratory, North Eastern France. Physics and Chemistry of the Earth, Parts A/B/C 32, 2-18.

Detzner K. and Kober F. (2015) FEBEX-DP drilling and sampling report sections 32-34, Internal report, AN15-714, NAGRA.

Dittrich, T. M., Boukhalfa, H., Ware, S. D., and Reimus, P. W. (2015). Laboratory investigation of the role of desorption kinetics on americium transport associated with bentonite colloids. *Journal of environmental radioactivity*, 148, 170-182.

Docrat, T. I., Mosselmans, J. F. W., Charnock, J. M., Whiteley, M. W., Collison, D., Livens, F. R., Jones, C., & Edmiston, M. J. (1999). X-ray Absorption Spectroscopy of Tricarbonatodioxouranate(V), [UO2(CO3)3]5-, in Aqueous Solution. *Inorganic Chemistry*, *38*(8), 1879–1882. https://doi.org/10.1021/ic9814423

DOPAS. (2016). DOPAS 2016 Proceedings (Deliverable n°7.3). https://igdtp.eu/activity/dopas-full-scale-demonstration-plugs-seals/

Eberl, D. (1977). The Hydrothermal Transformation of Sodium and Potassium Smectite into Mixed-Layer Clay. *Clays and Clay Minerals*, *25*(3), 215–227. https://doi.org/10.1346/ccmn.1977.0250308

Eberl, D. (1978). Reaction Series for Dioctahedral Smectites. *Clays and Clay Minerals*, *26*(5), 327–340. https://doi.org/10.1346/ccmn.1978.0260503

el Mendili, Y., Abdelouas, A., Ait Chaou, A., Bardeau, J. F., & Schlegel, M. (2014). Carbon steel corrosion in clay-rich environment. *Corrosion Science*, *88*, 56–65. https://doi.org/10.1016/j.corsci.2014.07.020

ENRESA (2000) Full-scale engineered barriers experiment for a deep geological repository in crystalline host rock FEBEX Project, European Commission: 403.

Ewing, R. C., Runde, W., & Albrecht-Schmitt, T. E. (2010). Environmental impact of the nuclear fuel cycle: Fate of actinides. *MRS Bulletin*, *35*(11), 859–866. https://doi.org/10.1557/mrs2010.712

Farahmandjou, M., & Golabiyan, N. (2019). Synthesis and characterisation of Al2O3 nanoparticles as catalyst prepared by polymer co-precipitation method. *Materials Engineering Research*, *1*(2), 40–44. https://doi.org/10.25082/mer.2019.02.002

Feng, Y., Lu, W., Zhang, L., Bao, X., Yue, B., Lv, Y., & Shang, X. (2008). One-Step Synthesis of Hierarchical Cantaloupe-like AlOOH Superstructures via a Hydrothermal Route. *Crystal Growth & Design*, *8*(4), 1426–1429. https://doi.org/10.1021/cg7007683

Fernández, A., Cuevas, J., & Rivas, P. (2000). Pore Water Chemistry of the Febex Bentonite. *MRS Proceedings*, *663*. https://doi.org/10.1557/proc-663-573

Fernández, A., Baeyens, B., Bradbury, M., & Rivas, P. (2004). Analysis of the porewater chemical composition of a Spanish compacted bentonite used in an engineered barrier. *Physics and Chemistry of the Earth, Parts A/B/C*, *29*(1), 105–118. https://doi.org/10.1016/j.pce.2003.12.001

Fernández, R., Cuevas, J., and Mäder, U. K. (2009). Modelling concrete interaction with a bentonite barrier. *European Journal of Mineralogy*, 21(1), 177-191.

Fernández, A., & Villar, M. (2010). Geochemical behaviour of a bentonite barrier in the laboratory after up to 8years of heating and hydration. *Applied Geochemistry*, *25*(6), 809–824. https://doi.org/10.1016/j.apgeochem.2010.03.001

Fernández, R., Torres, E., Ruiz, A. I., Cuevas, J., Alonso, M. C., Calvo, J. L. G., ... and Turrero, M. J. (2017). Interaction processes at the concrete-bentonite interface after 13 years of FEBEX-Plug operation. Part II: Bentonite contact. *Physics and Chemistry of the Earth*, Parts A/B/C, 99, 49-63.

Ferrage, E. (2005). Investigation of smectite hydration properties by modeling experimental X-ray diffraction patterns: Part I. Montmorillonite hydration properties. *American Mineralogist*, *90*(8–9), 1358–1374. https://doi.org/10.2138/am.2005.1776

Figueiredo, B., Tsang, C. F., Niemi, A., and Lindgren, G. (2016). The state-of-art of sparse channel models and their applicability to performance assessment of radioactive waste repositories in fractured crystalline formations. *Hydrogeology Journal*, 24(7), 1607-1622.

Fiorin, G., Klein, M. L., & Hénin, J. (2013). Using collective variables to drive molecular dynamics simulations. *Molecular Physics*, *111*(22–23), 3345–3362. https://doi.org/10.1080/00268976.2013.813594

Franks, G. V., & Gan, Y. (2007). Charging Behavior at the Alumina–Water Interface and Implications for Ceramic Processing. *Journal of the American Ceramic Society*, *90*(11), 3373–3388. https://doi.org/10.1111/j.1551-2916.2007.02013.x

Garcia-Garcia, S., Wold, S., & Jonsson, M. (2009). Effects of temperature on the stability of colloidal montmorillonite particles at different pH and ionic strength. *Applied Clay Science*, *43*(1), 21–26. https://doi.org/10.1016/j.clay.2008.07.011

García-Gutiérrez, M., Missana, T., Mingarro, M., Samper, J., Dai, Z., & Molinero, J. (2001). Solute transport properties of compacted Ca-bentonite used in FEBEX project. *Journal of Contaminant Hydrology*, *47*(2–4), 127–137. https://doi.org/10.1016/s0169-7722(00)00143-1

Garcia-Sineriz, J.L., Abós, H., Martínez, V., De la Rosa, C., Mäder, U. and Kober, F. (2016) FEBEX-DP Dismantling of the heater 2 at the FEBEX "in situ" test. Nagra Arbeitsbericht NAB 16-011. p. 92

Gardolinski, J. E. F. C., & Lagaly, G. (2005a). Grafted organic derivatives of kaolinite: I. Synthesis, chemical and rheological characterization. *Clay Minerals*, *40*(4), 537–546. https://doi.org/10.1180/0009855054040190

Gardolinski, J. E. F. C., & Lagaly, G. (2005b). Grafted organic derivatives of kaolinite: II. Intercalation of primary n-alkylamines and delamination. *Clay Minerals*, *40*(4), 547–556. https://doi.org/10.1180/0009855054040191

Gaudin, A., Bartier, D., Truche, L., Tinseau, E., Foct, F., Dyja, V., Maillet, A. and Beaufort, D. (2013). First corrosion stages in Tournemire claystone/steel interaction: In situ experiment and modelling approach. *Applied clay science*, 83, 457-468.

GENS, A. (2010). Soil–environment interactions in geotechnical engineering. *Géotechnique*, *60*(1), 3–74. https://doi.org/10.1680/geot.9.p.109

Giguere, A. T., Eichorst, S. A., Meier, D. V., Herbold, C. W., Richter, A., Greening, C., & Woebken, D. (2020). Acidobacteria are active and abundant members of diverse atmospheric H2-oxidizing communities detected in temperate soils. *The ISME Journal*, *15*(2), 363–376. https://doi.org/10.1038/s41396-020-00750-8

Giraudeau, C., d'Espinose De Lacaillerie, J. B., Souguir, Z., Nonat, A., & Flatt, R. J. (2009). Surface and Intercalation Chemistry of Polycarboxylate Copolymers in Cementitious Systems. *Journal of the American Ceramic Society*, *92*(11), 2471–2488. https://doi.org/10.1111/j.1551-2916.2009.03413.x

Gómez-Espina, R., & Villar, M. (2010). Geochemical and mineralogical changes in compacted MX-80 bentonite submitted to heat and water gradients. *Applied Clay Science*, *47*(3–4), 400–408. https://doi.org/10.1016/j.clay.2009.12.004

Greening, C., Berney, M., Hards, K., Cook, G. M., & Conrad, R. (2014). A soil actinobacterium scavenges atmospheric H2 using two membrane-associated, oxygen-dependent [NiFe] hydrogenases. *Proceedings of the National Academy of Sciences*, *111*(11), 4257–4261. https://doi.org/10.1073/pnas.1320586111

Grossfield, A., Patrone, P. N., Roe, D. R., Schultz, A. J., Siderius, D., & Zuckerman, D. M. (2019). Best Practices for Quantification of Uncertainty and Sampling Quality in Molecular Simulations [Article v1.0]. *Living Journal of Computational Molecular Science*, *1*(1). https://doi.org/10.33011/livecoms.1.1.5067

Gueven, N., and Huang, W. L. (1990). Effects of Mg^{2+} and Fe^{3+} substitutions on the crystallization of discrete illite and illite/smectite mixed layers. Int. rep. Dept. Geosciences Texas Tech University, Exxon Production research Co, Houston, Texas.

Guillaume, D., Neaman, A., Cathelineau, M., Mosser-Ruck, R., Peiffert, C., Abdelmoula, M., Dubessy, J., Villieras, F., and Michau, N. (2004). Experimental study of the transformation of smectite at 80 to 300 °C in the presence of Fe oxides. *Clay Minerals*, 39, 17-34.

Guimarães, L. N., Gens, A., Sánchez, M., & Olivella, S. (2013). A chemo-mechanical constitutive model accounting for cation exchange in expansive clays. *Géotechnique*, *63*(3), 221–234. https://doi.org/10.1680/geot.sip13.p.012

Günther, Thomas & Rücker, Carsten. (2012). Boundless Electrical Resistivity Tomography (BERT) v. 2.0 - Open Access Software for Advanced and Flexible Imaging.

Guo, Y., Xu, K., Wu, C., Zhao, J., & Xie, Y. (2015). Surface chemical-modification for engineering the intrinsic physical properties of inorganic two-dimensional nanomaterials. *Chemical Society Reviews*, *44*(3), 637–646. https://doi.org/10.1039/c4cs00302k

Guyonnet, D., Touze-Foltz, N., Norotte, V., Pothier, C., Didier, G., Gailhanou, H., Blanc, P., & Warmont, F. (2009). Performance-based indicators for controlling geosynthetic clay liners in landfill applications. *Geotextiles and Geomembranes*, *27*(5), 321–331. https://doi.org/10.1016/j.geotexmem.2009.02.002

Hadi, J., Wersin, P., Serneels, V., and Greneche, J. M. (2019). Eighteen years of steel–bentonite interaction in the FEBEX in situ test at the Grimsel Test Site in Switzerland. *Clays and Clay Minerals*, 67(2), 111-131.

Hakuta, Y., Adschiri, T., Hirakoso, H., & Arai, K. (1999). Chemical equilibria and particle morphology of boehmite (AlOOH) in sub and supercritical water. *Fluid Phase Equilibria*, *158–160*, 733–742. https://doi.org/10.1016/s0378-3812(99)00118-1

Hammond, G. E., Lichtner, P. C., & Mills, R. T. (2014). Evaluating the performance of parallel subsurface simulators: An illustrative example with PFLOTRAN. *Water Resources Research*, *50*(1), 208–228. https://doi.org/10.1002/2012wr013483

Hardin, Ernest, Hadgu, Teklu, and Clayton, Daniel James. (2015). Cavern/Vault Disposal Concepts and Thermal Calculations for Direct Disposal of 37-PWR Size DPCs. United States: N. Web. doi:10.2172/1172177.

Hassanvand, A., Wei, K., Talebi, S., Chen, G., & Kentish, S. (2017). The Role of Ion Exchange Membranes in Membrane Capacitive Deionisation. *Membranes*, *7*(3), 54. https://doi.org/10.3390/membranes7030054

He, T., Xiang, L., Zhu, W., & Zhu, S. (2008). H2SO4-assisted hydrothermal preparation of γ-AlOOH nanorods. *Materials Letters*, *62*(17–18), 2939–2942. https://doi.org/10.1016/j.matlet.2008.01.078

Hiemstra,T, Yong, H., & van Riemsdijk, W. H. (1999). Interfacial Charging Phenomena of Aluminum (Hydr)oxides. *Langmuir*, *15*(18), 5942–5955. https://doi.org/10.1021/la981301d

Ho, T. A., Criscenti, L. J., & Greathouse, J. A. (2019). Revealing Transition States during the Hydration of Clay Minerals. *The Journal of Physical Chemistry Letters*, *10*(13), 3704–3709. https://doi.org/10.1021/acs.jpclett.9b01565

Hochepied, J. F., & Nortier, P. (2002). Influence of precipitation conditions (pH and temperature) on the morphology and porosity of boehmite particles. *Powder Technology*, *128*(2–3), 268–275. https://doi.org/10.1016/s0032-5910(02)00178-x

Holm, C. H., Adams, C. R., & Ibers, J. A. (1958). The Hydrogen Bond in Boehmite. *The Journal of Physical Chemistry*, *62*(8), 992–994. https://doi.org/10.1021/j150566a027

Honorio, T., Brochard, L., & Vandamme, M. (2017). Hydration Phase Diagram of Clay Particles from Molecular Simulations. *Langmuir*, *33*(44), 12766–12776. https://doi.org/10.1021/acs.langmuir.7b03198

Horseman, S., & McEwen, T. (1996). Thermal constraints on disposal of heat-emitting waste in argillaceous rocks. *Engineering Geology*, *41*(1–4), 5–16. https://doi.org/10.1016/0013-7952(95)00046-1

Hsiao, Y. W., & Hedström, M. (2017). Swelling Pressure in Systems with Na-Montmorillonite and Neutral Surfaces: A Molecular Dynamics Study. *The Journal of Physical Chemistry C*, *121*(47), 26414–26423. https://doi.org/10.1021/acs.jpcc.7b09496

Idemitsu, K., Kozaki, H., Yuhara, M., Arima, T., & Inagaki, Y. (2016). Diffusion behavior of selenite in purified bentonite. *Progress in Nuclear Energy*, *92*, 279–285. https://doi.org/10.1016/j.pnucene.2015.08.012

Iler, R. K. (1961). Fibrillar Colloidal Boehmite; Progressive Conversion to Gamma, Theta, and Alpha Aluminas. *Journal of the American Ceramic Society*, *44*(12), 618–624. https://doi.org/10.1111/j.1151-2916.1961.tb11669.x

Ilton, E. S., Boily, J. F., & Bagus, P. S. (2007). Beam induced reduction of U(VI) during X-ray photoelectron spectroscopy: The utility of the U4f satellite structure for identifying uranium oxidation states in mixed valence uranium oxides. *Surface Science*, *601*(4), 908–916. https://doi.org/10.1016/j.susc.2006.11.067

Inoue, M. (1989). Alcohothermal Treatments of Gibbsite: Mechanisms for the Formation of Boehmite. *Clays and Clay Minerals*, *37*(1), 71–80. https://doi.org/10.1346/ccmn.1989.0370109

Inoue, M. (2004). Glycothermal synthesis of metal oxides. *Journal of Physics: Condensed Matter*, *16*(14), S1291–S1303. https://doi.org/10.1088/0953-8984/16/14/042

Inoue, M., Kominami, H., & Inui, T. (1991). Reaction of aluminium alkoxides with various glycols and the layer structure of their products. *Journal of the Chemical Society, Dalton Transactions*, *12*, 3331. https://doi.org/10.1039/dt9910003331

Inoue, M., Kominami, H., & Inui, T. (1994). Synthesis of large pore-size and large pore-volume aluminas by glycothermal treatment of aluminium alkoxide and subsequent calcination. *Journal of Materials Science*, *29*(9), 2459–2466. https://doi.org/10.1007/bf00363440

Inoue, M., Kondo, Y., & Inui, T. (1988). An ethylene glycol derivative of boehmite. *Inorganic Chemistry*, *27*(2), 215–221. https://doi.org/10.1021/ic00275a001

Itasca, (2009). FLAC3D, Fast Lagrangian Analysis of Continua in 3 Dimensions, Version 4.0, Minneapolis, Minnesota, Itasca Consulting Group.

Jarzynski, C. (1997). Nonequilibrium Equality for Free Energy Differences. *Physical Review Letters*, *78*(14), 2690–2693. https://doi.org/10.1103/physrevlett.78.2690

Jenny, H. (1936). Simple Kinetic Theory of Ionic Exchange. I. Ions of Equal Valency. *The Journal of Physical Chemistry*, *40*(4), 501–517. https://doi.org/10.1021/j150373a010

Johannesson, L. E., Börgesson, L., Goudarzi, R., Sandén, T., Gunnarsson, D., & Svemar, C. (2007). Prototype repository: A full scale experiment at Äspö HRL. *Physics and Chemistry of the Earth, Parts A/B/C*, *32*(1–7), 58–76. https://doi.org/10.1016/j.pce.2006.04.027

Jolivet, J.-P., Henry, M., LIvage, J., Bescher, E. (2000). Metal Oxide Chemistry and Synthesis. John Wiley & Sons, New York

Jolivet, J. P., Froidefond, C., Pottier, A., Chanéac, C., Cassaignon, S., Tronc, E., & Euzen, P. (2004). Size tailoring of oxide nanoparticles by precipitation in aqueous medium. A semi-quantitative modelling. *J. Mater. Chem.*, *14*(21), 3281–3288. https://doi.org/10.1039/b407086k

Jónsson, E., Thygesen, K. S., Ulstrup, J., & Jacobsen, K. W. (2011). Ab Initio Calculations of the Electronic Properties of Polypyridine Transition Metal Complexes and Their Adsorption on Metal Surfaces in the Presence of Solvent and Counterions. *The Journal of Physical Chemistry B*, *115*(30), 9410–9416. https://doi.org/10.1021/jp200893w

Jové Colón, C. F., Caporuscio, F. A., Levy, S. S., Sutton, M., Blink, J., Greenberg, H. R., Fratoni, M., Halsey, W. G., Wolery, T. J., Rutqvist, J., et al. (2011). Disposal systems evaluations and tool development - Engineered Barrier System (EBS) Evaluation (Fuel Cycle Research and Development). Sandia National Laboratory, (FCRD-USED-2011- 000132), 1-192.

Jové Colón, C. F., Caporuscio, F. A, Sauer, K., and Cheshire, M. C. (2019). Engineered barrier material interactions at elevated temperatures: Bentonite-metal interactions under elevated temperature conditions. Sandia National Laboratories: SAND2019-0714C. https://www.osti.gov/servlets/purl/1595898.

Kalam, S., Basu, A., Ahmad, I., Sayyed, R. Z., El-Enshasy, H. A., Dailin, D. J., & Suriani, N. L. (2020). Recent Understanding of Soil Acidobacteria and Their Ecological Significance: A Critical Review. *Frontiers in Microbiology*, *11*. https://doi.org/10.3389/fmicb.2020.580024

Karnland, O. (1997). Cement/bentonite interaction. Results from 16 month laboratory tests (No. SKB-TR--97-32). Swedish Nuclear Fuel and Waste Management Co.

Karnland, O. (2010). Chemical and mineralogical characterization of the bentonite buffer for the acceptance control procedure in a KBS-3 repository. SKB Report, TR 10–60. Swedish Nuclear Fuel and Waste Management, Stockholm, Sweden. www.skb.se.

Katz, J. E., Zhang, X., Attenkofer, K., Chapman, K. W., Frandsen, C., Zarzycki, P., Rosso, K. M., Falcone, R. W., Waychunas, G. A., & Gilbert, B. (2012). Electron Small Polarons and Their Mobility in Iron (Oxyhydr)oxide Nanoparticles. *Science*, *337*(6099), 1200–1203. https://doi.org/10.1126/science.1223598

Kaufhold, S., Hassel, A. W., Sanders, D., & Dohrmann, R. (2015). Corrosion of high-level radioactive waste iron-canisters in contact with bentonite. *Journal of Hazardous Materials*, 285, 464-473.

Kerisit, S., Zarzycki, P., & Rosso, K. M. (2015). Computational Molecular Simulation of the Oxidative Adsorption of Ferrous Iron at the Hematite (001)–Water Interface. *The Journal of Physical Chemistry C*, *119*(17), 9242–9252. https://doi.org/10.1021/jp512422h

Kersting, A., Zavarin, M., Zhao, P., Dai, Z., Carroll, S., Wang, Y., Miller, A., James, S., Reimus P., Zheng, L., Li, L., Rutqvist, J., Liu, H., and Birkholzer, J. (2012). Radionuclide Interaction and Transport in Representative Geologic Media. Lawerence-Livermore National Lab: FCRD-UFD-2012-000154. https://www.energy.gov/sites/prod/files/2013 /06/f1/FY12%20Radionuclide%20Interaction%20and%20Transport%20in%20Represent ative%20Geologic%20Media.pdf

Kickelbick, G., (2007). Hybrid Materials: Synthesis, Characterization, and Applications. John Wiley & Sons, Inc

Kloprogge, J. T. (1999). Synthesis of Smectite Clay Minerals: A Critical Review. *Clays and Clay Minerals*, *47*(5), 529–554. https://doi.org/10.1346/ccmn.1999.0470501

Kober, F. (2020), HOTBent (High Temperature Bentonite), Presentation given at 18th International Steering Committee Meeting (ISCO 2020), Grimsel Test Site Phase IV, Virtual Meeting, June 3, 2020.

Kober, F., et al. (2017). FEBEX-DP. Metal Corrosion and Iron-Bentonite Interaction Studies. Nagra Arbeitsbericht, NAB 16–16, Nagra, Wettingen, Switzerland, 300 pp.

Kober F. and Vomvoris S. (2021) Minutes of 6th HotBENT Partner Executive Meeting - DRAFT, Nagra technical report, AN 21-516.

Kololuoma, T., Leppäniemi, J., Majumdar, H., Branquinho, R., Herbei-Valcu, E., Musat, V., Martins, R., Fortunato, E., & Alastalo, A. (2015). Gravure printed sol–gel derived AlOOH hybrid nanocomposite thin films for printed electronics. *Journal of Materials Chemistry C*, *3*(8), 1776–1786. https://doi.org/10.1039/c4tc02022g

Komori, Y., Enoto, H., Takenawa, R., Hayashi, S., Sugahara, Y., & Kuroda, K. (2000). Modification of the Interlayer Surface of Kaolinite with Methoxy Groups. *Langmuir*, *16*(12), 5506–5508. https://doi.org/10.1021/la991453o

Kosmulski, M. (2003). A literature survey of the differences between the reported isoelectric points and their discussion. *Colloids and Surfaces A: Physicochemical and Engineering Aspects*, *222*(1–3), 113–118. https://doi.org/10.1016/s0927-7757(03)00240-1

Kuang, D., Fang, Y., Liu, H., Frommen, C., & Fenske, D. (2003). Fabrication of boehmite AlOOH and γ-Al2O3 nanotubes via a soft solution route. *Journal of Materials Chemistry*, *13*(4), 660–662. https://doi.org/10.1039/b212885c

Kurosawa, S., James, S. C., Yui, M., and Ibaraki, M. (2006). Model analysis of the colloid and radionuclide retardation experiment at the Grimsel Test Site. *Journal of colloid and interface science*, 298(1), 467-475.

Kursten, B., Cornelis, B., Labat, S. and Van Iseghem, P. (1996). Geological Disposal of Conditioned High-Level and Long Lived Radioactive Waste. In situ experiments, Report R-3121, SCK•CEN (Mol, Belgium).

Kursten, B., Cornelis, B., Labat, S. and Van Iseghem, P. (1997). Completion of the Corrosion Programme in Boom Clay – in situ experiments, Report EUR-17105, SCK•CEN (Mol, Belgium).

Kursten, B., Smailos, E., Azkarate, I., Werme, L., Smart, N.R. and Santarini, G. (2004). COBECOMA. State of the art document on the Corrosion Behaviour of Container Materials.

Laird, D. (1997). Relationship Between Cation Exchange Selectivity and Crystalline Swelling in Expanding 2:1 Phyllosilicates. *Clays and Clay Minerals*, *45*(5), 681–689. https://doi.org/10.1346/ccmn.1997.0450507

Lammers, L. N., Bourg, I. C., Okumura, M., Kolluri, K., Sposito, G., & Machida, M. (2017). Molecular dynamics simulations of cesium adsorption on illite nanoparticles. *Journal of Colloid and Interface Science*, *490*, 608–620. https://doi.org/10.1016/j.jcis.2016.11.084

Landau, L.D.; Lifshitz, E.M.; Pitaevskii, L.P.; Sykes, J.B.; Kearsley, M.J. (1980). Statistical Physics. Volume 5 of Course of Theoretical Physics. Part 1 Volume 5 of Course of Theoretical Physics. Part 1; 1980; ISBN 978-1-4831-0337-2.

Lantenois, S. (2003). Réactivité fer métal/smectites en milieu hydraté à 80°C (Doctoral dissertation).

Lantenois, S., Lanson, B., Muller, F., Bauer, A., Jullien, M., & Plançon, A. (2005). Experimental study of smectite interaction with metal Fe at low temperature: 1. Smectite destabilization. *Clays and Clay Minerals*, 53(6), 597-612.

Lepot, N., van Bael, M., van den Rul, H., D'Haen, J., Peeters, R., Franco, D., & Mullens, J. (2008). Synthesis of platelet-shaped boehmite and γ-alumina nanoparticles via an aqueous route. *Ceramics International*, *34*(8), 1971–1974. https://doi.org/10.1016/j.ceramint.2007.07.022

Letaief, S., & Detellier, C. (2009). Clay−Polymer Nanocomposite Material from the Delamination of Kaolinite in the Presence of Sodium Polyacrylate. *Langmuir*, *25*(18), 10975–10979. https://doi.org/10.1021/la901196f

Leupin, O. X., and Johnson, L. H. (2013). Buffer requirements for a SF/HLW repository in Opalinus Clay. Nagra working report, NAB 13-46, Nagra, Wettingen, Switzerland. www.nagra.ch.

Li, G., Liu, Y., Liu, D., Liu, L., & Liu, C. (2010). Synthesis of flower-like Boehmite (AlOOH) via a simple solvothermal process without surfactant. *Materials Research Bulletin*, *45*(10), 1487–1491. https://doi.org/10.1016/j.materresbull.2010.06.013

Li, Y. W., and Schulthess, C. P. (2020). ION-EXCHANGE MODELING OF MONOVALENT ALKALI CATION ADSORPTION ON MONTMORILLONITE. *Clays and Clay Minerals*, *68*(5), 476–490. https://doi.org/10.1007/s42860-020-00091-9

Liu, H.H., Houseworth, J., Rutqvist, J., Zheng, L., Asahina, D., Li, L., Vilarrasa, V., Chen, F., Nakagawa, S., Finsterle, S., Doughty, C., Kneafsey, T. and Birkholzer, J. (2013) Report on THMC modeling of the near field evolution of a generic clay repository: Model validation and demonstration, Lawrence Berkeley National Laboratory, August, 2013, FCRD-UFD-2013-0000244.

Liu, T., Chen, B., & Evans, J. R. G. (2008). Ordered assemblies of clay nano-platelets. *Bioinspiration & Biomimetics*, *3*(1), 016005. https://doi.org/10.1088/1748-3182/3/1/016005

Liu, Y., Ma, D., Han, X., Bao, X., Frandsen, W., Wang, D., & Su, D. (2008). Hydrothermal synthesis of microscale boehmite and gamma nanoleaves alumina. *Materials Letters*, *62*(8–9), 1297–1301. https://doi.org/10.1016/j.matlet.2007.08.067 (Y. Liu et al., 2008)

Liu, Z., Ma, R., Osada, M., Iyi, N., Ebina, Y., Takada, K., & Sasaki, T. (2006). Synthesis, Anion Exchange, and Delamination of Co−Al Layered Double Hydroxide: Assembly of the Exfoliated Nanosheet/Polyanion Composite Films and Magneto-Optical Studies. *Journal of the American Chemical Society*, *128*(14), 4872–4880. https://doi.org/10.1021/ja0584471

Lothenbach, B., Scrivener, K. and Hooton, R. D. (2011). Supplementary cementitious materials. *Cement and Concrete Research*, 41(12), 1244-1256.

Lutterotti, L., Voltolini, M., Wenk, H. R., Bandyopadhyay, K., & Vanorio, T. (2009). Texture analysis of a turbostratically disordered Ca-montmorillonite. *American Mineralogist*, *95*(1), 98–103. https://doi.org/10.2138/am.2010.3238

Ma, B., Charlet, L., Fernandez-Martinez, A., Kang, M., & Madé, B. (2019). A review of the retention mechanisms of redox-sensitive radionuclides in multi-barrier systems. *Applied Geochemistry*, *100*, 414–431. https://doi.org/10.1016/j.apgeochem.2018.12.001

Ma, C., Chang, Y., Ye, W., Duan, L., & Wang, C. (2008a). Hexagon γ-alumina nanosheets produced with the assistance of supercritical ethanol drying. *The Journal of Supercritical Fluids*, *45*(1), 112–120. https://doi.org/10.1016/j.supflu.2008.01.001

Ma, C., Chang, Y., Ye, W., Shang, W., & Wang, C. (2008b). Supercritical preparation of hexagonal γ-alumina nanosheets and its electrocatalytic properties. *Journal of Colloid and Interface Science*, *317*(1), 148–154. https://doi.org/10.1016/j.jcis.2007.07.077

Ma, R., & Sasaki, T. (2010). Nanosheets of Oxides and Hydroxides: Ultimate 2D Charge-Bearing Functional Crystallites. *Advanced Materials*, *22*(45), 5082–5104. https://doi.org/10.1002/adma.201001722

Makarova, V. V., Tolstykh, M. Y., Picken, S. J., Mendes, E., & Kulichikhin, V. G. (2013). Rheology–Structure Interrelationships of Hydroxypropylcellulose Liquid Crystal Solutions and Their Nanocomposites under Flow. *Macromolecules*, *46*(3), 1144–1157. https://doi.org/10.1021/ma301095t

Malucelli, G., Alongi, J., Gioffredi, E., & Lazzari, M. (2012). Thermal, rheological, and barrier properties of waterborne acrylic nanocomposite coatings based on boehmite or organo-modified montmorillonite. *Journal of Thermal Analysis and Calorimetry*, *111*(2), 1303–1310. https://doi.org/10.1007/s10973-012-2510-4

Mangiante, D. M., Schaller, R. D., Zarzycki, P., Banfield, J. F., & Gilbert, B. (2017). Mechanism of Ferric Oxalate Photolysis. *ACS Earth and Space Chemistry*, *1*(5), 270–276. https://doi.org/10.1021/acsearthspacechem.7b00026

Marcus, R. A. (1956). On the Theory of Oxidation-Reduction Reactions Involving Electron Transfer. I. *The Journal of Chemical Physics*, *24*(5), 966–978. https://doi.org/10.1063/1.1742723

Marcus, R. A. (1957a). On the Theory of Oxidation-Reduction Reactions Involving Electron Transfer. II. Applications to Data on the Rates of Isotopic Exchange Reactions. *The Journal of Chemical Physics*, *26*(4), 867–871. https://doi.org/10.1063/1.1743423

Marcus, R. A. (1957b). On the Theory of Oxidation-Reduction Reactions Involving Electron Transfer. III. Applications to Data on the Rates of Organic Redox Reactions. *The Journal of Chemical Physics*, *26*(4), 872–877. https://doi.org/10.1063/1.1743424

Marcus, Y. (2014). Concentration Dependence of Ionic Hydration Numbers. *The Journal of Physical Chemistry B*, *118*(35), 10471–10476. https://doi.org/10.1021/jp5039255

Mariner, P. E., Lee, J. H., Hardin, E. L., Hansen, F. D., Freeze, G. A., Lord, A. S., ... & Price, R. H. (2011). Granite disposal of US high-level radioactive waste. SAND2011-6203, Sandia, California.

Martin, P. L., Barcala, J. M. and Huertas, F. (2006). Large-scale and long-term coupled thermo- hydro-mechanic experiments with bentonite: the FEBEX mock-up test. *Journal of Iberian Geology*, 32, 259–282.

Martinez, V., Abós, H. and García-Siñeriz, J. L. (2016). FEBEXe: Final Sensor Data Report (FEBEX "in situ" Experiment) - Arbeitsbericht NAB 16-19, National Cooperative for the Disposal of Radioactive Waste (NAGRA), Wettingen, Switzerland.

Marty, N. C. M., Bildstein, O., Blanc, P., Claret, F., Cochepin, B., Gaucher, E. C., Jacques, D., Lartigue, J. E., Liu, S., Mayer, K. U., Meeussen, J. C. L., Munier, I., Pointeau, I., Su, D., & Steefel, C. I. (2015). Benchmarks for multicomponent reactive transport across a cement/clay interface. *Computational Geosciences*, *19*(3), 635–653. https://doi.org/10.1007/s10596-014-9463-6

Massat, L., Cuisinier, O., Bihannic, I., Claret, F., Pelletier, M., Masrouri, F., & Gaboreau, S. (2016). Swelling pressure development and inter-aggregate porosity evolution upon hydration of a compacted swelling clay. *Applied Clay Science*, *124–125*, 197–210. https://doi.org/10.1016/j.clay.2016.01.002

Matamoros-Veloza, A., Barker, R., Vargas, S., & Neville, A. (2020). Iron Calcium Carbonate Instability: Structural Modification of Siderite Corrosion Films. *ACS Applied Materials & Interfaces*, *12*(43), 49237–49244. https://doi.org/10.1021/acsami.0c14513

Mathieu, Y., Lebeau, B., & Valtchev, V. (2007). Control of the Morphology and Particle Size of Boehmite Nanoparticles Synthesized under Hydrothermal Conditions. *Langmuir*, *23*(18), 9435–9442. https://doi.org/10.1021/la700233q

Matteo, E., Hardin, E., Hadgu T., Park, H., Rigali, M., and Jove-Colon, C. F. (2016). Status of Progress Made Toward Preliminary Design Concepts for the Inventory in Select Media for DOE-Managed HLW/SNF. SAND2016-9823 R; FCRD-UFD-2016-000081. Sandia National Laboratories, Albuquerque, NM

Matusik, J., Gaweł, A., & Bahranowski, K. (2012). Grafting of methanol in dickite and intercalation of hexylamine. *Applied Clay Science*, *56*, 63–67. https://doi.org/10.1016/j.clay.2011.11.023

Mayer, J. M. (2004). Proton-Coupled Electron Transfer: A Reaction Chemist's View. *Annual Review of Physical Chemistry*, *55*(1), 363–390. https://doi.org/10.1146/annurev.physchem.55.091602.094446

Meetei, T. T., Devi, Y. B., & Chanu, T. T. (2020). Ion Exchange: The Most Important Chemical Reaction on Earth after Photosynthesis. *International Research Journal of Pure and Applied Chemistry*, 31–42. https://doi.org/10.9734/irjpac/2020/v21i630174

Missana, T., and Geckeis, H. (2006). Grimsel Test Site–Investigation Phase V. The CRR Final Project Report Series II: Supporting Laboratory Experiments with Radionuclides and Bentonite Colloids NAGRA Technical Report Series NTB, 03-02.

Missana, T., Alonso, R., García-Gutiérrez, M., & Mingarro, M. (2008). Role of bentonite colloids on europium and plutonium migration in a granite fracture. *Applied Geochemistry*, *23*(6), 1484–1497. https://doi.org/10.1016/j.apgeochem.2008.01.008

Missana, T., Alonso, Ú., and Turrero, M. J. (2003). Generation and stability of bentonite colloids at the bentonite/granite interface of a deep geological radioactive waste repository. *Journal of Contaminant Hydrology*, 61(1-4), 17-31.

Missana, T., Alonso, U., & García-Gutiérrez, M. (2009). Experimental study and modelling of selenite sorption onto illite and smectite clays. *Journal of Colloid and Interface Science*, *334*(2), 132–138. https://doi.org/10.1016/j.jcis.2009.02.059

Missana, T., Benedicto, A., García-Gutiérrez, M., & Alonso, U. (2014). Modeling cesium retention onto Na-, K- and Ca-smectite: Effects of ionic strength, exchange and competing cations on the determination of selectivity coefficients. *Geochimica et Cosmochimica Acta*, *128*, 266–277. https://doi.org/10.1016/j.gca.2013.10.007

Mizuguchi, K., Park, Y. Y., Tomiyasu, H., & Ikeda, Y. (1993). Electrochemical and Spectroelectrochemical Studies on Uranyl Carbonato and Aqua Complexes. *Journal of Nuclear Science and Technology*, *30*(6), 542–548. https://doi.org/10.1080/18811248.1993.9734516

Mon, A., Samper, J., Montenegro, L., Naves, A., & Fernández, J. (2017). Long-term non-isothermal reactive transport model of compacted bentonite, concrete and corrosion products in a HLW repository in clay. *Journal of Contaminant Hydrology*, *197*, 1–16. https://doi.org/10.1016/j.jconhyd.2016.12.006

Montavon, G., Guo, Z., Lützenkirchen, J., Alhajji, E., Kedziorek, M., Bourg, A., & Grambow, B. (2009). Interaction of selenite with MX-80 bentonite: Effect of minor phases, pH, selenite loading,

solution composition and compaction. *Colloids and Surfaces A: Physicochemical and Engineering Aspects*, *332*(2–3), 71–77. https://doi.org/10.1016/j.colsurfa.2008.09.014

Moore, D. M. and Reynolds, R.C. (1997). X-ray Diffraction and the identification and analysis of clay minerals. Oxford University Press, New York, New York, 377.

Mori, H., Müller, A. H., and Klee, J. E. (2003). Intelligent colloidal hybrids via reversible pH- induced complexation of polyelectrolyte and silica nanoparticles. *Journal of the American Chemical Society*, 125(13), 3712-3713.

Mosser-Ruck, R., Cathelineau, M., Guillaume, D., Charpentier, D., Rousset, D., Barres, O., and Michau, N. (2010). Effects of temperature, pH, and iron/clay and liquid/clay ratios on experimental conversion of dioctahedral smectite to berthierine, chlorite, vermiculite, or saponite. *Clays and Clay Minerals*, 58, 280-291.

Mosser-Ruck, R., Pignatelli, I., Bourdelle, F., Abdelmoula, M., Barres, O., Guillaume, D., Charpentier, D., Rousset, D., Cathelineau, M., & Michau, N. (2016). Contribution of long-term hydrothermal experiments for understanding the smectite-to-chlorite conversion in geological environments. *Contributions to Mineralogy and Petrology*, *171*(11). https://doi.org/10.1007/s00410-016-1307-z

Motta, A., Gaigeot, M. P., & Costa, D. (2012). Ab Initio Molecular Dynamics Study of the AlOOH Boehmite/Water Interface: Role of Steps in Interfacial Grotthus Proton Transfers. *The Journal of Physical Chemistry C*, *116*(23), 12514–12524. https://doi.org/10.1021/jp3000812

NAGRA, 2019. Implementation of the Full-scale Emplacement Experiment at Mont Terri: Design, Construction and Preliminary Results. Nagra Technical Report 15-02.

Naguib, M., Halim, J., Lu, J., Cook, K. M., Hultman, L., Gogotsi, Y., & Barsoum, M. W. (2013). New Two-Dimensional Niobium and Vanadium Carbides as Promising Materials for Li-Ion Batteries. *Journal of the American Chemical Society*, *135*(43), 15966–15969. https://doi.org/10.1021/ja405735d

Necib, S., Diomidis, N., Keech, P., & Nakayama, M. (2017). Corrosion of carbon steel in clay environments relevant to radioactive waste geological disposals, Mont Terri rock laboratory (Switzerland). *Swiss Journal of Geosciences*, *110*(1), 329–342. https://doi.org/10.1007/s00015-016-0259-7

Nguyen-Thanh, L., Hoang-Minh, T., Kasbohm, J., Herbert, H. J., Thuy, D. N., & Le Thi, L. (2014). Characterization of Fe-smectites and their alteration potential in relation to engineered barriers for HLW repositories: The Nui Nua clay, Thanh Hoa province, Vietnam. *Applied Clay Science*, 101, 168-176.

Norrish, K. (1954). Crystalline Swelling of Montmorillonite: Manner of Swelling of Montmorillonite. *Nature*, *173*(4397), 256–257. https://doi.org/10.1038/173256a0

Nutt, M. Voegele, M., Jove Colón, C.F., Wang, Y., Howard, R., Blink, J., Liu, H.H., Hardin, E., and Jenni, K. (2011). Used fuel disposition campaign disposal research and development road map (Fuel cycle research and development). Sandia National Laboratory, (FCRD- USED-2011-000065), 1-121.

Obodovskiy, I. (2019). Radiation Fundamentals, Applications, Risks, and Safety. Amsterdam, Elsevier.

Oestreicher, V., Jobbágy, M., & Regazzoni, A. E. (2014). Halide Exchange on Mg(II)–Al(III) Layered Double Hydroxides: Exploring Affinities and Electrostatic Predictive Models. *Langmuir*, *30*(28), 8408–8415. https://doi.org/10.1021/la5015187

Ohmoto, H., Hayashi, K. I., & Kajisa, Y. (1994). Experimental study of the solubilities of pyrite in NaCl-bearing aqueous solutions at 250–350°C. *Geochimica et Cosmochimica Acta*, *58*(10), 2169–2185. https://doi.org/10.1016/0016-7037(94)90003-5

Palmer, D. A., Bénézeth, P., & Wesolowski, D. J. (2001). Aqueous high-temperature solubility studies. I. The solubility of boehmite as functions of ionic strength (to 5 molal, NaCl), temperature (100–290°C), and pH as determined by in situ measurements. *Geochimica et Cosmochimica Acta*, *65*(13), 2081–2095. https://doi.org/10.1016/s0016-7037(01)00584-1

Park, S., & Schulten, K. (2004). Calculating potentials of mean force from steered molecular dynamics simulations. *The Journal of Chemical Physics*, *120*(13), 5946–5961. https://doi.org/10.1063/1.1651473

Patra, D., Vangal, P., Cain, A. A., Cho, C., Regev, O., & Grunlan, J. C. (2014). Inorganic Nanoparticle Thin Film that Suppresses Flammability of Polyurethane with only a Single Electrostatically-Assembled Bilayer. *ACS Applied Materials & Interfaces*, *6*(19), 16903–16908. https://doi.org/10.1021/am504455k

Perronnet, M. (2004). Réactivité des matériaux argileux dans un contexte de corrosion métallique: application au stockage des déchets radioactifs en site argileux (Doctoral dissertation).

Pettit, L. H. (1979). Metal ions in solution. *Biochemical Education*, *7*(4), 102. https://doi.org/10.1016/0307-4412(79)90105-5

Piché-Choquette, S., & Constant, P. (2019). Molecular Hydrogen, a Neglected Key Driver of Soil Biogeochemical Processes. *Applied and Environmental Microbiology*, *85*(6). https://doi.org/10.1128/aem.02418-18

Pignatelli, I., Mugnaioli, E., Hybler, J., Mosser-Ruck, R., Cathelineau, M., & Michau, N. (2013). A multi-technique characterization of cronstedtite synthesized by iron-clay interaction in a step-by-step cooling procedure. *Clays and Clay Minerals*, 61(4), 277-289.

Pignatelli, I., Bourdelle, F., Bartier, D., Mosser-Ruck, R., Truche, L., Mugnaioli, E., & Michau, N. (2014). Iron–clay interactions: Detailed study of the mineralogical transformation of claystone with emphasis on the formation of iron-rich T–O phyllosilicates in a step-by- step cooling experiment from 90° C to 40° C. Chemical Geology, 387, 1-11.

Plimpton, S.; Kohlmeyer, A.; Thompson, A.; Moore, S.; Berger, R. (2020). LAMMPS Stable Release 29 October 2020; Zenodo, 2020;

Pullman, B. (2010). Intermolecular Forces: Proceedings of the Fourteenth Jerusalem Symposium on Quantum Chemistry and Biochemistry Held in Jerusalem, Israel, April 13-16, 1981.; Springer Netherlands: Dordrecht, 2010; ISBN 978-94-015-7658-1.

Pusch, R. (1995). Aspects on the Illitization of the Kinnekulle Bentonites. *Clays and Clay Minerals*, *43*(3), 261–270. https://doi.org/10.1346/ccmn.1995.0430301

Pusch, R., & Karnland, O. (1996). Physico/chemical stability of smectite clays. *Engineering Geology*, *41*(1–4), 73–85. https://doi.org/10.1016/0013-7952(95)00027-5

Pusch, R., Kasbohm, J., & Thao, H. T. M. (2010). Chemical stability of montmorillonite buffer clay under repository-like conditions—A synthesis of relevant experimental data. *Applied Clay Science*, *47*(1–2), 113–119. https://doi.org/10.1016/j.clay.2009.01.002

Pusch, R., Prikryl, R., Weishauptová, Z., Xiaodong, L., & Knutsson, S. (2012). Role of clay microstructure in expandable buffer clay. *Journal of Purity, Utility Reaction and Environment*, 1(6), 267-292.

Pusch, R., Kasbohm, J., Knutsson, S., Yang, T., & Nguyen-Thanh, L. (2015). The role of smectite clay barriers for isolating high-level radioactive waste (HLW) in shallow and deep repositories. *Procedia Earth and Planetary Science*, 15, 680-687.

Ram, S. (2001). Infrared spectral study of molecular vibrations in amorphous, nanocrystalline and AlO(OH)·αH2O bulk crystals. *Infrared Physics & Technology*, *42*(6), 547–560. https://doi.org/10.1016/s1350-4495(01)00117-7

Ramírez, S., Cuevas, J., Vigil, R., & Leguey, S. (2002). Hydrothermal alteration of "La Serrata" bentonite (Almeria, Spain) by alkaline solutions. *Applied Clay Science*, *21*(5–6), 257–269. https://doi.org/10.1016/s0169-1317(02)00087-x

Rasband, W.S. Image J, U. S. National Institutes of Health, Bethesda, Maryland, USA, https://imagej.nih.gov/ij/, 1997–2020.

Rasband, W.S., ImageJ, U. S. National Institutes of Health, Bethesda, Maryland, USA, https://imagej.nih.gov/ij/, 1997-2018.

Reimus, P. W. (2012). Preliminary Interpretation of a Radionuclide and Colloid Tracer Test in a Granodiorite Shear Zone at the Grimsel Test Site, Switzerland (No. LA-UR-12-24411). Los Alamos National Lab. (LANL), Los Alamos, NM (United States).

Romaine, A., Sabot, R., Jeannin, M., Necib, S., & Refait, P. (2013). Electrochemical synthesis and characterization of corrosion products on carbon steel under argillite layers in carbonated media at 80 °C. *Electrochimica Acta*, *114*, 152–158. https://doi.org/10.1016/j.electacta.2013.09.163

Rotenberg, B., Morel, J. P., Marry, V., Turq, P., & Morel-Desrosiers, N. (2009). On the driving force of cation exchange in clays: Insights from combined microcalorimetry experiments and molecular simulation. *Geochimica et Cosmochimica Acta*, *73*(14), 4034–4044. https://doi.org/10.1016/j.gca.2009.04.012

Rutqvist, J., Ijiri, Y., & Yamamoto, H. (2011). Implementation of the Barcelona Basic Model into TOUGH–FLAC for simulations of the geomechanical behavior of unsaturated soils. *Computers & Geosciences*, *37*(6), 751–762. https://doi.org/10.1016/j.cageo.2010.10.011

Rutqvist, J., Zheng, L., Chen, F., Liu, H. H., & Birkholzer, J. (2013). Modeling of Coupled Thermo-Hydro-Mechanical Processes with Links to Geochemistry Associated with Bentonite-Backfilled Repository Tunnels in Clay Formations. *Rock Mechanics and Rock Engineering*, *47*(1), 167–186. https://doi.org/10.1007/s00603-013-0375-x

Salles, F., Douillard, J. M., Bildstein, O., Gaudin, C., Prelot, B., Zajac, J., & van Damme, H. (2013). Driving force for the hydration of the swelling clays: Case of montmorillonites saturated with alkaline-earth cations. *Journal of Colloid and Interface Science*, *395*, 269–276. https://doi.org/10.1016/j.jcis.2012.12.050

Sánchez, M., Gens, A., do Nascimento Guimarães, L., & Olivella, S. (2005). A double structure generalized plasticity model for expansive materials. *International Journal for Numerical and Analytical Methods in Geomechanics*, *29*(8), 751–787. https://doi.org/10.1002/nag.434

Sato, H., Yui, M., & Yoshikawa, H. (1994). Diffusion Behavior for Se and Zr in Sodium-Bentonite. *MRS Proceedings*, *353*. https://doi.org/10.1557/proc-353-269

Sauer, K., Caporuscio, F., Rock, M., Cheshire, M., & Jové-Colón, C. (2020). HYDROTHERMAL INTERACTION OF WYOMING BENTONITE AND OPALINUS CLAY. *Clays and Clay Minerals*, *68*(2), 144–160. https://doi.org/10.1007/s42860-020-00068-8

Savage, D. (1997). Review of the potential effects of alkaline plume migration from a cementitious repository for radioactive waste. Research & Development Technical Report P60, UK Environment Agency, Bristol, UK.

Savage, D., Benbow, S., Watson, C., Takase, H., Ono, K., Oda, C., & Honda, A. (2010). Natural systems evidence for the alteration of clay under alkaline conditions: An example from Searles Lake, California. *Applied Clay Science*, *47*(1–2), 72–81. https://doi.org/10.1016/j.clay.2009.08.024

Savage, D., Noy, D., & Mihara, M. (2002). Modelling the interaction of bentonite with hyperalkaline fluids. *Applied Geochemistry*, *17*(3), 207–223. https://doi.org/10.1016/s0883-2927(01)00078-6

Savage, D., Walker, C., Arthur, R., Rochelle, C., Oda, C., & Takase, H. (2007). Alteration of bentonite by hyperalkaline fluids: A review of the role of secondary minerals. *Physics and Chemistry of the Earth*, Parts A/B/C, 32(1-7), 287-297.

Schneider, C. A., Rasband, W. S., & Eliceiri, K. W. (2012). NIH Image to ImageJ: 25 years of image analysis. *Nature Methods*, *9*(7), 671–675. https://doi.org/10.1038/nmeth.2089

Sellin, P., & Leupin, O. X. (2013). The Use of Clay as an Engineered Barrier in Radioactive-Waste Management – A Review. *Clays and Clay Minerals*, *61*(6), 477–498. https://doi.org/10.1346/ccmn.2013.0610601

Seyfried, J.R., Janecky, D.R., and Berndt, M.E. (1987). Rocking autoclaves for hydrothermal experiments II. The flexible reaction-cell system. Hydrothermal Experimental Techniques, Eds. Ulmer, G.C. and Barnes, H.L. John Wiley & Sons, pp. 216 – 239.

Shainberg, I. (1987). Charge Density and Na-K-Ca Exchange on Smectites1. *Clays and Clay Minerals*, *35*(1), 68–73. https://doi.org/10.1346/ccmn.1987.0350109

Shen, X., & Bourg, I. C. (2021). Molecular dynamics simulations of the colloidal interaction between smectite clay nanoparticles in liquid water. *Journal of Colloid and Interface Science*, *584*, 610–621. https://doi.org/10.1016/j.jcis.2020.10.029

SKB, (2011). Long-term safety for the final repository for spent nuclear fuel at Forsmark. Main report of the SR-Site project. Swedish Nuclear Fuel and Waste Management Co.

Smailos, E., Cuñado, M. A., Azkarate, I., Kursten, B. and Marx, G. (2002). Long-Term Performance of Candidate Materials for HLW/Spent Fuel Disposal Containers, Report FZKA 6706, FZK.INE (Karlsruhe, Germany).

Smart, N. R., et al. (2004). The anaerobic corrosion of carbon and stainless steels in simulated cementitious repository environments: A summary review of NIREX research. Harwell, England, AEA Technology.

Smith, D. E., Wang, Y., Chaturvedi, A., & Whitley, H. D. (2006). Molecular Simulations of the Pressure, Temperature, and Chemical Potential Dependencies of Clay Swelling. *The Journal of Physical Chemistry B*, *110*(40), 20046–20054. https://doi.org/10.1021/jp062235o

Soltis, J. A., Schwartzberg, A. M., Zarzycki, P., Penn, R. L., Rosso, K. M., & Gilbert, B. (2017). Electron Mobility and Trapping in Ferrihydrite Nanoparticles. *ACS Earth and Space Chemistry*, *1*(4), 216–226. https://doi.org/10.1021/acsearthspacechem.7b00030

Somerton, W.H., A.H. El-Shaarani, and S.M. Mobarak (1974) High temperature behavior of rocks associated with geothermal-type reservoirs. Paper SPE-4897. Proceedings of the 44th Annual California Regional Meeting of the Society of Petroleum Engineers. Richardson, TX: Society of Petroleum Engineers.

Steefel, C. I., Yabusaki, S. B., & Mayer, K. U. (2015). Reactive transport benchmarks for subsurface environmental simulation. *Computational Geosciences*, *19*(3), 439–443. https://doi.org/10.1007/s10596-015-9499-2

Stöber, S., & Pöllmann, H. (1999). Synthesis of a lamellar calcium aluminate hydrate (AFm phase) containing benzenesulfonic acid ions. *Cement and Concrete Research*, *29*(11), 1841–1845. https://doi.org/10.1016/s0008-8846(99)00146-5

Subramanian, N., Whittaker, M. L., Ophus, C., & Lammers, L. N. (2020). Structural Implications of Interfacial Hydrogen Bonding in Hydrated Wyoming-Montmorillonite Clay. *The Journal of Physical Chemistry C*, *124*(16), 8697–8705. https://doi.org/10.1021/acs.jpcc.9b11339

Suchanek, W. L., Garcés, J. M., Fulvio, P. F., & Jaroniec, M. (2010). Hydrothermal Synthesis and Surface Characteristics of Novel Alpha Alumina Nanosheets with Controlled Chemical Composition. *Chemistry of Materials*, *22*(24), 6564–6574. https://doi.org/10.1021/cm102158w

Svemar, C., 2005. Cluster Repository Project (CROP). Final Report of European Commission Contract FIR1-CT-2000-2003, Brussels, Belgium.

Svoboda, M., Moučka, F., & Lísal, M. (2018). Saturated aqueous NaCl solution and pure water in Na-montmorillonite clay at thermodynamic conditions of hydraulic fracturing: Thermodynamics, structure and diffusion from molecular simulations. *Journal of Molecular Liquids*, *271*, 490–500. https://doi.org/10.1016/j.molliq.2018.08.144

Tachi, Y., Nakazawa, T., Ochs, M., Yotsuji, K., Suyama, T., Seida, Y., Yamada, N., & Yui, M. (2010). Diffusion and sorption of neptunium(V) in compacted montmorillonite: effects of carbonate and salinity. *Ract*, *98*(9–11), 711–718. https://doi.org/10.1524/ract.2010.1772

Teychené, J., Balmann, H. R. D., Maron, L., & Galier, S. (2019). Investigation of ions hydration using molecular modeling. *Journal of Molecular Liquids*, *294*, 111394. https://doi.org/10.1016/j.molliq.2019.111394

Teich-McGoldrick, S. L., Greathouse, J. A., Jové-Colón, C. F., & Cygan, R. T. (2015). Swelling Properties of Montmorillonite and Beidellite Clay Minerals from Molecular Simulation: Comparison of Temperature, Interlayer Cation, and Charge Location Effects. *The Journal of Physical Chemistry C*, *119*(36), 20880–20891. https://doi.org/10.1021/acs.jpcc.5b03253

Telfeyan, K., Reimus, P. W., Boukhalfa, H., & Ware, S. D. (2020). Aging effects on Cesium-137 (137Cs) sorption and transport in association with clay colloids. *Journal of Colloid and Interface Science*, 566, 316-326.

Teppen, B. J., & Miller, D. M. (2006). Hydration Energy Determines Isovalent Cation Exchange Selectivity by Clay Minerals. *Soil Science Society of America Journal*, *70*(1), 31–40. https://doi.org/10.2136/sssaj2004.0212

Tettenhorst, R., Hofmann, D.A., (1980). Crystal Chemistry of Boehmite. *Clays and Clay Minerals*, *28*(5), 373–380. https://doi.org/10.1346/ccmn.1980.0280507

Tinnacher, R. M., Holmboe, M., Tournassat, C., Bourg, I. C., & Davis, J. A. (2016). Ion adsorption and diffusion in smectite: Molecular, pore, and continuum scale views. *Geochimica et Cosmochimica Acta*, *177*, 130–149. https://doi.org/10.1016/j.gca.2015.12.010

Tournassat, C., & Appelo, C. (2011). Modelling approaches for anion-exclusion in compacted Na-bentonite. *Geochimica et Cosmochimica Acta*, *75*(13), 3698–3710. https://doi.org/10.1016/j.gca.2011.04.001

Tournassat, C., Gailhanou, H., Crouzet, C., Braibant, G., Gautier, A., & Gaucher, E. C. (2009). Cation Exchange Selectivity Coefficient Values on Smectite and Mixed-Layer Illite/Smectite Minerals. *Soil Science Society of America Journal*, *73*(3), 928–942. https://doi.org/10.2136/sssaj2008.0285

Tournassat, C., Steefel, C.I., Bourg, I.C., and Bergaya, F. (2015) Natural and engineered clay barriers. Elsevier.

Tournassat, C., & Steefel, C. I. (2019a). Modeling diffusion processes in the presence of a diffuse layer at charged mineral surfaces: a benchmark exercise. *Computational Geosciences*, *25*(4), 1319–1336. https://doi.org/10.1007/s10596-019-09845-4

Tournassat, C., & Steefel, C. I. (2019b). Reactive Transport Modeling of Coupled Processes in Nanoporous Media. *Reviews in Mineralogy and Geochemistry*, *85*(1), 75–109. https://doi.org/10.2138/rmg.2019.85.4

Tournassat, C., Tinnacher, R., Grangeon, S., & Davis, J. (2018). Modeling uranium(VI) adsorption onto montmorillonite under varying carbonate concentrations: A surface complexation model accounting for the spillover effect on surface potential. *Geochimica et Cosmochimica Acta*, *220*, 291–308. https://doi.org/10.1016/j.gca.2017.09.049

Tseng, I. H., Tsai, M. H., & Chung, C. W. (2014). Flexible and Transparent Polyimide Films Containing Two-Dimensional Alumina Nanosheets Templated by Graphene Oxide for Improved Barrier Property. *ACS Applied Materials & Interfaces*, *6*(15), 13098–13105. https://doi.org/10.1021/am502962b

Tunega, D., Pašalić, H., Gerzabek, M. H., & Lischka, H. (2011). Theoretical study of structural, mechanical and spectroscopic properties of boehmite (γ-AlOOH). *Journal of Physics: Condensed Matter*, *23*(40), 404201. https://doi.org/10.1088/0953-8984/23/40/404201

Tunney, J. J., & Detellier, C. (1996a). Aluminosilicate Nanocomposite Materials. Poly(ethylene glycol)−Kaolinite Intercalates. *Chemistry of Materials*, *8*(4), 927–935. https://doi.org/10.1021/cm9505299

Tunney, J. J., & Detellier, C. (1996b). Chemically modified kaolinite. Grafting of methoxy groups on the interlamellar aluminol surface of kaolinite. *Journal of Materials Chemistry*, *6*(10), 1679. https://doi.org/10.1039/jm9960601679

Turrero M.J. and Cloet V. (2017). FEBEX-DP concrete ageing, concrete/bentonite and concrete/rock interaction analysis, Nagra technical report, NAB 16-18

Underwood, T. R., & Bourg, I. C. (2020). Large-Scale Molecular Dynamics Simulation of the Dehydration of a Suspension of Smectite Clay Nanoparticles. *The Journal of Physical Chemistry C*, *124*(6), 3702–3714. https://doi.org/10.1021/acs.jpcc.9b11197

van Loon, L., Soler, J., & Bradbury, M. (2003). Diffusion of HTO, 36Cl− and 125I− in Opalinus Clay samples from Mont Terri. *Journal of Contaminant Hydrology*, *61*(1–4), 73–83. https://doi.org/10.1016/s0169-7722(02)00114-6

Vatanpour, V., Madaeni, S. S., Rajabi, L., Zinadini, S., & Derakhshan, A. A. (2012). Boehmite nanoparticles as a new nanofiller for preparation of antifouling mixed matrix membranes. *Journal of Membrane Science*, *401–402*, 132–143. https://doi.org/10.1016/j.memsci.2012.01.040

Villar, M. V., Fernandez, A. M., Martin, P. L., Barcala, J. M., Gomez-Espina, R., and Rivas, P. (2008). Effect of Heating/hydration on Compacted Bentonite: tests in 60-cm Long Cells. Spain: Editorial CIEMAT.

Villar, M.V., Armand, G., Conil, N., de Lesquen, Ch., Herold, Ph., Simo, E., Mayor, J.C., Dizier, A., Li, X., Chen, G., Leupin, O., Niskanen, M., Bailey, M., Thompson, S., Svensson, D., Sellin, P.,

Hausmannova, L. (2020a). D7.1 HITEC. Initial State-of-the-Art on THM behaviour of i) Buffer clay materials and of ii) Host clay materials. Deliverable D7.1 HITEC. EURAD Project, Horizon 2020 No 847593. 214 pp.

Villar, M. V., Iglesias, R. J., & García-Siñeriz, J. L. (2020b). State of the in situ Febex test (GTS, Switzerland) after 18 years: a heterogeneous bentonite barrier. *Environmental Geotechnics*, *7*(2), 147–159. https://doi.org/10.1680/jenge.17.00093

Villar, M. V., Iglesias, R. J., Gutiérrez-Álvarez, C., & Carbonell, B. (2018). Hydraulic and mechanical properties of compacted bentonite after 18 years in barrier conditions. *Applied Clay Science*, *160*, 49–57. https://doi.org/10.1016/j.clay.2017.12.045

Villar, M. A. M. Fernández, E. Romero, A. Dueck, J. Cuevas, M. Plötze, S. Kaufhold, R.Dohrmann, R. J. Iglesias, T. Sakaki, L. Zheng, K. Kawamoto, F. Kober (2017). FEBEX-DP Post-mortem THM-THG Analysis Report. NAGRA technical report: NAB 16-017

Wander, M. C. F., Kerisit, S., Rosso, K. M., & Schoonen, M. A. A. (2006). Kinetics of Triscarbonato Uranyl Reduction by Aqueous Ferrous Iron: A Theoretical Study. *The Journal of Physical Chemistry A*, *110*(31), 9691–9701. https://doi.org/10.1021/jp062325t

Wang, L., & Sun, H. (2013). Prediction of Na+/NH4+ Exchange in Faujasite Zeolite by Molecular Dynamics Simulation and Thermodynamic Integration Method. *The Journal of Physical Chemistry C*, *117*(27), 14051–14060. https://doi.org/10.1021/jp403326n

Wang, Z., Wang, H., Li, Q., Xu, M., Guo, Y., Li, J., & Wu, T. (2016). pH effect on Re(VII) and Se(IV) diffusion in compacted GMZ bentonite. *Applied Geochemistry*, *73*, 1–7. https://doi.org/10.1016/j.apgeochem.2016.07.015

Watson, C., Hane, K., Savage, D., Benbow, S., Cuevas, J. and Fernandez, R. (2009). Reaction and diffusion of cementitious water in bentonite: results of 'blind' modelling. *Applied Clay Science*, 45(1-2), 54-69.

Watson, C., Wilson, J., Savage, D. Norris, S. (2018). Coupled reactive transport modelling of the international Long-Term Cement Studies project experiment and implications for radioactive waste disposal. *Applied Geochemistry*, 97, 134-146.

Waxman, M., & Smits, L. (1968). Electrical Conductivities in Oil-Bearing Shaly Sands. *Society of Petroleum Engineers Journal*, *8*(02), 107–122. https://doi.org/10.2118/1863-a

Weinberg, D. R., Gagliardi, C. J., Hull, J. F., Murphy, C. F., Kent, C. A., Westlake, B. C., Paul, A., Ess, D. H., McCafferty, D. G., & Meyer, T. J. (2012). Proton-Coupled Electron Transfer. *Chemical Reviews*, *112*(7), 4016–4093. https://doi.org/10.1021/cr200177j

Wen, J. R., Liu, M. H., & Mou, C. Y. (2015). Synthesis of curtain-like crumpled boehmite and γ-alumina nanosheets. *CrystEngComm*, *17*(9), 1959–1967. https://doi.org/10.1039/c4ce02506g

Wersin, P., Johnson, L., & McKinley, I. (2007). Performance of the bentonite barrier at temperatures beyond 100°C: A critical review. *Physics and Chemistry of the Earth, Parts A/B/C*, *32*(8–14), 780–788. https://doi.org/10.1016/j.pce.2006.02.051

Wersin, P., Birgersson, M., Olsson, S., Karnland, O. and Snellman, M. (2008). Impact of corrosion-derived iron on the bentonite buffer within the KBS-3H disposal concept. The Olkiluoto site as case study (No. SKB-R--08-34). Swedish Nuclear Fuel and Waste Management Co.

Wester, D. W., & Sullivan, J. C. (1980). Electrochemical and spectroscopic studies of uranium(IV), -(V), and -(VI) in carbonate-bicarbonate buffers. *Inorganic Chemistry*, *19*(9), 2838–2840. https://doi.org/10.1021/ic50211a072

Whitley, H. D., & Smith, D. E. (2004). Free energy, energy, and entropy of swelling in Cs–, Na–, and Sr–montmorillonite clays. *The Journal of Chemical Physics*, *120*(11), 5387–5395. https://doi.org/10.1063/1.1648013

Whittaker, M. L., Lammers, L. N., Carrero, S., Gilbert, B., & Banfield, J. F. (2019). *Ion exchange selectivity in clay is controlled by nanoscale chemical–mechanical coupling* (Vol. 116, Issue 44). Proceedings of the National Academy of Sciences. https://doi.org/10.1073/pnas.1908086116

Wilson, J., Savage, D., Cuadros, J., Shibata, M., & Ragnarsdottir, K. V. (2006a). The effect of iron on montmorillonite stability.(I) Background and thermodynamic considerations. *Geochimica et Cosmochimica Acta*, 70(2), 306-322.

Wilson, J., Cressey, G., Cressey, B., Cuadros, J., Ragnarsdottir, K. V., Savage, D., and Shibata, M. (2006b). The effect of iron on montmorillonite stability.(II) Experimental investigation. *Geochimica et Cosmochimica Acta*, 70(2),

Wu, T., Wang, H., Zheng, Q., Zhao, Y. L., & van Loon, L. R. (2014). Diffusion behavior of Se(IV) and Re(VII) in GMZ bentonite. *Applied Clay Science*, *101*, 136–140. https://doi.org/10.1016/j.clay.2014.07.028

Wu, T., Wang, Z., Wang, H., Zhang, Z., & van Loon, L. R. (2017). Salt effects on Re(VII) and Se(IV) diffusion in bentonite. *Applied Clay Science*, *141*, 104–110. https://doi.org/10.1016/j.clay.2017.02.021

Wu, X., Zhang, B., & Hu, Z. (2013). Large-scale and additive-free hydrothermal synthesis of lamellar morphology boehmite. *Powder Technology*, *239*, 155–161. https://doi.org/10.1016/j.powtec.2013.02.013

Xu, H., Rutqvist, J., Plúa, C., Armand, G., & Birkholzer, J. (2020). Modeling of thermal pressurization in tight claystone using sequential THM coupling: Benchmarking and validation against in-situ heating experiments in COx claystone. *Tunnelling and Underground Space Technology*, *103*, 103428. https://doi.org/10.1016/j.tust.2020.103428

Xu, H., Zheng, L., Rutqvist, J., & Birkholzer, J. (2021). Numerical study of the chemo-mechanical behavior of FEBEX bentonite in nuclear waste disposal based on the Barcelona expansive model. *Computers and Geotechnics*, *132*, 103968. https://doi.org/10.1016/j.compgeo.2020.103968

Xu, T., Spycher, N., Sonnenthal, E., Zhang, G., Zheng, L., & Pruess, K. (2011). TOUGHREACT Version 2.0: A simulator for subsurface reactive transport under non-isothermal multiphase flow conditions. *Computers & Geosciences*, *37*(6), 763–774. https://doi.org/10.1016/j.cageo.2010.10.007

Xu, T., Sonnenthal, E., Spycher, N., and Zheng, L. (2014) TOUGHREACT V3. 0-OMP reference manual: a parallel simulation program for non-isothermal multiphase geochemical reactive transport. University of California, Berkeley.

Yoldas, B.E., (1975). Alumina Sol Preparation from Alkoxides. Am Ceram Soc Bull 54, 289-290.

Yu, J., Bai, H., Wang, J., Li, Z., Jiao, C., Liu, Q., Zhang, M., & Liu, L. (2013). Synthesis of aluminananosheetsvia supercritical fluid technology with high uranyl adsorptive capacity. *New J. Chem.*, *37*(2), 366–372. https://doi.org/10.1039/c2nj40514h

Zacharias, M., Straatsma, T. P., & McCammon, J. A. (1994). Separation-shifted scaling, a new scaling method for Lennard-Jones interactions in thermodynamic integration. *The Journal of Chemical Physics*, *100*(12), 9025–9031. https://doi.org/10.1063/1.466707

Zarzycki, P., Kerisit, S., & Rosso, K. (2011). Computational methods for intramolecular electron transfer in a ferrous–ferric iron complex. *Journal of Colloid and Interface Science*, *361*(1), 293–306. https://doi.org/10.1016/j.jcis.2011.05.070

Zarzycki, P., Kerisit, S., & Rosso, K. M. (2015). Molecular Dynamics Study of Fe(II) Adsorption, Electron Exchange, and Mobility at Goethite (α-FeOOH) Surfaces. *The Journal of Physical Chemistry C*, *119*(6), 3111–3123. https://doi.org/10.1021/jp511086r

Zarzycki, P., & Rosso, K. M. (2017). Stochastic Simulation of Isotopic Exchange Mechanisms for Fe(II)-Catalyzed Recrystallization of Goethite. *Environmental Science & Technology*, *51*(13), 7552–7559. https://doi.org/10.1021/acs.est.7b01491

Zarzycki, P., & Rosso, K. M. (2018). Surface Charge Effects on Fe(II) Sorption and Oxidation at (110) Goethite Surfaces. *The Journal of Physical Chemistry C*, *122*(18), 10059–10066. https://doi.org/10.1021/acs.jpcc.8b02099

Zarzycki, P., Smith, D. M., & Rosso, K. M. (2015). Proton Dynamics on Goethite Nanoparticles and Coupling to Electron Transport. *Journal of Chemical Theory and Computation*, *11*(4), 1715–1724. https://doi.org/10.1021/ct500891a

Zhang, X., Cui, W., Page, K. L., Pearce, C. I., Bowden, M. E., Graham, T. R., Shen, Z., Li, P., Wang, Z., Kerisit, S., N'Diaye, A. T., Clark, S. B., & Rosso, K. M. (2018). Size and Morphology Controlled Synthesis of Boehmite Nanoplates and Crystal Growth Mechanisms. *Crystal Growth & Design*, *18*(6), 3596–3606. https://doi.org/10.1021/acs.cgd.8b00394

Zheng L., Rutqvist J. Kim, K. and Houseworth J. (2015a) Investigation of Coupled Processes and Impact of High Temperature Limits in Argillite Rock. FCRD-UFD-2015-000362, LBNL-187644.

Zheng, L., Rutqvist, J., Birkholzer, J. T., & Liu, H. H. (2015b). On the impact of temperatures up to 200 °C in clay repositories with bentonite engineer barrier systems: A study with coupled thermal, hydrological, chemical, and mechanical modeling. *Engineering Geology*, *197*, 278–295. https://doi.org/10.1016/j.enggeo.2015.08.026

Zheng, L., Samper, J., & Montenegro, L. (2011). A coupled THC model of the FEBEX in situ test with bentonite swelling and chemical and thermal osmosis. *Journal of Contaminant Hydrology*, *126*(1–2), 45–60. https://doi.org/10.1016/j.jconhyd.2011.06.003

Zheng, L., Li, L., Rutqvist, J., Liu, H. and Birkholzer, J.T., (2012). Modeling Radionuclide Transport in Clays. Lawrence Berkeley National Laboratory. FCRD-URD-2012-000128

Zheng, L. J. Rutqvist, C. Steefel, K. Kim, F. Chen, V. Vilarrasa, S. Nakagawa, J. Zheng, J. Houseworth, J. Birkholzer. (2014). Investigation of Coupled Processes and Impact of High Temperature Limits in Argillite Rock. FCRD-UFD-2014-000493, LBNL-6719E

Zheng, L., Kim, K., Xu, H., and Rutqvist, J. (2016) DR Argillite Disposal R&D at LBNL. FCRD-UFD-2016-000437, LBNL-1006013, Lawrence Berkeley National Laboratory.

Zheng, L., Rutqvist, J., Xu, H., & Birkholzer, J. T. (2017). Coupled THMC models for bentonite in an argillite repository for nuclear waste: Illitization and its effect on swelling stress under high temperature. *Engineering Geology*, *230*, 118–129. https://doi.org/10.1016/j.enggeo.2017.10.002

Zheng, L., Xu H., Fox P., Nico P. Birkholzer J. (2018) Engineered Barrier System Research Activities at LBNL: FY18 Progress Report. SFWD-SFWST-2018-000040, LBNL-200117. Lawrence Berkeley National Laboratory.

Zheng, L., P. Fox, P. Zarzycki, E. Sonnenthal, S. Borglin, C. Chang, C. Chou, Y. Wu, H. Xu, P. Nico, B. Gilbert, T. Kneafsey, Y. Cheng and J. Birkholzer (2019) Engineered Barrier System Research

Activities at LBNL Via International Collaboration: FY19 Progress Report, Lawrence Berkeley National Laboratory, LBNL-2001210.

Zheng, L., Xu, H., Rutqvist, J., Reagan, M., Birkholzer, J., Villar, M. V., & Fernández, A. M. (2020a). The hydration of bentonite buffer material revealed by modeling analysis of a long-term in situ test. *Applied Clay Science*, *185*, 105360. https://doi.org/10.1016/j.clay.2019.105360

Zheng, L., H. Xu, B. Gilbert, N. Subramanian, L. Lammers, P. Nico, P. Fox, C. Tournassat, M. Whittaker, S. Borglin, Y. Wu, C. Chang, C. Chou, T. Kneafsey (2020b) Engineered Barrier System Research Activities at LBNL: FY20 Progress Report, Lawrence Berkeley National Laboratory, LBNL- 2001331

Zhou, H., Chen, M., Zhu, R., Lu, X., Zhu, J., & He, H. (2020). Coupling between clay swelling/collapse and cationic partition. *Geochimica et Cosmochimica Acta*, *285*, 78–99. https://doi.org/10.1016/j.gca.2020.07.007